University of Southampton

Faculty of Engineering and Physical Sciences

School of Chemistry

The analysis of polymeric excipients using Ultra-High-Performance Supercritical Fluid Chromatography and Mass Spectrometry

Volume 1 of 1

by

Sergio Cancho Gonzalez

Thesis for the degree of Doctor of Philosophy

June 2022

University of Southampton

Abstract

Faculty of Engineering and Physical Sciences

School of Chemistry

Thesis for the degree of Doctor of Philosophy

The analysis of polymeric excipients using ultra-high-performance supercritical fluid chromatography and mass spectrometry

by

Sergio Cancho Gonzalez

Even though the approval of small molecules is still of great importance, the expansion towards newer modalities requires the development of druggable large biomolecules with inherent challenges in their delivery due to their toxicity, poor bioavailability, or lack of cell specificity. The result is that drugs are being formulated in complex drug-excipient conjugates to address the emerging challenges in drug delivery. Polymers are popular excipients due to their synthetic versatility, allowing for achieving the desired pharmacological and physicochemical characteristics of the final product. The use of poly(ethylene) glycols or cyclodextrins as excipients in some formulations enables the production of robust formulations. Poly(ethylene) glycols are safe materials that improve drug delivery by drug encapsulation or binding. Cyclodextrins host drug molecules in their cavity to improve their solubility.

The polymeric nature of the materials requires control of their quality from the early stages of drug development. The synthetic approaches of poly(ethylene) glycols as the raw material and the possible degradation pathways lead to the formation of undesired subproducts. The synthesis of 2-hydroxypropyl cyclodextrin produces a complex mixture that is difficult to characterise. The resulting heterogeneity can lead to sub-potency, so the dose is not administered as required, compromising the treatment reaching the patient. These findings showed the need for further characterisation of the excipients used.

This research proposes the combination of ultra-high-performance supercritical fluid chromatography and mass spectrometry to characterise and quantify polymeric excipients, specifically poly(ethylene) glycols and 2-hydroxypropyl cyclodextrin. The aim was to facilitate the characterisation and quantitation of the materials.

Table of Contents

Table of Contents ..... **i**

Table of Tables ..... **ix**

Table of Figures ..... **xv**

Research Thesis: Declaration of Authorship ..... **xxxiii**

Acknowledgements ..... **xxxv**

Definitions and Abbreviations ..... **xxxix**

Chapter 1 Introduction **1**

1.1 Synopsis of the research 1

1.2 Polymeric excipients and the pharmaceutical industry 2

1.2.1 Medicines and drug delivery 2

1.2.2 Polymeric excipients 5

1.2.3 Selection of surfactants for drug formulation 6

1.3 Poly(ethylene) glycols in the drug formulation 8

1.3.1 PEG Excipients *vs* PEGylation 9

1.3.2 Brij®: polyoxyethylene alkyl ethers or ethoxylated fatty alcohols 14

1.3.3 Acidic poly(ethylene) glycols: polyoxyethylene ethers derived from carboxylic acids 14

1.3.4 Gelucires®: polyoxylglycerides 15

1.3.5 Tween®: polysorbates 16

1.3.6 Other poly(ethylene) glycols not investigated in this research 19

1.3.7 Regulatory aspects in the quality control of the materials 20

1.3.8 Literature approaches for characterisation 28

1.3.8.1 Characterisation of linear PEGs 28

1.3.8.2 Characterisation of linear PEGs using SFC 29

1.3.8.3 Characterisation of PEGylated molecules 30

1.3.8.4 Characterisation of polysorbates 30

1.3.8.5 Advantages of MS for characterisation 32

1.3.9 Literature approaches for quantitation 33

1.3.9.1 Quantitation using SEC 33

1.3.9.2 Quantitation using MS 33
1.3.9.3 Challenges in quantitation data comparison 34
1.4 Cyclodextrins 35
1.4.1 Cyclodextrins as hosts for drug molecules 35
1.4.2 Synthetic challenges in cyclodextrin modification 37
1.4.3 Pharmaceutical uses of (2-hydroxypropyl)-β-cyclodextrins 38
1.4.4 Synthetic challenges of (2-hydroxypropyl)-β-cyclodextrins 38
1.4.5 Literature approaches for characterisation of (2-hydroxypropyl)-β-cyclodextrins 39
1.5 Instrumentation 40
1.5.1 Chromatography 40
1.5.1.1 Chromatographic nomenclature 40
1.5.1.2 Classification of chromatographic techniques 49
1.5.2 Supercritical fluid chromatography 52
1.5.2.1 Basics 52
1.5.2.2 Instrumentation 54
1.5.2.3 Mobile phases 55
1.5.2.4 Columns for achiral separations 57
1.5.2.5 Columns for chiral separations 60
1.5.2.6 Injection solvent composition 61
1.5.2.7 Role of the column temperature and the active backpressure regulator 62
1.5.2.8 Chromatographic detection 62
1.5.2.9 Capillary supercritical fluid chromatography and flame ionisation detection 63
1.5.2.10 Packed column supercritical fluid chromatography and UV-Visible detection 63
1.5.2.11 Coupling of packed column supercritical fluid chromatography to mass spectrometry and aerosols detectors: role of the make-up solvent and the ABPR 64
1.5.2.12 Aerosol detectors 66

1.5.3 Mass spectrometry....68
1.5.3.1 Ionisation sources....69
1.5.3.2 Unispray™ ionisation source....72
1.5.3.3 Mass analysers....77
1.5.3.4 Ion mobility mass spectrometry....85
1.6 Project scope....88
Chapter 2 Experimental....91
2.1 Chemicals....91
2.1.1 Reagents used during the method development....91
2.1.2 Project samples....91
2.1.3 Reagents used for quantitation....92
2.1.4 Mass spectrometry calibrant standards....92
2.2 Sample preparation....92
2.2.1 Mobile phase preparation....92
2.2.2 Sample preparation of poly(ethylene) glycols for characterisation....93
2.2.3 Sample preparation of poly(ethylene) glycols for external calibration....93
2.2.4 Sample preparation of poly(ethylene) glycols for internal calibration....93
2.2.5 Sample preparation of lauric acid for external calibration....93
2.2.6 Sample preparation of (2-hydroxypropyl)-β-cyclodextrins....93
2.3 Chromatographic columns....94
2.4 Direct infusion methods....95
2.5 Connection of the UPC² to the Synapt™ G2-*Si* instrument....95
2.6 Developed methods for poly(ethylene) glycol analysis....96
2.6.1 Ultra-high-performance supercritical fluid chromatographic method....96
2.6.2 Ionisation source voltage and make-up solvents....97
2.6.3 Conditions of the Xevo SQD 2 (single quadrupole mass analyser) and Xevo TQD (triple quadrupole mass analyser)....98
2.6.4 Conditions of the Synapt™ G2-*Si* (quadrupole time-of-flight mass analyser)....98
2.7 Developed methods for (2-hydroxypropyl)-β-cyclodextrin characterisation....98
2.7.1 Ultra-high-performance supercritical fluid chromatographic method....98

2.7.2 Conditions of the Xevo SQD 2 (single quadrupole mass analyser) and Synapt™ G2-*Si* (quadrupole time-of-flight mass analyser) 99

2.8 Data processing 100

2.8.1 Ionisation of PEGs and data processing of the mass spectra 100

2.8.2 Data processing of the chromatogram: TICC *vs* BPICC *vs* RICC 102

2.8.3 Data processing using ion maps 103

2.8.4 Determination of polymeric end groups using linear fittings and MS 106

2.8.5 Other information required for determining polymeric end groups 108

2.9 Data analysis 110

2.9.1 Chemical information 110

2.9.2 Data smoothing 110

2.9.3 Data deconvolution using Waters® Transform™ 111

2.9.4 Data quantitation 112

2.9.5 Ion mobility data processing 112

2.9.6 Data visualisation 112

Chapter 3 Optimisation of the supercritical fluid chromatography separation and mass spectrometry ionisation of poly(ethylene) glycols 113

3.1 Initial screening method: poly(ethylene) glycols with alcohol and methoxy end groups 113

3.1.1 Ion source selection 113

3.1.2 Mobile phase and column matching screening 114

3.1.3 Initial optimisation of the sample diluent 116

3.1.4 Initial optimisation of the column temperature 118

3.1.5 Initial optimisation of the ABPR 119

3.2 Addition of poly(ethylene) glycols with acidic end groups to the screening method 120

3.2.1 Selection of the ionisation polarity for analysis of poly(ethylene) glycols 120

3.2.2 Column and mobile phase screening re-evaluation 123

3.2.3 Column temperature re-evaluation 125

3.2.4 ABPR re-evaluation and optimisation of the flow rate 126

3.3 Challenges observed in the screening method 127

3.3.1 Unusual chromatographic peak shape in acidic poly(ethylene) glycols 128
3.3.2 Non-selective ionisation of poly(ethylene) glycols 129
3.4 Forcing the selective ionisation of ammoniated adducts and optimisation of the chromatographic peak shape of acidic poly(ethylene) glycols 130
3.4.1 Mobile phase optimisation 130
3.4.2 Optimisation of the positive ion electrospray mass spectrometry desolvation process 137
3.4.3 Reconsideration of the choice of injection solvent for PEGs with acidic end groups 139
3.4.4 Active backpressure regulator to control the mobile phase acidity 140
3.4.5 Mass spectra improvements resulting from the selective ionisation 141
3.5 The ionisation of poly(ethylene) glycols 142
3.5.1 Effect of the oligomer chain length 143
3.5.2 Effect of the end group: length of the aliphatic chain 144
3.5.3 Effect of the end group: acidic poly(ethylene) glycols 145
3.5.4 Overall conclusions 147
3.5.5 The limit of the selective ionisation: small oligomers 148
3.6 Connecting the UPC^2 and the Synapt^{TM} G2-*Si* instruments 149
3.7 Final chapter thoughts 151
Chapter 4 Impurity profiling of complex poly(ethylene) glycol-based excipients 153
4.1 Application to poly(ethylene) glycols with acidic end groups 153
4.2 Application to Brij® 159
4.3 Application to Gelucire® 164
4.3.1 Characterisation of Gelucire® 44/14 164
4.3.2 Evaluation of the degradation of Gelucire® 44/14 165
4.4 Application to polysorbates 167
4.4.1 Analysis of Tween®20 167
4.4.2 Supplier and batch comparison of Tween® 20 products 173
4.4.3 Analysis of Tween® 80 and the differences from other polysorbates 176
4.5 Final chapter remarks 182

Chapter 5 Quantitation of poly(ethylene) glycols based on the deconvolution of the oligomer mass spectra 185

5.1 Comparison between small and large molecule quantitation 185

5.2 Development of an oligomer-based deconvolution approach 186

5.2.1 Generation of the polymer mass spectra 186

5.2.2 Questioning the non-quantitative aspect of the Waters® Transform™ algorithm 190

5.3 Proposed approaches using the single quadrupole mass analyser 192

5.3.1 Approaches for quantitation based on a surrogate oligomer 193

5.3.2 Approaches for quantitation based on the overall polymeric distribution 194

5.3.3 Comparison of quantitative approaches 195

5.4 Intercomparison study: effect of the mass analyser 198

5.4.1 Effect on the mass spectra and deconvoluted mock spectra 199

5.4.2 Effect on the quantitation and polydispersity 204

5.5 Evaluation of an internal standard for quantitation 208

5.6 Final chapter remarks 213

Chapter 6 Optimisation of the separation and ionisation of (2-hydroxypropyl)-β-cyclodextrins 217

6.1 Understanding the mass spectra 217

6.1.1 Evaluation of the direct infusion mass spectra 217

6.1.2 Initial considerations of the analysis 219

6.1.2.1 Excessive retention and evaluation of the gradient elution 219

6.1.2.2 Benefits of changing the mass analyser 219

6.2 Evaluation of the injection, mobile phase, and mass spectrometry make-up solvents 220

6.2.1 Evaluation of the injection and mass spectrometry make-up solvents 221

6.2.2 Optimisation of the mobile phase and achievement of selective ionisation 222

6.2.3 Investigation of the effect of the column temperature and ABPR 224

6.3 Investigation of achiral stationary phase 226

6.3.1 Elution order of oligomers 226
6.3.2 Separation using achiral stationary phases 227
6.4 Need for chiral stationary phases 231
6.4.1 Method translation 231
6.4.2 Separation using chiral stationary phases 232
6.5 Final column evaluation 234
6.5.1 Stationary phase evaluation using high-resolution mass spectrometry 234
6.5.2 Stationary phase selection using ion mobility mass spectrometry 236
6.5.3 Peak shape explanation using ion mobility mass spectrometry 239
6.6 Final chapter remarks 241
Chapter 7 Conclusions and future work 243
7.1 Research summary 243
7.2 Summary of contributions in poly(ethylene) glycol analysis 243
7.2.1 Primary contributions 243
7.2.2 Limitations of the research and future work 247
7.2.3 Final remarks 249
7.3 Summary of contributions in (2-hydroxypropyl)-β-cyclodextrins 250
7.3.1 Primary contributions 250
7.3.2 Limitations of the research and future work 250
7.3.3 Final remarks 251
7.4 Final thesis remarks 251
Appendix A Prediction of acidic dissociation constants of acidic PEGs using surrogate molecules 252
A.1 Acidic dissociation constant prediction for mPEG acid 2000 252
A.2 Acidic dissociation constant prediction for PEG diacid 2000 252
Appendix B Calibration curves used in poly(ethylene) glycol quantitation 253
B.1 Approaches for quantitation using a surrogate oligomer and quadrupole mass analyser. External calibration linear fittings 253

B.1.1 Selective ion monitoring acquisition of the most intense ion in the mass spectra. External calibration linear fittings 254
B.1.2 Use of the reconstructive ion current chromatogram of the most intense oligomer. External calibration linear fittings 258
B.1.3 Deconvolution of the mass spectra of a surrogate oligomer. External calibration linear fittings 262
B.2 Approaches for quantitation using the whole distribution and quadrupole mass analyser. External calibration linear fittings 266
B.2.1 Sum of the peak areas of the reconstructive ion current chromatograms of all ions in the whole distribution. External calibration linear fittings 267
B.2.2 Sum of all the oligomer Transform^{TM} deconvoluted response. External calibration linear fittings 271
B.3 Approaches for quantitation using the quadrupole time-of-flight mass analyser. External calibration linear fittings 275
B.3.1 Mass spectra deconvolution of a surrogate oligomer. External calibration linear fittings 276
B.3.2 Mass spectra deconvolution of the whole distribution. External calibration linear fittings 280
B.4 Approaches for quantitation using the quadrupole mass analyser and internal calibration linear fitting 284
B.4.1 Mass spectra deconvolution of a surrogate oligomer. Internal standard calibration linear fittings 285
B.4.2 Mass spectra deconvolution of the whole distribution. Internal calibration linear fittings (0.5 µg/mL 18-crown-6 in CH_3CN) 289
List of References 293

Table of Tables

Table 1. Different pharmaceutical excipients and their roles in formulations [5] 3

Table 2. Polymers used as excipients in the pharmaceutical industry based on their source. Cyclodextrins were not included on the table as they are polysaccharides (natural) that follow synthetic reactions to become cyclic and later on substituted 5

Table 3. Correlation between the API log P value and the surfactant HLB value 8

Table 4. Examples of commercially approved drugs that use PEG as an excipient 10

Table 5. Examples of commercially approved PEGylated small drug molecules 11

Table 6. Examples of commercially approved PEGylated large biomolecules drugs 12

Table 7. Examples of PEG derivatives used in drug formulations 13

Table 8. Marketed Gelucire®, their role in the formulation and their composition, showing the most predominant fatty acid observed. Notice that all fatty acids are vegetable-based fatty acids [65] 16

Table 9. Most common polysorbates and their HLB values. Table adapted from Pasquali *et al.* [38] 18

Table 10. The reporting, identification, and qualification threshold of organic, inorganic, and residual solvent impurities. TDI: Total daily intake [94] 23

Table 11. The reporting thresholds for degradation impurities [95] 24

Table 12. The identification thresholds for degradation impurities. TDI: Total daily intake [95] 24

Table 13. The qualification thresholds for degradation impurities. TDI: Total daily intake [95] 24

Table 14. Summary of liquid chromatography modes 50

Table 15. Comparison of the density, diffusion and viscosity of gases, supercritical fluids, and liquids [222] 53

Table 16. Achiral stationary phases used in this research. In black BEH particles. In Green HSS particles 60

Table 17. Investigated chiral stationary phases 61

Table of Tables

Table 18. Classification of typical chromatographic detectors and MS ionisation sources based on the response provided 63

Table 19. UV-Vis cut-off of common solvents used in SFC [284] 64

Table 20. Different make-up solvents used in aerosol detection and MS 65

Table 21. Lasers used in modern MALDI sources [334-336] 76

Table 22. Scan modes of triple quadrupole mass analyser. Note that m_1^+ is the product ion, m_2^+ is the fragment ion and *n* a neutral lost from the fragmentation reaction 82

Table 23. Types of fragmentations in the Waters® Synapt™ G2-*Si* 88

Table 24. Materials provided by AstraZeneca plc (Macclesfield, UK) 92

Table 25. Columns investigated in this research 94

Table 26. Direct infusion method conditions for high-resolution mass measurements. [a]: +2.5 kV for positive ion ESI QToF MS and -2.5 kV for negative ion ESI QToF MS 95

Table 27. UHPSFC method conditions for PEG analysis. [a]: CH_3OH was used for positive ion APPI MS experiments due to the quenching product by ammonium salts in the ionisation source. [b]: CH_3CN + 0.1% HCOOH was used for PEGs with acidic end groups to favour the formation of the carboxylate anion 97

Table 28. Ionisation sources tested, their voltages used and corresponding make-up solvents for PEG analysis. [a]: Note that acidic PEGs were detected using the chromatographic method in positive ion ESI MS whilst both positive and negative ion ESI MS were used for direct infusion experiments 97

Table 29. Q and QqQ method conditions for PEG analysis 98

Table 30. QToF MS method conditions for PEG analysis 98

Table 31. UHPSFC method conditions for 2HPBCD analysis. [a]: conditions for analysis using FPP columns with chiral stationary phases 99

Table 32. Positive ion ESI Q MS and positive ion ESI QqQ MS method conditions used in the analysis of 2HPBCD 99

Table 33. Positive ion ESI Q IM ToF MS method conditions for 2HPBCD analysis 100

Table 34. Coding modification of the [SpeTransform] of MassLynx.ini file (C:\MassLynx) within the MassLynx® 4.1 software package to deconvolute ammoniated adducts. Key changes are in bold. Other parameters were adjusted to maximise ion count 112

Table 35. Selected columns for initial screening of PEGs with alcohol and aliphatic end groups 115

Table 36. Effect of the sample diluent on the peak area of alcohol (PEG 200) and aliphatic (mPEG 350) PEGs. Samples analysed in triplicate. Note that the protic solvent methanol showed the lowest solubility for these neutral polymers 117

Table 37. Optimisation of the column temperature of PEG 600. R_s: chromatographic resolution at half-width calculated using the RICC of two contiguous oligomer peaks (*m/z* 520.5 and 564.5). Samples analysed in triplicate 119

Table 38. ABPR optimisation for PEG 600 oligomer separation. Samples analysed in triplicate 120

Table 39. Evaluation of the ionisation efficiency of ESI MS of acidic PEGs using different ESI source polarities. Direct infusion MS experiment of 100 µg/mL acidic PEG in CH_3OH. Samples analysed in triplicate 123

Table 40. Relationship of the column temperature with the chromatographic resolution of PEGs with acidic end groups. The chromatographic resolution was calculated using the RICC of two contiguous peaks of mPEG acid 2000 (*m/z* 664.2 and 649.5) at baseline. Samples analysed in triplicate 126

Table 41. Comparison of the theoretical aqueous pK_a of two buffers used in the mobile phase and the predicted pK_a of surrogate molecules with two repeating units of mPEG acid 2000 and PEG diacid 2000 using ACDLabs 2017 (see supporting information) 134

Table 42. Effect of the sample diluent in the peak area of mPEG acid 2000 and PEG diacid 2000. Peak areas were calculated using the RICC of *m/z* 650.5 for one oligomer of mPEG acid 2000 and PEG diacid 2000. Samples were analysed in triplicates 139

Table 43. Differences in the analysis time when using two computers to control the Waters® UPC^2 and the Waters® Synapt™ G2-*Si* systems 151

Table 44. Calculated monoisotopic masses and reduced monoisotopic masses (ethylene oxide mass: 44.0261 Da) of acidic PEGs. [a] isobaric masses that require accurate mass measurements for identification. [b] isobaric masses that require chromatography for identification 156

Table of Tables

Table 45. Calculated monoisotopic masses and reduced monoisotopic masses (ethylene oxide mass: 44.0261 Da) of Brij® species 163

Table 46. Calculated logP (clogP) for the possible synthetic subproducts of the cyclisation of sorbitol. * clogP calculated using ChemDraw® Professional 21.0.0 169

Table 47. Calculated monoisotopic masses and reduced monoisotopic masses (ethylene oxide mass: 44.0261 Da) of Tween® 20 species. [a] MW': Reduced MW calculated by subtracting the mass of the ethylene oxide repeating unit to the molecule end group MW 172

Table 48. Quantitation of free lauric acid of different quality products of different batches and suppliers of Tween® 20 (as received in the lab). Three replicates analysed 174

Table 49. Calculated monoisotopic masses and reduced monoisotopic masses (ethylene oxide mass: 44.0261 Da) of Tween® 80 species. [a] MW': Reduced MW calculated by subtracting the mass of the ethylene oxide repeating unit to the molecule end group MW. [b] isobaric masses that require high-resolution mass spectrometry for identification 179

Table 50. Coding modification of the [SpeTransform] section of the MassLynx.ini file (C:\MassLynx) within the MassLynx® 4.1 software package to deconvolute ammoniated adducts (18.033826 = NH_3 + H - e). Key changes are in bold. Other parameters were adjusted to maximise ion count 189

Table 51. Evaluation of the quantitative aspect of Waters® Transform™ algorithm by comparing experimental and reported M_n, M_w and PDI. Manufacturer data acquired using SEC 192

Table 52. Selected surrogate PEG oligomers used for polymer quantitation when analysed using UHPSFC positive ion ESI Q MS 194

Table 53. Comparison of different approaches for external calibration quantitation based on the LDR and R^2 196

Table 54. Comparison of different approaches for external calibration quantitation based on the data processing time 198

Table 55. Effect of the mass analyser (Q and QToF) in the quantitation, compared based on the LDR and R^2 205

Table 56. Comparison of the effect of the mass analyser on the data processing time for external calibration quantitation 207

Table 57. Comparison of the effect of the mass analyser (Q *vs* QToF) in the M_n, M_w and PDI of different PEGs as obtained using UHPSFC positive ESI MS and 0.5 µg/mL (Q) and 0.2 µg/mL (QToF) of 18-crown-6 in acetonitrile. Samples analysed in triplicates. The error corresponds to 1 stdev. Manufacturer values acquired using SEC 208

Table 58. Investigated columns with achiral SPs for the evaluation of the oligomer elution and the inclusion-exclusion mechanism for SP selection 228

Table 59. Method translation from sub-2 µm/SPP particles to HPLC columns 232

Table 60. Chiral SPs selected to investigate the possible inclusion-exclusion mechanism 233

Table 61. Columns selected for 2HPBCD screening 235

Table 62. Detected peak list for *m/z* 1506 and $^{TW}CCS_{N2}$ 140 ± 2 Å2 using the C18+ 240

Table 63. Detected peak list for *m/z* 1506 and $^{TW}CCS_{N2}$ 202 ± 2 Å2 using the C18+ 240

Table 64. Experimental $^{TW}CCS_{N2}$ (Å2) of α-CD and β-CD. Data obtained by infusion of 50 µg/mL solution in H_2O + 1% HCOOH 240

Table 65. Experimental $^{TW}CCS_{N2}$ (Å2) of α-CD and β-CD. Data obtained by infusion of 50 µg/mL solution in H_2O + 1% HCOOH and using polyalanine/acetaminophen as calibrants 241

Table of Figures

Figure 1. Drug delivery systems: a) molecules used as drugs and their delivery challenges, b) possible molecular modifications to improve drug delivery, and c) macromolecular design of drug delivery systems. Adapted from Vargason *et al.* [9] 4

Figure 2. Surfactants and formation of micelles: a) amphiphilic molecule, b) normal micelle, and c) reverse micelle 7

Figure 3. Synthesis of PEG *via* anionic living polymerisation 9

Figure 4. Common pharmaceutical dosage forms where PEGs are found 9

Figure 5. Prodrug approach using PEG. Example of a marketed drug that benefitted from using PEGylation: a) Naloxol (free drug), b) Naloxegol (PEGylated drug) 10

Figure 6. Chemical structures of: a) Brij® 58 (n_{av} = 20) and b) Brij S 100 (n_{av} = 100) 14

Figure 7. Chemical structures of acidic PEGs: a) mPEG acid 2000 (n_{av} = 45) and b) PEG diacid 2000 (n_{av} = 45) 15

Figure 8. Structures of a) PEG monoester and b) PEG diester. R_4, R_5 and R_6 are the alkyl chains of vegetable-based fatty acids 15

Figure 9. Hydrolysis (right) and transesterification (left) of acylglycerols: monoacylglycerols (MAG), diacylglycerols (DAG), and triacylglycerols (TAG). R_1, R_2 and R_3 are the alkyl chains of vegetable-based fatty acids 15

Figure 10. Generic synthesis of polysorbates from sorbitol 17

Figure 11. Dehydration of sorbitol showing the different synthetic sub-products 18

Figure 12. Chemical structure of the most abundant polymer in Tween® 20 (polyoxyethylene sorbitan monolaurate) showing the *w+x+y+z* value 18

Figure 13. Structure of nonoxynol or poly(ethylene glycol) nonyl phenyl ether 19

Figure 14. Chemical structures of a) Triton X-100 (n_{av} = 9), b) reduced Triton X-100 (n_{av} = 10) and c) Nereid (n_{av} = 9) 19

Figure 15. Chemical structures of a) lauryl methyl gluceth-10 hydroxypropyl dimonium chloride (Glucquat 125) and b) PEG propylene glycol cocoates 20

Table of Figures

Figure 16. Examples of copolymers of PEG: a) Poloxamers or PEG-PPG-PEG (PPG: poly(propylene glycol) and b) Poly(ethylene glycol)-polyvinyl alcohol or PEG-PVA [80] 20

Figure 17. Attributes that alter the quality of polymeric materials and explain the differences in suppliers or batches 21

Figure 18. Resulting MW distribution from a synthetic polymerisation reaction, showing the dependence of the amount of each oligomer, the $M_{n,}$ and the M_w values 22

Figure 19. PEG impurity of 1,4-dioxane generated by dimerisation of ethylene oxide 25

Figure 20. Degradation of the PEG chain by oxidation [97] 25

Figure 21. Degradation of varenicline to produce formaldehyde and formic acid 26

Figure 22. Drug dimerization produced by formaldehyde 26

Figure 23. The dimerisation of Rebeccamycin. The electrophilic addition of formaldehyde activates the aromatic rings of the drug molecule and induces the dimerisation 27

Figure 24. Oxidation of the unsaturated site in fatty acids to produce aldehydes and ketones 27

Figure 25. RPLC-CAD separation of PEGs using an endcapped C18 and H_2O + 0.1% HCOOH/CH_3CN + 0.1% HCOOH. a) Oligomer separation of PEG with alcohol end groups. b) Separation of Brij® species. FAA: fatty acid alcohol. B/BO: Brij species, Mix: mixed sample of fatty acids and fatty acid alcohols (C12:0, C16:0, C17:0, C18:0, C18:1 and C18:2). Reproduced with permission from Theiss *et al.* [110] 29

Figure 26. Analysis of PEGylated cetirizine using SFC-UV/Vis-ELSD, a BEH column and CO_2/CH_3OH. The authors use the selectivity of UV-Vis to distinguish PEGylated cetirizine from PEG, from Schou-Pedersen *et al.* [117] 30

Figure 27. RPLC-CAD separation of PEGs using an endcapped C18 and H_2O + 0.1% HCOOH/CH_3CN + 0.1% HCOOH. Separation of polysorbates: T: Tween®. Mix: mixed sample of fatty acids and fatty acid alcohols (C12:0, C16:0, C17:0, C18:0, C18:1 and C18:2). Reproduced with permission from Theiss *et al.* [110] 31

Figure 28. Separation of various polysorbates using UHP RPLC positive ion ESI QToF MS using a BEH C4 and H_2O + 0.1% HCOOH/CH_3CN. The number indicates the species observed: 1: PEG, 2: POE sorbitan (POE S), 3: POE isosorbitan (POE IS), 4: POE S monooleate (POE S MO), 5: POE IS MO, 6: POE MO, 7: POE S dioleate (POE S DO), 8: POE IS DO, 9: POE DO, 10: POE S trioleate (POE S TO), 11: POE S monostereate (POE S MS), 12: POE IS MS, 13: POE MS, 14: POE S DS,

15: POE IS DS, 16: POE DS, 17: POE S TS, 18: POE S monopalmitate (POE S MP), 19: POE IS MP, 20: POE MP, 21: POE S dipalmitate (POE S DP), 22: POE IS DP, 23: POE DP, 24: POE S tripalmitate (POE S TP), 25: POE S ML, 26: POE IS ML, 27: POE ML, 28: POE S DL, 29: POE IS DL, 30: POE DL, 31: POE S DL. Reproduced with permission from Wang *et al.* [125] 31

Figure 29. Parameters that contribute to the variability in the reported value of M_n, M_w and PDI values of polymers 35

Figure 30. Chemical structure of a CD. n=6: α-CD, n=7: β-CD and n=8: γ-CD 36

Figure 31. 3D-molecular structure of a CD, highlighting the truncated cone and the cavity that allows drug allocation 36

Figure 32. Planar representation of a β-CD indicating the three types of hydroxy groups in the molecular structure (blue for OH-2, green for OH-3 and pink for OH-6). The letters inside the glucose units indicate the terminology in the CD ring when fragmenting 37

Figure 33. 2HPBCD used in this research project 38

Figure 34. The synthetic reaction of 2HPBCD showing examples of subproducts and the presence of molecules with isobaric masses 39

Figure 35. Data analysis of a chromatogram for the separation of two analytes [199] 41

Figure 36. Relationship between the band broadening observed with the time the analyte spends in the column (assuming isocratic mobile phase conditions) 42

Figure 37. Schematic of the Eddy diffusion effect (A). Notice the band broadening due to different paths that the same analyte might have in the chromatographic columns [199-201] 42

Figure 38. Schematic of the longitudinal diffusion effect, B. Notice the band broadening [199-201] 43

Figure 39. $C_{MP:}$ mass transfer related to the movement of the analyte inside/outside the pores in the stationary phase particles [199-201] 44

Figure 40. C_{SP}, mass transfer of the analyte movement between mobile and stationary phases. a) Ideal equilibrium, b), c) The analyte movement disrupts the equilibrium, and the diffusion tries to re-establish the equilibrium (arrows). d) Re-established equilibrium with a broader analyte band [199-201] 45

Table of Figures

Figure 41. van Deemter plot of the height equivalent to a theoretical plate (H or HETP) showing the individual contribution of the three kinetic variables A, B and C based on the linear velocity of the analyte (μ) 46

Figure 42. Correlation between the distribution isotherm (*K*) and the peak shape 47

Figure 43. Calculation of A_s and T_f in a chromatographic peak [199] 47

Figure 44. Definition of resolution (R_s) in a chromatogram 48

Figure 45. Effect of α, N and k in the chromatographic resolution (R_s) 49

Figure 46. Mechanism separation in HILIC: a) Formation of a thin layer of in the stationary, and b) possible interactions between different analytes and a stationary phase particle 51

Figure 47. Mechanism of separation in SEC for three analytes of different size explaining how the size sieve retain small analytes for longer than larger analytes 52

Figure 48. Phase diagram of CO_2 showing the triple and the critical points 53

Figure 49. UPC^2 Waters® instrument used in this research 55

Figure 50. Effect of the addition of different modifiers to the CO_2 polarity. Adapter from Berger *et al.* [233] 55

Figure 51. In-situ formation of carbonic acid from H_2O and $scCO_2$ [240] 56

Figure 52. Particle technology of FPP: a) TEOS, b) PEOS, c) BTEE, d) BPEOS 58

Figure 53. Differences between an FPP (left) and an SPP (right). The light blue indicates the porous site, and the dark blue is the rounded, solid bead 58

Figure 54. Structures of polysaccharide-based stationary phases used in chiral separations: a) cellulose, b) amylose. Reproduced with permission from Gübitz and Schmid [272] 61

Figure 55. Schematic of the splitter used in the Waters® UPC^2 system 65

Figure 56. Diagram illustrating the differences between aerosol-based detectors [297] 67

Figure 57. Schematic of the ELSD. Reproduced with permission from Megoulas and Koupparis, 2005 [288] 67

Figure 58. Schematic of the CAD [307, 308] 68

Figure 59. Schematic of an MS instrumentation 69

Figure 60. Schematic of the ESI source showing the processes that occur 70

Figure 61. Schematic of the possible desolvation mechanisms occurring in ESI: a) IEM by Iribarne and Thomson, b) CRM by Dole *et al.*, and c) CEM by Konermann *et al.* [317-319] 71

Figure 62. Differences in the positive ion ESI mass spectrum between a) a small molecule (terfenadine) and b) a large biomolecule (horse heart myoglobin) 72

Figure 63. Schematic of the UNI source 73

Figure 64. Schematic of the APCI source 75

Figure 65. Diagram of the APPI source 76

Figure 66. The desorption/ionisation processes in the source MS 77

Figure 67. Schematic of a) Q mass analyser and b) hyperbolic section of the Q mass analyser 78

Figure 68. Mathieu diagram showing stable region according to the Mathieu equation. Areas labelled as A, B, C and D denote stability areas for an ion in the *x*- and *y*- axes 79

Figure 69. Stability diagram as a function of U and V for three ions of masses m_1, m_2 and m_3 (assuming singly charged species), showing the scan line 80

Figure 70. Schematic of a triple quadrupole detector 81

Figure 71. Schematic of a ToF mass analyser 82

Figure 72. Refocussing of ions in a ToF mass analyser using a reflectron 83

Figure 73. Differences in the configuration between ToF mass analyser: a) linear configuration and b) orthogonal configuration 84

Figure 74. Different configurations of ToF mass analysers based on the number of reflectron plates and their position: a) basic, b) V and c) W 85

Figure 75. Schematic of the ion mobility separation line in Waters® Synapt™ G2-*Si* 86

Figure 76. Schematic of the ion mobility separation using TWIMS: a) the stacked ring ion guides that allow the application of the travelling wave, b) the ion mobility line, and c) the electric field waves that allow for ion mobility separation 87

Figure 77. Connection of the UPC^2 system to the Synapt™ G2-*Si* system 96

Table of Figures

Figure 78. 3D-structure of the gas-phase adduct of PEG $[P_5 + Na]^+$ (drawn using ChemDraw 3D®). H atoms in light grey, C atoms in dark grey, O atoms in red and Na atoms in yellow. Adapted from Gidden *et al.* [364] 100

Figure 79. The complexity of the mass spectra of PEGs highlighting the effect of increasing the polymer molecular weight in the mass spectra and the requirement for chromatographic separation 101

Figure 80. UHPSFC positive ion ESI Q MS. Generation of the mass spectra of individual oligomers of PEG 600 (b) based on the chromatographic separation using UHPSFC positive ion ESI MS (a) and simplification of the oligomer mass spectra 102

Figure 81. Different approaches for polymer data processing using LC-MS-like data. a) TICC, b) BPICC, c) RICC of one *m/z* value, d) ion map 103

Figure 82. UHPSFC positive ion ESI MS. Correlation between the BPICC (top) and the ion map (bottom), showing how data is interpreted based on the recognition of an ion, the polymeric repeating unit, and the polymeric charge trends 104

Figure 83. UHPSFC positive ion ESI MS. Ion map. Data visualisation using ion maps of the same sample. Differences between a) MassLynx® and b) MZmine 105

Figure 84. Calculation of the polymer end group by a linear fitting of the oligomer molecular weight to the repeating unit 106

Figure 85. Proposed chemical structures for the impurity identified in PEG diacid 2000: a) mPEG 2000, b) PEG monoacid 2000 107

Figure 86. Examples of structure reduction using poly(ethoxylate) sorbitan monolaurate 107

Figure 87. UHPSFC positive ion ESI Q MS. BPICC. 10 μg/mL PEG 600 in CH_3CN, 50 μg/mL PEG 1000 in CH_3CN, 50 μg/mL PEG 1450 in CH_3CN and 100 μg/mL PEG 2000 in CH_3CN 108

Figure 88. UHPSFC positive ion ESI Q MS. BPICC. Influence of the end group polarity in the retention. a) 50 μg/mL PEG 600 in CH_3CN and 50 μg/mL PEG 600 mPEG 550 in CH_3CN, b) 1000 μg/mL mPEG acid 2000 and 1000 μg/mL PEG diacid 2000 in CH_3CN + 1% HCOOH 109

Figure 89. UHPSFC positive ion ESI Q MS. BPICC. 1000 μg/mL Tween® 20 in CH_3CN. Influence of PEG structure on the retention 110

Figure 90. UHPSFC MS. Mass spectra. 300 μg/mL PEG 600 in CH_3OH. Comparison of the mass spectra of alcohol PEGs when using different ionisation sources. The ion response was

optimised for each ionisation source. Measurements taken in triplicates (ion response error: ±3%). 113

Figure 91. UHPSFC-MS positive ion ESI MS. BPICC. 100 µg/mL PEG 350 in CH_3OH. Effect of the mobile phase co-solvent composition in the chromatographic separation when using a BEH stationary phase (5-40% co-solvent gradient), showing the importance of a methanolic co-solvent with CH_3COONH_4 as additive 114

Figure 92. UHPSFC-MS positive ion ESI MS. BPICC. 100 µg/mL of mPEG 350 in CH_3OH with the presence of an alcohol PEG impurity. Column screening when using a co-solvent of CH_3OH + 25 mM CH_3COONH_4 115

Figure 93. UHPSFC-MS positive ion ESI MS. RICC (*m/z* 300). 25 µg/mL of PEG 200 using different sample diluents: a) $CH_3COOCH_2CH_3$, b) CH_2Cl_2, c) CH_3CN, and d) CH_3OH 117

Figure 94. UHPSFC-MS positive ion ESI MS. RICC (*m/z* 314). 25 µg/mL of mPEG 350 using different sample diluents: a) $CH_3COOCH_2CH_3$, b) CH_2Cl_2, c) CH_3CN, and d) CH_3OH 118

Figure 95. UHPSFC positive ion ESI MS. BPICC. 100 µg/mL PEG 600 in CH_3CN. Optimisation of the column temperature at ABPR 150 bar for analysis of PEGs with alcohol and alkoxy end groups 119

Figure 96. UHPSFC positive ion ESI MS. BPICC. 100 µg/mL PEG 600 in CH_3CN. Optimisation of the ABPR at 70 °C for PEGs with alcohol and alkoxy end groups 120

Figure 97. Chemical structures of acidic PEGs: a) mPEG acid 2000 (n_{av} = 45), and b) PEG diacid 2000 (n_{av} = 45) 120

Figure 98. Direct infusion. Mass spectra. 100 µg/mL mPEG acid 2000 in CH_3OH. Comparison in the ionisation of mPEG acid in a) positive ion ESI MS, b) negative ion ESI MS 122

Figure 99. Direct infusion MS. Mass spectra. 100 µg/mL PEG diacid 2000 in CH_3OH. Comparison in the ionisation of PEG diacid in: a) positive ion ESI MS showing the presence of an impurity, and b) negative ion ESI MS without the presence of the impurity 123

Figure 100. UHPSFC positive ion ESI MS. BPICC 1000 µg/mL mPEG acid 2000 and 1000 µg/mL PEG diacid 2000 in CH_3CN. Column screening for PEGs with acidic end groups 124

Figure 101. UHPSFC positive ion ESI MS. BPICC 1000 µg/mL mPEG acid 2000 and 1000 µg/mL PEG diacid 2000 in CH_3CN. Strong retention of PEGs with acidic end groups in the T1-AA column was observed (data was shown unsmoothed on purpose) 125

Table of Figures

Figure 102. UHPSFC positive ion ESI MS. BPICC 1000 µg/mL mPEG acid 2000 in CH_3CN. Influence of the column temperature in the separation at ABPR 200 bar 126

Figure 103. UHPSFC positive ion ESI MS. RICC (*m/z* 650.5). 1000 µg/mL of mPEG acid 2000 in CH_3CN. Influence of the flow rate at ABPR a) 105 bar, b) 150 bar, and c) 200 bar 127

Figure 104. Carboxylic acids and chromatography: a) Biphasic diagram showing the species formed, and b) Energy released of the intermolecular interactions that occur during the chromatographic separation 128

Figure 105. UHPSFC positive ion ESI MS. RICC (*m/z* 650.5). 1000 µg/mL of mPEG acid 2000 in CH_3CN. Challenge in the chromatographic peak shape 129

Figure 106. UHPSFC positive ion ESI MS. Mass spectra. Non-selective ionisation of PEG 600 showing the ions generated by a) one oligomer, b) the polymeric distribution 130

Figure 107. Visual representation of the ionisation current trends of: a) singly charged species and b) doubly charged species of PEG 600 based on the oligomer n value. Colours indicate the distributions of different ionisation events 131

Figure 108. Visual representations of the relative formation of the singly and doubly charged species for PEG 600. Colours indicate the charged states 131

Figure 109. UHPSFC positive ion ESI MS. 50 µg/mL PEG 600 in CH_3CN. Differences in the ion current trends of singly charged species formed for PEG 600 when using different combinations of mobile phase co-solvent and additives. The make-up solvent corresponded to CH_3OH with 50 µM of the ammoniated salt added to the co-solvent 133

Figure 110. UHPSFC positive ion ESI MS. 50 µg/mL PEG 600 in CH_3CN. Differences in the ion current trends of doubly charged species formed for PEG 600 when using different mobile phase co-solvents and additives. The make-up solvent corresponded to CH_3OH with 50 µM of the ammoniated salt added to the co-solvent 134

Figure 111. UHPSFC positive ion ESI MS. RICC of a representative oligomer of mPEG acid 2000 (n=41, *m/z* 650, $[M + 3NH_4]^{3+}$). 100 µg/mL mPEG acid 2000 in CH_3CN + 0.1% HCOOH. Optimisation of the mobile phase co-solvent and additive combination 136

Figure 112. UHPSFC positive ion ESI MS. RICC (*m/z* 650) of a representative oligomer of mPEG acid 2000 (n=41, *m/z* 650, $[M + 3NH_4]^{3+}$). 100 µg/mL mPEG acid in CH_3CN + 0.1% HCOOH. Optimisation of the co-solvent: a) CH_3OH / H_2O (v/v)+ 25 mM CH_3COONH_4), and b) the

additive concentration CH_3OH / H_2O 94%/6% (v/v) + X mM CH_3COONH_4). A_s values calculated at half-width 137

Figure 113. UHPSFC positive ion ESI MS. Mass Spectra. 50 µg/mL PEG 200 in CH_3CN. In-source fragmentation of PEG chains: a) fragmentation mechanism via cleavage, and b) fragments observed 137

Figure 114. UHPSFC positive ion ESI MS. Differences in the ion current trends of doubly charged species formed for PEG 600 when using different cone voltage and desolvation temperature for a) singly and b) doubly charged species 138

Figure 115. Effect of increasing the cone voltage and/or the desolvation temperature to the ammoniated species: a) loss of ammonia (increase both), b) charge stripping (increase cone voltage), and c) formation of Na adducts (increase cone voltage) 139

Figure 116. UHPSFC positive ion ESI MS. RICC (*m/z* 650.5). 1000 µg/mL mPEG acid 2000 dissolved in: a) CH_3CN, b) CH_3CN + 1% HCOOH, c) CH_3OH + 50 mM CH_3COONH_4, d) CH_3OH + 15 mM CH_3COONH_4 + 6% H_2O 140

Figure 117. UHPSFC positive ion ESI MS. RICC (*m/z* 650.5). 1000 µg/mL mPEG acid 2000 in CH_3CN + 1% HCOOH. Effect of the ABPR: a) 200 bar and b) 150 bar 141

Figure 118. UHPSFC positive ion ESI MS. Mass spectra. 50 µg/mL of PEG 600 in CH_3CN. Effect of a selective adduct formation for PEG 600 in the ions generated by: a) one oligomer, b) the polymeric distribution 142

Figure 119. Relative formation of the different ionisation states for PEG 600, 1000, 1450 and 2000. The contribution of the protonated molecules was neglected for PEG 600 and PEG 1000 (*ca.* 1%) 143

Figure 120. Effect of the chain length on the average charge state of alcohol PEGs 143

Figure 121. Ionisation current trends showing the percentage of different ionisation events of alcohol PEG oligomers. Graph produced using a mixture of 50 µg/mL in CH_3CN (per component) of PEG 600, 1000, 1450 and 2000 144

Figure 122. Ionisation current trends showing the percentage of different ionisation events of methoxy PEG oligomers 144

Figure 123. Ionisation current trends showing the percentage of different ionisation events for Brij® 58 oligomers 145

Table of Figures

Figure 124. Relative formation of the different ionisation states for PEGs with aliphatic end groups and MW: mPEGs and Brij® 58 145

Figure 125. Relative formation of the different ionisation states for mPEG acid 2000 and PEG diacid 2000, compared to PEG 2000 and mPEG 2000 146

Figure 126. Ionisation current trends showing the percentage of different ionisation events of mPEG acid 2000 oligomers 146

Figure 127. Ionisation current trends showing the percentage of different ionisation events of PEG diacid 2000 oligomers 147

Figure 128. Comparison of the ion current trends between PEG 200 and PEG 600 148

Figure 129. The influence of different make-up solvents in the formation of $[M + H]^+$, $[M + NH_4]^+$ and $[M + Na]^+$ species for PEG 200 oligomers. Graph produced using 10 µg/mL PEG 200 in CH_3CN 148

Figure 130. Comparison in the ionisation current trends of PEG 200 under two mobile phases 149

Figure 131. Picture of the connection of the UPC^2 system to the Synapt^{TM} G2-*Si* system. In red, the PEEK tubing 149

Figure 132. UHPSFC positive ion ESI MS. PEG 1450 (RICC shown of two oligomers). Impact in the chromatographic band broadening of introducing a long PEEK tubing: a) Waters® UPC^2 to Waters® SQD 2, b) Waters® UPC^2 to the Waters® Synapt^{TM} G2-*Si* using the PEEK tubing 150

Figure 133. UHPSFC positive ion ESI MS. Differences in the mass spectra of PEG 1450 between a) Q, and b) QToF mass analysers 151

Figure 134. Chemical structures of: a) mPEG acid 2000 (n_{av} = 45), and b) PEG diacid 2000 (n_{av} = 45). Notice that both molecules have the same nominal mass 153

Figure 135. UHPSFC positive ion ESI Q MS. BPICC of 1000 µg/mL mPEG acid 2000 and 1000 µg/mL PEG diacid 2000 in CH_3CN + 1% HCOOH 153

Figure 136. UHPSFC positive ion ESI Q MS. Ion map. Comparison of the effect of the mass analyser for the acidic PEGs mixture: a) 500 µg/mL in CH_3CN Q, b) 50 µg/mL QToF. mPa: mPEG acid 2000, Pda: PEG diacid 2000 154

Figure 137. UHPSFC positive ion ESI Q MS. BPICC. Observation of a PEG-based impurity in PEG diacid 2000 using mPEG acid 2000 and PEG diacid 2000 at 500 µg/mL in CH_3CN 155

Figure 138. Proposed structures for the PEG-based impurity identified in PEG diacid 2000: a) mPEG, and b) PEG monoacid 155

Figure 139. Determination of an impurity in PEG diacid 2000. Evaluation of the linear fitting assuming n values corresponding to mPEG using all data points available 156

Figure 140. Determination of an impurity in PEG diacid 2000. Evaluation of the linear fitting assuming n values corresponding to mPEG using three data points 157

Figure 141. Determination of an impurity in PEG diacid 2000. Evaluation of the linear fitting assuming n values corresponding to PEG monoacid 157

Figure 142. DI positive ion ESI MS. Mass spectra. 100 µg/mL PEG diacid 2000 in CH_3OH. Observation of the charge distributions of singly, doubly, and triply charged species of PEG diacid 2000 and the charge distributions of singly and doubly charged species of the PEG impurity 158

Figure 143. DI negative ion ESI MS. Mass spectra. 100 µg/mL PEG diacid 2000 in CH_3OH. Observation of the charge distribution of singly and doubly charged species of PEG diacid 2000 and the lack of ionisation of the impurity 159

Figure 144. Chemical structures of: a) Brij® 58 (n_{av} = 20), and b) Brij® S 100 (n_{av} = 100) 159

Figure 145. UHPSFC positive ion ESI Q MS. BPICC. 100 µg/mL Brij® 58 in CH_3CN. Analysis of Brij® 58 (n_{av} = 20) 160

Figure 146. UHPSFC positive ion ESI MS. Ion map. Comparison of the effect of changing the mass analyser for Brij® 58: a) Q, b) QToF. B: Brij oligomers 161

Figure 147. UHPSFC positive ion ESI Q MS. BPICC. 2500 µg/mL Brij® S 100 in CH_3CN. Analysis of Brij® S 100 (n_{av} = 100) 161

Figure 148. UHPSFC positive ion ESI Q MS. Ion map. 1000 µg/mL in CH_3CN. Comparison of the effect of the mass analyser for Brij® S 100. FA PEG refers to an unknown impurity characterised as stearate PEG. B S: Brij S oligomers 162

Figure 149. UHPSFC positive ion ESI QToF MS. Ion map. 200 µg/mL in CH_3CN. Comparison of the effect of the mass analyser for Brij® S 100: FA PEG referred to an unknown impurity characterised as stearate PEG. B S: Brij S oligomers 163

Figure 150. Proposed structure of the fatty-acid derivative impurity (stearate PEG); labelled as FA PEG in the ion map 163

Table of Figures

Figure 151. UHPSFC positive ion ESI Q MS. BPICC. 5000 µg/mL Gelucire® 44/14 in CH_3CN 164

Figure 152. UHPSFC positive ion ESI MS. Ion map. Comparison of the effect of the mass analyser for Gelucire® 44/14: a) Q, 5000 µg/mL in CH_3CN, b) QToF 500 µg/mL in CH_3CN 165

Figure 153. UHPSFC positive ion ESI QToF MS. 500 µg/mL Gelucire® 44/14 in CH_3CN. Overlapping of three samples: Sample A (blue): no treatment, sample B (red): after one cycle of heat-up / cool-down processes and sample C (green): after two cycles 166

Figure 154. Differential scanning calorimetry (DSC) thermogram of Gelucire ® 44/14. Blue (top): Gelucire® 44/14 curve thermogram, Orange (middle): Glyceride fraction thermogram, Green (bottom): PEG-ester fraction thermogram. Reproduced with permission from Gatteffosé [65]. Original work from Jannin [376] 167

Figure 155. UHPSFC positive ion ESI Q MS. BPICC. 2500 µg/mL Tween® 20 in CH_3CN. Analysis of the elution of species present in polysorbates 168

Figure 156. UHPSFC positive ion ESI Q MS. RICC. 2500 µg/mL Tween® 20 in CH_3CN. Unusual chromatographic peak shapes of POE S of different chain lengths 168

Figure 157. Chemical structure of POE S ML 169

Figure 158. Dehydration of sorbitol showing the different synthetic sub-products 169

Figure 159. UHPSFC positive ion ESI Q MS. Ion map. 2500 µg/mL Tween® 20 in CH_3CN. Analysis of the components 170

Figure 160. UHPSFC positive ion ESI QToF MS. Ion map. 500 µg/mL Tween® 20 in CH_3CN. Analysis of the components 171

Figure 161. UHPSFC negative ion ESI Q MS. BPICC 2500 µg/mL Tween® 20 in CH_3CN. Determination of free fatty acids in the polysorbate 172

Figure 162. UHPSFC negative ion ESI Q MS. 2500 µg/mL Tween® 20 in CH_3CN. Development of a SIM acquisition approach for quantitation of free lauric acid in Tween® 20 for batch and supplier comparison: a) negative ion ESI mass spectrum, b) comparison of chromatographic peak shape and improvements on S/N when collecting using SIM, and c) linear fitting of the calibration (samples analysed in triplicates, the error bars correspond to 1 stdev) 174

Figure 163. UHPSFC positive ESI Q MS. a) BPICC, b) Ion map. 2500 µg/mL Tween® 20 in CH_3CN. Differences between two suppliers of Tween® 20 (in red supplier A, in blue supplier B) 175

Figure 164. UHPSFC positive ion ESI Q MS. Ion map. 2500 µg/mL Tween® 20 in CH_3CN. Differences in the quality of Tween® 20 products from the same supplier (in red the higher quality, in blue the lower quality) 176

Figure 165. UHPSFC positive ion ESI Q MS. BPICC. 2500 µg/mL Tween® 20 and 2500 µg/mL Tween® 80 in CH_3CN. Differences in the pattern of the BPICC between a) Tween® 20 and Tween® 80, and b) two suppliers of Tween® 80 177

Figure 166. UHPSFC positive ion ESI MS. Ion map. Comparison of the effect of the mass analyser for Tween® 80: a) Q 2500 µg/mL in CH_3CN, b) QToF 500 µg/mL in CH_3CN 178

Figure 167. UHPSFC positive ion ESI QToF MS. Ion map. 1000 µg mL Tween® 80 in CH_3CN. Comparison of different suppliers: a) supplier A, b) supplier B 180

Figure 168. UHPSFC negative ion ESI Q MS. BPICC. 2500 µg/mL Tween® 20 in CH_3CN. Differences in the fatty acid composition of different polysorbates: C12:0, C14:0, C16:0, C18:0, C18:1 and C18:2 180

Figure 169. UHPSFC positive ion APPI Q MS (dopped with toluene). BPICC. 2500 µg/mL Tween® 20 in CH_3CN. Differences in the composition of substituted saturated fatty acid of different polysorbates: oleic acid (C18:1, OL) and linoleic acid (C18:2) 181

Figure 170. Deconvolution of the mass spectra of a large biomolecule a) mass spectrum of a small molecule (terfenadine) in an *m/z* scale, b) characteristic mass spectrum of a large biomolecule showing the charge envelope in an *m/z* scale, and c) deconvoluted mass spectrum of the large biomolecule in an MW scale 186

Figure 171. The advantages of chromatography in PEG analysis: a) Comparison of the mass spectra of PEG 600 and PEG 2000 and the need for chromatography, and b) generation of the mass spectra of individual oligomers of PEG 600 (bottom) based on the chromatographic separation using UHPSFC-MS (top) 187

Figure 172. Stepwise approach of the deconvolution of one single oligomer mass spectra using Waters® Transform™ deconvolution. a) identification of the oligomer in the chromatogram, b) oligomer mass spectra, c) deconvoluted oligomer 189

Figure 173. Stepwise deconvolution of the mass spectra of PEG 1450 using Waters® Transform™ algorithm 190

Figure 174. Effect of increasing the cone voltage to the ammoniated molecules of PEGs 191

Table of Figures

Figure 175. Evaluation of the quantitative aspect of Waters® Transform™ algorithm using linear fitting (3 replicates, error bars correspond to 1 stdev) 191

Figure 176. Proposed approaches for PEG quantitation based on a) a surrogate oligomer that represents the whole distribution, and b) the whole polymeric distribution 192

Figure 177. Selection of the surrogate oligomer for polymer quantitation. Example showed using PEG 1450 193

Figure 178. Quantitation approaches of PEGs using a surrogate oligomer: a) RICC of the most intense ion with/without SIM acquisition, and b) mass spectra deconvolution of the surrogate oligomer 194

Figure 179. Quantitation approaches of PEGs using the whole distribution: a) sum of the RICCs of all PEG ions in the mass spectra, and b) sum of the oligomer Transform™ deconvoluted response 195

Figure 180. Examples of calibration curves for quantitation using a surrogate oligomer: a) SIM acquisition, b) use of the RICC, and c) deconvolution of the mass spectra (samples analysed in triplicates, the error bars correspond to 1 stdev) 197

Figure 181. Examples of calibration curves for quantitation using the whole distribution: a) Sum of the peak areas of the RICC of all ions, and b) sum of the oligomer Transform™ deconvoluted response (samples analysed in triplicates, the error bars correspond to 1 stdev) 197

Figure 182. Evaluation of the effect of the mass analyser ion transmission and collision gas in the mass spectra of PEG 1450: a) Q: beam mass analyser without collision gas Q, b) QqQ: beam mass analyser with collision gas QqQ, and c) QToF: pulsed mass analyser with collision gas 200

Figure 183. Ionisation current trends of different ionisation events of alcohol PEG oligomers. Data acquired using UHPSFC positive ion ESI Q MS and mixture of 50 µg/mL in CH_3CN (per component) of PEG 600, 1000, 1450 and 2000 200

Figure 184. UHPSFC positive ion Q MS. Mass spectra. 100 µg/mL PEG 1450 in CH_3CN. Effect of a) HM, and b) LM in the sensitivity and resolving power of the Q mass analyser 202

Figure 185. Simplification of the deconvolution trace of PEG 1450 to allow data analysis comparison between mass analysers. The response of the Q was increased by a factor corresponding to the relative differences between the oligomer intensity of the most intense oligomer in each deconvoluted trace 202

Figure 186. UHPSFC positive ESI MS. PEG 600, 1000, 1450 and 2000. Comparison of the mass spectra deconvolution traces of a) PEG 600, b) PEG 1000, c) PEG 1450, and d) PEG 2000 when using the Q (blue) and QToF (orange) mass analysers. Note that the Q mass analyser response was adjusted to align the graphs based on sensitivity and concentration differences 203

Figure 187. UHPSFC positive ion ESI Q MS. PEG 600, 1000, 1450 and 2000. Ionisation current trends when using the Q mass analyser 204

Figure 188. Examples of calibration curves of PEG 600 using deconvolution approaches of a surrogate oligomer. Effect of the mass analyser: a) Q, b) QToF (samples analysed in triplicates, the error bars correspond to 1 stdev) 206

Figure 189. Examples of calibration curves of PEG 600 using deconvolution approaches of the whole distribution. Effect of the mass analyser: a) Q, and b) QToF (samples analysed in triplicates, the error bars correspond to 1 stdev) 207

Figure 190. Crown ethers evaluated in this research and their chelation to different cations: a) 15-crown-5 for Na^+, b) 18-crown-6 for K^+, and c) 18-crown-6 for NH_4^+ 209

Figure 191. UHPSFC positive ion ESI Q MS. 50 µg/mL 15-crown 5 (*m/z* 238) and 18-crown-6 (*m/z* 282) in CH_3CN: a) BPICC, and b) mass spectra 210

Figure 192. Linear range scoping for 18-crown-6 using UHPSFC positive ion ESI Q MS (samples analysed in triplicates, the error bars correspond to 1 stdev) 211

Figure 193. UHPSFC positive ion ESI Q MS. BPICC. 50 µg/mL PEG 1000 + 0.5 µg/mL 18-crown-6 (18C6) in CH_3CN. Co-elution between the ISTD and the oligomer P_{14} of PEG 1000 211

Figure 194. Evaluation of the interference produced by the ISTD in the response of PEG 1000. 50 µg/mL PEG 1000 + 0.5 µg/mL 18-crown-6 in CH_3CN. a) Evaluation of the matrix effect based on the peak area. b) Effect of introducing the ISTD when calculating M_n, M_w and PDI. Samples analysed in triplicates. The error correspond to 1 stdev 212

Figure 195. Effect of the ISTD of 18-crown-6 in the calibration curve of PEG 600. a) External calibration, and b) Internal calibration (samples analysed in triplicates, the error bars correspond to 1 stdev) 213

Figure 196. Proposed protocol for PEG quantitation using Transform™ deconvolution 215

Table of Figures

Figure 197. DI positive ion ESI QToF MS. Mass spectra. 10 µg/mL of 2HPBCD in H_2O. The formation of the multiply charged ions in the 2HPBCD are highlighted 217

Figure 198. DI positive ion ESI QToF MS. Mass spectra. 10 µg/mL of 2HPBCD in H_2O. The degree of substitution of the singly charged area of the mass spectra showing the polymeric character. Oligomer ions were labelled based on the DS of the central β-CD ring. The first number corresponds to the number of positions substituted by the HP chain, and the second number is the amount of free hydroxy groups 218

Figure 199. DI positive ion ESI QToF MS. Mass spectra. 10 µg/mL of 2HPBCD in H_2O. The formation of Na salts of 2HPBCD. An example is shown for singly charged species 218

Figure 200. UHPSFC positive ion ESI QToF MS. BPICC. 1000 µg/mL in CH_3OH + 1% HCOOH. The requirement to increase the gradient percentage 219

Figure 201. UHPSFC positive ion ESI MS. Ion map. Effect of the mass analyser in the ion map of 2HPBCD. a) Q 1000 µg/mL in CH_3OH + 1% HCOOH, b) QToF 100 µg/mL in CH_3OH + 1% HCOOH 220

Figure 202. UPSFC positive ion ESI QToF MS. RICC (*m/z* 1448). 10 mg/mL 2HPBCD. Peak shapes when using three different injection solvents 221

Figure 203. UPSFC positive ion ESI QToF MS. Mass spectra. 10 mg/mL 2HPBCD using of CH_3O+ 1% HCOOH. Mass spectra obtained when using three different make-up solvents. Notice the formation of Na salts when using 50 µM HCOONa showing low levels of Na salt ($) 222

Figure 204. UHPSFC positive ion ESI QToF MS. RICC (*m/z* 1448). 10 mg/mL 2HPBCD in CH_3OH + 1% HCOOH. Optimisation of HCOOH concentration in the mobile phase 223

Figure 205. UPSFC positive ion ESI QToF MS. 10 mg/mL 2HPBCD using of CH_3OH + 1% HCOOH. Mass spectra obtained using CH_3OH + 1% HCOOH showing low levels of Na salt ($) 223

Figure 206. UHPSFC positive ion ESI QToF MS. 10 mg/mL 2HPBCD in CH_3OH + 1% HCOOH. Optimisation of the H_2O concentration in the mobile phase. a) RICC of two consecutive oligomers, and b) mass spectra showing relative levels of Na adducts ($) 224

Figure 207. UHPSFC positive ion ESI QToF MS. RICC *m/z* 1622 and *m/z* 1564. 1000 µg/mL 2HPBCD in CH_3OH. Effect of the column temperature in the separation 225

Figure 208 UHPSFC positive ion ESI QToF MS. RICC *m/z* 1622 and *m/z* 1564. 1000 µg/mL 2HPBCD in CH_3OH. Effect of the ABPR in the separation 226

Figure 209. UHPSFC positive ion ESI MS. 1000 µg/mL 2HPBCD in CH_3OH. RICC of the singly charged species showing the oligomer elution. Data acquired using the BEH-2EP SP 227

Figure 210. UHPSFC positive ion ESI MS. 1000 µg/mL 2HPBCD in CH_3OH + 1% HCOOH. RICC *m/z* 1448 (top) and *m/z* 1622 (bottom) when using the BEH-2EP SP 228

Figure 211. UHPSFC positive ion ESI MS. 1000 µg/mL 2HPBCD in CH_3OH + 1% HCOOH. RICC *m/z* 1448 (top) and *m/z* 1622 (bottom) when using the T2Pic SP 229

Figure 212. UHPSFC positive ion ESI MS. 1000 µg/mL 2HPBCD in CH_3OH + 1%HCOOH. RICC *m/z* 1448 (top) and *m/z* 1622 (bottom) when using the TDiol SP 229

Figure 213. UHPSFC positive ion ESI MS. 1000 µg/mL 2HPBCD in CH_3OH + 1% HCOOH. RICC *m/z* 1448 (top) and *m/z* 1622 (bottom) when using the DEA SP 230

Figure 214. UHPSFC positive ion ESI MS. 1000 µg/mL 2HPBCD in CH_3OH + 1% HCOOH. RICC *m/z* 1448 (top) and *m/z* 1622 (bottom) when using the C18+ SP 230

Figure 215. The instrumental challenge of using HPLC columns (250 mm) in a UPC^2 system: a) Differences in column size between FPP for achiral analysis (100 mm), SPP for achiral analysis (100 mm) and FPP for chiral analysis (250 mm) columns, and b) the set-up of the FPP for chiral analysis column in the UPC^2 column compartment 232

Figure 216. UHPSFC positive ion ESI TQD MS. BPICC. 1000 µg/mL 2HPBCD in CH_3OH + 1% HCOOH. Analysis of 2HPBCD using FPP columns designed for chiral screening 234

Figure 217. UHPSFC positive ion ESI QToF MS. Ion map. 1000 µg/mL 2HPBCD in CH_3OH + 1% HCOOH. Comparison of the selected columns screened for the 2HPBCD separation 236

Figure 218. Different representations of UHPSFC positive ion ESI Q IM ToF MS 237

Figure 219. UHPSFC positive ion ESI Q IM ToF MS. 100 µg/mL 2HPBCD in CH_3OH + 1% HCOOH. Mobiligrams (retention time *vs* drift time) were acquired using SIM *m/z* 1506 237

Figure 220. UHPSFC positive ion ESI Q IM ToF MS. 100 µg/mL 2HPBCD in CH_3OH + 1% HCOOH. Mobiligrams (retention time *vs* drift time) were acquired using SIM *m/z* 1506. Separation of up to 4 conformers of the 2HPBCD oligomer with 6 hydroxypropyl and 15 hydrogens. Comparison between a) Chiralcel OD, b) 2-PIC, c) Chiralpack AD, d) C18+, e) PFP, and f) BEH 2-EP SPs 239

Research Thesis: Declaration of Authorship

Print name: Sergio Cancho Gonzalez

Title of thesis: The analysis of polymeric excipients using Ultra-High-Performance Supercritical Fluid Chromatography and Mass Spectrometry

I declare that this thesis and the work presented in it are my own and have been generated by me as the result of my own original research. I confirm that:

1. This work was done wholly or mainly while in candidature for a research degree at this University
2. Where any part of this thesis has previously been submitted for a degree or any other qualification at this University or any other institution, this has been clearly stated
3. Where I have consulted the published work of others, this is always clearly attributed
4. Where I have quoted from the work of others, the source is always given. With the exception of such quotations, this thesis is entirely my own work
5. I have acknowledged all main sources of help
6. All work has been conducted wholly by myself with the exception of the following:
   - Appendix A performed by Dr Paul Ferguson, AstraZeneca, UK
   - Coding modification of the [SpeTransform] of the MassLynx.ini file of the MassLynx® 4.1 software; modified with suggestions of Ed Sparke, Waters® Corporation, UK
7. Part of this work has been published before submission:
   - In six internal, national, and international conferences and with specialised, pharmaceutical, and general audiences
   - As part of: *"Practical Application of Supercritical Fluid Chromatography for Pharmaceutical Research and Development, M.B. Hicks and P.D. Ferguson, Separation Science and Technology, Volume 14, Academic Press, Elsevier; 2022"*, where Sergio Cancho Gonzalez co-authored *Chapter 10. Different detectors used with SFC*, in conjunction with Dr G. John Langley and Dr Julie M. Herniman

Signature:	Sergio Cancho Gonzalez	Date:	19-June-2022

Acknowledgements

This research project would not have been started if the initial questions were not raised by the Rebecca Cross in AstraZeneca and without the funding that AstraZeneca and EPSRC provided.

I am grateful for the advice and motivation from my industrial peers: Dr Paul Ferguson, Dr Sophie Bailes, Matt Osborne, Rebecca Cross and Fiona Bell and the AstraZeneca team. Their extensive knowledge of the pharmaceutical industry has helped me understand my project better. Also, I would like to thank Ed Sprake and the Waters® team that helped develop the deconvolution algorithm.

I would like to acknowledge the academic supervisory team, Dr G. John Langley, Julie M. Herniman and Dr Matthias Baud, for their emotional and research support throughout the PhD. Their support has given me the independence and confidence I have today as an analytical chemist, which helped me navigate this project and my future career.

At the University of Southampton. Thanks to many members of the Langley research group: Dr Maria Ashe, Dr Anastarsia Carter, Dr Tom Sutton and Fabien Hannauer for their continuous challenges and discussions of topics. I am thanking my examiner, Dr Sam Thompson, for pushing my research knowledge to the limits and challenging me to prove myself as an independent scientist. I am incredibly grateful to Marina Carravetta and Louise Fay for their support over the last year.

Thank you to many people that supported me through my Southampton route. Fabien and Aleksandra for believing in me when no one did, Rosie and Simon for providing support when I was in my lowest days, Ravi for being the best PhD thesis partner that one can have, and Sofia for helping me settle down in Southampton.

Special thanks go to those closest to me. Tomás and Pablo for being the best friends that one can get in the world. Alejandro, Carlos, Cristian, Juan Miguel, and Macarena for all the support and jokes that helped me to disconnect from the research topic.

I would not have done this without Kitty, my house cat, for proving the company and the unconditional love of a pet and for always being there during my writing breaks.

And finally, a message to my mum, dad and aunt for the constant strived to support me in every endeavour. I cannot convey enough how much I appreciate them.

“Chemists are dreamers: We think up new molecules and bring them to life”

Carolyn Bertozzi, Nobel Prize in Chemistry, 2022

Definitions and Abbreviations

2HPBCD	(2-hydroxypropyl)-β-cyclodextrin derivative
ABPR	Active backpressure regulator
APCI	Atmospheric pressure chemical ionisation
API	Active pharmaceutical molecule
APPI	Atmospheric pressure photo-ionisation
B	Brij® 58 oligomer
B S	Brij® S 100 oligomer
BPICC	Base peak ion current chromatogram
CAD	Charged aerosol detector/detection
CD	Cyclodextrins
CID	Collision-induced dissociation fragmentation
CLAD	Chemiluminescence aerosol detector/detection
CMC	Critical micelle concentration
CNLSD	Condensation nucleation light-scattering detector
cSFC	Capillary supercritical fluid chromatography
Da	Dalton
DS	Degree of substitution of a cyclodextrin
ECD	Electron capture detector/detection
ELSD	Evaporative light scattering detector/detection
EMA	European Medicines Agency
ESI	Electrospray ionisation source
FDA	U.S. Food and Drug Administration

FID	Flame ionisation detector/detection
FT-ICR MS	Fourier-transform ion cyclotron resonance mass spectrometry
GC	Gas Chromatography
GPC	Gel permeation chromatography
HIC	Hydrophobic interaction chromatography
HILIC	Hydrophilic interaction liquid chromatography
HLB	Hydrophilic-lipophilic balance
HP	Hydroxypropyl chains in a (2-hydroxypropyl)-β-cyclodextrin derivative
IARC	The International Agency for Research on Cancer
ICH	International Council for Harmonisation of Technical Requirements for Pharmaceuticals for Human Use
IEX-LC	Ion-exchange liquid chromatography
IMMS	Ion mobility mass spectrometry
ISTD	Internal standard
LC	Liquid chromatography
m/z	Mass-to-charge ratio of an ion
MALDI	Matrix-assisted laser desorption/ionization source
MaxEnt	Maximum Entropy® algorithm
Mn	Number average molecular weight
MP	Mobile phase
MS	Mass spectrometry
MW	Molecular weight
Mw	Weight average molecular weight
NMR	Nuclear magnetic resonance spectroscopy

NPD	Nitrogen phosphorous detector
O/W	Oil dispersed in water emulsion
PDI	Polydispersity: IUPAC term is Đ: dispersity
PEG	Poly(ethylene) glycol
POE DL	Polyoxyethylene dilaurate
POE DO	Polyoxyethylene dioleate
POE DP	Polyoxyethylene dipalmitate
POE DS	Polyoxyethylene distereate
POE IS	Polyoxyethylene isosorbitan
POE IS DL	Polyoxyethylene isosorbitan dilaurate
POE IS DO	Polyoxyethylene isosorbitan dioleate
POE IS DP	Polyoxyethylene isosorbitan dipalmitate
POE IS DS	Polyoxyethylene isosorbitan distereate
POE IS ML	Polyoxyethylene isosorbitan dilaurate
POE IS MO	Polyoxyethylene isosorbitan monooleate
POE IS MP	Polyoxyethylene isosorbitan monopalmitate
POE IS MS	Polyoxyethylene isosorbitan monostereate
POE ML	Polyoxyethylene monolaurate
POE MO	Polyoxyethylene monooleate
POE MP	Polyoxyethylene monopalmitate
POE MS	Polyoxyethylene monostereate
POE S	Polyoxyethylene sorbitan
POE S DL	Polyoxyethylene sorbitan dilaurate
POE S DO	Polyoxyethylene sorbitan dioleate

POE S DP	Polyoxyethylene sorbitan dipalmitate
POE S DS	Polyoxyethylene sorbitan distereate
POE S ML	Polyoxyethylene sorbitan monolaurate
POE S MO	Polyoxyethylene sorbitan monooleate
POE S MP	Polyoxyethylene sorbitan monopalmitate
POE S MS	Polyoxyethylene sorbitan monostereate
POE S QL	Polyoxyethylene sorbitan tetralaurate
POE S QP	Polyoxyethylene sorbitan tetrapalmitate
POE S QS	Polyoxyethylene sorbitan tetrastereate
POE S TL	Polyoxyethylene sorbitan trilaurate
POE S TO	Polyoxyethylene sorbitan trioleate
POE S TP	Polyoxyethylene sorbitan tripalmitate
POE S TS	Polyoxyethylene sorbitan tristereate
prepSFC	Preparative supercritical fluid chromatography
pSFC	Packed column supercritical fluid chromatography
Q	Quadrupole mass analyser
QqQ	Triple quadrupole mass analyser
QToF	Quadrupole time-of-flight mass analyser
RI	Refractive index detector/detection
RICC	Reconstructed Extracted ion current chromatogram; also known as XICC: Extracted ion current chromatogram
RPLC	Reversed-phase liquid chromatography
SEC	Size exclusion chromatography
SFC	Supercritical fluid chromatography

SP	Stationary phase
TWIMS	Travelling wave ion mobility spectrometry
UHP	Ultra-high-performance chromatographic technique
UHPLC	Ultra-high-performance liquid chromatography
UHPSFC	Ultra-high-performance supercritical fluid chromatography
UV-Vis	Ultraviolet-visible detector/detection
W/O	water dispersed in oil emulsion

Chapter 1 Introduction

1.1 Synopsis of the research

Even though the approval of small molecules is still of great importance, the expansion towards newer modalities requires the development of druggable large biomolecules. However, the use of these molecules has inherent challenges in their delivery due to their toxicity, poor bioavailability, or lack of cell specificity. Drugs are now being developed and formulated in complex drug-excipient conjugates to address these emerging challenges in drug delivery. Drug delivery refers to approaches, formulations, manufacturing techniques, storage systems, and technologies to administer a pharmaceutical compound in systemic circulation to its target biological site to achieve a therapeutic effect in humans or animals. Polymers are popular among all the excipients due to their synthetic versatility as structural variations allow achieving the desired pharmacological and physicochemical characteristics of the final product. These modifications improve drug protection and delivery and enable the production of robust formulations, resulting in the use of poly(ethylene) glycols (PEG) or cyclodextrins (CD) as excipients in some formulations. PEGs are safe materials that improve drug delivery by drug encapsulation or binding. CDs can host drug molecules inside their cavity to highly improve their solubility.

The polymeric nature of the materials requires control of their quality from the early stages of drug development. The non-specific synthetic processes used to produce PEGs as raw materials lead to the formation of undesired subproducts that emerge from their synthesis or degradation (discussed in Chapter 4). Even though the synthesis of substituted cyclodextrin is controlled, the synthetic challenge of the 2-hydroxypropyl derivate (discussed in Chapter 6) leads to a complex mixture that is difficult to characterise. The resulting heterogeneity can lead to sub-potency, so the dose is not administered as required, compromising the treatment reaching the patient. These findings showed the need for further characterisation of the excipients used.

This research proposes the combination of ultra-high-performance supercritical fluid chromatography and mass spectrometry (UHPSFC-MS) to characterise and quantify polymeric excipients, specifically of PEGs and CDs. The aim was to explore and facilitate data interpretation by optimising the separation and ionisation of the individual components using appropriate visualisation and quantitation tools.

1.2 Polymeric excipients and the pharmaceutical industry

1.2.1 Medicines and drug delivery

Medicinal drug formulations comprise an active pharmaceutical molecule (API – the drug molecule), excipients, and other minor substances (impurities and degradants) [1, 2]. The API is a molecule that produces a beneficial biological response in a disease state [1, 2]. They must be stable in plasma, target the tissue, bind to the cell, and improve the intracellular delivery and trafficking to the relevant cellular compartment [1, 3]. Generally, a low amount of the API is added when formulating the medicinal product resulting in the excipients being the main component [2, 3]. Excipients are molecules added to aid the formulation of the final product used for administration and improve API pharmacokinetics activity leading to an improved delivery to the active biological target [4]. Excipients are either inorganic molecules (*e.g.,* calcium phosphate), small organic molecules as neutral (*e.g.,* mannitol) or salt species (*e.g.,* sodium citrate) or polymers - either synthetic (*e.g.,* PEGs) or naturally derived (*e.g.,* starch) and play different roles within the formulations (see Table 1) [5]. Selecting the right excipient combination is crucial for protecting the API during delivery, achieving stable dosage forms, and minimising the drug administration dose and regime [3, 4]. The product performance, manufacturability, excipient functionality and compatibility are important factors that affect the final formulation [6-8].

Category	**Function**	**Example**
Adjuvants	Enhance/modify the immune system response	Aluminium hydroxide
Binders	Provide cohesiveness	PEG
Disintegrants	Aid break-up of solid oral dosage forms	Starch glycolate
Fillers	Provide chemical ballast	Stearic acid
Lubricants	Reduce friction during processing	Silica
Glidants	Enhance powder flowability	Starch
Coatings	For aesthetic and protective purposes	Gelatin
Anti-adherents	Prevent adhesion	Polyplasdone
Artificial flavours	Imparting aroma	Vanillin
Taste-masking	Improve patience compliance	Ethylcellulose

Preservatives	Control the microbial bioburden	Bronopol
Solubilisers	Enhance the solubility	Poly(vinylpyrrolidone)
Sorbents	For moisture-proofing	Nylon
Surfactants	Modulate the solubility	Polysorbates
Sweeteners	Impart sweetness	Table sugar
Colours	Improve the appearance	Iron oxide
Vehicles	The bulk excipient that conveys the API	Mineral oil

Table 1. Different pharmaceutical excipients and their roles in formulations [5]

During the process of drug development, molecule are selected as drugs (API – the drug molecule) as they have therapeutic role; their interaction with a biological entity induces a beneficial biological response that can be used in a disease state [1]. The selected molecule, whether small or large, must be delivered to the correct biological target when formulating a drug product [1]. Conventional drug delivery systems are the traditional framework for small drug molecule delivery and integrate classical methods, including the preferred non-invasive peroral, topical, transmucosal and inhalation routes [9]. Traditionally, small molecule drug delivery is governed by their physicochemical properties (often Lipinski's rule of five) [7, 10, 11]. Their small size involves that these drugs can rapidly diffuse across many biological barriers [12]. Efforts focus on improving drug bioavailability by altering solubility, controlling the release, and adjusting pharmacokinetics [13, 14]. However, the use of small molecules is imperfect due to a probability of missing the drug dose during delivery (pharmacokinetics), resulting in the need for frequent drug administration as the peak valley plasma concentration-time profile challenges the attainment of a steady-state condition [7, 12, 15]. The use of conventional dosage forms causes oscillation of plasma drug levels and accelerates drug release [12, 15]. Novel drug delivery systems were developed to maintain the desired drug concentration within the therapeutical window, minimise the undesired effects and maximise therapeutic benefits [6-8].

In recent years, the market trends of the food and drug administration (FDA) approvals have evolved from using small molecules to large biomolecules, including more complex molecules such as oligonucleotides [9, 16]. Over time, the therapeutic landscape evolved toward new drugs with chemical entities based on peptides, proteins, monoclonal antibodies, live cells, vaccines, or genes (Figure 1 a) [9]. As the therapeutic landscape evolved, delivery strategies and technologies quickly adapted due to the changes in drug delivery needs by either modifying the drug or

introducing environmental (Figure 1 b) [9]. These new drugs provided new solutions to existing and new diseases. Still, their use brought additional challenges in stability (for proteins and peptides), intracellular delivery requirements (for nucleic acids) and viability and expansion (for live cells) as a result of susceptibility to enzymatic degradation, poor bioavailability or poor penetration of the intestinal mucosa [9]. As a result, the improved delivery approaches used in formulations account for the disease biology, physicochemical properties of the therapeutic entities, and the physiology and anatomy of the route of administration to achieve the desired medicinal outcome [6-8]. The latest advances include microparticles, nanoparticles, liposomes, niosomes, transdermal drug delivery and drug microencapsulation (Figure 1 c) [9, 17]. Their use improves site-targeting *in-vivo*, drug potency and control drug release with prolonged pharmacological effect, leading to better, safer drugs with longer half-life and large therapeutic indices [6, 9]. These systems combine innovative development in formulations, new technologies, and novel methodologies for drug delivery to achieve the desired pharmacological effects.

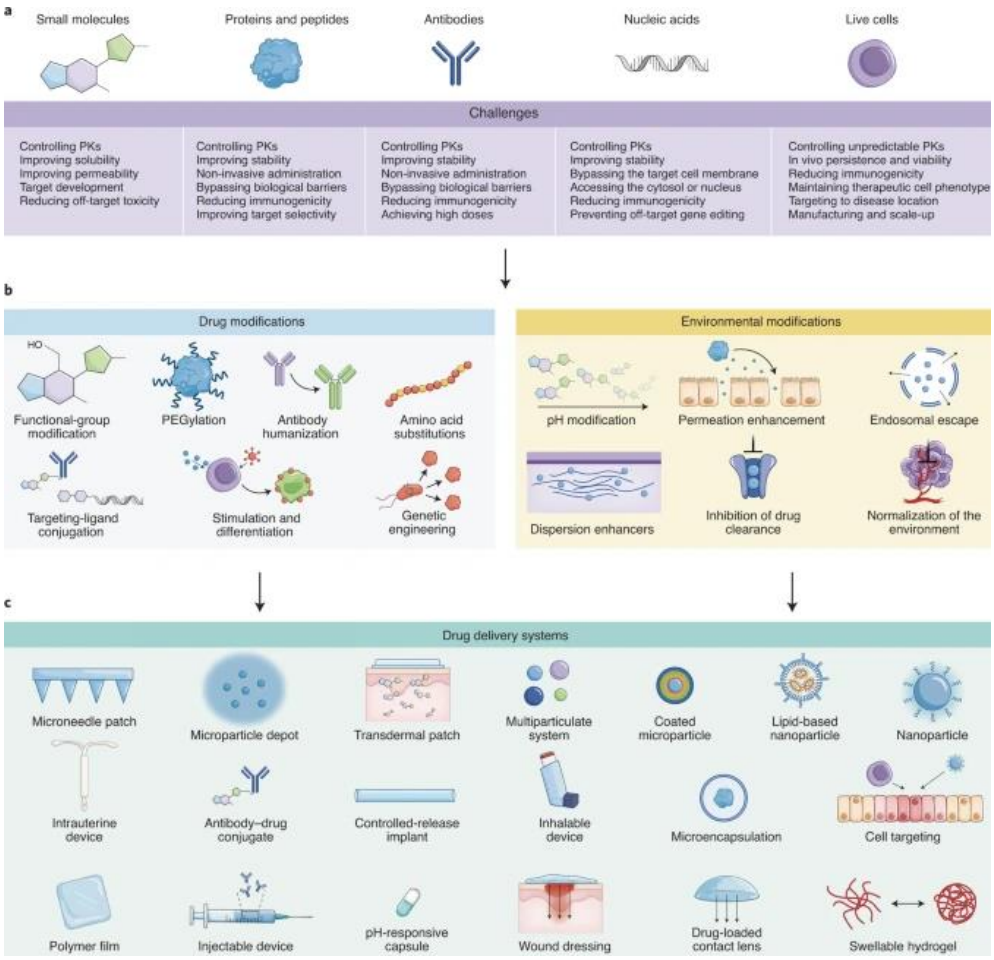

Figure 1. Drug delivery systems: a) molecules used as drugs and their delivery challenges, b) possible molecular modifications to improve drug delivery, and c) macromolecular design of drug delivery systems. Adapted from Vargason *et al.* [9]

Advantages of novel drug delivery systems over traditional ones include controlled delivery through maintenance of the desired drug concentration, accurate dosing, and enhanced efficacy due to a site/target-specific drug delivery at an optimum dose, decreasing the toxicity/side effects and improving patient comfort [6, 7, 9, 17]. The increased challenges in drug delivery results in the addition of complex molecules as excipients, such as polymers [6, 18, 19].

1.2.2 Polymeric excipients

Polymers are versatile molecules that can differ in molecular weight (MW), the structure of their monomer, the use of copolymerisation or blending, or the modification of the end groups [20]. Polymers are popular among all excipients due to their synthetic versatility [21]. The possibility of altering their structure can help achieve the desired pharmacological and physicochemical characteristics of the final product, resulting in more robust formulations[21]. They are either synthetic or found in nature (Table 2) [21, 22]. Most polymers are binders that provide weight and mechanical strength to the formulation ensuring rigid shape, high stability, and extended storage lifetimes, which in turn, allows the manufacture of capsules or tablets [20, 21]. Therefore, polymers are an essential component in pharmaceutical formulation [22].

Synthetic polymers		**Natural polymers**
Polyethers	Polyphosphoesters	Cellulose ethers polymers
Poly(ethylene imine)s	Poly(vinyl ester/alcohol/ether)s	Polysaccharides
Polyesters	Poly(*N*-vinyl amide)s	Elastin
Polysiloxanes	Poly(allylamine)s	Gelatine
Polycarbonates	Poly(methacrylate)s	
Poly(amino acid)s	Polyacrylonitriles	
Poly(peptoid)s	Polyurethanes	
Poly(2-oxazoline)s	Poly(anhydride)s	
Poly(*N*-acrylamide)s	Poly(olefin)s	
Silicones		

Table 2. Polymers used as excipients in the pharmaceutical industry based on their source. Cyclodextrins were not included on the table as they are polysaccharides (natural) that follow synthetic reactions to become cyclic and later on substituted

Not all polymers provide the same outcomes in drug delivery, with benefits in either the control drug release to the bloodstream, the improvement of the specific drug delivery to the biological

target, or the enhancement of the drug solubility [20]. Controlled release is achieved by encapsulating the drug molecule inside the polymer (micelle-like), protecting it against metabolism and slowly diffusing the drug molecule into the bloodstream [20]. This diffusion maintains the therapeutic concentration in plasma and, as a result, reduces the dose regime [23]. Additionally, some polymers improve the binding of the drug to the biological target [24, 25]. Other polymers modify drug lipophilicity, enhancing their solubility [26]. Also, the innocuous nature of the material is required to determine the applicability of excipients [20]. Polymers must be non-immunogenic, either by biocompatibility or biodegradability [27].

Overall, the process of discovering a drug is a meticulous analysis to check whether the drug fits the purpose and is economically rentable. As a result, the throughput of each stage tends to be improved and accelerated by overlapping stages as a manner to save in costs and transforming how new medicines are created. The use of new technologies for drug delivery such as polymers appeared to facilitate this process as they open a new world in how APIs are formulated by improved drug delivery and drug release to the biological target [28-31]. New chemical entities based on PEG or CD emerged to overcome some of the challenges in drug delivery mentioned above. PEGs are safe materials that benefit drug delivery by drug encapsulation or binding, and cyclodextrins host drugs inside their cavity to improve their solubility [32-34]. The polymeric nature of these materials results in increased demand from the industry for a deeper understanding of the starting materials and the development of improved approaches for quality control processes from the early stages of drug development. The heterogeneities in the materials lead to variations between batches and suppliers that may compromise the treatment reaching the patient, requiring the industry to develop better approaches to characterise these excipients.

1.2.3 Selection of surfactants for drug formulation

Surfactants are amphiphilic molecules (Figure 2 a) that, in solution, tend to form aggregates of colloidal dimensions (micelles, Figure 2 b and c), which exist in equilibrium with the molecules from which they were formed [35]. Micelle formation allows encapsulating drugs to improve solubility or delivery [36]. Above a particular concentration of surfactant (critical micelle concentration, CMC) in a bulk phase, the aggregation is observed, and micelles start to form [35]. Below the CMC, adsorption occurs at the surface of the solution until it is fully overlaid, corresponding to the minimum surface tension value [35]. The CMC specifies the limiting concentration for meaningful use and measures the efficiency of a surfactant [35]. Micelles are classified as normal or reverse based on how the hydrophilic and hydrophobic sites of the

amphiphilic molecule are located in the colloidal aggregation [35]. Oil-soluble surfactants form normal micelles (Figure 2 b) in aqueous solutions (oil dispersed in water emulsions (O/W)) by allocating their polar heads in the exterior of the core and the hydrophobic site of the molecule in the interior [37]. Water-dispersible surfactants form reverse micelles (Figure 2 c) in hydrophobic oily media (water dispersed in oil emulsions (W/O)) by locating the hydrophilic site of the surfactant in the interior of the core and the hydrophobic site in the exterior [35].

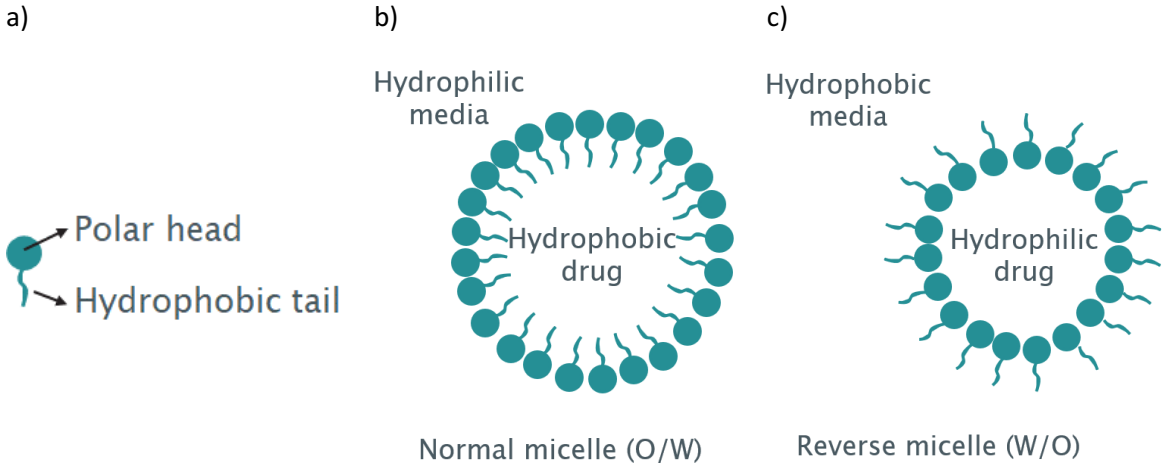

Figure 2. Surfactants and formation of micelles: a) amphiphilic molecule, b) normal micelle, and c) reverse micelle

The capacity of a surfactant to encapsulate a drug molecule can be obtained by measuring the hydrophilic-lipophilic balance (HLB). HLB measures the balance between the hydrophilic and lipophilic moieties in the structure (Equation 1) and represents the preference of the surfactant in the emulsion. Surfactants with lower values (HLB < 10) are suitable for W/O emulsions, whereas those with higher values (HLB > 10) are used for O/W emulsions.[37, 38].

$$HLB = 20\left(1 - \frac{M_o}{M}\right)$$

M_o: Mass of the lipophilic part

M: Mass of the molecule

Equation 1

The selection of a surfactant is based on the correlation between API logP value and the surfactant HLB value [38]. LogP measures the drug lipophilicity and relates to the drug ADME (administration, distribution metabolism and excretion). Tuning a drug lipophilicity involves a compromise between the location of the biological target, the non-polar biological membranes that the drug needs to diffuse through to reach the biological target and its solubility in body fluids that affect drug metabolism.

The partition coefficient (logP, Equation 2) is defined as the ratio of drug concentration in two immiscible solvents. The organic solvent varies depending on the different environments where the biological target is located. Octan-1-ol, chloroform, cyclohexane and propylene glycol dipelargonate were proposed. When using aqueous buffers at the pH of the media, different ionic and neutral species might coexist at a certain pH with different physicochemical and biological characteristics. The term is renamed as the distribution coefficient (D_{pH}, Equation 3). Noteworthy that this simplistic model simulates the behaviour of highly complex biolipidic membranes. [39-42]

$$logP = \log_{10}\left(\frac{[Drug\ in\ the\ organic\ phase]}{[Drug\ in\ the\ water\ phase]}\right) \qquad \text{Equation 2}$$

$$D_{pH} = \frac{[Drug\ unionised]_{org\ phase}}{[Drug\ unionised]_{aqu\ phase} + [Drug\ ionised]_{aqu\ phase}} \qquad \text{Equation 3}$$

The correlation between the API log P value and the surfactant HLB value is shown in Table 3 [38].

API logP value	< 3	3 - 5	5 - 7	≥ 8
Type of surfactant	Aqueous solubilisers	Water-dispersible surfactants	Oil-soluble surfactants	Oily solubilisers
Surfactant HLB value	HLB > 11	7 < HLB < 11	3 < HLB < 7	1 < HLB < 3

Table 3. Correlation between the API log P value and the surfactant HLB value

1.3 Poly(ethylene) glycols in the drug formulation

PEGs are linear or branched polyethers (repeating unit -CH_2-CH_2-O-) terminated with two hydroxyl groups and an MW below 100,000 Da. Higher MW PEGs are named poly(ethylene) oxide (PEO). Low MW ones (< 1,000 Da) are colourless viscous liquids, whilst higher MW ones (over 1,000 Da) are waxy or white solids [27, 43]. Either acidic or basic catalysis can be used when manufacturing PEGs. Basic catalysis allows for narrower MW distributions due to the synthetic anionic polymerisation mechanism (Figure 3). The reaction initiates by a nucleophilic attack of the epoxide ring with the nucleophilic hydroxide or alkoxide, resulting in the opening of the epoxide ring and forming the propagating species. PEGs with low MW dispersion are manufactured using ethylene glycol as the starting material. PEG derivatives are formed by protecting one end group

of ethylene glycol (*e.g.,* methoxy ethylene glycol to obtain mPEG) whilst the other end can be functionalised using specific terminating agents [44-47].

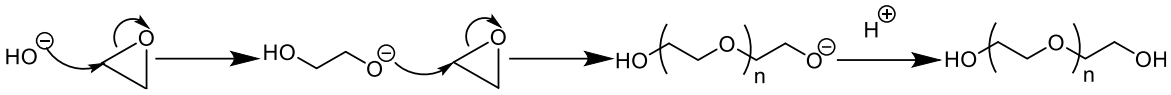

Figure 3. Synthesis of PEG *via* anionic living polymerisation

The use of PEGs finds many applications in biomedical research (drug delivery, tissue engineering scaffolds, surface functionalisation, *etc.*) and consumer care products (laxatives, toothpaste, hair shampoo, *etc.*). Daily examples containing PEGs include several tablet formulations of acetaminophen or ibuprofen, eye drops for hay fever treatment, some topical foams or injectables for cancer therapy, influenza, or COVID-19 vaccination (Figure 4). An extensive range of MW of PEGs is used in most pharmaceutical formulations. Whilst short-chain PEGs (400 Da) predominate in eye drop treatments; higher MW PEGs are common in injectables [27, 43].

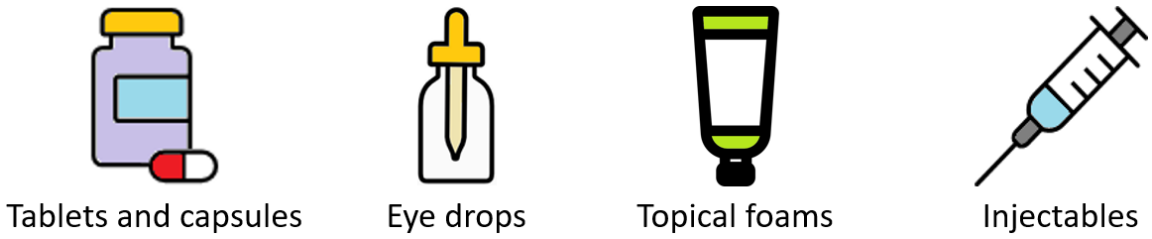

Figure 4. Common pharmaceutical dosage forms where PEGs are found

1.3.1 PEG Excipients *vs* PEGylation

The amphiphilic properties of PEG explain their use in formulations. Even though a common approach for PEGs is their use as excipients due to the advantage observed in drug delivery [48] and solubility through drug encapsulation; the solution can be stabilised by reaction with drug molecules (PEGylation) [25] via a covalent bond (prodrug) to enhance drug protection against metabolism. End groups are altered to modify drug lipophilicity and improve biological targeting. These advantages result when PEGs are added to drug treatments as excipients or PEGylating small drug molecules or large biomolecules [27, 43].

PEG excipients (Table 4) are amphiphilic surfactants that increase the solubility of components in the formulation in water and many organic solvents by encapsulating the API inside a normal micelle which improves drug delivery [49-52].

API	Treatment
Acetaminophen	Analgesic and antipyretic effects
Cetirizine	Allergic rhinitis, chronic hives, and pollen-induced asthma
Cyclobenzaprine	Acute back injuries, including patients with muscle spasms or significant tightness in their back
Diclofenac	Antipyretic and analgesic actions
Diphenhydramine	Seasonal allergies, antiemetic, antitussive, hypnotic, and antiparkinsonian properties
Methocarbamol	Musculoskeletal conditions associated with a painful muscle spasm
Morphine	Chronic pain
Oxycodone	Opiate painkiller for around-the-clock pain
Tramadol hydrochloride	Moderate to severe pain

Table 4. Examples of commercially approved drugs that use PEG as an excipient

Additionally, PEGs can react with the free API molecule to form a prodrug (see Figure 5) (PEGylation approach) [24, 43, 53]. Figure 5 shows a marketed drug molecule that benefited from PEGylation.

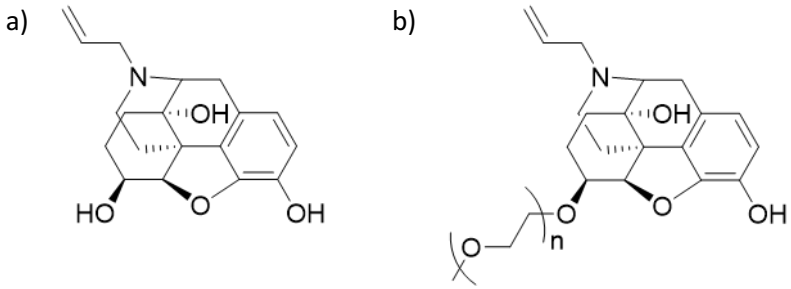

Figure 5. Prodrug approach using PEG. Example of a marketed drug that benefitted from using PEGylation: a) Naloxol (free drug), b) Naloxegol (PEGylated drug)

The biodegradable polymer forms stable covalent bonds to improve delivery (*e.g.,* masking the lipophilic moieties of the drug) and preserve the biological-active sides of the API structure (carboxy, alcohol, thiol, amine, *etc.*) against metabolism [49, 50]. A discharge of the drug molecule

occurs when reaching the site of action, releasing the active site of the drug molecule to interact with the therapeutic biological target. PEGylation protects the drug molecule by releasing degradable linkages of ethane-1,2-diol from the PEG chain [24, 43]. Additionally, membrane transportation changes from diffusion (small molecules) to endocytosis (PEGylated drug) [54].

Many approved drugs contain PEGylated small drug molecules and large biomolecules. Examples are shown in Table 5 (PEGylated small drug molecules) and Table 6 (large biomolecules).

API	**Treatment**
Paclitaxel	Ovarian, breast, lung, cervical and pancreatic cancers, and Kaposi sarcoma
Cisplatin	Sarcomas, some carcinomas, lymphomas, and germ cell tumours
Doxorubicin	Breast and bladder cancers, Kaposi's sarcoma, lymphoma, and acute lymphocytic leukaemia
Irinotecan	Colorectal and advanced pancreatic cancers
Wortmannin	Inhibitor of Phosphatidylinositol-3-Kinases and alloantigen-specific activation of T Lymphocytes in human tumour cell lines
Pemetrexed	Pleural mesothelioma and non-small cell lung cancer
Saquinavir	HIV/AIDS. Used with ritonavir or lopinavir/ritonavir
Gentamicin	Bacterial infections
Curcumin	Proteinuria, multiple myeloma, depression, and breast and non-small cell lung cancers
Naloxegol	Opioid-induced constipation in adult patients with chronic non-cancer pain
Camptothecin	Antitumor activity

Table 5. Examples of commercially approved PEGylated small drug molecules

Commercial name	**PEGylated molecule**	**Treatment**
Adagen	Enzyme	Severe combined immunodeficiency disease
Oncaspar	Enzyme	Acute lymphoblastic leukaemia
PEGasys	Liposome	Cancer
PegIntron	Protein	Hepatitis C
Neulasta	Protein	Chemotherapy-induced neutropenia
Somavert	Protein	Acromegaly
Macugen	Aptamer	Neovascular age-related macular degeneration
Mircera	Protein	Anaemia associated with chronic kidney disease
Cimzia	FAB' fragment	Crohn's disease, Rheumatoid arthritis, psoriatic arthritis, ankylosing spondylitis
Pegloticase / Krystexxa	Enzyme	Severe, refractory and chronic gout
Sylatron	Protein	Melanoma
Omontys	Peptide	Anaemia associated with chronic kidney disease

Table 6. Examples of commercially approved PEGylated large biomolecules drugs

When synthesising PEG for PEGylation, both hydroxyl groups can be functionalised to modify drug lipophilicity or increase the loading capacity (Table 7). Monomethoxy (mPEG) and alcohol (unmodified) PEGs are commonly used when lipophilicity modification is required. Derivatisation with anhydrides to form esters (*e.g.,* mPEG acid or PEG diacid) was reported. Still, one limitation is the number of active sites in the PEG molecule. When increasing the number of sites, the use of mono-functional or poly-functional PEG depends on the size of the drug. Contrariwise, mono-functional PEG (*e.g.,* mPEG) is preferred when working with poly-functional or high MW drugs. Equally, small mono-functional drugs tend to be conjugated with poly-functional polymers due to the lower risk of cross-linking, benefiting the drug/polymer ratio. Approaches used to increase the number of sites include the derivatisation with succinimidyl salts (succinate, glutarate, *etc.*) or

small amino acids. These small amino acids (α-amino acids excluding proline) are coupled with mPEG to prepare α-alkoxy amides PEG conjugates and allow an umbrella-like covering in peptide conjugation of branched PEG that can be extended to obtain dendrimers [23-25, 27, 43, 49-52, 54-57].

	Name	**Structure**
Modify drug lipophilicity	PEG	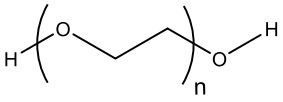
	Monomethoxy PEG	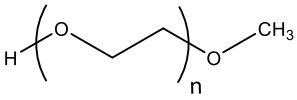
	mPEG acid	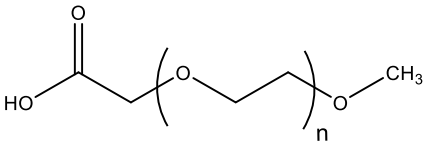
	PEG diacid	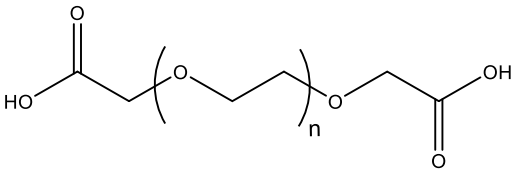
Increase the number of sites	α-alkoxy amides PEG (Leu)	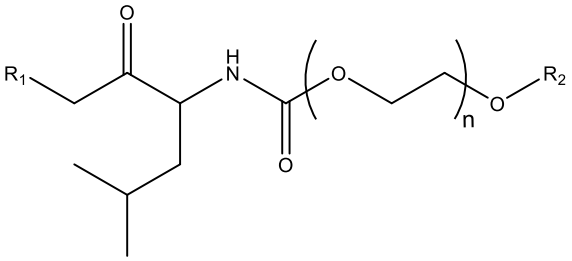
	mPEG-succinimidyl succinate	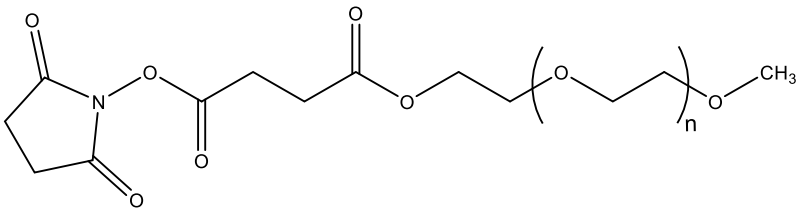
	mPEG-succinimidyl glutarate	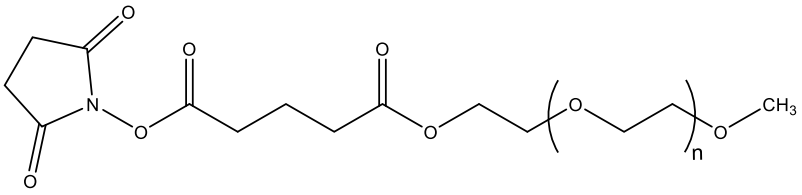

Table 7. Examples of PEG derivatives used in drug formulations

In this research, several PEGs based on the needs of the project sponsor were selected for characterisation and quantitation: Brij®, acidic PEGs, Gelucires®, and Tween®. The research was structured based on simplicity, where short PEGs with known end groups (alcohols and methoxy) were initially analysed, followed by applying the developed methods to more complex ones. The most important ones from a pharmaceutical point-of-view are described below.

1.3.2 Brij®: polyoxyethylene alkyl ethers or ethoxylated fatty alcohols

Brijs® are a family of non-ionic surfactants used in many formulations but extensively in cosmetics that follow a chemical formula as $HO(CH_2CH_2O)_nC_xH_{2x+1}$ [58]. They are non-ionic ethylene oxide adducts of linear alcohols derived from vegetable fatty acids: lauryl, oleyl, myristyl, cetyl and stearyl alcohols. Their nomenclature usually follows a letter that indicates the alcohol used and a number that refers to the average PEG chain length. Their synthesis results from the condensation between linear fatty alcohol and ethylene oxide followed by polymerisation with ethylene oxide to the desired MW [59, 60]. Brij® 58 and Brij S 100 (Figure 6) are analysed in this research.

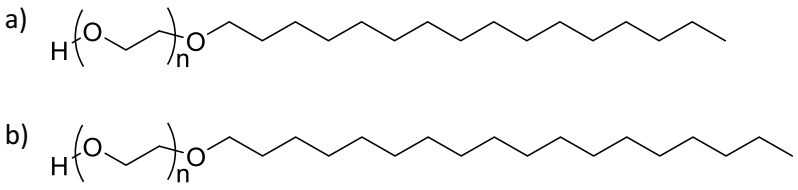

Figure 6. Chemical structures of: a) Brij® 58 (n_{av} = 20) and b) Brij S 100 (n_{av} = 100)

1.3.3 Acidic poly(ethylene) glycols: polyoxyethylene ethers derived from carboxylic acids

Polyoxyethylene alkyl ethers derived from carboxylic acids are PEGs with a carboxylic acid and another terminal group that could be a carboxymethyl or a lipophilic alkyl chain. Their development comes from a structural similarity to fatty acids. When considering fatty acids as excipients for pharmaceutical formulations, issues regarding high stability and the presence of a hydrophobicity non-ionised site are found. Inserting a PEG chain increases the water solubility without modifying the pH of the media and provides similar CMC values to alcohol or alkyl PEGs. Additionally, the pH-responsive carboxylic headgroup opens many possibilities for PEGylation due to the option of releasing the drug molecule at the site of action. The result is a surfactant that combines an ionic (carboxylic end) and a non-ionic (PEG) sites in the same molecule [61-64]. The acidic PEGs analysed in this research are in Figure 7: mPEG acid 2000 and PEG diacid 2000.

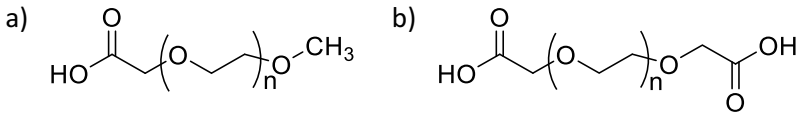

Figure 7. Chemical structures of acidic PEGs: a) mPEG acid 2000 (n_{av} = 45) and b) PEG diacid 2000 (n_{av} = 45)

1.3.4 Gelucires®: polyoxylglycerides

Gelucires® are semi-solid excipients of esterified PEGs (Figure 8) that may contain acylglycerols (Figure 9): monoacylglycerols (MAG), diacylglycerols (DAG), and triacylglycerols (TAG).

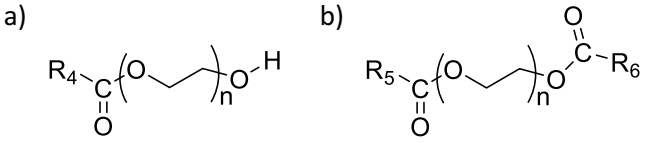

Figure 8. Structures of a) PEG monoester and b) PEG diester. R_4, R_5 and R_6 are the alkyl chains of vegetable-based fatty acids

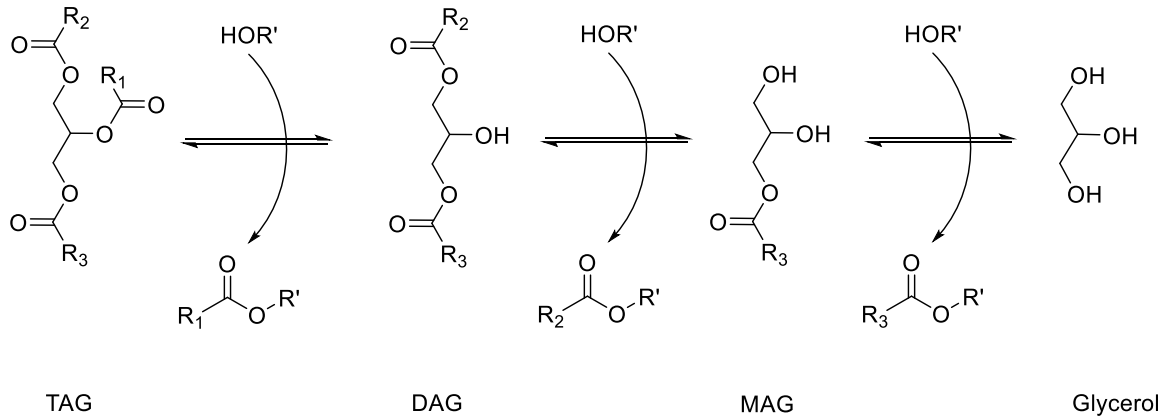

Figure 9. Hydrolysis (right) and transesterification (left) of acylglycerols: monoacylglycerols (MAG), diacylglycerols (DAG), and triacylglycerols (TAG). R_1, R_2 and R_3 are the alkyl chains of vegetable-based fatty acids

The numbers in the name of each Gelucire® indicate the melting point in Celsius degree (first) and the theoretical HLB value (second). The most commonly used are the 48/16, 44/14 and 50/13, used to increase the aqueous solubility and oral bioavailability of highly lipophilic drug molecules (non-ionic surfactant). The 43/01, 39/01 and 33/01 are encountered in formulations that require the protection of drugs sensitive to oxidation, humidity, or light (matrix former). A summary of the characteristics and compositions of different Gelucire® is shown in Table 8.

Gelucire® type	Role	Composition	Predominant fatty acid
48/16	Water-soluble non-ionic surfactants	PEG esters	Stearic and palmitic acids
44/14	Water-dispersible non-ionic surfactants	PEG esters and acylglycerols	Lauric acid
50/13	Water-dispersible non-ionic surfactants	PEG esters and acylglycerols	Stearic and palmitic acids
43/01, 39/01 and 33/01	Matrix former	PEG esters and acylglycerols	C8 to C18

Table 8. Marketed Gelucire®, their role in the formulation and their composition, showing the most predominant fatty acid observed. Notice that all fatty acids are vegetable-based fatty acids [65]

Gelucire® 44/14 (under investigation in this research) is prepared by an alcoholysis reaction between coconut oil and PEG 1500. The product is a mixture of PEG esters of fatty acids of varying chain length and mono, di and triacylglycerides (MAGs, DAGs and TAGs) [32, 65, 66]. Gelucire® 44/14 is a versatile and suitable excipient for many formulation processes, such as capsule moulding, melt granulation and spray cooling. Upon contact with an aqueous media, an emulsion is formed (self-emulsion drug delivery system, SEDDS) due to the different affinity of the components for water: PEGs are water-soluble, PEG esters and MAGs are amphiphilic, and DAGs and TAGs are hydrophobic [65].

1.3.5 Tween®: polysorbates

Polysorbates are non-ionic surfactants used in food, pharmaceuticals, or personal care as emulsifiers, solubilisers, wetting agents or dispersants [67, 68]. Figure 10 shows the synthetic process. The synthesis starts with the dehydration of sorbitol using acidic catalysis to form 1,4-sorbitan and isosorbide. A polymerisation reaction occurs with ethylene oxide to produce PEGylated sorbitol (poly(ethoxylate) sorbitan, POE S). Finally, an esterification reaction with vegetable-based fatty acids leads to the mono, di, tri or tetra-substituted esters. The final product is an unequal mixture of non-esterified and esterified products. [67-69]

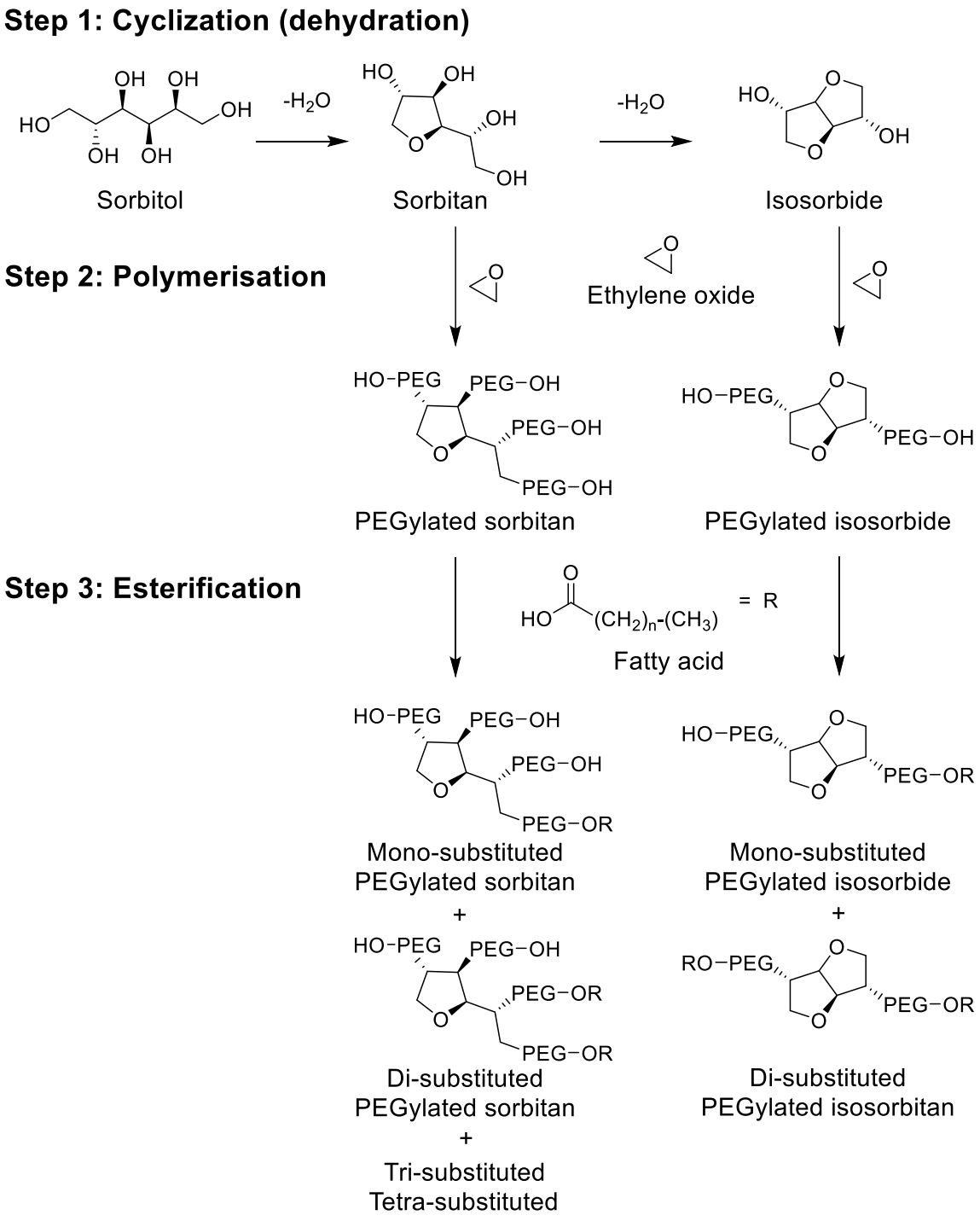

Figure 10. Generic synthesis of polysorbates from sorbitol

Also, longer reaction times or strong acids can lead to further cyclization of 1,4-sorbitan to form isosorbide that results in poly(ethoxylate) isosorbide and the corresponding esters. Even though other cyclization routes were reported (Figure 11), studies of the synthetic routes showed that their formation is minimal and in low abundance, as tested by using the acid value or by RPLC-ELSD/MS [67, 69].

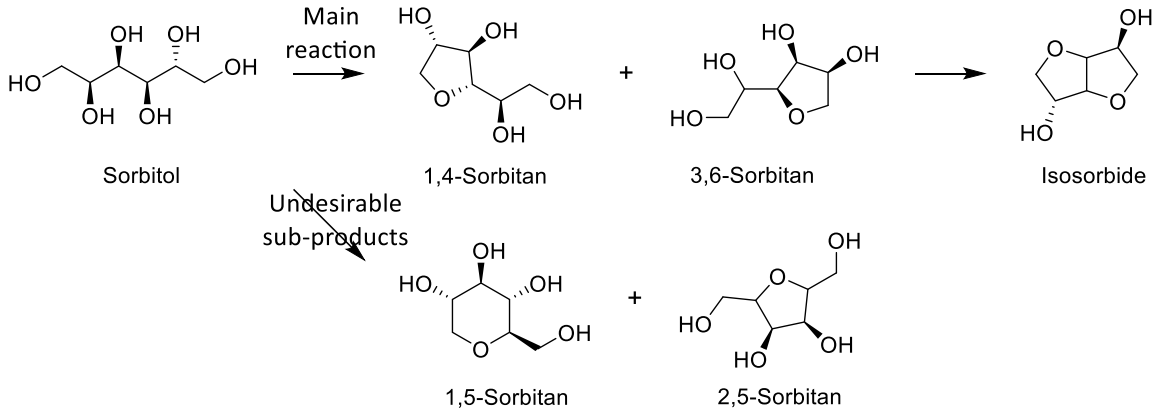

Figure 11. Dehydration of sorbitol showing the different synthetic sub-products

The selection of polysorbates depends on the HLB value required in the formulation (Table 9). The HLB value of polysorbates depends on the *w+x+y+z* value and the fatty acid substitution. The *w+x+y+z* value is the sum of the length of each PEG chain and reflects the hydrophilic sites of the surfactant (Figure 12). The hydrophobic area is characterised by the primary fatty acid and degrees of substitution. Tween® 20 tends to be used for more aqueous media, whilst Tween®80 is for more hydrophobic water-in-oil solutions [38].

Polysorbate	***w+x+y+z* value**	**Main fatty acid**	**HLB value**
Tween®20	20	Lauric acid (C12:0)	16.7
Tween®40	40	Palmitic acid (C16:0)	15.6
Tween®60	60	Stearic acid (C18:0)	14.9
Tween®80	80	Oleic acid (C18:1)	15.0

Table 9. Most common polysorbates and their HLB values. Table adapted from Pasquali *et al.* [38]

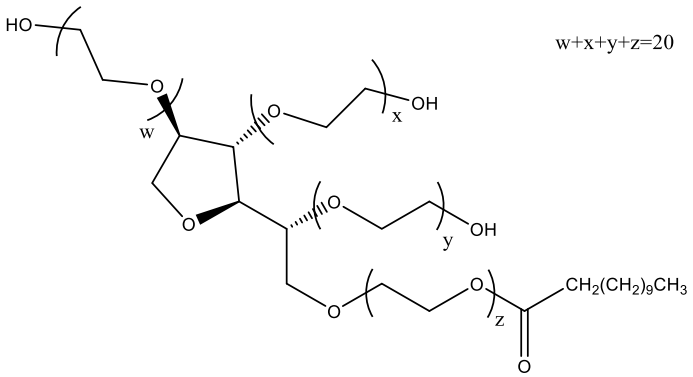

Figure 12. Chemical structure of the most abundant polymer in Tween® 20 (polyoxyethylene sorbitan monolaurate) showing the *w+x+y+z* value

1.3.6 Other poly(ethylene) glycols not investigated in this research

The amphiphilic characteristics of the PEGs make them excellent non-ionic surfactants. For example, phenyl-based PEGs are used as detergents, emulsifiers, wetting agents or defoaming agents. Nonoxynol-9 (Figure 13) is a spermicide used as an HIV /AIDS prophylactic in vaginal foams and creams; however, the current effectiveness of this PEG is yet to be drawn due to the presence of inconclusive research [70].

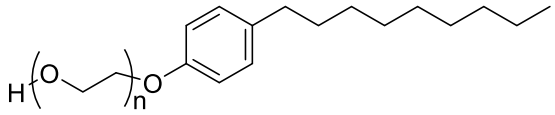

Figure 13. Structure of nonoxynol or poly(ethylene glycol) nonyl phenyl ether

Another appealing phenyl-based PEGs is Triton X-100 (4-(1,1,3,3-tetramethyl butyl)-phenyl PEG) (Figure 14 a), used in cleaning products or biopharmaceuticals. The discovery of the ecotoxicity of a degradation product of Triton X-100 led the European Chemicals Agency (ECHA) to require their removal from formulations in December 2012. Reduced Triton X-100 (Figure 14 b) and Nereid (Figure 14 c) are safer alternatives that were developed by removal of the chemical entities that led to the formation of the reported degradation product [71-75]:

a) b) c)

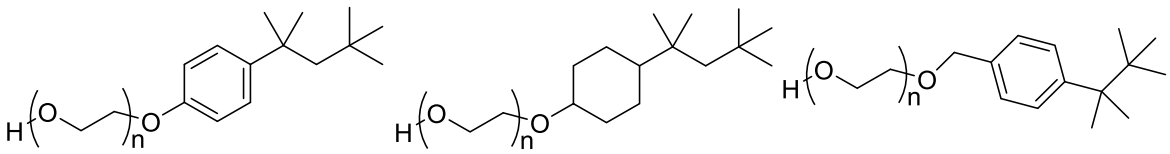

Figure 14. Chemical structures of a) Triton X-100 (n_{av} = 9), b) reduced Triton X-100 (n_{av} = 10) and c) Nereid (n_{av} = 9)

Other standard PEGs with no phenyl end groups that are non-ionic surfactants and used in cosmetics include Glucquat (lauryl methyl gluceth-10 hydroxypropyl dimonium chloride, Figure 15 a) and the PEG propylene glycol cocoates (Figure 15 b) [76, 77].

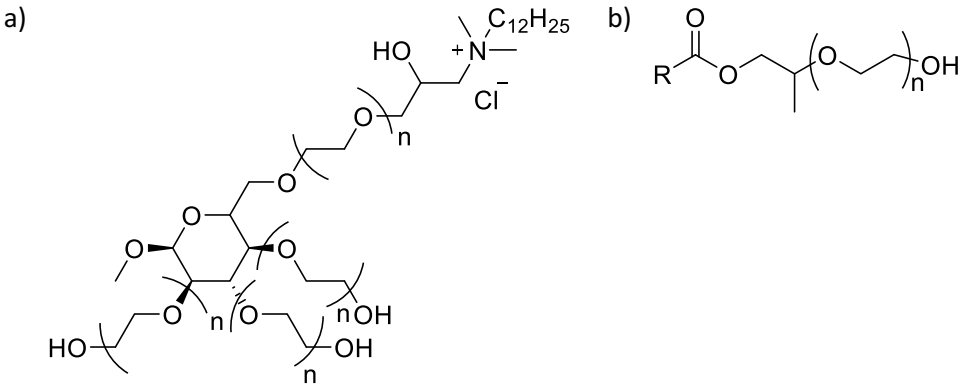

Figure 15. Chemical structures of a) lauryl methyl gluceth-10 hydroxypropyl dimonium chloride (Glucquat 125) and b) PEG propylene glycol cocoates

Well-known copolymers with PEG include poloxamers and PEG-PVA (Figure 16). Poloxamers are non-ionic triblock copolymers composed of a central hydrophobic chain of poly(propylene) oxide flanked by two PEGs resulting in their use as cosmetics and pharmaceuticals in synthesising mesoporous materials or forming hydrogels [78]. PEG-PVA or Kollicoat IR® is a multifunctional excipient used as a pill and a wet binder composed of PEG and poly(vinyl alcohol) (PVA). The most common composition is a combination of 25% PEG and 75% PVA [79, 80].

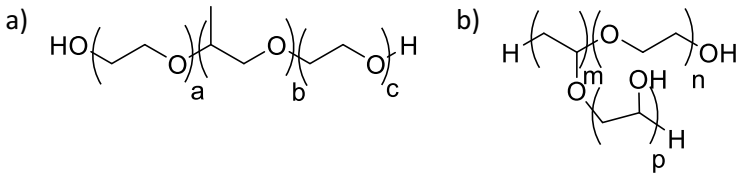

Figure 16. Examples of copolymers of PEG: a) Poloxamers or PEG-PPG-PEG (PPG: poly(propylene glycol) and b) Poly(ethylene glycol)-polyvinyl alcohol or PEG-PVA [80]

1.3.7 Regulatory aspects in the quality control of the materials

Even though PEGs are cheap low dispersed materials, approaches to control the quality of the final product are needed to ensure safety [81]. The variability of PEG batches and suppliers is understood by following the processes used during their manufacturing processes (Figure 17). The different reaction schemes and isolation procedures between manufacturers used during the synthesis of PEG materials causes heterogeneity that leads to differences in the drug residence time in plasma, immunogenicity, in-vivo adsorption, *etc.* [27, 43]. The nonuniformity in the chain length of polymeric molecules leads to an MW distribution. Also, the polymer can undergo degradation, which could lead to the formation of impurities that compromise the delivery of the

correct therapeutic dose of API (Figure 17). Consequently, the apparent differences in products in the market require control to understand the deviations between suppliers and batches.

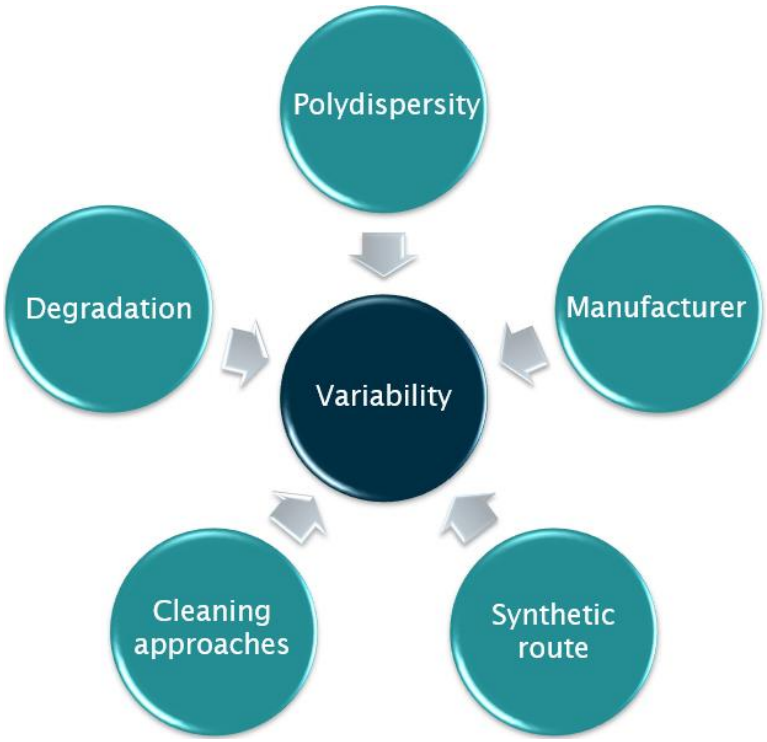

Figure 17. Attributes that alter the quality of polymeric materials and explain the differences in suppliers or batches

When the quality of PEG formulations is uncontrolled or not understood, patient safety may be impacted through potential hypersensitivity when PEG is administered intravenously, orally, or topically. Intravenous administration may result in nonspecific interactions of PEGs with blood that induce blood clotting and cell clumping, leading to embolism [82]. The administration of the mRNA COVID-19 vaccine led to some cases of patients with anaphylactic reactions caused by a release of chemicals by the immune system that generated a shock through a sudden drop in the blood pressure and a narrowing of the airways [83]. Oral administration to patients for colonoscopy led to hypersensitivity reactions due to the decreased gastrointestinal adsorption of PEG when MW increases [84]. Contact dermatitis was reported in topical formulations of dentifrice (PEG MW 4 to 20 kDa) or multivitamin tablets (PEG MW 8 to 20 kDa) [85].

Similarly, PEGylated drug molecules can display unexpected changes in pharmacokinetics. Examples include accelerated blood clearance after the second dose when using PEGylated liposomes (PEG MW 2 kDa) [86, 87]. Besides, the non-biodegradability of the material enhances these effects, suggesting the use of low MW PEGs. However, low MW PEGs (PEG 400) undergo bio-oxidative degradations by the alcohol and the aldehyde dehydrogenases into diacid and

hydroxy acid metabolites [88]. Still, toxicity significantly decreases when increasing the MW [89]. Also, low MW PEGs (< 1,000 Da) are rapidly eliminated unaltered from the body, whilst higher MW ones (over 1,000 Da) that take much longer to be metabolised [27, 43].

Rogošić *et al.* described dispersity (Đ) to quantify the heterogeneity of the MW distribution in a polymer. They discovered that the polymer Đ could not be associated with the width of the MW distribution as a deviation from the ideal Gaussian distribution occurs towards higher MWs (Poisson distribution). To quantify Đ, the number average (M_n, Equation 4) and the weighted average (M_w, Equation 5) MWs are defined based on the *ith* oligomer with n_i mer units and a M_i MW. N_i is determined based on the analytical method, typically the peak area for chromatographic analysis. M_n and M_w relate to the MW of some of the most abundant oligomers in the distribution (Figure 18). Đ is quantified by dividing these values (Equation 6). [90-92].

$$\overline{M_n} = \frac{\sum_i N_i M_i}{\sum_i N_i} \qquad \text{Equation 4}$$

$$\overline{M_w} = \frac{\sum_i N_i M_i^2}{\sum_i N_i M_i} \qquad \text{Equation 5}$$

$$Đ = \frac{\overline{M_w}}{\overline{M_n}} \qquad \text{Equation 6}$$

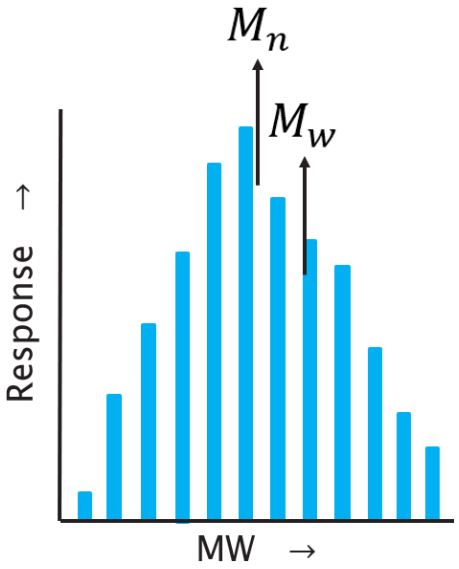

Figure 18. Resulting MW distribution from a synthetic polymerisation reaction, showing the dependence of the amount of each oligomer, the M_n, and the M_w values

Monodispersed polymers show a value of Đ of 1.00. This document uses the term *polydispersity* (PDI) instead due to its wide use in the pharmaceutical industry. M_n, M_w, and PDI quantify the

heterogeneity caused by the polymer MW distribution and can explain the performance of the polymer when included in the formulation.

Impurities are undesired components in a drug formulation. Their presence can compromise the integrity of the API structure and the formulation. Impurity profiling and allocating regions where degradation can occur are crucial to improving the synthetic and manufacturing processes. The International Council for Harmonisation of Technical Requirements for Pharmaceuticals for Human Use (ICH) provides insights into their chemistry aspects (classification, characterisation, *etc.*) and safety levels (quantitation reporting levels).

ICH classifies impurities as organic, inorganic, or residual solvent impurities. Organic impurities arise from the manufacturing and storage of the product and are sourced from by-products, intermediates, degradation products, reagents, ligands and/or catalysts. Inorganic impurities occur during the manufacturing process or are sourced from starting materials, reagents, ligands, catalysts, residual metals, inorganic salts, or other materials used in the process (*e.g.*, filter aids, charcoal). Residual solvents refer to liquids used during the synthesis. Other impurities can arise during the manufacturing processes (different polymorphic forms or possible enantiomeric impurities) or result from degradation due to light, temperature, pH, hydrolysis, or reactions occurring between the API and the excipients, between excipients, or within a closed container.

The source and potential degradation pathways must be reported, and the impurities should be investigated by comparing various batches. Based on the amount and source, the impurity must be reported (reporting threshold), characterised (identification threshold), or requires a biological safety evaluation (qualification threshold) (Table 10 to 13) [93-95].

Maximum daily dose	**Reporting threshold**	**Identification threshold**	**Qualification threshold**
≤ 2 g/day	0.05%	0.10% or 1 mg TDI (whichever is lower)	0.15% or 1.0 mg TDI (whichever is lower)
> 2 g/day	0.03%	0.05%	0.05%

Table 10. The reporting, identification, and qualification threshold of organic, inorganic, and residual solvent impurities. TDI: Total daily intake [94]

Maximum daily dose	Reporting threshold
≤ 1 g	0.10%
> 1 g	0.05%

Table 11. The reporting thresholds for degradation impurities [95]

Maximum daily dose	Identification threshold
≤ 1 mg	1.0% or 5 µg TDI (whichever is lower)
1 mg – 10 mg	0.5% or 20 µg TDI (whichever is lower)
> 10 mg – 2 g	0.2% or 2 mg TDI (whichever is lower)
> 2 g	0.10%

Table 12. The identification thresholds for degradation impurities. TDI: Total daily intake [95]

Maximum daily dose	Qualification threshold
≤ 10 mg	1.0% or 50 µg TDI (whichever is lower)
10 mg – 100 mg	0.5% or 200 µg TDI (whichever is lower)
> 100 mg - 2 g	0.2% or 3 mg TDI (whichever is lower)
> 2 g	0.15%

Table 13. The qualification thresholds for degradation impurities. TDI: Total daily intake [95]

Polymer degradation introduces undesirable impurities and possible chain cleavage that affects the oligomer distribution or can react with the API drug molecule. The examination of the synthetic and oxidation mechanisms of PEGs allows for identifying possible impurities present and potential sources of induced degradation in the API or other excipients. This approach permits the investigation of batches that fall outside the established specifications. PEG impurities originated from the initial reactants, and catalytic products result from the anionic polymerisation. The initial ethylene oxide reactant can be deactivated to produce 1,4-dioxane (Figure 19). The control of both products is required due to their oxidative properties and carcinogenic characteristics. The International Agency for Research on Cancer (IARC) classifies

ethylene oxide as carcinogenic in humans and 1,4-dioxane as possibly carcinogenic in humans, with sufficient evidence from animal experiments. [44, 69, 96-99]

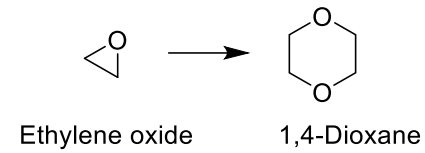

Figure 19. PEG impurity of 1,4-dioxane generated by dimerisation of ethylene oxide

PEG auto-oxidation can also generate impurities. The chain breakdown *via* an oxidative radical (Figure 20) produces formic acid and formaldehyde, a carcinogenic in humans (IARC) [99].

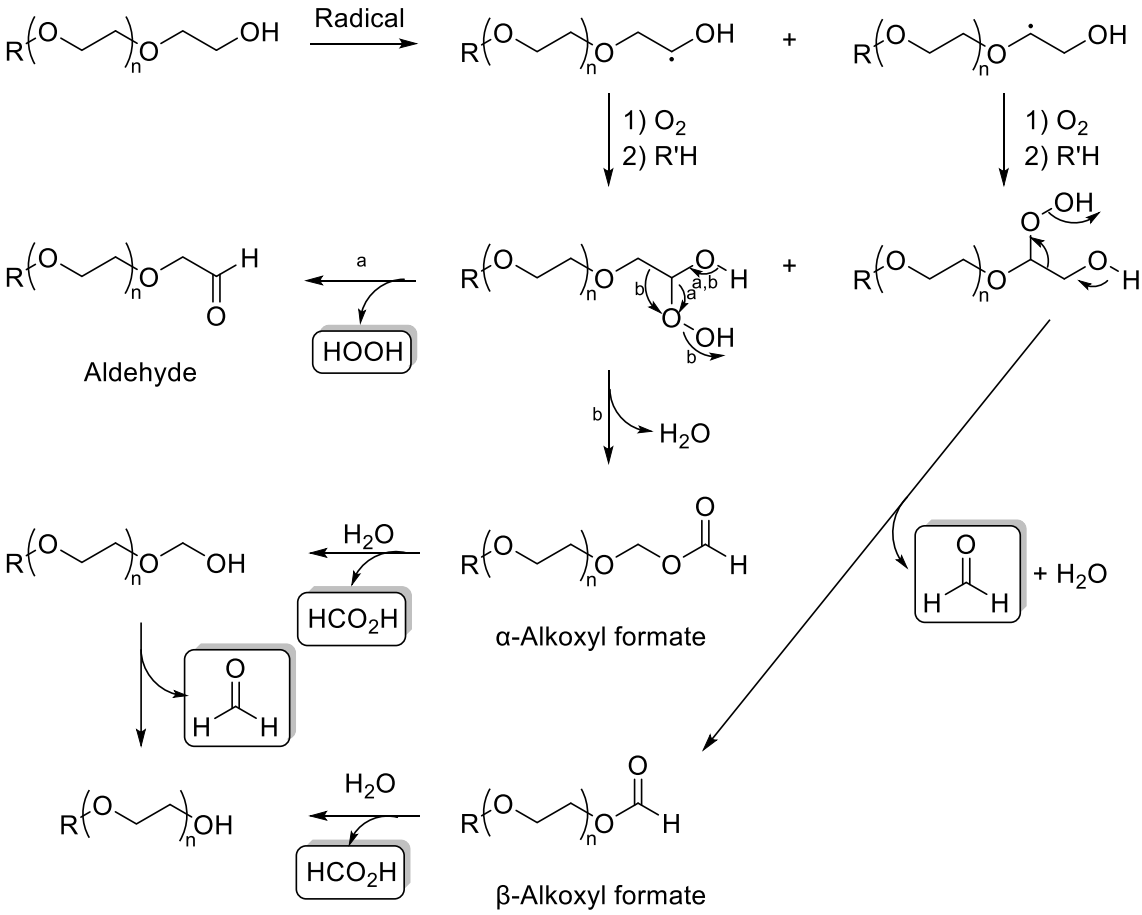

Figure 20. Degradation of the PEG chain by oxidation [97]

The presence of formaldehyde and formic acid can interact with drug molecules and result in toxic degradants. For example, the interaction of formaldehyde with drugs with primary amines can produce N-methylation *via* condensation, whilst N-formylation degradants are observed when using formic acid *via* the Eschweiler-Clarke reaction (Figure 21) [100].

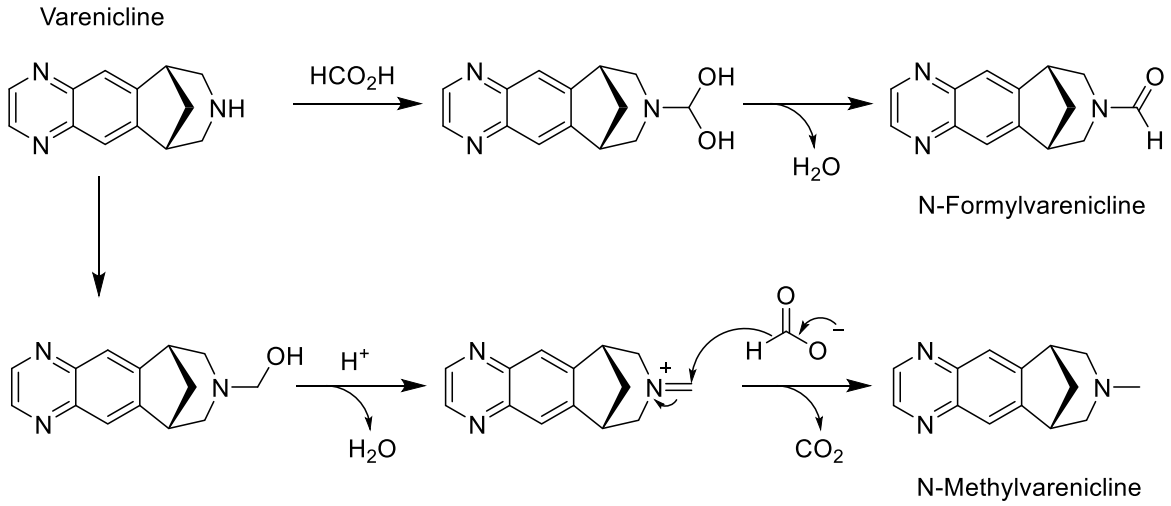

Figure 21. Degradation of varenicline to produce formaldehyde and formic acid

Formaldehyde can induce undesirable drug dimerisation, either with an amino group that degrades *via* formaldehyde/methylene-bridged dimerisation (Figure 22) [101, 102] or *via* electrophilic addition to activated aromatic rings (Figure 23) [100, 103, 104].

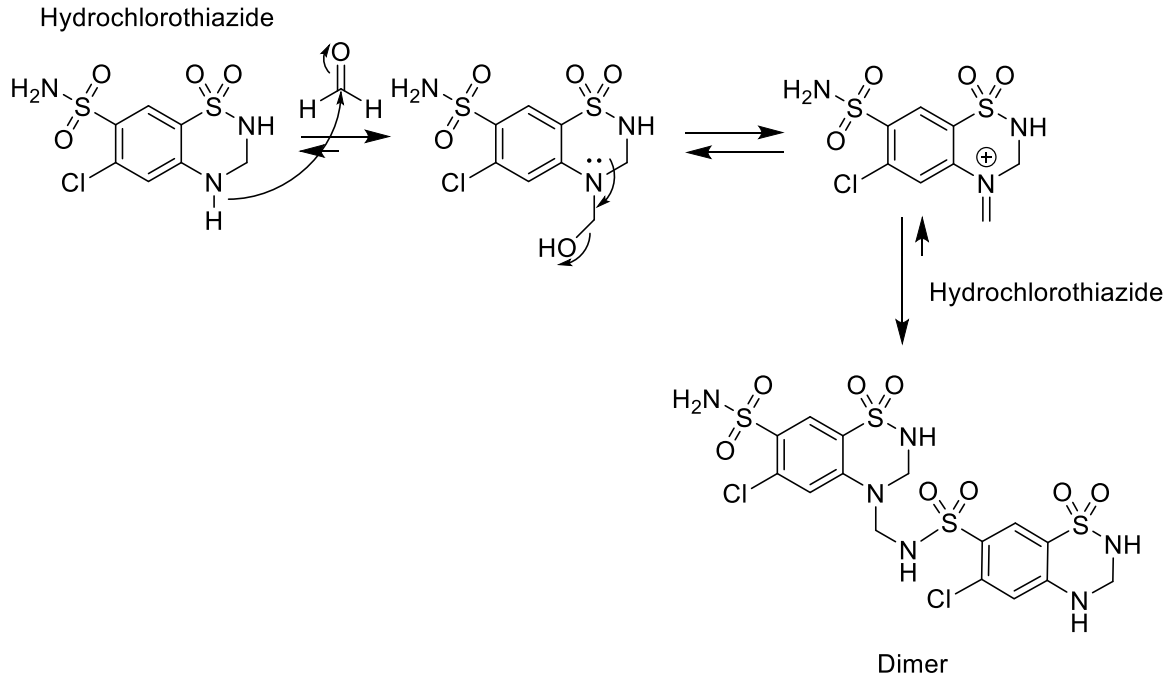

Figure 22. Drug dimerization produced by formaldehyde

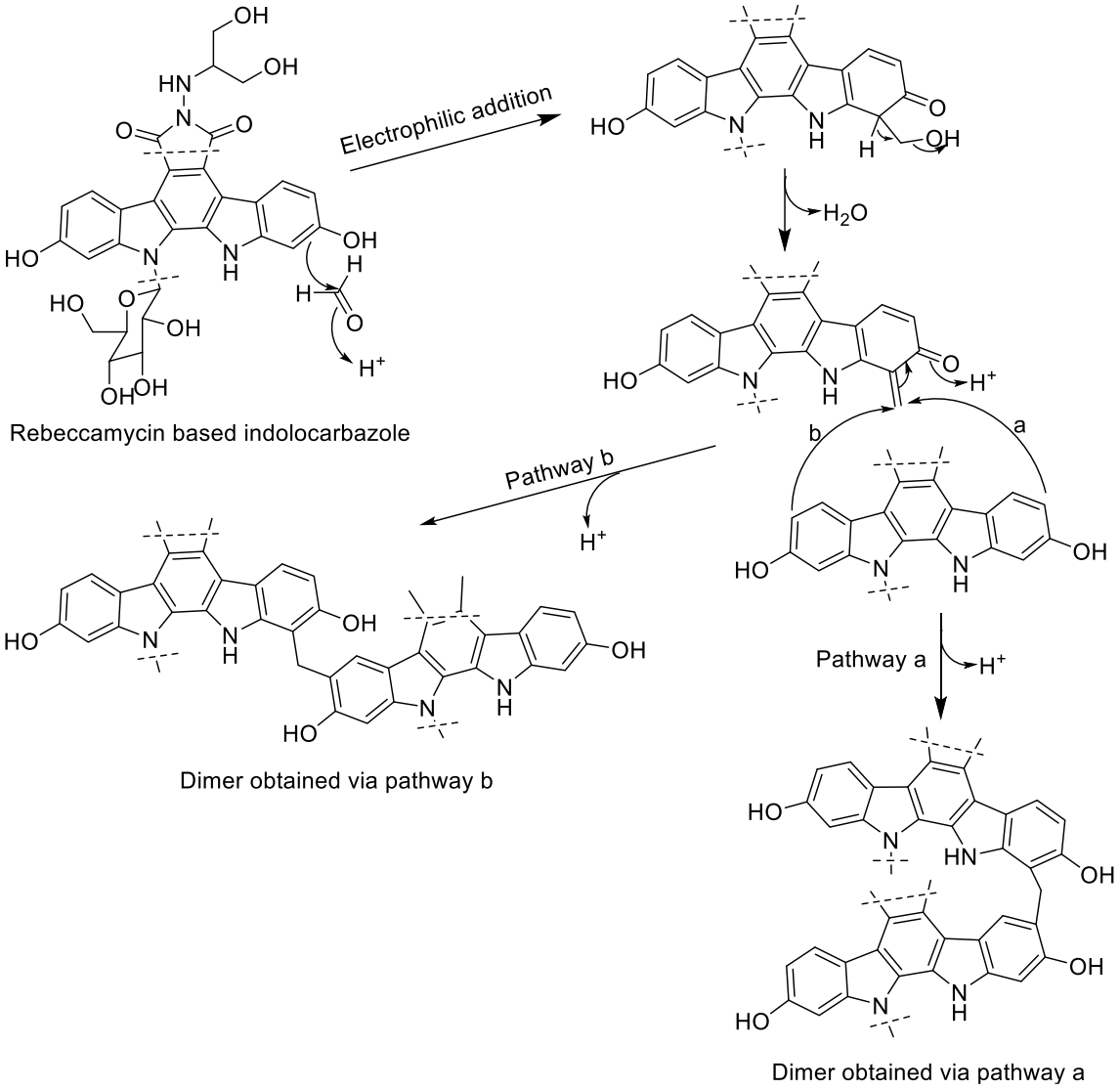

Figure 23. The dimerisation of Rebeccamycin. The electrophilic addition of formaldehyde activates the aromatic rings of the drug molecule and induces the dimerisation

Similar degradation can occur due to the double bonds in some substituted PEGs. This degradation is significant in PEGs that contain fatty acids within their structure (Figure 24) [105].

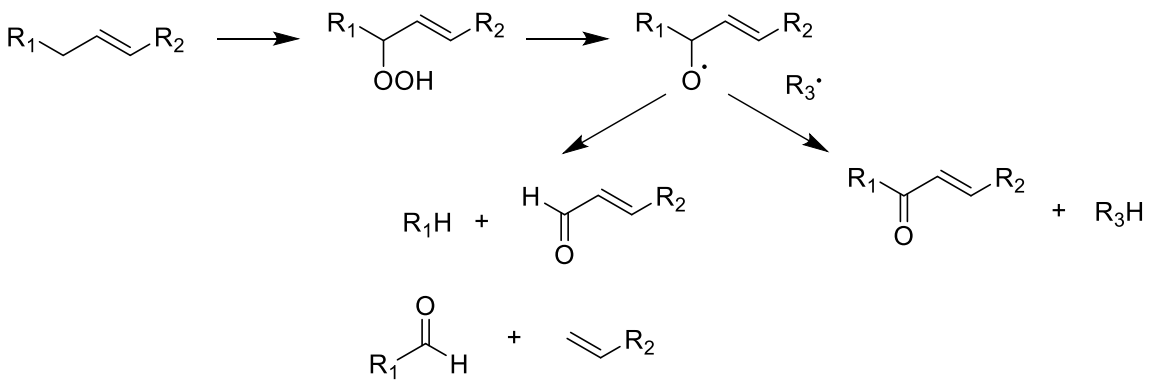

Figure 24. Oxidation of the unsaturated site in fatty acids to produce aldehydes and ketones

The variations encountered in PEGs due to the synthesis, MW distribution and impurities led to apparent differences in products on the market and a need to control differences between suppliers and batches. The overall result is that variations in the final product may be observed in their physical (melting temperature, crystallinity, loss on drying, particle size distribution, morphology, *etc.*) and chemical characteristics (delivery, drug structure integrity, *etc.*) that may compromise drug efficacy. Quantitation of PEGs and their impurities is therefore crucial in the pharmaceutical industry to control the quality of the material and ensure patient safety. [106-109]

1.3.8 Literature approaches for characterisation

1.3.8.1 Characterisation of linear PEGs

The traditional method for polymer characterisation is size exclusion chromatography (SEC), combining three detectors (refractive index, ultraviolet-visible (UV-Vis), and aerosol detector). SEC methods cannot resolve PEGs that vary in the end group, whereas their coupling to MS can lead to complex mass spectra that are challenging to interpret. Even though reversed-phase liquid chromatography (RPLC) provides some end group separation, oligomer separation of linear PEGs becomes more challenging when the MW increases (Figure 25 a) [110]. Examples of polymer separations using RPLC include the analysis of mPEG and vinyl PEG [111] or the complex differentiation of PEGs with highly hydrophobic end groups (Figure 25 b) [110]. Coupling RPLC with MS is rare for linear PEGs due to the extensive price, resulting in the use of aerosol detectors as a popular option due to their lower price and applicability to development and quality control environments as an alternative to UV detection [110, 112]. The most popular aerosol detectors are evaporative light-scattering (ELSD) and charged aerosol (CAD). However, RPLC-MS can characterise complex (polysorbates) due to a higher degree of end group separation; but a complete oligomer separation is challenging [67]. The lack of hydrophilic liquid interaction chromatography (HILIC) or normal-phase LC in the literature possibly relates to the strong retention of PEG within these separation modes, resulting in extended and impractical analysis times. Alternative approaches for characterising PEGs include capillary zone electrophoresis for PEG 400, 1000 and 1500 [113] or micellar electrokinetic chromatography for PEG with MW between 200 and 2000 [114].

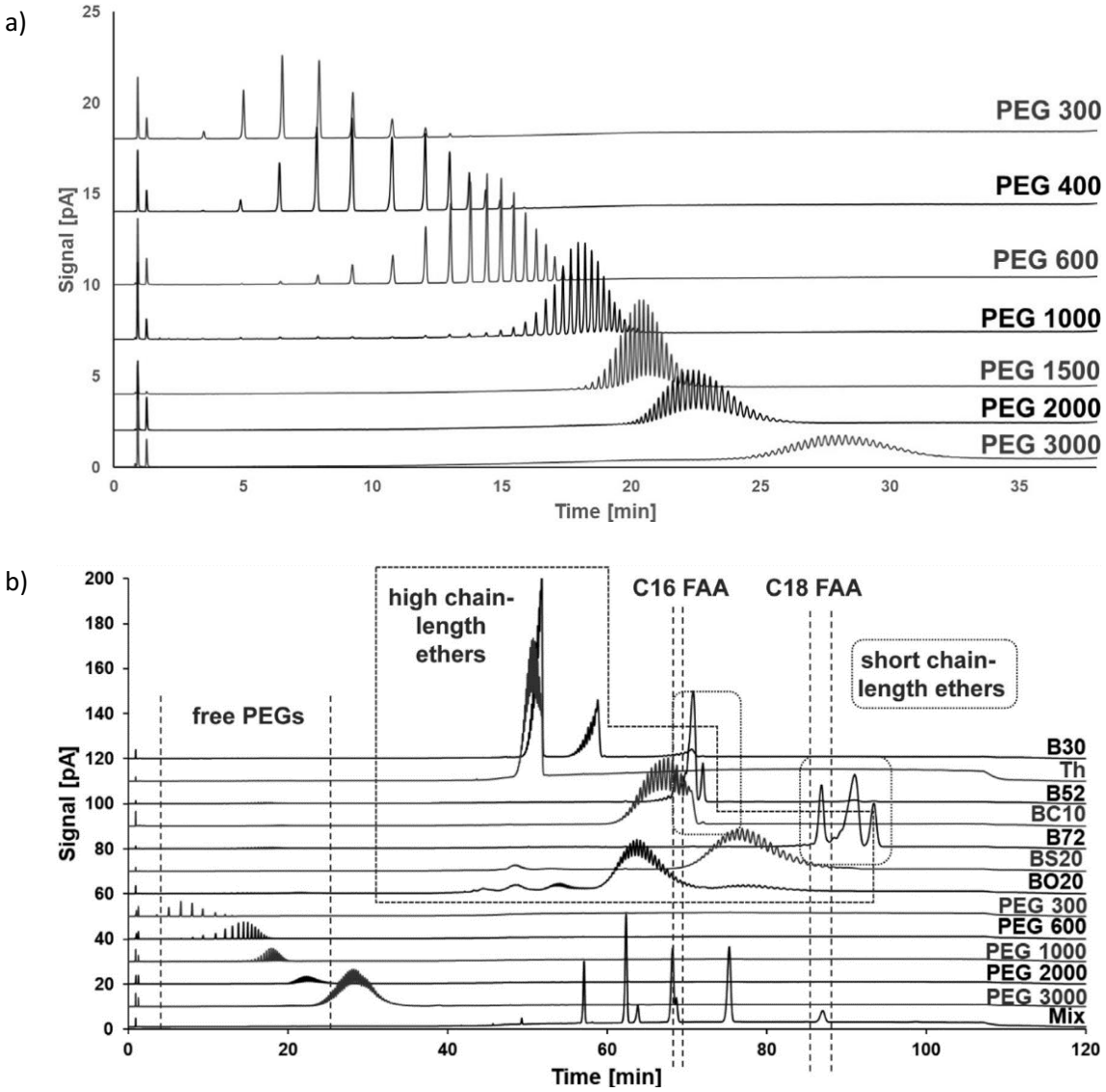

Figure 25. RPLC-CAD separation of PEGs using an endcapped C18 and H_2O + 0.1% HCOOH/CH_3CN + 0.1% HCOOH. a) Oligomer separation of PEG with alcohol end groups. b) Separation of Brij® species. FAA: fatty acid alcohol. B/BO: Brij species, Mix: mixed sample of fatty acids and fatty acid alcohols (C12:0, C16:0, C17:0, C18:0, C18:1 and C18:2). Reproduced with permission from Theiss *et al.* [110]

1.3.8.2 Characterisation of linear PEGs using SFC

The potential of capillary supercritical fluid chromatography (cSFC) for PEG characterisation was explored by Just *et al.* [115]. They successfully differentiated PEG 440, PEG 600 and derivatives (end groups: *n*-octyl, *p*-isoalkylphenyl and *p*-isononylphenyl) using cSFC coupled to flame ionisation detection (FID), CO_2, and a fused silica column with an SB Biphenyl-30 stationary phase. However, a lack of developments in the technique meant that using cSFC for PEG characterisation was

limited to higher MW polymers. Modern packed column SFC (pSFC – referred to as 'SFC' from this point on) provides improved oligomer resolution compared to LC or SEC. [116]

1.3.8.3 Characterisation of PEGylated molecules

Moreover, the absence of chromophores in the structure can be an advantage in characterising PEGylated small drug molecules that absorb in the UV-Vis range (Figure 26). Free PEG does not absorb in the UV-Vis range, whilst the PEGylated cetirizine or indomethacin do because of the presence of chromophores in the drug structure [117]. The UV transparency of pure CO_2 can be advantageous for detection of PEGs when using derivatisation reagents [118]. However, the use of aerosol detection is preferred for PEG analysis due to the lack of chromophores in the structure [116, 117, 119-121]. Coupling SFC to MS is ideal for polymer characterisation as the improved oligomer separation provides minimal ionisation suppression, increasing the MS impurity response and facilitating their profiling [122].

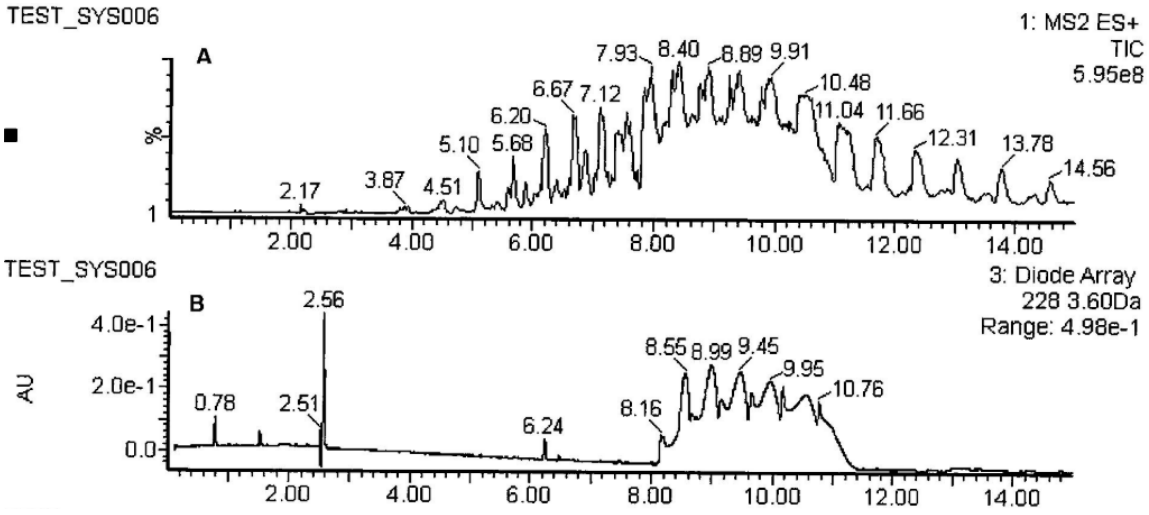

Figure 26. Analysis of PEGylated cetirizine using SFC-UV/Vis-ELSD, a BEH column and CO_2/CH_3OH. The authors use the selectivity of UV-Vis to distinguish PEGylated cetirizine from PEG, from Schou-Pedersen *et al.* [117]

1.3.8.4 Characterisation of polysorbates

Many techniques emerged for polysorbates analysis, but specific approaches require extended analysis times to elute multi-chain products (Figure 27) [110]. RPLC is the most common technique for polysorbate separation due to the enhanced separation of the different polymers based on the hydrophobicity of the end group, with minimal oligomer separation (Figure 28) [123]. The absence of chromophores in the structure suggests that the analysis would be better served by

aerosol detection or MS [124]. MS typically uses electrospray ionisation (ESI) sources and quadrupole time-of-flight (QToF) mass analysers.

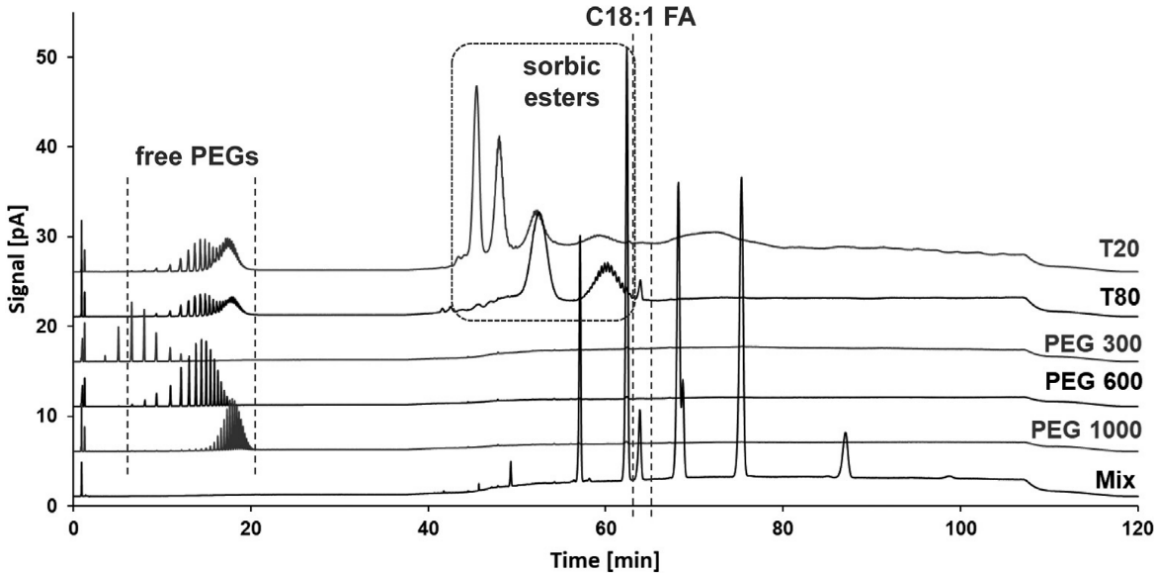

Figure 27. RPLC-CAD separation of PEGs using an endcapped C18 and H_2O + 0.1% HCOOH/CH_3CN + 0.1% HCOOH. Separation of polysorbates: T: Tween®. Mix: mixed sample of fatty acids and fatty acid alcohols (C12:0, C16:0, C17:0, C18:0, C18:1 and C18:2). Reproduced with permission from Theiss *et al.* [110]

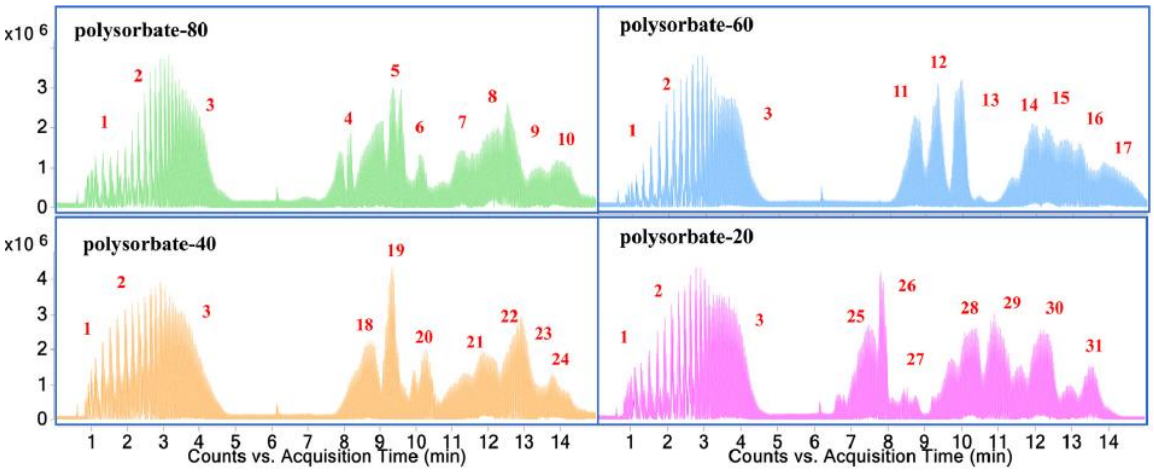

Figure 28. Separation of various polysorbates using UHP RPLC positive ion ESI QToF MS using a BEH C4 and H_2O + 0.1% HCOOH/CH_3CN. The number indicates the species observed: 1: PEG, 2: POE sorbitan (POE S), 3: POE isosorbitan (POE IS), 4: POE S monooleate (POE S MO), 5: POE IS MO, 6: POE MO, 7: POE S dioleate (POE S DO), 8: POE IS DO, 9: POE DO, 10: POE S trioleate (POE S TO), 11: POE S monostereate (POE S MS), 12: POE IS MS, 13: POE MS, 14: POE S DS, 15: POE IS DS, 16: POE DS, 17: POE S TS, 18: POE S monopalmitate (POE S MP), 19: POE IS MP, 20: POE MP, 21: POE S dipalmitate (POE S

DP), 22: POE IS DP, 23: POE DP, 24: POE S tripalmitate (POE S TP), 25: POE S ML, 26: POE IS ML, 27: POE ML, 28: POE S DL, 29: POE IS DL, 30: POE DL, 31: POE S DL. Reproduced with permission from Wang *et al.* [125]

SFC-MS has been applied to separate complex PEG species. Poulton *et al.* proposed the first modern SFC-ELSD-MS method that separated PEGs with methoxy and acidic end groups; however, details about the mobile phase selection, the make-up solvent used, or the ions observed in the mass spectra were not reported [126]. Ma *et al.* reported the benefits of increased peak capacity and improved separation achieved when analysing octyl phenol and fatty alcohol ethoxylates using SFC coupled with ion mobility mass spectrometry (IMMS) [127].

1.3.8.5 Advantages of MS for characterisation

MS is excellent for polymer characterisation due to the added value of the technique to achieve accurate mass measurements, especially for high-resolution instruments [128]. Characterisation of end groups and repeating units occurs *via* a linear fitting of the monoisotopic masses of the oligomers against their repeating unit value [129, 130]. Also, representations of the Kendrick mass defect can be plotted to aid characterisation [131]. When using this representation, the oligomer ions in the mass spectrum are classified based on the differences in the repeating unit and end groups, independently of the charged state.

Direct infusion mass spectrometry approaches such as matrix-assisted laser desorption/ionization MS (MALDI MS) are extended for their applicability in polymer analysis. Examples are the work of Hoogland *et al.* for the characterisation of Triton™ X-405 and sulfated PEG in acrylic paints and the work of Ayorinde *et al.* for polysorbate analysis [132, 133]. However, Ayorinde *et al.* showed that MALDI ToF MS is limited when characterising commercial Tween® 80 samples due to the presence of isobaric species [133]. The higher resolution achieved by Fourier-transform ion cyclotron resonance (FT-ICR) MS with a 12T magnet can resolve the isobaric ions in Tween® 80; however, coupling to chromatography is challenging due to the potential of overloading the cyclotron cell with too many ions, which leads to a reduced system performance due to space-charge effects [134]. The use of ion mobility MS (IMMS) adds an extra level of separation that allows unravelling the sample complexity through its ability to differentiate molecules in terms of charge, shape, and size [127, 135-137].

Coupling MS with chromatography is still preferred as ion suppression is minimised with the added potential of using ion maps to identify trends in polymeric species at different ionisation charge states. Ion maps are 3D representations of the chromatographic retention time (t_R) on the

x-axis, the ion *m/z* value on the *y-axis* and the reconstructive ion current chromatogram (RICC) of the ion on the *z-axis* [127].

Many techniques emerged for more complex PEG analysis to deal with the material complexity, with nuclear magnetic resonance (NMR) spectroscopy or RPLC being the most common approach. NMR spectroscopy was applied to identify different species of polysorbates [138] whilst the separation provided by RPLC enhanced the analysis of these excipients [123]. RPLC methods allow for the separation of several chemical entities based on the hydrophobicity of the end group of each polymer with minimal separation of the oligomers [123, 139]. The absence of chromophores in the PEG structure led to MS or aerosol detection (ELSD or CAD) being the preferred approach [110, 124, 126].

1.3.9 Literature approaches for quantitation

1.3.9.1 Quantitation using SEC

The essential characteristics (*i.e.,* polymer MW distribution, chemical composition, and end group composition) are mainly determined by established analytical techniques such as SEC and nuclear magnetic resonance (NMR) spectroscopy. SEC with different detectors (UV-Vis, light scattering detectors, *etc.*) is the standard technique for quantitation in the pharmaceutical industry [128, 140]. The use of aerosol detectors has demonstrated the accurate calculation of the number average, weight average MW and polydispersity of linear polymers [116, 119-121, 126]. In SEC, the elution volume of polymeric standards based on polystyrene or PEG is correlated to the unknown polymer elution volume [141]. However, this approach cannot be extrapolated to other separation techniques as the elution volume of the polymers/oligomers cannot be obtained. Additionally, quantitation using UV-Vis or fluorescence is common; however, the lack of chromophores within the core PEG structure means that this detector is only possible when chromophores are part of the chemical structure of the end groups - *i.e.,* for Triton or some PEGylated molecules [142]. NMR spectroscopy can quantify polymers to some degree [138].

1.3.9.2 Quantitation using MS

Quantitation using MS is challenging due to the complexity of the mass spectra generated [128, 143, 144]. One approach is the use of deconvolution approaches to the mass spectra. A deconvolution approach is a mathematical algorithm to group multiply charged ions in a mass spectrum into the MW of the molecule. Gruendling *et al*. proposed the most successful deconvolution approach using poly(methyl methacrylate) mass spectra with data generated using SEC positive ion ESI MS

[143]. Their deconvolution approach took advantage of the complementary strengths of RI detection to separately measure the ESI mass spectra and deconvolution via Maximum Entropy® (MaxEnt). MaxEnt is a deconvolution algorithm that uses Bayesian statistics to predict the most likely molecular mass spectrum based on similarities of patterns after several iterations (see Chapter 5, page 185, to learn more about deconvolution algorithms) [145-147]. Alternatively, MALDI MS allows for quantifying without using chromatography [148]; however, inconsistent sample preparation leads to an uncertainty in the resulting polymer PDI, resulting in differences compared to SEC data [122]. Also, mass discrimination was observed due to the detector, laser power and cationisation-dependent effects. This disadvantage can be overcome in polymer samples that exhibit broad MW distributions (PDI exceeding 1.1) by offline or online pre-fractionating using preparative SEC [149]. Some attempts using stable isotope dilution [150] were successfully applied with [151, 152] or without [153] internal standards (ISTD), although the incorporation of ISTD is rare. The inclusion of polymeric ISTD adds unnecessary complexity, whilst using small molecules can potentially lead to ion suppression. Other approaches to increase the method precision include the creation of an absolute molecular mass distribution polymer standard based on the Taylor expansion approach (a mathematical algorithm) [154] or the isolation of oligomers to produce certified reference materials [155]. The characteristic PEG fragment (*m/z* 133) obtained *via* collision-induced dissociation (CID) fragmentation can quantify PEGylated proteins and free PEGs as the fragments are distinguishable [156, 157]. Nevertheless, the similarities in the fragmentation routes of more complex PEGs result in a challenge when tracking back the fragmented mass spectra to assign the polymer end group. Lingaityte proposed a SFC positive ion atmospheric pressure photoionisation (APPI) MS approach for methylene diphenyl diisocyanate polymer quantitation and proved a constant APPI ionisation efficiency independent of the number of aromatic rings and equal for different functional groups [158].

1.3.9.3 Challenges in quantitation data comparison

Additionally, identifying the intrinsic differences between quantitation approaches are required to ensure consistency and facilitate data comparison between instrumentation set-ups. This evaluation is essential when quantifying large biomolecules and polymers, as many aspects can affect the ions produced in the ion source [159]. Figure 29 shows that the sample preparation [154], the ion source desolvation environment [160-162] and the ion source [163, 164]/mass analyser [165, 166] design can result in slightly differences in the reported M_n, M_w and PDI values of polymers. Trathnigg and Maier reported 2% differences between chromatographic techniques with several detectors, SEC with a refractive index or light scattering detector and MALDI-ToF MS for PPG 450

[122]. Poulton *et al.* showed slight differences in the reported PDI of PEGs with different end groups between SEC coupled to a triple detector array to those obtained using SFC coupled to ELSD and MS of up to 2.5% [126].

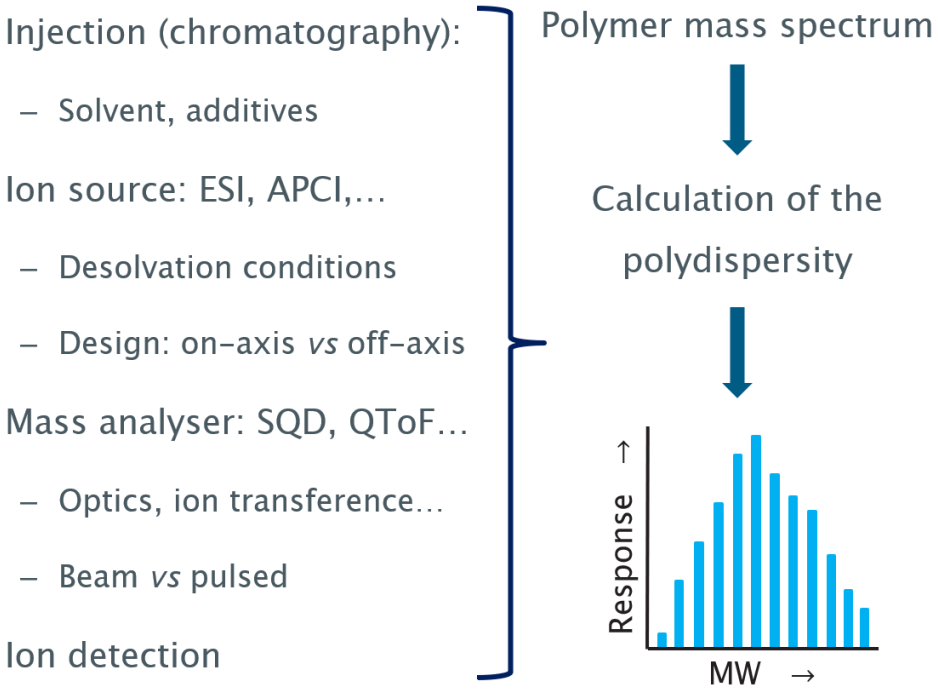

Figure 29. Parameters that contribute to the variability in the reported value of M_n, M_w and PDI values of polymers

1.4 Cyclodextrins

1.4.1 Cyclodextrins as hosts for drug molecules

Cyclodextrins or CDs are cyclic oligosaccharides composed of several glucose units linked with α-1,4 glycosidic bonds in the form of a ring. These excipients are produced by enzymatic degradation of starch or a starch hydrolysate using 1,4-α-D-glucan 4-α-D-(1,4-α-D-glucano)-transferase (CGTase). CGTase hydrolyses the starch, catalyses different transglycosylation steps (intermolecular coupling, disproportionation, *etc.*), reacts at the α(1-4) positions of the oligosaccharides and modifies the length of non-cyclic dextrins [167, 168]. Either solvent-based or non-solvent-based processes are used for their manufacture. Solvent-based processes use an organic solvent to direct the reaction and prevent the growth of microorganisms and a complexing reagent to selectively control the synthesis to produce one type of CD, whilst a mixture is obtained in non-solvent-based processes [167, 168].

CDs are named based on the number of glucopyranose units: the α-CD has six, the β-CD has seven, and the γ-CD has eight units (Figure 30). Each glucose in the CD has a rigid chair conformation, shaping the molecule into a hollow truncated cone (Figure 31). The OH-2 and OH-3 are on the broader rim and relatively rigid, while the OH-6 is on the narrower rim and can rotate, allowing partial cavity blockage [169]. The H-3, H-5 and glycosidic oxygen are located inside the hydrophobic cavity, whilst the other protons (H-1, H-2, H-4, and H-6) are in the hydrophilic outside region.

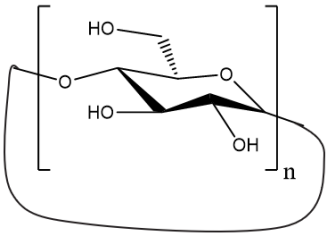

Figure 30. Chemical structure of a CD. n=6: α-CD, n=7: β-CD and n=8: γ-CD

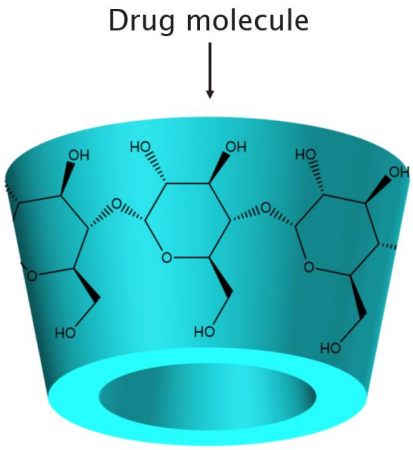

Figure 31. 3D-molecular structure of a CD, highlighting the truncated cone and the cavity that allows drug allocation

Their capacity as complexing agents explains the use of CDs in formulations as they can allocate hydrophobic drug molecules in a host-guest inclusion complex as electrostatic, van der Waals and hydrogen bonding interactions occur [169-173]. CDs are ideal polymeric excipients that improve the solubility and bioavailability of liposoluble drug molecules and prevent their degradation [170]. The inclusion of drugs in CDs has been proven to reduce gastrointestinal and ocular irritation, mask unpleasant smells or tastes, prevent drug-drug or drug-additive interactions within a formulation, or convert oily or liquid drugs into microcrystalline or amorphous drugs. [26]

1.4.2 Synthetic challenges in cyclodextrin modification

Modifications can happen in the ring size, substituent, substitution position, and substitution pattern. Increasing the ring size (γ > β > α) leads to a larger cavity for hosting larger drug molecules. Substitution can occur in OH-2, OH-3, and OH-6; however, their reactivity is different (Figure 32): OH-2 is more acidic and can form reactive oxyanions, OH-3 is less accessible and least reactive, whilst OH-6 is the most nucleophilic and basic. [169-171, 173]

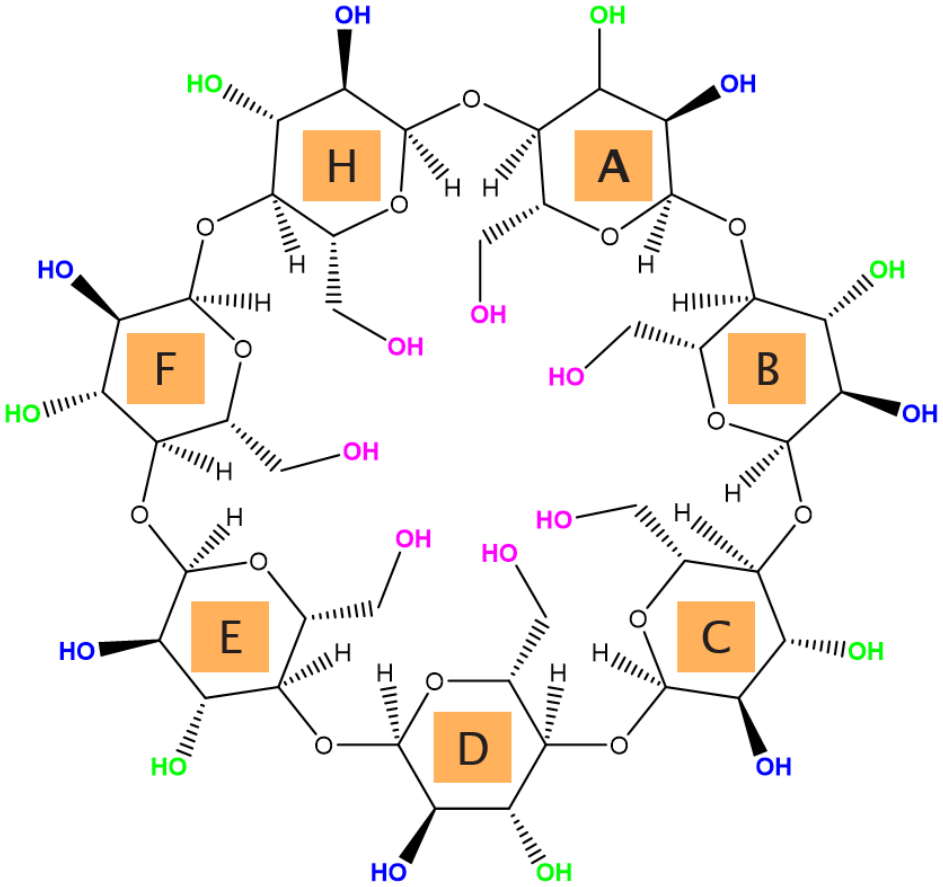

Figure 32. Planar representation of a β-CD indicating the three types of hydroxy groups in the molecular structure (blue for OH-2, green for OH-3 and pink for OH-6). The letters inside the glucose units indicate the terminology in the CD ring when fragmenting

Substitutions in the OH-2 and OH-3 may extend the hydrophobic cavity, whereas substituents at OH-6 may narrow the cavity openings [174]. Also, the type of substituent alters the encapsulation as specific substituents can block the encapsulation by steric hindrance of the entrance of the cavity whilst others extend it, whereas charged substituents vary the complexation capacity. Even with the existing competition of the three hydroxy groups for the derivatising agent, regiospecificity can be achieved using reagent excess or appropriate capping reagents [175]. Note that the selectivity of the different glucose units varies when a substitution occurs. The substitutions of

pharmaceutical interest are the hydroxypropyl derivatives of β and γ-CD, the randomly methylated-β-CD, sulfobutylether-β-CD, citrate-β-CD, succinyl-β-CD, and the branched CDs such as glucosyl-β-CD [171, 172, 176]. This document only focuses on the (2-hydroxypropyl)-β-cyclodextrin derivative (2HPBCD).

1.4.3 Pharmaceutical uses of (2-hydroxypropyl)-β-cyclodextrins

The extended use of the 2HPBCD (Figure 33) comes from a dramatic increase in aqueous solubility compared to the β-CD [175]. Janssen Pharmaceutica (1983) [177] and the National Institute of Health (1984) [178] concurrently patented their use as an excipient. Over 3000 articles and 1000 patents on HPBCD in the literature recognise the importance of this excipient for the industry [179]. Its uses cover oral, rectal, dermal, ocular, and parenteral formulations, mainly solutions that take advantage of the solubilising and stabilising effect of HPBCDs [180]. One of the most famous applications is their use in patients with Niemann Pick Type C disease. This fatal metabolic disorder enhances cholesterol accumulation in the brain and other organs. Apart from delivering the appropriate drug molecule for treatment, the use of HPBCD slows down the progression of the disease due to the encapsulation of cholesterol within the cavity. Other applications when HPBCDS showed advantages over other excipients are the treatment of Alzheimer's, atherosclerosis [181, 182], HIV/AIDS [183], influenza A [184], Herpes simplex [185], Vibrio cholera [186] and leukaemia [187].

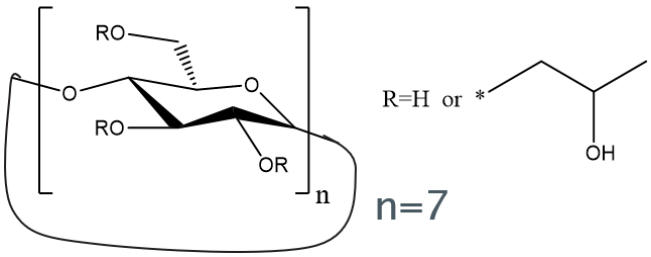

Figure 33. 2HPBCD used in this research project

1.4.4 Synthetic challenges of (2-hydroxypropyl)-β-cyclodextrins

Pitha highlighted the synthetic challenge and complex analysis of 2HPBCD in 1992 at the 6th International Cyclodextrin Symposium in Chicago: *"HPBCDs mixtures are beautiful if properly characterised"*. The synthetic reaction of 2HPBCD occurs *via* hydroxypropylation of the β-CD in the OH-2 using propylene oxide. However, the similar reactivity of three OH groups means that specific regioselectivity is not achieved, and a mixture of isomers with various degrees and

substitution patterns is obtained (Figure 34) [188, 189]. Furthermore, hydroxypropylation in the alcohols of the hydroxypropyl chains (HP) can lead to further reaction subproducts.

Understanding the substitution pattern and the degree of substitution (DS) of the final product is essential in determining the solubility and complexation capacity of the final excipient and identifying how the 2HPBCD allocates the drug and increases its solubility. DS refers to the average number of substituents in the initial HPBCD molecule. Even though DS can vary from 1 to 21, the acceptable range is between 2.8 to 10.5 (0.4 to 1.5 substituents per glucose unit). The DS of the HPBCD alters the solubility of the final product in H_2O as values below 2.5 show poorer solubility than β-CD [190], whilst HPBCDs with DS over 3 are highly soluble [188].

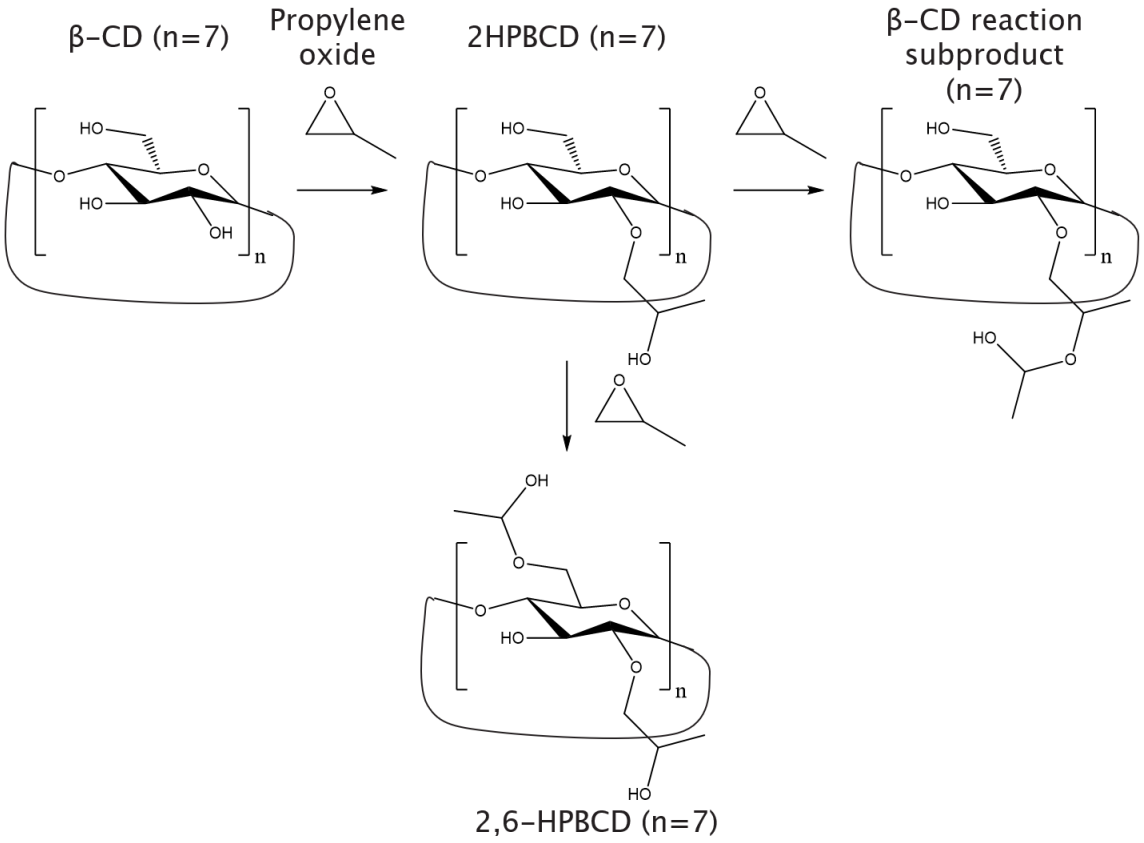

Figure 34. The synthetic reaction of 2HPBCD showing examples of subproducts and the presence of molecules with isobaric masses

1.4.5 Literature approaches for characterisation of (2-hydroxypropyl)-β-cyclodextrins

The non-selective synthesis of 2HPBCD results in a complex mixture that is challenging to characterise. Approaches that estimate DS include NMR spectroscopy, reductive-cleavage method and methylation analysis, differential scanning calorimetry [191], microcalorimetric titration [192], thermogravimetric-differential thermal analysis [193], Fourier transform infrared spectroscopy

[193], near-infrared reflectance spectroscopy [194], or colourimetric determination of 1,2-propanediol [195]. Even though the standard Pharmacopoeia approach is NMR spectroscopy, no information about the isomer distribution is provided. Other techniques include gas chromatography (GC)-MS, RPLC-ELSD [189, 196, 197], RPLC-MS [189, 198], MALDI MS [189], IMMS or 2D NMR spectroscopy [189]. Isobaric masses must be considered during MS analysis, as hydroxypropylation of the OH groups on the β-CD or in the HP chains leads to subproducts with isobaric masses and an extra level of complexity. No applications were found that use SFC for 2HPBCD characterisation and analysis; the only application of SFC in CD analysis was reported by Salvador *et al.* to characterise methylated β-CDs.

1.5 Instrumentation

1.5.1 Chromatography

Chromatography is an analytical technique to separate mixtures between stationary and mobile phases. The separated components are introduced in a detector (hyphenated techniques), either a UV-Vis, an aerosol-based, a mass spectrometer or other detectors (see sections 1.5.2 page 62 and 1.5.3 page 68 for more information).

1.5.1.1 Chromatographic nomenclature

A chromatogram represents the chemical separation of a mixture based on the peak response of each analyte at different elution times of the analyte (t_R). The main components are (see Figure 35): (i) the hold-up time (t_0) is the time a non-retained analyte takes from injection to elute, (ii) the retention time (t_R) is the time the analyte spends in the mobile phase, and (iii) the peak width of the analyte is measured at the base of the peak *(w)* or half-height *($w_{1/2}$)*.

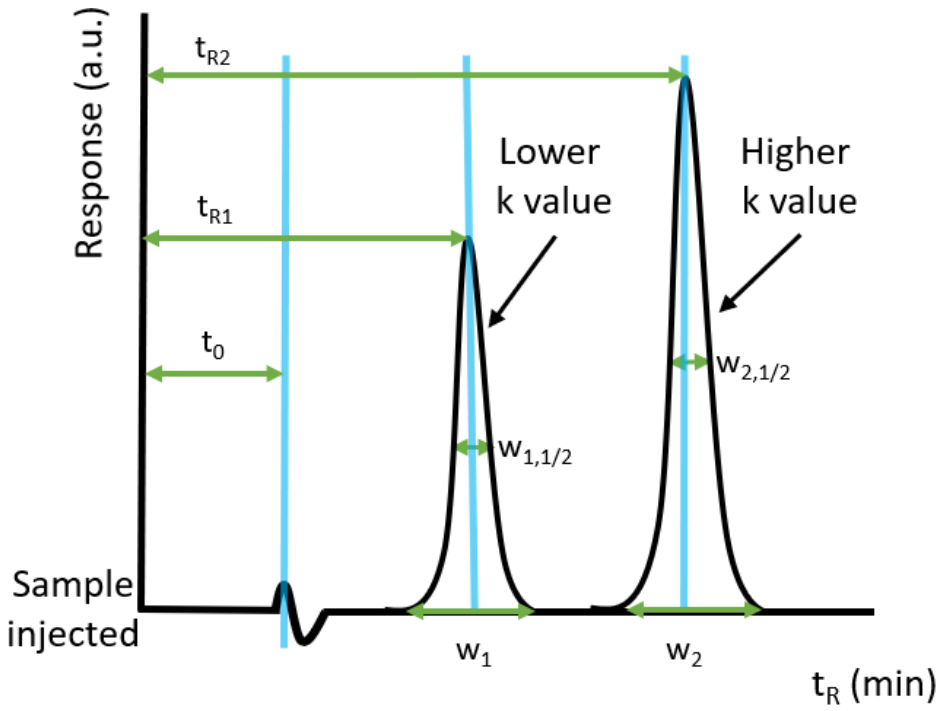

Figure 35. Data analysis of a chromatogram for the separation of two analytes [199]

Based on these parameters, the retention factor (*k*) is a value that represents the distribution of each analyte between the mobile and stationary phases (Equation 7).

$$k = (t_R - t_0)/t_0 \qquad \text{Equation 7}$$

During the separation, the mobile phase continuously flows through the stationary phase. For one analyte, each equilibrium that the analyte encounters between mobile and stationary phases when passing through the analytical column is called a theoretical plate. The separation efficiency of each analyte (N) relates to the number of theoretical plates the analyte encounters and links to the band broadening of the peak (Equation 8).

$$N = 5.54\left(\frac{t_R}{w_{1/2}}\right)^2 \qquad \text{Equation 8}$$

The faster the kinetics of these equilibria, the chromatographic peak shapes of the analyte are sharper; however, a loss in efficiency in the column due to three kinetic diffusions (Eddy, longitudinal and mass transfer diffusions) compromise the chromatographic resolution achieved and results in a band broadening of the chromatographic peak shape (see Figure 36).

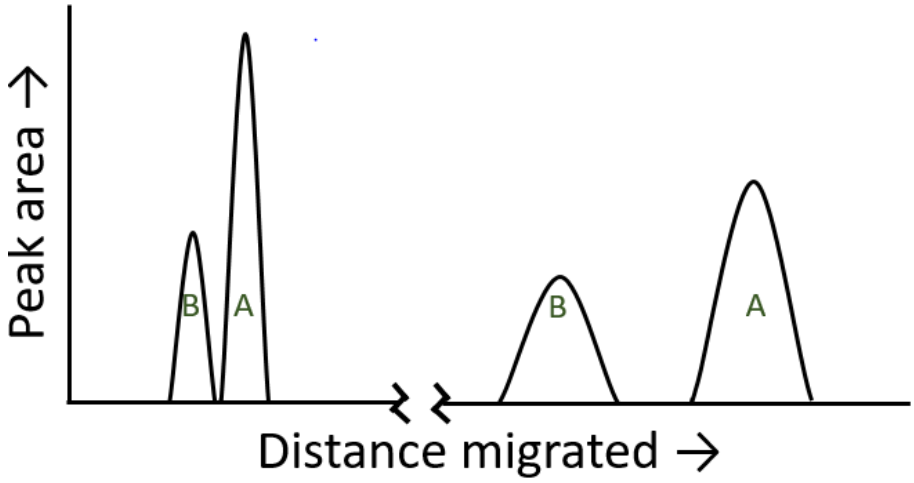

Figure 36. Relationship between the band broadening observed with the time the analyte spends in the column (assuming isocratic mobile phase conditions)

Eddy diffusion (A) refers to the multiple paths the analyte can have due to the packing distribution inside the analytical column, producing a dispersion of the molecules (see Figure 37). The more paths available, the larger A and the broader the chromatographic peak. Also, the more regular and spherical-like the particle shape is, the easier the packed column bed is formed. The smaller the particle size (d_p) and the more compact the particle distribution (λ), the time that the analyte spends on the column is reduced, and the lower A (Equation 9).

$$A = 2\lambda d_p \qquad \text{Equation 9}$$

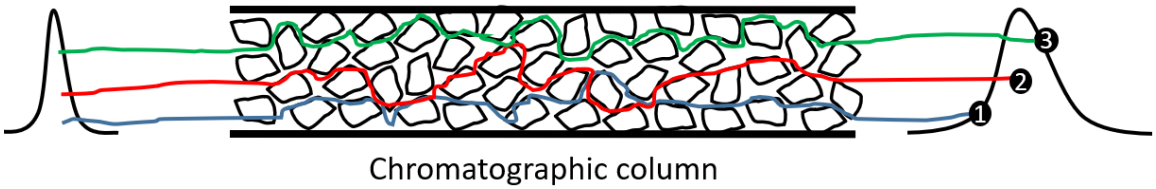

Figure 37. Schematic of the Eddy diffusion effect (A). Notice the band broadening due to different paths that the same analyte might have in the chromatographic columns [199-201]

The longitudinal diffusion (B) relates to the solute diffusion along the column in the mobile phase (Figure 38) and depends on the column packing (γ) and the analyte diffusion coefficient (D_{MP}) (Equation 10). This parameter is essential as concentration gradients diffuse the analytes from the centre of the band to the edges. Minimal dead volumes (shorter tubing and correct fitting) and higher flow rate reduce B as the most significant diffusion occurs in the flow direction.

$$B = 2\gamma D_{MP} \qquad \text{Equation 10}$$

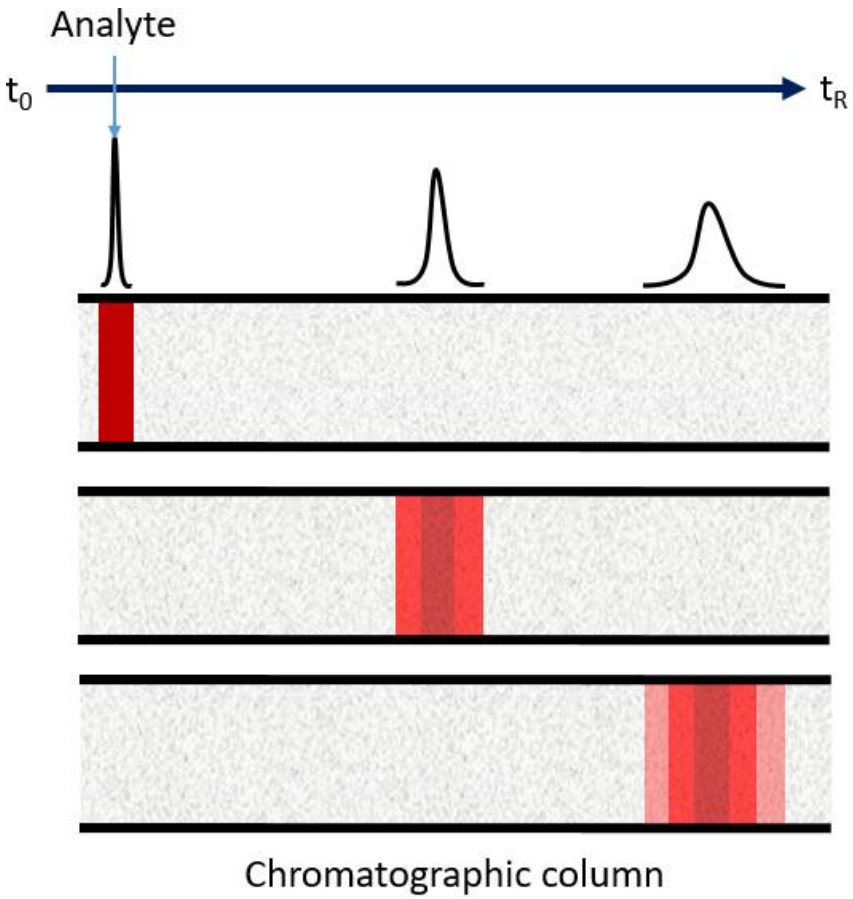

Figure 38. Schematic of the longitudinal diffusion effect, B. Notice the band broadening [199-201]

The mass transfer diffusion (C) refers to the dynamic equilibria of transference of the analyte between the mobile and stationary phases and relates to two mass transfers, C_{MP} and C_{SP}: C_{MP} (Figure 39) is the mass transfer that occurs due to the differences in the rate of diffusion of the analyte between the mobile phase outside the pores of the support (flowing mobile phase) and the mobile phase within the pores of the support (stagnant mobile phase).

The mass transfer from C_{MP} contributes to the band broadening depending on the size, shape, and pore structure of the packing material (ω), the particle diameter (d_p), the diffusion of the analyte in the mobile phase (D_{MP}) and the flow rate of the solute through the column (Equation 11). The deeper an analyte travels inside a pore, the higher C_{MP} and the broader the band observed.

$$C_{MP} = \omega d_p^2 / D_{MP} \qquad \text{Equation 11}$$

The smaller the particle, the shallower the pores and a reduced mass transfer is achieved. At lower flow rates, the molecules that do not enter the pores do not travel as far along the column as those that penetrate further into the pore, resulting in lower C_{MP}. At the same time, an

increase in column temperature increases the diffusion rate of molecules out of the pores and reduces the band broadening effect.

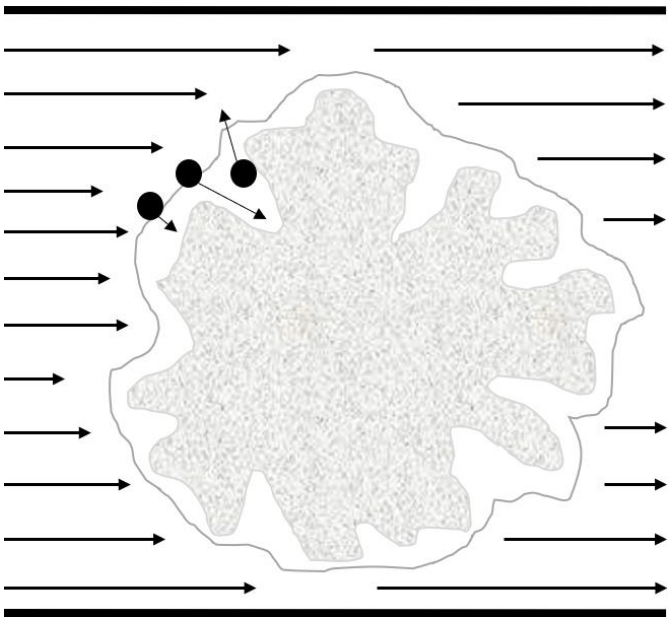

Figure 39. $C_{MP:}$ mass transfer related to the movement of the analyte inside/outside the pores in the stationary phase particles [199-201]

C_{SP} (see Figure 40) is the mass transfer that occurs due to the movement of the analyte between the stationary phase and the mobile phase.

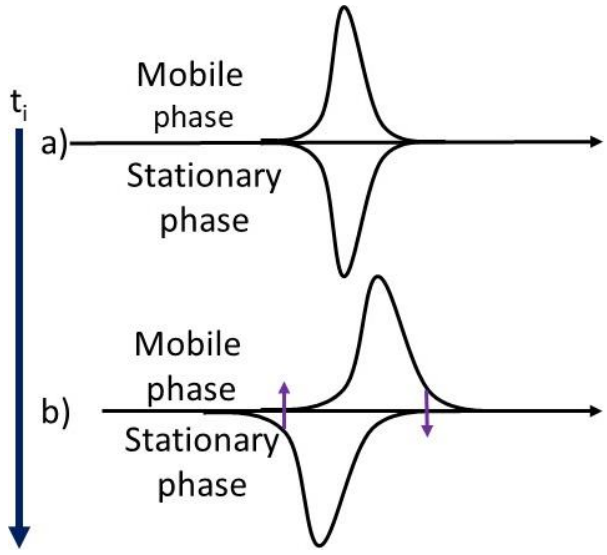

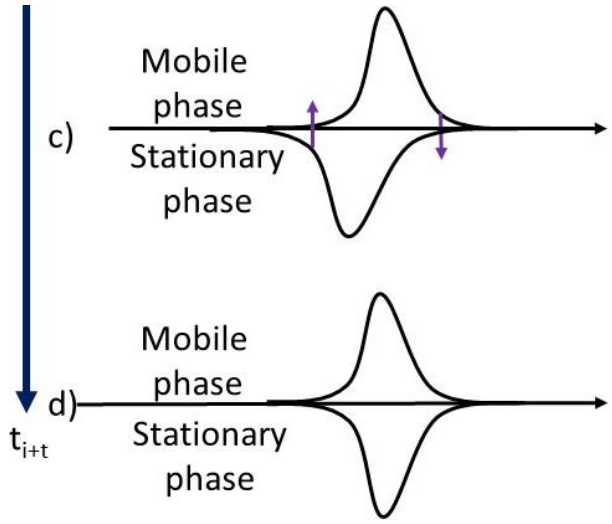

Figure 40. C_{SP}, mass transfer of the analyte movement between mobile and stationary phases. a) Ideal equilibrium, b), c) The analyte movement disrupts the equilibrium, and the diffusion tries to re-establish the equilibrium (arrows). d) Re-established equilibrium with a broader analyte band [199-201]

The height equivalent to a theoretical plate (H or HETP) represents the efficiency of plates for one analyte. The smaller H, the more theoretical plates are established (Equation 12). As the plate number of an analyte is independent of the retention, the height of a single theoretical plate H depends on the length of the column (L) and the separation efficiency (N):

$$H = L/N \qquad \text{Equation 12}$$

van Deemter *et al.* introduced Equation 13 to assess the impact of A, B and C on H based on the linear velocity of the analyte (μ) [202]. The best chromatographic separation (see Figure 41) is achieved when minimising the contribution of A, B, and C as smaller H values lead to sharper peaks due to more equilibria occurring per unit length of the column:

$$H = A + B/\mu + C\mu \qquad \text{Equation 13}$$

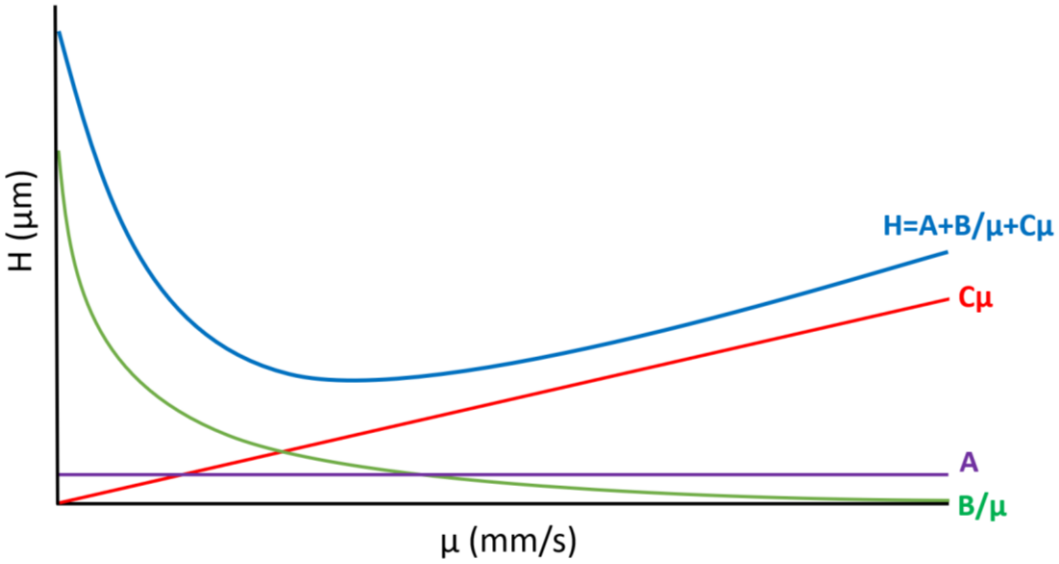

Figure 41. van Deemter plot of the height equivalent to a theoretical plate (H or HETP) showing the individual contribution of the three kinetic variables A, B and C based on the linear velocity of the analyte (µ)

Similar to band broadening, deviations can occur in the shape of the chromatographic peak shape. Ideally, the chromatographic band of an analyte is a Gaussian distribution of molecules of analytes because each analyte follows an isotherm (distribution coefficient, *K*) marked by the relation of the analyte C_{SP} and C_{MP} mass transfers (Equation 14).

$$K = C_{SP}/C_{MP} \qquad \text{Equation 14}$$

During the separation, when a compound elutes from the column, if *K* remains constant throughout the separation process, the detector registers a peak corresponding to a Gaussian distribution of molecules. The variation of *K* is one factor that leads to asymmetric peaks, observed in the form of either fronting or tailing (see Figure 42). Other aspects that can affect the symmetry of a peak relate to column overloading or secondary interactions with the silanol in the stationary phase.

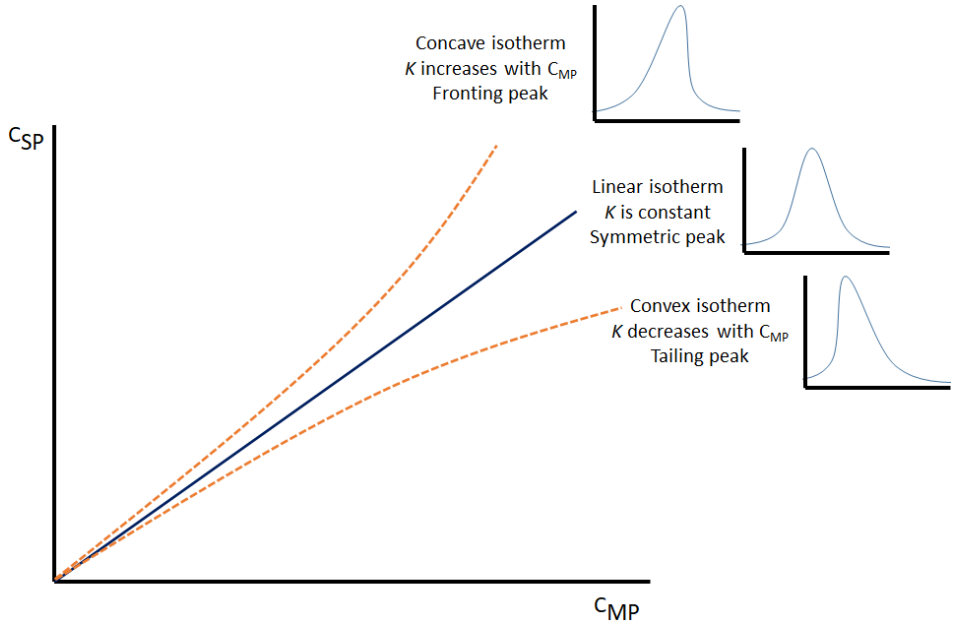

Figure 42. Correlation between the distribution isotherm (*K*) and the peak shape

The asymmetry generated in the chromatography peak can be quantified (Figure 43) using the asymmetric factor (A_s) at 10% peak height (Equation 15) or the tailing factor (T_f, used in the United States Pharmacopoeia) at 5% peak height (Equation 16). This research uses A_s due to its extensive application in the chemical industry.

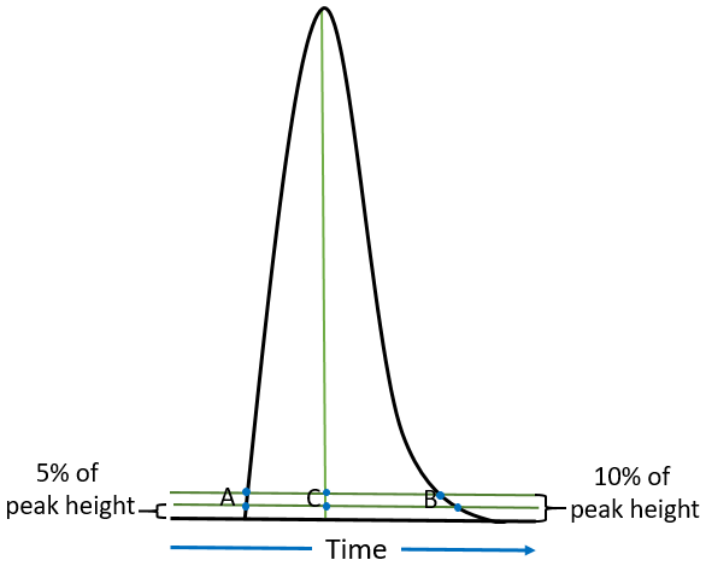

Figure 43. Calculation of A_s and T_f in a chromatographic peak [199]

$$A_s = \frac{BC_{10\%}}{BA_{10\%}} \qquad \text{Equation 15}$$

$$T_f = \frac{AB_{5\%}}{2AC_{5\%}} \qquad \text{Equation 16}$$

The chromatographic resolution (R_s) quantifies the degree of separation of two adjacent peaks (see Figure 44, Equation 17). A value of 1.00 means 94.00% separation, and a value of 1.50 means 99.99% separation. Typically, a value of 1.30 is an acceptable compromise between analysis time and good chromatography practices.

$$R_s = 1.177\frac{(t_{R2} - t_{R1})}{w_{1/2,2} + w_{1/2,1}} \qquad \text{Equation 17}$$

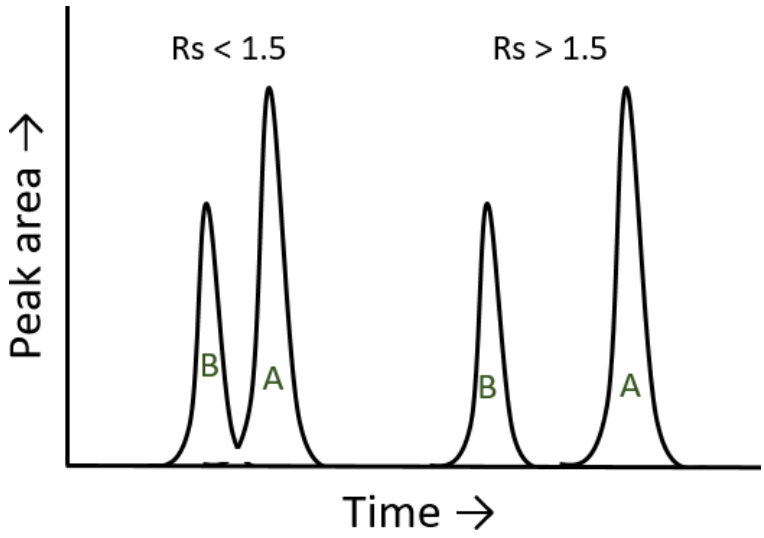

Figure 44. Definition of resolution (R_s) in a chromatogram

The separation factor (α) (Equation 18) describes the selectivity of the technique to separate two adjacent peaks and depends on the interaction of each analyte with the mobile and stationary phases. Separation is possible if α ≥ 1.

$$\alpha = k_2/k_1 \qquad \text{Equation 18}$$

The previous R_s equation can be adapted (Equation 17) to understand how the method development impacts the separation based on physical ($\sqrt{N}/4$) term) and chemical ($k/(k+1)$ and $(\alpha - 1)/\alpha$) aspects (Equation 19). Even though the stationary phase, the gradient delay volume, the mobile phase, the pressure, the flow rate, and the temperature affect the separation, the plotting of this equation reveals the significant impact of the stationary phase (α term) on the selectivity (Figure 45). Also, mobile phase acidity plays a vital role in the chromatographic resolution of ionic compounds. A change in the acidity of the media can result in tremendous changes in the retention time of the analyte by controlling the acid-base equilibrium of the functional group with the ionic characteristics.

$$R_s = \frac{\sqrt{N}}{4}\left(\frac{\alpha - 1}{\alpha}\right)\left(\frac{k}{k+1}\right) \qquad \text{Equation 19}$$

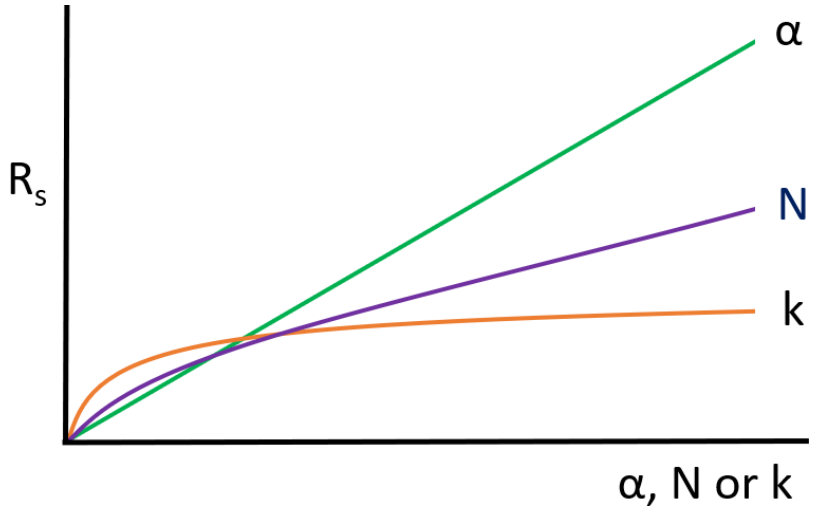

Figure 45. Effect of α, N and k in the chromatographic resolution (R_s)

1.5.1.2 Classification of chromatographic techniques

The separation of mixtures is possible if the molecules interact differently with the mobile and stationary phases, with different rates of migration of the analytes depending on the nature of the stationary (whether solid, liquid or gel) and the mobile (whether gas (GC), liquid (LC) or supercritical fluid (SFC)) phases [203-207]. The most common interactions are partitioning, dipole-dipole, hydrogen bonding, adsorption and/or ionic.

Twsett first reported a chromatographic separation in 1906 by separating green and yellow pigments of chloroplasts using an early version of thin-layer chromatography (TLC) that used $CaCO_3$ as early stationary phase support and petroleum ether as an early mobile phase) [207, 208]. Later, changing from paper to silica gel on a flat inert substrate in TLC significantly improved the separation and allowed the selection of different mobile phases to alter selectivity. Developments in TLC led to column chromatography, where a glass column is packed using silica particles and separated using a non-polar mobile phase. Further developments in the instrumentation and the technique resulted in James and Martin developing GC in 1954 using a capillary column and introducing a carrier gas as a mobile phase [209]. The result is that GC can provide suitable separation with narrower peaks due to the rapid diffusion of the analyte molecules in the gas phase; however, derivatisation is required when analysing thermally labile and non-volatile compounds, which involves that is not suitable for most of the small and the large molecules used as API. Besides that, GC finds applications in the pharmaceutical industry when analysing residual solvents, small synthetic chemistry starting materials or drugs of abuse, determining the percentage of purity of APIs, for identifying similar classes of compounds in complex mixtures or in metabolomics studies. Subsequently, LC emerged to analyse thermally

unstable compounds unamenable to GC. LC used a liquid mobile phase and a packed column [210] and became the most extended chromatographic technique, as various separation mechanisms are possible (Table 14). LC predominates in the routine analysis of API and many excipients and research and development. LC can separate polar [207, 208, 211] and non-polar [210, 212] analytes, whether ionic [213, 214] or not, or based on their molecule size [205, 206]. HILIC and SEC are described in this document due to their correlation with SFC and importance in PEG analysis [203-207].

LC Mode	**Stationary phase (SP)**	**Mobile phase (MP)**	**Main mechanism**
RPLC [210]	Non-polar silica-based bonded phases (Si-C18, Si-C8)	Polar eluents (H_2O, CH_3CN, CH_3OH)	Partition
Hydrophobic interaction chromatography (HIC) [212]	Low hydrophobicity sorbent with concentrated buffer (Si-C4)	H_2O or aqueous buffers	Adsorbed to SP with concentrated buffer and eluted with lower concentration buffer
NP-LC [207, 208]	Polar sorbent (Silica, alumina)	Non-polar eluent (hexanes, chlorinated hydrocarbons) / $(CH_3)_2CHOH/CH_3OH$	Adsorption
HILIC [211]	Polar sorbent (silica, polar ligand bonded silica)	Non-polar solvents with a low amount of H_2O or aqueous buffer	Partition in a thin aqueous film on the SP surface
Ion-exchange LC (IEX-LC) [213, 214]	Charged SP surfaces *via* acidic or basic functionality attached to silica or polymer particles	Aqueous buffers with a low amount of CH_3OH	Ionic interactions
Gel permeation chromatography (GPC) or SEC [205, 206]	Controlled porosity polymeric SP	Hydrophobic/hydrophilic solvents	Sieving by analyte size. Larger analytes elute first

Table 14. Summary of liquid chromatography modes

HILIC was first described by Alpert *et al.*; however, the first use belongs to Martin and Synge [211, 215]. HILIC is ideal for separating hydrophilic and polar molecules, including polar neutral and ionised analytes, with logP values of around zero [216-220]. The main challenges relate to the re-equilibration of the thin water layer formed in the stationary phase as the mobile phase should enrich the stationary phase and forms a thin layer of water on the surface of the stationary phase (see Figure 46 a) [216-220]. The water content in the mobile phase should be between 3 and 30% as a higher amount of water reduces the partition mechanism occurring [216-220]. The complex separation combines a partitioning mechanism, dipole-dipole interactions, hydrogen bonding, adsorption, and ionic interactions (see Figure 46 b) [216-220]. The predominance of a separation mechanism over others depends on the disposition of residual silanol groups. However, in HILIC, both adsorption and partitioning mechanisms are interrelated. The adsorption mechanism results from the analyte and mobile phase competing for the polar sites on the stationary phase. The partitioning mechanism occurs from the different solubility of the analyte in the mobile phase and the layer of water absorbed on the surface of the stationary phase [216-220].

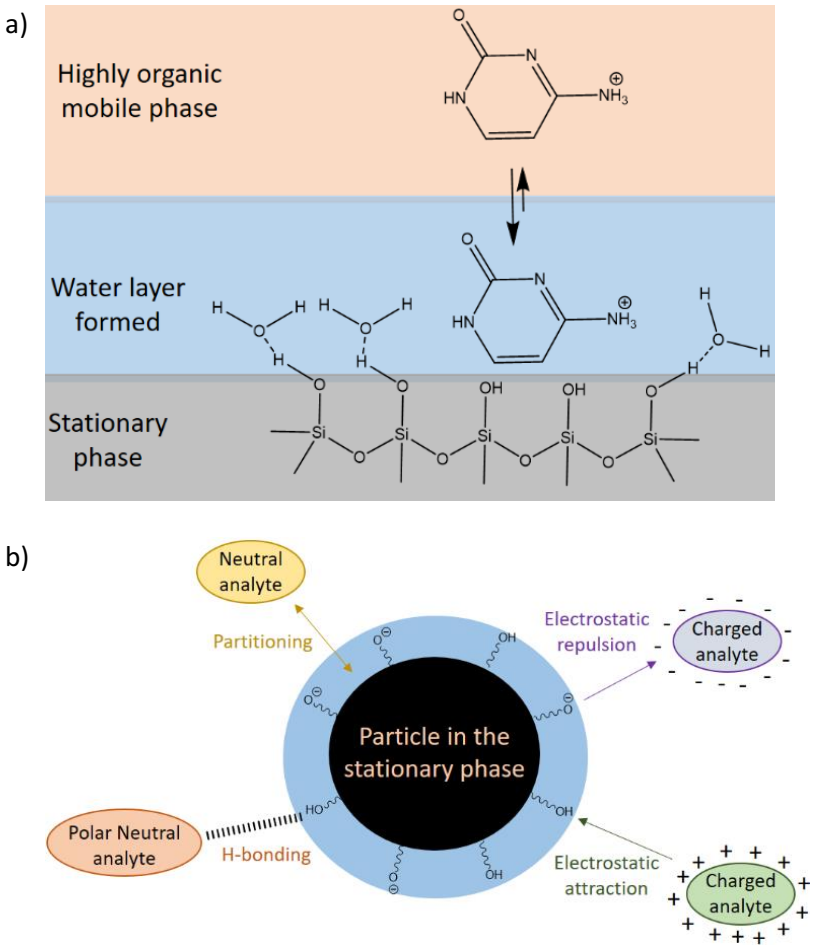

Figure 46. Mechanism separation in HILIC: a) Formation of a thin layer of in the stationary, and b) possible interactions between different analytes and a stationary phase particle

SEC started when Synge *et al.* and Wheaton *et al.* reported a size-based separation where the analytes diffuse inside and outside specific-size pores [205, 206]. The differences in size drive the separation, with other interactions minimised during the method development. The elution profile depends on the analyte hydrodynamic radius and the mobile phase composition, with up to three columns connected in series to increase the number of plates and the separation efficiency. Larger analytes elute earlier than small analytes due to smaller analytes being retained in the sieved SP (Figure 47) [205, 206]. SEC is widely used to purify proteins or DNA and impurity profiling biomolecules. GPC is typically used when analysing polymers. However, both terms are acceptable and interchangeable. The terminology SEC is used in this document.

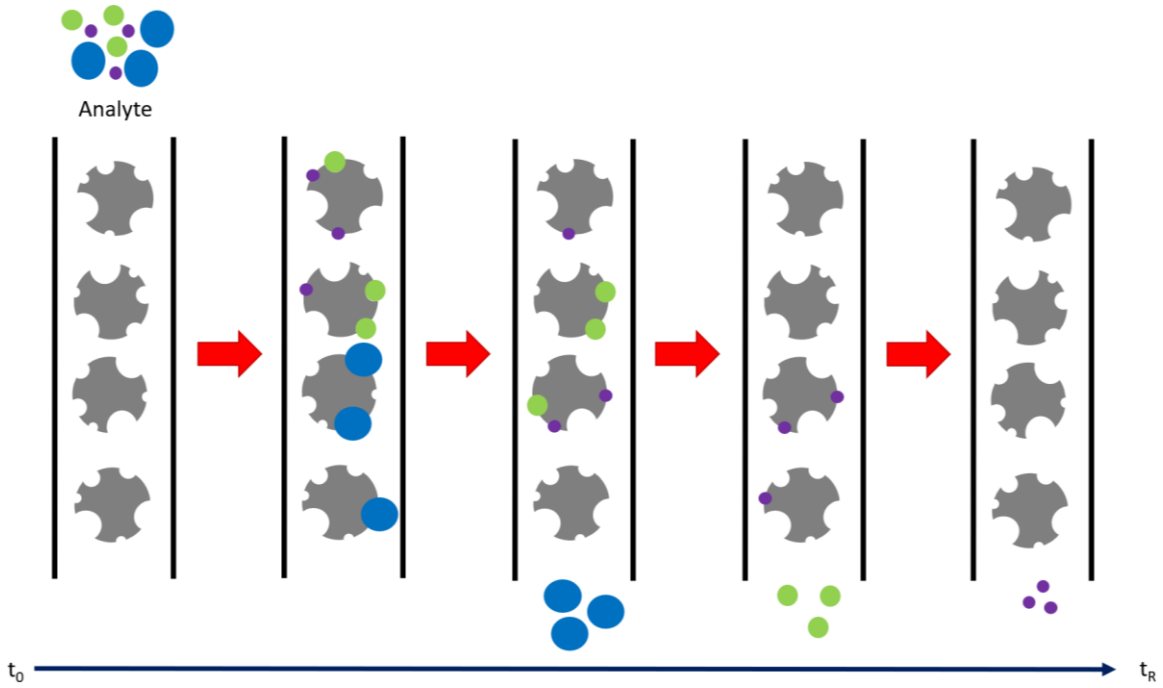

Figure 47. Mechanism of separation in SEC for three analytes of different size explaining how the size sieve retain small analytes for longer than larger analytes

1.5.2 Supercritical fluid chromatography

1.5.2.1 Basics

Supercritical fluid chromatography (SFC) is becoming important these days as a substitution for HILIC due to the speed of analysis and the greener capacity of the technique, allowing for faster analysis with lower solvent consumption [221]. SFC is a chromatographic technique in which the mobile phase mainly uses supercritical fluid CO_2 ($scCO_2$). When looking at the phase diagram of CO_2 (see Figure 48), the triple point is a specific temperature and pressure (-57°C, 5 bar) at which solid, liquid and gas phases co-exist. The critical point is defined as specific temperature (31°C)

and pressure (74 bar) conditions where liquid, gas and supercritical fluid phases co-exist. At higher temperature and pressure conditions, a supercritical fluid exists. Supercritical fluids possess intermediate properties between gases and liquids (Table 15), resulting in a technique with better solvating capacities than GC and higher diffusivities and flow rates than LC without seriously compromising the efficiency. [222]

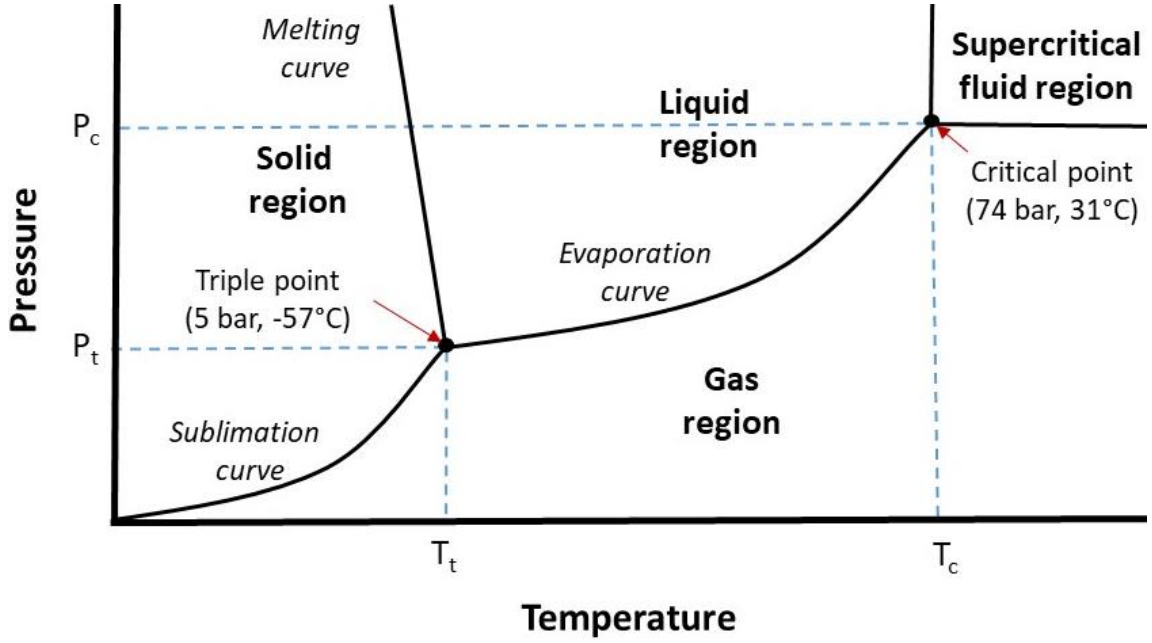

Figure 48. Phase diagram of CO_2 showing the triple and the critical points

	Density ($g.cm^{-3}$)	Diffusivity ($cm^2.s^{-1}$)	Viscosity ($g.cm^{-1}.s^{-1}$)
Gas	10^{-3}	10^{-1}	10^{-4}
Supercritical fluid	10^{-1}-1	10^{-4}-10^{-3}	10^{-4}-10^{-3}
Liquid	1	$<10^{-5}$	10^{-2}

Table 15. Comparison of the density, diffusion and viscosity of gases, supercritical fluids, and liquids [222]

SFC had an unlucky and delayed development because of inadequate instrumentation. Klesper *et al.* used a GC system and a supercritical fluid (CCl_2F_2 and $CHClF_2$) to separate nickel etioporphyrin II and nickel mesoporphorin IX dimethyl ester [204]. Later, Sie *et al.* used CO_2 gas in a GC system [223]. Giddings *et al.* used $scCO_2$ two years later and started capillary SFC (cSFC) [224]. The same research group later discussed the convergence between gas and liquid chromatography [224], which allowed for the investigation of Jentoft and Gouw to use pressure programming to modify retention times and suggested the use of packed columns for SFC separation [225]. The development of the first

commercial liquid chromatography instrument in 1967 [222] and research [224, 226] that reported the limitations of packed column SFC delayed the development of packed column SFC. The interest for packed column SFC gained a great deal of interest in 1981 when Springston and Novotny reported that the intermediate properties of supercritical fluid to gases and liquids (Table 15) could be advantageous as a chromatographic technique [227]. As a result, in 1982, Gere *et al.* modified a liquid chromatography system to operate at supercritical conditions by adding a backpressure regulator and a high-pressure UV-Vis detector cell and demonstrated high efficiency with no significant impact of pressure drop on the efficiency or peak shape [228]. The substitution from capillary to packed columns (packed SFC, pSFC) improved separation performance and solute flexibility, resulting in ultra-high-performance (UHP) LC instruments being adapted to SFC which minimised some of the previous difficulties in backpressure regulation, sample injection and flow rate stability [229, 230]. UHP techniques significantly increase the analysis speed and improve the separation by increasing the column efficiency, reducing the particle size, and shortening the column, allowing the use of higher flow rates [222].

1.5.2.2 Instrumentation

The research here uses SFC instrumentation developed by Waters® (Waters® Acquity™ UPC²), and this instrumentation is described (Figure 49). The experiment starts with converting gaseous CO_2 to a supercritical fluid ($scCO_2$) in the Convergence Manager by the action of heat and a compressor. The $scCO_2$ is mixed with a liquid (co-solvent) in a mixing chamber at specific percentages depending on the gradient. The mobile phase mixture passes through an injection valve (6-port Rheodyne) that introduces the sample and directs the flow to a column. A pre-heater at the beginning of the column preserves the supercritical state of the mobile phase. The column is connected to a UV-Vis detector and a splitter. The splitter is composed of two T-pieces connected in series. The first T-piece mixes the column flow with the make-up solvent from the Isocratic Solvent Manager. The role of the make-up solvent is described in section 1.5.2.3, page 64, due to the dependence on whether aerosol detectors or mass spectrometry is used. The second T-piece splits the flow to the aerosol detector or mass spectrometry and the convergence manager. The mobile phase density is maintained constant with the help of an active backpressure regulator (ABPR) located in the Convergence Manager. [230, 231]

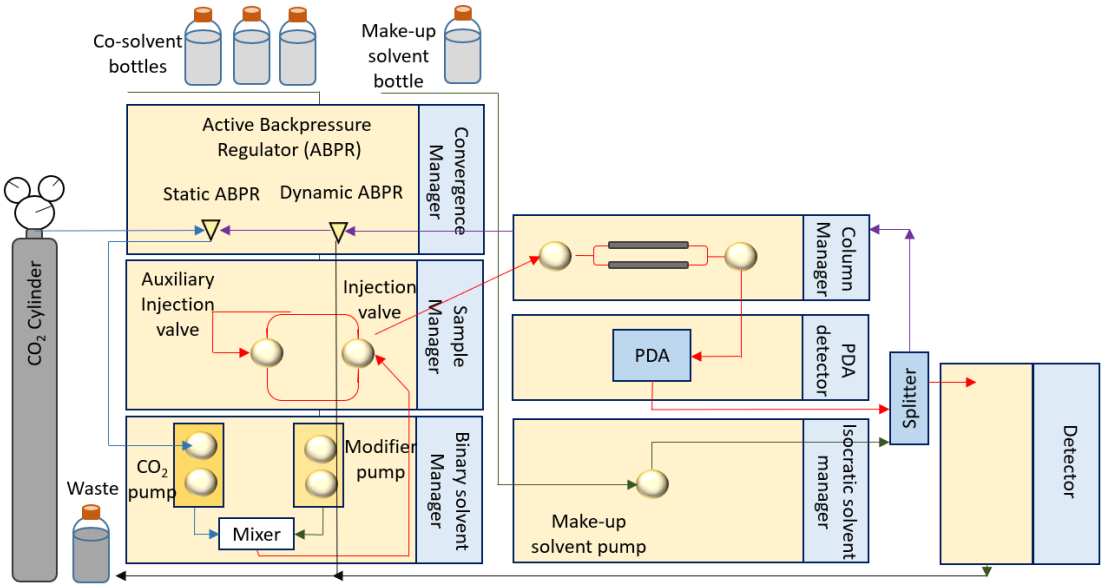

Figure 49. UPC² Waters® instrument used in this research

1.5.2.3 Mobile phases

The most common supercritical fluid used in the mobile phase is CO_2 due to its low cost, safety (non-flammable gas) and easy capacity to reach the supercritical state. Literature proposed other supercritical fluids (hydrofluorocarbons, NH_3, SO_2 and N_2O); however, the extreme conditions required to reach the supercritical point make them unpractical, resulting in the only use of CO_2 in modern applications. Modifiers are added to increase CO_2 polarity and change the mobile phase density (Figure 50) [232, 233]. The most common is CH_3OH; however, other reported solvents are CH_3CH_2OH, $(CH_3)_2CHOH$, CH_2Cl_2, tetrahydrofuran, and CH_3CN.

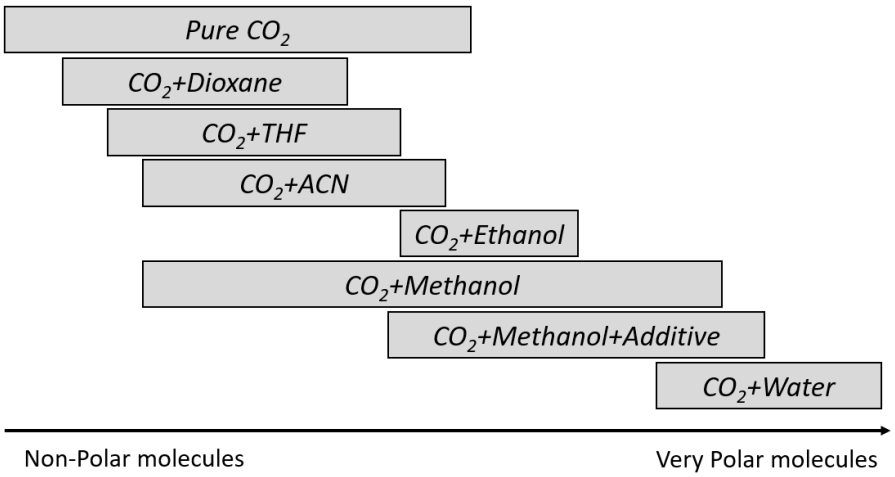

Figure 50. Effect of the addition of different modifiers to the CO_2 polarity. Adapter from Berger *et al.* [233]

Additives are added to the modifier in small amounts (<1% v/v) to improve the peak shape and selectivity as they interact with the active sites of the stationary phase. They can slightly modify the polarity of the mobile phase (Figure 50). Either acidic, neutral, or basic additives are used based on the stationary phase and the analyte chemistry [233].

Organic acids (trifluoroacetic acid, formic acid, acetic acid or citric acid) are added for acidic analytes (lower than 0.3% v/v) to suppress peak tailing and improve the peak shape [229, 230, 234-239]. H_2O is a co-solvent; however, the improvements observed in peak shape when using this solvent suggest that some authors denominate H_2O as acidic additive due to the formation of carboxylic acids when reacting with $scCO_2$ and CH_3OH under high pressure and temperature (Figure 51). The amount of H_2O should be kept low due to the lack of miscibility with CO_2 at 8% v/v or higher. Also, some authors reported the formation of a thin layer of water in the silica bed, involving a HILIC-like mechanism that improves separation, which could explain the higher polarity observed when using $scCO_2$-H_2O mixtures and their categorisation as a $scCO_2$ co-solvent (Figure 50) [233, 234, 240-243].

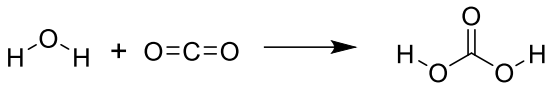

Figure 51. In-situ formation of carbonic acid from H_2O and $scCO_2$ [240]

Aliphatic amines are used as additives for basic analytes (lower than 0.3% v/v, diethylamine, dimethylethylamine, isopropylamine or triethylamine). Volatile ammonium salts were reported to avoid the difficulties of choosing an additive for basic analytes. These salts enhance the separation due to an ion-pairing interaction between the analyte, the ammoniated ion, and the bare silica stationary phase. Zheng *et al.* proposed that the ammonium ions form an ion pair with the alkoxide groups of the stationary phase. Also, basic analytes form a second ion pair with the ammonium ions. The flow of the salt counterions breaks the ion pair leading to the subsequent equilibria being the most common the formate, the acetate and the hydroxide. Ammonium formate and ammonium acetate produce sharper chromatographic peaks and improve ESI ionisation with significant enhancements noticed when using 25 mM but lead to a noisier baseline. Ammonium hydroxide helps decrease the baseline noise, enhancing the limit of detection. Ammonia was reported as an alternative to aliphatic amines to improve the peak shape of drug-like molecules. [230, 234, 235, 244-249].

1.5.2.4 Columns for achiral separations

Modern SFC separation is achieved using packed steel columns (pSFC) with similar technology to that used in LC. These columns measure 50 to 100 cm in length, 2.1 to 4.6 mm in internal diameter and have particles with a size that varies from 2 to 5 µm. The columns for achiral analysis consist of several particle morphologies (monoliths, fully porous particles, or core-shell) with different chemistries as SPs fused onto them.

Monolith columns are organic polymers with rod-shaped structures with structures based on silica. Even though the structure is unevenly unpacked, no interparticle voids are present as a single piece of porous material comprises the structure. Lower system backpressures and higher flow rates (up to 10 mL/min) are achieved than in silica-based columns; however, the lower column efficiency due to broadly distributed stagnant meso- (15 nm) or macro/flow- (1.15 µm) pores involves that monolith columns are less common [250, 251].

Fully porous particles (FPP) are the most common in modern applications due to their improved column efficiency, resolution, sensitivity, and analysis speed compared to monolith columns. The reduction of particle size (from 10 µm in the 1970s to sub-2 µm in 2004) resulted in significant improvements in column efficiency at the cost of higher backpressures. All technologies are based on silica particles (tetraethoxysilane, TEOS, Figure 52 a): high-strength silica (HSS), ethylene bridged hybrid (BEH), and charged surface hybrid (CSH) particles. All three technologies vary in silanol activity, shape, selectivity, and hydrophobicity. HSS particles contain TEOS joined into a poly(ethoxy silane) (PEOS, Figure 52 b). BEH technology provides a variation of such chemistry as the particles have bridged ethane groups within a silica matrix where the bis(triethoxy silyl)ethane (BTEE, Figure 52 c) reacts with TEOS to form poly(ethoxy silane) (BPEOS, Figure 52 d). CSH are BEH-like particles with an added low-level charge to the particle surface before chemically bonding the stationary phase [252, 253].

a)

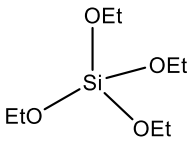

b)

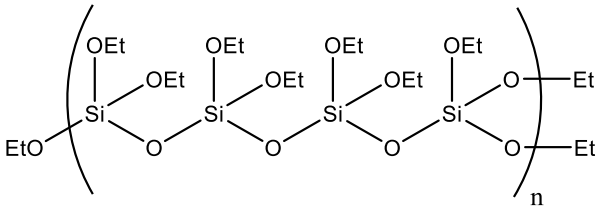

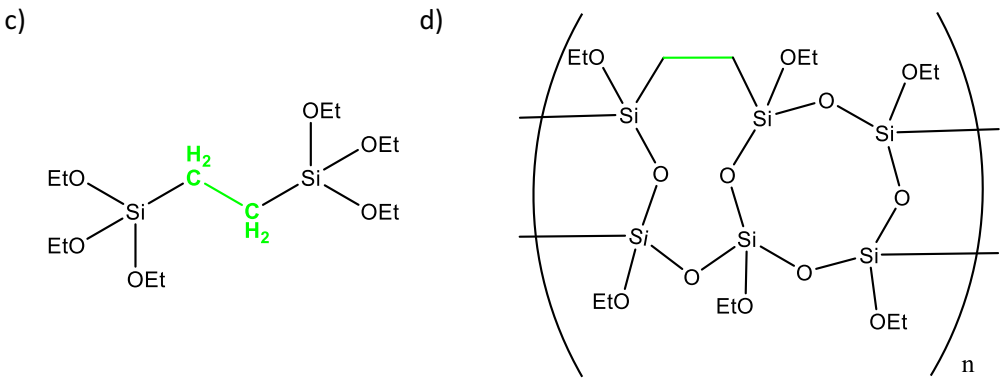

Figure 52. Particle technology of FPP: a) TEOS, b) PEOS, c) BTEE, d) BPEOS

Superficially porous particles (SPP) were developed in recent years as an alternative to FPP to provide increased column efficiency due to improved particle distribution (lower A), smaller pores (lower B) and shorter diffusion path length (lower C). These particles consist of a solid core 1.7 µm silica bead fused with a 0.5 µm porous layer (Figure 53), resulting in a final microsphere of 2.7 µm. Their manufacturing starts with producing the non-porous core using a Stöber method of monodisperse silica spheres, where alcohol is added to TEOS in the presence of ammonia as the catalyst. The core particle can be produced in many configurations: from a single sphere, aggregation of several small spheres, or a rattle-like hollow shell with a small sphere inside. The solid core spheres are coated with an oppositely charged polymer, and the coated sphere is immersed in a dispersion of nanoparticles with opposite charges to the polyelectrolyte. The result is a porous shell that could be a continuous layer or an aggregation of smaller spheres onto a larger core. The most common synthetic approach is an accurate and precise layer-by-layer approach, leading to narrower particle size distribution than FPPs [202, 254-257].

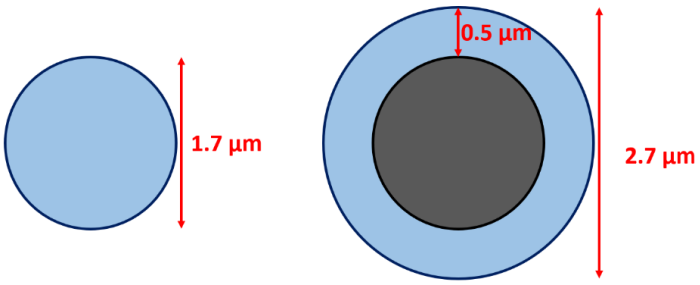

Figure 53. Differences between an FPP (left) and an SPP (right). The light blue indicates the porous site, and the dark blue is the rounded, solid bead

Different ligands with achiral chemistries are fused on the particle to alter the selectivity for either LC or SFC separations. Packed columns SFC uses similar technology to packed column LC separations. The typical modifications of the stationary phase for achiral separations include

aliphatic chains with one (methyl, C1), four (butyl, C4), (octyl, C8) or 18 (octadecyl, C18) carbon atoms, cyclohexyl, phenyl hexyl, amide, diol and cyanopropyl ligands that are connected to the O atom in the silica particle via a covalent bond. The remaining hydroxy end groups (silanols) can be either end-capped or not, whilst the ligands can have polar atoms embedded into the chain to improve the retention of polar analytes. Other less common modifications include poly(4-vinyl pyridine) for planar compound analysis or C30 for highly hydrophobic separations. Also, Waters® has developed the Torus™ patents for specific SFC separations based on BEH particles with 2-picolylamine (2-PIC), diethylamine (DEA), 1-aminoanthracene (1-AA) or diol (Diol) modifications. The achiral stationary phases investigated in this research are shown in Table 16. [229, 230, 234, 258-262]

Commercial name of the stationary phase	**Structure**
Waters® Acquity™ UPC² BEH (BEH)	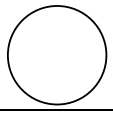
Waters® Acquity™ UPC² Torus™ Diol (Diol)	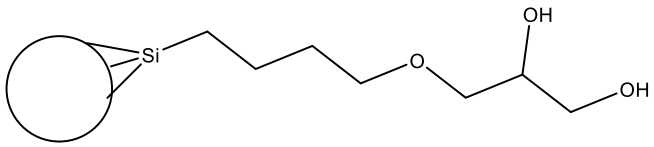
Waters® Acquity™ UPC² BEH-2-Ethylpyridine (2EP)	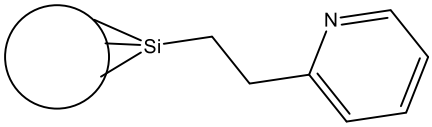
Waters® Acquity™ UPC² Torus™ 2-Picolamine (2Pic)	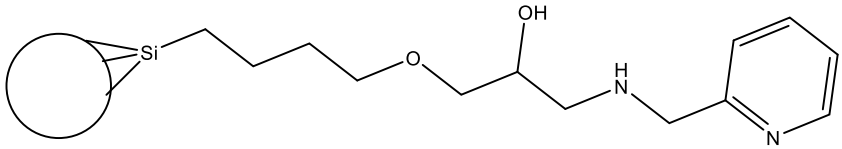
Waters® Acquity™ UPC² Torus™ 1-aminoanthracene (1AA)	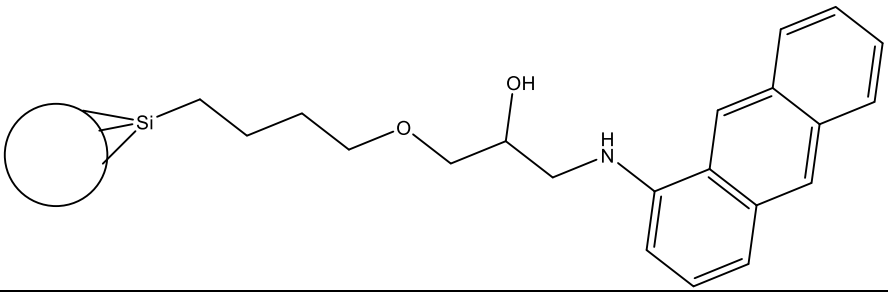
Waters® Acquity™ UPC² HSS Cyano (Cyano)	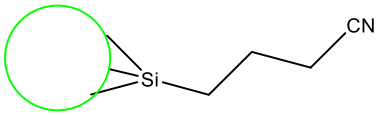

Waters® Acquity™ UPLC™ HSS Pentafluorophenyl (PFP)	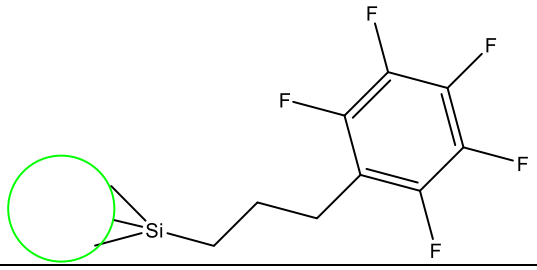
Waters® Viridis® HSS C18 SB (C18)	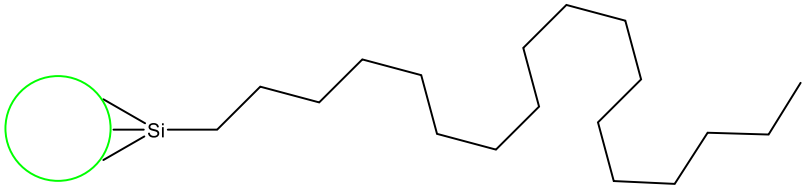

Table 16. Achiral stationary phases used in this research. In black BEH particles. In Green HSS particles

1.5.2.5 Columns for chiral separations

Chiral separations are critical in the pharmaceutical industry to assess the enantiomeric purity of chiral API as they recognise the 3D structure (regiochemical) of the molecule. The enantiomeric separation uses chiral selectors based on brush type (Pirkle), polysaccharides, inclusion (CDs, macrocyclic glycoproteins, *etc.*), ligand exchangers and proteins. Specific column technologies for chiral SFC analysis include the Waters® Trefoil™ products. In this project, polysaccharide-based supports were used. [229, 230, 263-272].

Polysaccharide-based SPs use cellulose or amylose as chiral supports due to incorporating chiral recognition sites in their structures. Both polysaccharides are based on glucose units bonded with a 1,4- linkage (α- in cellulose and β- in amylose) (Figure 54) [272].

a)

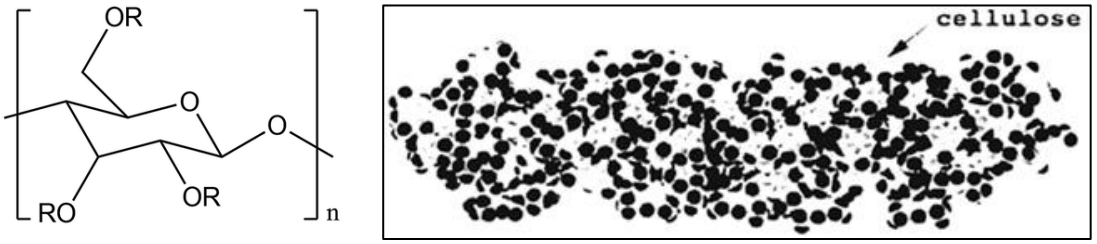

b)

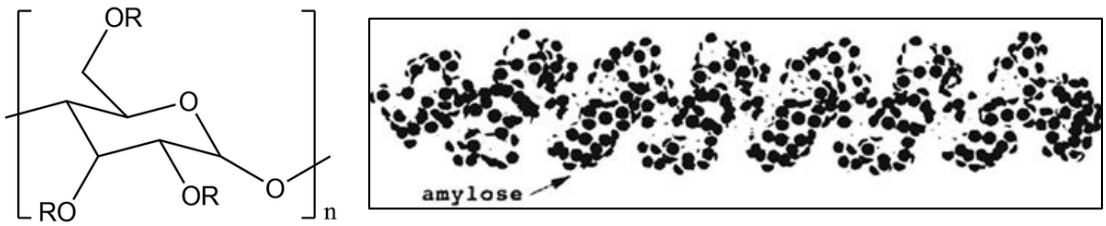

Figure 54. Structures of polysaccharide-based stationary phases used in chiral separations: a) cellulose, b) amylose. Reproduced with permission from Gübitz and Schmid [272]

The main drawback of these stationary phases is their instability to medium-polarity and polar organic solvents. Polysaccharide immobilisation can happen *via* chemical bonding to a solid support or *via* coating the chiral polysaccharide onto the support, followed by photochemical cross-linking. The result is a minor sacrifice in the enantioselectivity with the gain of unique selectivity, broader temperature operation range, solubility-guided method development, and the possibility of regeneration using harsh solvent systems. Derivatisation of polysaccharide-based SPs broads the chiral recognition capacity of these SPs (Table 17). [229, 230, 263-271]

Column	**Ligand**
Chiralcel OD	Tris(3,5-dimethylphenyl carbamate) 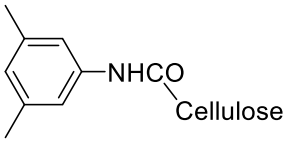
Chiralcel OD-H	Tris(3,5-dimethylphenyl) carbamate 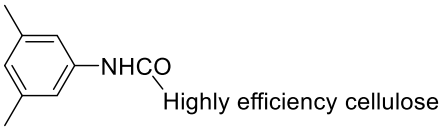
Chiralcel OG	Tris(4-methylphenyl carbamate) 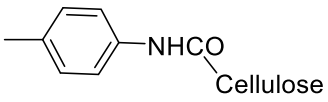
Chiralpack AD	Tris(3,5-dimethylphenyl carbamate) 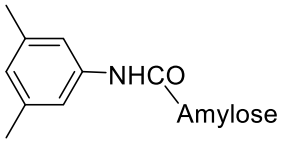
Chiralpack AS	Tris[(S)-1-phenyl ethyl carbamate] 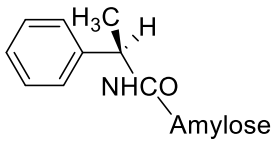

Table 17. Investigated chiral stationary phases

1.5.2.6 Injection solvent composition

The solvent composition of the sample before injection (injection solvent) affects the chromatographic peak shape. Ideally, the injection solvent composition should match the mobile phase composition at the beginning of the gradient. This matching in SFC is impossible as the standard experiment starts at low polarity with high percentages of CO_2 (95-99%) and low

amounts of modifier (1-5%). Using CH_3OH is not advised when started at low co-solvent percentages as polar organic solvent changes the mobile phase polarity and viscosity (*i.e.*, density), affecting the analyte peak shape as distortion or tailing, resulting in possible selectivity changes of early eluting components. [273-275]

1.5.2.7 Role of the column temperature and the active backpressure regulator

Optimisation of the column temperature (30-70 °C) and ABPR (105-200 bar) usually occur at the end of the method development to improve the peak shape and selectivity. These modifications alter the pure CO_2 density from 0.2 to 1.1 g/mL, with reduced densities observed at higher column temperatures and lower ABPR back pressures. Additionally, the column temperature and ABPR affect the viscosity of the supercritical fluid, the solute solubility in CO_2 and the solute diffusivity. Changing the viscosity affects the column efficiency and the mass transference of the analyte in the mobile phase. Similarly, the column temperature has two opposite effects; when the column temperature increases, the mass transference of the analyte to the mobile phase decreases the retention time of the analyte, whilst increasing the column temperature decreases the viscosity of the supercritical fluid, decreasing the fluid density and retaining the analytes more. Therefore, the column temperature can play different roles in the separation based on the interactions of the analyte with the mobile and stationary phases. [230, 276]

1.5.2.8 Chromatographic detection

The main challenge in chromatographic detection is that the analyte, the mobile phase, and the detector must be compatible. GC can be coupled to FID, nitrogen phosphorous (NPD) or electron capture (ECD) detectors as the inert gas (N_2, He and H_2) used in the mobile phase is not detected using FID, NPD or ECD. LC detection occurs *via* UV-Vis, aerosol detectors (mainly using ELSD or CAD), refractive index detector (RI) or polarimetry. The coupling to these detectors is possible as they are designed to remove the solvent particles from the liquid mobile phase before detecting the analyte. MS detection allows for analyte identification due to the remarkable capacity of the technique to provide structural information on the eluted compounds.

SFC uses supercritical fluids that have an intermediate character between liquid and gases, and theoretically, the technique can be coupled to most of the detectors available. The initial coupling of cSFC was with FID, as no organic modifier was used. Further development in the technique that resulted from adding a modifier and using packed columns required liquid-based detection systems such as UV-Vis, ELSD and CAD. The most extended choice is the coupling of

pSFC with MS, which allows for analyte identification, followed by aerosol detectors due to their quantitative capacity and lower price.

Detectors are classified as mass or concentration-dependent based on the response of the analyte (Table 18). For mass-dependent, the signal is proportional to the mass of the analyte, with better responses at higher flow rates. For concentration-dependent, the signal is proportional to the analyte concentration. A similar classification can be proposed for MS ionisation sources (ESI, atmospheric pressure chemical ionisation (APCI) or APPI) as the analyte response in MS instruments does not depend on the mass analyser or detector used. [230, 277, 278]

Concentration-dependent	ESI – MS	UNI – MS	UV-Vis
Mass-dependent	APCI – MS	APPI – MS	Aerosols

Table 18. Classification of typical chromatographic detectors and MS ionisation sources based on the response provided

1.5.2.9 Capillary supercritical fluid chromatography and flame ionisation detection

Early cSFC was coupled to FID due to the gaseous character of CO_2; however, several instrumental challenges related to the presence of spiking signals in the detector from the irregular formation of aggregated clusters of desolvated molecules slowed the progression [224]. Only one modern cSFC-FID instrument was found, with no application in the pharmaceutical industry [279-281].

1.5.2.10 Packed column supercritical fluid chromatography and UV-Visible detection

Modern pSFC uses UV-Vis, aerosols, or MS to detect and quantify the analytes. Most packed-column UHPSFC instruments install a UV detector immediately after the chromatographic elution and before the splitter due to their non-destructive nature. A deuterium lamp emits UV-Vis radiation that transfers electrons to high-energy orbitals of chromophores sites of the molecule. The Beer-Lambert law dictates the amount of monochromatic electromagnetic radiation absorbed [282]. Equation 20 establishes that the amount of light absorbed by an analyte (A) is proportional to the path length (b) through which the radiation passes and the concentration of the analyte in solution (c). The proportion is the molar absorptivity (ε), a coefficient that depends on the nature of the analyte that absorbs the light, the absorbance wavelength λ (UV range 200-400 nm), and the solvent used.

$$A = \varepsilon bc \qquad \text{Equation 20}$$

The chromatographic eluent passes through a sapphire flow cell that can withstand backpressures of at least 400 bar (for the Waters® UPC^2 instrument) [230, 283]. Detection of UV light usually occurs *via* a photodiode array in the range of 190 to 500 nm (Waters® UPLC PDA detector). Still, the mobile phase may impair detection due to the UV-Vis cut-off wavelength of solvents and additives used. The UV-Vis cut-off in colourimetry is the wavelength at which the solvent absorbance in a 1 cm path length cell equals 1 AU (absorbance unit) using water in the reference cell [282]. Table 19 shows the UV-Vis cut-off of common co-solvents used in SFC. Even though CO_2 has excellent UV transparency [284], the pressure fluctuations lead to higher background noise than in LC-UV due to changing the mobile phase density and the refractive index fluctuations in the flow cell [230, 285]. Still, the lower cut-off of CO_2 (190 nm) makes it ideal for most pharmaceutical applications.

Solvent	CO_2	CH_3OH	CH_3CH_2OH	$(CH_3)_2CHOH$	CH_3CN
UV-Vis cut-off (nm)	190	205	210	205	190

Table 19. UV-Vis cut-off of common solvents used in SFC [284]

1.5.2.11 Coupling of packed column supercritical fluid chromatography to mass spectrometry and aerosols detectors: role of the make-up solvent and the ABPR

The coupling of SFC to aerosol detectors or MS involves a decompression step of the mobile phase followed by nebulisation [286]. Compared to LC, the lower viscosity of supercritical fluids and the post-column decompression complicates the nebulization process [230]. The low viscosity requires the addition of a backpressure regulator to control the pressure and flow rates [230]. The endothermic nature of the process leads to the formation of solid particulates of icy CO_2 that results in the possible precipitation of analytes with low solubility in the gas phase and increases background noise, requiring additional heating of the interfacing tube to mitigate the impact [287]. Even though a heating regulator valve can aid decompression, a more efficient approach is using a two-step procedure [288]. In the first instance, the pressure decreases to maintain the mobile phase in super/sub-critical conditions. Then the eluent enters the detector using a heated capillary silica restriction that simultaneously decompresses and nebulises the mobile phase [286, 289]. Alternatively, the use of a make-up solvent is adequate as the flow rate of the solvent regulates the backpressure produced by the heated capillary silica restrictor [290]. Suppose the eluent is connected pre-BPR (backpressure regulator) (also called active BPR (ABPR)). In that case, the

nebulization occurs in the nebulisation chamber, requiring a higher percentage of organic modifier for best sensitivity [282, 291]. If the connection occurs post-BPR, nebulisation occurs in the transfer line, with a higher response observed at a lower percentage of the organic modifier [292].

The connection of the eluent in the Waters® UPC^2 is pre-ABPR, with an interface using a splitter (Figure 55), a make-up solvent, and an active backpressure regulator. The rationale is that a make-up solvent can be added pre-depressurisation to avoid analyte precipitation or segmented flow due to separated phases in the transfer line at lower percentages of the organic modifier [293-295]. The make-up solvent regulates the backpressure produced by the heated capillary silica restrictor and provides a more uniform response in gradient elution SFC, similar to LC [287, 292].

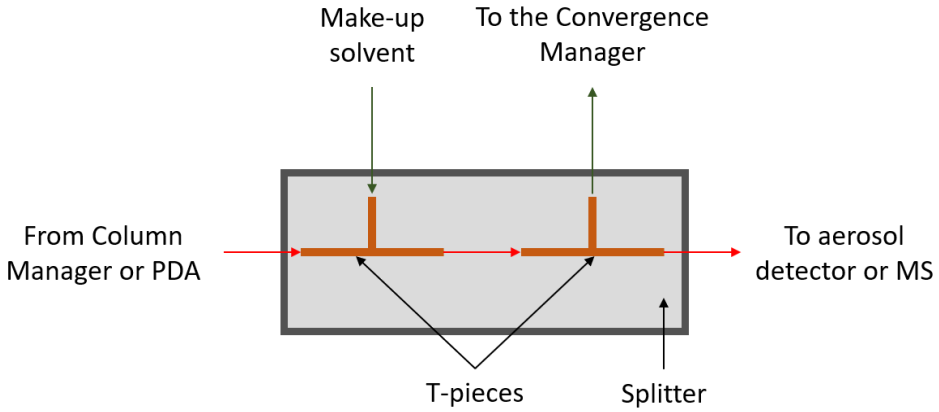

Figure 55. Schematic of the splitter used in the Waters® UPC^2 system

The make-up solvent selection depends on whether aerosol detection or the ionisation source in MS is used (Table 20). A nebulising gas is required with aerosol detectors to decrease the background noise and improve detection. In MS, the make-up solvent, the heat, and the gas flow stabilise the spray, whilst the solvents and additives provide an ionisation media that can direct the MS ionisation to the primary formation of one species over others [287, 292].

	Aerosol detector (ELSD, CAD)	**ESI-MS**	**APCI-MS**	**APPI-MS**
Make-up solvent	CH_3OH with low levels of HCOOH, CF_3COOH, or with low levels of $N(CH_2CH_3)_3$, $(CH_3)_2NC_2H_5$ or NH_4OH	CH_3OH or $(CH_3)_2CHOH$ with low levels of HCOOH, volatile ammonium or Na salts, or NH_4OH	CH_3OH or $(CH_3)_2CHOH$ with low levels of HCOOH	Toluene or $(CH_3)_2CO$

Table 20. Different make-up solvents used in aerosol detection and MS

1.5.2.12 Aerosol detectors

Alternatively, aerosol detectors are coupled to detect non-volatile analytes that do not absorb UV light, as their response is independent of the chemical structure. These detectors generate an aerosol *via* nebulisation, typically pneumatically assisted using N_2 to convert the effluent into a fine mist. The largest droplets are removed before evaporation to maintain a uniform distribution and reduce the evaporation temperature. Removing these largest droplets is essential for compatibility with the conventional flow rates used in LC [288]; however, the facile evaporation of supercritical mobile phases involves these detectors potentially performing better with SFC than with LC [286]. The improved performance observed results from a dependence of their signal on the size of the analyte particles, the mobile phase composition and surface tension, the chromatographic flow rate, the detector temperature, and the nebulising gas [287].

They are classified based on the following steps to the nebulisation (Figure 56): ELSD, CAD, condensation nucleation light-scattering (CNLSD), and chemiluminescence aerosol (CLAD) detectors. ELSD and CAD are the most used due to their sensitivity, broad dynamic range, and ease of use [296]. CNLSD requires further studies, but some papers have already shown the enhanced capacities of this detector [120]. The current document describes ELSD and CAD due to their use in the routine analysis and quantitation of PEG materials.

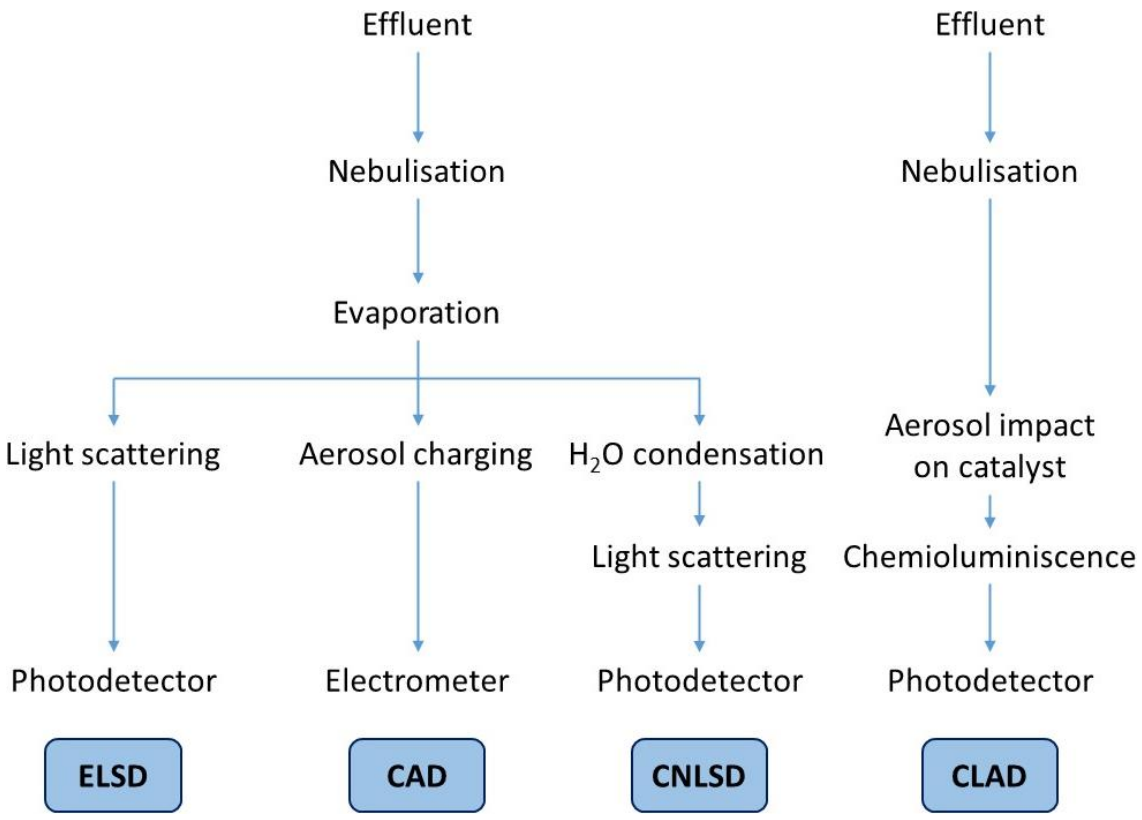

Figure 56. Diagram illustrating the differences between aerosol-based detectors [297]

In an ELSD (Figure 57), the aerosol enters a nebulisation chamber where high-sized drops are condensed on the chamber's walls and diverted to waste. The proportion of waste depends on the mobile phase volatility: >90% for aqueous to 10% for organic mobile phases. A long-coiled heated drift tube with an upward direction evaporates the mobile phase, converting the droplets into a stream of tiny particles of the analyte, eliminating the solvent and leaving the less volatile analytes in the gas stream like a dry solute [298-300]. After the evaporation, the dry solute enters the optical cell and passes through a light beam. A collimated light beam produced using a pair of optical fibres is focused on the particles in the optical cell. The particles disperse the beam, and the radiation produced by elastic light scattering is detected by a photomultiplier or a photodiode, providing the output signal. A tungsten filament, halogen lamp, or secondary gas can be used to favour the scattering and not absorbing phenomenon. The tungsten filament or halogen lamp produces a continuous spectrum of wavelengths that suppress the absorption. The secondary gas concentrates the particulates in the centre of the detection cell and prevents deposition on the inner surfaces [298-300]. Although ELSD is a robust detector, controlling the droplet size is critical to ensure good linearity, as the scattered light depends on the particle diameter, the wavelength, and the angle of the scattered light. [288, 298, 301-304]

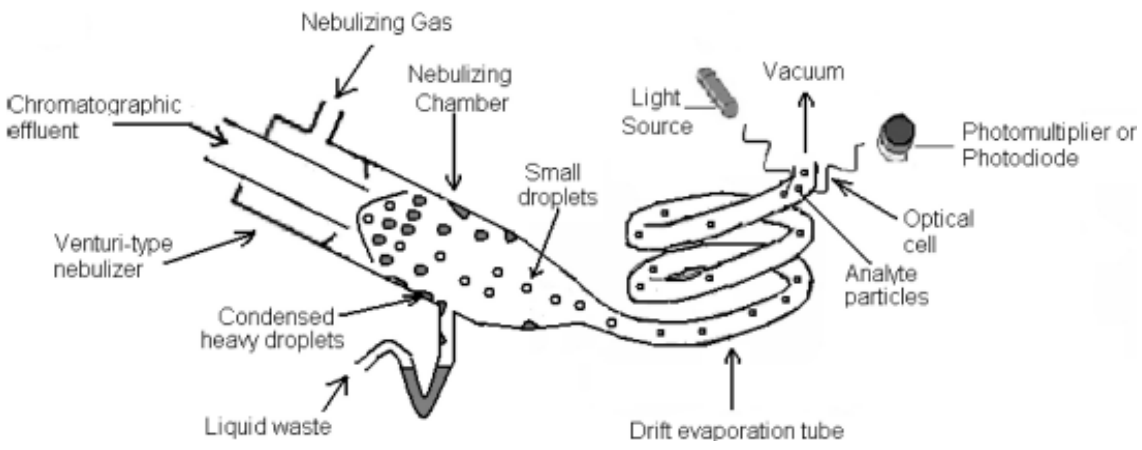

Figure 57. Schematic of the ELSD. Reproduced with permission from Megoulas and Koupparis, 2005 [288]

CAD (Figure 58) provides a more efficient application to particulates smaller than 100 nm [292, 305], improving detection limits compared to ELSD [155, 301]. The first step is the ionisation of a dried stream of N_2 (positively charged) by a corona discharge needle (a high-voltage platinum wire). The eluent is nebulised and vaporised, and the particulates collide with the charged N_2 stream that transfers the charge to the analyte particles by diffusion. Then, the flux of charged analyte

particles is collected and measured by a highly sensitive electrometer [305, 306]. Compared to ELSD, CAD provides higher sensitivity and a more uniform response throughout a broader dynamic range. [296, 305]

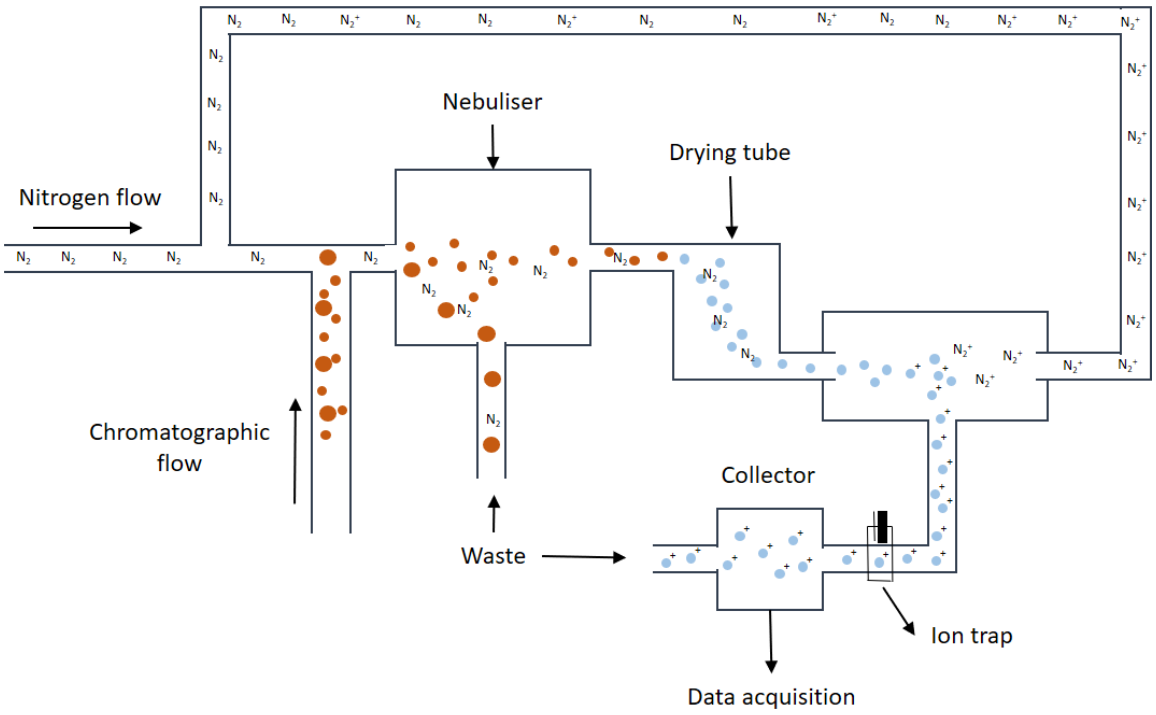

Figure 58. Schematic of the CAD [307, 308]

1.5.3 Mass spectrometry

MS is a powerful technique that provides numerous advantages when coupled with chromatography. The unique capacity to deliver structural information of the eluted compounds and the better detection limit reached when compared to classical detectors have increased the popularity of the hyphenation. Figure 59 shows a schematic of a mass spectrometer. The first step is forming gas-phase charged species in the ionisation source, making coupling to GC ideal. As the gas molecules elute, the ionisation source converts them to gas-phase ions.

The coupling to LC or pSFC is challenging as the liquid-like mobile phase affects the required operating vacuum and the reproducibility of the analysis. The introduction of atmospheric pressure ionisation interfaces overcomes the challenge by efficiently desolvating the liquid-like mobile phase. Now, electrospray ionisation (ESI), unispray ionisation (UNI), atmospheric pressure chemical ionisation (APCI) or atmospheric pressure photoionisation (APPI) sources are easily coupled to LC or SFC. The main differences result from the aided desolvation when using SFC due to the gaseous nature of the CO_2. The choice of one ionisation technique over another depends

on the chemical characteristics of the analyte. Even though matrix-assisted laser desorption/ionisation (MALDI) is not coupled to SFC, the ionisation source is described due to its wide application to polymer and PEG analyses.

Figure 59. Schematic of an MS instrumentation

After the ionisation occurs, the gas-phase ions produced in the ionisation source are transferred into the mass analyser. Examples of mass analysers are the single quadrupole mass analyser (Q), the triple quadrupole mass analyser (QqQ), the time of flight (ToF), the magnetic sector, the Orbitrap™ (OT), ion mobility mass spectrometry (IMMS) or Fourier-transform ion cyclotron resonance (FT-ICR). Ions are differentiated in the mass analyser based on different phenomena, either by using electromagnetic and/or magnetic fields (Q, QqQ, OT, FT-ICR), time of flight (ToF) or shape and size (IMMS). Sometimes, molecule fragmentation can be induced to obtain rich structural information. The selection of a mass analyser is based on the mass range, the mass resolution, and the mass accuracy required. The mass range is the range of *m/z* over which a mass spectrometer can detect ions or is operated to record a mass spectrum [309]. The resolving power is defined as the ability of an instrument or measurement procedure to distinguish between two peaks at *m/z* differing by a small amount and expressed as the peak width in mass units [309]. The accurate mass is the experimentally determined mass of an ion of known charge [309]. The last two terms are essential in the correct prediction of the chemical formula of the analyte and its fragments. A measurable electric signal detects the gas-phase ions separated in the mass analysers. The obtained data is a mass spectrum, a plot of *m/z* ratios on the *x-axis* and the relative abundance of the ions on the *y-axis*. A pump maintains the whole system under a high vacuum to allow reproducibility and avoid further undesirable fragmentation inside the system.

1.5.3.1 Ionisation sources

1.5.3.1.1 Electrospray ionisation source

ESI is a soft ionisation source (low to no fragmentation) (Figure 60). The process starts with the introduction of the analyte into a capillary. The source region is heated and a strong electrical potential is applied between the capillary and the counter-electrode (sample cone in Waters® mass spectrometers) that generates a voltage between the end of the capillary and the entrance to the MS. A Taylor cone is formed when applying a potential to the capillary; physical

phenomenon that occurs when the surface tension of the eluent emerging from the capillary is higher than the voltage applied. When the opposite occurs and the capillary is above a threshold voltage, the Taylor cone breaks and a jet of charged droplets emanates by nebulisation. In the limit (Rayleigh limit), the charge excess produces a Coulombic explosion that disintegrates the droplet. As they approach the sample cone, these smaller droplets lose solvent, releasing gas-phase ions that are transferred toward the mass analyser. If the voltage applied between the capillary and the counter-electrode is positive (positive ion ESI), the positive ions being repelled from the tip and focused on the mass analyser. The opposite occurs in negative ion ESI. In pneumatically-assisted ESI MS (a newer variant of ESI MS), an N_2 flow is added to favour solvent desolvation and results in the disruption of the Taylor cone, avoiding its formation. [310-316]

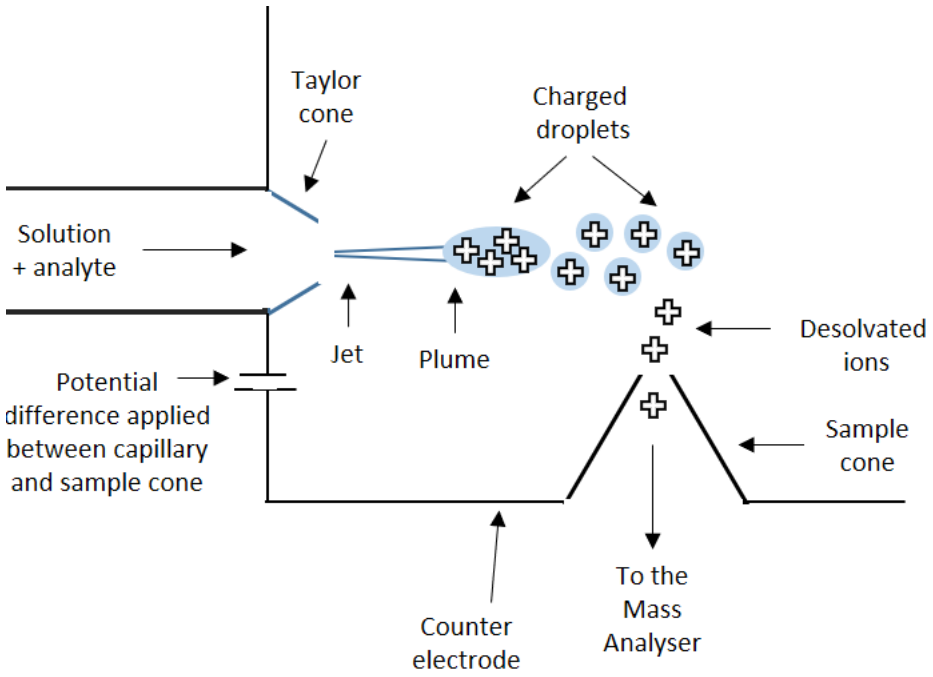

Figure 60. Schematic of the ESI source showing the processes that occur

Three desolvation mechanisms have been accepted that explain the formation of ions (Figure 61). Iribarne and Thomson proposed the ion evaporation model (IEM) [317], Dole *et al.* proposed the charged residue model (CRM) [318], and Konermann *et al.* recently proposed the chain ejection model (CEM) [319]. The IEM (Figure 61 a) applies to ions from low MW species (*e.g.*, small drug molecules). The CRM (Figure 61 b) is mainly considered when the size of the analyte dramatically exceeds the size of the solute (*e.g.,* large biomolecules such as globular proteins). The CEM (Figure 61 c) falls between the IEM and the CRM (*e.g.*, non-polar polymers or unfolded proteins) [320]. The IEM proposes that solvent evaporation causes the droplet to shrink until the field strength at the droplet surface is sufficiently large that the analyte ions can be ejected from the

droplet. The CRM proposes that ions are solvent droplets containing an analyte molecule that evaporates to dryness. The solvent and analyte molecules remain close to the Rayleigh limit, the Coulombic fissions cause the small solvent molecules to eject from the droplet and charges are balanced during the shrinkage process as the solvent evaporation from the analyte induces a charge transfer from the solvent to the analyte. The CEM proposes that exposure to an acidic environment denatures and unfolds proteins, making accessible the hydrophobic core of the molecule for dissolution. Then, the partially unfolded hydrophobic region side of the chain is expelled from the droplet surface and subsequently ejected into the gas phase, charging the chain as it leaves the solvent droplet. Typically, more charges are observed in analytes that follow the CEM than the CRM due to a higher number of exposed ionisable side chains and a larger surface area.

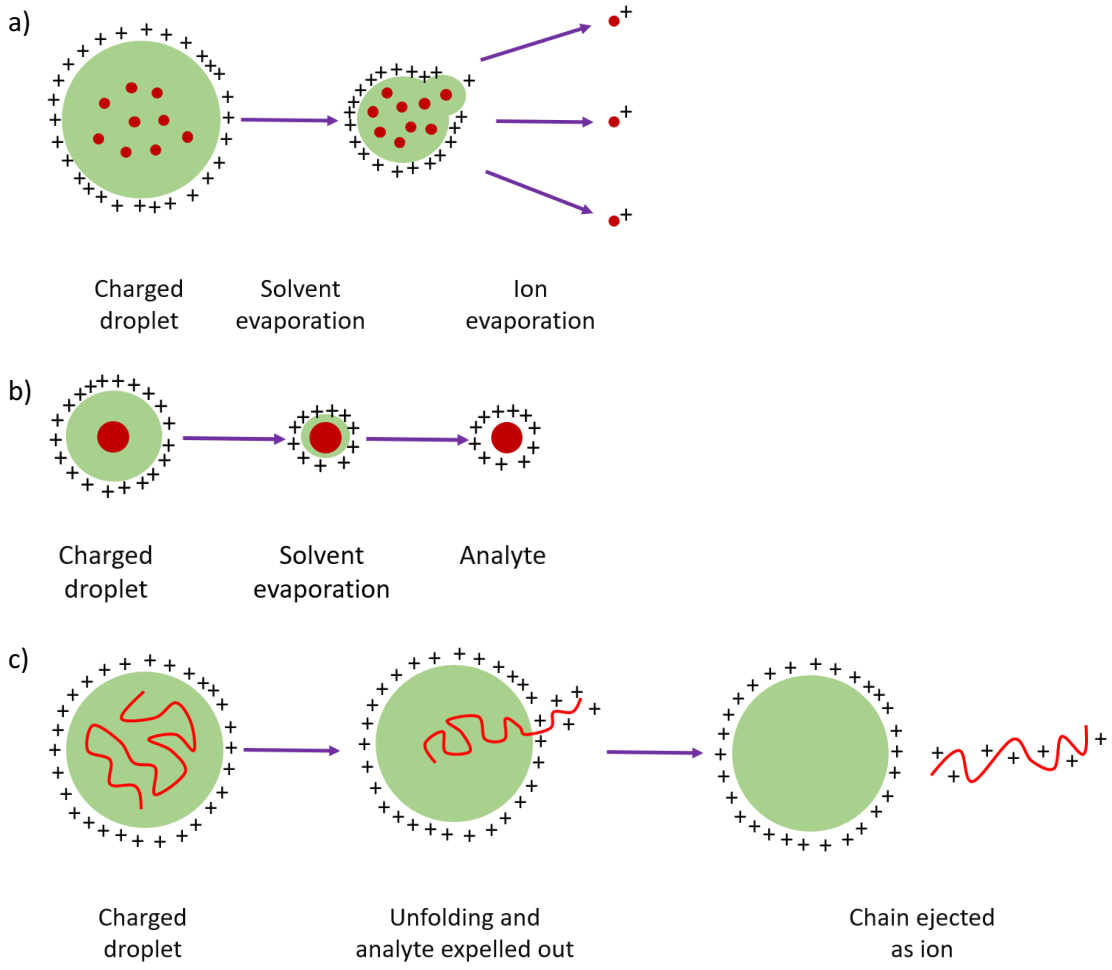

Figure 61. Schematic of the possible desolvation mechanisms occurring in ESI: a) IEM by Iribarne and Thomson, b) CRM by Dole *et al.*, and c) CEM by Konermann *et al.* [317-319]

The ion formation in ESI MS relies on the presence of acidic and basic sites of the analyte. In positive ion ESI MS, analytes mainly form protonated ($[M + nH]^{n+}$) or cationised molecules of NH_4^+,

Na^+ or K^+ ($[M + nX]^{n+}$) (Figure 62 a) due to the presence of basic sites. In negative ion ESI MS, deprotonated ($[M - nH]^{n-}$) or anionised molecules of formate or citrate can be formed ($[M - nX]^{n-}$) due to the presence of acidic sites. For larger molecules, the presence of several ionisation sites of protonation/deprotonation in the molecule results in multiply charged species (Figure 62 b), either in positive or negative ion ESI MS (*e.g.*, proteins, large molecules, etc.). The observation of M^+ or M^- is rare and mainly observed for some quaternary ammonium salts. [310, 321, 322]

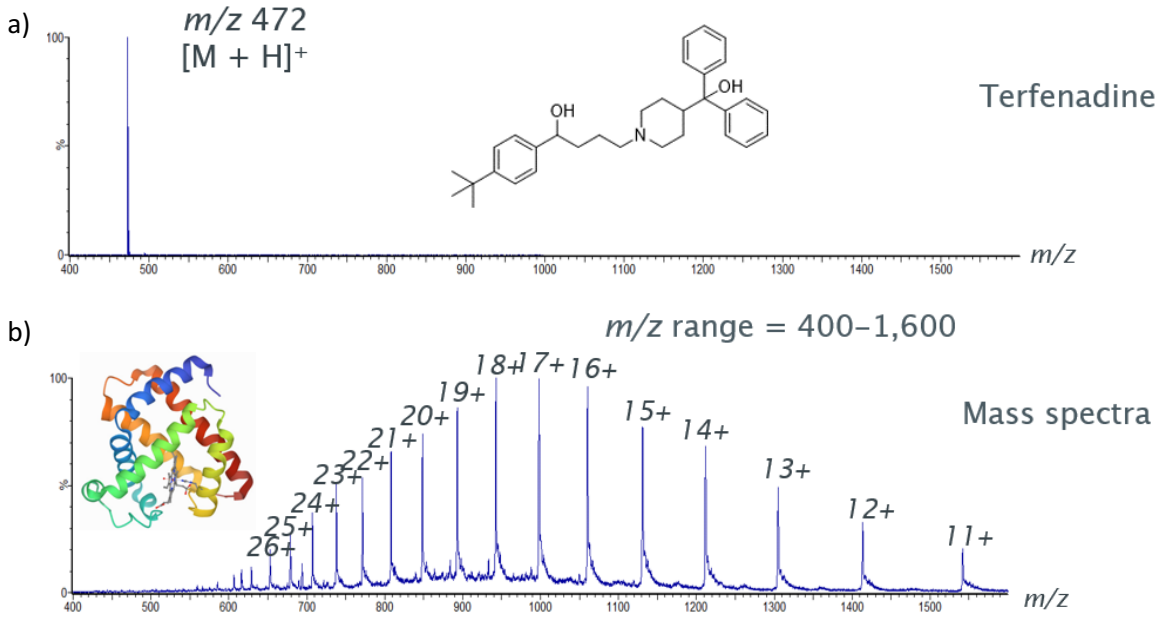

Figure 62. Differences in the positive ion ESI mass spectrum between a) a small molecule (terfenadine) and b) a large biomolecule (horse heart myoglobin)

Applications of ESI include polar analytes with acidic or basic sites due to the higher ionisation efficiency and excellent sensitivity observed; however, matrix effects can be observed that result in ion suppression or enhancement. The positive ion polarity is ideal for analysing peptides, proteins, small polar drugs and their metabolites, pesticides, dyes, and organometallic compounds, whilst negative ion ESI is applicable for proteins, drug metabolites, oligonucleotides, carboxylic acids, saccharides, and polysaccharides. [310, 322-324]

1.5.3.2 Unispray™ ionisation source

In pneumatically-assisted ESI, the large droplets formed during the nebulisation process have a reduced time to evaporate the solvent before reaching the mass analyser, decreasing the ionisation efficiency. UNI overcome this challenge by introducing several modifications to the design. Firstly, UNI incorporates a metallic pin orthogonal to the spray and the sample cone (Figure 63). Then, a voltage is applied between the pin and the sample cone, which no longer

occurs between the spray capillary and the sample cone. This voltage is typically lower (1.5 kV) than pneumatically-assisted ESI (3.5 kV). [325]

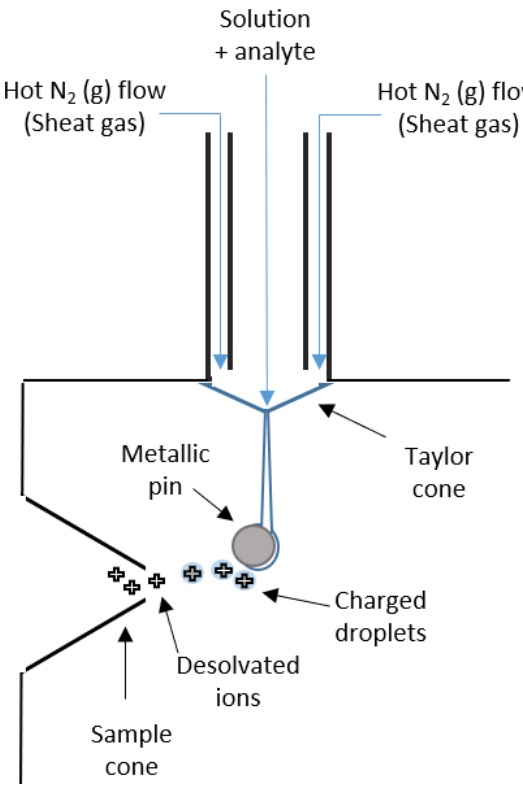

Figure 63. Schematic of the UNI source

In UNI, the spray is nebulised using a coaxial hot N_2 gas, and the nebulised (primary) droplets impact a hot cylindric pin made of stainless steel, forming smaller (secondary) droplets. The location of impact and the distance to the pin are critical for good ionisation efficiency. The optimum impact location typically happens on the top right quadrant of the pin (opposite the sample cone) so that the Coandă phenomenon can occur [325]. The distance is crucial due to the need for the primary droplets to reach supersonic velocities before colliding with the pin. As the fluid collides with the pin, the stream of droplets is attached to the convex surface, following around the curve of the pin, deflecting from its original trajectory, and pointing the fluid to the sample cone. Whilst this process, the primary droplets are charged and disintegrated, leading to smaller droplets that desolvate producing the ions as they approach the sample cone. The ionisation mechanism is believed to be similar to ESI. As the secondary droplets are smaller than the primary droplets, the desolvation process in UNI is more efficient when compared to ESI, leading to higher ionisation efficiency. Even though Ciclet *et al.* reported that the UNI signal is up to 20 times higher, some analytes show higher responses under ESI conditions. [325, 326]

1.5.3.2.1 Other atmospheric pressure ionisation sources used in chromatography

ESI is an excellent ionisation source for non-volatile, polar, and semi-polar small and large molecules with acidic/basic characteristics. However, other ionisation sources can be used for polymer analysis, and Waters® offer these interchangeable ionisation sources requiring minimal instrument downtime. APCI is suitable for low polar analytes with MWs below 2000 Da, whilst APPI applies to the analysis of non-polar compounds that contain either unsaturated double bonds or aromatic systems. Changes in the ionisation source require changes in the flow rate and make-up solvent, especially when quantifying. Whilst ESI or APCI typically uses CH_3OH/HCOOH, for APPI, the make-up solvent requires changes from CH_3OH/HCOOH to toluene/acetone. APCI proved to work with polymers such as poly(tetrahydrofuran), poly(ethylene terephthalate) or poly(caprolactone). APPI found applications for poly(styrene) or polymers with unsaturated end groups. [323, 324, 327, 328]

APCI is a soft ionisation source in which an ionised gas (N_2, O_2, H_2O, NH_3) reacts with gas-phase analytes to produce either protonated or deprotonated molecules. In APCI (see Figure 64), the mobile phase is vaporised by a heated fused silica capillary assisted by a coaxial nitrogen flow that produces a neutral spray. The analyte is nebulised using a hot auxiliary gas to tiny droplets by solvent evaporation. An electric field produced by a corona discharge needle breaks these droplets resulting in serial chemical reactions between the analyte and the plasma ions. Ions produced are protonated/deprotonated molecules ($[M + H]^+$ or $[M - H]^-$) *via* proton transfer or abstraction and radical ions (M^{*+} or M^{*-}) *via* charge exchange or electron capture. Even though adduct ions $[M + X]^+$ are rarely formed, their formation depends on the analyte and is associated with a secondary ESI process. [329]

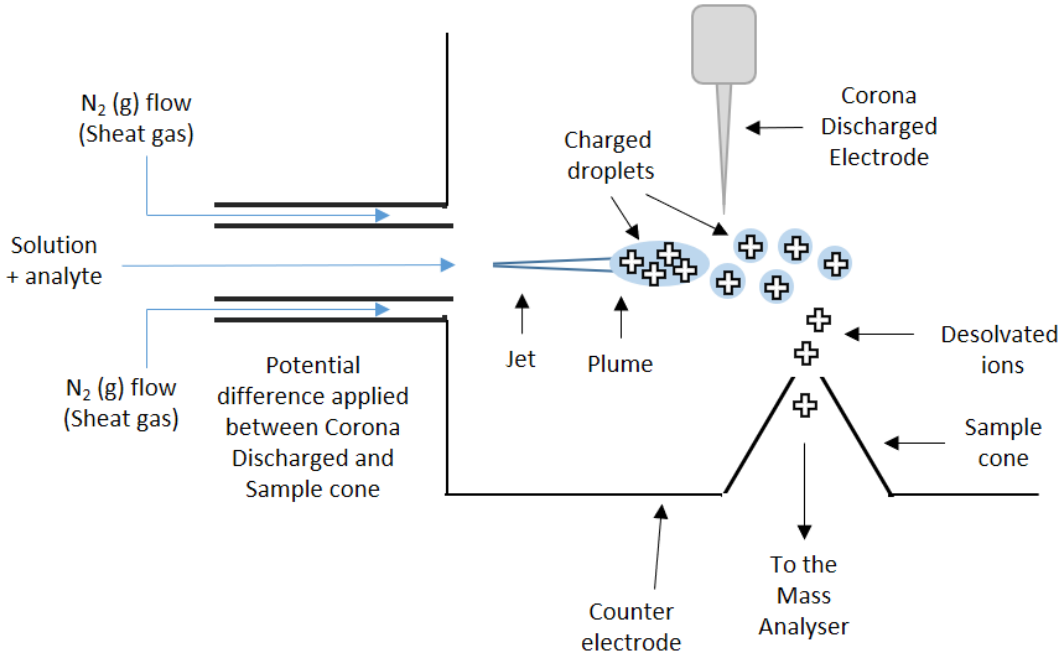

Figure 64. Schematic of the APCI source

APPI accomplishes ionisation by photoirradiation (see Figure 65). A heated fused silica capillary vaporises the mobile phase, producing an aerosol. The aerosol droplets are irradiated using a Krypton UV discharged lamp that emits a photon absorbed by the analyte. Radical ions (M^{*+} or M^{*-}) are produced if the photon exceeds the ionisation potential of the molecule. Protonated molecules ($[M + H]^+$) are observed if solvent molecules are at the ionisation site. As common chromatographic solvents (CH_3OH or CH_3CN) can absorb irradiating photons resulting in poor ionisation or quenching, the ionisation is enhanced using photoionisable dopants (toluene, acetone) that favour the formation of radical cations. Dopants are commonly infused into a stream of hot gas through the auxiliary gas port of the source or introduced directly into the solvent flow post-column. APPI works for aromatic and olefinic compounds. [327, 330-332]

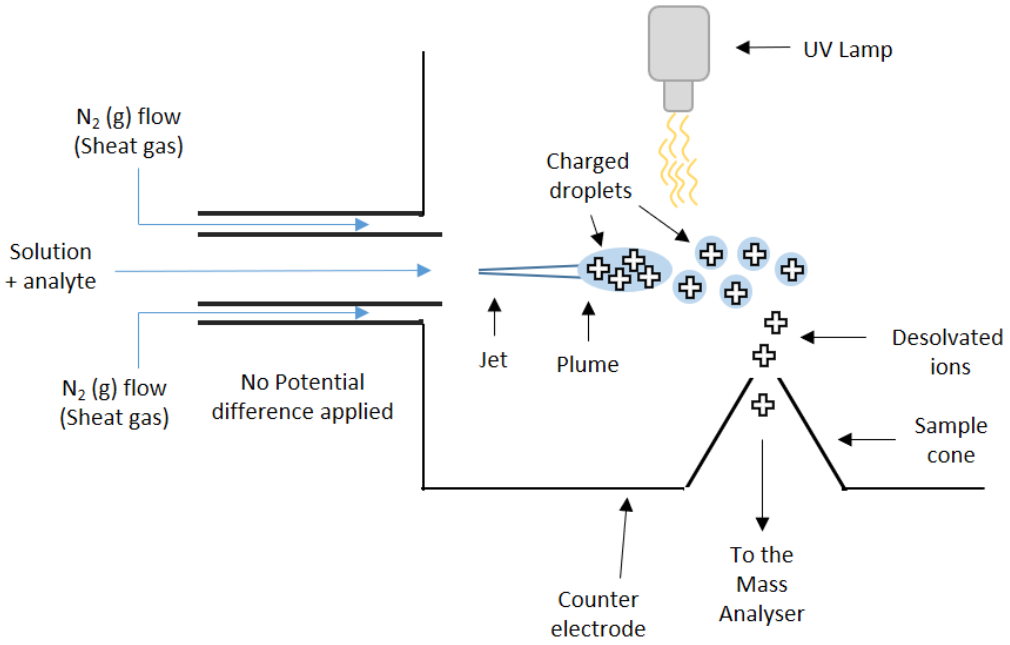

Figure 65. Diagram of the APPI source

1.5.3.2.2 Other atmospheric pressure ionisation sources not coupled to chromatography

MALDI MS is common in polymer analysis as chromatographic separation is not required [333]. In MALDI, the sample is prepared with a matrix co-crystallised with the analytes once solvent evaporation is observed. Easily ionised polymers (such as PEG or PPG) typically include an alkali metal to aim ionisation and form $[M + nX]^{n+}$ molecules, whilst more challenging ones (PS) require silver trifluoroacetate. A highly energetic photon beam laser removes a fragment of the sample-matrix crystal (desorption). The laser energy is controlled and emitted by specifying the corresponding wavelength (ranging from UV to infrared) and fluence of the laser pulses. Some commonly used lasers are provided in Table 21.

Laser type	**Gas**	**Solid-state**			
	N_2	**Nd:YAG**			**Er:YAG**
		Fundamental	**Frequency-tripled**	**Frequency-quadrupled**	
Wavelength	337 nm	1.06 µm	355 nm	266 nm	2.94 µm
Pulse width	Few ns	Few ns			Few tens ps

Table 21. Lasers used in modern MALDI sources [334-336]

Pulsed lasers are more common than continuous laser designs due to the standard coupling of MALDI with ToF mass analysers. The pulses allow enough time for the ion packet to reach the

detector before the next one arrives. As a result, the energy per pulse is more important than the energy of the photon. Evaluating the pulse width (duration of a pulse) and fluence (energy of the laser per area) is required to control the energy of each laser pulse available for ionisation. These two parameters are controlled using optics that adjust the spot size of the beam at the surface and focus the energy distribution on a near-Gaussian or Top-Hat distribution.

The absorption of the laser energy from the matrix produces matrix excitation (electronic, vibrational, and kinetic energy) and increases the temperature of the sample-matrix complex. Then, the matrix desorbs from the complex, evaporates, and transfers the correct amount of energy to the analyte by an induced electron-proton transference, resulting in the ionisation of analytes without fragmenting. The ion beam of analytes in the gas phase is focused and accelerated to the mass analyser using several Einzel lenses and electric fields.

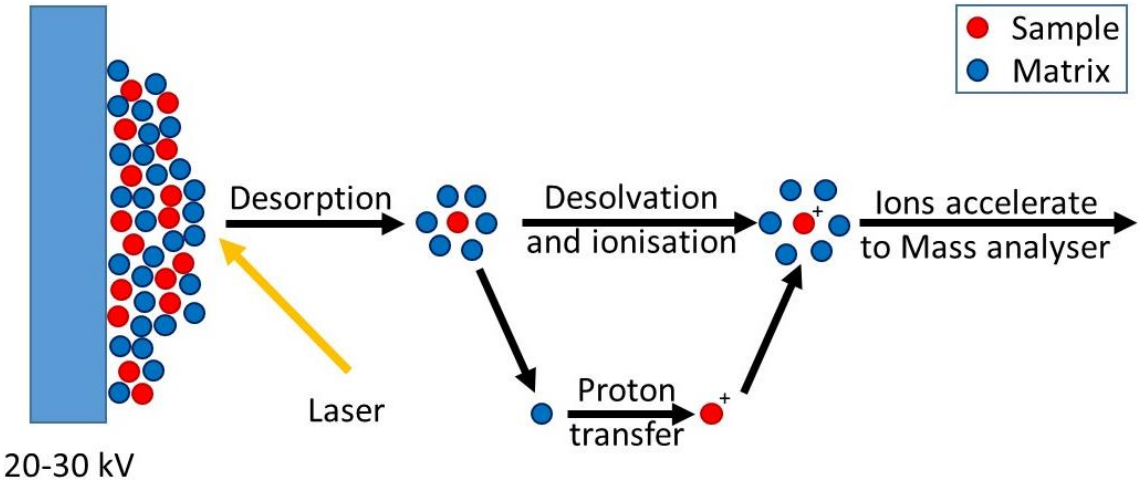

Figure 66. The desorption/ionisation processes in the source MS

1.5.3.3 Mass analysers

1.5.3.3.1 Single quadrupole mass analyser

The single quadrupole mass analyser (Q) from Waters® is the Xevo SQD 2. In 1953, Paul and Steinwegen described the principle of the Q mass analyser. Figure 67 a shows the schematic of a Q mass analyser. The structure consists of two pairs of metallic rods parallel and equidistant from the central axis (Figure 67 b). Each opposite pair is electrically connected with opposite potentials +Φ and -Φ. Gas-phase ions travel in the middle of the hyperbolic cross-section of the four rods, where no electric field is applied.

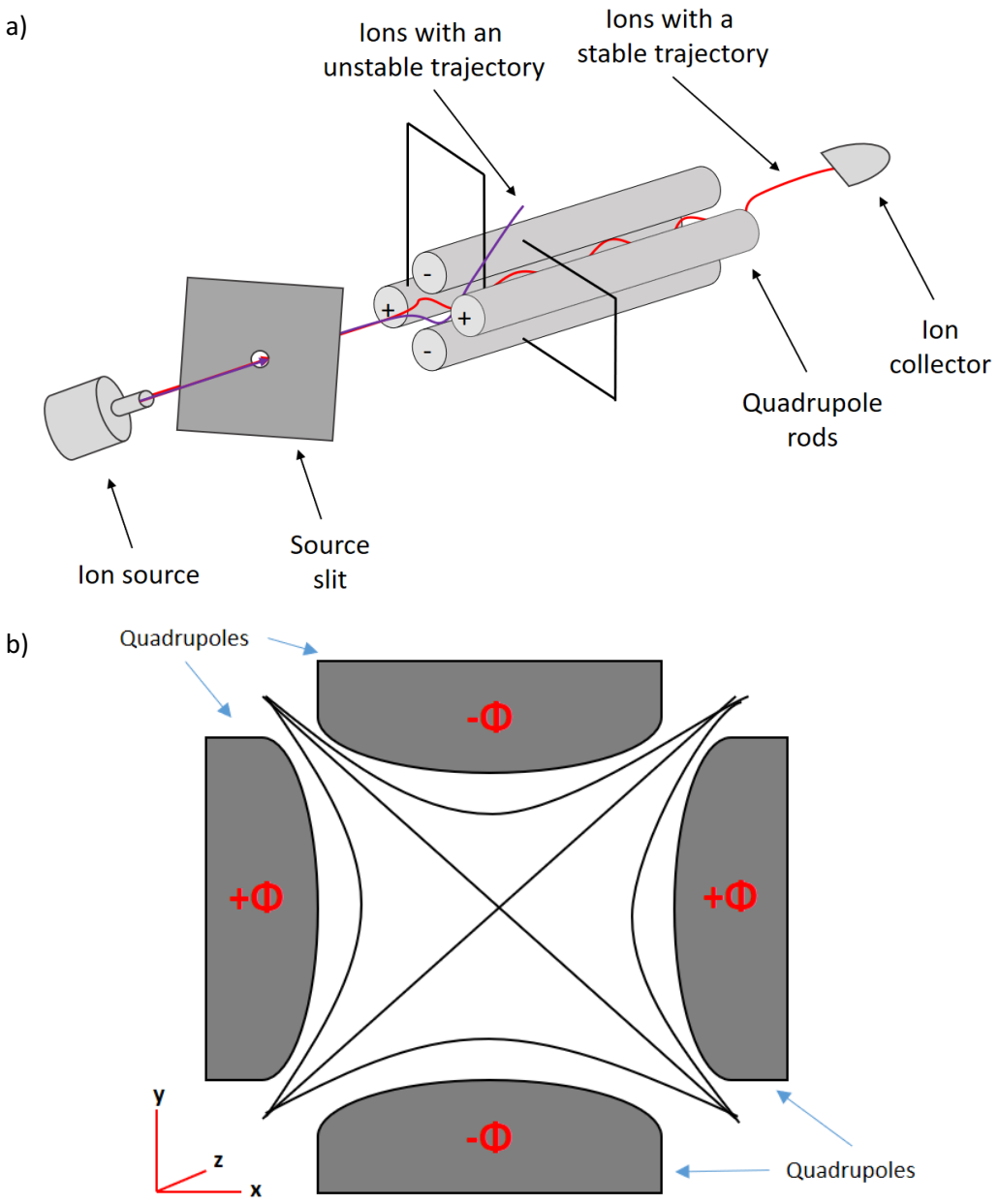

Figure 67. Schematic of a) Q mass analyser and b) hyperbolic section of the Q mass analyser

Both direct and alternating currents are applied to both pairs of rods, generating two voltages (+Φ and -Φ, Equation 21and Equation 22). One voltage is generated by applying the direct current to a pair of opposite rods (U), whilst the application of the alternating current at a varying radio frequency (ωt) to the other pair of rods generates the second voltage (Vcos(ωt)).

$$+\Phi = +(U + V\cos\omega t) \qquad \text{Equation 21}$$

$$-\Phi = -(U + V\cos\omega t) \qquad \text{Equation 22}$$

Applying the Mathieu equations to the voltages generated on the four rods of a Q led to two critical variables, *a* and *q*, also called Mathieu solutions (Equation 23 and Equation 24).

$$a = a_x = -a_y = \frac{8zU}{mr_0^2\omega^2} \qquad \text{Equation 23}$$

$$q = q_x = -q_y = \frac{4zV}{mr_0^2\omega^2} \qquad \text{Equation 24}$$

The overlapping of the Mathieu solutions allows the observation of areas where ions are stable (Mathieu diagrams, Figure 68). The intersections of the representation of the curves in Equation 23 and Equation 24 allows to establish regions (A, B, C and D) which contain stables *x*- and *y*-trajectories, as such allowing the transference of the ion through the Q. Most commercial Q operates in the A region.

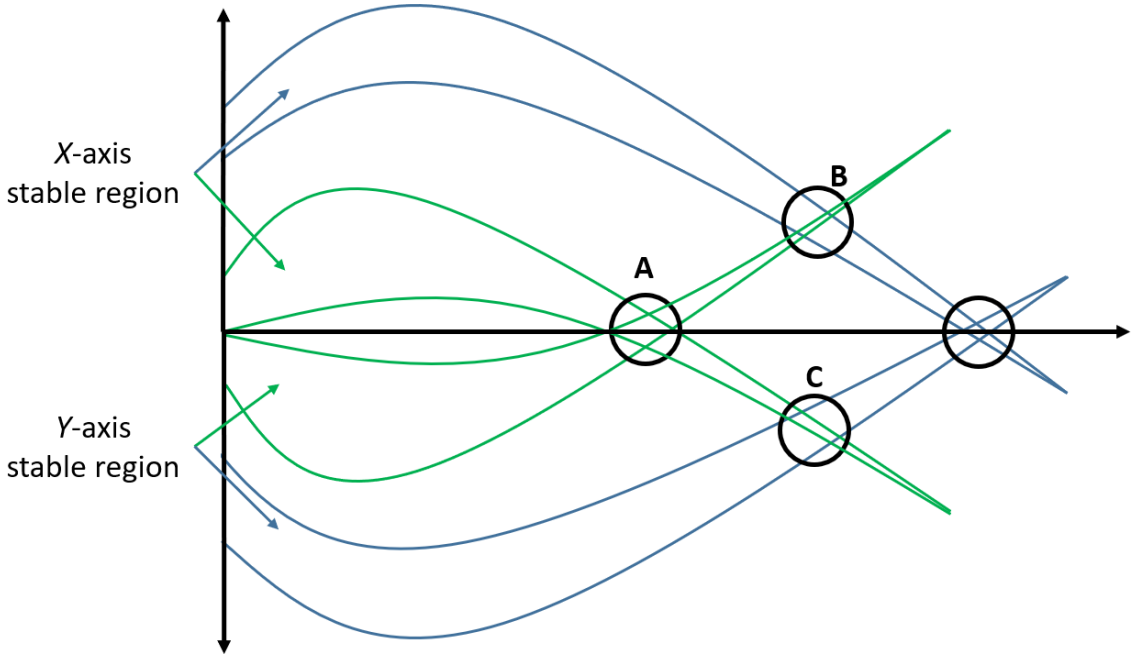

Figure 68. Mathieu diagram showing stable region according to the Mathieu equation. Areas labelled as A, B, C and D denote stability areas for an ion in the *x*- and *y*- axes

When an ion enters the quadrupolar field, the constant current attracts ions into one consistent direction towards one pair of electrodes. In contrast, the alternating current moves ions in spirals through the detector (along with the *z-axis*). During the analysis, the radiofrequency voltage is sequentially positively and negatively charged. Therefore, both voltages simultaneously attract and repel the ions from the rods. Small ions pass through a significant distance by the alternating field; however, the stronger electric regions of the field produce that these ions have unstable trajectories and quickly collide with the rods, deactivating them. For large ions, the direct current

part of the field is responsible for the unstable trajectories of these ions and the subsequent deactivation. The voltages are compensated when ions undergo stable trajectories. This compensation involves that the ions remain stable in both axes until they reach the mass detector. In a Q, the rods in the *x-axis* act as a high-pass mass filter for heavy ions, whilst the *y-axis* rods act as a low-pass mass filter for light ions. Then, ions of a specific *m/z* value have stable trajectories depending on the direct current and alternating radiofrequency applied to each pair of rods. [337-340]

As the Mathieu solutions depend on the mass and charge of the ion, the Mathieu diagrams are specific to the ions. Suppose we assume ions at singly charged states (z=1). In that case, a scan line can be drawn that intercepts the stability region A for each ion (Figure 69) and illustrates the mass filter character of the mass analyser.

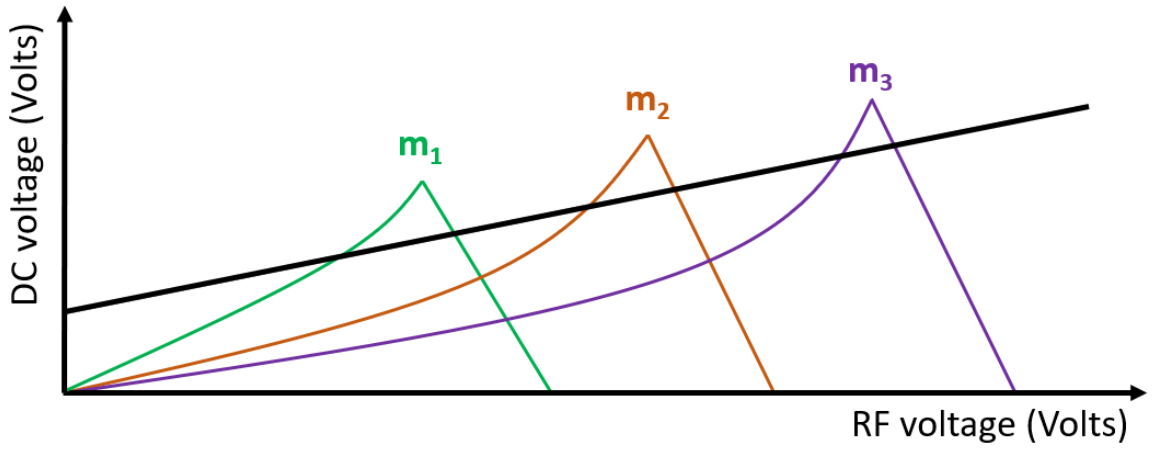

Figure 69. Stability diagram as a function of U and V for three ions of masses m_1, m_2 and m_3 (assuming singly charged species), showing the scan line

The scan line can be modified to alter the sensitivity and mass resolution that the Q provides. These changes can be made in Waters® MassLynx™ software by modifying the low-mass (LM) and the high-mass (HM) resolution values of the instrument tune page, as they modify the resolving DC on the Q. These values relate to the slope (HM) and the *y*-offset (LM) of the scan line rate of the Q. Their modifications move the scan line away from the stability region of the Mathieu diagram of the Q. Decreasing the slope or the *y*-offset allows the scan line to pass through a major area of the stability diagram, resulting in higher sensitivity at the cost of a wider mass peak. On the other hand, increasing the slope or the y-offset involves covering a smaller stability region, resulting in lower sensitivity; however, the mass resolution increases. As a result, the mass resolution varies over the *m/z* range, resulting in Q mass analysers being considered low-

resolution instruments. However, due to their low-duty cycle, Qs are ideal for interfacing with many chromatographic systems.

1.5.3.3.2 Triple quadrupole mass analyser

The information provided by one mass analyser is often insufficient to distinguish between molecules, or extra fragmentation is required for the unique assignation of the molecule of interest. In these cases, tandem MS results are helpful. Several mass analysers are combined (see Figure 70) to selectively fragment specific ions to facilitate an understanding of the fragmentation pattern of the ion and distinguish molecules that co-eluted during the chromatographic process. In a triple quadrupole mass analyser, three quadrupoles (Q1, q2, Q3) are aligned in series. Several ion lenses located in the gaps between Qs focus the ions on the mass analyser. Whereas Q1 and Q3 work as standard quadrupole mass analysers (as described in section 1.5.3.3.1, page 77), q2 is a radiofrequency-only quadrupole. Sometimes, a collision gas (N_2 or Ar) is introduced inside q2 to produce a Collision-Induced Dissociation process (CID), *i.e.*, collisional activation followed by fragmentation of the ion. [309, 337, 341-343]

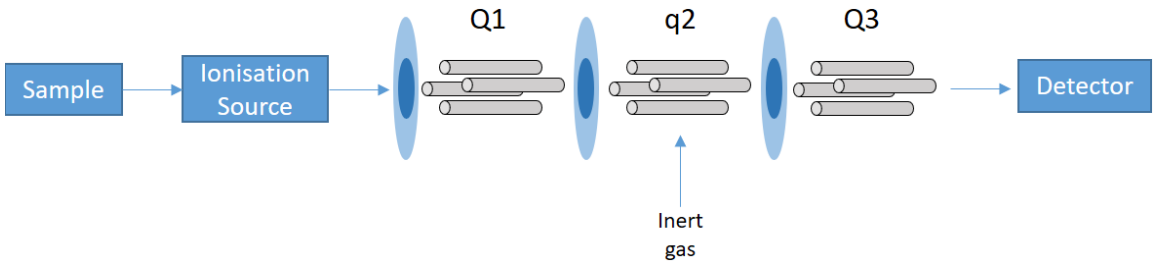

Figure 70. Schematic of a triple quadrupole detector

Assuming the reaction $m_1^+ \rightarrow m_2^+ + n$, several scanning modes can be performed (see Table 22): product ion scan, precursor ion scan and neutral loss scan. In a product ion scan, a chosen *m/z* selected in Q1 collides with a gas (collision-induced dissociation) in q2, and the fragments are analysed in Q3. In precursor ion scan, Q3 focus the selection on one ion whilst Q1 scans the masses. Therefore, all ions that followed a specific fragmentation or reaction are detected. In a neutral loss scan, both Q1 and Q3 scan simultaneously; when the loss of one particular mass α occurs, an ion with mass m is detected when it undergoes a mass fragmentation (*m*-α). Similarly, a given mass increase can be detected if a reactive gas is introduced within the collision cell located in q2. [343]

Scan mode	Q1	q2	Q3

Product ion scan, define m_1^+	No scan, select m_1^+	Metastable or CID	Scan up to m_1^+ to collect its fragments
Precursor ion scan, define m_2^+	Scan from m_2^+ upwards to cover potential precursors	Metastable or CID	No scan, select m_2^+
Neutral loss scan, define n	Scan desired range	Metastable or CID	Scan range shifted by Δm to low mass

Table 22. Scan modes of triple quadrupole mass analyser. Note that m_1^+ is the product ion, m_2^+ is the fragment ion and *n* a neutral lost from the fragmentation reaction

1.5.3.3.3 Time-of-flight mass analyser

ToF is a mass analyser where ions fly through a drift region in a vacuum, a field-free path, inside a tube of known length (l), after being accelerated by an electrical potential (Figure 71).

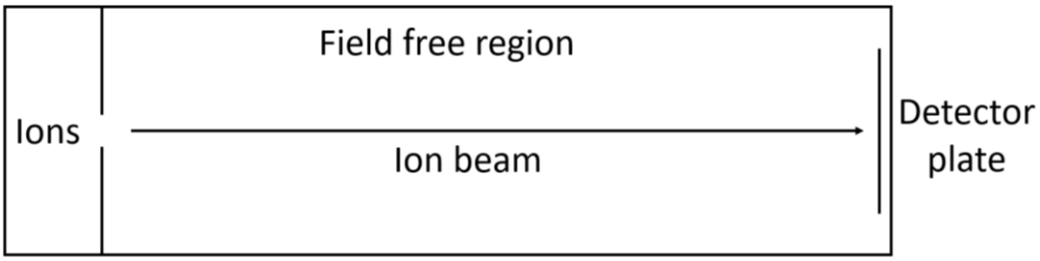

Figure 71. Schematic of a ToF mass analyser

The kinetic energy administered to an ion (E_K, Equation 25) and the time of flight (t_{ToF}, Equation 26) depend on the ion *m/z* value; hence, the ions separate according to their *m/z* value as they have different velocities (v_{ToF}, Equation 27).

$$E_K = \frac{m v_{ToF}^2}{2} = zeV \qquad \text{Equation 25}$$

$$t_{ToF} = \frac{m}{z}\left(\frac{l^2}{2eV}\right) \qquad \text{Equation 26}$$

$$v_{ToF} = \frac{l}{t_{ToF}} = \sqrt{\frac{2zeE}{m}} \qquad \text{Equation 27}$$

As the ions travel through the mass analyser, the differences in ion evaporation and ionisation result in unequal E_K, leading to a spatial spread of the ion cloud according to a distribution of E_K and, as such, the resolving power of the instrument is affected. During the ionisation, the use of a delayed or pulsed extraction can minimise these differences. Also, the addition of a reflectron

(*i.e.,* ion mirror) located before the detector (Figure 72) minimises the ion spread [344, 345]. This device consists of equally spaced electrodes that reflect the ions along the flight tube and compensate for the differences in the ion t_{ToF}, as ions with greater v_{ToF} penetrate deeper, spending more time in the accelerating potential and experiencing a slightly longer flight path than those with lower E_K [345-347]. The ions with lower E_K experience the opposite, as the penetration is shallower [347]. The incorporation of a reflectron provides two main advantages [347, 348]. Firstly, the kinetic spread of the ion cloud of the same *m/z* value that occurs during the ionisation is minimised, resulting in the focusing of the ion beam. Likewise, the longer length of the flying path that the ion travels (length of the ion beam) results in improved mass resolution.

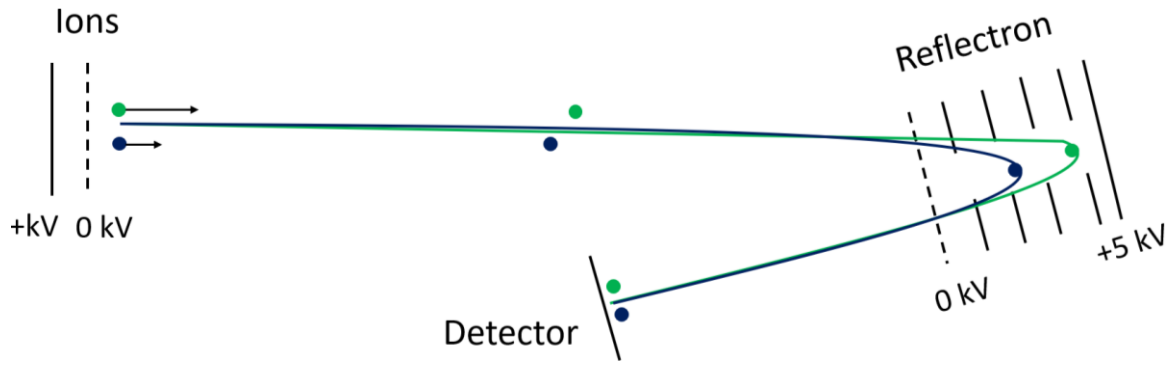

Figure 72. Refocussing of ions in a ToF mass analyser using a reflectron

ToF mass analysers are orientated in two configurations from the ion source: the linear and the axial (orthogonal) configurations (Figure 73) [349]. The use of an orthogonal design highly improves the resolution achieved, being *ca.* 1,500 for linear MALDI and *ca.* 30,000 in the orthogonal configuration (resolution values for cytochrome C with an MW *ca.* 12 kDa) [350]. The linear configuration, where ions travel when ionised directly to the detector (MALDI-ToF), and the orthogonal configuration, where ions travel through an initial path (typically an RF quadrupole) and then a pusher plate, produces the orthogonal acceleration of the ions towards the field-free path [349, 350]. Development of the orthogonal configuration occurred due to the constant introduction of ions from atmospheric pressure ionisation sources [349]. These ionisation sources can introduce neutral molecules from the mobile phase that can affect the reliability of the measurement of the ion t_{TOF} [349, 350].

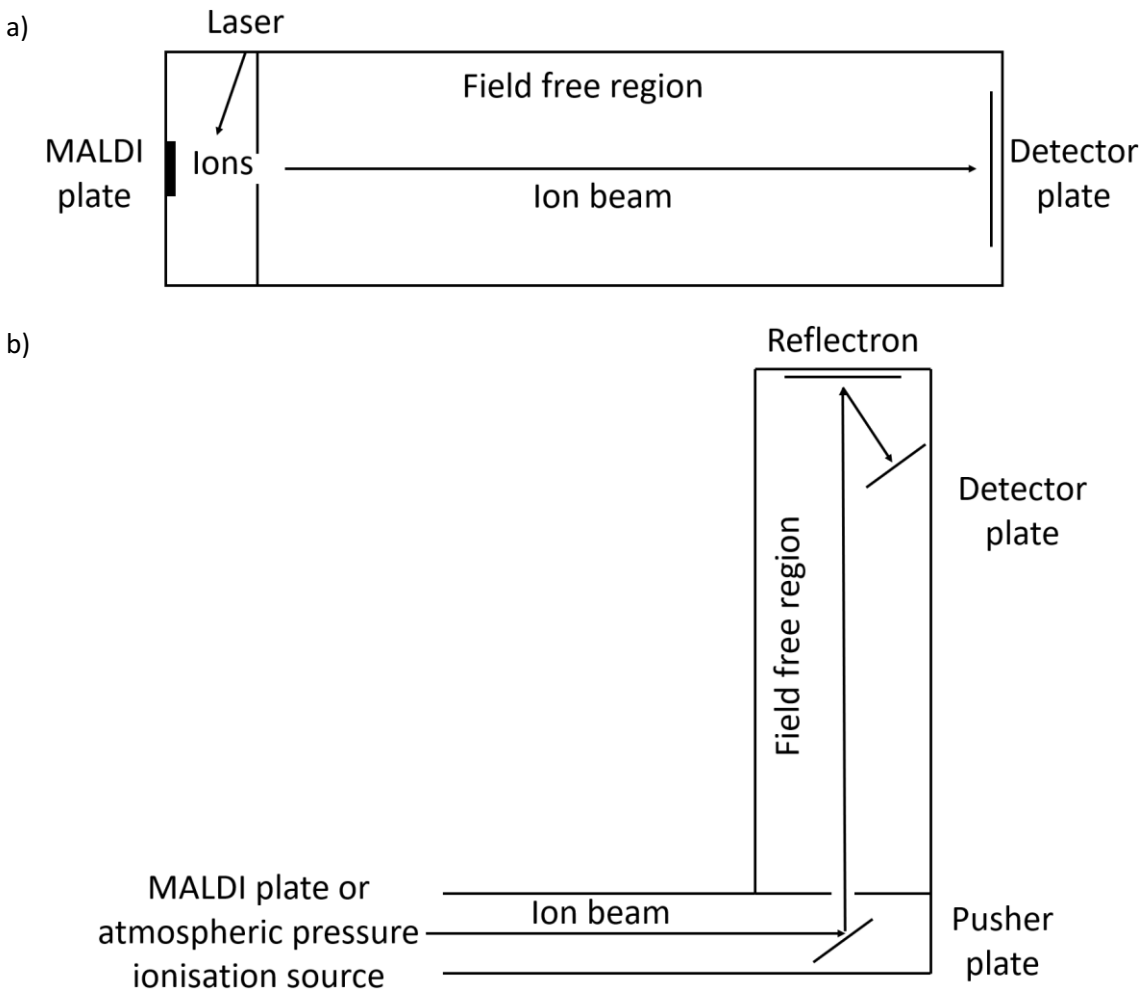

Figure 73. Differences in the configuration between ToF mass analyser: a) linear configuration and b) orthogonal configuration

Additionally, any slight variation that alters the initial sample height affects the obtained ion t_{TOF}, compromising the mass resolution of the instrument. These challenges directly conflict with the ToF, leading to instruments with lower mass resolution [349]. The introduction of a perpendicular ion beam to the axis of the ToF allows the elimination of most neutral molecules [349]. The perpendicular ion beam is achieved by adding a pulse towards the ToF region (produced by a pusher plate), resulting in an ion beam that is not continuous as in Q mass analysers[349]. As the ions are pulsed to travel in packets, a lower duty cycle is obtained (< 50%), resulting in differences in the t_{TOF} between small and large molecules [351]. Understanding the effect of this pulse is vital in polymer analysis as the obtained mass spectra are affected due to the various orders of magnitude of the oligomers MW.

Theoretically, ToF mass analysers have no upper mass limit; however, smaller differences are observed in t_{ToF} of molecules of higher masses when compared to smaller molecules. Orthogonal

ToF mass analyser usually incorporates several reflectron plates with different system configurations (V, N, W, *etc.*), especially in orthogonal ToF (Figure 74) [352]. The increased resolving power achieved due to a longer flight path compromises the sensitivity and possible fragmentation of metastable ions [350, 352]. The Waters® Synapt™ G2-*Si* instrument used in this research has the configuration Figure 74 c.

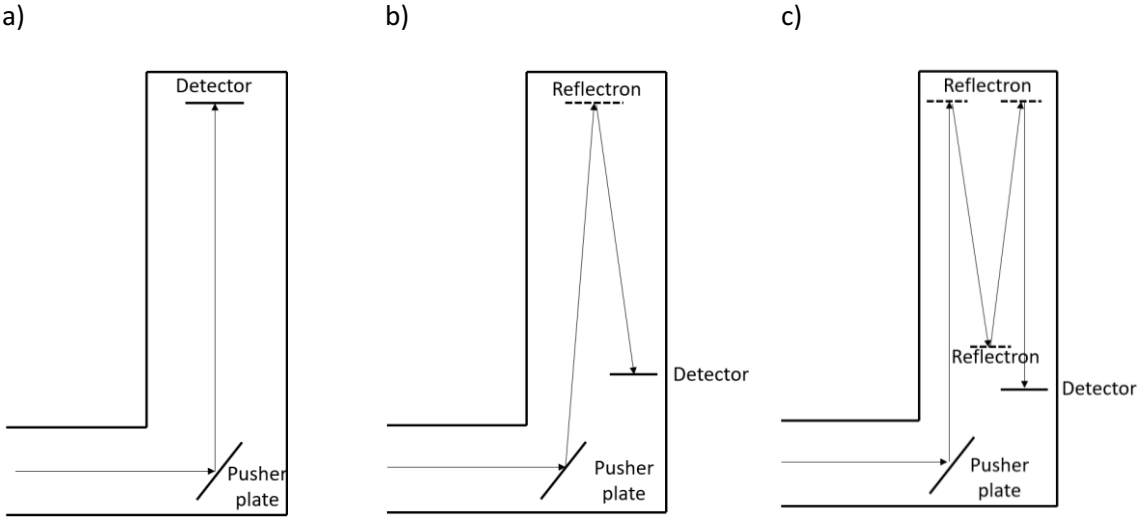

Figure 74. Different configurations of ToF mass analysers based on the number of reflectron plates and their position: a) basic, b) V and c) W

1.5.3.4 Ion mobility mass spectrometry

Ion mobility MS (IMMS) started when McDaniel *et al.* combined a ToF mass analyser with an ion mobility spectrometry (IMS) [353]. Ion mobility MS (IMMS) or ion mobility spectrometry (IMMS) are terms that refer to an MS technique that can separate ions as they drift through an inert gas at a constant gas pressure in an electric field based on the mass (*m*), charge (*z*), size and shape [354-356]. Separation occurs according to the *m/z* and the ion mobility (K) through the mobility drift gas (typically He, N_2 or air). The ions with an open conformation will travel slower than those with a more compact conformation. A ToF mass analyser usually detects the separated ions. In the early version, the ions from the ionisation source are accumulated and pulsed to an ion mobility cell (drift tube or DTIMS). However, modern versions include IMS such as the field asymmetric waveform IMS (FAIMS), the differential mobility spectrometry (DMS), the trapped IMS (TIMS), the travelling wave IMS (TWIMS) or the cyclic IMS (Cyclic IMS).

Each gas-phase ion with a known *m/z* value and a specific size and shape is characterised by the collisional cross-section (CCS or Ω) of the ion. The normalised ion mobility of an ion (K_0, Equation 28), defined as the ion mobility at p_0 760 Torr and T_0 273.15 K, relates to the collisional CCS of the

ion by the Mason-Schamp modification of the fundamental zero-field equation (Equation 29). This equation depends on the ionic charge (q = ze, z is the nominal ion charge state, and e is the elementary charge), the gas density (N_0) at p_0 and T_0, the Boltzmann constant (k_B), the gas temperature (T), the mass of the buffer gas (m) and the mass of the ion (M).

$$K_0 = K\frac{p}{p_0}\frac{T_0}{T} \qquad \text{Equation 28}$$

$$K_0 = \frac{3q}{16N_0}\left(\frac{2\pi}{k_B T}\right)^{1/2}\left(\frac{1}{m}+\frac{1}{M}\right)^{1/2}\frac{1}{\Omega} \qquad \text{Equation 29}$$

The use of specific calibration protocols allow obtaining experimental Ω values of the ion [357, 358]. The experimental Ω values allow the distinction of isobaric ions with different shapes and sizes or obtaining information on the conformational landscape and the ion dynamics. The Waters® Synapt™ G2-S*i* system used in this research uses a travelling wave for ion separation (TWIMS) [359], where an ion mobility separation is introduced before the QToF (Q-IM-ToF). A schematic of the ion mobility line in the system is shown in Figure 75.

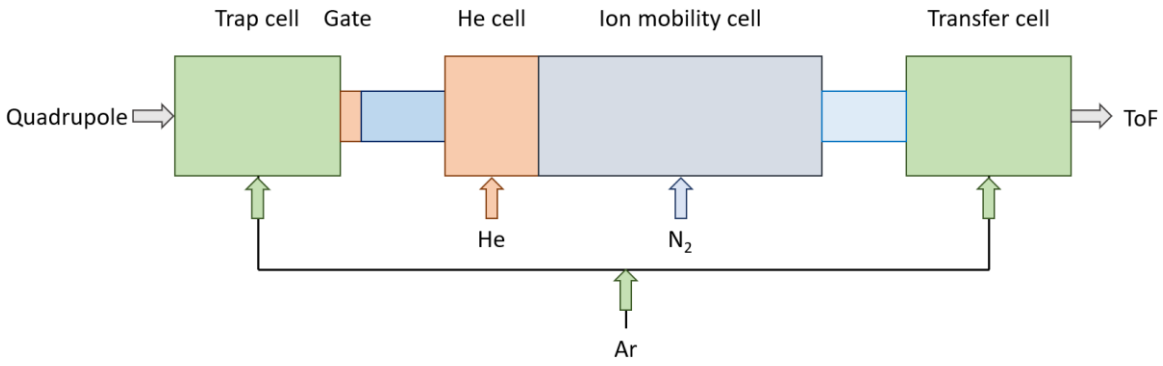

Figure 75. Schematic of the ion mobility separation line in Waters® Synapt™ G2-*Si*

In TWIMS, ion separation occurs by a non-uniform electric field located in three stacked ring ion guides (SRIGs, Figure 76 a) that consist of four regions: the trap ion guide, the helium cell, and the ion mobility cell, and the transfer ion guide (TriWave™). Ions are trapped in the trap ion guide (helped by the helium cell) to simultaneously release all ions to the IM cell (Figure 76 b). In the IM cell, a travelling wave of potential is created by applying a direct current superimposed on the confining radiofrequency of an electron and then transferred to the adjacent electrode. As ions pass through the wave (Figure 76 c), they can either tumble over the waves into adjacent potential wells or be carried through, based on the interactions with the opposite drift gas, resulting in a separation by shape and size. Ions focused on the ToF in the transfer ion guide as the ions leave the IM cell [360-363]. The CCS values in TWIMS are called $^{TW}CCS_{N2}$, as the CCS values depend on the ion mobility technique (TWIMS = TW) and the gas used for the separation (N_2).

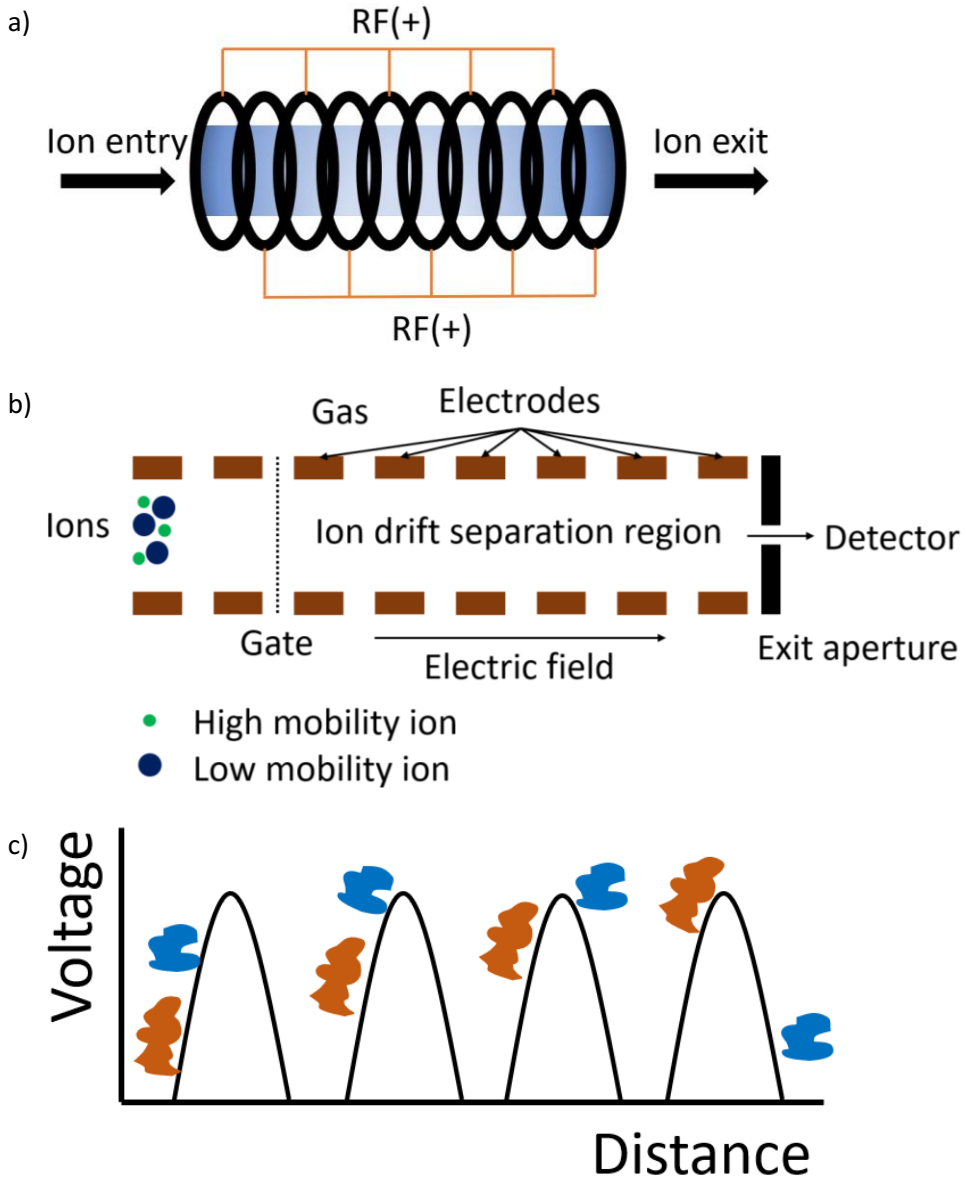

Figure 76. Schematic of the ion mobility separation using TWIMS: a) the stacked ring ion guides that allow the application of the travelling wave, b) the ion mobility line, and c) the electric field waves that allow for ion mobility separation

Additionally, collision-induced dissociation (MS^n in space) can be accomplished in the trap and transfer ion guides region of the Waters® Synapt™ G2-*Si* system, meaning that mobility information of the molecule and/or the fragments can be obtained; leading to three different types of fragmentation experiments: trap, transfer and time-aligned-parallel (TAP). In these fragmentation experiments, the Q select the precursor ion, and the fragmentation happens in the trap, the ion mobility and/or the transfer cells (see Table 23).

Experiment	Trap cell	Ion mobility cell	Transfer cell
Trap fragmentation	Fragmentation 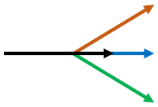	Mobility separation 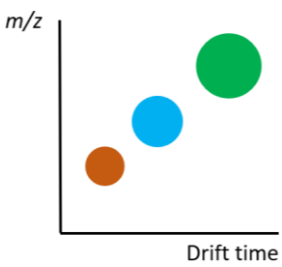	Transference 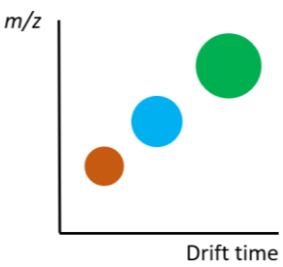
Transfer fragmentation	Transference	Mobility separation 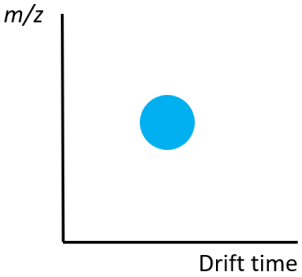	Fragmentation 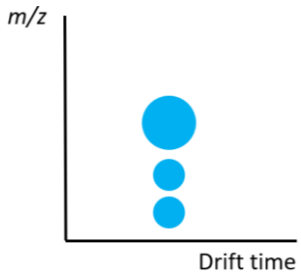
Time-aligned-parallel (TAP) fragmentation	Fragmentation 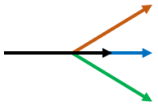	Mobility separation 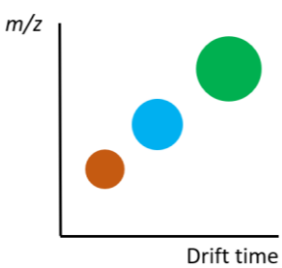	Fragmentation 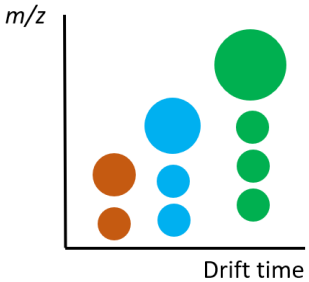

Table 23. Types of fragmentations in the Waters® Synapt™ G2-*Si*

1.6 Project scope

While SEC predominates in characterising impurities and quantitation of linear polymers, RPLC-MS is extended to analyse complex polymers. MALDI MS can be used; however, the lack of chromatography leads to a complicated data analysis for complex polymeric mixtures. The current literature lacks research using modern chromatographic approaches. This project proposes the combination of UHPSFC-MS using ESI to characterise and quantify polymeric excipients to evaluate the material quality and composition and complement the current techniques used in the pharmaceutical industry. Even though the project sponsor team (AstraZeneca) initially developed some approaches to quantify PEG using this technique, a more

extensive investigation was required for complex polymeric mixtures [126]. The research rationale was to exploit the enhanced oligomer separation of SFC and force the ionisation towards one type of adduct to simplify the complex polymer mass spectra and help investigate the composition of more complex polymeric excipients used in the industry. Also, the lack of quantitative approaches using MS leads to challenging intercomparison studies, especially when using different mass analysers in MS or instrumental configurations. Newer quantitation approaches should be developed to improve accuracy and precision and facilitate data comparison.

Chapter 2 Experimental

2.1 Chemicals

2.1.1 Reagents used during the method development

A-grade helium, industrial-grade argon and food-grade carbon dioxide (CO_2) were purchased from BOC Special Gases (Manchester, UK). Nitrogen (N_2) was supplied by an in-house nitrogen generator that varied for the instrument: a Whatman N_2 generator when using the Waters® single quadrupole detector (SQD) (Waters Corp., Milford, USA) mass analyser and a STREAM 120 N_2 generator when using the Waters® Triple quadrupole detector (TQD) (Waters Corp., Milford, USA) and the Waters® Synapt™ G2-S*i* (Q-IM-TOF-MS) (Waters Corp., Milford, USA) mass analysers. Laboratory-grade ammonium acetate (CH_3COONH_4) and laboratory-grade 15-crown-5 were obtained from Sigma−Aldrich (Gillingham, UK). Laboratory-grade ammonium formate ($HCOONH_4$) was purchased from Acros Organics (Basingstoke, UK). Laboratory-grade formic acid (HCOOH) and glacial acetic acid (CH_3COOH) were purchased from Fisher Scientific Ltd (Basingstoke, UK). LC-MS-grade methanol (CH_3OH), isopropanol ($(CH_3)_2CHOH$), and HPLC-grade acetonitrile (CH_3CN) were purchased from ThermoFisher Scientific (Loughborough, UK). LC-MS-grade water (H_2O) and HPLC-grade ethyl acetate ($CH_3CO_2C_2H_5$) were obtained from Fisher Scientific Ltd (Basingstoke, UK).

2.1.2 Project samples

Poly(ethylene) glycol (PEG) derivatives and (2-hydroxypropyl)-β-cyclodextrin (2HPBCD) samples were provided by AstraZeneca plc (Macclesfield, UK) (Table 24).

Material	Material quality and characteristics
mPEG 350, 550-750	Pharmaceutical reagent
mPEG acid 2000	Pharmaceutical reagent
PEG diacid 2000	Pharmaceutical reagent
Brij® 58	Pharmaceutical reagent
Brij® S 100	Pharmaceutical reagent
Gelucire® 44/14	Pharmaceutical reagent and treated samples
Tween® 20	Pharmaceutical reagent – several suppliers and batches qualities

Tween® 80	Pharmaceutical reagent – several suppliers
2HPBCD	Pharmaceutical reagent – several suppliers

Table 24. Materials provided by AstraZeneca plc (Macclesfield, UK)

2.1.3 Reagents used for quantitation

Laboratory grade PEG 200, 400, 600, 1000, 1450 and 2000, 18-crown-6 and lauric acid were purchased from Sigma−Aldrich (Gillingham, UK).

2.1.4 Mass spectrometry calibrant standards

A Waters® Synapt^{TM} G2-S*i* instrument was used to acquire accurate mass and ion mobility measurements. Accurate mass measurements were obtained using an external calibration of Waters® NaCsI pre-prepared tuning mixture (MS calibration solution for atmospheric pressure ionisation) obtained from Waters® (Manchester, UK). The NaCsI mixture consisted of 2 µg/mL NaI and 50 ng/mL in 50%/50% (v/v) $H_2O/(CH_3)_2CHOH$ and calibrated the *m/z* scale in the range *m/z* 300-3000 that led into an RMS in the range of [0.323 – 0.785]. Internal calibration was performed using a lock mass of *m/z* 758.2218 $[(C_2H_6SiO)_{10} + NH_4]^+$ that corresponded to an ion from dimethyl poly(siloxane) sourced from the PEEK tubing in the system. A supplementary internal calibration was performed using the ammoniated adducts of the most abundant PEG in the sample. Ion mobility $^{TW}CCS_{N2}$ calibration in positive ion ESI MS was achieved using a mixture of 0.1 µg/mL of acetaminophen (Sigma−Aldrich, Gillingham, UK) and 10 µg/mL poly-DL-alanine (MW 1,000-5,000 Da) (Sigma−Aldrich, Gillingham, UK) in 50%/50% (v/v) CH_3CN/H_2O. The measured drift times of the known components were converted to $^{TW}CCS_{N2}$ values following established procedures [360].

2.2 Sample preparation

2.2.1 Mobile phase preparation

Mobile phases composed of CH_3OH with either HCOOH, CH_3COOH or H_2O were prepared by mixing the required percentages of volume. The amount of ammonium formate or acetate salt - either $HCOONH_4$ or CH_3COONH_4 - required to achieve the desired concentration was calculated without considering volume contraction.

2.2.2 Sample preparation of poly(ethylene) glycols for characterisation

Stock solutions of 1000 µg/mL (linear PEG) or 5000 µg/mL (complex PEGs) in CH_3CN were prepared. Solutions of acidic PEGs were prepared in CH_3CN/HCOOH 99%/1% (v/v). Stock solutions were diluted using the same solvent until neither column nor detector overloading was observed.

2.2.3 Sample preparation of poly(ethylene) glycols for external calibration

The calibration solutions of PEG 600, 1000, 1450 and 2000 were prepared by several dilutions (factor 1:10) of the stock solutions of 1000 µg/mL in CH_3CN up to the highest number of the desired concentration. The required volumes of the corresponding diluted solution and CH_3CN were calculated to prepare the desired concentration of calibrant.

2.2.4 Sample preparation of poly(ethylene) glycols for internal calibration

Stock solutions of 1000 µg/mL PEG 600, 1000, 1450 and 2000 and 100 µg/mL of 18-crown-6 used as the internal standard (ISTD) in CH_3CN were prepared. The stock solution of PEG was diluted using several dilutions (factor 1:10) up to the highest number of the desired concentration. The stock solution of ISTD was diluted using several dilutions (factor 1:10) up to the highest number of the desired concentration. The required volumes of the diluted ISTD solution to achieve the final ISTD concentration in the calibrant solution were considered when calculating the final volume of CH_3CN added to reach the final concentration of the PEG calibrant.

2.2.5 Sample preparation of lauric acid for external calibration

A stock solution of 100 µg/mL lauric acid in CH_3CN was prepared. The calibration solutions of lauric acid were prepared by several dilutions (factor 1:10) of stock solutions up to the highest number of the desired concentration. The required volumes of the diluted solution and CH_3CN were calculated to prepare the desired calibrant concentration.

2.2.6 Sample preparation of (2-hydroxypropyl)-β-cyclodextrins

Stock solutions of 1000 µg/mL 2HPBCD in CH_3OH/HCOOH 99%/1% (v/v) was prepared for characterisation. The stock solution was diluted to the desired concentration using CH_3OH/HCOOH 99%/1% (v/v) until no overloading was observed.

2.3 Chromatographic columns

Fully porous (FPP) and superficially porous (SPP) particle columns for achiral analyses were purchased from Waters® (Waters Corp., Manchester, UK). FPP columns for chiral analyses were acquired from Daicel (Chiral technologies, Illkirch-Graffenstaden, France). The stationary phases are shown in Table 25.

Particle type and column size	**Stationary phase**	**Particle size (µm)**
FPP for achiral analysis (3.0 mm x 100 mm)	Acquity™ UPLC™ HSS PFP	1.8
	Acquity™ UPC² BEH	1.7
	Acquity™ UPC² BEH 2-Ethylpyridine	1.7
	Viridis HSS C18 SB	1.8
	Acquity™ HSS Cyano	1.8
	Acquity™ UPC²™ Torus™ Diol	1.7
	Acquity™ UPC² Torus™ 2-Picolamine	1.7
	Acquity™ UPC² Torus™ Diethylamine	1.7
	Acquity™ UPC² Torus™ 1-Aminoanthracene	1.7
SPP for achiral analysis (3.0 mm x 100 mm)	Acquity™ Cortecs™ C18+	2.7
FPP for chiral analysis (4.6 mm x 250 mm)	Chiralcel OD	3
	Chiralcel OD-H	3
	Chiralcel OG	3
	Chiralpack AD	3
	Chiralpack AS	3

Table 25. Columns investigated in this research

2.4 Direct infusion methods

Direct infusion experiments of mPEG acid 2000, PEG diacid 2000 and 2HPBCD were undertaken using a Waters® ZSpray™ electrospray ionisation (ESI) source located in a Waters® Synapt™ G2-S*i* QToF MS instrument. The sample diluent was collected using a 100 µL Hamilton 1710 syringe. The analyses were aided by a Chemyx 100 syringe pump driver that delivered a flow rate of 40 µL/min of the sample solution from the Hamilton syringe. The syringe was connected using a syringe fill port and one piece of PEEK connector. The sample was fused *via* PEEK tubing to the ionisation source using a PEEK fitting (method conditions in Table 26).

Ionisation voltage (kV)	±2.5[a]	**Desolvation gas flow (L/Hr)**	550
Cone voltage (V)	40	**Cone gas flow (L/Hr)**	50
Source offset (V)	40	**Nebuliser (bar)**	7
Source temperature (°C)	150	**Scan mode**	Full scan *m/z* 300-3000
Desolvation temperature (°C)	350		

Table 26. Direct infusion method conditions for high-resolution mass measurements. [a]: +2.5 kV for positive ion ESI QToF MS and -2.5 kV for negative ion ESI QToF MS

2.5 Connection of the UPC^2 to the Synapt™ G2-*Si* instrument

The Waters® Acquity™ UPC^2 instrument was connected to a Waters® ZSpray™ ESI source located before the Waters® Synapt™ G2-*Si* system using an additional piece of red PEEK tubing (1/16" OD x 0.005" ID x 2 m) (Figure 77). The piece of red PEEK tubing was connected to the splitter in the Waters® UPC^2 system using a piece of PEEK connector and to the ESI source in the Waters® Synapt™ G2-*Si* by using a PEEK fitting. The impact of adding a long piece of PEEK tubing in the chromatographic is discussed in section 3.6, page 149.

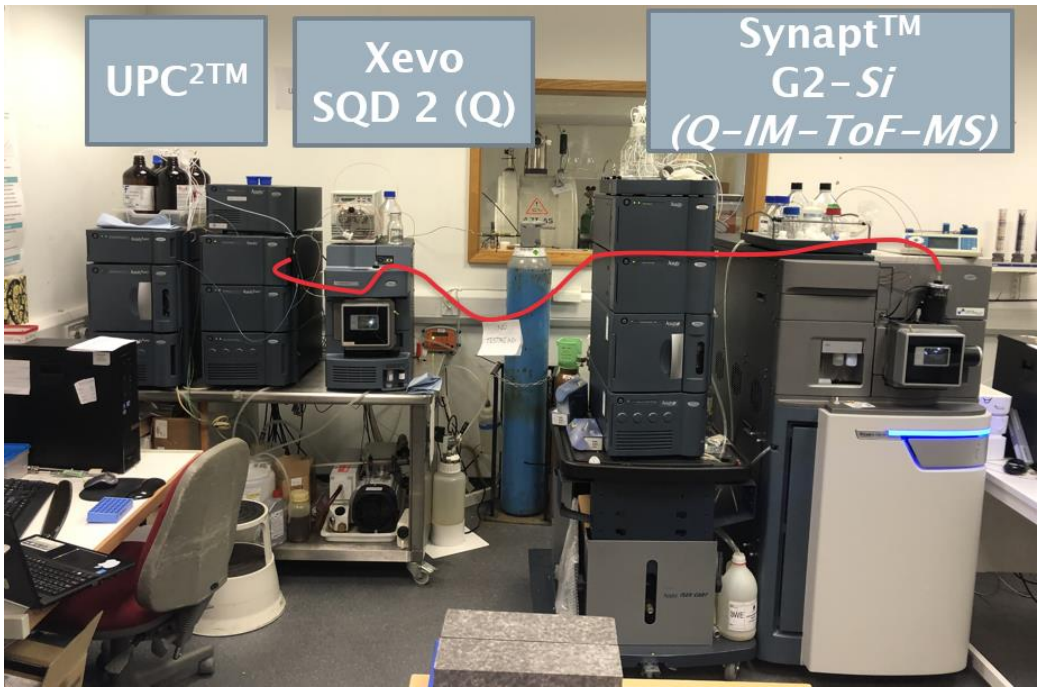

Figure 77. Connection of the UPC^2 system to the Synapt^{TM} G2-*Si* system

2.6 Developed methods for poly(ethylene) glycol analysis

2.6.1 Ultra-high-performance supercritical fluid chromatographic method

UHPSFC analysis was achieved using a Waters® Acquity^{TM} UPC^2 system(Waters Corp., Milford, USA). The sample manager was cooled at 10°C. An integral partial loop needle overfill (PLNO) injection mode injected 2 µL of each sample *via* the Acquity^{TM} Sample Manager. The needle and injection port were cleaned using one cycle of strong solvent (600 µL) and one cycle of weak solvent (600 µL) in PLNO injection mode, and the seal was washed between injections. The method conditions are presented in Table 27.

Mobile phase	A: CO_2 / 150 bar ABPR
	B: CH_3OH + 15 mM CH_3COONH_4 + 6.0% H_2O (CH_3OH [a])
	Linear gradient 2-40% at 1.3 mL/min
Column	Waters® Acquity^{TM} UPC^{2TM} Torus^{TM} Diol
	(130 Å, 1.7 µm, 3.0 X 100 mm) at 70 °C
Syringe wash	Weak wash: 600 µL CH_3CN
	Strong wash: 600 µL $(CH_3)_2CHOH$
	Seal wash: CH_3CN

Sample dissolution solvent CH_3CN (CH_3CN + 0.1% HCOOH [b])

Table 27. UHPSFC method conditions for PEG analysis. [a]: CH_3OH was used for positive ion APPI MS experiments due to the quenching product by ammonium salts in the ionisation source. [b]: CH_3CN + 0.1% HCOOH was used for PEGs with acidic end groups to favour the formation of the carboxylate anion

2.6.2 Ionisation source voltage and make-up solvents

The chromatographic system was directly coupled to several Waters® ZSpray™ ionisation sources before the Waters® SQD 2 mass analyser. Different ionisation sources were investigated (Waters Corp., Milford, USA): ESI, unispray ionisation (UNI), atmospheric pressure chemical ionisation (APCI) and atmospheric pressure photoionisation (APPI). The make-up solvent was changed accordingly to promote the favoured ionisation. The applicability, voltages and make-up solvents used for each ionisation source are presented in Table 28.

Ionisation source	**Applicability**	**Voltage (kV)**	**Make-up solvent used (flow rate 0.45 mL/min)**
Positive ion ESI MS	All PEGs [a]	+2.5 (capillary)	CH_3OH + 50 µM CH_3COONH_4
Negative ion ESI MS	Free fatty acids and acidic PEGs [a]	-2.5 (capillary)	CH_3OH + 50 µM CH_3COONH_4
Positive ion UNI MS	Source screening	+1.4 (capillary)	CH_3OH + 50 µM CH_3COONH_4 CH_3OH + 50 µM HCOONa
Positive ion APCI MS	Source screening	+2.5 (corona)	CH_3OH
Positive ion APPI MS	PEGs and fatty acids with unsaturation sites	+1.0 (repeller)	Toluene

Table 28. Ionisation sources tested, their voltages used and corresponding make-up solvents for PEG analysis. [a]: Note that acidic PEGs were detected using the chromatographic method in positive ion ESI MS whilst both positive and negative ion ESI MS were used for direct infusion experiments

2.6.3 Conditions of the Xevo SQD 2 (single quadrupole mass analyser) and Xevo TQD (triple quadrupole mass analyser)

The mass spectra were acquired using a Waters® Xevo SQD 2 or a Waters® Xevo TQD. The same method was used for both mass analysers (Table 29).

Cone voltage (V)	20	**Scan mode**	Full scan *m/z* 270-1500
Source temperature (°C)	150	**Scan time (s)**	0.2
Desolvation temperature (°C)	350	**LM**	14
Desolvation gas flow (L/Hr)	550	**HM**	16
Cone gas flow (L/Hr)	50		

Table 29. Q and QqQ method conditions for PEG analysis

2.6.4 Conditions of the Synapt™ G2-*Si* (quadrupole time-of-flight mass analyser)

The Waters® ZSpray™ ESI conditions in the positive and negative ionisation polarities in the Synapt™ G2-S*i* are presented in Table 30.

Cone voltage (V)	20	**Desolvation gas flow (L/Hr)**	550
Source offset (V)	40	**Cone gas flow (L/Hr)**	50
Source temperature (°C)	150	**Nebuliser (bar)**	7
Desolvation temperature (°C)	350	**Scan mode**	Full scan *m/z* 270-3000

Table 30. QToF MS method conditions for PEG analysis

2.7 Developed methods for (2-hydroxypropyl)-β-cyclodextrin characterisation

2.7.1 Ultra-high-performance supercritical fluid chromatographic method

UHPSFC analysis was achieved using a Waters® Acquity™ UPC^2. The sample manager was cooled at 10°C. An integral partial loop needle overfill (PLNO) injection mode injected 2.0 µL of each sample *via* the Acquity™ Sample Manager. The needle and injection port were cleaned using one

cycle of strong solvent (600 µL) and one cycle of weak solvent (600 µL) in PLNO injection mode, and the seal was washed between injections. The method is presented in Table 31.

Mobile phase	A: CO_2 / 105 bar
	B: CH_3OH + 1% HCOOH
Flow rate	Linear gradient 5-50% over 5 min at 1.1 mL/min (2.5 mL/min [a])
Column	Waters® Acquity™ Torus™ 2-Picolamine (130Å, 1.7 µm, 2.1 mm X 100 mm) at 30 °C (room temperature [a])
Make-up solvent	CH_3OH + 1% HCOOH at 0.45 mL/min
Syringe wash	Weak wash: 600 µL CH_3OH
	Strong wash: 600 µL CH_3CN
	Seal wash: CH_3OH
Dissolution solvent	CH_3OH + 1% HCOOH

Table 31. UHPSFC method conditions for 2HPBCD analysis. [a]: conditions for analysis using FPP columns with chiral stationary phases

2.7.2 Conditions of the Xevo SQD 2 (single quadrupole mass analyser) and Synapt™ G2-*Si* (quadrupole time-of-flight mass analyser)

The Waters® ZSpray™ ESI source conditions in the mass analysers are presented in Table 32. The mass spectra were acquired using a Waters® Xevo SQD 2, a Waters® Xevo TQD and the Waters® Synapt™ G2-*Si*. The ion mobility data were acquired using the Waters® Synapt™ G2-*Si*. The Waters® ZSpray™ ESI source in the Waters® Xevo SQD 2 and Waters® Xevo TQD method conditions are presented in Table 32.

Capillary voltage (kV)	2.5	**Cone gas flow (L/Hr)**	50
Cone voltage (V)	40	**Scan mode**	Full scan *m/z* 300-1800
Source temperature (°C)	150	**Scan time (s)**	0.2
Desolvation temperature (°C)	350	**LM**	14
Desolvation gas flow (L/Hr)	550	**HM**	16

Table 32. Positive ion ESI Q MS and positive ion ESI QqQ MS method conditions used in the analysis of 2HPBCD

The Waters® ZSpray™ ESI source in the Waters® Synapt™ G2-*Si* and travelling-wave ion mobility method conditions are presented in Table 33.

Capillary voltage (kV)	4.0	**T-wave velocity (m/s)**	500
Cone voltage (V)	40	**T-wave height (V)**	40
Source Offset (V)	40	**He cell gas flow (mL/min)**	180
Source temperature (°C)	150	**He cell pressure (bar) (mbar)**	4
Desolvation temperature (°C)	550	**IMS gas (N_2) flow (mL/min)**	90
Desolvation gas flow (L/Hr)	650	**IMS pressure (mbar)**	3
Cone gas flow (L/Hr)	50	**Scan mode**	Full scan *m/z* 200-2000
Nebuliser (bar)	7		

Table 33. Positive ion ESI Q IM ToF MS method conditions for 2HPBCD analysis

2.8 Data processing

2.8.1 Ionisation of PEGs and data processing of the mass spectra

Polyethers such as PEGs produce cationised molecules arising from host-guest complexation of the cation by the polyether chain and the formation of a podand [364]. Podands are supramolecular hosts for metal cations based on an open-chain acyclic structure [365]. PEGs form podand structures when ionising win cations (Figure 128).

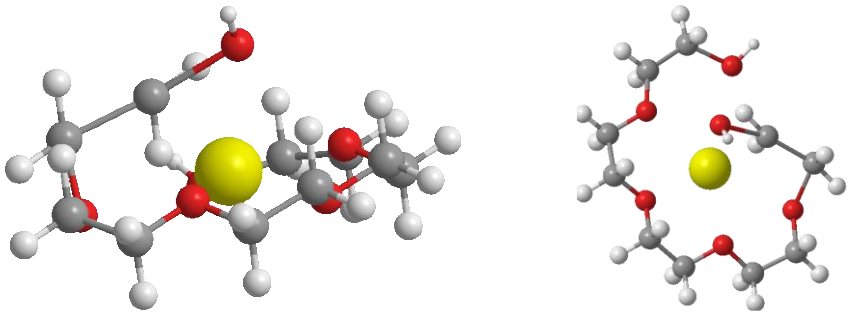

Figure 78. 3D-structure of the gas-phase adduct of PEG $[P_5 + Na]^+$ (drawn using ChemDraw 3D®). H atoms in light grey, C atoms in dark grey, O atoms in red and Na atoms in yellow. Adapted from Gidden *et al.* [364]

The gas-phase conformation consists of a *syn* position of the ethylene mer units that chelate the cation in the centre by the electrostatic attraction produced by the lone pair of electrons of the oxygen atoms in the chain [310, 364-366]. Multiply charged species are formed when increasing the

oligomer chain length due to (i) the increase in the number of oxygen atoms (ionisation sites) and (ii) the charge repulsion between cations is reduced (see section 3.5, page 142 for more information). The *m/z* value of a molecule relates to the MW via the adduct mass (X) and the charged state of the ion observed (n) (Equation 30).

$$m/z = \frac{MW + nX}{n}$$ Equation 30

The complexity is evident when observing the PEG mass spectra due to the presence of charge envelopes of ions with the same charge states (Figure 79). The complexity increases further when increasing the PEG molecular weight, as the larger oligomer chain lengths allow the location of more cations in the structure, achieving higher charged states.

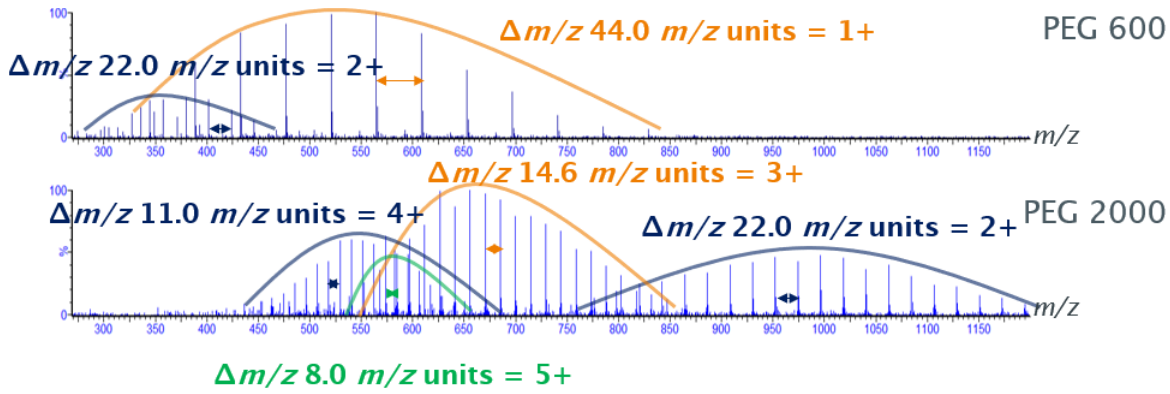

Figure 79. The complexity of the mass spectra of PEGs highlighting the effect of increasing the polymer molecular weight in the mass spectra and the requirement for chromatographic separation

The complex mass spectrum highlights the need for chromatography to simplify data analysis. When using the improved oligomer separation of ultra-high-performance supercritical fluid chromatography (UHPSFC), the mass spectra of the polymer can be simplified into the mass spectra of the individual oligomers (Figure 80). The mass spectrum of an individual oligomer is a charge envelope of multiply charged ions. An oligomer with n+1 repeating units shows a mass spectrum displaced by Δ*m/z* 44/n *m/z* units. The overlapping of the mass spectra of all individual oligomers explains the curves of ions with the same ionisation charged state in the polymer mass spectra, as shown in Figure 79.

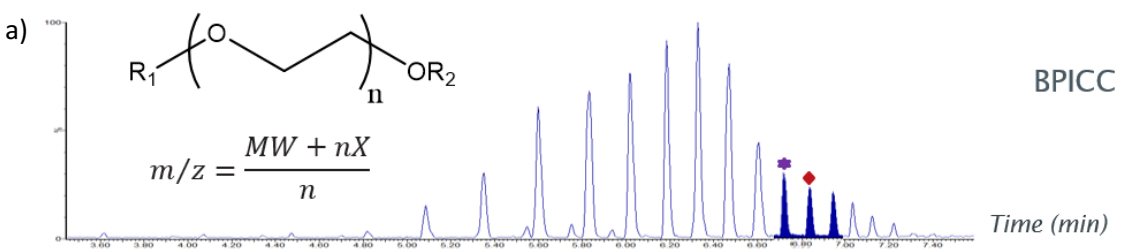

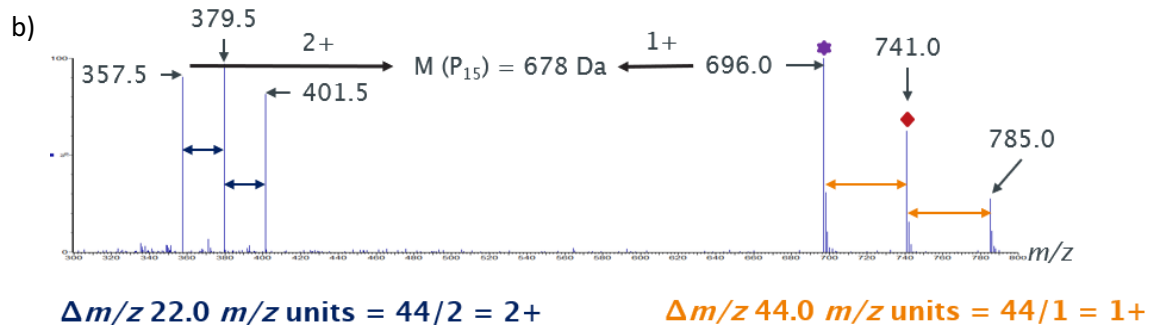

Figure 80. UHPSFC positive ion ESI Q MS. Generation of the mass spectra of individual oligomers of PEG 600 (b) based on the chromatographic separation using UHPSFC positive ion ESI MS (a) and simplification of the oligomer mass spectra

The polymer mass spectrum shows differences between oligomer ions that correspond to a nominal mass of 44.0261 Da of the ethylene oxide mer unit -CH_2-CH_2-O- divided by the charge state of the ions observed [45, 46, 310, 322] (Equation 31). The difference is 44 *m/z* units for singly charged species, for doubly charged 22 *m/z* units, for triply charged 14.6 *m/z* units, for quadruply charged 11 *m/z* units *etc.* [310, 322].

$$Repeating\ value = \frac{Nominal\ mass\ of\ the\ repeating\ mer\ unit}{Charge\ of\ the\ molecular\ specie\ observed} = \frac{44.0261}{n} \qquad \text{Equation 31}$$

Even though in positive ion ESI MS PEGs ionise via cationisation (Figure 78), the chemical characteristics of the end group can influence the ionisation and allow the polymer ionisation using negative ion ESI MS or other ionisation sources. For example, the carboxylic end groups in acidic PEGs allow these polymers to be detected using negative ion ESI MS, whilst the olefinic or aromatic rings in the Triton family allow ionisation using APPI MS or detection using UV-Vis.

2.8.2 Data processing of the chromatogram: TICC *vs* BPICC *vs* RICC

Depending on how the ion current data is represented, LC-MS data can be viewed using different chromatogram displays: either using the total ion current (TICC), the base peak ion current (BPICC) or the reconstructed (or extracted) ion current (RICC or EICC) chromatograms. The TICC represents the signal as a sum of all the separate ion currents carried by the ions of different *m/z* contributing to a mass. The BPICC is obtained by plotting the ion signals represented by the base peak detected in each mass spectra series. The RICC is created by plotting the signal intensity observed at a chosen *m/z* value [309]. The formation of multiply charged PEG species alters the chromatographic data representation due to a heterogeneous distribution of ion current in the charge states. The TICC resembles the Gaussian distributions of polymers obtained when using

size-exclusion chromatography (Figure 81 a) provides data representation that is more similar to the MW distribution. The BPICC shows an altered representation altered based on the intensities of the charged states of the oligomers; however, BPICC aids interpretation by excluding background ions (Figure 81 b). The RICC represents the ion abundance for one ion (Figure 81 c). The combination of chromatography with MS allows for data visualisation using ion maps (*i.e.,* heat maps, Figure 81 d).

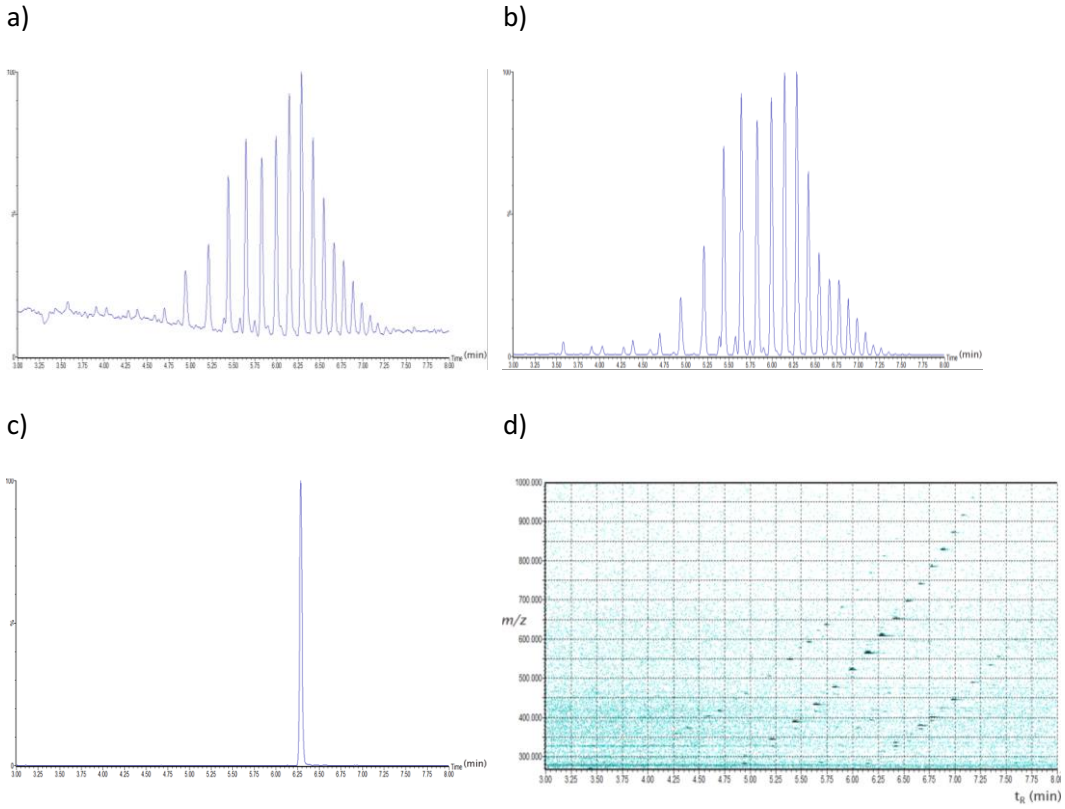

Figure 81. Different approaches for polymer data processing using LC-MS-like data. a) TICC, b) BPICC, c) RICC of one *m/z* value, d) ion map

2.8.3 Data processing using ion maps

The use of the chromatogram is time-consuming and challenging data processing for polymer interpretation. Ion intensity maps or ion maps are three-dimensional representations that allow the visualisation of complex LC-MS data. These representations show ions using the chromatographic retention time (*x-axis*), the *m/z* value (*y-axis*) and the intensity of the peak (*z-axis*). Figure 82 shows how the BPICC correlates to the ion map and data is interpreted. The analyst should identify an area of interest in the ion map and collect the chromatographic retention time (t_R) and the *m/z* value of the specific ion. Then, the MW of the molecule can be obtained using Equation 30 and correlated to the BPICC using the RICC of that specific ion. The charge state (n) can be obtained based on the differences in the $^{12}C/^{13}C$ isotopic distribution or

between within oligomer ions at the same charge state. Polymers are recognised as trends at each ionisation charge state with the difference between two consecutive oligomer ions corresponding to a Δ*m/z* value associated with the polymer repeating unit. For PEGs, the Δ*m/z* value is 44/n *m/z* units. Any small pharmaceutical drug molecules are easily spotted as single dots located within or away from the polymeric trends. An analyst can perform the identification without using ion maps; however, their use results in a facile manner to visualise data, resulting in an acceleration of the data processing and essential when unravelling the complexity of mixtures and performing non-targeted analyses.

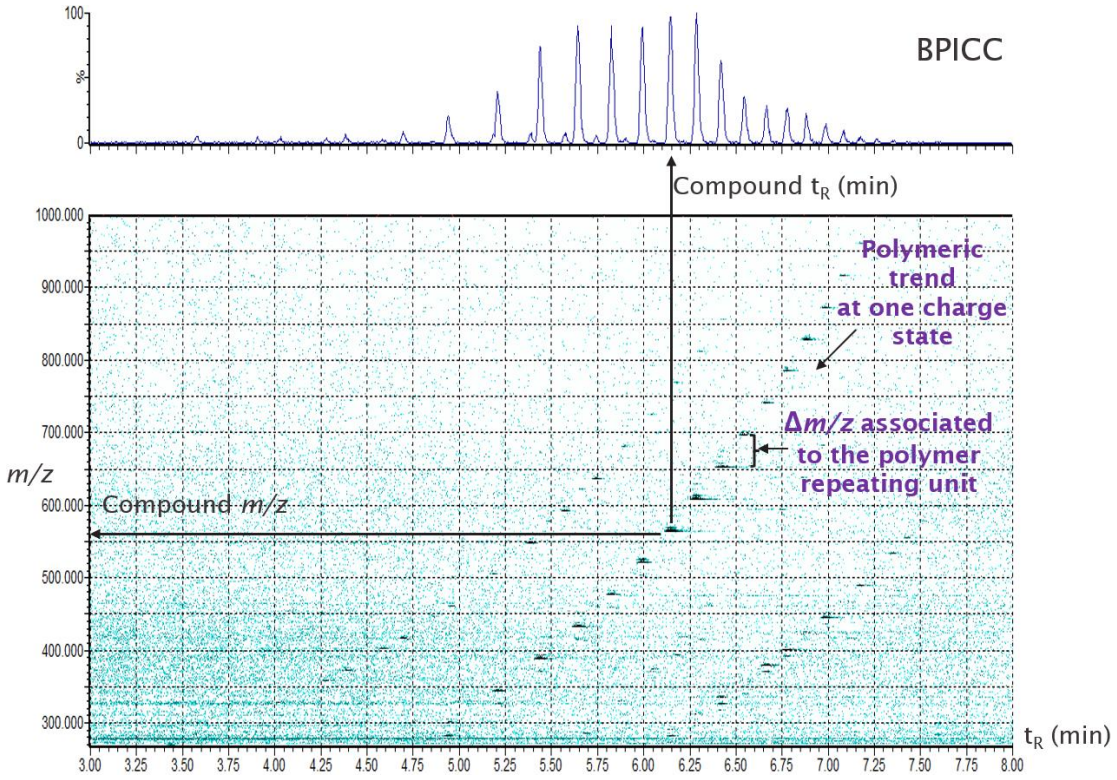

Figure 82. UHPSFC positive ion ESI MS. Correlation between the BPICC (top) and the ion map (bottom), showing how data is interpreted based on the recognition of an ion, the polymeric repeating unit, and the polymeric charge trends

Several software options are available to visualise LC-MS-like data as ion maps. Commercial software such as Waters® MassLynx® 4.1 displays a two-dimensional space with t_R (*x*-axis), *m/z* (*y*-axis), and the abundance of ions in the MS signal (*z-axis*) represented as the darkness of the colour (Figure 83 a). Alternatively, Pluskal *et al.* developed an open-source software called MZmine to deal with some of the ongoing challenges in data processing of complex *-omics* samples [367]. MZmine ion maps are three-dimensional pictures showing the ion intensity as the RICC (Figure 83 b).

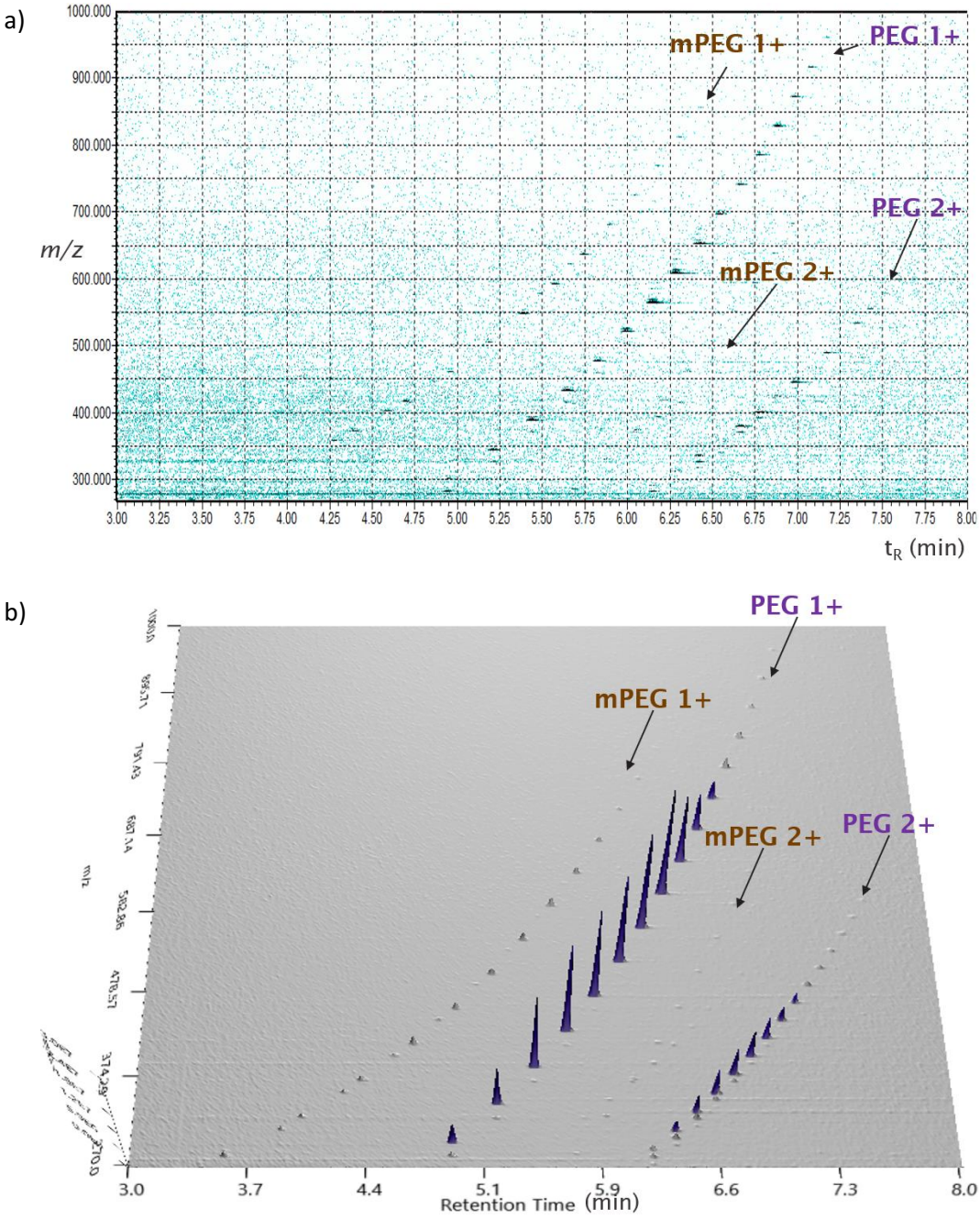

Figure 83. UHPSFC positive ion ESI MS. Ion map. Data visualisation using ion maps of the same sample. Differences between a) MassLynx® and b) MZmine

It is worth noting that both Waters® MassLynx® and MZmine ion maps provide the same information, being the only difference in how data is visualised. Still, improved data mining is achieved using MZmine due to the incorporation of facilitating functions such as zoom in certain areas, graph rotation or overlapping of ion maps to facilitate data comparison, suggesting that this software is more orientated to the user for routine data analysis.

2.8.4 Determination of polymeric end groups using linear fittings and MS

Mass spectrometry allows end group characterisation by converting the *m/z* values of the oligomers into their corresponding MW using the monoisotopic mass of the adduct (X) and the charged state of the ion formed (n) using Equation 30. The resulting oligomer MW (*y-axis*) can be plotted against a proposed value of the repeating unit (*x-axis*) and adjusted to a linear fitting model (Figure 84) [129, 368].

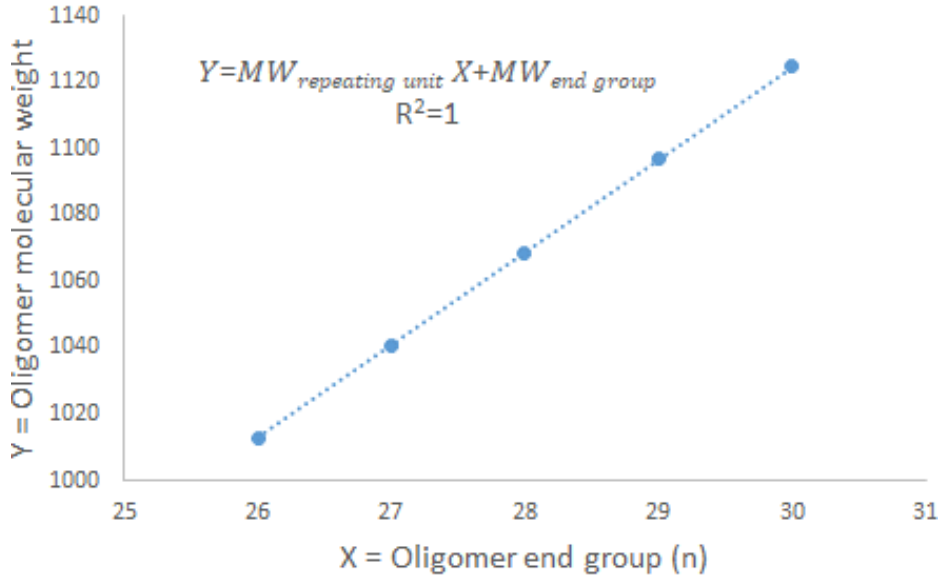

Figure 84. Calculation of the polymer end group by a linear fitting of the oligomer molecular weight to the repeating unit

The equation that fits the linear fitting model (Equation 32 and Equation 33) shows a slope that depends on the MW of the repeating unit of the polymer ($MW_{repeating\ unit}$) and the *y-axis* intercept that corresponds to the sum of MW in both end groups of the polymer $MW_{end\ group}$.

$$Y = MW_{repeating\ unit}X + MW_{end\ group} \qquad \text{Equation 32}$$

$$MW_{end\ group} = MW_{end\ group,one\ side} + MW_{end\ group,other\ side} \qquad \text{Equation 33}$$

If we consider a simple alcohol PEG, the MW (in nominal masses), these values correspond to $MW_{repeating\ unit}$ of 44 Da and a $MW_{end\ group}$ of 18 Da (17 Da OH + 1 Da H).

If we consider a PEG with end groups with a MW larger than 18 Da, such as mPEG (Figure 85 a) with a $MW_{end\ group}$= 32 Da (CH_3 15 Da + OH 17 Da), then the assignation of the end group is delicate and requires further evaluation. Notice that mPEG has an isobaric mass to that of PEG monoacid (Figure 85 b) with a $MW_{end\ group}$= 76 Da (CH_3 59 Da + OH 17 Da); therefore, mPEG and

PEG monoacid are undistinguishable using monoisotopic masses and other information is required such as the acquisition of accurate mass measurements, the mass defect, the selectivity of the ionisation source, the ionisation source polarity, or the elution profile in the chromatographic separation.

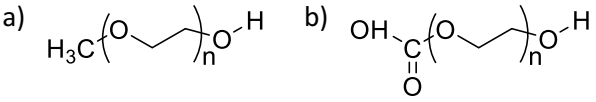

Figure 85. Proposed chemical structures for the impurity identified in PEG diacid 2000: a) mPEG 2000, b) PEG monoacid 2000

Also, the end group calculation of multi-chain complex PEGs required a simplification by using a simplified small molecule as the end group with the removal of the PEG chain. An example is shown in Figure 86.

Original chemical structure

MW = 346 + 44(w+x+y+z) Da

Simplified molecule considered to be the end group

MW = 346 Da

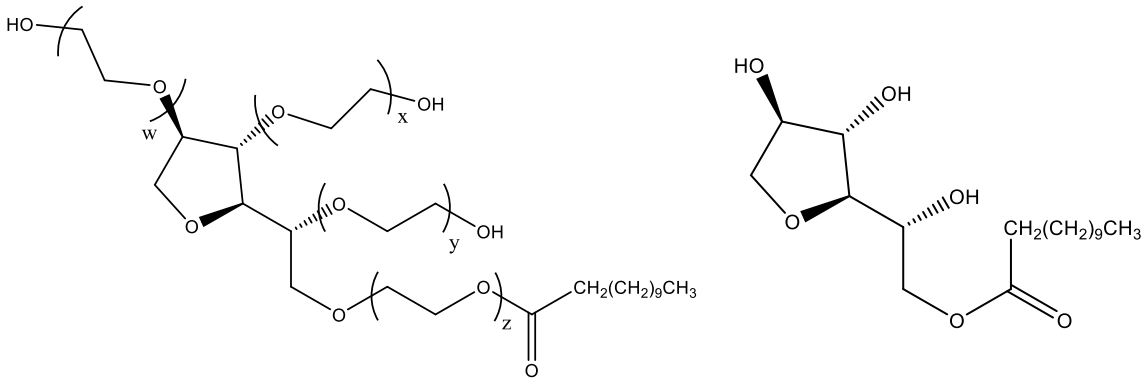

Figure 86. Examples of structure reduction using poly(ethoxylate) sorbitan monolaurate

In any of the two previously explained cases (and for most PEGs in this research), the $MW_{end\ group}$ was higher than the $MW_{repeating\ unit}$. These differences required recalculating the $MW_{end\ group}$ to use the linear fitting model (Equation 34). The reduced end group molecular weight (MW') is calculated by subtracting the $MW_{repeating\ unit}$ to $MW_{end\ group}$ until the value was lower than the $MW_{repeating\ unit}$.

$$MW' = MW_{end\ group} - n\left(MW_{repeating\ unit}\right)$$

$$0 < MW' < MW_{repeating\ unit}$$

Equation 34

2.8.5 Other information required for determining polymeric end groups

For this research, acquiring accurate mass measurements using high-resolution MS might not be sufficient to characterise polymeric end groups due to the presence of isobaric masses and the challenge of distinguishing these species. Other tools such as (i) the chromatographic elution, (ii) the selectivity of the ionisation source, (iii) the ionisation source polarity or (iv) the use of standards are required to distinguish polymers with isobaric masses.

The chromatographic separation of polymer standards suggested that the elution order highly depends on the oligomer chain length, the PEG structure, and the end group. Whilst shorter oligomers are resolved at baseline level (PEG 600, n_{av} = 14), the chain elongation compromises the separation (PEG 2000, n_{av} = 45) as the differences in polarity between consecutive oligomers are minimised (Figure 87).

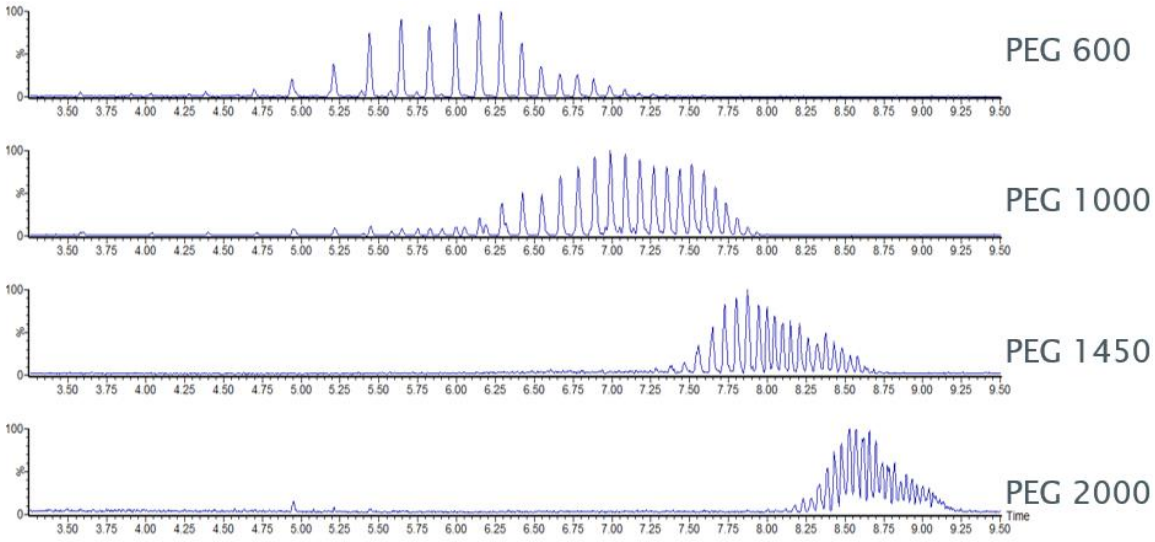

Figure 87. UHPSFC positive ion ESI Q MS. BPICC. 10 µg/mL PEG 600 in CH_3CN, 50 µg/mL PEG 1000 in CH_3CN, 50 µg/mL PEG 1450 in CH_3CN and 100 µg/mL PEG 2000 in CH_3CN

At equal chain length, PEG derivatives eluted based on the polarity of the end group (Figure 88), with non-polar end groups eluting earlier than polar end groups. Ethers were the first eluted PEGs, followed by esters and alcohols (alcohols eluted slightly later), and lately, PEGs with acidic end groups showed the strongest retention eluting at the latest time.

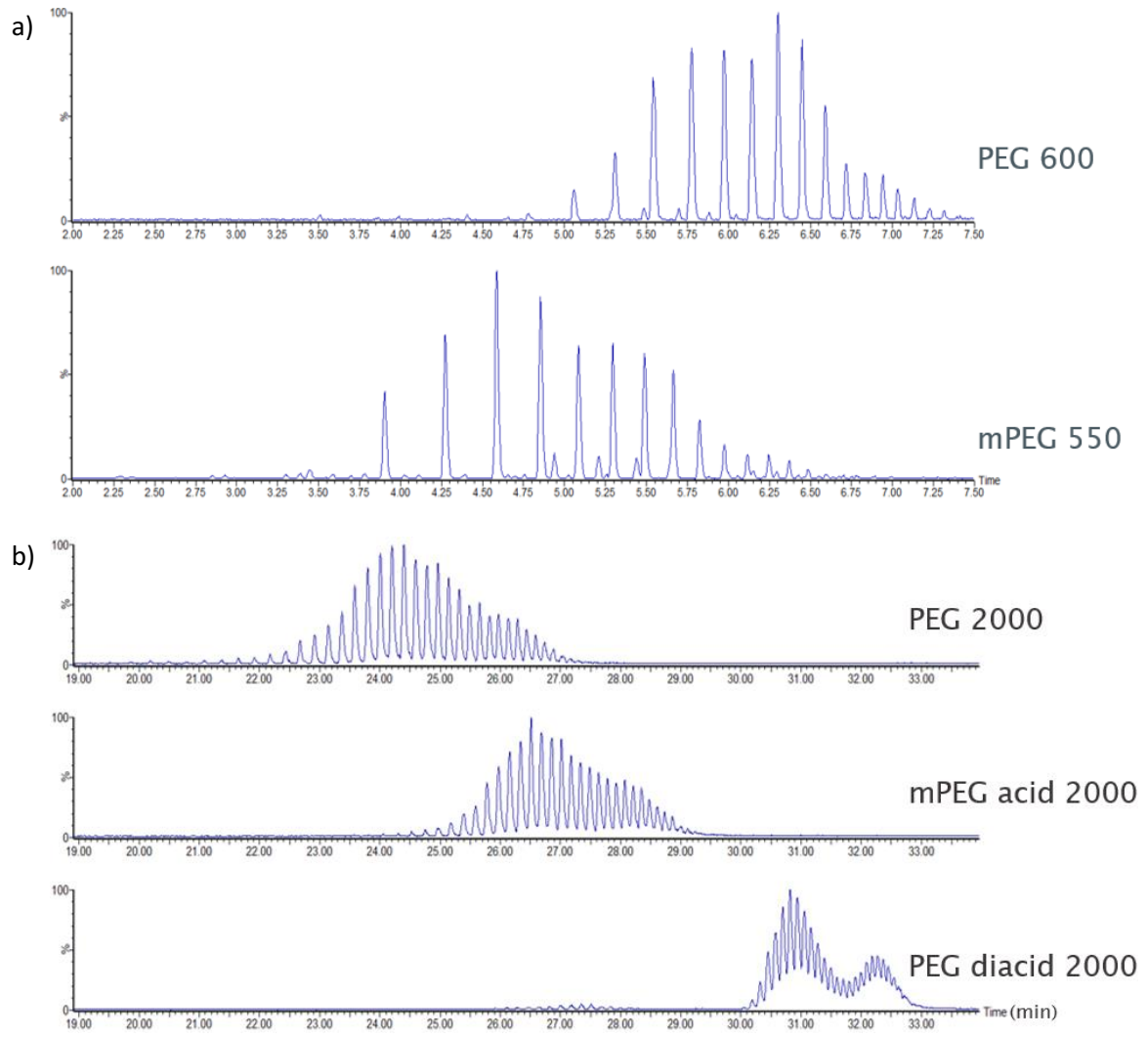

Figure 88. UHPSFC positive ion ESI Q MS. BPICC. Influence of the end group polarity in the retention. a) 50 µg/mL PEG 600 in CH_3CN and 50 µg/mL PEG 600 mPEG 550 in CH_3CN, b) 1000 µg/mL mPEG acid 2000 and 1000 µg/mL PEG diacid 2000 in CH_3CN + 1% HCOOH

Structure-related separation occurred based on whether the molecule is linear or contains multiple PEG chains with multi-chain polysorbates eluting later than linear PEG (Figure 89). This dependence is unsure whether it relates to the multi-chain structure or the amount of repeating ethylene oxide units, with the second being the most likely.

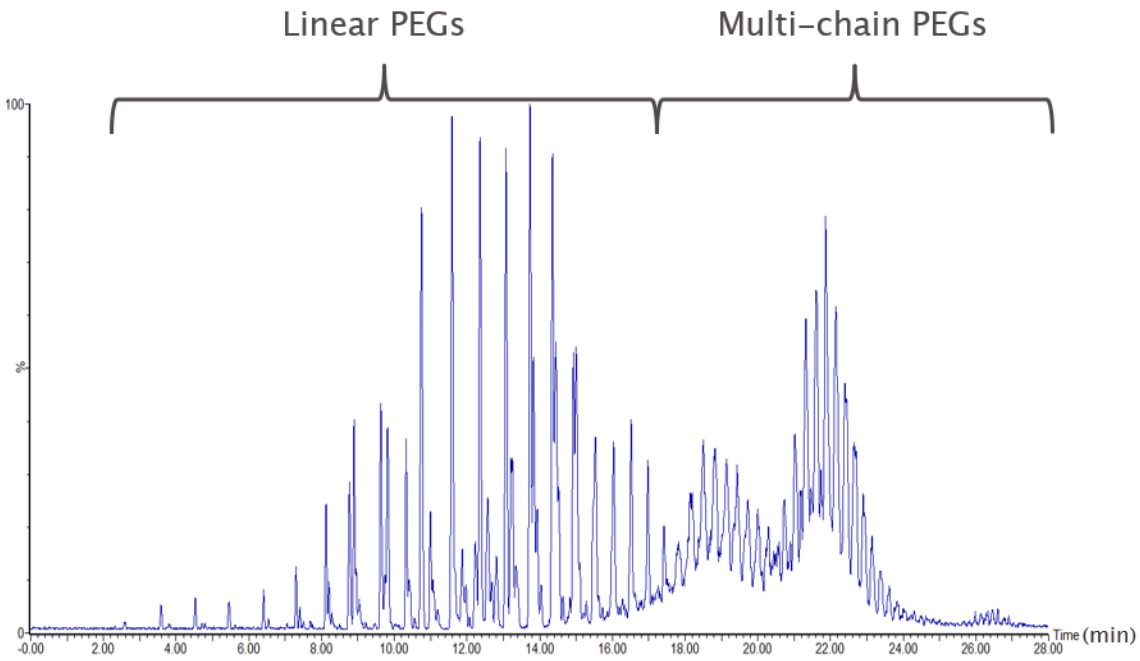

Figure 89. UHPSFC positive ion ESI Q MS. BPICC. 1000 µg/mL Tween® 20 in CH_3CN. Influence of PEG structure on the retention

2.9 Data analysis

SFC and MS data were recorded using MassLynx™ v.4.1 SCN 855 software. Data processing was achieved using MassLynx™ v.4.1 SCN 855, DriftScope™ v2.9 and Microsoft Office 365 (Excel) software as described.

2.9.1 Chemical information

Modelling of chemicals and prediction of their physicochemical properties was achieved using ACDLabs 2017.1 and ChemDraw® Professional 21.0.0. 3D modelling of chemical structures was conducted using ChemDraw 3D® within the ChemDraw® Professional 21.0.0 software.

2.9.2 Data smoothing

Data smoothing was performed by a Savitzky–Golay filtering using the algorithm with the window 2, the number of smooths 2, as per the dialogue box of the algorithm in the Waters® MassLynx™ v.4.1 SCN 855 software.

2.9.3 Data deconvolution using Waters® Transform™

Deconvolution using Transform™ required the introduction of ammoniated ions in the algorithm. The coding of the [SpeTransform] section of the MassLynx.ini file (C:\MassLynx) was modified (Table 34) by changing the accurate mass of the Na ion (22.989768 = Na - e) for the accurate mass of the ammonium ion (18.033826 = NH_3 + H - e).

Initial coding:	**New coding:**
TransformMinMass=200.00	TransformMinMass=200.00
TransformMaxMass=3000.00	TransformMaxMass=3000.00
TransformRes=0.1250	TransformRes=0.1250
TransformMinLen=1	TransformMinLen=1
TransformThreshold=10.00	TransformThreshold=10.00
TransformWindow=1.00	TransformWindow=0.30
TransformReject=2.00	TransformReject=2.00
TransformDimers=FALSE	TransformDimers=FALSE
TransformAdduct=22.989768	**TransformAdduct=18.033826**
TransformCut=MIDDLE	TransformCut=MIDDLE
TransformReplace=APPEND	TransformReplace=APPEND
TransformMz1=689.97	TransformMz1=689.97
TransformMz2=466.32	TransformMz2=466.32
TransformNumSinglePeaks=0	TransformNumSinglePeaks=0
TransformMaxStandardDeviation=2.00	TransformMaxStandardDeviation=1.00
TransformPeptide=FALSE	TransformPeptide=FALSE
TransformDelimiter=TRUE	TransformDelimiter=TRUE
TransformDelimChar=5	TransformDelimChar=5
AutoPos=TRUE,SW_SHOWNORMAL,38,85,511,259	**AdductPos=TRUE,SW_SHOWNORMAL,523,395,750,515**
ManualPos=TRUE,SW_SHOWNORMAL,268,419,718,591	ManualPos=TRUE,SW_SHOWNORMAL,268,419,718,591
EditPos=TRUE,SW_SHOWNORMAL,446,231,814,595	**EditPos=TRUE,SW_SHOWNORMAL,615,228,983,592**

Table 34. Coding modification of the [SpeTransform] of MassLynx.ini file (C:\MassLynx) within the MassLynx® 4.1 software package to deconvolute ammoniated adducts. Key changes are in bold. Other parameters were adjusted to maximise ion count

2.9.4 Data quantitation

The oligomer responses (obtained as the ion peak area, ion count or Waters® Transform™) were processed using Microsoft Office 365 (Excel) software. This software was used to obtain the calibration curves and calculate the number average (M_n) and weight average (M_w) molecular weights and polydispersity (PDI) values using established equations (Equation 35, Equation 36 and Equation 37). The values N_i corresponded to the response of the *ith* oligomer, whilst the M_i values were obtained by calculating the accurate mass of the oligomer MW using the monoisotopic masses of the elements that compose it (see section 5.2, page 186 for further details):

$$\overline{M_n} = \frac{\sum_i N_i M_i}{\sum_i N_i} \qquad \text{Equation 35}$$

$$\overline{M_w} = \frac{\sum_i N_i M_i^2}{\sum_i N_i M_i} \qquad \text{Equation 36}$$

$$PDI = \frac{\overline{M_w}}{\overline{M_n}} \qquad \text{Equation 37}$$

2.9.5 Ion mobility data processing

The reported values of $^{TW}CCS_{N2}$ were obtained by processing the travelling-wave ion mobility data using DriftScope™ v2.9 software.

2.9.6 Data visualisation

MassLynx™ v.4.1 SCN 855 and MZmine 2.52 software were used to visualise chromatographic-mass spectrometry data using the total ion current (TICC), the base peak ion current (BPICC) or the reconstructed (or extracted) ion current (RICC or EICC) chromatograms and 3D-ion maps. MZmine 2.52 software was used to visualise chromatographic-mass spectrometry data using 3D-ion maps. The analysis of chromatographic-mass spectrometry data is described in detail in section 4.2.3, page 103.

Ion mobility data was visualised using DriftScope™ v2.9 software.

Chapter 3 Optimisation of the supercritical fluid chromatography separation and mass spectrometry ionisation of poly(ethylene) glycols

3.1 Initial screening method: poly(ethylene) glycols with alcohol and methoxy end groups

3.1.1 Ion source selection

The polymeric chain suggested that positive ion electrospray ionisation mass spectrometry (ESI MS) can be used [364]; however, atmospheric pressure chemical ionisation (APCI) has also been reported in the literature for polymer analysis [369]. Unispray (UNI MS) was tested due to the similarities to ESI MS. The ion response of the base peak ion was used for comparison between ionisation sources (Figure 90). Compared to ESI MS; UNI MS produces more sodiated adducts due to incorporating a metallic pin, which leads to a preferential desolvation that favours ionisation to form sodiated molecules over other cations. Their comparison (Figure 90) showed the preference for ESI MS – as visualised through a higher ion response and more prominent formation of multiply charged species. Further details of PEG ionisation are discussed in section 3.5, page 142.

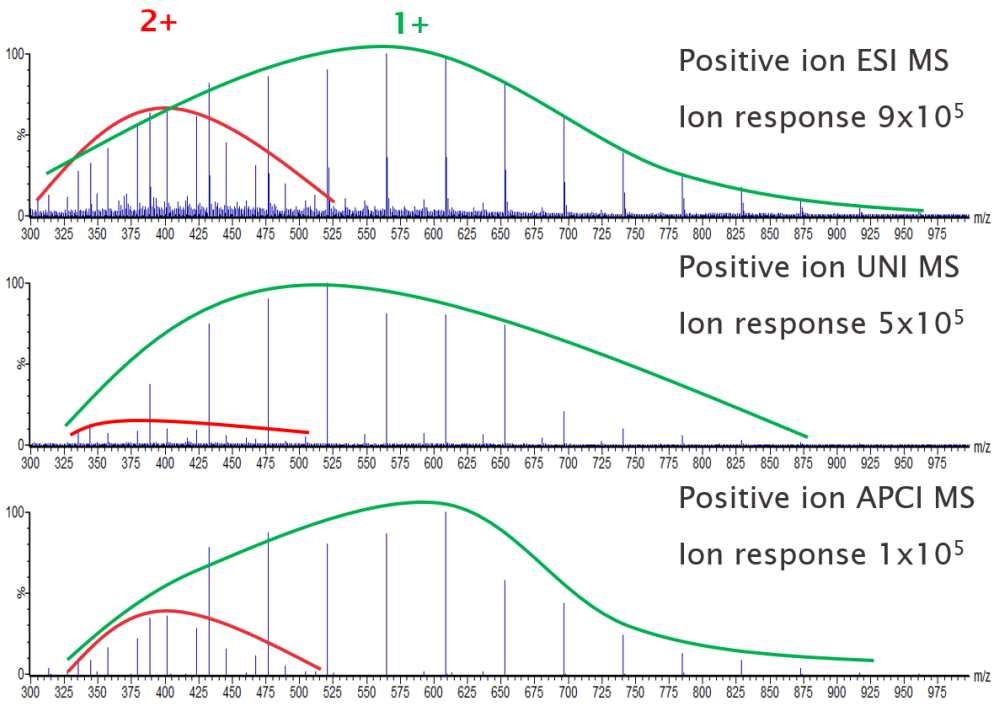

Figure 90. UHPSFC MS. Mass spectra. 300 µg/mL PEG 600 in CH_3OH. Comparison of the mass spectra of alcohol PEGs when using different ionisation sources. The ion response

was optimised for each ionisation source. Measurements taken in triplicates (ion response error: ±3%).

3.1.2 Mobile phase and column matching screening

Figure 91 shows the effect of the co-solvent in the separation of mPEG 350 (with an impurity characterised as alcohol PEG). Three co-solvents were evaluated: CH_3OH, CH_3OH + 25 mM CH_3COONH_4 and CH_3CN. Their evaluation showed that the oligomer separation occurred due to a size-related mechanism and that the use of CH_3CN as a co-solvent did not have enough elution strength to elute the oligomers, suggesting the use of CH_3OH. The addition of CH_3COONH_4 to CH_3OH led to a further improved chromatographic peak shape and response. The improvements in the oligomer separation when using ammoniated salts were associated with the formation of an ion-pairing mechanism between the ammonium ions, the (3,5-dialcoxy)pentyl chains of the Diol stationary phase, and the lone pair of electrons in the oxygen atoms of PEG, similarly to the proposal of Zheng *et al.* [247]. The response improvements when using the ammonium acetate as an additive were associated with a higher formation of ammoniated molecules in the ionisation source. These improvements were related to a depreciation of the sodiated molecules due to the high concentration of ammonium acetate in the co-solvent.

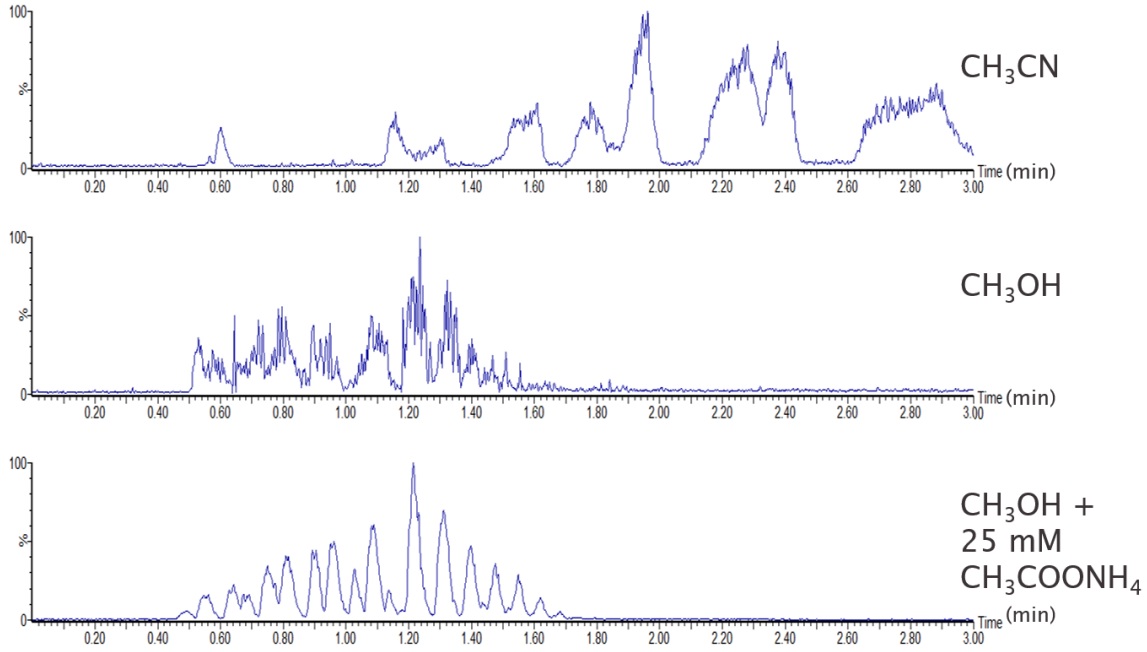

Figure 91. UHPSFC-MS positive ion ESI MS. BPICC. 100 µg/mL PEG 350 in CH_3OH. Effect of the mobile phase co-solvent composition in the chromatographic separation when using a BEH stationary phase (5-40% co-solvent gradient), showing the importance of a methanolic co-solvent with CH_3COONH_4 as additive

The selected columns screened in this work (Table 35) provided a wide range of column selectivity for separating compounds based on the interactions of the analytes with the stationary phase [260, 370-372].

Particle type and column size	**Stationary phase**	**Particle size (µm)**	**Terminology in this document**
FPP for achiral analysis (3.0 mm x 100 mm)	Acquity™ UPC² BEH	1.7	BEH
	Acquity™ UPC² BEH 2-Ethylpyridine	1.7	BEH-2-EP
	Viridis HSS C18 SB	1.8	C18
	Acquity™ HSS Cyano	1.8	Cyano
	Acquity™ UPC² Torus™ Diol	1.7	Diol
	Acquity™ UPC² Torus™ 1-Aminoanthracene	1.7	1-AA

Table 35. Selected columns for initial screening of PEGs with alcohol and aliphatic end groups

The column screening (Figure 92) showed that the BEH, BEH-2-EP and Diol provided a similar degree of selectivity due to the facile accessibility of the hydroxy groups that allowed for an ion-pairing mechanism (Zheng *et al.*) to occur [247].

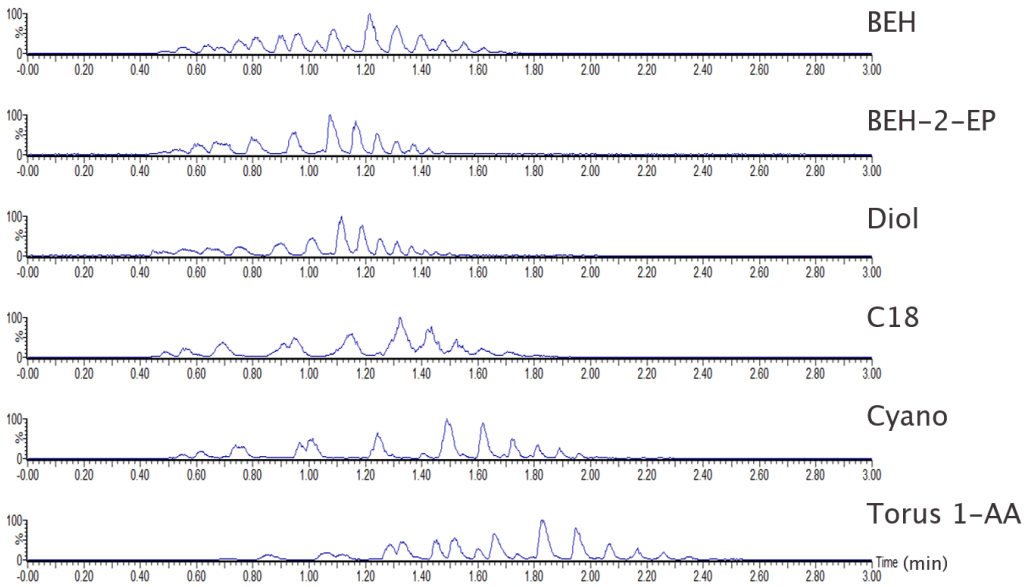

Figure 92. UHPSFC-MS positive ion ESI MS. BPICC. 100 µg/mL of mPEG 350 in CH_3OH with the presence of an alcohol PEG impurity. Column screening when using a co-solvent of CH_3OH + 25 mM CH_3COONH_4

A similar interaction was observed with the Cyano stationary phase; however, the minor hydrogen-bonding capacity of this stationary phase could involve that the partitioning mechanism was more important. The effect of a partitioning mechanism in the separation could be observed when using the C18 stationary phase as the longer length of the aliphatic chain involves that these interactions are more important. The 1-AA phases improved the end group separation but provided a similar degree of selectivity to the BEH.

The current experiment showed the difficulty in selecting the stationary phase due to the different types of selectivity provided in terms of oligomer and end group separations. The TDiol was selected for future experiments due to the improved oligomer separation provided; however, all stationary phases provide useful chromatographic information. None of them was discarded at this stage of the method development.

3.1.3 Initial optimisation of the sample diluent

$CH_3COOCH_2CH_3$, CH_3CN, CH_2Cl_2 and CH_3OH were tested as possible sample diluents for PEG analysis with PEG alcohol (Figure 93) and aliphatic (Figure 94) end groups. The peak area was used for comparison (Table 36) due to the distortion of the peak shape; thus, the asymmetry values (A_s) could not be calculated. $CH_3COOCH_2CH_3$ showed the best peak shape and highest peak area (Figure 93 a and Figure 94 a); however, the use of this solvent is unusable due to its inability to dissolve alcohol PEGs with high MW. CH_2Cl_2 (Figure 93 b and Figure 94 b) and CH_3CN (Figure 93 c and Figure 94 c) provided the best peak areas and shapes. The high volatility of CH_2Cl_2 compromised sample stability and led to unreliable quantitation, so CH_3CN was preferred. Using CH_3OH (Figure 93 d and Figure 94 d) illustrated issues with polarity and viscosity differences between the sample diluent and the low percentages of the co-solvent, leading to broad peak shapes. PEGs with either alcohol or alkoxy end groups showed similar results, suggesting that polar solvents were preferable due to their facility to dissolve the alcohol and aliphatic PEGs and favoured the selection of CH_3CN. Also, even though certain solvents showed significant results for PEGs with lower molecular weight (MW) (MW < 600 Da), longer chains (MW > 1000Da) showed poor solubility in $CH_3COOCH_2CH_3$ and CH_3OH and showed the effect of the oligomer chain length on the solubility.

	Sample diluent	$CH_3COOCH_2CH_3$	CH_2Cl_2	CH_3CN	CH_3OH
Peak area x 10^{-7} (a.u.)	PEG 200	9.37 ± 0.12	9.05 ± 0.13	9.16 ± 0.09	5.85 ± 0.11
	mPEG 350	9.31 ± 0.10	8.81 ± 0.15	8.99 ± 0.11	7.04 ± 0.14
Solubility	Low MW	Complete	Complete	Complete	Complete
	High MW	Insoluble	Complete	Complete	Requires heat

Table 36. Effect of the sample diluent on the peak area of alcohol (PEG 200) and aliphatic (mPEG 350) PEGs. Samples analysed in triplicate. Note that the protic solvent methanol showed the lowest solubility for these neutral polymers

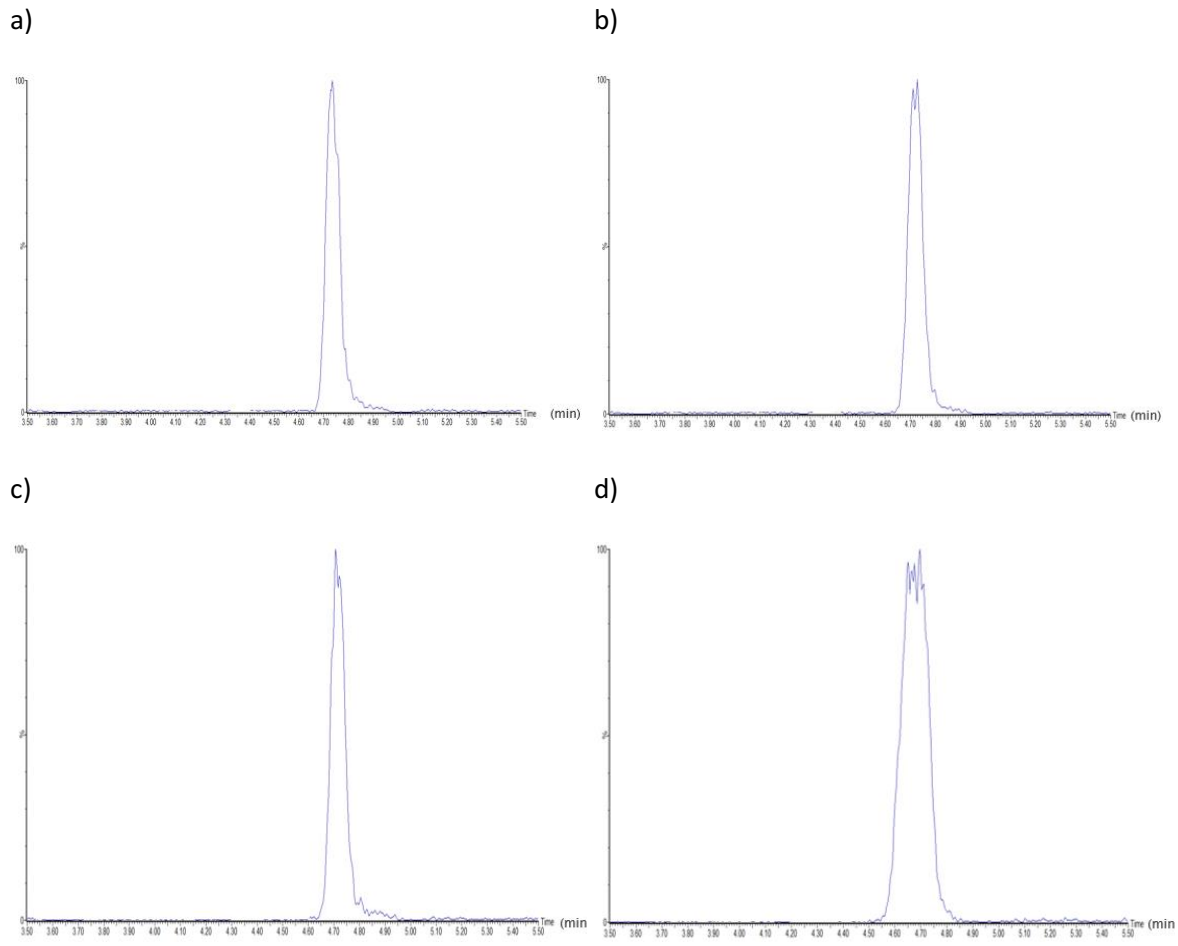

Figure 93. UHPSFC-MS positive ion ESI MS. RICC (*m/z* 300). 25 µg/mL of PEG 200 using different sample diluents: a) $CH_3COOCH_2CH_3$, b) CH_2Cl_2, c) CH_3CN, and d) CH_3OH

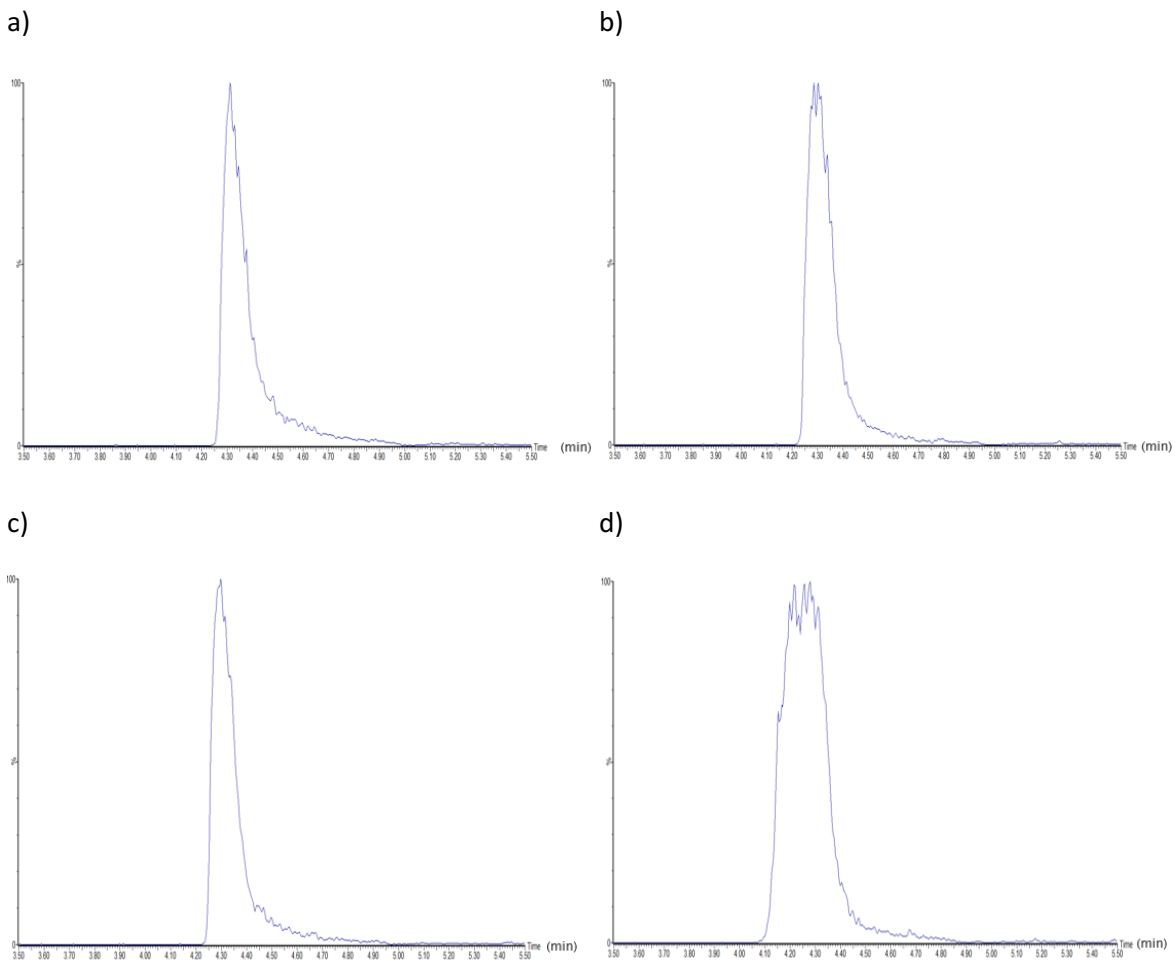

Figure 94. UHPSFC-MS positive ion ESI MS. RICC (*m/z* 314). 25 µg/mL of mPEG 350 using different sample diluents: a) $CH_3COOCH_2CH_3$, b) CH_2Cl_2, c) CH_3CN, and d) CH_3OH

3.1.4 Initial optimisation of the column temperature

Samples required ultrasonication in a water bath (*ca.* 50–60 °C) to dissolve PEGs of higher MW completely and suggested the need for increasing the column temperature for a complete solubility of the components in the mobile phase (Figure 95).

The column temperature was screened between 30 to 70 °C. Higher values were not tested due to a compromise in the stability of the stationary phase. The increased in column temperature (Table 37 and Figure 95) improved the chromatographic resolution without a detriment in the peak shape when increasing the column temperature. The improvements in the chromatographic resolution was associated to: (i) the supercritical fluid state of CO_2 was maintained for longer at the lower volume fractions of co-solvent before reaching the sub-critical state, resulting in sharper chromatographic peaks and (ii) an improved diffusion of the analyte at higher temperature leading to improved mass transfer in the less dense mobile phase. Besides, when

the column temperature increases, the density and viscosity of the mobile phase decrease, resulting in a mobile phase with a lower elution strength and, consequently, leading to longer elution times.

Column temperature (°C)	40	50	60	70
R_s (a.u.)	1.27 ± 0.02	1.85 ± 0.02	2.52 ± 0.02	2.53 ± 0.02

Table 37. Optimisation of the column temperature of PEG 600. R_s: chromatographic resolution at half-width calculated using the RICC of two contiguous oligomer peaks (*m/z* 520.5 and 564.5). Samples analysed in triplicate

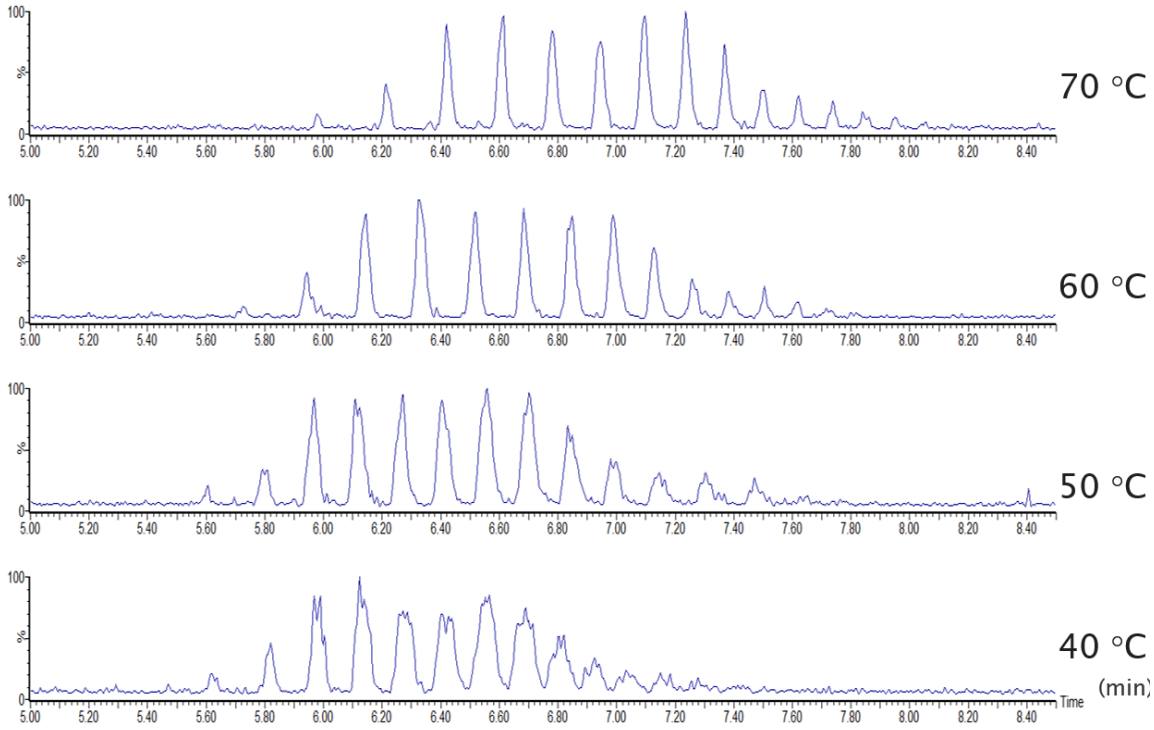

Figure 95. UHPSFC positive ion ESI MS. BPICC. 100 µg/mL PEG 600 in CH_3CN. Optimisation of the column temperature at ABPR 150 bar for analysis of PEGs with alcohol and alkoxy end groups

3.1.5 Initial optimisation of the ABPR

The ABPR was screened at 105, 150 and 200 bar. When increasing the ABPR (Figure 96), the chromatographic peaks became sharper (Table 38) due to an increase in the mobile phase density that increases the elution strength and decreases the retention time of the analytes. A value of 200 bar was selected for further analysis.

ABPR (bar)	105	150	200
A_s (a.u.)	1.34 ± 0.03	1.27 ± 0.02	1.21 ± 0.03

Table 38. ABPR optimisation for PEG 600 oligomer separation. Samples analysed in triplicate

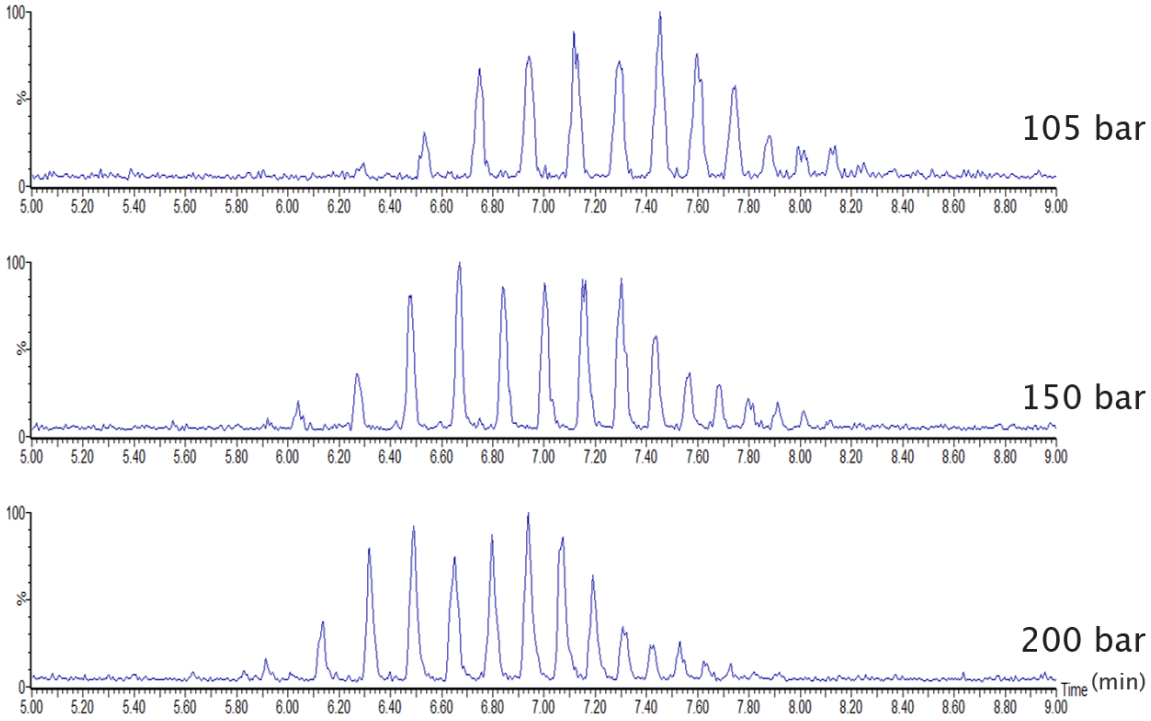

Figure 96. UHPSFC positive ion ESI MS. BPICC. 100 µg/mL PEG 600 in CH_3CN. Optimisation of the ABPR at 70 °C for PEGs with alcohol and alkoxy end groups

3.2 Addition of poly(ethylene) glycols with acidic end groups to the screening method

3.2.1 Selection of the ionisation polarity for analysis of poly(ethylene) glycols

The polyether chain and the carboxylic end group in acidic PEGs (Figure 97) meant that either positive or negative ion ESI source polarity could be used for their analysis.

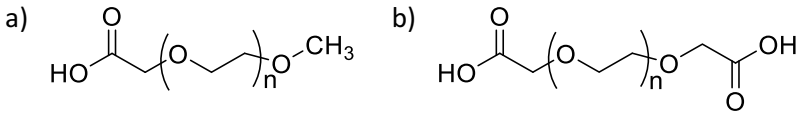

Figure 97. Chemical structures of acidic PEGs: a) mPEG acid 2000 (n_{av} = 45), and b) PEG diacid 2000 (n_{av} = 45)

A direct infusion analysis of each acidic PEG was proposed to identify the appropriate ionisation source polarity. When infusion a solution in the positive ion ESI MS source (Figure 98 a) lead to either the formation of multiply sodiated adducts of the carboxylic acid [mPEG-COOH + n Na]$^{n+}$ or the corresponding salt [mPEG-COONa - H + n Na]$^{n+}$ (theoretical *m/z* 113.6099, experimental *m/z* 1113.6141, mass error 3.8 ppm). Minor formation of potassiated molecules [mPEG-COOH + n K]$^{n+}$ was also observed. The analysis of mPEG acid 2000 in negative ion ESI MS (Figure 98 b) showed the deprotonated molecule of the carboxylic acid [mPEG-COOH - H]$^{-}$ and other adducts likely from the ionisation source, flow path and reagents (such as Na formate).

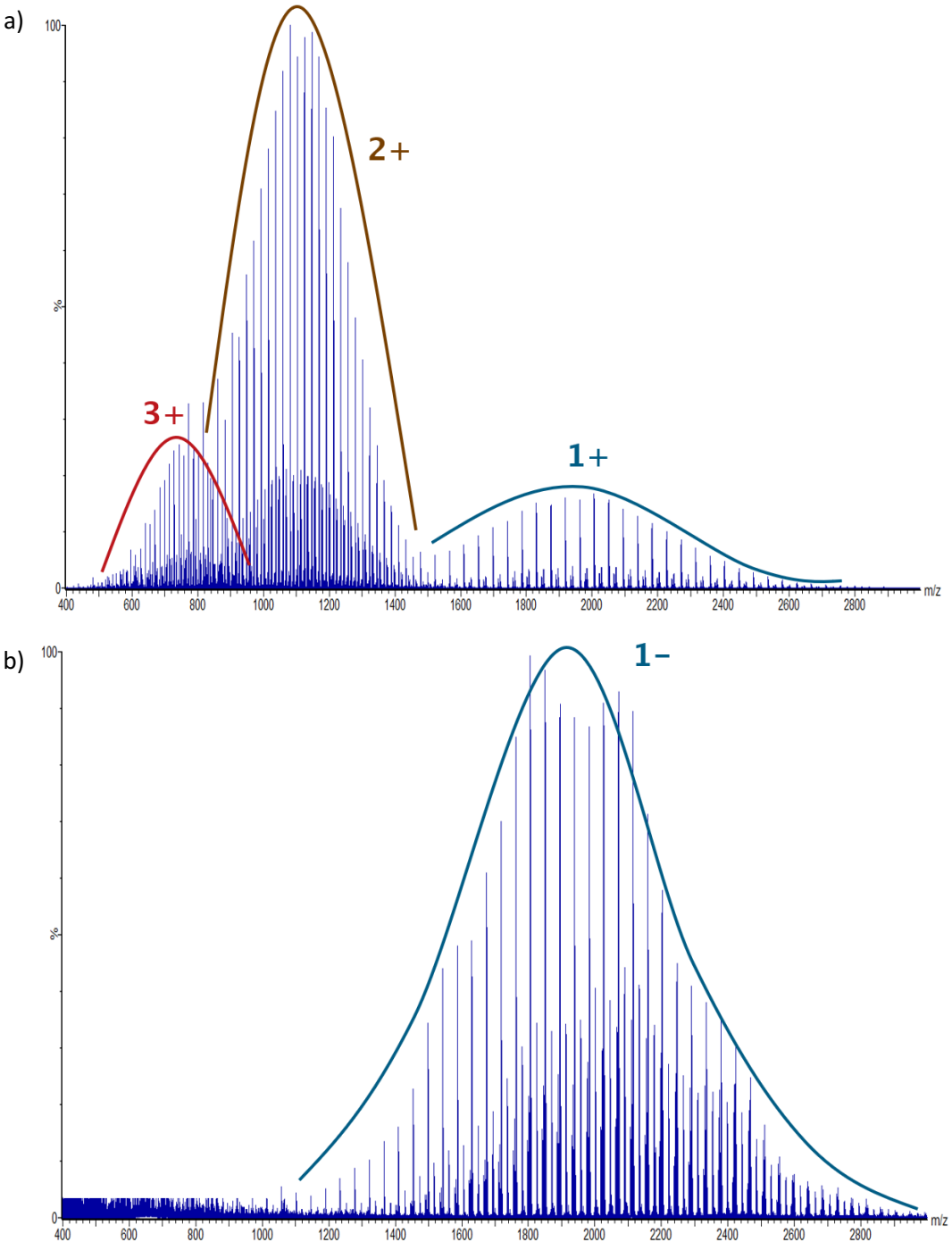

Figure 98. Direct infusion. Mass spectra. 100 µg/mL mPEG acid 2000 in CH_3OH. Comparison in the ionisation of mPEG acid in a) positive ion ESI MS, b) negative ion ESI MS

The analysis of PEG diacid (mPda) 2000 using positive ion ESI MS experiment (Figure 99 a) showed the presence of multiply charged ions and the formation of salt $[mPda + (n+1)\ Na - H]^{n+}$, along with the presence of an unknown impurity. The analysis using negative ion ESI MS (Figure 99 b) showed the presence of deprotonated molecules (deprotonated the carboxylic acids) in the form of singly $[mPda - H]^-$ and doubly $[mPda - 2\ H]^{2-}$ charged states.

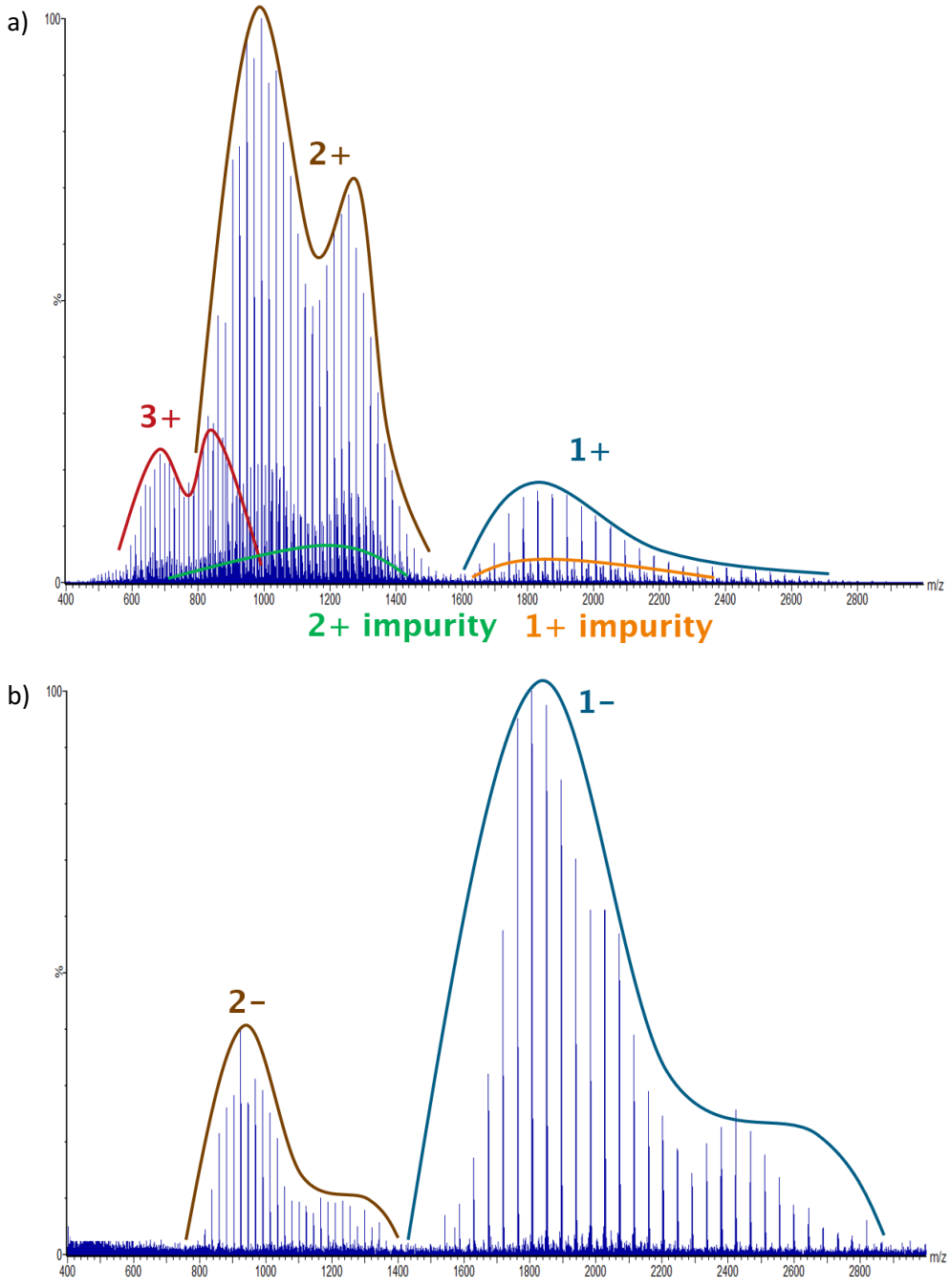

Figure 99. Direct infusion MS. Mass spectra. 100 µg/mL PEG diacid 2000 in CH_3OH. Comparison in the ionisation of PEG diacid in: a) positive ion ESI MS showing the presence of an impurity, and b) negative ion ESI MS without the presence of the impurity

The response of the base peak ion of each polymer mass spectra in each ionisation source polarities were compared (Table 39). The base peak ion in a mass spectrum is the peak corresponding to the separated ion beam which has the greatest intensity [309]. As the ion response in positive ion ESI MS was significantly higher than in the negative ion polarity, the ionisation efficiency of the PEG chain in positive ion ESI MS was higher than the ionisation efficiency of the carboxylic acid in negative ion ESI MS. The lower ionisation efficiency of the carboxylic acid in positive ion ESI MS was associated with the tendency of these molecules to form $[M + H]^+$ species. The results showed a preference of PEGs with carboxylic groups for ionising when using ESI in the positive polarity [373].

		mPEG acid 2000	**PEG diacid 2000**
Base peak ion response x 10^{-3} (a.u.)	**Positive ion ESI MS**	72 ± 4	103 ± 6
	Negative ion ESI MS	15 ± 2	4 ± 1

Table 39. Evaluation of the ionisation efficiency of ESI MS of acidic PEGs using different ESI source polarities. Direct infusion MS experiment of 100 µg/mL acidic PEG in CH_3OH. Samples analysed in triplicate

The higher response in positive ion ESI MS (Table 39) and the observation of a PEG-based impurity in PEG diacid 2000 in the positive polarity and not in the negative one (Figure 99) highlighted that positive ion was the correct ionisation source polarity for the method development.

3.2.2 Column and mobile phase screening re-evaluation

The previously discussed column screening (Figure 92) was re-evaluated by analysing PEGs with acidic end groups as the interactions of the analyte with the mobile phase can change due to the presence of an ionisable, more polar carboxylic end group. The experiment aimed to find a stationary phase that allowed a fully resolved separation of mPEG acid 2000, PEG diacid 2000 distributions and some degree of oligomer separation.

The column screening experiment of the acidic PEGs (Figure 100) showed an earlier elution of an mPEG acid 2000 distribution and a later elution of the PEG diacid 2000 distribution. When using the BEH and C18 columns, a lower degree of oligomer separation was noticed that was associated with lower accessibility of the hydroxy groups in the stationary phase (silanols). Even though the ion-pairing interactions between the NH_4^+ ions and the stationary phase were higher with the BEH

column, the oligomers barely separated. The higher degree of a partitioning mechanism in the ligands of the BEH-2EP and the TDiol stationary phase could explain the improved oligomer separation achieved when using these stationary phase. Also, in the BEH-2EP, a secondary interaction of the carboxylate group of each acidic PEGs with a possible charged amine group of the 2-ethylpyridine ligand in the BEH-2EP could neglect the separation of both polymeric distributions. The lack of ionisable groups in the (3,5-dialcoxy)pentyl chains of the TDiol stationary phase involves the adsorption of oligomer chains in the stationary phase ligands, the partitioning interaction of the ligand and the oligomer, and the ion-pairing interactions between the hydroxy groups of the ligand and the oligomers were responsible for the baseline separation of the acidic PEGs.

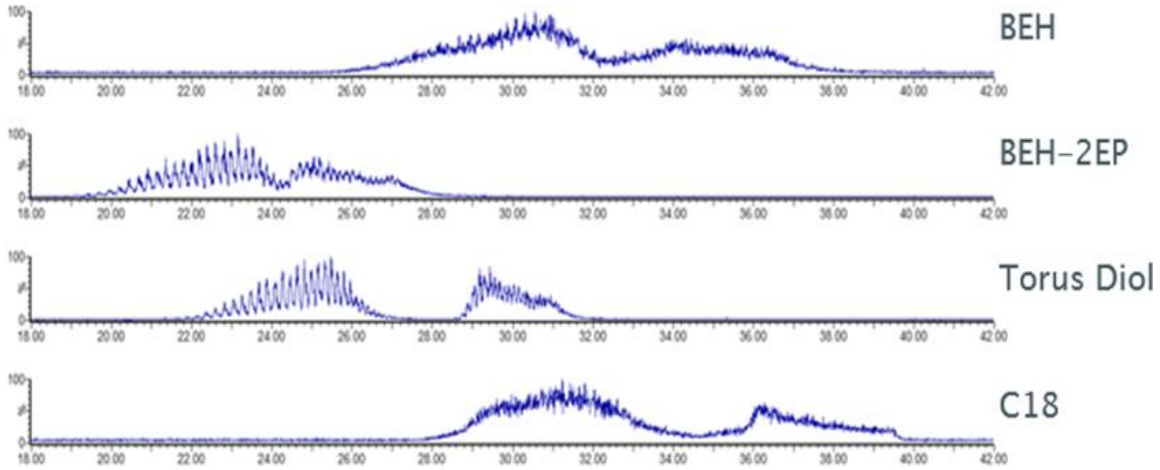

Figure 100. UHPSFC positive ion ESI MS. BPICC 1000 µg/mL mPEG acid 2000 and 1000 µg/mL PEG diacid 2000 in CH_3CN. Column screening for PEGs with acidic end groups

The screening of the Cyano stationary phase is not shown due to a similar selectivity to the C18 phase. The screening of the 1-AA phase (Figure 101) required a mobile phase with a substantial elution power to elute the PEG diacid oligomers. The elution of PEG diacid 2000 in a consecutive injection was explained by strong ionic interactions between the carboxylic acid end group of the acidic PEG with the amino group in the ligand chain of the stationary phase, which suggested that the 1-AA was inappropriate for analysis.

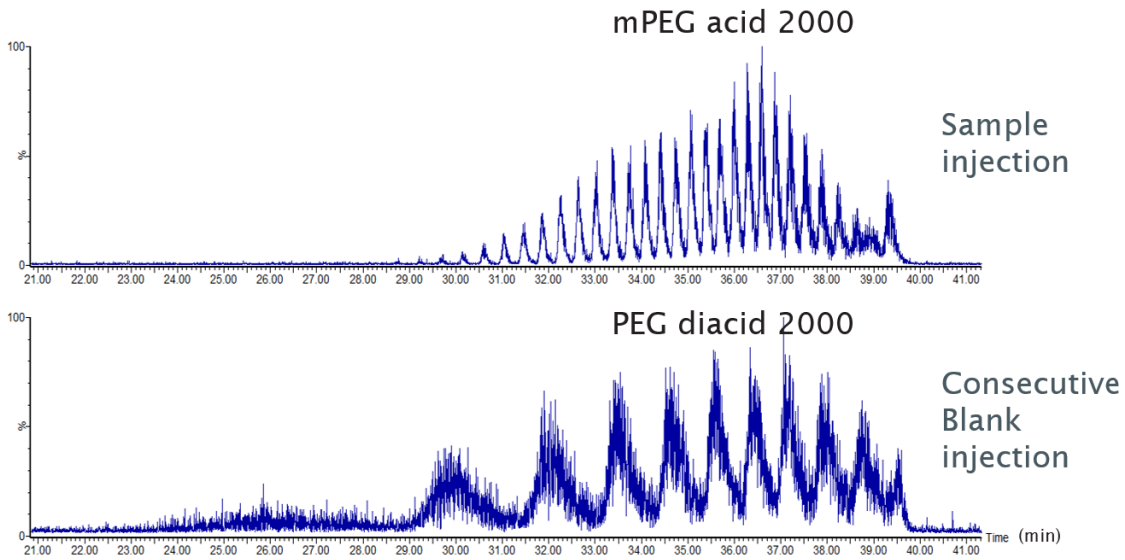

Figure 101. UHPSFC positive ion ESI MS. BPICC 1000 µg/mL mPEG acid 2000 and 1000 µg/mL PEG diacid 2000 in CH_3CN. Strong retention of PEGs with acidic end groups in the T1-AA column was observed (data was shown unsmoothed on purpose)

The Diol column was selected for the improved oligomer separation and the full separation of both polymeric distributions. It is worth noting that the column screening of PEGs with alcohol and methoxy end groups showed that column selection is not a straightforward decision. The analysis of both column screening experimental data showed that oligomer separation was related to a size-related mechanism and was improved in stationary phases with several hydroxy substituents - either silanols or hydroxy groups of the ligands – that can interact with the ammonium ions. On the other hand, the end group separation depended on all interactions between the end group and the stationary phase. The investigation revealed the influence of the stationary phase on the SFC selectivity of PEGs and the importance of their selection for SFC separations.

3.2.3 Column temperature re-evaluation

Evaluation of the column temperature when analysing the acidic PEGs (Figure 102, Table 40) led to similar conclusions to the analysis using PEGs with alcohol end groups (Figure 95, Table 37), showing the little effect of the column temperature in the chromatographic resolution between various end groups. However, increasing the column temperature led to slight changes in chromatographic resolution and a significant shift in the retention time when using acidic PEGs. Even though the changes in the resolution were minor ($\Delta R_s \approx 0.10$) when increasing the column temperature, a considerable increase in the separation was noticed between the first and the last chromatographic peak. The elution of the polymer at 40 °C occurs in *ca.* 4 min, whilst the elution at 70 °C occurs in *ca.* 5 min. The extra minute achieved at 70 °C (refer to Figure 102) was required

to minimise the ion suppression of possible impurities and facilitate their identification, as the overall separation improved.

Column temperature (°C)	40	50	60	70
Rs (a.u.)	0.95 ± 0.02	1.00 ± 0.02	1.01 ± 0.02	1.05 ± 0.02

Table 40. Relationship of the column temperature with the chromatographic resolution of PEGs with acidic end groups. The chromatographic resolution was calculated using the RICC of two contiguous peaks of mPEG acid 2000 (*m/z* 664.2 and 649.5) at baseline. Samples analysed in triplicate

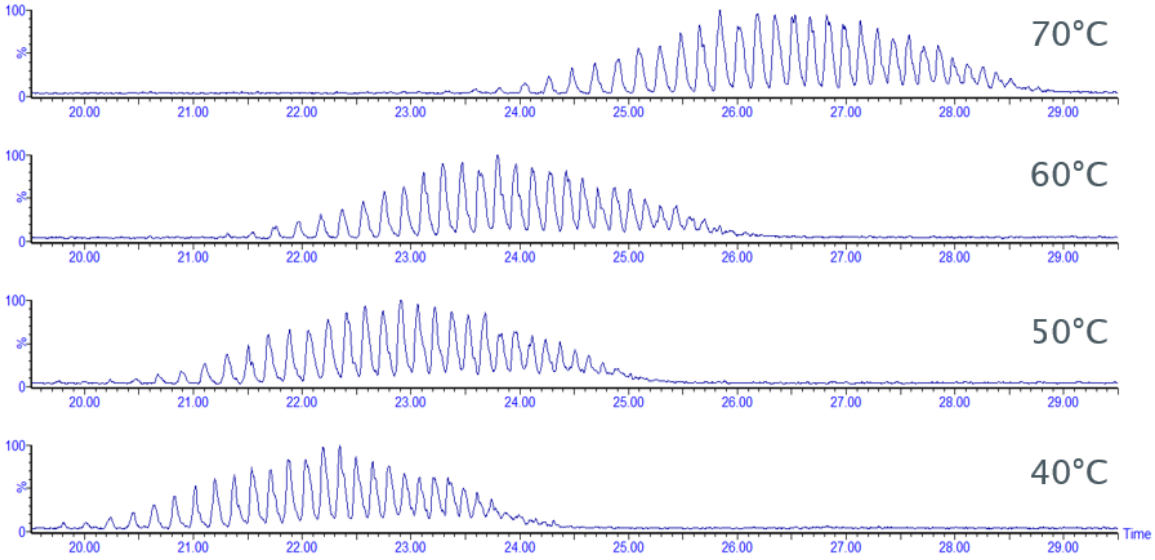

Figure 102. UHPSFC positive ion ESI MS. BPICC 1000 µg/mL mPEG acid 2000 in CH_3CN. Influence of the column temperature in the separation at ABPR 200 bar

3.2.4 ABPR re-evaluation and optimisation of the flow rate

Optimisation of the ABPR and the flow rate occurred in parallel due to a need to work at a linear velocity of the analyte close to the optimum (in the van Deemter equation) to achieve higher peak heights and better LOD for quantitation. Figure 103 shows the optimisation of these parameters. Increasing the ABPR improved the peak shape but compromised the resolution due to reduced retention. Increasing the flow rate over 1.4 mL/min compromised the method backpressure and the peak shape resulting in two peaks being observed at low ABPR values. The final conditions chosen were a flow rate of 1.3 mL/min and an ABPR of 200 bar, as they were a good compromise between an acceptable separation and peak shape.

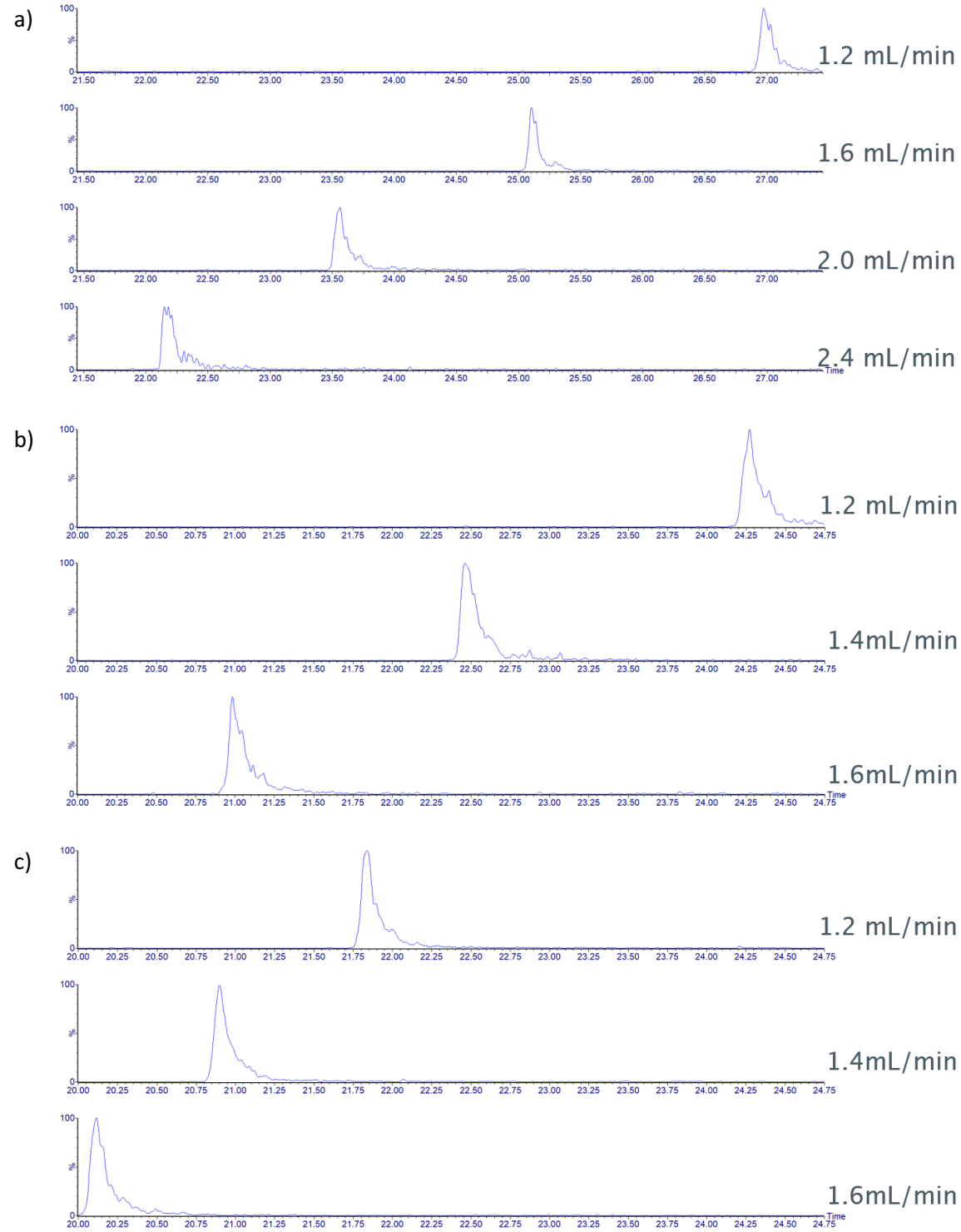

Figure 103. UHPSFC positive ion ESI MS. RICC (*m/z* 650.5). 1000 µg/mL of mPEG acid 2000 in CH_3CN. Influence of the flow rate at ABPR a) 105 bar, b) 150 bar, and c) 200 bar

3.3 Challenges observed in the screening method

Two main concerns were identified during the initial method of screening. The first concern was a distorted peak shape of PEGs with acidic end groups related to an acid-base equilibrium within

the mobile phase. The second concern was a non-selective ionisation that complicated the qualitative and quantitative analyses.

3.3.1 Unusual chromatographic peak shape in acidic poly(ethylene) glycols

Analytes with carboxylic acids such as mPEG acid 2000 and PEG diacid 2000 could show chromatographic separation between the carboxylic acid and the carboxylate anion due to the acid-base equilibria between both species (Figure 104 a). The evaluation of the energy of intermolecular interactions showed that ionic interactions are stronger than any other intermolecular interaction (Figure 104 b). As a result, the neutral carboxylic acid elutes earlier than the ionic carboxylate anion due to the lower hydrophilicity and lack of ionic interactions. The observed chromatographic peak shape of the neutral species is sharper but shows tailing due to the presence of a lower proportion of the carboxylate anion. More symmetric but broader chromatographic peak shapes are observed when the carboxylate anion predominates.

a)

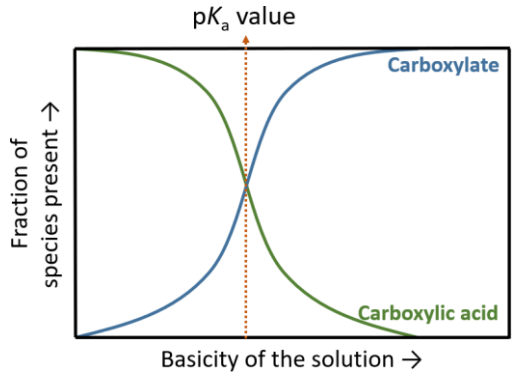

b)

Intermolecular interaction	Energy (Kcal/mol) [200]
Ionic	50 – 200
Hydrogen bonding	5 – 10
Partition, dipole-dipole, *etc.*	< 5

Figure 104. Carboxylic acids and chromatography: a) Biphasic diagram showing the species formed, and b) Energy released of the intermolecular interactions that occur during the chromatographic separation

The chromatographic method at this point showed a suboptimal peak shape (see Figure 105) with a large peak width (*w*: 0.70 minutes) and peak splitting (top side of the peak at t_R = 22.20 min), and several shoulders (t_R = 22.40 min). These peak shape issues were related to the selected mobile phase acidity and additives. The lack of a buffering capacity suggested that the working acidity was close to the analyte pK_a; as such, the proportion of the neutral and ionic forms of the acidic PEGs was poorly controlled, resulting in broader peak shapes.

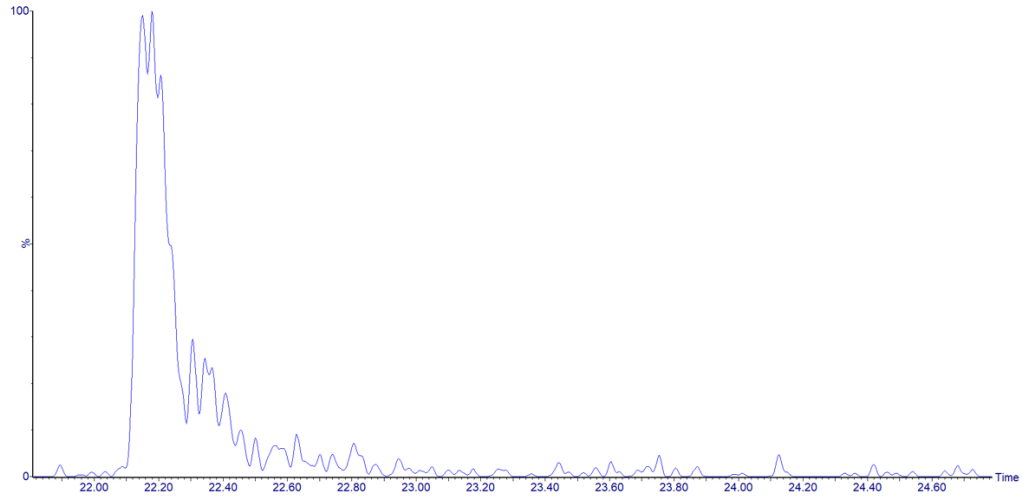

Figure 105. UHPSFC positive ion ESI MS. RICC (*m/z* 650.5). 1000 µg/mL of mPEG acid 2000 in CH_3CN. Challenge in the chromatographic peak shape

When dealing with acid-base equilibria, a common practice in liquid chromatography (LC) is the control of the mobile phase acidity by working at pH values of at least one unit (ideally ±2) from the analyte pK_a. This control of the mobile phase acidity is challenging in SFC due to changes in the mobile phase composition derived from the gradient analysis and the gas/supercritical fluid nature of CO_2. West *et al.* showed that the percentage of co-solvent governs the acidity of the SFC mobile phase, being more acidic at lower percentages of the gradient and more basic at higher percentages [374].

3.3.2 Non-selective ionisation of poly(ethylene) glycols

The current method showed a non-selective ionisation (Figure 106) that complicated data treatment and a qualitative analysis due to overcrowded mass spectra and increased variability of the quantitative method, resulting in inconsistent experimental values of number average (M_n), weight average (M_w) MWs and polydispersity (PDI). The observed challenges suggested optimising the method conditions and forcing the ionisation to form only one ionised species. Selective ionisation was considered essential and suggested for polymer analysis, as the generated mass spectra are complicated by nature.

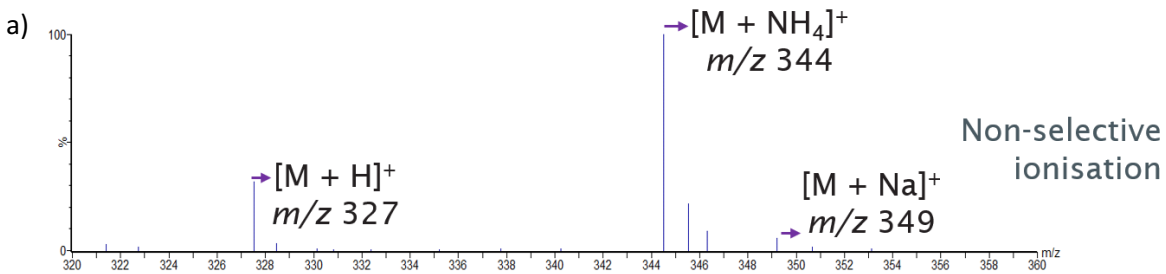

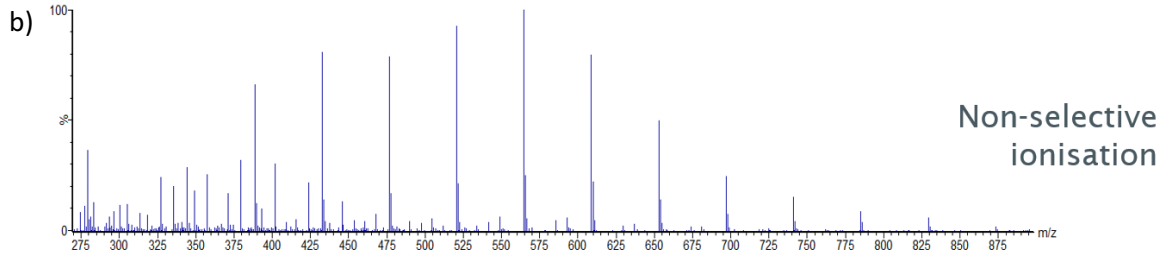

Figure 106. UHPSFC positive ion ESI MS. Mass spectra. Non-selective ionisation of PEG 600 showing the ions generated by a) one oligomer, b) the polymeric distribution

The injection solvent, the mobile phase co-solvent and additives, the make-up solvent, the desolvation conditions in the ionisation source and the ion source/mass analyser design (as shown in Figure 29) can control the ionisation event followed by a molecule. The following section 3.4 covers those aspects related to the chromatography and the ESI desolvation event, whilst those associated with the design of the mass analyser are discussed in Chapter 5. The ion source design is not covered in this study.

3.4 Forcing the selective ionisation of ammoniated adducts and optimisation of the chromatographic peak shape of acidic poly(ethylene) glycols

3.4.1 Mobile phase optimisation

Initial chromatographic studies (discussed in section 3.1.2, page 114) showed the requirement of using CH_3OH as a co-solvent (size-based mechanism) and ammoniated salts as additives (ion-pairing mechanism, Zheng *et al.*) to allow for an oligomer separation [247]. Similarly, the formation of ammoniated molecules was designated because (i) selective ionisation of sodiated adducts was impossible due to the introduction of the highly concentrated solution of ammonium acetate, and (ii) removal of the ammoniated salt compromised the chromatographic separation.

A qualitative comparison of the formed ionised species was performed to aim at achieving selective ionisation. Visual representations of the ionisation current trends at different charged states were proposed. The peak area of the reconstructed ion current chromatograms (RICC) of all the ionisation states was represented against the oligomer repeating unit, assuming an equal positive ion ESI MS response for the protonated, ammoniated, and sodiated molecules. Responses below 3% were removed as this value corresponded to the average standard deviation of the peak area of the RICC of each ionisation state. Examples are shown for (i) singly charged

species based on the oligomer n value (Figure 107 a), (ii) doubly charged species based on the oligomer n value (Figure 107 b), and (iii) relative formation of singly and doubly charged species (Figure 108). These visual representations of the ion current trends were proposed to help optimise the positive ion ESI MS species, and they do not represent their actual response.

The visual representations of the singly charged species based on the oligomer n value (Figure 107 a) show the ion response based on the n value of the polymer and represent the observed response for the formation of PEG ions at singly charged states: $[M + H]^+$, $[M + NH_4]^+$, $[M + Na]^+$ and the total ion response. The visual representations of the doubly charged species based on the oligomer n value (Figure 107 b) are the same representation for singly charged species (Figure 107 a) but for ions that are doubly charged: $[M + 2H]^{2+}$, $[M + H + NH_4]^{2+}$, $[M + 2NH_4]^{2+}$, $[M + NH_4 + Na]^{2+}$ and their total ion response.

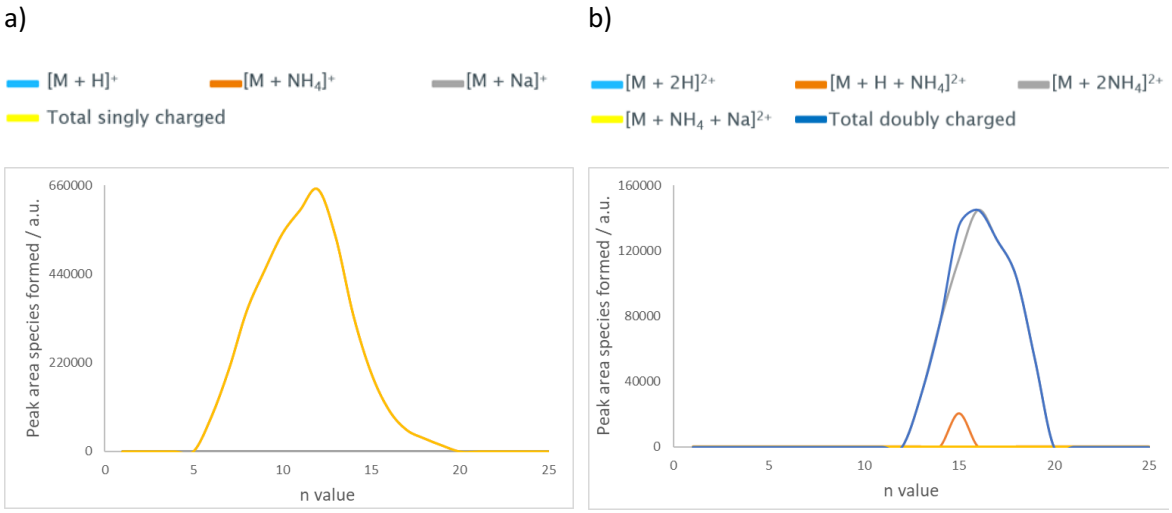

Figure 107. Visual representation of the ionisation current trends of: a) singly charged species and b) doubly charged species of PEG 600 based on the oligomer n value. Colours indicate the distributions of different ionisation events

The visual representation of the relative formation of singly and doubly charged species (Figure 108) shows the relative proportion of the different ionisation charged states for a specific polymeric distribution with a defined MW.

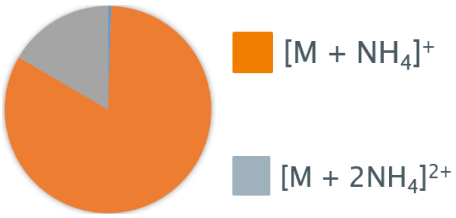

Figure 108. Visual representations of the relative formation of the singly and doubly charged species for PEG 600. Colours indicate the charged states

Either buffering the mobile phase with the corresponding counter-acid (formic/formate or acetic/acetate) or partial substitution of methanol with H_2O were initially proposed to control the ionisation species based on the mobile phase acidity. Figure 109 and Figure 110 showed that mobile phases based on formates favoured protonation to a higher degree than those based on acetates due to their higher acidity. Removing the counter-acid and partial substitution of CH_3OH for H_2O decreased the mobile phase acidity leading to a higher formation of ammoniated molecules. The use of higher percentages of H_2O increased the basicity of the mobile phase, reducing undesirable ionisation species. Higher substitution of H_2O than 6% (v/v) was not tested due to immiscibility with the $scCO_2$. The singly charged trends (Figure 109) and the doubly charged trends (Figure 110) suggested that a concentration between 15 to 50 mM of ammonium acetate was suitable as the mobile phase additive. It is worth noting the negligible number of species not related to singly or multiply ammoniated molecules when using conditions that forced ionisation to these events: Figure 109 e and f for singly, and Figure 110 e and f for the doubly charged trends.

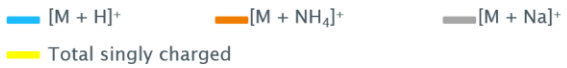

a) 25 mM $HCOONH_4$ + 1% HCOOH in CH_3OH

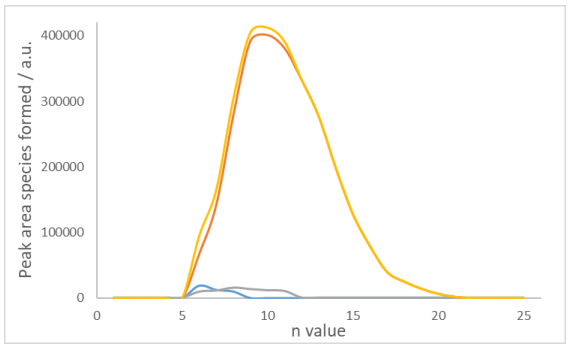

b) 25 mM CH_3COONH_4 + 1% CH_3COOH in CH_3OH

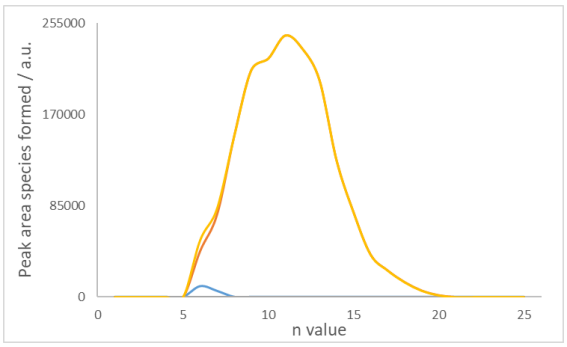

c) 25 mM CH_3COONH_4 in 98% CH_3OH / 2% H_2O

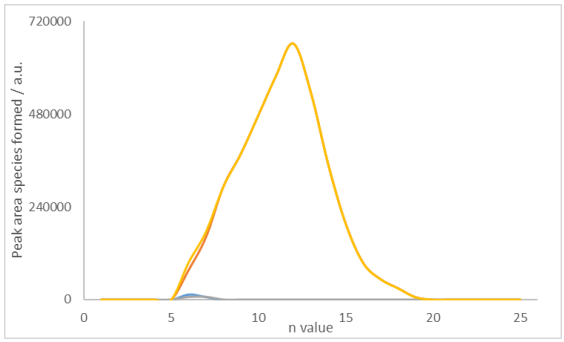

d) 25 mM CH_3COONH_4 in 94% CH_3OH / 6% H_2O

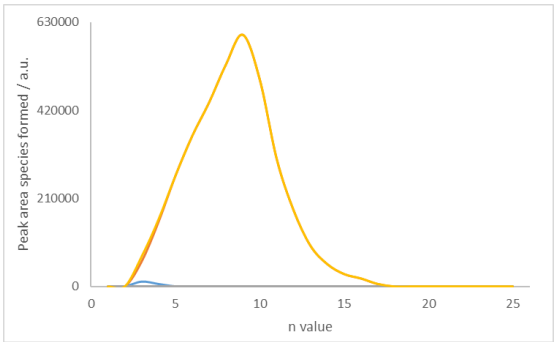

e) 15 mM CH_3COONH_4 in 94% CH_3OH / 6% H_2O

f) 50 mM CH_3COONH_4 in 94% CH_3OH / 6% H_2O

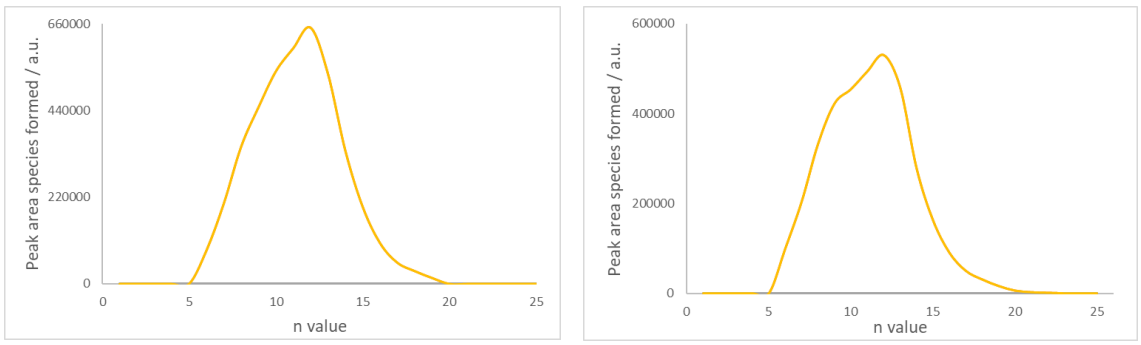

Figure 109. UHPSFC positive ion ESI MS. 50 µg/mL PEG 600 in CH_3CN. Differences in the ion current trends of singly charged species formed for PEG 600 when using different combinations of mobile phase co-solvent and additives. The make-up solvent corresponded to CH_3OH with 50 µM of the ammoniated salt added to the co-solvent

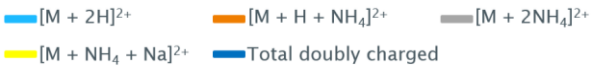

a) 25 mM $HCOONH_4$ + 1% HCOOH in CH_3OH

b) 25 mM CH_3COONH_4 + 1% CH_3COOH in CH_3OH

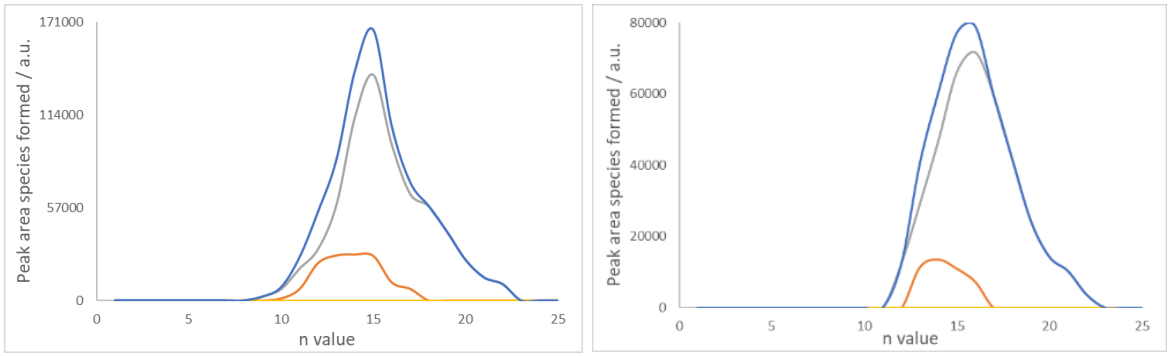

c) 25 mM CH_3COONH_4 in 98% CH_3OH / 2% H_2O

d) 25 mM CH_3COONH_4 in 94% CH_3OH / 6% H_2O

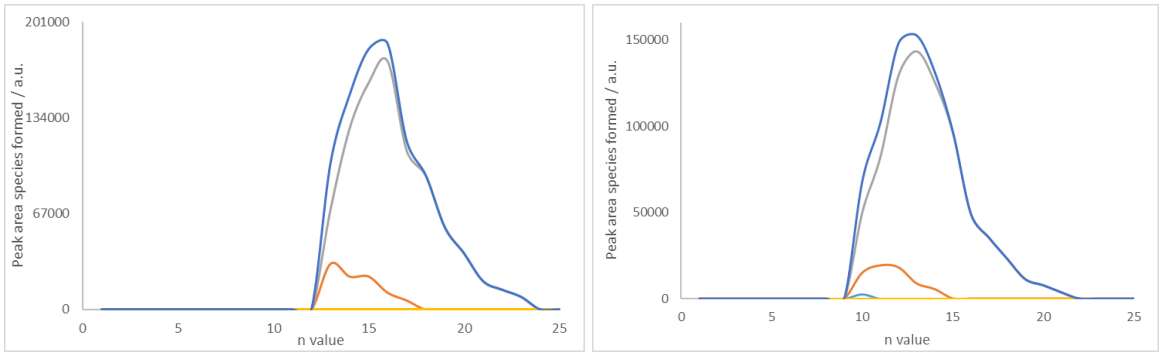

e) 15 mM CH_3COONH_4 in 94% CH_3OH / 6% H_2O f) 50 mM CH_3COONH_4 in 94% CH_3OH / 6% H_2O

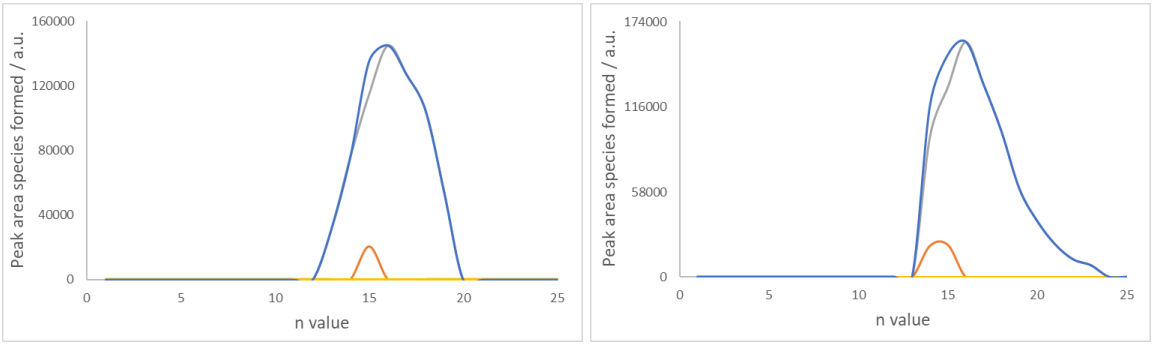

Figure 110. UHPSFC positive ion ESI MS. 50 µg/mL PEG 600 in CH_3CN. Differences in the ion current trends of doubly charged species formed for PEG 600 when using different mobile phase co-solvents and additives. The make-up solvent corresponded to CH_3OH with 50 µM of the ammoniated salt added to the co-solvent

A parallel evaluation of the chromatographic peak shape of some PEGs with acidic end groups confirmed previous thoughts about the mobile phase acidity. Either buffering the ammonium salt with the corresponding counter-acid (formic/formate or acetic/acetate) or partial substitution of the co-solvent with H_2O were proposed to control the ionisation event and the mobile phase acidity. A comparison of the theoretical aqueous buffer pK_a and the predicted pK_a of surrogate oligomers of the acidic PEGs (Table 41) allowed the evaluation of the mobile phase acidity.

	mPEG acid surrogate	**PEG diacid surrogate**	**$HCOOH/HCOONH_4$ buffer**	**CH_3COOH/CH_3COONH_4 buffer**
pK_a (a.u.)	3.39*	3.09*, 3.70*	3.75	4.76

Table 41. Comparison of the theoretical aqueous pK_a of two buffers used in the mobile phase and the predicted pK_a of surrogate molecules with two repeating units of mPEG acid 2000 and PEG diacid 2000 using ACDLabs 2017 (see supporting information)

When using the formic acid/formate buffer (Figure 111 a), a distorted peak resulted from a partial neutralisation of the carboxylate anions that was minimised when using the acetic/acetate buffer due to the higher basicity of the counterion (Figure 111 b). The differences in retention time between buffers were associated with the ionic strength and bulkiness of the ammonium salt counterion and increased the hydrophilicity of the analyte due to a displacement of the fraction of the neutral form of the end group to the ionic form. Removal of the buffer counter-acid

decreased the mobile phase acidity and favoured the carboxylate anion leading to a more symmetrical peak shape and extra retention (Figure 111 b and c). The chromatographic peak shape was enhanced when eliminating the salt counter-acid and partially substituting the methanolic co-solvent with H_2O (Figure 111 e and f) due to an increase in the mobile phase basicity. The increased retention when using H_2O resulted from the solvation of the stationary phase (HILIC-like mechanism, Taylor, Liu *et al.*) and the larger hydrodynamic size of the analytes (size-related mechanism, Poulton *et al.*) [126, 241-243].

a) CH_3OH + 25 mM $HCOONH_4$ + 0.1% HCOOH

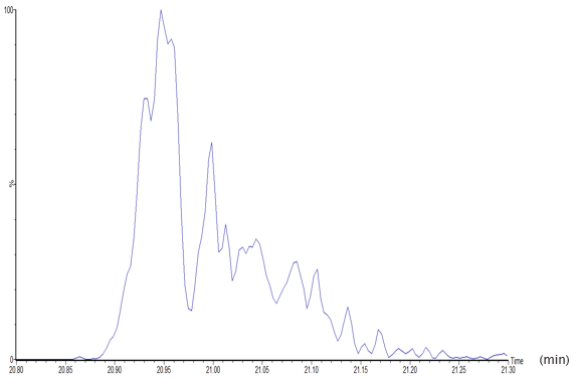

b) CH_3OH + 25 mM CH_3COONH_4 + 0.1%CH_3COOH

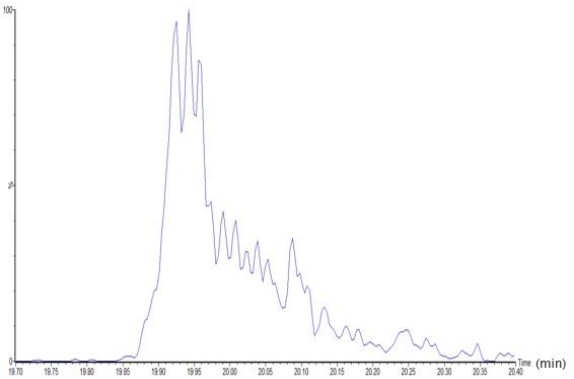

c) CH_3OH + 25 mM $HCOONH_4$

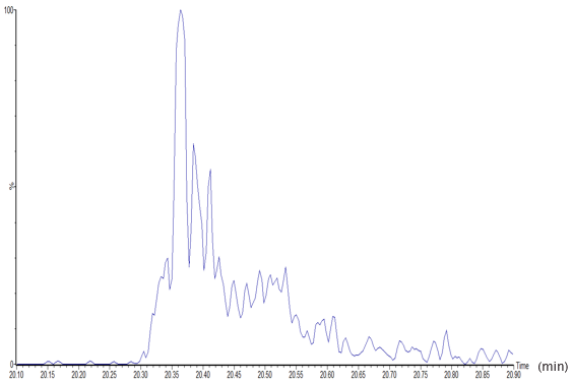

d) CH_3OH + 25 mM CH_3COONH_4

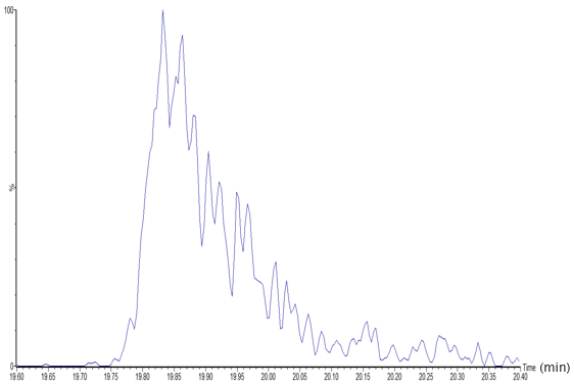

e) CH_3OH + 25 mM $HCOONH_4$ + 2% H_2O

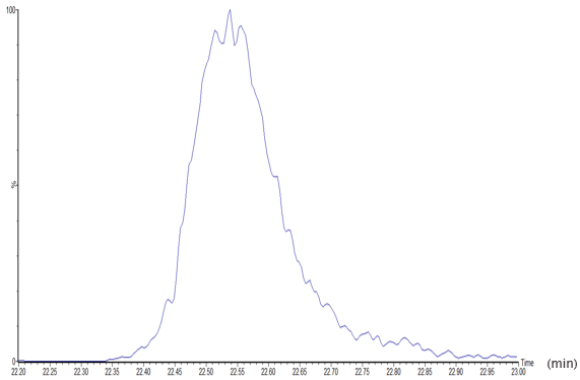

f) CH_3OH + 25 mM CH_3COONH_4 + 2% H_2O

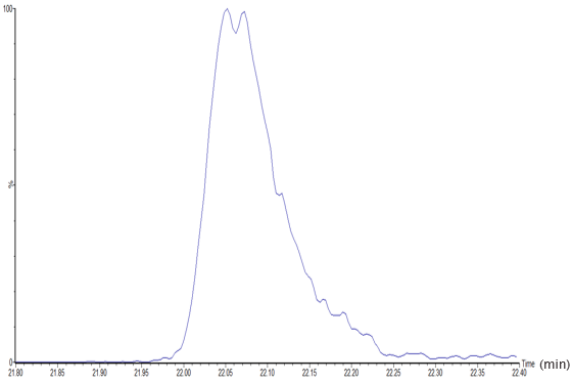

Figure 111. UHPSFC positive ion ESI MS. RICC of a representative oligomer of mPEG acid 2000 (n=41, *m/z* 650, $[M + 3NH_4]^{3+}$). 100 µg/mL mPEG acid 2000 in CH_3CN + 0.1% HCOOH. Optimisation of the mobile phase co-solvent and additive combination

The evaluation of the percentage of H_2O partially substituting the methanolic co-solvent suggested that higher water fractions improved the peak shape (Figure 112 a), highlighting 6% (v/v) as the optimum value. The evaluation of the concentration of CH_3COONH_4 (Figure 112 b) showed that decreasing the amount of salt improved the peak shape due to a decrease in acidity. Lower concentrations were not tested due to the need for NH_4^+ ions for chromatographic separation and ionisation. A co-solvent combination of 94 CH_3OH / 6 H_2O (% v/v) + 15 mM CH_3COONH_4 was selected. The make-up solvent consisted of CH_3OH + 50 µM CH_3COONH_4.

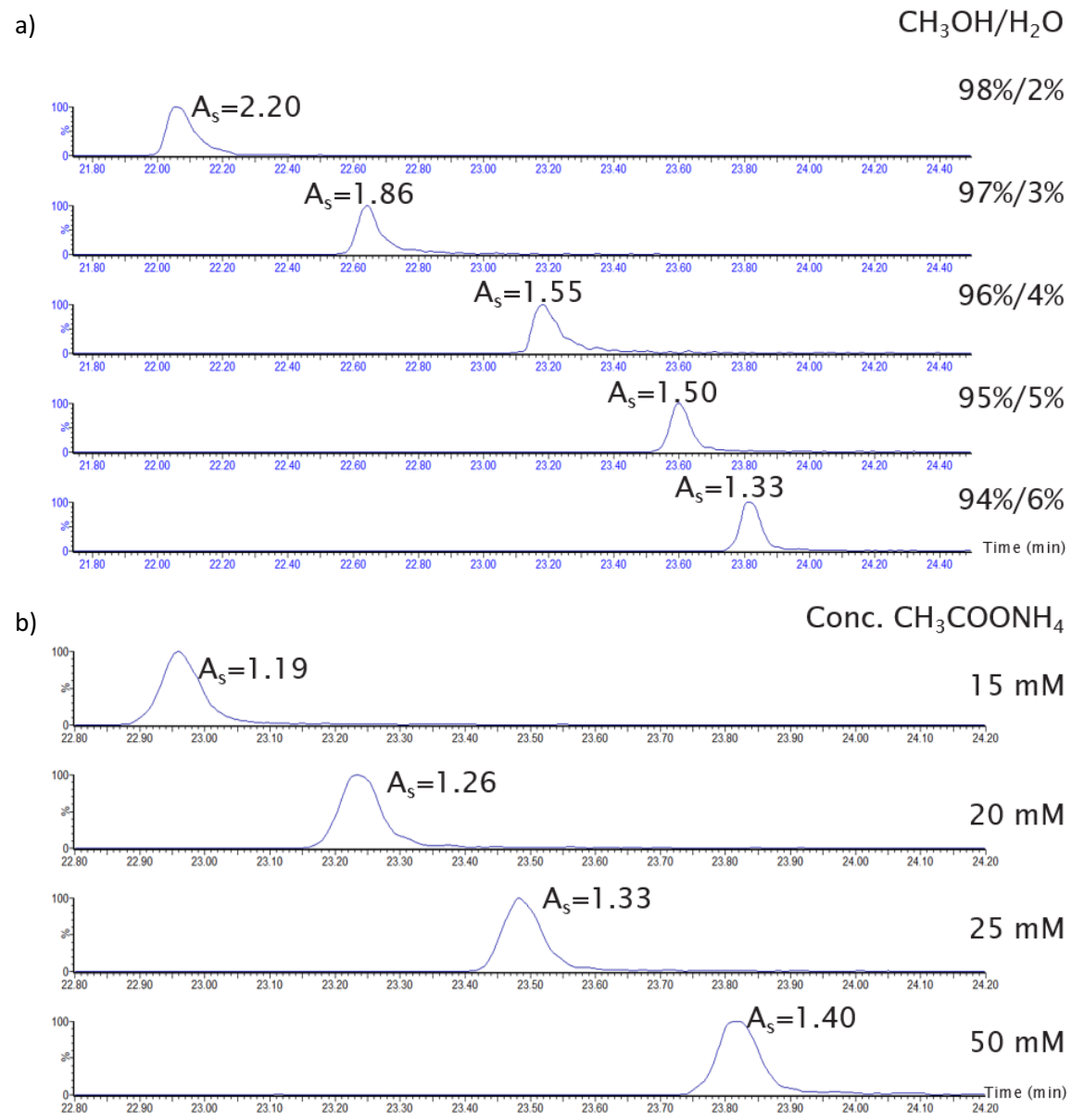

Figure 112. UHPSFC positive ion ESI MS. RICC (*m/z* 650) of a representative oligomer of mPEG acid 2000 (n=41, *m/z* 650, $[M + 3NH_4]^{3+}$). 100 µg/mL mPEG acid in CH_3CN + 0.1% HCOOH. Optimisation of the co-solvent: a) CH_3OH / H_2O (v/v)+ 25 mM CH_3COONH_4), and b) the additive concentration CH_3OH / H_2O 94%/6% (v/v) + X mM CH_3COONH_4). A_s values calculated at half-width

3.4.2 Optimisation of the positive ion electrospray mass spectrometry desolvation process

The similarities observed during the mobile phase optimisation suggested that a generic method was possible independent of the MS desolvation conditions related to the polymer end group. Previous analyses showed that selective ionisation was already achieved; however, the positive ion ESI MS compromised the ions arriving at the mass analyser due to an uncontrolled in-source fragmentation leading to the formation of $[M + H]^+$ through loss of ammonia from $[M + NH_4]^+$. The cone voltage and the desolvation temperature were investigated due to their relation to in-source CID fragmentation. When increasing the cone voltage, the first noticeable point was an in-source fragmentation of the smaller PEG chains via cleavage (Figure 113 a), producing fragments in the mass spectra with *m/z* 44.9 + 44x *m/z* units (Figure 113 b). The smaller PEG chains, either $[M + NH_4]^+$ or $[M + H]^+$ species formed by loss of ammonia, compromised the quantitation of low MW PEGs.

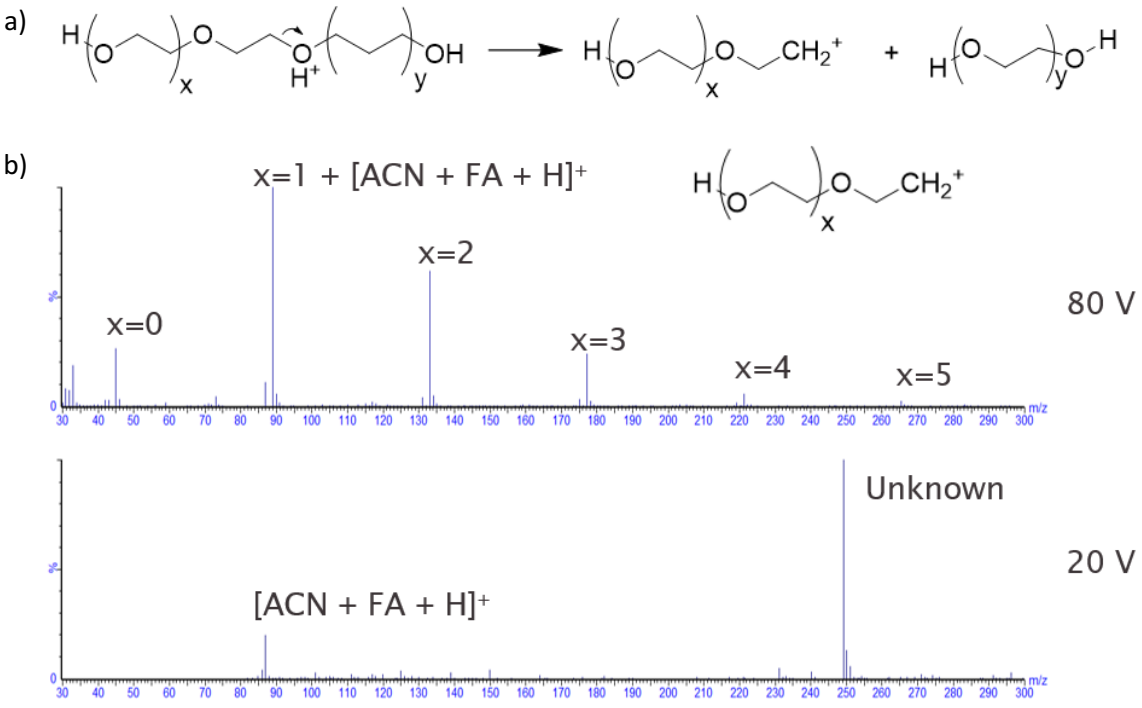

Figure 113. UHPSFC positive ion ESI MS. Mass Spectra. 50 µg/mL PEG 200 in CH_3CN. In-source fragmentation of PEG chains: a) fragmentation mechanism via cleavage, and b) fragments observed

The undesirable formation of protonated molecules was associated with an in-source fragmentation of ammoniated molecules. Increasing the cone voltage and the desolvation temperature (Figure 114) promoted the ion source CID fragmentation. Also, higher values of the cone voltage (over 50 V) induced a formation of sodiated molecules; however, selective ionisation was not possible due to the high ammonium ions concentration from the mobile phase.

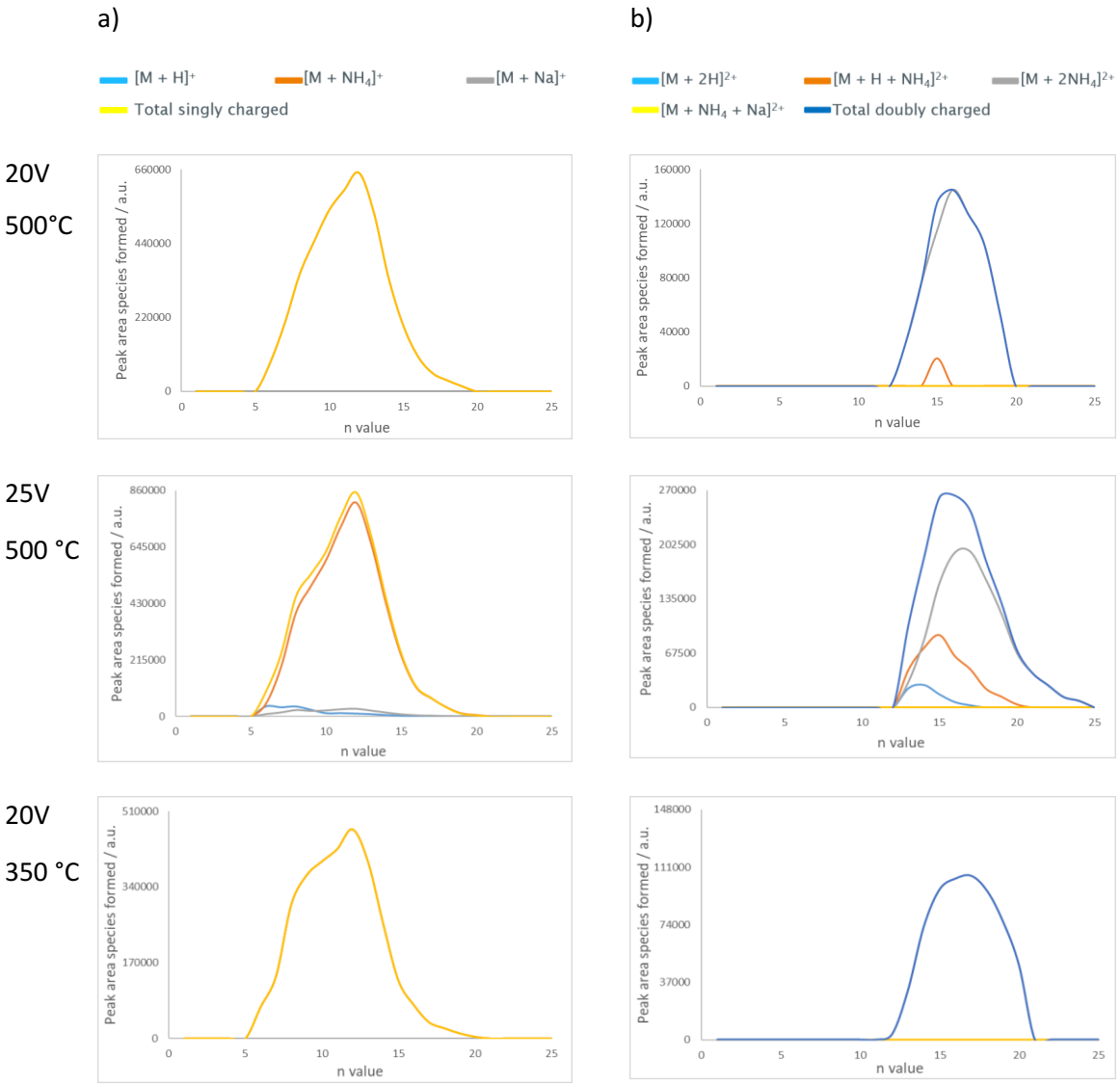

Figure 114. UHPSFC positive ion ESI MS. Differences in the ion current trends of doubly charged species formed for PEG 600 when using different cone voltage and desolvation temperature for a) singly and b) doubly charged species

Even though protonation of PEG was observed for small oligomers (n 2-5) (discussed in detail in section 3.5, page 142), cationisation becomes the dominant process for larger chains when forcing their ionisation. Increasing the cone voltage or the desolvation temperature resulted in harsher CID conditions observed, leading to loss of ammonia from the ammoniated oligomers

(Figure 115), suggesting that the best conditions are a 20 V cone voltage and 350 °C as the desolvation temperature, as shown in Figure 114.

a) $[M + NH_4]^+ - NH_{3(g)} \uparrow\rightarrow [M + H]^+$

b) $[M + nNH_4]^{n+} \rightarrow [M + (n - x)NH_4]^{(n-x)+} + xNH_4^{x+}$

c) $[M + nNH_4]^{n+} + yNa^+ \rightarrow [M + (n - y)NH_4 + yNa^+]^{n+}$

Figure 115. Effect of increasing the cone voltage and/or the desolvation temperature to the ammoniated species: a) loss of ammonia (increase both), b) charge stripping (increase cone voltage), and c) formation of Na adducts (increase cone voltage)

3.4.3 Reconsideration of the choice of injection solvent for PEGs with acidic end groups

When analysing carboxylic acids, the addition of trifluoroacetic acid (pK_a 0.23) in small amounts (0.1% v/v) is recommended to maintain weaker carboxylic acids (pK_a 3-5) in the neutral form. However, the use of trifluoroacetic acid leads to significant ion suppression effects within the ESI source. The use of formic acid is a better agent to achieve the ionic form when coupling the chromatography to ESI MS. Previous tests concluded that CH_3CN was the best injection solvent for PEGs with alcohol and aliphatic end groups and this injection solvent was compared to CH_3CN +1% HCOOH, CH_3OH + 15 mM $HCOONH_4$ and 94 CH_3OH/6 H_2O (v/v) + 15 mM $HCOONH_4$ (Table 42 and Figure 116). More symmetrical peaks were obtained when using CH_3CN or adding HCOOH. Combinations with protic solvents (either CH_3OH or H_2O) showed the worst peak shapes due to the higher solvent strengths of these solvents to the lower percentages of the mobile phase gradient, confirming the need to use CH_3CN and HCOOH (Figure 116 b). It is worth noting that contrary to alcohol and aliphatic PEGs, acidic PEGs were soluble in protic solvents at room temperature, even with their high MW, due to the presence of the carboxylic end group.

	Peak area x 10^{-7} (a.u.)	
Sample diluent	**mPEG acid 2000**	**PEG diacid 2000**
CH_3CN	1.19 ± 0.13	1.41 ± 0.14
CH_3CN + 1% HCOOH	1.05 ± 0.14	1.22 ± 0.10
CH_3OH + 50 mM CH_3COONH_4	1.25 ± 0.11	1.43 ± 0.13
CH_3OH + 15 mM $HCOONH_4$ + 6% H_2O	1.40 ± 0.12	1.56 ± 0.14

Table 42. Effect of the sample diluent in the peak area of mPEG acid 2000 and PEG diacid 2000. Peak areas were calculated using the RICC of *m/z* 650.5 for one oligomer of mPEG acid 2000 and PEG diacid 2000. Samples were analysed in triplicates

a) CH_3CN b) CH_3CN + 1% HCOOH

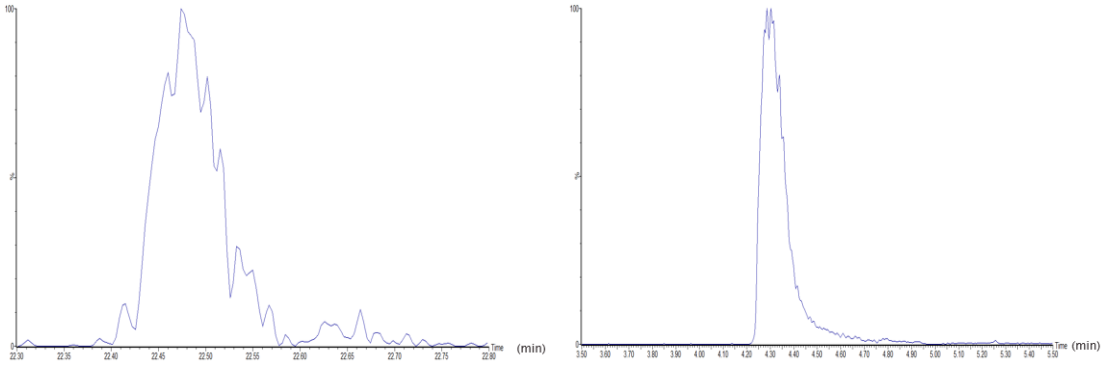

c) CH_3OH + 50 mM CH_3COONH_4 d) CH_3OH + 15 mM CH_3COONH_{4+} + 6% H_2O

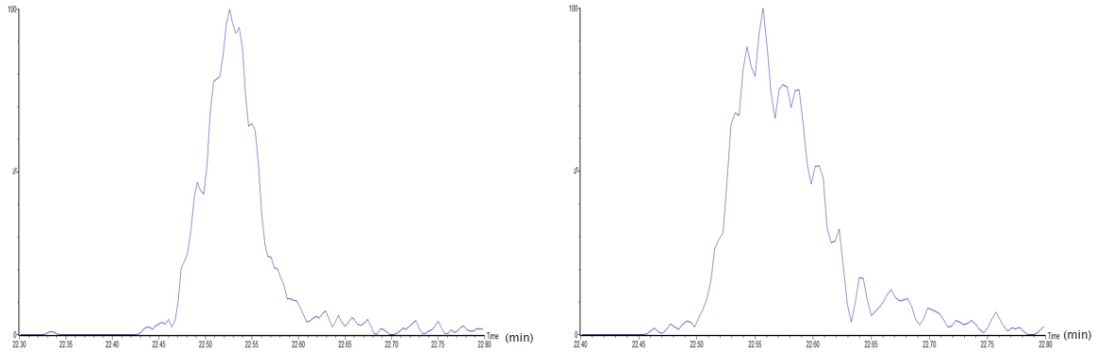

Figure 116. UHPSFC positive ion ESI MS. RICC (*m/z* 650.5). 1000 µg/mL mPEG acid 2000 dissolved in: a) CH_3CN, b) CH_3CN + 1% HCOOH, c) CH_3OH + 50 mM CH_3COONH_4, d) CH_3OH + 15 mM CH_3COONH_4 + 6% H_2O

3.4.4 Active backpressure regulator to control the mobile phase acidity

The Gibbs equation relates the temperature with the analyte pK_a. As such, the column temperature affects the mobile phase acidity, as increasing the column temperature should decrease the acidity of the mobile phase, varying the ionisation state of the analytes (Equation 38); hence, 70 °C is the optimum column temperature.

$$pK_a = \frac{\Delta G}{2.303RT} \qquad \text{Equation 38}$$

The variation of the ABPR backpressure is performed at the end of the method development for fine-tuning. The ABPR back pressure was tested at 200 and 150 bar as previous analysis showed that the peak shape was poor at 105 bar. Decreasing the ABPR to 150 bar resulted in a slightly more symmetric peak shape (A_s 1.15) than 200 bar (A_s 1.19) (Figure 117).

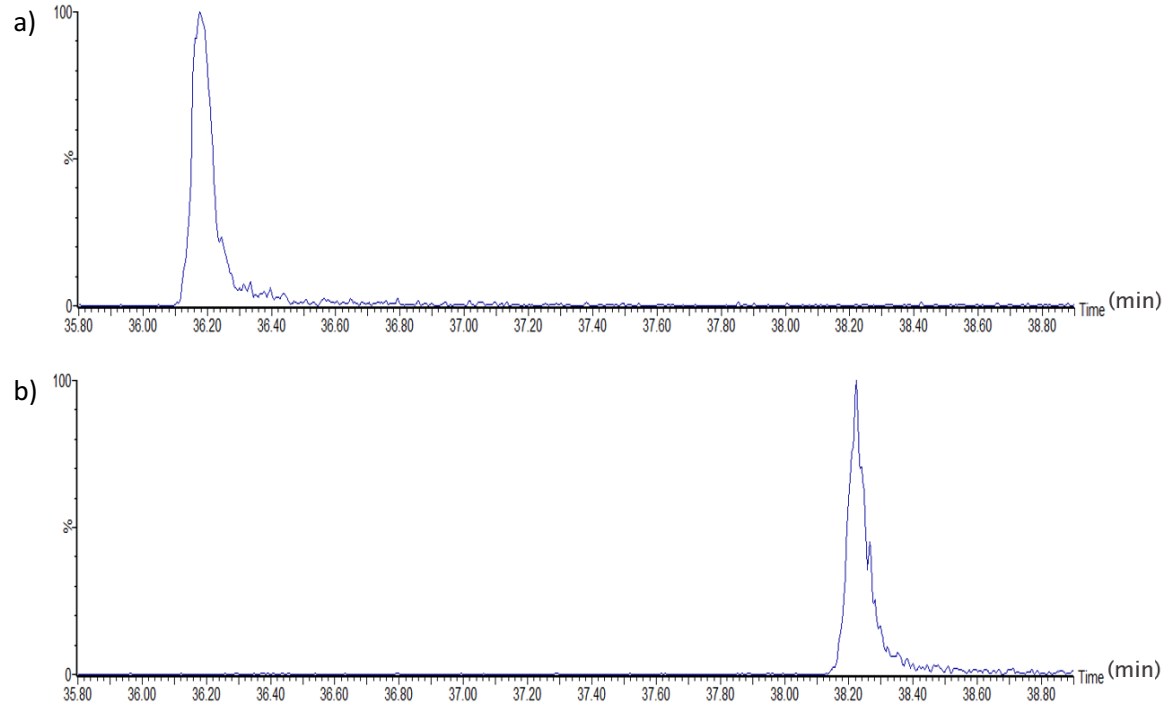

Figure 117. UHPSFC positive ion ESI MS. RICC (*m/z* 650.5). 1000 µg/mL mPEG acid 2000 in CH_3CN + 1% HCOOH. Effect of the ABPR: a) 200 bar and b) 150 bar

3.4.5 Mass spectra improvements resulting from the selective ionisation

Figure 118 shows the differences in the MS ionisation between the previous method (non-selective) and the new method (selective) for one oligomer (Figure 118 a) and the whole polymer distribution (Figure 118 b), showing the benefits of the selective ionisation. The selective ionisation of ammoniated adducts was selected due to the need for ammonium ions in chromatographic separation. Achieving the selective ionisation provided cleaner mass spectra that facilitated the impurity observation and decreased variance in the measured signal, resulting in improved characterisation and quantitation of the material.

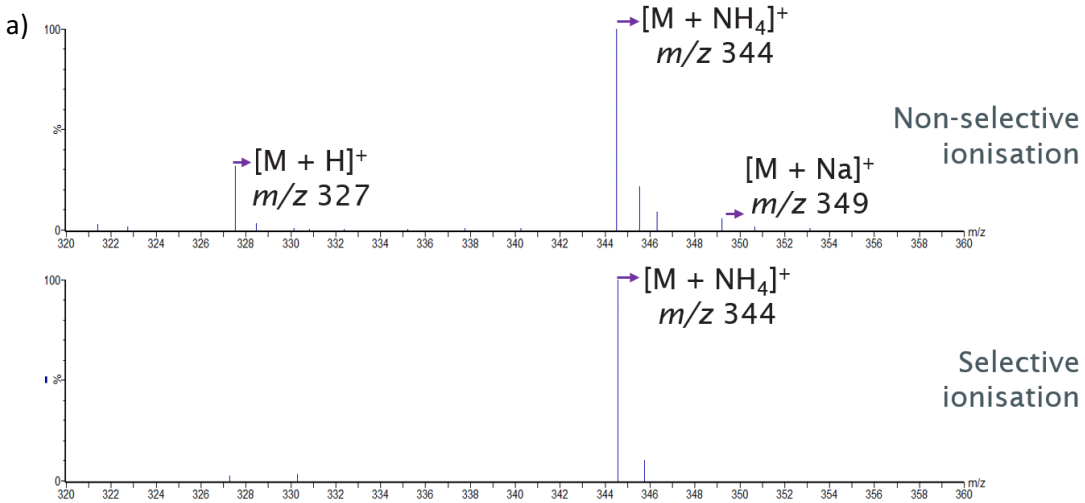

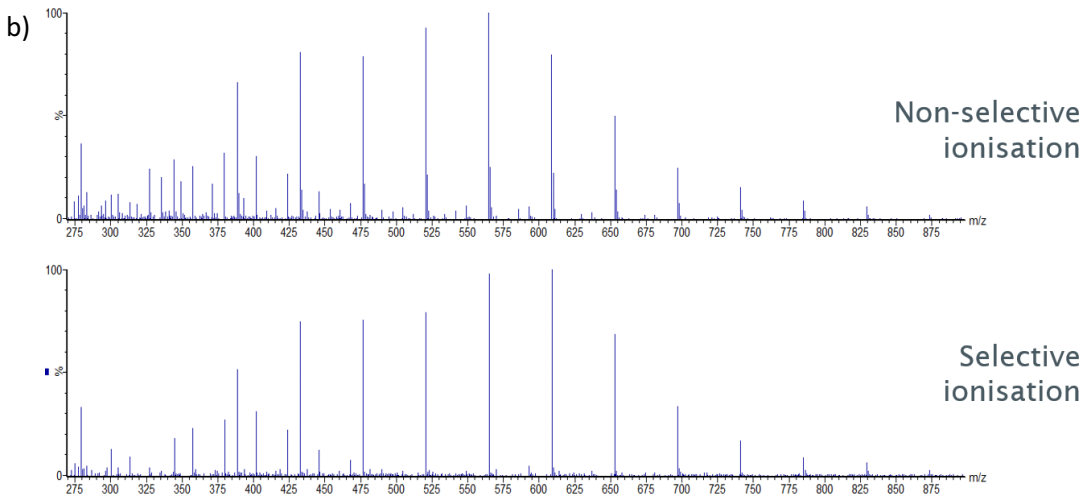

Figure 118. UHPSFC positive ion ESI MS. Mass spectra. 50 µg/mL of PEG 600 in CH_3CN. Effect of a selective adduct formation for PEG 600 in the ions generated by: a) one oligomer, b) the polymeric distribution

3.5 The ionisation of poly(ethylene) glycols

Gidden *et al.* showed the dependence of the polymer MW on the ion charge state [364]. Even though the repeating unit and the end group might affect the quantitation, no profound insights were found into their influence on ionisation. The calculation of the average charge state (z_{avg}) of Lavarone and Williams [375] and visual representations of the relative ion current trends (pie charts and 2D graphs) were proposed to quantify the influence of the chain length and the end group. Pie charts were helpful when comparing polymers and showed the relative formation of the different ionisation states based on the MW. The 2D-graphs were better suited to the oligomers within a polymer and showed the relative formation of the different ionisation states based on the oligomer number. These representations were possible when following the assumption that the ion current produced by singly charged species is equal to that of doubly charged and equal to that of triply charged, *etc.* This statement was proved later on section 5.2.2.

$$z_{avg} = \frac{\sum_{i=1}^{N} z_i \, w_i}{\sum_{i=1}^{N} w_i}$$ Equation 39

N Number of observed analyte charge states in the mass spectrum

z_i The *i*th charge state

w_i The sum of the peak areas of the RICC of all oligomers in the *i*th charge state

3.5.1 Effect of the oligomer chain length

Analysis of the relative formation of the different ionisation states (Figure 119) and the z_{avg} to the manufacturer MW (Figure 120) for PEG 600, 1000, 1450 and 2000 confirmed that multiply charged species are formed based on chain length, with longer oligomer chains favouring multiple cationic species; as discussed by Gidden *et al.* [364].

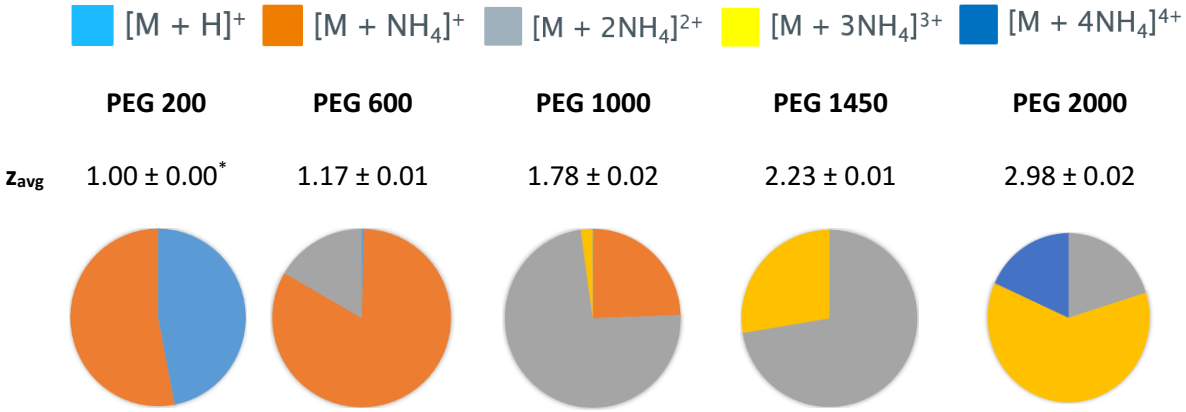

Figure 119. Relative formation of the different ionisation states for PEG 600, 1000, 1450 and 2000. The contribution of the protonated molecules was neglected for PEG 600 and PEG 1000 (*ca.* 1%)

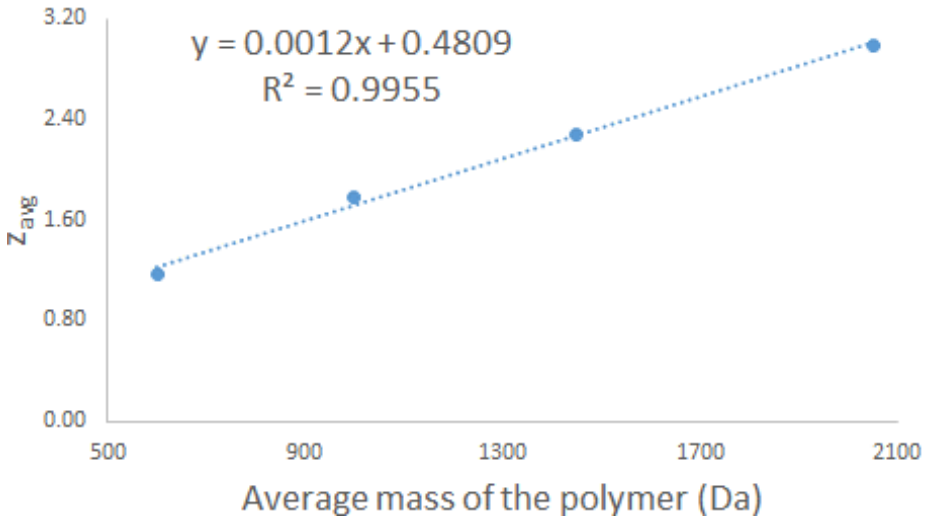

Figure 120. Effect of the chain length on the average charge state of alcohol PEGs

The relative ionisation current trends of the oligomers (Figure 121) showed how increasing the chain length allowed the accommodation of more ammonium ions, possibly due to fewer Coulombic repulsions occurring between the cations. Whilst short oligomers preferred the formation of protonated molecules up to n=5, singly charged ammoniated molecules became predominant for n=6. Doubly charged species were firstly observed from n=10 and overcame the ionisation for oligomers with n=20-30. Triply charged ions were observed from n=23 and

quadruply charged ions at n=35. The abnormality appearing from n=53 in triply and quadruply charged ions was explained by a possible conformational change of the gas-phase oligomer ions.

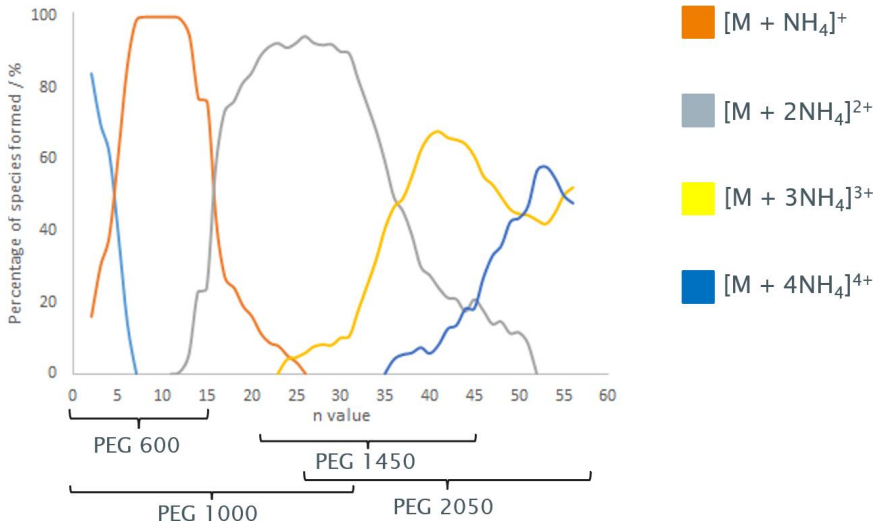

Figure 121. Ionisation current trends showing the percentage of different ionisation events of alcohol PEG oligomers. Graph produced using a mixture of 50 µg/mL in CH_3CN (per component) of PEG 600, 1000, 1450 and 2000

3.5.2 Effect of the end group: length of the aliphatic chain

The ionisation current trends for mPEG (Figure 122) and Brij® 58 (Figure 123) showed a formation of singly, doubly and triply ammoniated charged molecules similarly to alcohol PEGs with a shift of -1 *n value* in the graph (compare Figure 121 with Figure 122). Note that protonated molecules were not observed for aliphatic PEGs.

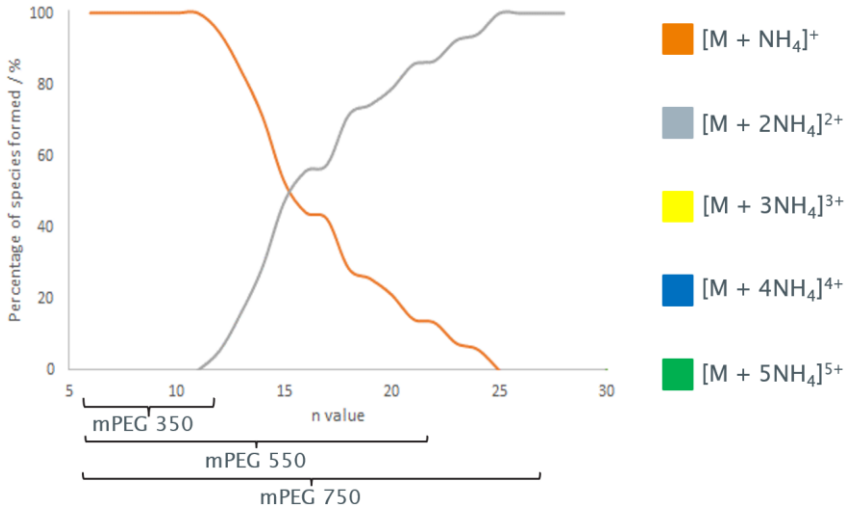

Figure 122. Ionisation current trends showing the percentage of different ionisation events of methoxy PEG oligomers

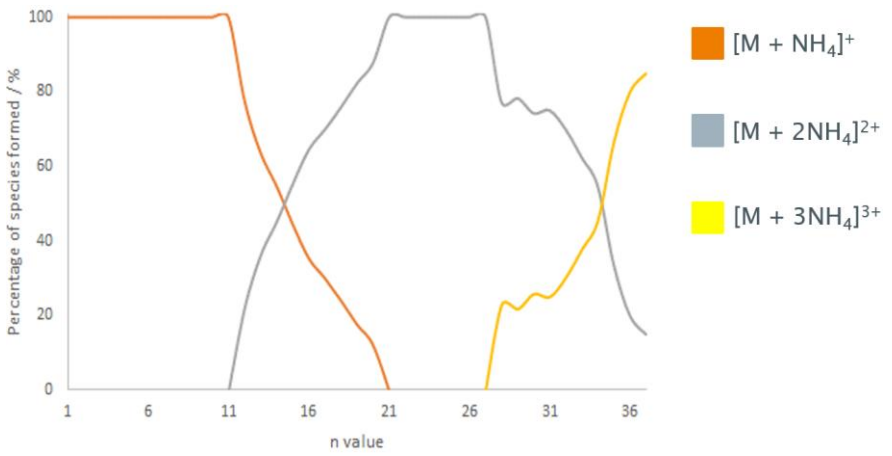

Figure 123. Ionisation current trends showing the percentage of different ionisation events for Brij® 58 oligomers

A comparison of the oligomer ionisation current trends between mPEG to Brij® 58 (Figure 122 and Figure 123) showed that the length of the aliphatic chain displaced the formation of doubly charged species by -4 *n values*, possibly due to a substantial inductive effect.

The relative formation of the different ionisation states and z_{avg} for mPEG and Brij® showed similar trends to the alcohol PEGs, confirming a shape-driven phenomenon in the formation of multiply charged species (Figure 119 and Figure 124).

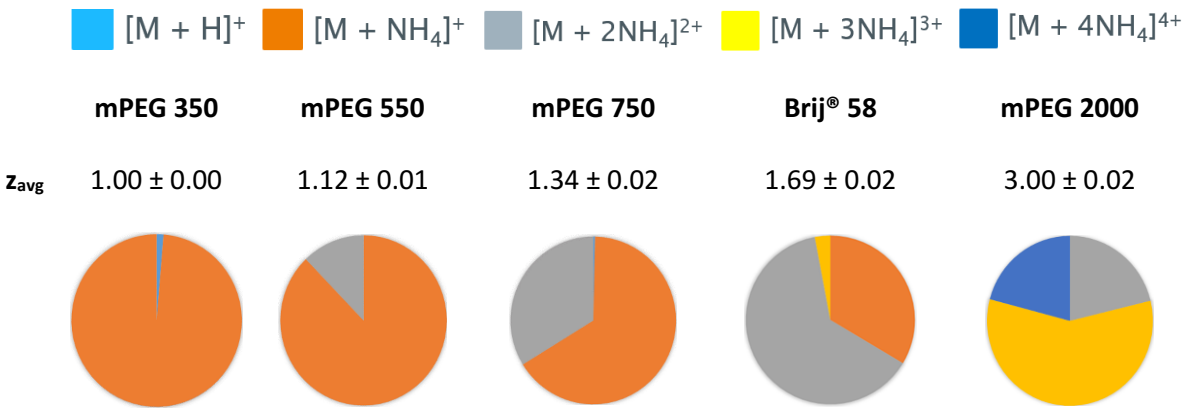

Figure 124. Relative formation of the different ionisation states for PEGs with aliphatic end groups and MW: mPEGs and Brij® 58

3.5.3 Effect of the end group: acidic poly(ethylene) glycols

The acidic end group showed a significant effect in the formation of multiply charged species (Figure 125) due to the ionisable side of the end group. The more charges accommodated in mPEG acid 2000 and PEG diacid 2000 indicate an evident influence of the acidic end group in the overall charge state (Figure 122 and Figure 126) that was associated with the ionic character of

the functional group. For PEG diacid 2000 (Figure 127), the abnormality observed between the oligomers 45 and 55 could be explained by a lower S/N ratio of the oligomers in that region, as these oligomers corresponded to the overlapping of the two PEG diacid distributions.

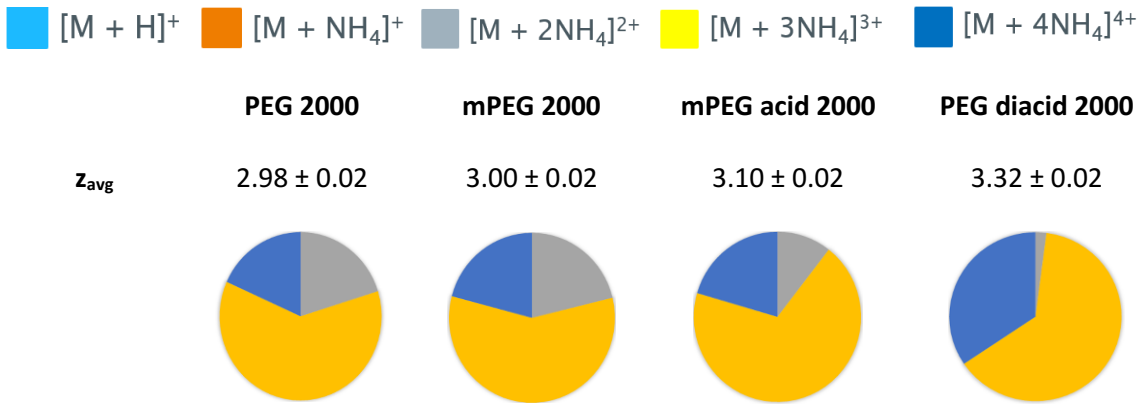

Figure 125. Relative formation of the different ionisation states for mPEG acid 2000 and PEG diacid 2000, compared to PEG 2000 and mPEG 2000

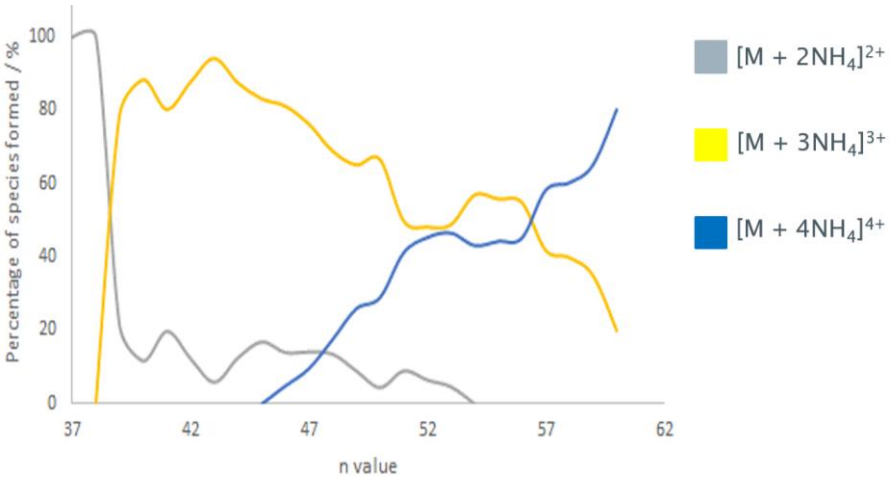

Figure 126. Ionisation current trends showing the percentage of different ionisation events of mPEG acid 2000 oligomers

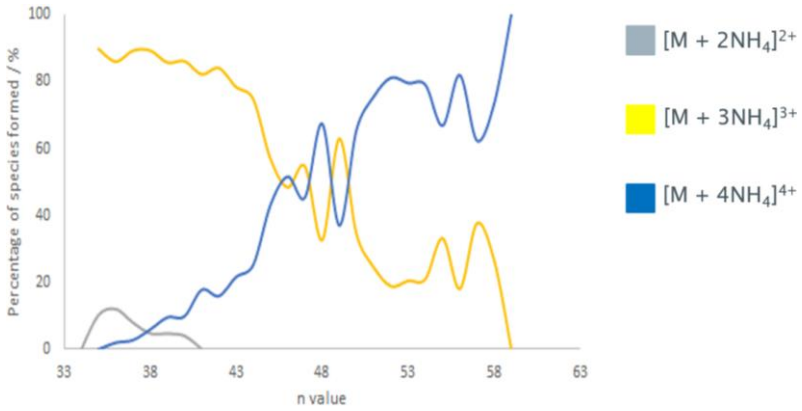

Figure 127. Ionisation current trends showing the percentage of different ionisation events of PEG diacid 2000 oligomers

3.5.4 Overall conclusions

The calculation of z_{avg} and the proposed visual representations of the relative ion current allowed the evaluation of the influence of the chain length and the end group in the ionisation of PEGs. Both representations showed an evidence influence of the polymer MW to the ionisation, similarly to the conclusions of Gidden *et al.* [364]. In any case, the impact of the MW of the polymer on the ionisation charged of the ion was significantly higher than that from the end group, except when the end group had an ionisable character (carboxylic acid, amines, etc.)

For PEGs with the same end groups but that differing in their MW, an independent ionisation response to the charge state was noticed when observing a linear fitting of z_{avg} to the reported MW of different alcohol PEGs and the relative formation of the different ionisation states. The 2D-graphical representation of the oligomer repeating unit showed the dependence of the oligomer chain length on the ion formed and charged state of the ion; and explained how long chains could accommodate more charges due to a depreciation of the Coulombic repulsions between cations located in the ethylene oxide and a shape-driven phenomenon.

For PEGs with different end groups but the same MW, a comparison between the z_{avg} and the relative formation of the different ionisation states showed a noticeable influence of the end group on the charge state. The similarities between z_{avg} values and the 2D graphs suggested that end groups shifted the oligomer at which the different ionisation charge states are formed. The impact of the end group on the ionisation was attributed to an inductive effect of the end group that disturbed the lone pair of electrons of the first neighbouring O atom of the chain, resulting in an alteration of the electron cloud within the PEG chain and the corresponding charge states observed. These findings suggested that electron-donating groups (aliphatic chain in mPEG or Brij® or the H in PEG) destabilised the closest O of the PEG chain (more electronegative), pushing the electron density towards the PEG chain, showing a slight displacement towards fewer charges accommodated. Differences observed between mPEG and Brij® 58 oligomers could relate to the length of the aliphatic chain. On the other side, electron-withdrawing groups (carboxylic acids in mPEG acid or PEG diacid) can deactivate the O of the PEG chain (less electronegative), delocalising the electron cloud and allowing the accommodation of more charges.

3.5.5 The limit of the selective ionisation: small oligomers

When analysing alcohol PEGs with an MW below 600, the selective formation of $[M + nNH_4]^{n+}$ species was compromised for the oligomers, with the smallest chain lengths being the oligomer with n=6 being the smallest where selective ionisation was observed (Figure 128).

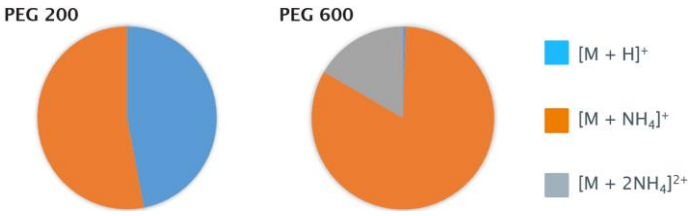

Figure 128. Comparison of the ion current trends between PEG 200 and PEG 600

The make-up solvent and the mobile phase were considered to aid the promotion of selective ionisation for smaller PEGs, for which PEG 200 was used as a model. Figure 129 showed that increasing the CH_3COONH_4 concentration on the make-up solvent from 50 to 1000 µM was insufficient to produce selective ionisation. Changing the make-up solvent for CH_3OH + 1.0% HCOOH (v/v) was sufficient to induce some level of protonation and sodiation; however, achieving a more selective ionisation was not possible. The negligible effect in the ionisation of each of the make-up solvents related to a mobile phase that provided sufficient ammonium ions (CH_3OH / H_2O 94%/6% (v/v) + 15 mM CH_3COONH_4).

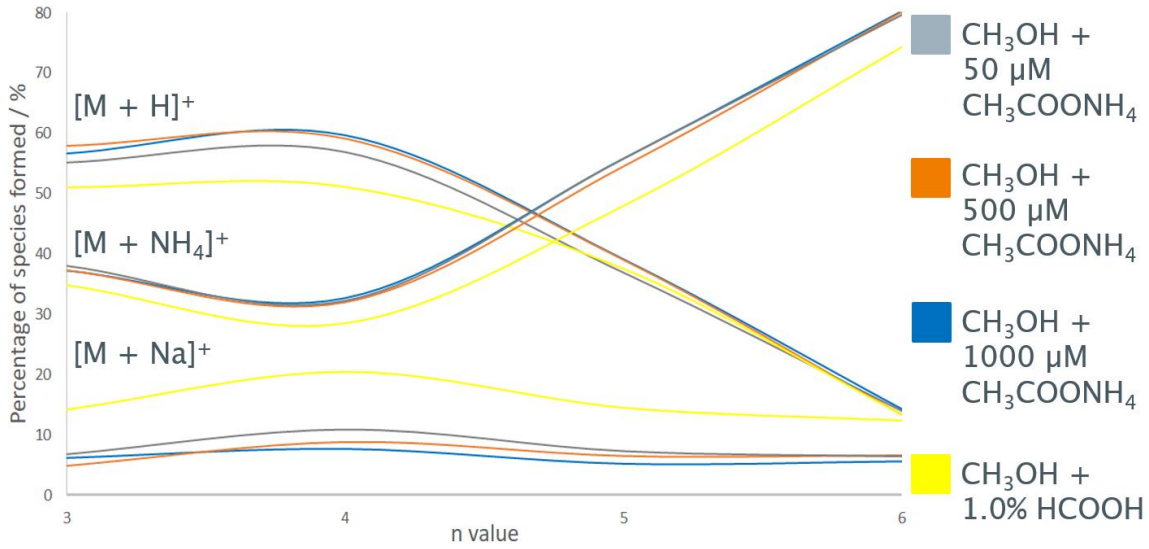

Figure 129. The influence of different make-up solvents in the formation of $[M + H]^+$, $[M + NH_4]^+$ and $[M + Na]^+$ species for PEG 200 oligomers. Graph produced using 10 µg/mL PEG 200 in CH_3CN

The substitution of both the mobile phase and the make-up solvent for CH_3OH + 1.0% HCOOH (v/v) (Figure 130) resulted in the selective formation of $[M + Na]^+$ species (96%) over $[M + H]^+$ species (*ca.* 4%). The lack of formation of protonated molecules in the shortest chains of PEG 200 was associated to a more efficient chelation of the Na^+ ions than the NH_4^+ ions.

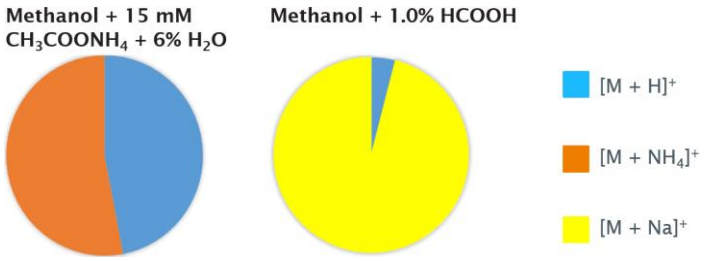

Figure 130. Comparison in the ionisation current trends of PEG 200 under two mobile phases

3.6 Connecting the UPC^2 and the Synapt^{TM} G2-*Si* instruments

The UPC^2 and the Synapt^{TM} G2-*Si* instruments were connected to obtain an UHPSFC positive ion ESI Q IM ToF MS (Figure 131) using a long additional piece of red PEEK tubing with dimensions 1/16" OD x 0.005" ID x 2 m (in red in Figure 131).

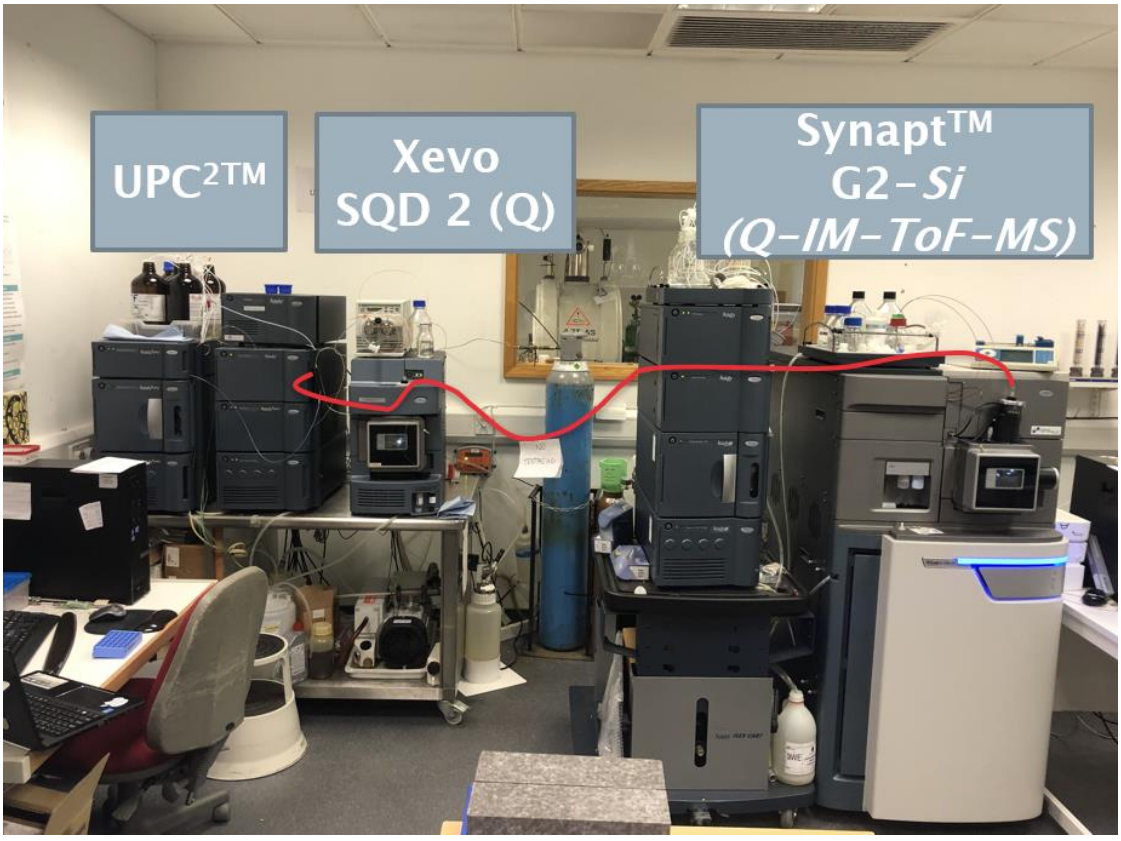

Figure 131. Picture of the connection of the UPC^2 system to the Synapt^{TM} G2-*Si* system. In red, the PEEK tubing

The introduction of the PEEK tubing resulted in a higher analyte retention time of *ca.* 0.2 min differences in the retention time to the TICC that was associated with the dead volume of the PEEK tubing ($\Delta\overline{w_{1/2}} = 0.2s$, $\Delta\overline{w} = 0.9s$). The minor impact in the dispersion (factor of 1.1, Figure 132) was associated with the supercritical character of CO_2 and the flow rate of the make-up solvent.

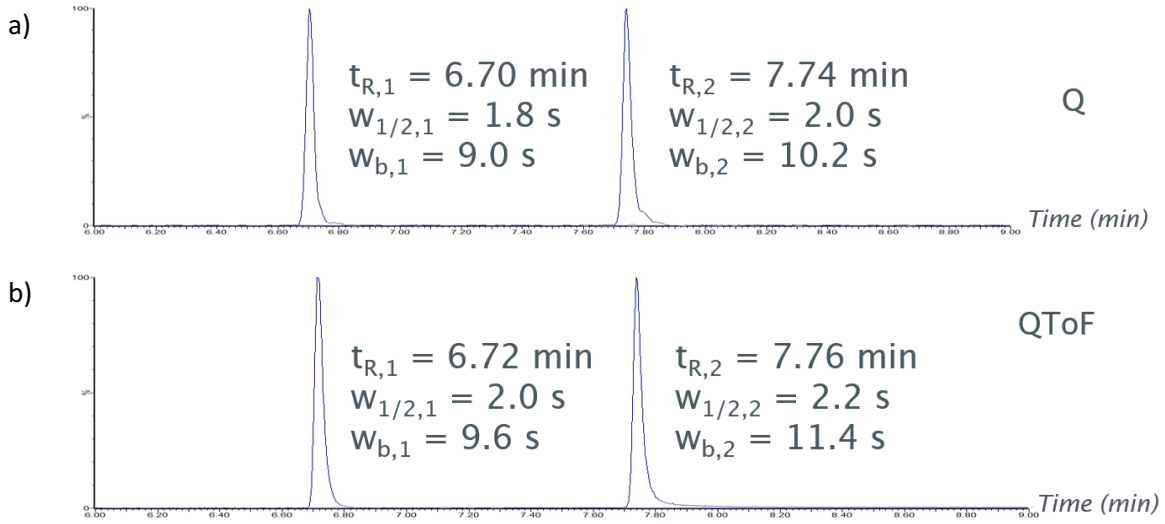

Figure 132. UHPSFC positive ion ESI MS. PEG 1450 (RICC shown of two oligomers). Impact in the chromatographic band broadening of introducing a long PEEK tubing: a) Waters® UPC^2 to Waters® SQD 2, b) Waters® UPC^2 to the Waters® Synapt™ G2-*Si* using the PEEK tubing

Additionally, the change in the mass analyser resulted in fewer charge states observed in the mass spectra (Figure 133), which was related to the change in the ion beam direction and transmission from a beam (Q) to a pulsed ion beam (QToF) instrumentation. This effect is discussed in detail in Chapter 4.

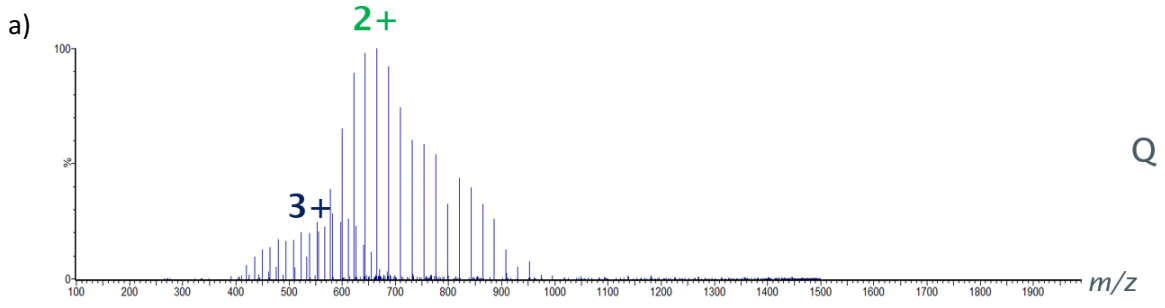

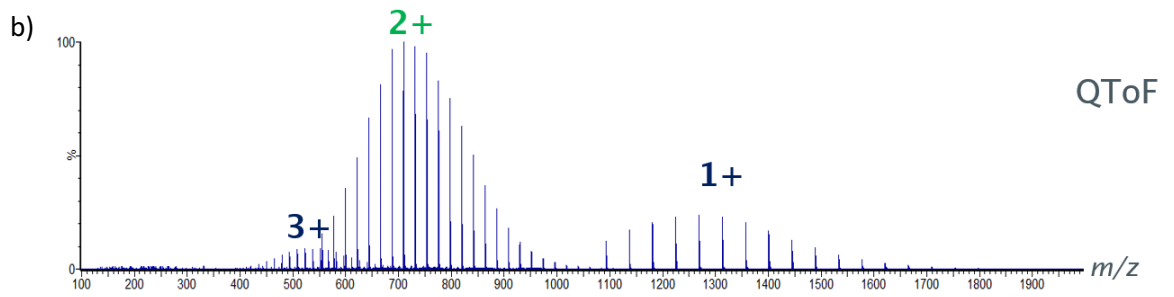

Figure 133. UHPSFC positive ion ESI MS. Differences in the mass spectra of PEG 1450 between a) Q, and b) QToF mass analysers

Apart from the observed effects, there was an analytical challenge due to two computers controlling the two different instruments. The method in the Synapt™ G2-*Si* must take longer and consider the pre-run, the run, the time the analyte spends in the PEEK tubing and the conditioning time (Table 43), resulting in an impractical variance of *ca.* 0.22 min. The obvious solution would be configuring the Waters® UPC^2 and the Waters® Synapt™ G2-*Si* as one system.

System	Pre-run time (min)	Run time (min)	Conditioning (min)	PEEK tubing (min)	Total time (min)
Waters® UPC^2	2.00	10.00	2.30	0.05	14.35 ± 0.22
Waters® Synapt™ G2-*Si*	0.00	0.00	0.00	0.00	14.35 ± 0.22

Table 43. Differences in the analysis time when using two computers to control the Waters® UPC^2 and the Waters® Synapt™ G2-*Si* systems

3.7 Final chapter thoughts

The current research provided a generic UHPSFC-MS approach that can be used for PEG characterisation. The optimised method showed minor dependence on the end group; however, the mobile phase composition significantly impacted the chromatographic separation and the peak shape of PEG with acidic end groups. The data suggested that some oligomer separation was possible independent of the stationary phase, and as such, the selection of the stationary phase should be based on the interactions with the end group and not on the chain itself. Similarly, the mobile phase composition hugely affected the positive ion ESI conditions; however, these conditions were independent of the end group due to chelation occurring between the PEG chain and the ammonium ions. One of the main drawbacks of the method is that it was not tested for PEGs with amino or basic end groups as it was out of the scope of this research project;

however, further investigation is required due to their enhanced use in modern vaccination formulations.

In terms of the evaluation of the ionisation, current data suggested that the positive ion ESI MS of PEG oligomers was influenced mainly by the chain length of the oligomer and, to a lesser extent, by the end group. The longer the chain length of the oligomer, the more charges can be accommodated in the structure because Coulombic repulsions are minimised (size-related effect). The influence of the end group on ionisation was related to an inductive effect that disturbs the lone pair of electrons of the neighbouring O atoms and alters the chelation event of the cation. Electron-donating groups (such as the aliphatic chain in mPEG or Brij® or the H in PEG) destabilise the closest O of the PEG chain (more electronegative), pushing the electron density towards the PEG chain, resulting in fewer charges being accommodated. Differences observed between mPEG and Brij® 58 oligomers could be explained by the length of the aliphatic chain, as the longer the aliphatic chain, the stronger this effect. Conversely, electron-withdrawing groups (such as acids in mPEG acid) deactivate the O of the PEG chain (less electronegative). The more delocalised electron cloud allowed for greater accommodation of charges.

The extensive range of MW PEGs used in the industry involves that singly charged protonated molecules, and singly and multiply charged ammoniated molecules could be observed in daily analyses of these molecules using positive ion ESI MS. Similarly, the extensive range of end groups used to deliver drug molecules to the different biological targets suggests that basic end groups require additional research.

Chapter 4 Impurity profiling of complex poly(ethylene) glycol-based excipients

4.1 Application to poly(ethylene) glycols with acidic end groups

An acidic PEG mixture was prepared by mixing equal amounts of mPEG acid 2000 and PEG diacid 2000 (Figure 134) at 1 mg/mL in CH_3CN. Figure 135 shows that both PEGs are fully resolved under current conditions and highlights two distinct distributions of PEG diacid 2000. Both mPEG acid and PEG diacid 2000 have isobaric molecular weight, and identification was possible because of the elution order of the polymer. mPEG acid is more non-polar due to the presence of a methoxy, rather than the carboxymethyl of PEG diacid, involving that their elution occurs at an earlier retention time. Similarly, the two distributions of PEG diacid 2000 were associated with a blend of two PEG diacid of different molecular weights; however, this assumption cannot be proved.

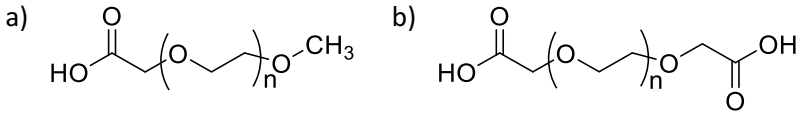

Figure 134. Chemical structures of: a) mPEG acid 2000 (n_{av} = 45), and b) PEG diacid 2000 (n_{av} = 45). Notice that both molecules have the same nominal mass

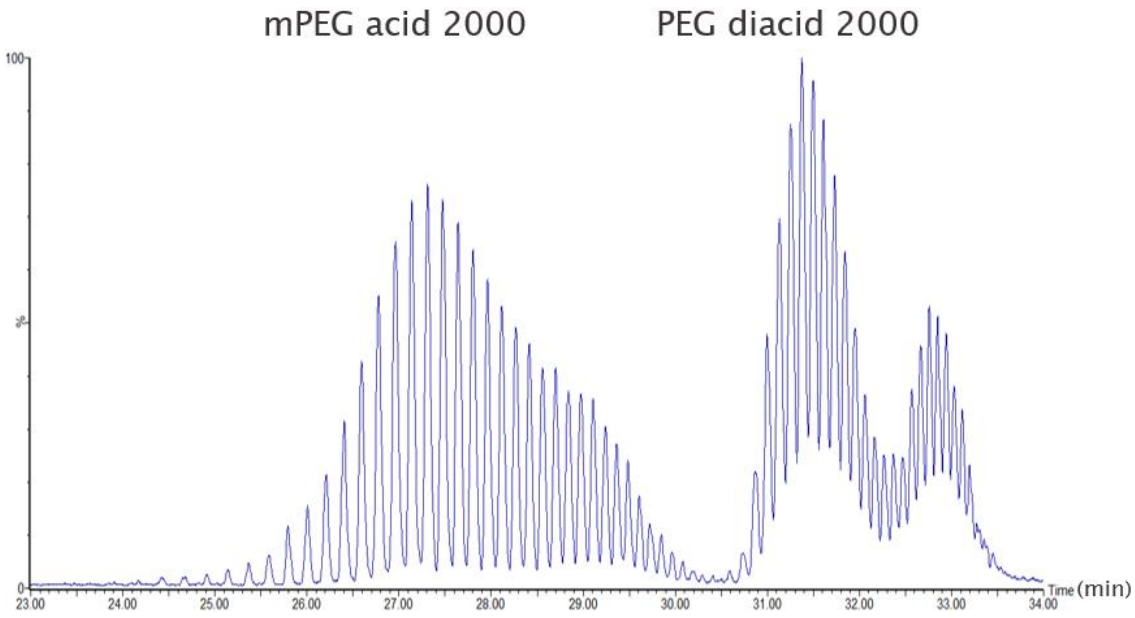

Figure 135. UHPSFC positive ion ESI Q MS. BPICC of 1000 µg/mL mPEG acid 2000 and 1000 µg/mL PEG diacid 2000 in CH_3CN + 1% HCOOH

The ion map (Figure 136 a) confirmed the two distributions of PEG diacid 2000 and highlighted the presence of a polymeric impurity. Changing the mass analyser from the Q to the QToF (Figure 136 b) facilitated the observation of the polymeric trends and the impurity. These observations were related to higher sensitivity and a movement of the charged states to lower charges. The higher sensitivity was associated with a larger hole in the sampling cone. The movement of the charge states from multiply charges to lower charges due to a charge stripping phenomenon resulting from a direction change in the ion beam from the linear beam mass analyser (Q) to the angular pulsed beam mass analyser (QToF).

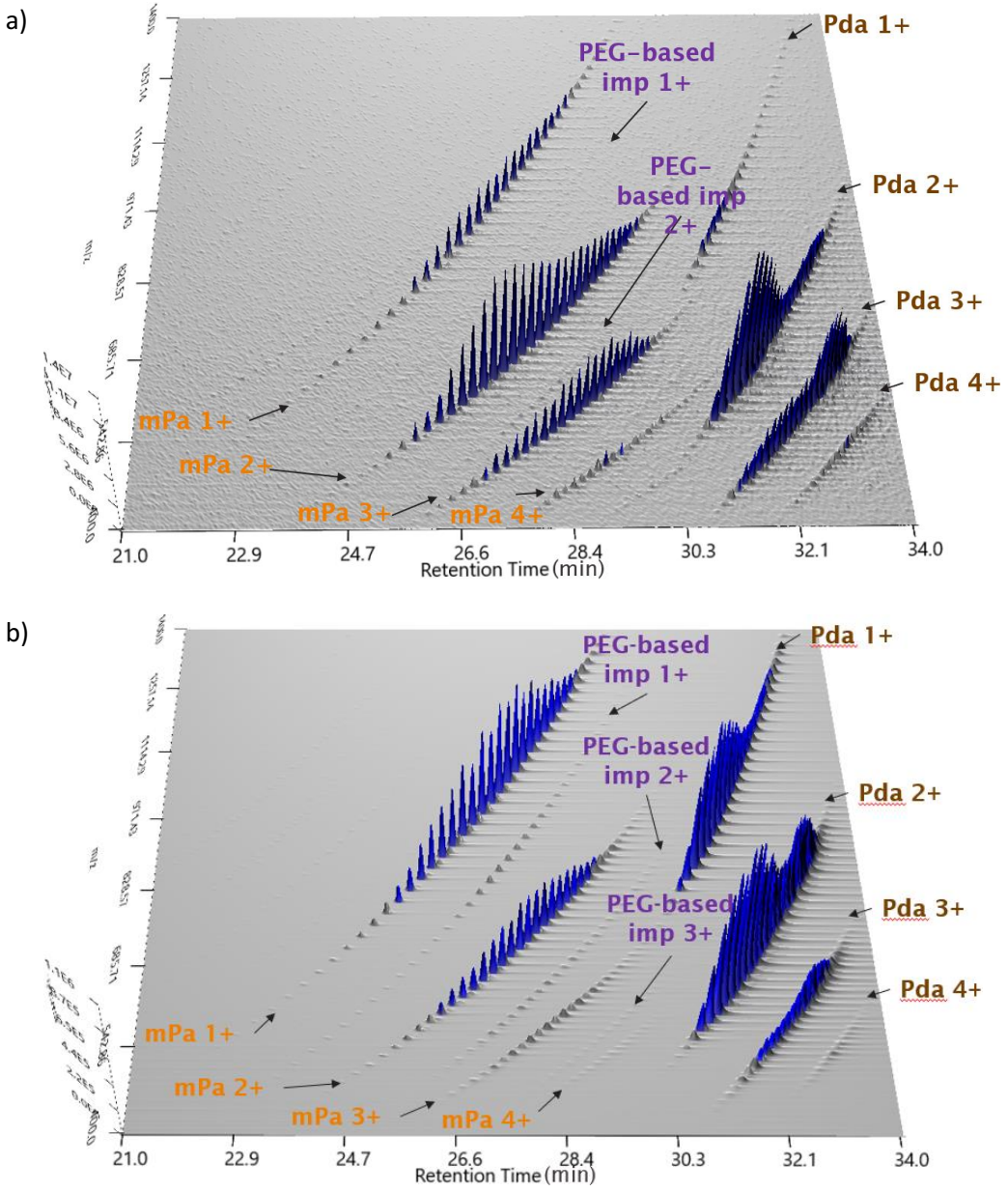

Figure 136. UHPSFC positive ion ESI Q MS. Ion map. Comparison of the effect of the mass analyser for the acidic PEGs mixture: a) 500 µg/mL in CH_3CN Q, b) 50 µg/mL QToF. mPa: mPEG acid 2000, Pda: PEG diacid 2000

Analysis of individual components of the mixture (Figure 137) highlighted the purity of mPEG acid 2000 and that the impurity was related to PEG diacid 2000. Using the RICC of low-resolution data (Q) of two contiguous ions within the polymeric trends suggested the characteristic of repeating unit of PEG (*m/z* 44/n *m/z* units).

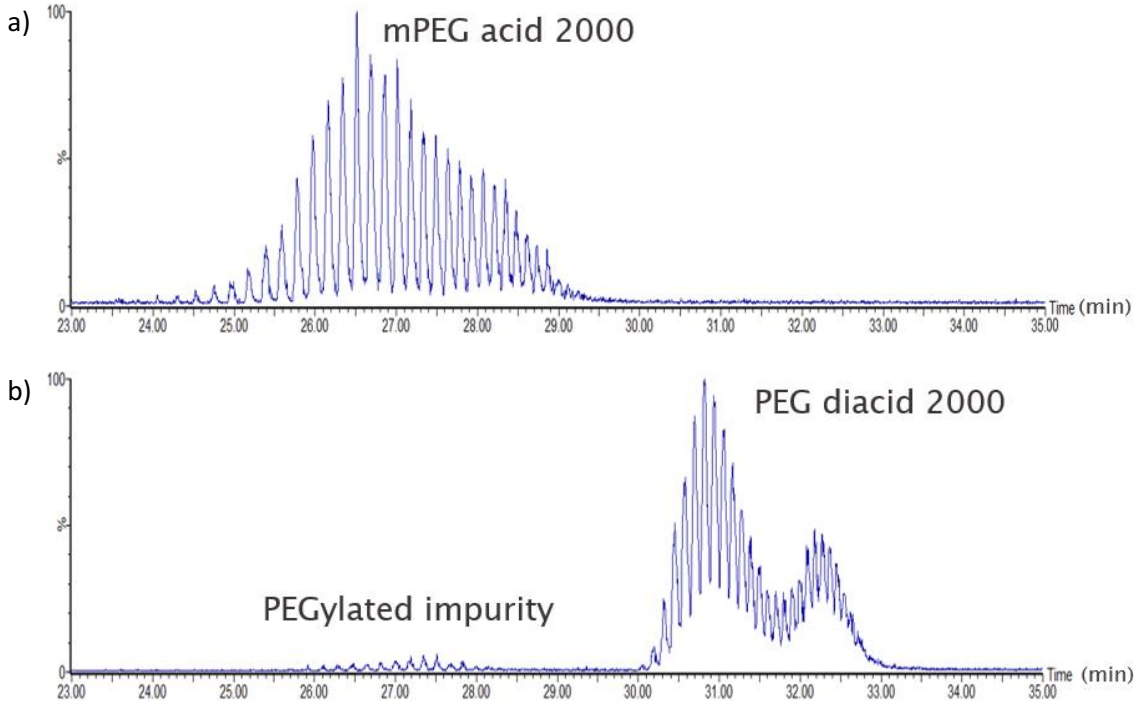

Figure 137. UHPSFC positive ion ESI Q MS. BPICC. Observation of a PEG-based impurity in PEG diacid 2000 using mPEG acid 2000 and PEG diacid 2000 at 500 µg/mL in CH_3CN

The evaluation of the PEG diacid synthetic route (see 1.3.3 page 14 for further information) allowed the proposal of mPEG and PEG monoacid (Figure 138) as possible impurities based on the low-resolution data.

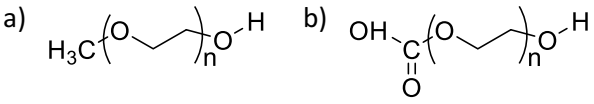

Figure 138. Proposed structures for the PEG-based impurity identified in PEG diacid 2000: a) mPEG, and b) PEG monoacid

The proposed structures of the impurity (Figure 138) are isobaric in low-resolution MS as the end group for mPEG is 32 Da, and for PEG monoacid is 76 Da, which corresponds to the repeating unit of PEG (44Da) plus 32 Da. The differentiation required the acquisition of accurate mass measurements for their distinction. An evaluation of high-resolution data suggested that both structures can be discriminated using the mass defect (Table 44), with mPEG showing a positive

mass defect (32.0261 Da) and PEG monoacid with a negative mass defect (76.0159 Da - 44.0261 Da = 31.9898 Da).

Polymer	R_1	R_2	MW (Da)	MW' (Da)
mPEG	CH_3O 31.0183	H 1.0078	32.026	32.0261 [a,b]
PEG monoacid	HO_2CH_2 59.0132	OH 17.0027	76.0159	31.9898 [a,b]
mPEG acid	HO_2CH_2 59.0132	CH_3O 31.0183	90.0315	1.1939 [b]
PEG diacid	HO_2CH_2 59.0132	HO_2CH_2O 75.0081	134.0213	1.9430 [b]

Table 44. Calculated monoisotopic masses and reduced monoisotopic masses (ethylene oxide mass: 44.0261 Da) of acidic PEGs. [a] isobaric masses that require accurate mass measurements for identification. [b] isobaric masses that require chromatography for identification

The linear fitting of the MW to the n values was used for end group identification (Figure 139) based on the oligomer *m/z* value, the charge state of the ion (n) and the observation of the formation of ammoniated molecules formation (X=NH_4^+ 18.0343 Da).

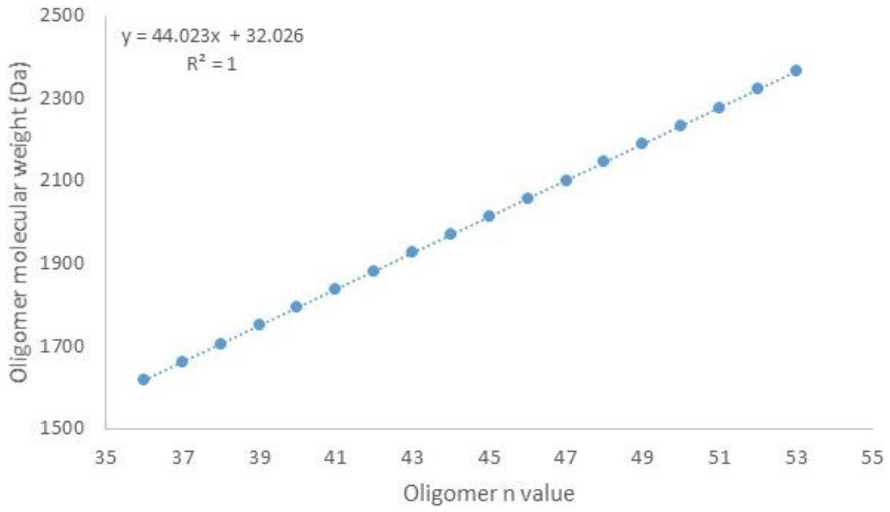

Figure 139. Determination of an impurity in PEG diacid 2000. Evaluation of the linear fitting assuming n values corresponding to mPEG using all data points available

The R^2 was equal to one independently of the PEG end groups. The slope of the predicted equation corresponded to the monoisotopic mass of the ethylene oxide repeating unit ($MW_{repeating\ unit}$) with a value of 44.0233 Da (0.06 ppm error, 2.8 mDa), and the intercept corresponded to the monoisotopic mass of the addition of both end groups of the PEG ($MW_{end\ group}$). Theoretical masses of the end group were calculated using monoisotopic masses

of the elements that composed the molecule; also, the mass of the electron was ignored as Waters® software does not account for it. The experimental mass of the end group was compared against the theoretical value and evaluated based on the closeness and the mass defect. The characteristic values (slope, intercept and R^2) remained constant independently of the number of data points, suggesting that only a few are needed, notably saving the analyst data processing time.

The evaluation of the linear fitting assuming n values corresponding to mPEG (Figure 140) suggested an end group with an experimental mass of 32.0977 Da (2.2 ppm error, 71.6 mDa).

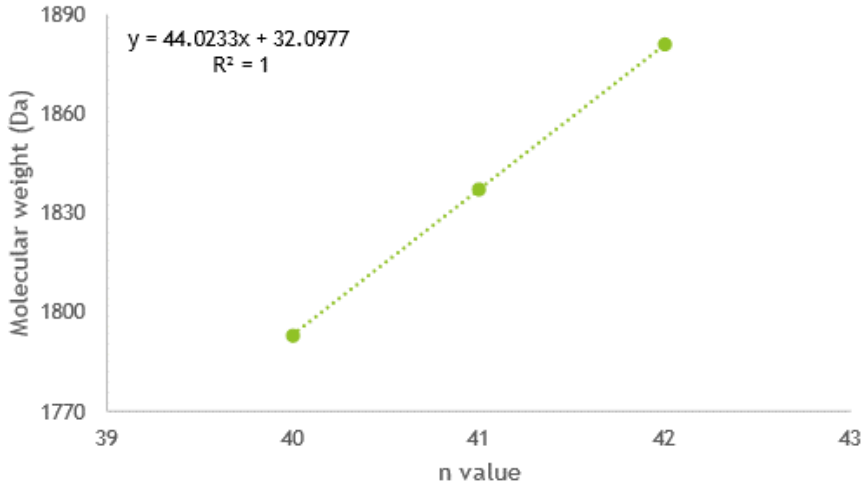

Figure 140. Determination of an impurity in PEG diacid 2000. Evaluation of the linear fitting assuming n values corresponding to mPEG using three data points

The linear fitting assuming n values corresponding to a monoacid PEG (Figure 141) suggested an experimental mass of the end group of 76.1210 Da (3.3 ppm error, 105.1 mDa).

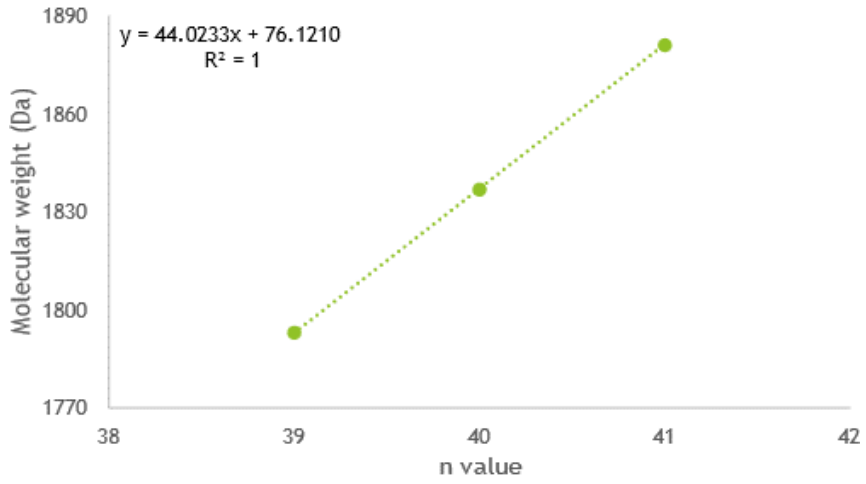

Figure 141. Determination of an impurity in PEG diacid 2000. Evaluation of the linear fitting assuming n values corresponding to PEG monoacid

The smaller error of the monoisotopic masses when assuming mPEG (Table 44, 2.2 *vs* 3.3 ppm) suggested this end group for the impurity. However, the closeness of the error in the monoisotopic masses involved in using high-resolution mass spectrometry was not enough to fully distinguish between both structural proposals (Figure 138 and Table 44). A direct infusion of PEG diacid 2000 analysed using direct infusion ESI MS in positive (Figure 142) and negative ion (Figure 143) modes was proposed to provide insights into the impurity structure.

The analysis of PEG diacid 2000 mass spectra under direct infusion (DI) positive ion ESI MS (Figure 142) did not provide impurity confirmation as both proposed structures of mPEG and PEG monoacid show ionisation in this polarity due to the presence of the PEG chain.

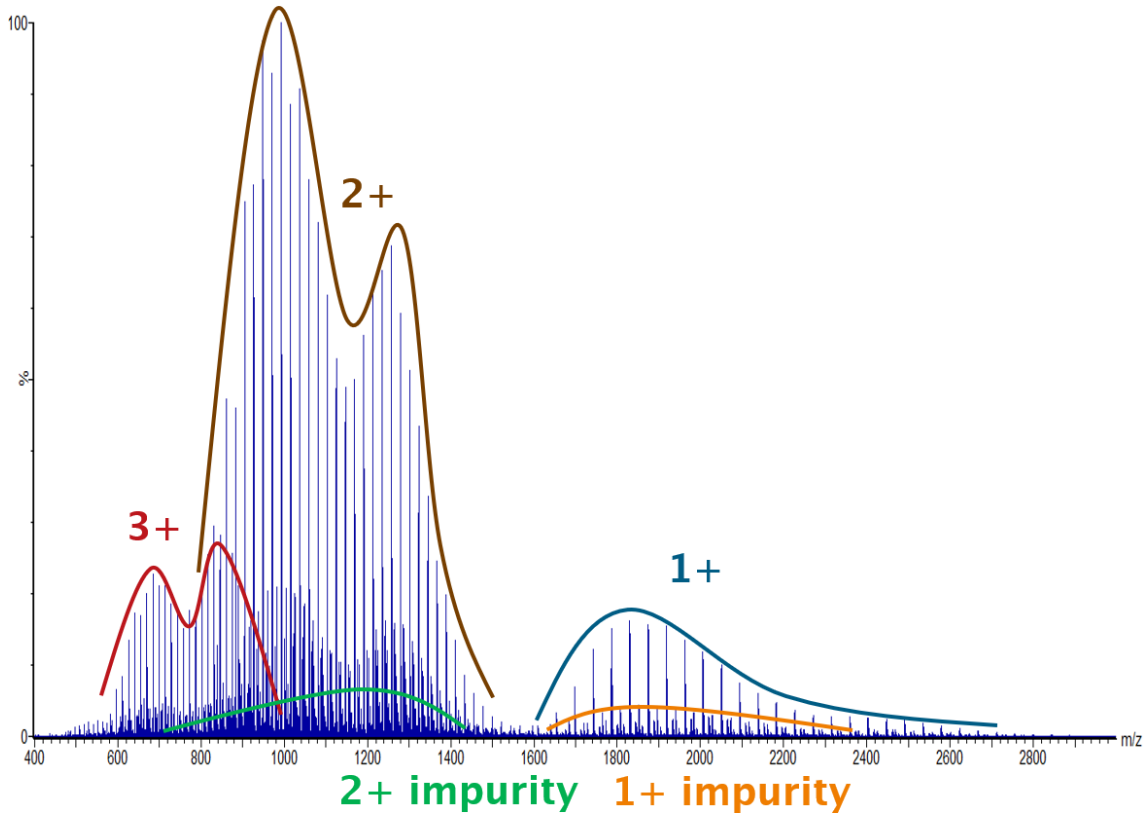

Figure 142. DI positive ion ESI MS. Mass spectra. 100 µg/mL PEG diacid 2000 in CH_3OH. Observation of the charge distributions of singly, doubly, and triply charged species of PEG diacid 2000 and the charge distributions of singly and doubly charged species of the PEG impurity

The lack of observation of the impurity under negative ion ESI MS (Figure 143) suggested the proposal of the mPEG impurity, as PEG monoacid should ionise due to the presence of the carboxylic acid in the structure, confirming the structure of the impurity as mPEG.

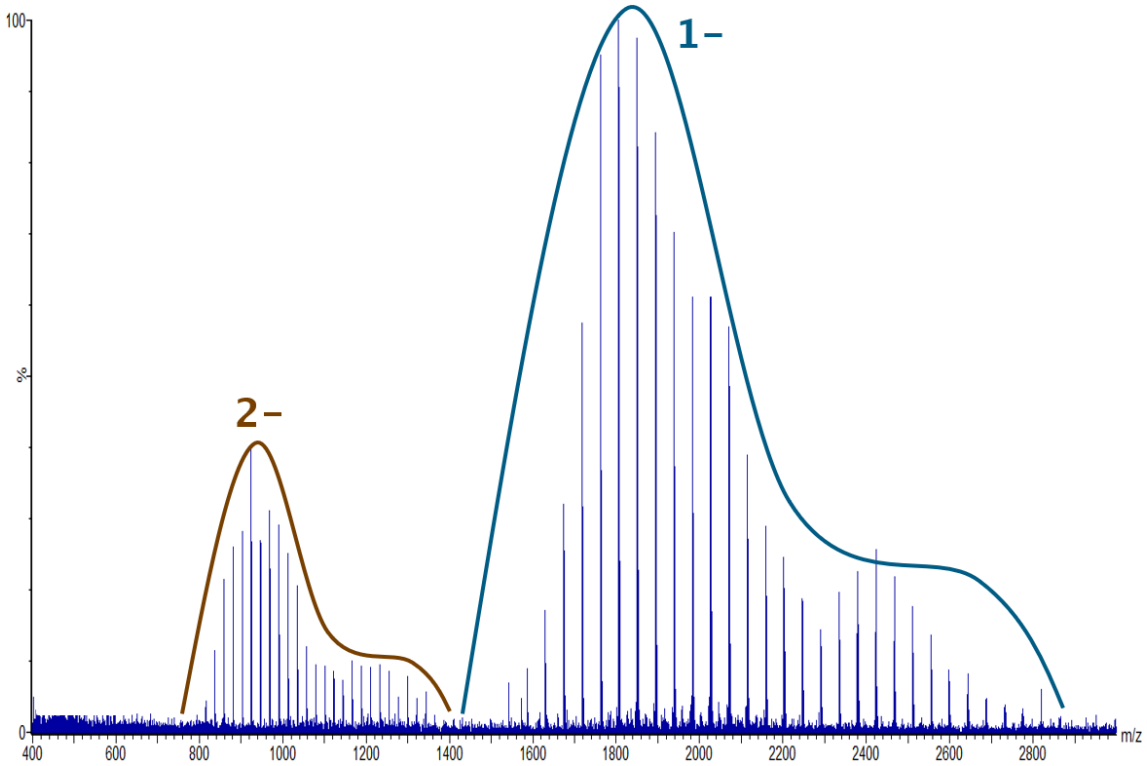

Figure 143. DI negative ion ESI MS. Mass spectra. 100 µg/mL PEG diacid 2000 in CH_3OH. Observation of the charge distribution of singly and doubly charged species of PEG diacid 2000 and the lack of ionisation of the impurity

4.2 Application to Brij®

Two Brij® excipients used in pharmaceutical formulations were tested: Brij® 58 and Brij S 100. These molecules are differentiated by the fatty alcohol chain length (16 for Brij® 58 *vs* 18 for Brij S 100) and the number of PEG repeating units (n_{av} = 20 for Brij® 58 and n_{av} = 100 for Brij® S 100). The structures are shown in Figure 144.

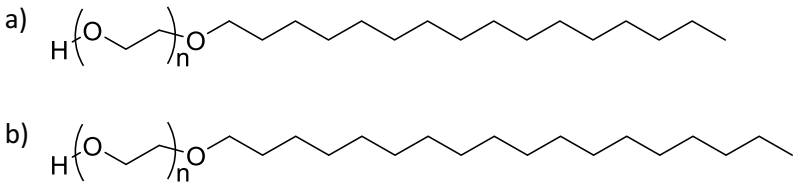

Figure 144. Chemical structures of: a) Brij® 58 (n_{av} = 20), and b) Brij® S 100 (n_{av} = 100)

Figure 145 shows the BPICC of Brij® 58 with a baseline oligomer separation and the identification of the expected oligomers. Additionally, the shape of the envelope of the chromatographic peaks of the BPICC can indicate possible chain cleavage via degradation or blend of polymers with different molecular weights.

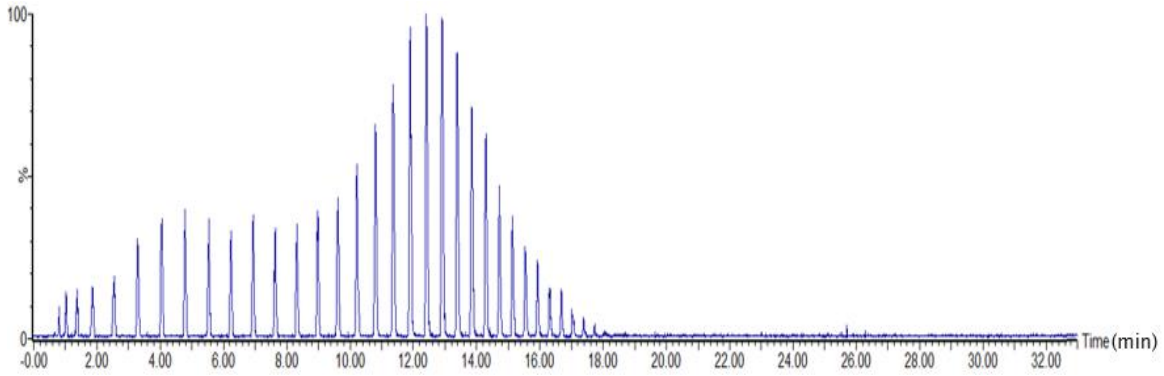

Figure 145. UHPSFC positive ion ESI Q MS. BPICC. 100 µg/mL Brij® 58 in CH_3CN. Analysis of Brij® 58 (n_{av} = 20)

Analysis of the ion map (Figure 146 a) showed two polymeric series between t_R [19.00 – 27.00] min that were associated with alcohol PEG. Changing the mass analyser to a QToF (Figure 146 b), which provides a higher response, showed that this possible impurity was not present. The alcohol PEG impurity in the ion map acquired when using the Q was associated with system contamination. Other than that, the change in the mass analyser led to no significant differences and did not provide new information.

a)

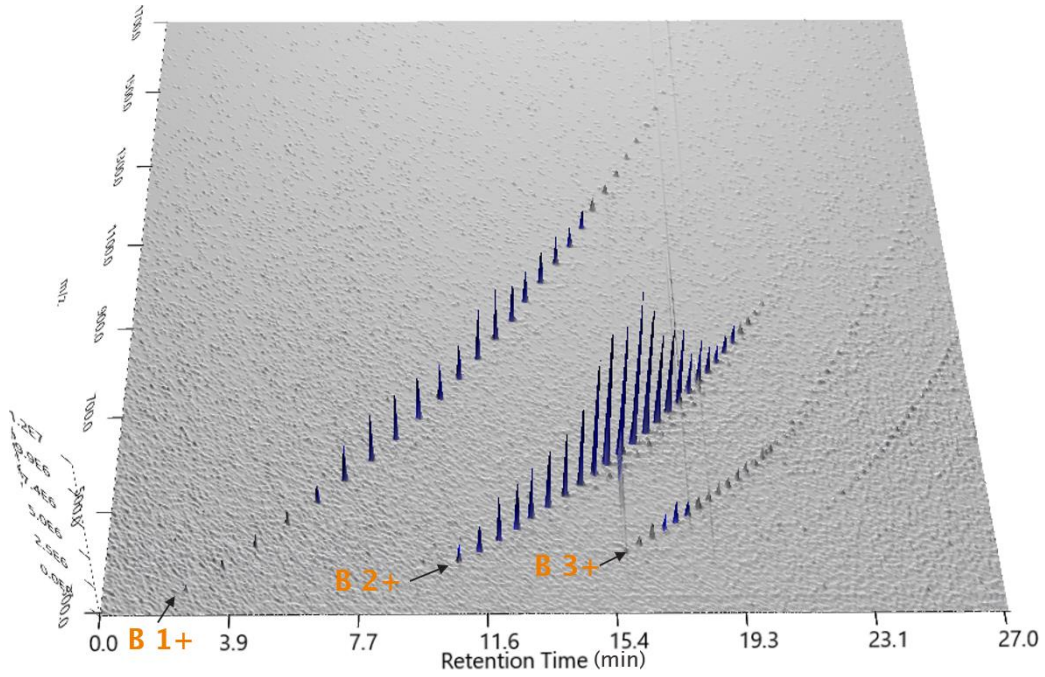

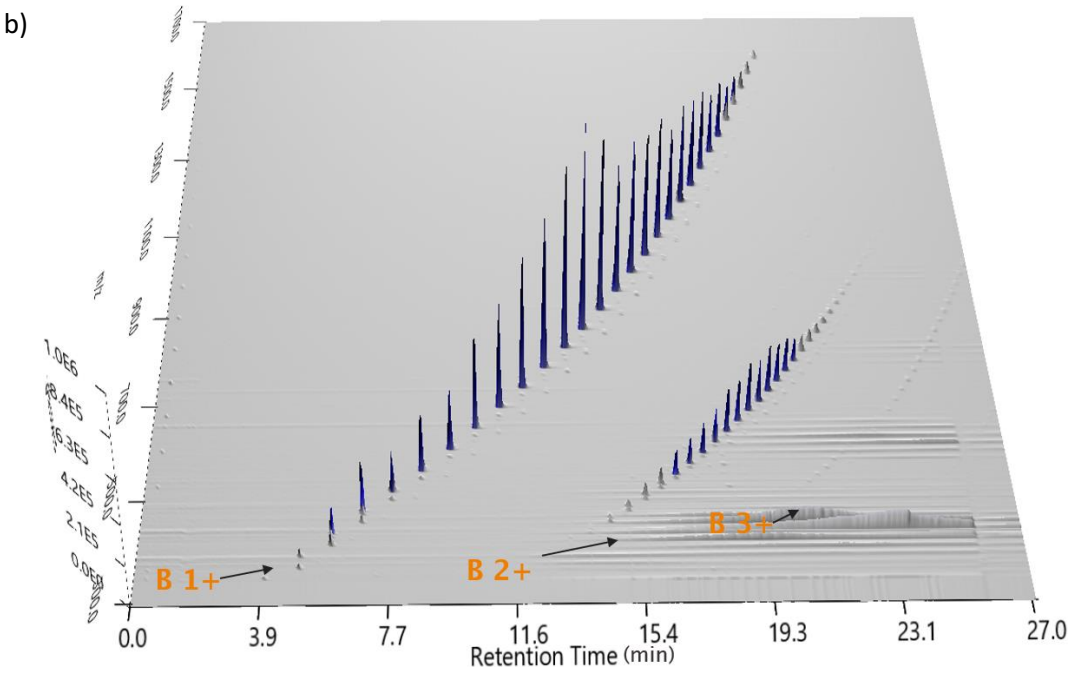

Figure 146. UHPSFC positive ion ESI MS. Ion map. Comparison of the effect of changing the mass analyser for Brij® 58: a) Q, b) QToF. B: Brij oligomers

Analysis of the BPICC of Brij® S 100 (Figure 147) showed the influence of the chain length of the PEG series in the polymer (n_{av} = 100) in the oligomer separation and how longer chains compromised the chromatographic separation. Additionally, the highly hydrophobic end group (aliphatic chain) involved some degree of oligomer separation at longer oligomer chain lengths. The higher degree of oligomer separation can be observed when comparing the retention times of oligomers of Brij® 58 and oligomers Brij® S 100 with the same chain length (Figure 145 and Figure 147); being more significant in Brij® S 100 as longer oligomer chains provide some degree of oligomer separation.

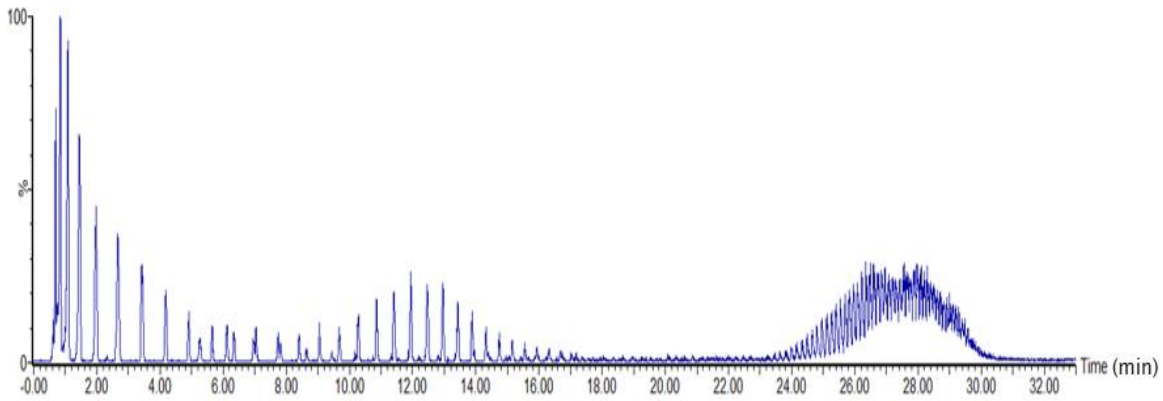

Figure 147. UHPSFC positive ion ESI Q MS. BPICC. 2500 µg/mL Brij® S 100 in CH_3CN. Analysis of Brij® S 100 (n_{av} = 100)

The analysis of the ion map of Brij® S 100 (Figure 148) revealed an alcohol PEG impurity and an unknown impurity nominated as FA PEG.

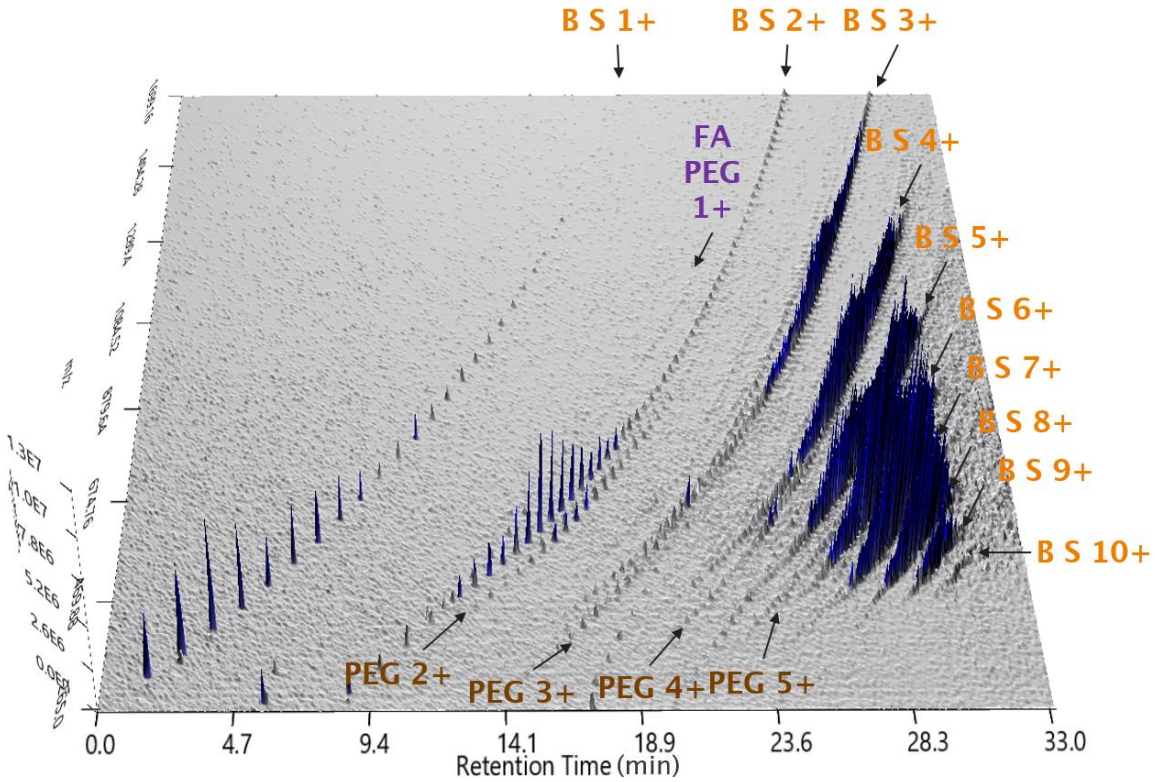

Figure 148. UHPSFC positive ion ESI Q MS. Ion map. 1000 µg/mL in CH_3CN. Comparison of the effect of the mass analyser for Brij® S 100. FA PEG refers to an unknown impurity characterised as stearate PEG. B S: Brij S oligomers

The proposal of the polymeric chain structure was possible by coupling UHPSFC to high-resolution MS (Figure 149) due to a decluttering of the region at t_R [9.00-33.00] min caused by a movement to lower charges when changing from the beam (Q) to the pulsed beam (QToF) mass analyser. Also, the use of the QToF increased the sensitivity, which facilitated the distinction of the impurity, allowing to distinguish the impurity from the background (S/N > 3) and confirm their presence. The alcohol PEG impurity was recognised by obtaining *m/z* values from the ion map and calculating the end group from the linear regression of the n values to the oligomer MW. This impurity was confirmed by superposing the Brij® S 100 ion map with a PEG 1000 standard. Identification of the FA PEG impurity was possible by collecting *m/z* values of polymeric series using RICC, converting these *m/z* values into MW values, assigning repeating unit values and plotting the values to obtain the calibration curve using the already discussed linear fitting approach. The change in the mass analyser allowed obtaining accurate mass measurements of

both impurities (Table 44) and confirmed their end group structure as alcohol PEG and stearate PEG (Figure 150).

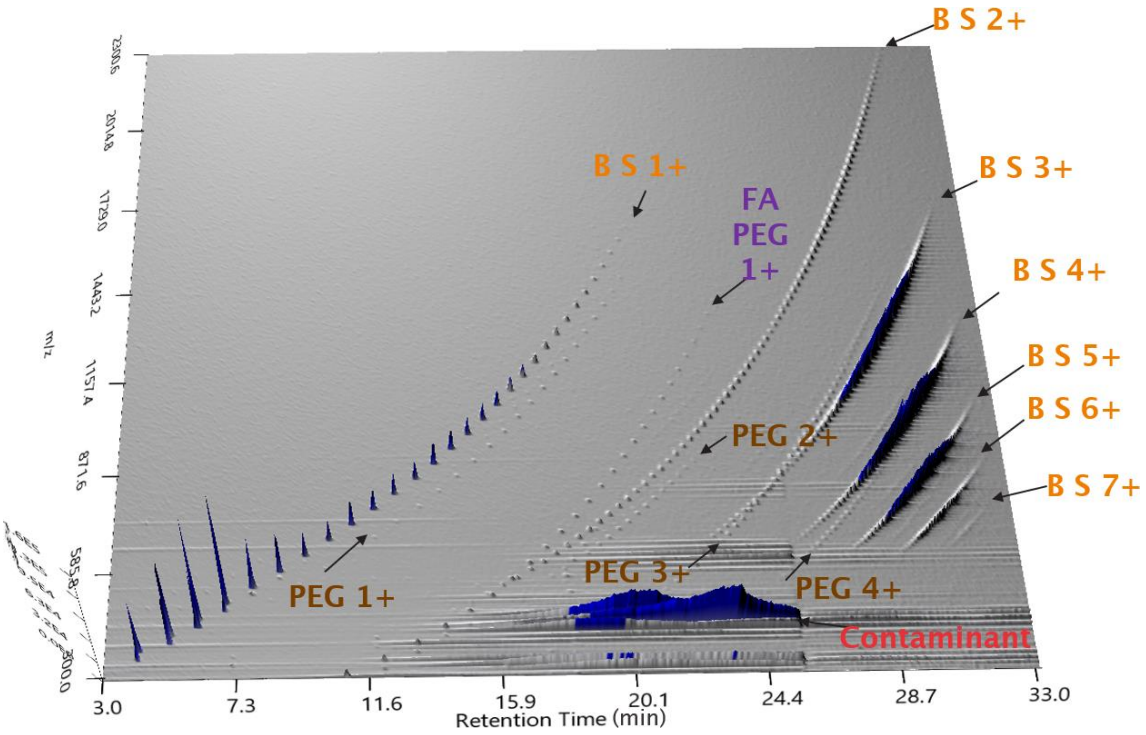

Figure 149. UHPSFC positive ion ESI QToF MS. Ion map. 200 µg/mL in CH_3CN. Comparison of the effect of the mass analyser for Brij® S 100: FA PEG referred to an unknown impurity characterised as stearate PEG. B S: Brij S oligomers

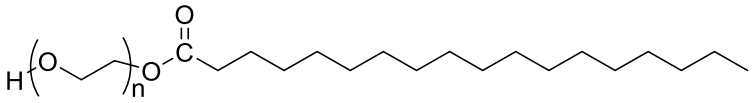

Figure 150. Proposed structure of the fatty-acid derivative impurity (stearate PEG); labelled as FA PEG in the ion map

Polymer	**R_1**	**R_2**	**MW**	**MW'**
PEG	OH 17.0027	H 1.0078	18.0105	18.0105
Brij® 58	$C_{16}H_{33}O$ 241.2523	H 1.0078	242.2601	22.1296
Brij® S 100	$C_{18}H_{37}O$ 269.2835	H 1.0078	270.2913	6.1347
Stearate PEG	$CH_3(CH_2)_{16}CO_2$ 282.2550	H 1.0078	283.2628	19.1062

Table 45. Calculated monoisotopic masses and reduced monoisotopic masses (ethylene oxide mass: 44.0261 Da) of Brij® species

4.3 Application to Gelucire®

4.3.1 Characterisation of Gelucire® 44/14

Gelucire® 44/14 is composed of PEG esters and monoacylglicerides (MAGs), diacylglycerides (DAGs) and triacylglycerides (TAGs); thus, observation of isobaric species is highly likely, requiring the use of chromatographic separation. Additionally, the synthetic reaction of these products results in a complex mixture of PEG derivatives. The BPICC revealed the sample complexity (Figure 151) with two main differentiated regions: (i) the early eluting region corresponded to the elution of MAGs, DAGs and TAGs with different fatty acid substitutions (Δ*m/z* 14/n *m/z* units), and (ii) related to a PEG series (Δ*m/z* 44/n *m/z* units) with different fatty acid substitutions (Δ*m/z* 14/n *m/z* units).

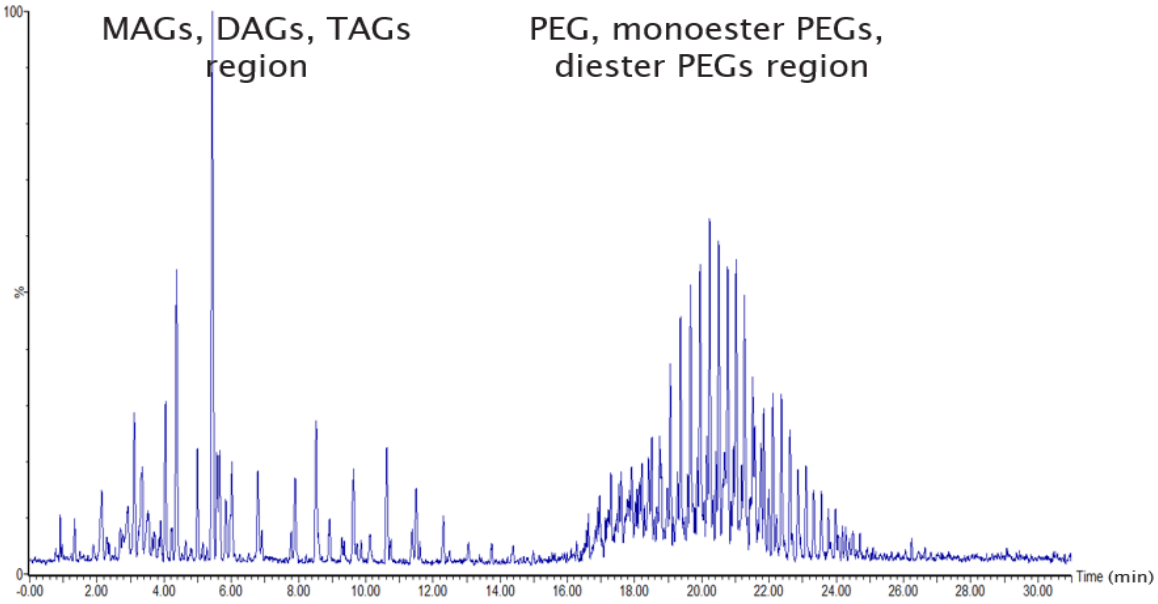

Figure 151. UHPSFC positive ion ESI Q MS. BPICC. 5000 µg/mL Gelucire® 44/14 in CH_3CN

Using the Q as the mass analyser was insufficient for characterisation due to an overcrowded ion map that challenged the interpretation (Figure 152 a) due to the overlapping of PEG 1500 with mono- and diesters PEGs. Changing the mass analyser (Figure 152 b) enabled the characterisation of the two main areas: (i) MAGs, DAGs, and TAGs eluted at the early states (ii) at higher retention times eluted several series of PEG monoesters at a lower *m/z* region, diesters at a higher *m/z* area, and some unreacted PEG 1450 co-eluting in the region. It is worth noting that free glycerol was not observed, even when using negative ion ESI MS or high-resolution MS. The presence of a poly(siloxane) contaminant was traced to the sample vial lids and was not present on the sample.

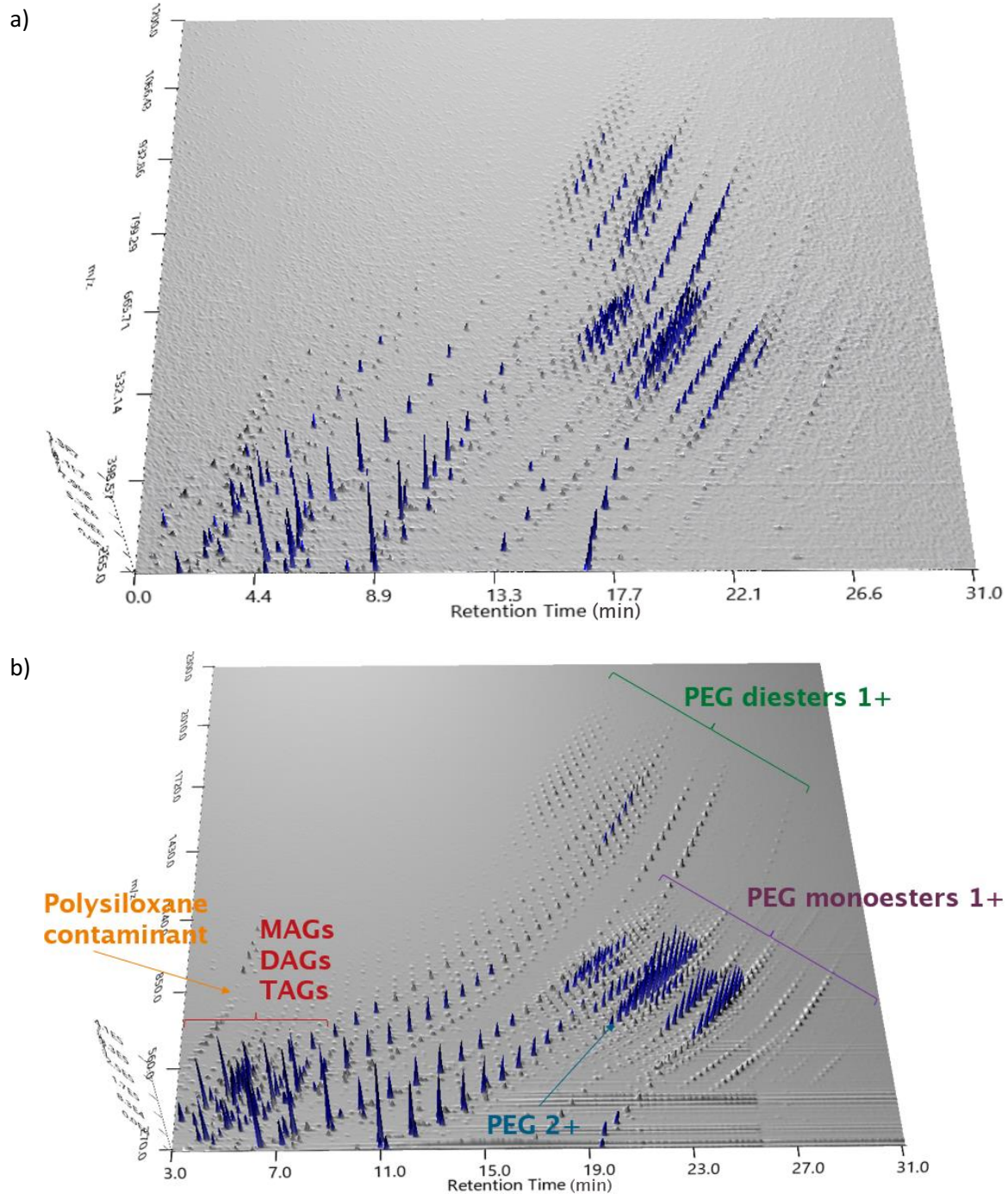

Figure 152. UHPSFC positive ion ESI MS. Ion map. Comparison of the effect of the mass analyser for Gelucire® 44/14: a) Q, 5000 µg/mL in CH_3CN, b) QToF 500 µg/mL in CH_3CN

4.3.2 Evaluation of the degradation of Gelucire® 44/14

Issues were reported when adding Gelucire® 44/14 in the manufacturing process of a drug formulation that resulted in changes in the physicochemical properties of the polymer after several cycles of heat-up/cool-down. Three samples that underwent none (sample A), one

(sample B) and two (sample C) heat-up/cool-down cycles were investigated using the developed UHPSFC positive ion ESI QToF MS approach. The study of the three samples and the overlapping of their ion map (Figure 153) showed that the differences in the samples were related to a suspected degradation via hydrolysis processes of the ester bonds. Di-ester PEGs hydrolysis led to an increase of mono-ester PEGs that further hydrolysed to free PEG. Similarly, it is proposed that TAGs hydrolysis led to the formation of DAGs, and DAGs hydrolysis led to the formation of MAGs.

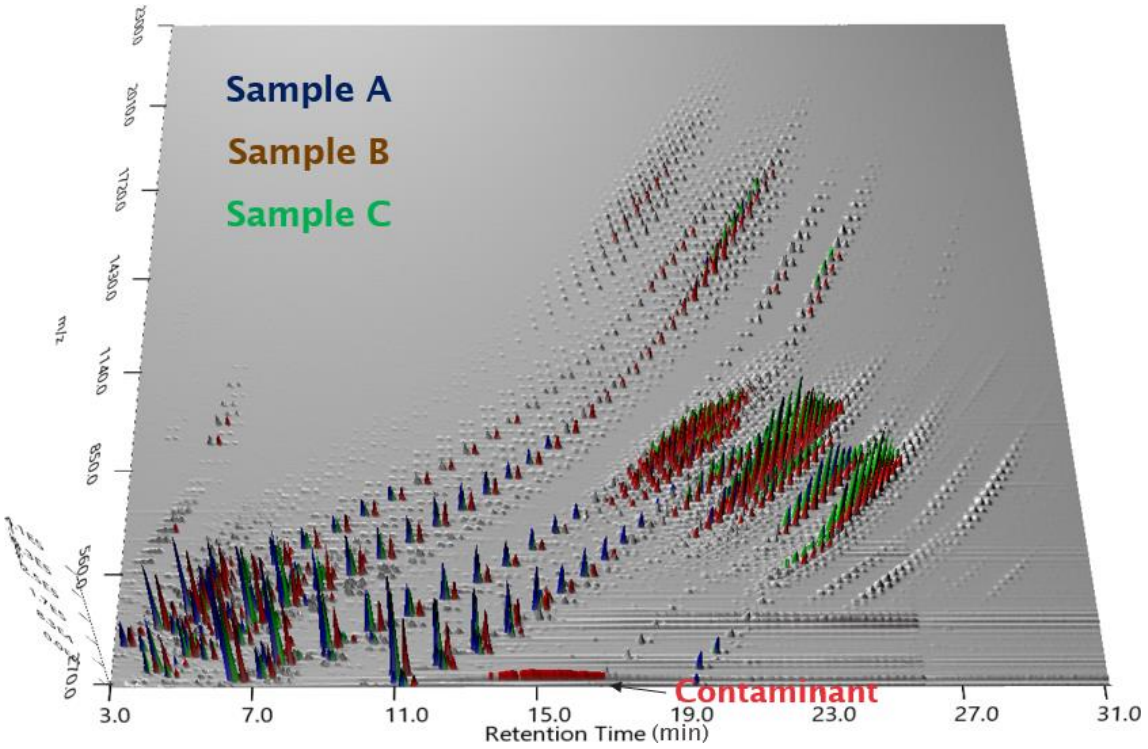

Figure 153. UHPSFC positive ion ESI QToF MS. 500 µg/mL Gelucire® 44/14 in CH_3CN. Overlapping of three samples: Sample A (blue): no treatment, sample B (red): after one cycle of heat-up / cool-down processes and sample C (green): after two cycles

The melting characteristics of Gelucire® 44/14 were confirmed by comparing the UHPSFC positive ion ESI MS ion maps (Figure 153) with differential scanning calorimetry (DSC) thermograms (Figure 154) from the literature. Jannin reported that the melting characteristics of Gelucire® 44/14 (Figure 154, blue line) were associated with the melting characteristics of the individual components as the acylglyceride fraction melted first (Figure 154, orange line), followed by the PEG-ester fraction (Figure 154, green line) [65, 376]. Hence, the differences in the composition between the untreated sample A and the treated samples B and C were related to thermal degradation occurring due to the melting characteristics of Gelucire® 44/14.

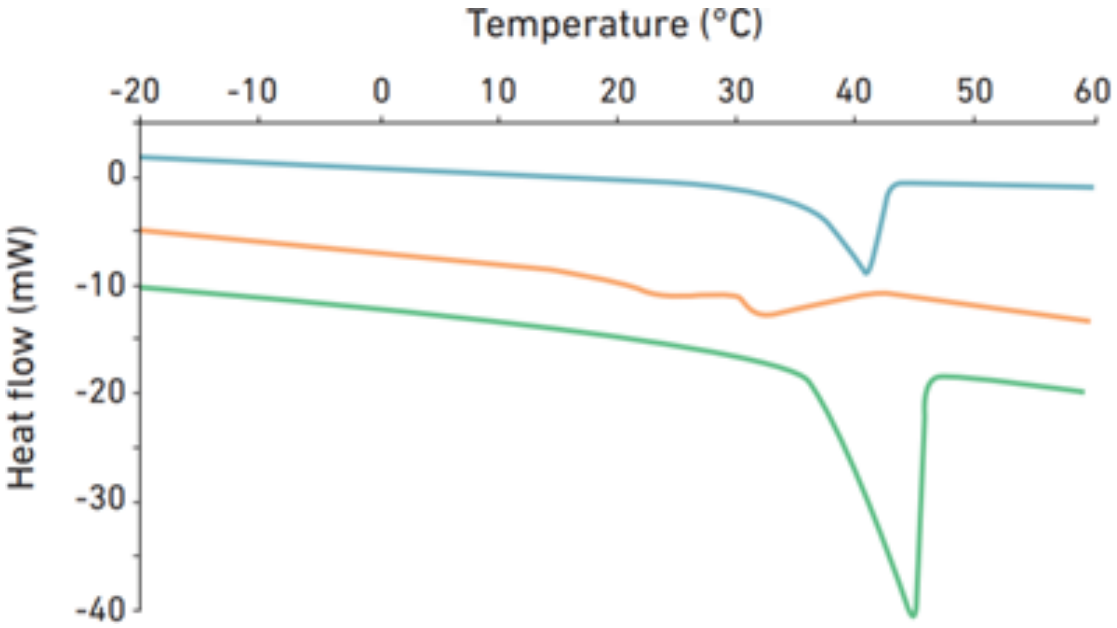

Figure 154. Differential scanning calorimetry (DSC) thermogram of Gelucire ® 44/14. Blue (top): Gelucire® 44/14 curve thermogram, Orange (middle): Glyceride fraction thermogram, Green (bottom): PEG-ester fraction thermogram. Reproduced with permission from Gatteffosé [65]. Original work from Jannin [376]

Both UHPSFC positive ion ESI QToF MS data and the DSC thermogram provided orthogonal information about the sample, allowing the understanding of the thermal degradation of the polymer. The extra benefit of overlapping UHPSFC positive ion ESI MS ion maps enables the follow-up of the process, highlighting the rich information provided by the developed method.

4.4 Application to polysorbates

4.4.1 Analysis of Tween®20

Polysorbate is a complex mixture composed of (polyoxyethylene) sorbitan, (polyoxyethylene) isosorbitan and PEG, where the end alcohols of the PEG chains can be substituted with fatty acids. The study of the BPICC (Figure 155) showed the complexity of the polymeric mixture, and characterisation using this tool was complicated as the co-elution of the different polymers meant that the mass spectra overlapped, challenging the assignment of the *m/z* value with the chromatographic peak in the polymer series.

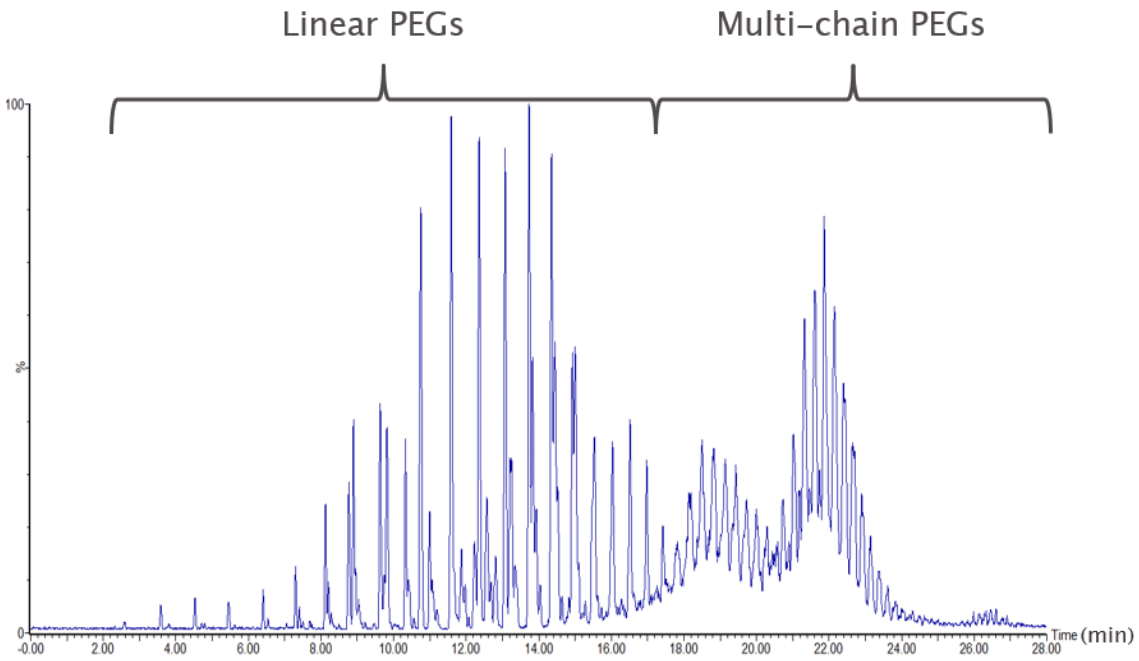

Figure 155. UHPSFC positive ion ESI Q MS. BPICC. 2500 µg/mL Tween® 20 in CH_3CN. Analysis of the elution of species present in polysorbates

The only explicit information that the BPICC provided was a complex peak shape (Figure 156) for the later eluting at t_R [18.00-24.00] min that was associated with (polyoxyethylene) sorbitan (POE S)-based polymers with a structure-style of Figure 157 (either substituted with a fatty acid or not).

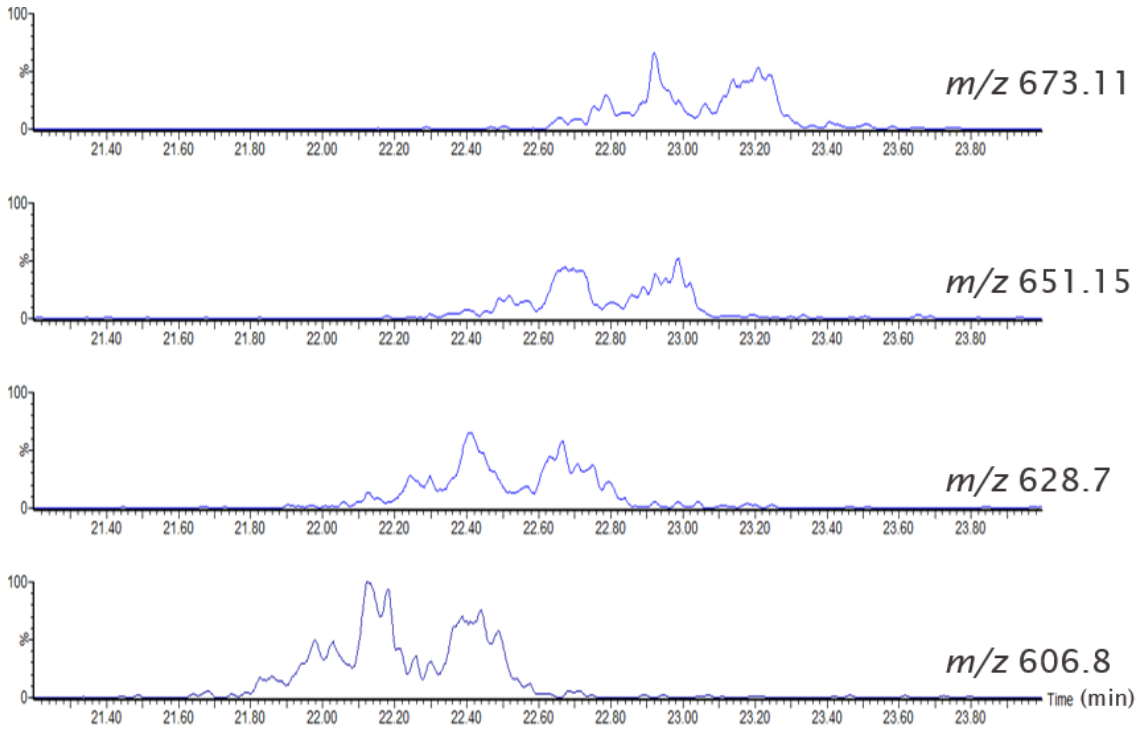

Figure 156. UHPSFC positive ion ESI Q MS. RICC. 2500 µg/mL Tween® 20 in CH_3CN. Unusual chromatographic peak shapes of POE S of different chain lengths

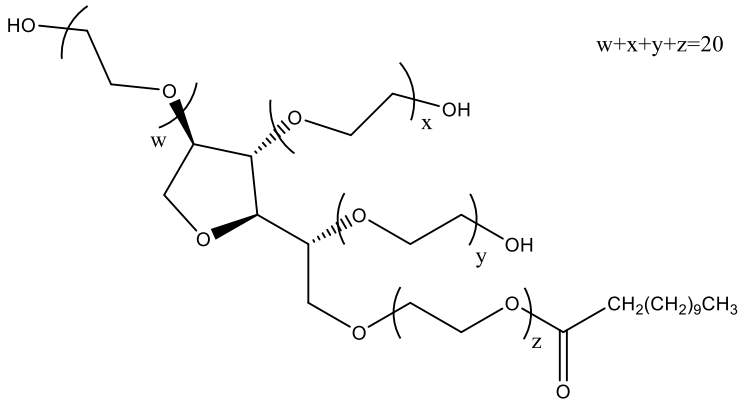

Figure 157. Chemical structure of POE S ML

The complex peak shape (Figure 156) was associated with by-products generated during the cyclisation of sorbitol (Figure 158). Evaluation of the subproduct calculated logP (clogP) using ChemDraw® Professional 21.0.0 allowed the suggestion of an elution order according to polarity (Table 46): 2,5-, 1,5-, 3,6- and 1,4-sorbitans. Other features that affect the peak shape are the possible commutations of the *w, x, y, z* values that produce the same n value or the different positions for fatty acids substitutions (see Figure 157).

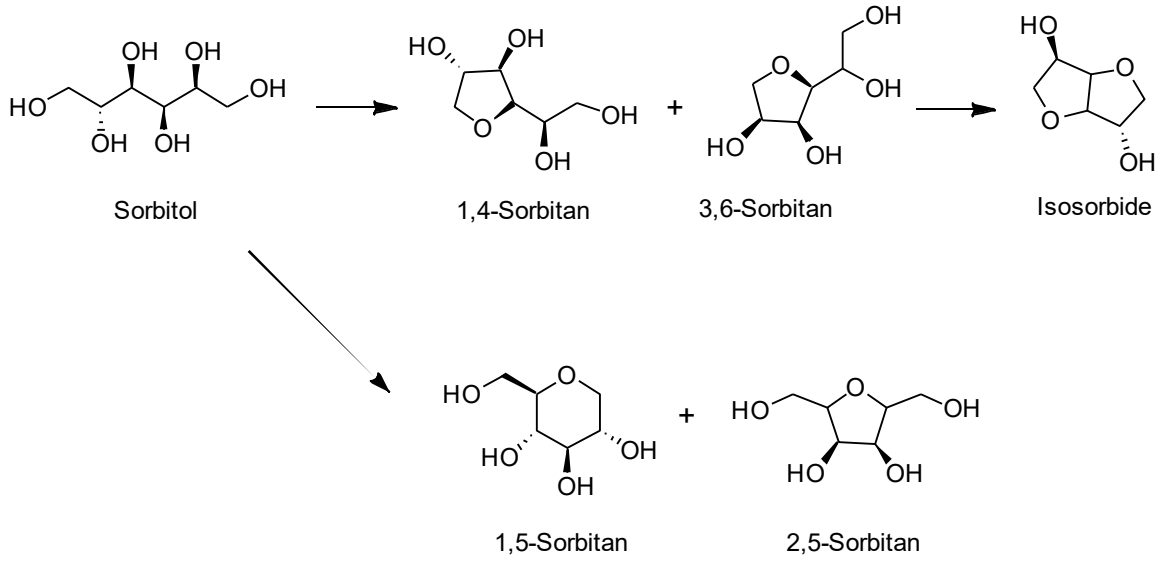

Figure 158. Dehydration of sorbitol showing the different synthetic sub-products

Molecule	2,5-Sorbitan	1,5-Sorbitan	1,4-Sorbitan	3,6-Sorbitan
clogP*	-1.30	-1.42	-2.09	-2.09
Elution order	1st	2nd	3rd	3rd

Table 46. Calculated logP (clogP) for the possible synthetic subproducts of the cyclisation of sorbitol. * clogP calculated using ChemDraw® Professional 21.0.0

Additionally, the Gaussian peak shape of (polyoxyethylene) isosorbitan (POE IS) polymers suggested the different substitution positions of the fatty acid and the interchanges in the *w, x, y* and *z* values were not significant contributors to the peak shape of POE S-based polymers. These observations confirmed that synthetic sub-products were the main factor in the observed complex peak shape and suggested that further investigation using IMMS was not required.

The analysis of the ion map of Tween® 20 allowed the identification of the different polymeric blends (Figure 159). The MW of the different polymeric series reported in the literature were used to calculate the accurate masses of the oligomers and the obtained *m/z* value were used to obtain the corresponding RICC and the chromatographic retention time in the ion map. This approach allowed to differentiate between polymeric series when using low-resolution MS, and was later confirmed using high-resolution data and the linear fitting approach already discussed.

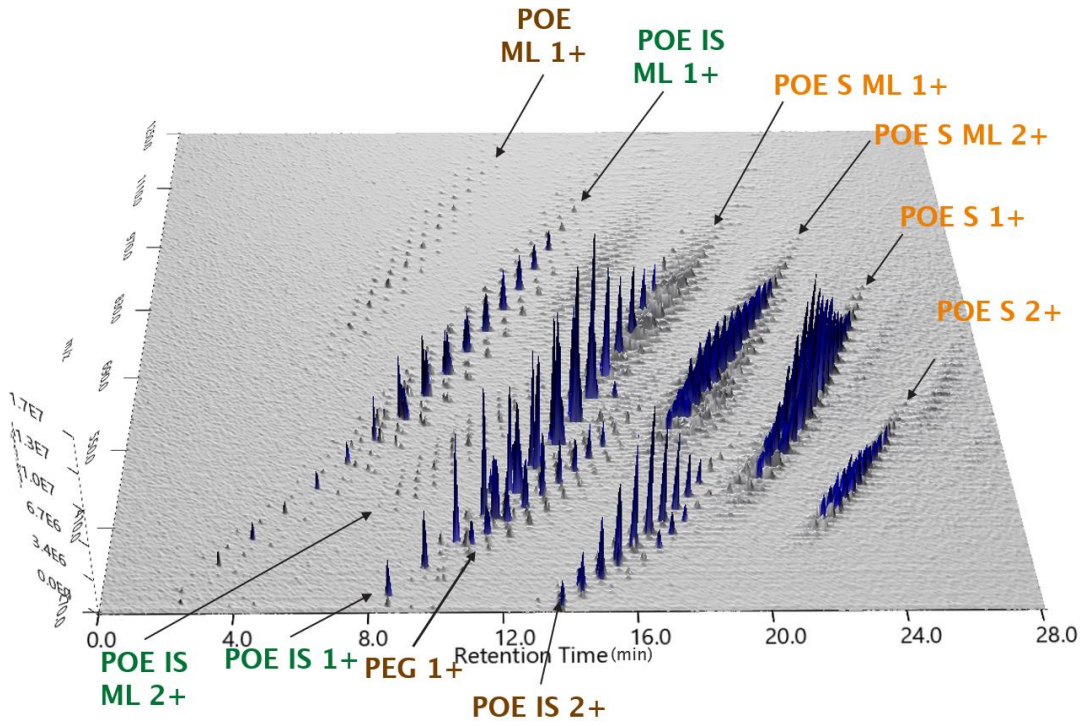

Figure 159. UHPSFC positive ion ESI Q MS. Ion map. 2500 µg/mL Tween® 20 in CH_3CN. Analysis of the components

When changing the mass analyser (Figure 160), the higher sensitivity and the shifting of the charged states towards lower charged states facilitated the visualisation and allowed the confirmation of the assigned structures to the species. Also, the identification of substituents of less abundant fatty acids (C12:0, C14:0, C16:0 and C18:0) was possible due to the higher sensitivity of the mass analyser. Overall, the early eluting polymers at t_R [4.00-18.00] min

corresponded to linear PEG and isosorbide-based polymers, whilst the most substituted sorbitan-based polymers elute later at t_R [18.00-24.00] min.

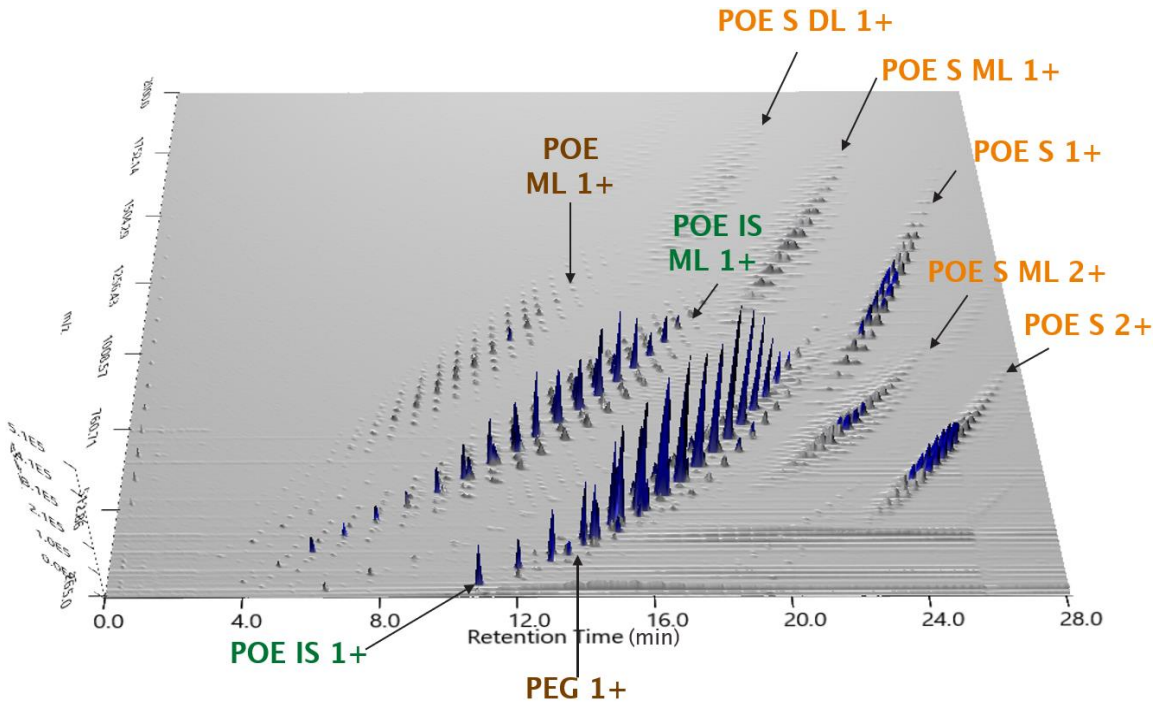

Figure 160. UHPSFC positive ion ESI QToF MS. Ion map. 500 µg/mL Tween® 20 in CH_3CN. Analysis of the components

The structural assignation of the different polymeric series was possible by acquiring accurate mass measurements and using linear fitting regression of the oligomer MW to the repeating unit (Table 47). The assigned polymeric trends using the Q (Figure 159) were confirmed using this approach.

Polymer	**MW**	**MW' [a]**
PEG	18.0105	18.0105
PEG monolaurate (POE ML)	217.1797	41.0753
POE dilaurate (POE DL)	416.3489	20.1140

Polymer	MW	MW' [a]
POE sorbitan (POE S)	164.0681	31.9898
POE sorbitan monolaurate (POE S ML)	346.2346	38.0519
POE sorbitan dilaurate (POE S DL)	528.4011	44.1140
POE sorbitan trilaurate (POE S TL)	710.5676	6.1500
POE sorbitan tetralaurate (POE S QL)	892.7341	12.2121

Polymer	MW	MW' [a]
POE isosorbide (POE IS)	146.0576	13.9793
POE isosorbide monolaurate (POE IS ML)	328.2241	20.0414
POE isosorbide dilaurate (POE IS DL)	510.3906	26.1035

Table 47. Calculated monoisotopic masses and reduced monoisotopic masses (ethylene oxide mass: 44.0261 Da) of Tween® 20 species. [a] MW': Reduced MW calculated by subtracting the mass of the ethylene oxide repeating unit to the molecule end group MW

As a characterisation of the polymeric series was possible, further characterisation was performed by calculating the free fatty acid content of the polysorbate as these values can correlate with degradation via hydrolysis or oxidation. The standardised method for fatty acid analysis involves a sample preparation step of complete hydrolysis of the polysorbate and analysis of the total content via HPLC-CAD [377]. When switching the ionisation source polarity of the developed method (SFC negative ion ESI Q MS, Figure 161), the free fatty acids present in the sample were revealed. This approach eliminated the sample preparation step, thus accelerating the analysis. A specific example is provided in section 4.6.2, page 173.

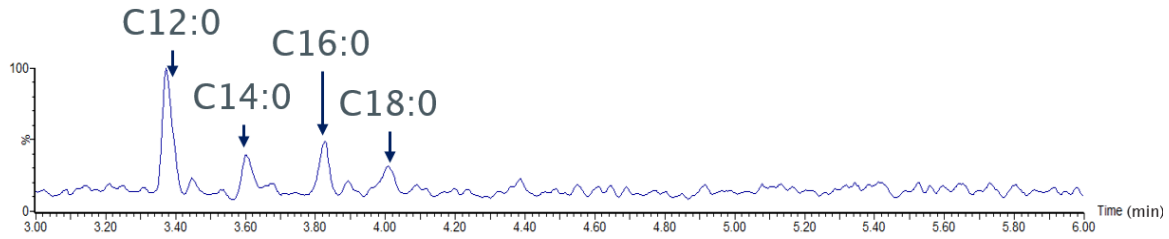

Figure 161. UHPSFC negative ion ESI Q MS. BPICC 2500 µg/mL Tween® 20 in CH_3CN. Determination of free fatty acids in the polysorbate

4.4.2 Supplier and batch comparison of Tween® 20 products

As the free fatty acid content indicates degradation, their quantitation correlates to product quality and can be used to compare suppliers and batches. A quantitation protocol was developed based on a selective ion monitoring (SIM) experiment of the deprotonated laurate ion ($[M - H]^-$ with *m/z* 199, Figure 162 a). The increased S/N (*ca.* 200) achieved using SIM (Figure 162 b) improved the limit of detection and allowed quantitation (Figure 162 c, $R^2 > 0.999$).

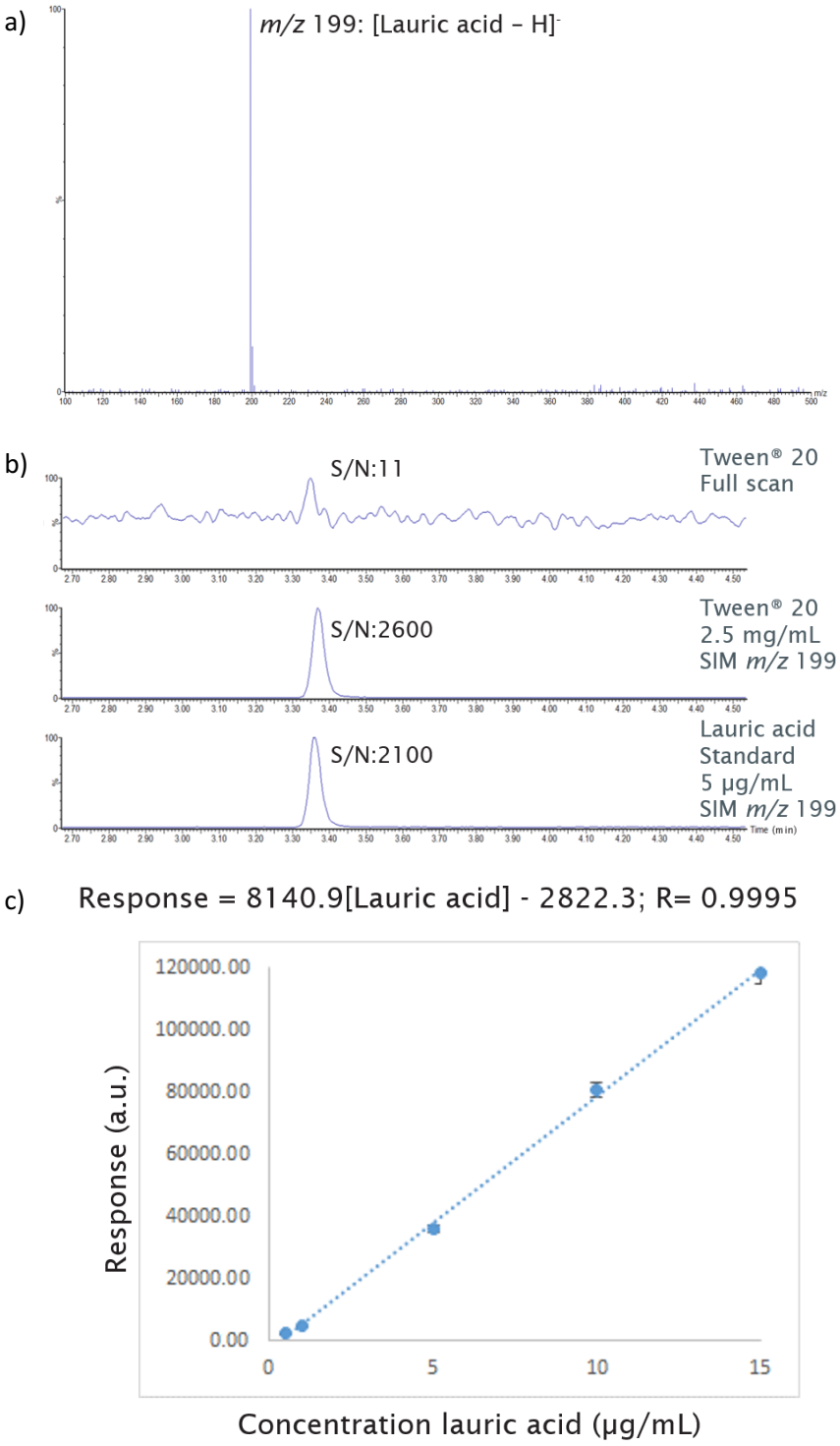

Figure 162. UHPSFC negative ion ESI Q MS. 2500 µg/mL Tween® 20 in CH_3CN. Development of a SIM acquisition approach for quantitation of free lauric acid in Tween® 20 for batch and supplier comparison: a) negative ion ESI mass spectrum, b) comparison of chromatographic peak shape and improvements on S/N when collecting using SIM, and c) linear fitting of the calibration (samples analysed in triplicates, the error bars correspond to 1 stdev)

The most abundant free fatty acid in Tween® 20 (lauric acid) was monitored (Table 48) using UHPSFC negative ion ESI MS in different suppliers/batches. The differences in the amount of lauric acid between both suppliers were apparent, being in the range of 6 µg/mg for supplier A and 0.2 µg/mg for supplier B. The qualities of supplier A were in the same range, with minimal differences apart from one outlier in one of the batches of the higher-quality product. Similarly, the amount of lauric acid did not increase for batches opened at different times.

Supplier	**Product quality**	**Batch**	**Opened**	**Lauric acid (µg/mg)**
A	Low	1	July 2020	6.46 ± 0.46
		2	July 2020	7.25 ± 0.35
		1	May 2020	6.17 ± 0.25
		1	December 2020	5.90 ± 0.22
		2	December 2020	6.04 ± 0.20
A	High	1	December 2020	6.34 ± 0.02
		2	December 2020	4.43 ± 0.12
B	High	2	December 2020	0.20 ± 0.02

Table 48. Quantitation of free lauric acid of different quality products of different batches and suppliers of Tween® 20 (as received in the lab). Three replicates analysed

The products of different suppliers and product quality were compared using the BPICC and the ion map. When comparing the two suppliers A and B (Figure 163), the BPICC (Figure 163 a) showed a clear difference between their composition that was further investigated using the ion map (Figure 163 b) and the obtained amount of lauric acid (Table 48). Supplier A was of lower quality with a more significant amount of free lauric acid (7.25 ± 0.35 µg/mg) and more hydrolysed products detected, either POE S, POE IS or free PEG. Supplier B was considered of higher quality and contained a lower amount of free lauric acid (0.20 ± 0.02 µg/mg) and a

considerable higher amount of either POE S ML, POE S DL, POE IS ML, and POE IS DL. Noteworthy that the differences between suppliers cannot be associated with either degradation or synthesis, and only information about the quality of the product at the moment of the analysis can be postulated.

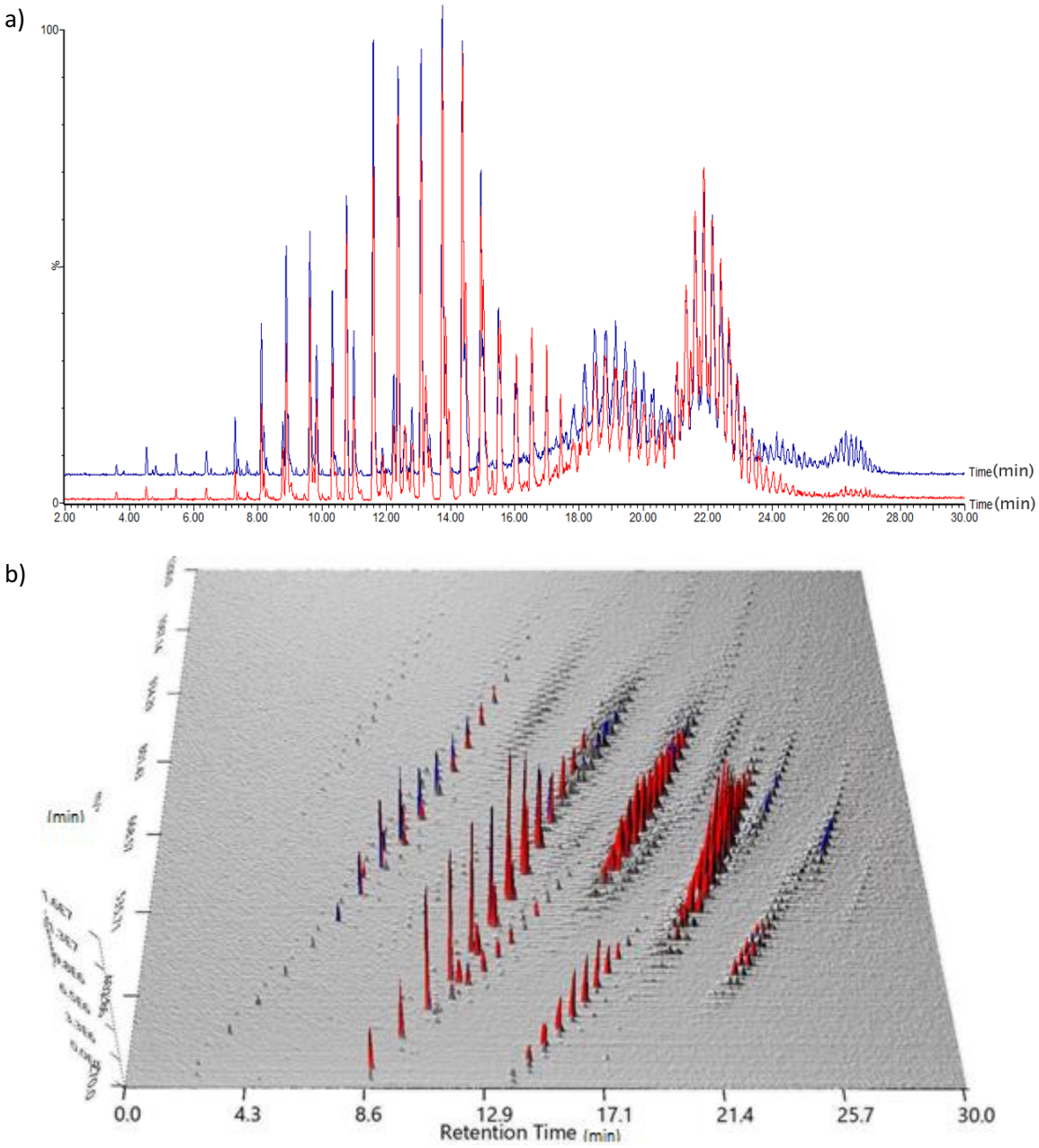

Figure 163. UHPSFC positive ESI Q MS. a) BPICC, b) Ion map. 2500 µg/mL Tween® 20 in CH_3CN. Differences between two suppliers of Tween® 20 (in red supplier A, in blue supplier B)

A comparison of products of the same supplier (supplier A) (Figure 164) noted minor differences between products of different qualities, suggesting a high degree of similarity. The main difference was the presence of slightly longer PEG chains in the high-quality product (red peaks).

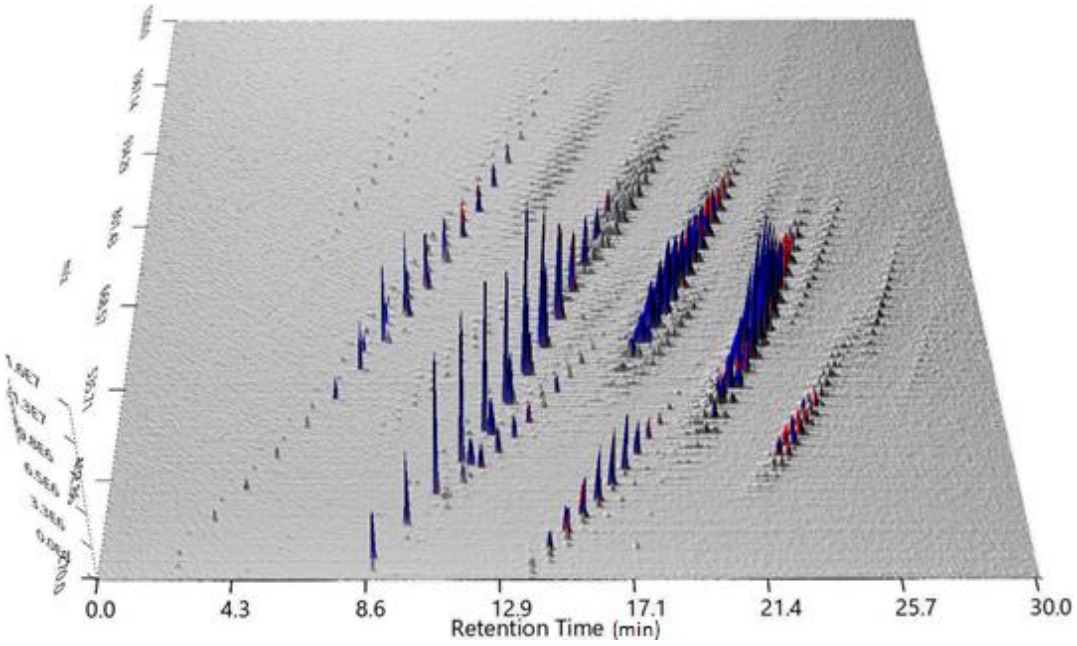

Figure 164. UHPSFC positive ion ESI Q MS. Ion map. 2500 µg/mL Tween® 20 in CH_3CN. Differences in the quality of Tween® 20 products from the same supplier (in red the higher quality, in blue the lower quality)

4.4.3 Analysis of Tween® 80 and the differences from other polysorbates

Tween® 80 analysis should be treated differently from other polysorbates due to an increased complexity that results from the number of isobaric species and the higher substitution of fatty acids in POE sorbitans, with mixtures of mono-, di-, tri- and tetra- substituted. An appropriate chromatographic separation and high-resolution mass spectrometry are required to decongest the mass spectra and aim for characterisation.

When comparing the BPICC of Tween®80 to Tween® 20 (Figure 165 a), the extra level of complexity of Tween®80 can be noticed; however, the subtle differences in the retention time and the complexity of the peak pattern are not that obvious for an untrained eye. Similarly, using the BPICC, differences in Tween®80 composition based on different suppliers can be noticed (Figure 165 b); however, using the BPICC is not enough for characterisation, showing the need for the ion map.

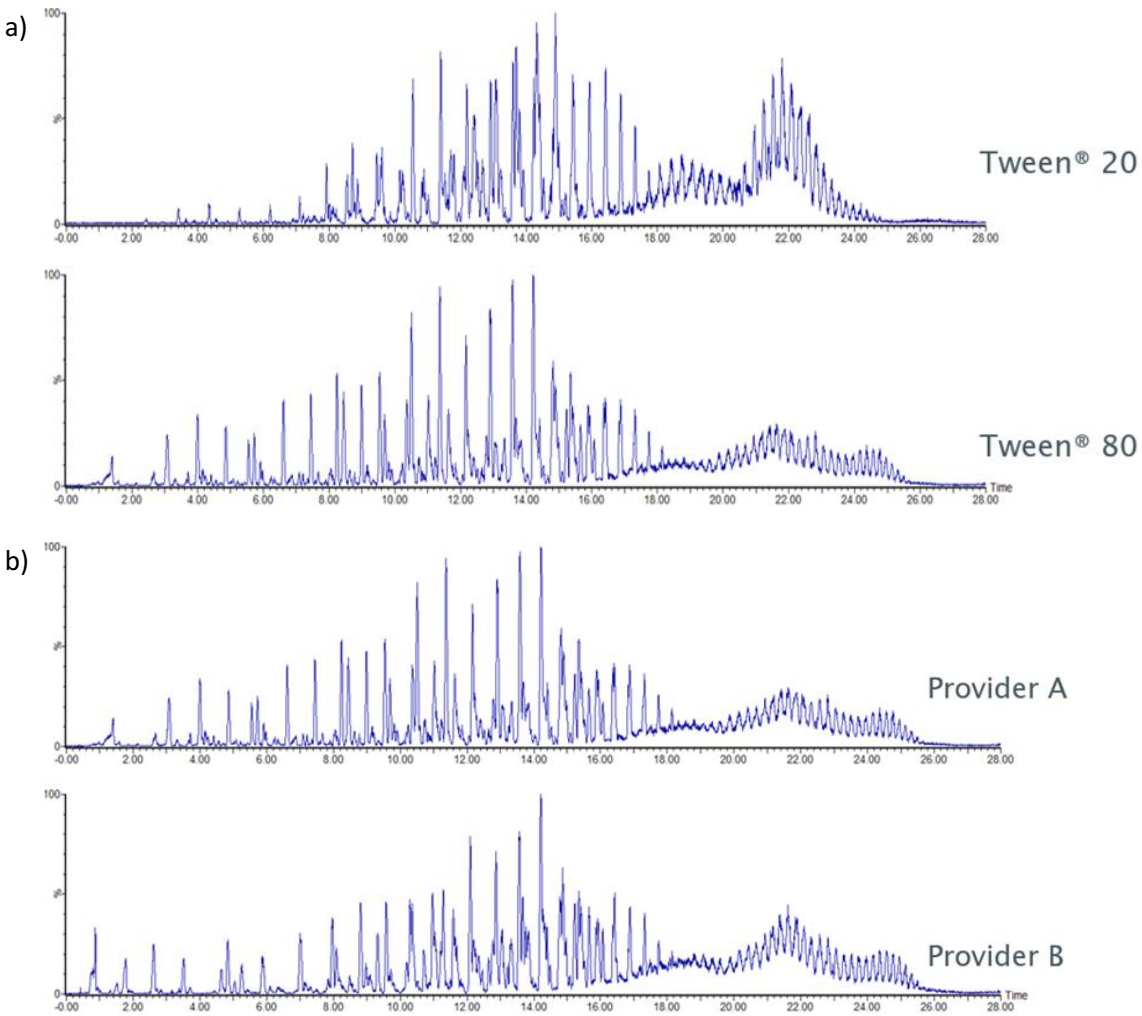

Figure 165. UHPSFC positive ion ESI Q MS. BPICC. 2500 µg/mL Tween® 20 and 2500 µg/mL Tween® 80 in CH_3CN. Differences in the pattern of the BPICC between a) Tween® 20 and Tween® 80, and b) two suppliers of Tween® 80

The increased complexity of Tween® 80 can be directly noticed in the ion map (Figure 163), where trends of the higher degree of oleate substitution in POE S become more noticeable and increase the complexity of the later eluted side of the chromatogram. The acquisition of the ion map using low-resolution mass spectrometry (Figure 166 a) involved the characterisation of Tween®80 was challenging and not possible. The change of the mass analyser to a high-resolution QToF (Figure 166 b) allowed the characterisation of the complex mixture (Table 49) due to the charge stripping observed and the higher sensitivity of the mass analyser. The polymeric chains were identified using the chromatographic elution of the polymers and accurate mass measurements. Similarly, the higher sensitivity of the QToF allowed the detection of other less abundant fatty acid substitutions that were not oleic acid. These were correlated to vegetable fatty acids due to differences of 28 Da in the MW of substituted POE sorbitan-based and POE IS-based polymers.

a)

b)

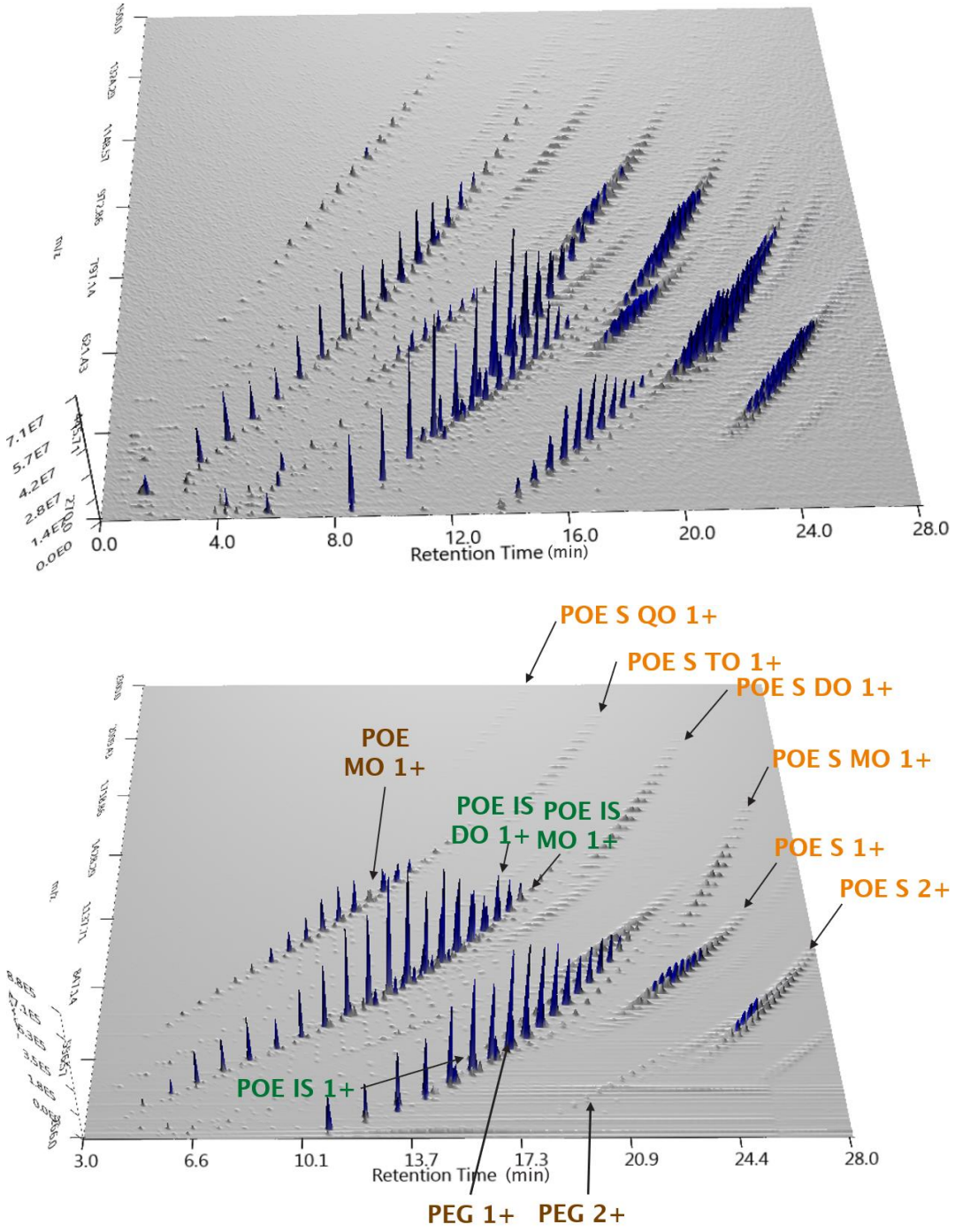

Figure 166. UHPSFC positive ion ESI MS. Ion map. Comparison of the effect of the mass analyser for Tween® 80: a) Q 2500 µg/mL in CH_3CN, b) QToF 500 µg/mL in CH_3CN

Polymer	**MW**	**MW'** [a]
PEG	18.0105	18.0105
PEG monooleate (POE ML)	299.2577	35.1011
POE dioleate (POE DL)	580.5049	8.1656

Polymer	MW	MW' [a]
POE sorbitan (POE S)	164.0681	31.9898 [b]
POE sorbitan monooleate (POE S MO)	428.3126	32.0777 [b]
POE sorbitan dioleate (POE S DO)	692.5571	32.1656 [b]
POE sorbitan trioleate (POE S TO)	956.8016	32.2535 [b]
POE sorbitan tetraoleate (POE S QO)	1221.0461	32.3414 [b]

Polymer	MW	MW' [a]
POE isosorbide (POE IS)	146.0576	13.9793 [b]
POE isosorbide monooleate (POE IS MO)	410.3021	14.0672 [b]
POE isosorbide dioleate (POE IS DO)	674.6466	14.1551 [b]

Table 49. Calculated monoisotopic masses and reduced monoisotopic masses (ethylene oxide mass: 44.0261 Da) of Tween® 80 species. [a] MW': Reduced MW calculated by subtracting the mass of the ethylene oxide repeating unit to the molecule end group MW. [b] isobaric masses that require high-resolution mass spectrometry for identification

When evaluating two suppliers of Tween® 80 (Figure 167), a high degree of similarity between products was noticed, with minor differences observed.

a)

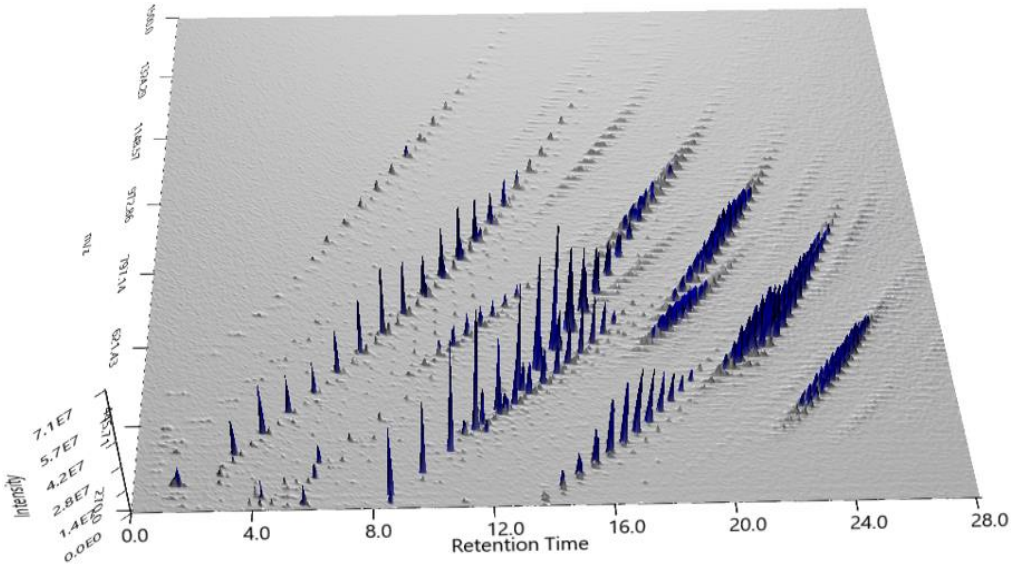

b)

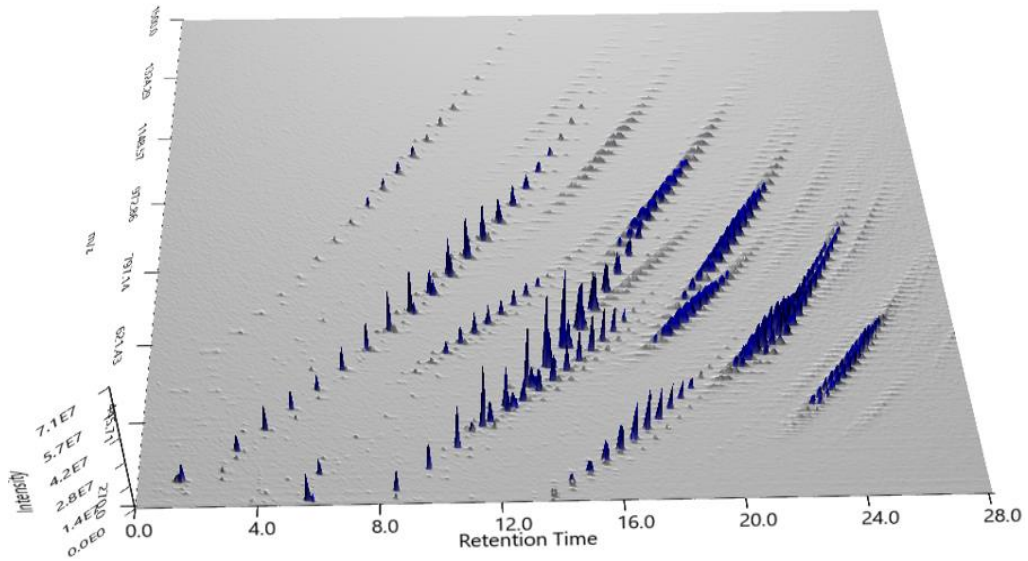

Figure 167. UHPSFC positive ion ESI QToF MS. Ion map. 1000 µg mL Tween® 80 in CH_3CN. Comparison of different suppliers: a) supplier A, b) supplier B

Analysis of Tween® 80 under negative ion ESI MS further characterised the polysorbate (Figure 168) by assigning the fatty acids present in the mixture. Analysis of the synthetic route of the products allowed assignation of the *m/z* values of the different $[M - H]^-$ ions to vegetable-fatty acids present in both Tween®20 and Tween®80 products. Whilst analysis of Tween®20 showed lauric acid (C12:0), myristic acid (C14:0), palmitic acid (C16:0) and stearic acid (C18:0), with lauric acid the most abundant, analysis of Tween®20 product showed oleic acid (C18:1) and linoleic acid (C18:2), with oleic acid the most abundant. Similarly, supplier differentiation was facilitated by the oleic acid and linoleic acid compositions.

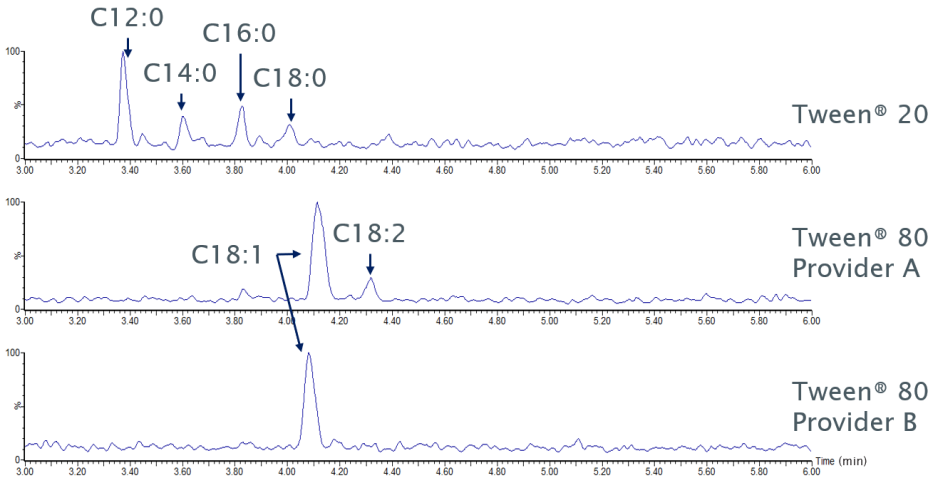

Figure 168. UHPSFC negative ion ESI Q MS. BPICC. 2500 µg/mL Tween® 20 in CH_3CN. Differences in the fatty acid composition of different polysorbates: C12:0, C14:0, C16:0, C18:0, C18:1 and C18:2

The analysis of the samples using UHPSFC dopant-assisted (toluene) positive ion APPI Q MS (Figure 169) allowed the identification of the *m/z* values of the protonated molecules $[M + H]^+$ to oleic and linoleic acids and some PEG series that showed double bonds in their chemical structure that allowed to be ionised using positive ion APPI MS.

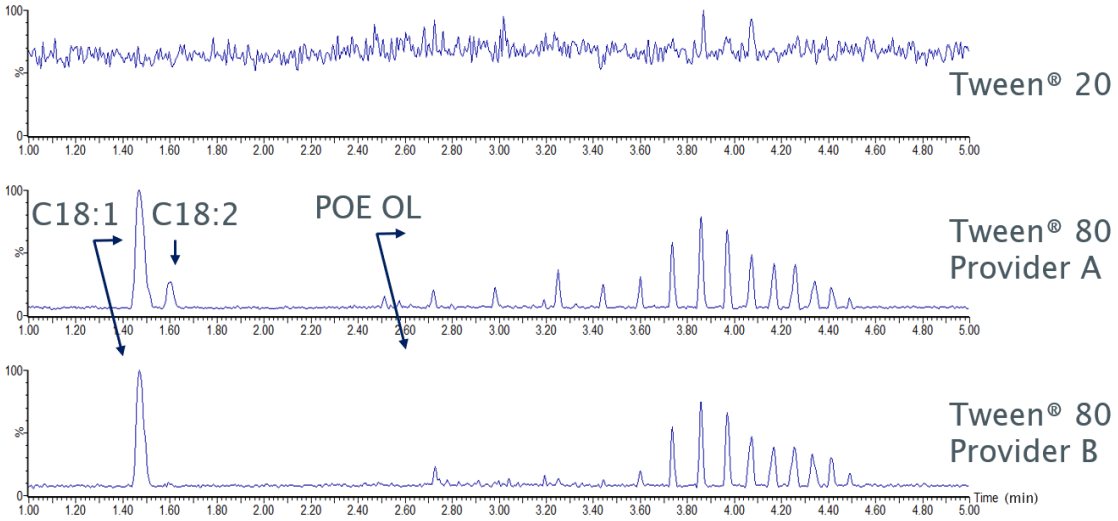

Figure 169. UHPSFC positive ion APPI Q MS (dopped with toluene). BPICC. 2500 µg/mL Tween® 20 in CH_3CN. Differences in the composition of substituted saturated fatty acid of different polysorbates: oleic acid (C18:1, OL) and linoleic acid (C18:2)

The experiments (Figure 169) were related to the previous UHPSFC positive and negative ion ESI MS data (Figure 165 to Figure 168). The comparison confirmed that the two first peaks in the UHPSFC positive ion APPI MS BPICC corresponded to oleic acid at t_R 1.45 min and linoleic acids at t_R 1.60 min due to the presence of unsaturation sites in their chemical structures. Additionally, the PEG series corresponded to POE monooleate (POE OL), where detection was possible due to the unsaturation site in the oleate substituent of the PEG chain. It is noteworthy that other species with oleate substitutions were not detected as the ions produced were outside of the scanned *m/z* range of the quadrupole. The ions produced in positive ion APPI MS when assisted with toluene as the dopant are $[M + H]^+$ species, rather than the multiply charged species $[M + nNH_4]^{n+}$ observed in positive ion ESI MS. The different ions observed illustrated that the $[M + H]^+$ species were outside the *m/z* scan range of the Q, showing that oleic and linoleic substituents of POE IS, and POE S-based polymers cannot be detected. The multiple charging afforded by positive ion ESI means that the ions fall into the *m/z* range of the Q, bringing down the molecule MW to the scan area of the mass analyser. The result is that only POE oleate is detected using UPHSFC positive ion APPI MS and not POE sorbitan or isosorbide oleate species. These data showed the power of combining ionisation sources to unravel the polysorbate composition.

4.5 Final chapter remarks

This chapter focused on addressing the complexity of the challenging PEG species used in pharmaceutical formulations and how the potential of UHPSFC hyphenated with MS methodologies has been developed to unravel their complexity. The current research offers a methodological approach to characterise PEG-based excipients using UHPSFC-MS and can be used as an alternative to the traditional RPLC-MS and NMR spectroscopy. The combination of UHPSFC and MS is critical and required to characterise complex polymeric mixtures due to the presence of isobaric species in many mixtures. The advantages of using the BPICC and the ion map were evaluated to characterise several PEGs of different levels of complexity in different scenarios for the pharmaceutical industry. Whilst the BPICC provides a screening approach to differentiate polymers and highlight differences in the material source from other suppliers, using the BPICC on its own is not enough to interpret polymeric mixtures. The powerful combination of the two techniques, together with data representation using ion maps (MZmine), improves visualisation and provides the analyst with an information-rich, visual representation of the data to observe the distribution of the polymer ionisation charged states and reveal impurities. Using ion maps proved an excellent analytical tool for characterising polymeric chains at different charge states and facilitating the observation of low-level impurities.

The selectivity of the ionisation source can be used to simplify the characterisation by detecting specific components. Whist ESI MS allows the determination of molecules with (either) basic (positive ion) and acidic (negative ion) sites, APPI MS ionises those components with unsaturation sites in the chemical structure. The selectivity of negative ion ESI MS facilitates the characterisation of PEGs with acidic end groups, whilst APPI MS provides insights for components with olefinic chains such as Tween® 80. An example of the benefit of using negative ion ESI MS was proposed to quantify free lauric acid, which provided good results and allowed supplier and product quality comparison. The proposed technique can be used as an alternative to headspace or liquid injection gas chromatography-MS. The approach eliminates most of the need for sample preparation that the standardised method of fatty acid analysis using HPLC-CAD requires [377]. The pitfall of using UHPSFC negative ion ESI MS is the lack of detection of free ethylene oxide or dioxin from the synthesis or degradation or other volatile molecules present in the mixture, which is possible using headspace or liquid injection gas chromatography-MS [378]. These techniques allow the identification of synthetic (ethylene oxide or dioxin) or oxidative degradation (formic acid) subproducts that are critical due to the possible interactions with the drug molecule.

The intercomparison study showed that the type and the data acquisition modes of mass analyser were critical factors for qualitative analysis. For beam instrumentation such as quadrupole mass analysers, the scan rate and duty cycle of modern instrumentation is fast (typically 15-20,000 *m/z* units per second) and can deliver the appropriate number of scans across the SFC peak to give a genuinely representative peak profile, this with the caveat of the scan rate being *m/z* range dependent. Note that at very fast scan rates (approaching their theoretical limit), the isotopic information of measured ions may be compromised and induce errors in assigning polymeric trends. Additionally, data processing is time-consuming and cannot provide accurate mass measurements. A change in the mass analyser from Q to QToF accelerated the characterisation due to a shifting in the mass spectra to lower charge states of the ions, decongesting the ion map and increased sensitivity that facilitates the observation of the polymeric trends at the different charge states and impurities. QToF instrumentation delivers high-resolution mass measurements, and because there is no *m/z* scan, all the ions are always recorded. The result is that the high-resolution capability allows for the separation of nominally isobaric species, and the accurate measurement of the *m/z* value of ions (typically to the fourth decimal place) allows chemical formulae for the ion to be postulated. The confidence in the identity of the ion is further enhanced by comparing the measured and theoretical isotope patterns. A benefit of quadrupole or QToF data is that data can be revisited to search for other species (non-targeted analysis).

The use of UHPSFC hyphenated to MS is appropriate for the investigation of PEG materials but cannot provide a complete picture of the polymeric mixture, and other techniques are required for this purpose. This conclusion is not new in polymer analysis and is well known within the field, with limitations, including the analysis of minor components within the mixture [379]. Typically, SEC is used to determine minor levels of impurities in polymeric materials as the impurities are separated away from the polymer due to the huge differences in size [380]. For example, the analysis of small drug molecules and excipients can be affected by the ion suppression produced by the polymeric chain, and their detection or quantitation might be compromised. Using gel permeation chromatography or a temperature-gradient analysis of atmospheric solids analysis probe (ASAP) MS can allow investigation of low levels of suppressed small molecule impurities.

Additionally, the capacity of UHPSFC to differentiate the initial cyclisation subproducts of sorbitol in polysorbate materials can provide insights into formulation development and suggests the requirement of improved synthetic routes. The technique itself might not be sufficient for a deeper investigation of polysorbate materials due to the unusual peak shapes of POE S-based polymers, and further investigation might be required with proposals including (i) the introduction

of IMMS to add an extra dimension in the separation and (ii) use of 2D hyphenated chromatographic techniques (LC x LC or SFC x LC or LC x SFC) [381] or (iii) the coupling of columns in series to improve peak resolution and peak capacity within the chromatographic separation.

The developed UHPSFC positive ion ESI MS method (section 2.6) is herein fit for purpose and can be added to the throughput of the pharmaceutical industry for investigation and quality purposes. The addition of UHPSFC-MS is recommended to investigate samples that cannot meet specifications due to in-process degradation, suppliers, or batches — *e.g.*, by using the benefit of ionisation selectivity to unravel polymer complexity. Whilst ESI MS is still a common ionisation source choice within the industry, the extension to other approaches such as positive ion APPI MS can facilitate data processing and improve the confidence of the assignation of chemical structures in a complementary manner to the use of high-resolution MS. The added benefit of changing the mass analyser for a high-resolution QToF MS can accelerate the characterisation and improve the confidence in the assignation of chemical structures.

Chapter 5 Quantitation of poly(ethylene) glycols based on the deconvolution of the oligomer mass spectra

5.1 Comparison between small and large molecule quantitation

When using positive ion ESI sources, quantitation of small molecules is straightforward and based on the response of the *m/z* value of the base peak ion in the mass spectrum (Figure 170 a) [382]. The ion response is obtained either in full scan (the whole *m/z* range is scanned based on the peak area of the corresponding reconstructive ion current chromatogram (RICC) or by monitoring an ion (selective ion monitoring, SIM mode) and obtaining the area under the peak. The peak area of the *m/z* value (obtained in either manner) is represented against the concentration to predict a least-square linear regression used for quantitation and to obtain the concentration values of unknowns.

Large biomolecule quantitation is not as simple as the multiple ionisation sites present in the molecule generate a mass spectrum characterised by a charged envelope (Figure 170 b); a set of *m/z* values of the same molecule differ by the charge states [310]. The large biomolecule MW is correlated to each ion in the charge envelope with an *m/z* value based on the charge state (n) and the adduct (X) of the ion formed (Equation 40).

$$MW = n(m/z - X) \qquad \text{Equation 40}$$

Charge envelopes of large biomolecules are interpreted using deconvolution tools that convert the multiply charged ions in the *m/z* scale into a single peak corresponding to the MW of the large biomolecule in a "reconstructed" mock spectrum in the mass scale (Figure 170 b and c). Quantitation is derived from the peak area of this deconvolved spectrum. Most deconvolution algorithms were developed based on Equation 40.

The initial approach for charge envelope deconvolution was described by Mann *et al.* and directly resolves a simultaneous set of equations by assigning values to the charge state (n) [322]. Recently, the most common approach is to use Maximum Entropy® (MaxEnt), which takes advantage of Bayesian statistics to predict the most likely molecular mass spectrum based on similarities of patterns after several iterations [145-147]. Figure 170 c shows an example of using the MaxEnt algorithm for deconvoluting the mass spectra of a horse heart myoglobin protein (left side of

Figure 170 b). Before MaxEnt, Waters® developed Transform™ to improve the process by resolving several combinatorial equations [383], an approach similar that of Mann *et al.* [322].

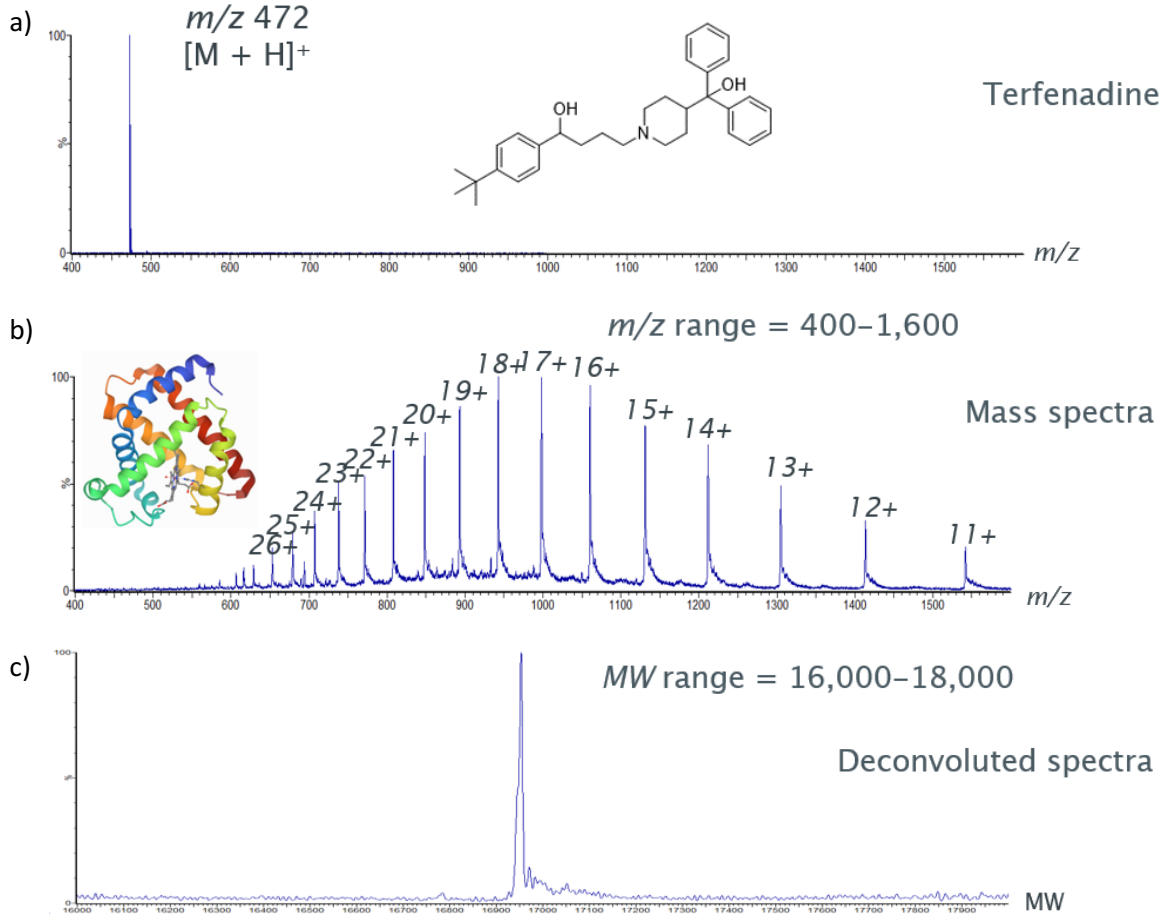

Figure 170. Deconvolution of the mass spectra of a large biomolecule a) mass spectrum of a small molecule (terfenadine) in an *m/z* scale, b) characteristic mass spectrum of a large biomolecule showing the charge envelope in an *m/z* scale, and c) deconvoluted mass spectrum of the large biomolecule in an MW scale

5.2 Development of an oligomer-based deconvolution approach

5.2.1 Generation of the polymer mass spectra

Quantitation of PEGs is challenging as the polymer ionisation under positive ion ESI MS results in a complex mass spectrum corresponding to an envelope of ions with the same charge states (Figure 171 a). The complexity of the mass spectra increases when increasing the MW of the molecule due to the higher presence of ionisation sites in the oligomer chain lengths, as discussed in section 3.5, page 142. The application of MaxEnt to these mass spectra is also challenging due to the intrinsic complexity, and alternatives are needed to facilitate data processing. The improved

oligomer separation obtained using ultra-high-performance supercritical fluid chromatography (UHPSFC) (Figure 171 b, top) allows for observing the individual mass spectra of each oligomer (Figure 171 b, bottom). Each oligomer mass spectra shows a charge envelope, similar to that of a large biomolecule (Figure 170 b), that can be resolved using Equation 40. The ions of this oligomer are separated from the following oligomer, with n+1 repeating units, by a displaced value (Equation 41) that depends on the charged state. The overlapping of the mass spectra of each oligomer explains the curves at the same charged state observed in the complex mass spectra (Figure 171 a).

$$\Delta m/z = \frac{MW_{repeating\ unit}}{n}\ m/z\ units \qquad \text{Equation 41}$$

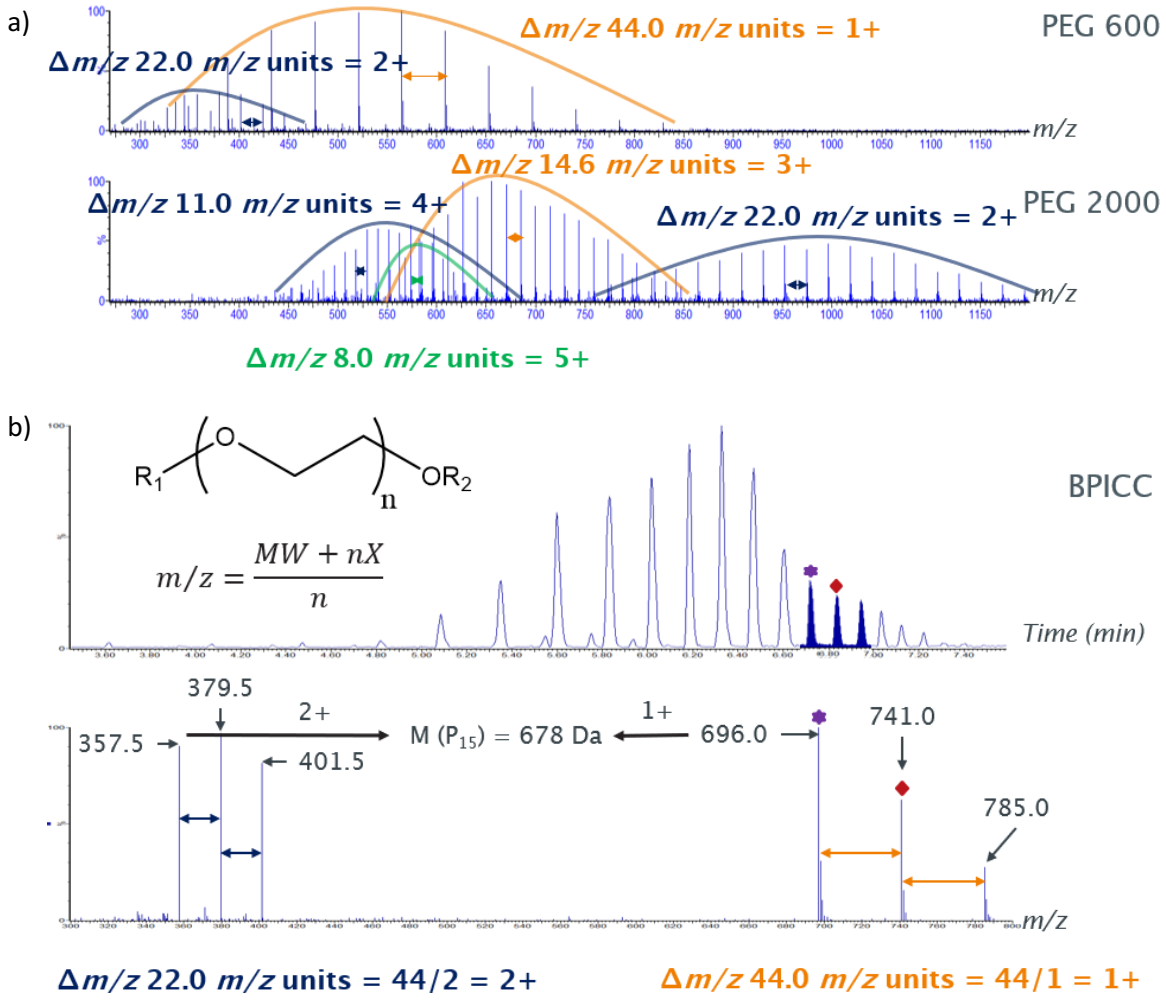

Figure 171. The advantages of chromatography in PEG analysis: a) Comparison of the mass spectra of PEG 600 and PEG 2000 and the need for chromatography, and b) generation of the mass spectra of individual oligomers of PEG 600 (bottom) based on the chromatographic separation using UHPSFC-MS (top)

The resemblance of the oligomer mass spectra to that of a large biomolecule (Figure 170 b and Figure 171 b) suggested that similar deconvolution approaches can be applied. Waters® offer two deconvolution approaches within the MassLynx® 4.1 software package: MaxEnt and Transform™. The application of MaxEnt was not possible due to a software limitation where the established *m/z* range in the add-on settings must be below the molecule MW. This restraint was not identified when using MaxEnt software from other manufacturers (*e.g.*, Bruker®). It was noted that Transform™ does not include ammoniated adducts in the algorithm involving that the coding required a modification to include these adducts (Table 50). This modification consisted in changing the value of the accurate mass of the Na ion (22.989768 - e) for the accurate mass of the ammonium ion (18.033826 = NH_3 + H - e).

Initial code:	**New code:**
TransformMinMass=200.00	TransformMinMass=200.00
TransformMaxMass=3000.00	TransformMaxMass=3000.00
TransformRes=0.1250	TransformRes=0.1250
TransformMinLen=1	TransformMinLen=1
TransformThreshold=10.00	TransformThreshold=10.00
TransformWindow=1.00	TransformWindow=0.30
TransformReject=2.00	TransformReject=2.00
TransformDimers=FALSE	TransformDimers=FALSE
TransformAdduct=22.989768	**TransformAdduct=18.033826**
TransformCut=MIDDLE	TransformCut=MIDDLE
TransformReplace=APPEND	TransformReplace=APPEND
TransformMz1=689.97	TransformMz1=689.97
TransformMz2=466.32	TransformMz2=466.32
TransformNumSinglePeaks=0	TransformNumSinglePeaks=0
TransformMaxStandardDeviation=2.00	TransformMaxStandardDeviation=1.00
TransformPeptide=FALSE	TransformPeptide=FALSE
TransformDelimiter=TRUE	TransformDelimiter=TRUE
TransformDelimChar=5	TransformDelimChar=5
AutoPos=TRUE,SW_SHOWNORMAL,38,85,511,259	**AdductPos=TRUE,SW_SHOWNORMAL,523,395,750,515**

ManualPos=TRUE,SW_SHOWNORMAL,268,419,718,591 **EditPos=TRUE,SW_SHOWNORMAL,446,231,814,595**	ManualPos=TRUE,SW_SHOWNORMAL,268,419,718,591 **EditPos=TRUE,SW_SHOWNORMAL,615,228,983,592**

Table 50. Coding modification of the [SpeTransform] section of the MassLynx.ini file (C:\MassLynx) within the MassLynx® 4.1 software package to deconvolute ammoniated adducts (18.033826 = NH_3 + H - e). Key changes are in bold. Other parameters were adjusted to maximise ion count

Polymer deconvolution was possible by gradually repeating a stepwise deconvolution process of the mass spectra of the oligomers. Initially, a single oligomer mass spectrum was identified in the chromatogram, and the coding modification allowed the successful deconvolution using Transform™ (Figure 172).

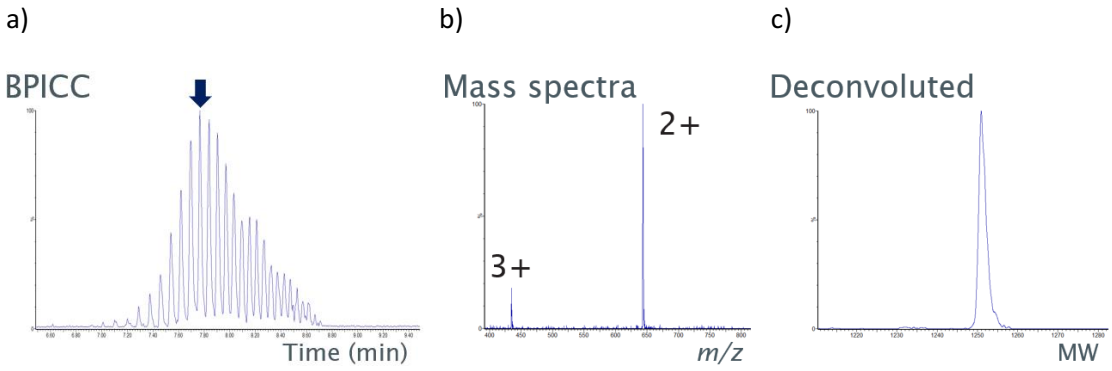

Figure 172. Stepwise approach of the deconvolution of one single oligomer mass spectra using Waters® Transform™ deconvolution. a) identification of the oligomer in the chromatogram, b) oligomer mass spectra, c) deconvoluted oligomer

The chromatographic separation (Figure 173 a) of the individual *"blue"* oligomer resulted in the mass spectrum for this oligomer (Figure 173 b) and subsequent deconvolution (Figure 173 c). This step was followed by selecting the *"red"* and *"green"* oligomers in the BPICC (Figure 173 a), obtaining their mass spectra (Figure 173 b) and then deconvoluting as previously (Figure 173 c). The deconvolution of the entire polymer mass spectra was gradually achieved using this protocol (Figure 173 d) in *ca.* 15 mins.

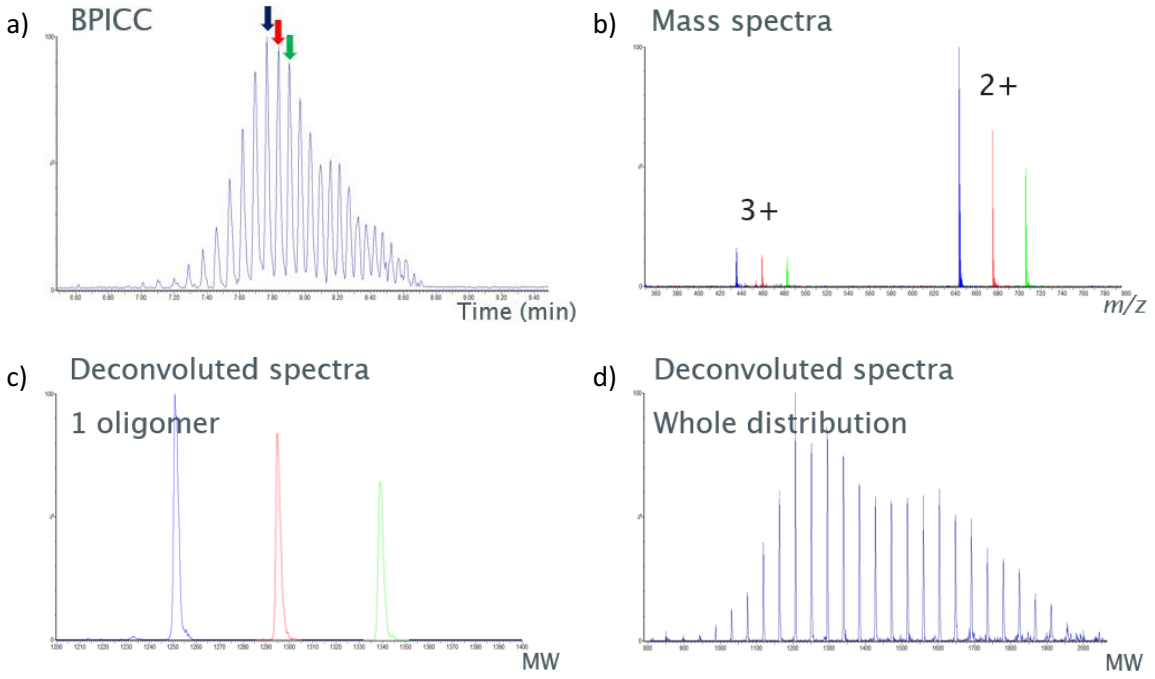

Figure 173. Stepwise deconvolution of the mass spectra of PEG 1450 using Waters® Transform™ algorithm

5.2.2 Questioning the non-quantitative aspect of the Waters® Transform™ algorithm

Even though early literature stated the non-quantitative aspect of the Waters® Transform™ algorithm [383], previous research group members challenged this statement for oligonucleotide quantitation with unsuccessful results, resulting in the application of MaxEnt due to the reliability of the approach [384]. The comparison of MaxEnt and Transform™ was presented in the work of Marty *et al.* where they compared these algorithms to the results of their proposed approach UniDec (based on Bayesian Statistics) for deconvolution of a membrane protein AqpZ with bound POPC lipid [385]. They found that Transform™ was quantitative; however, the algorithm relies on a user-defined mass window to simply sum up isolated charge states with no deconvolution [385]. However, the similarities in the polymeric nature between oligonucleotides and proteins and the obtain mass spectra of the PEG oligomers suggested that these results might be extrapolated.

An independent ionisation response to the charge state was proposed, and the hypothesis was disproved by assessing how the ion response changes using three approaches: (i) increasing the cone voltage to induce charge stripping without fragmentation, as if the ion response is maintained, then the charged state does not influence the ion response, (ii) Evaluating a linear least-squares fitting regression model of the Transform™ response to the polymer concentration, as diluting a sample by a certain amount should reduce the ion response, and (iii) a comparison

between the reported M_n, M_w, and PDI and the experimental values when calculated using the developed deconvolution approach and a classic approach of reconstructive ion current chromatograms (RICCs), as if the values are comparable to manufacturer values, the accuracy of the method is appropriate for quantitation.

When increasing the cone voltage (Figure 174), charge stripping of the ammoniated adducts was induced; however, an undesirable in-source collision-induced dissociation (CID) of ammoniated molecules added the protonated molecules to the mass spectra, undoing the desire to have one ion type per molecule delivered by the selective ionisation and hence, compromising the quantitation.

Charge stripping $[M + nNH_4]^{n+} \rightarrow [M + (n-x)NH_4]^{(n-x)+} + xNH_4^+ \quad x \leq n$

In-source CID $[M + NH_4]^+ \rightarrow [M + H]^+ + NH_3$

Consequence $[M + nNH_4]^{n+} \rightarrow [M + (n-x)NH_4]^{(n-x)+} + [M + (n-y)NH_4 + yH]^{n+} + (x+y)NH_3$

$(x+y) \leq n$

Figure 174. Effect of increasing the cone voltage to the ammoniated molecules of PEGs

Serial dilutions of the polymer at several concentrations allowed analysis of the dependence of the Transform™ response to the concentration. After deconvolution of the whole polymeric distribution, the resulting data was successfully correlated using a least-squares fitting model (Figure 175) that significantly represented the linear Transform™ response at different concentrations ($R^2 > 0.998$, $F_{(2\ tails,\ v=5,\ 0.05)} = 2287 > 6.61$).

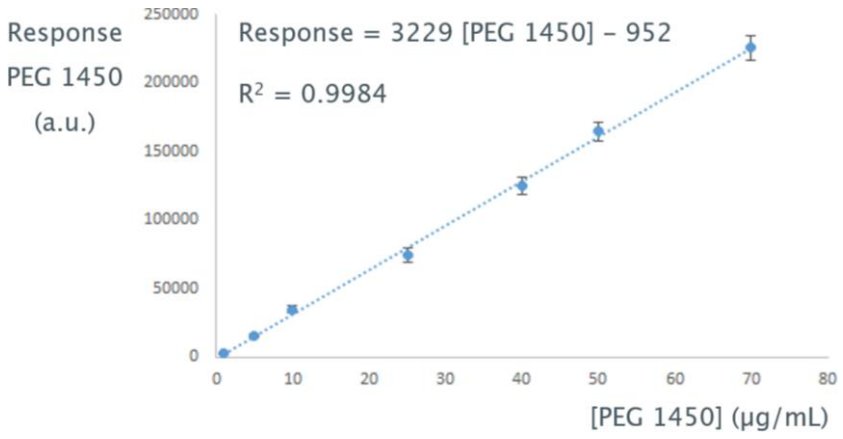

Figure 175. Evaluation of the quantitative aspect of Waters® Transform™ algorithm using linear fitting (3 replicates, error bars correspond to 1 stdev)

The last experiment compared the reported M_n, M_w and PDI values of PEG 1450 provided by the manufacturer acquired using SEC with the experimental values. This polymer was selected as the

resolving power of the Q is at the limit to resolve the isotopic distribution of $^{12}C/^{13}C$ for doubly charged species and could not resolve triply charged species, which could induce an error in the final value. The individual oligomer response, N_i, was either calculated by totalling all RICC peak areas of the oligomer ions or by the deconvoluted response of the individual oligomers. Either approach showed insignificant differences in the manufacturer values (p = 0.05, n = 5), proving the validity of both approaches (Table 51).

Method	**Sum of RICC peak area of each charge state**	**Ion response obtained using Transform™**	**Manufacturer**
M_n	1432 (-1.3%)	1443 (-0.6%)	1451
M_w	1477 (-0.9%)	1486 (-0.3%)	1491
PDI	1.03	1.02	1.03

Table 51. Evaluation of the quantitative aspect of Waters® Transform™ algorithm by comparing experimental and reported M_n, M_w and PDI. Manufacturer data acquired using SEC

The least-squares fitting model and the comparison of the M_n, M_w and PDI values proved the quantitative aspect of the Transform™ algorithm, showing the independence of the charged state to the ion response; hence, data suggested that the quantitative aspect of the response of the Transform™ deconvolution algorithm.

5.3 Proposed approaches using the single quadrupole mass analyser

Several approaches for quantitation were proposed based on either a single surrogate oligomer representing the whole polymeric distribution (Figure 176 a) or the whole polymeric distribution itself (Figure 176 b).

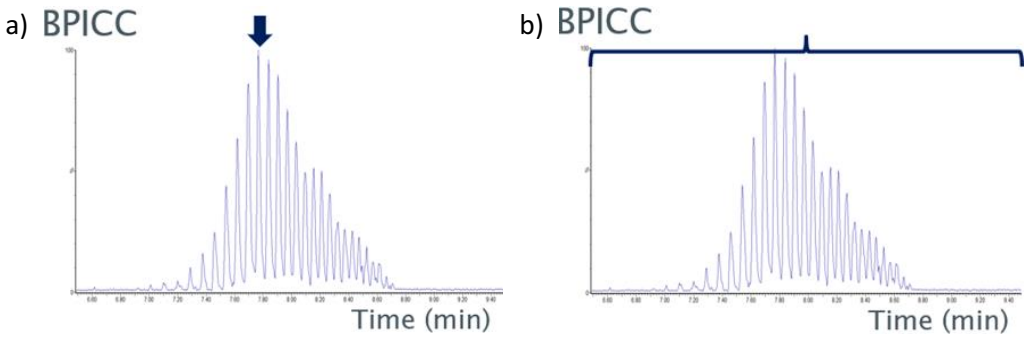

Figure 176. Proposed approaches for PEG quantitation based on a) a surrogate oligomer that represents the whole distribution, and b) the whole polymeric distribution

5.3.1 Approaches for quantitation based on a surrogate oligomer

The evaluation of the polymer mass spectra suggested that the surrogate oligomer to be used should be the oligomer with ions that correspond to the base peak ion that corresponded to the most intense peak in the BPICC (Figure 177). The selection of one ion resembled the approach used to quantify small molecules, whilst following the deconvolution approach resembled the quantitation of a large molecule; as such, similar approaches were assessed.

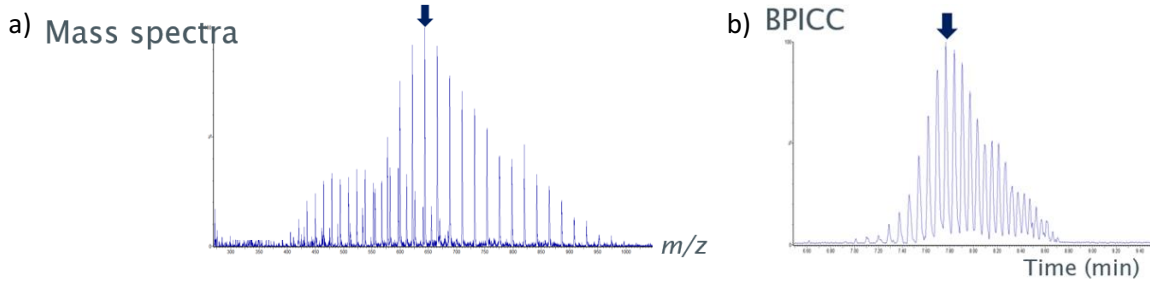

Figure 177. Selection of the surrogate oligomer for polymer quantitation. Example showed using PEG 1450

The ions produced by these oligomers were treated in three different manners to obtain the response used for the linear fitting for calibration – either (i) the response of the base peak ion acquired using selective ion monitoring (SIM) acquisition (Figure 178 a) that took *ca.* 0.5 min, (ii) the reconstructive ion current chromatogram (RICC) of oligomer that produced the base peak ion (Figure 178 a) that took *ca.* 0.5 min and c) the deconvolution of the oligomer mass spectra (Figure 178 b) took *ca.* 1.0 min.

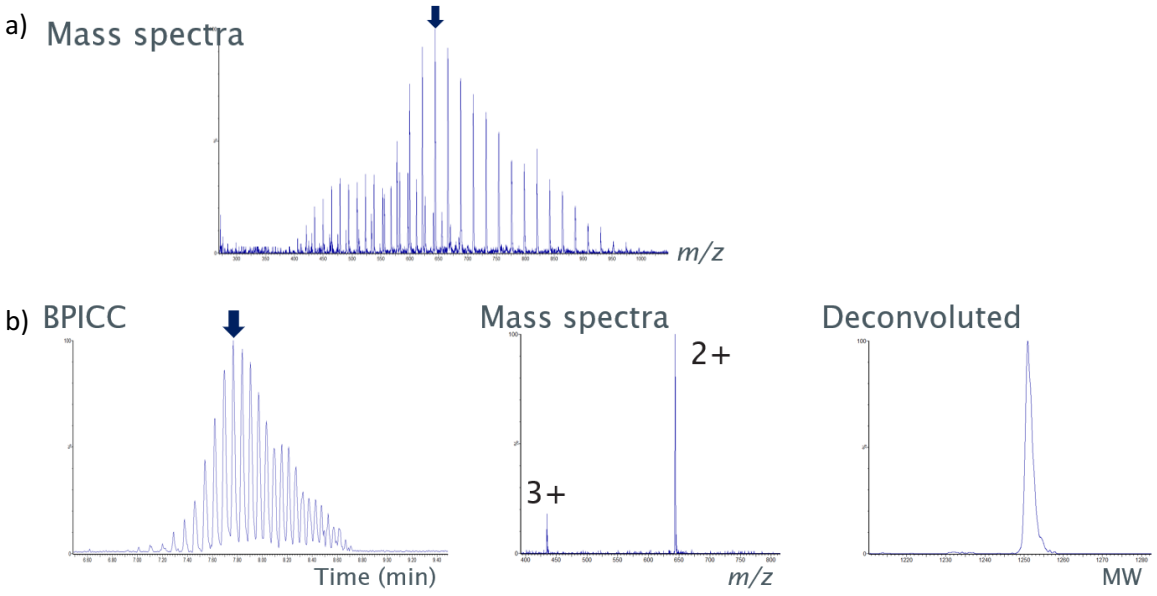

Figure 178. Quantitation approaches of PEGs using a surrogate oligomer: a) RICC of the most intense ion with/without SIM acquisition, and b) mass spectra deconvolution of the surrogate oligomer

The evaluation of the mass spectra of the polymeric distributions produced by each PEG standard (600, 1000, 1450 and 2000) allowed the identification of the oligomers/ions shown in Table 52 as representatives of the whole polymeric distribution.

PEG MW	600	1000	1450	2000
Ions produced	$[M + NH_4]^+$ $[M + 2NH_4]^{2+}$	$[M + NH_4]^+$ $[M + 2NH_4]^{2+}$	$[M + 2NH_4]^{2+}$ $[M + 3NH_4]^{3+}$	$[M + 2NH_4]^{2+}$ $[M + 3NH_4]^{3+}$ $[M + 4NH_4]^{4+}$
MW value of the selected oligomer	590.3	898	1471	1867
n value of the selected oligomer	13	20	33	42
Ion selected for SIM acquisition	$[M + NH_4]^+$ *m/z* 565.0	$[M + 2NH_4]^{2+}$ *m/z* 468.0	$[M + 2NH_4]^{2+}$ *m/z* 753.5	$[M + 3NH_4]^{3+}$ *m/z* 640.5
t_R ions selected for SIM acquisition (min)	6.44	7.53	7.68	8.47

Table 52. Selected surrogate PEG oligomers used for polymer quantitation when analysed using UHPSFC positive ion ESI Q MS

5.3.2 Approaches for quantitation based on the overall polymeric distribution

When quantifying based on the whole distribution, two approaches were considered that were an extension of the described surrogate oligomer approaches (i) sum of the RICCs of all the polymeric ions of the mass spectra (Figure 179 a) took *ca.* 30 min per sample and (ii) sum of the oligomer Transform™ deconvoluted response (Figure 179 b) took *ca.* 20 min.

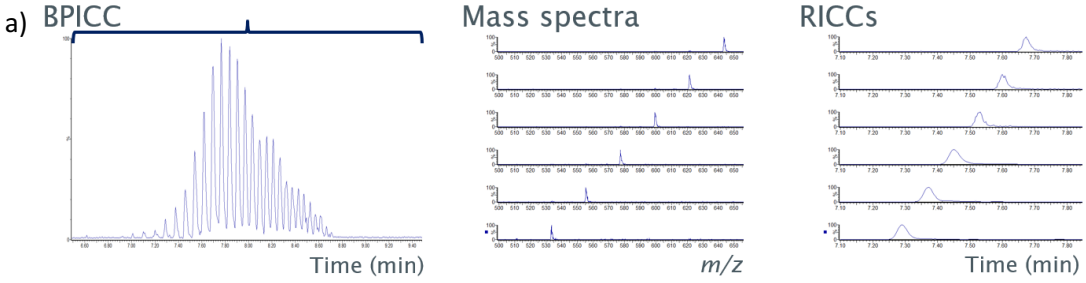

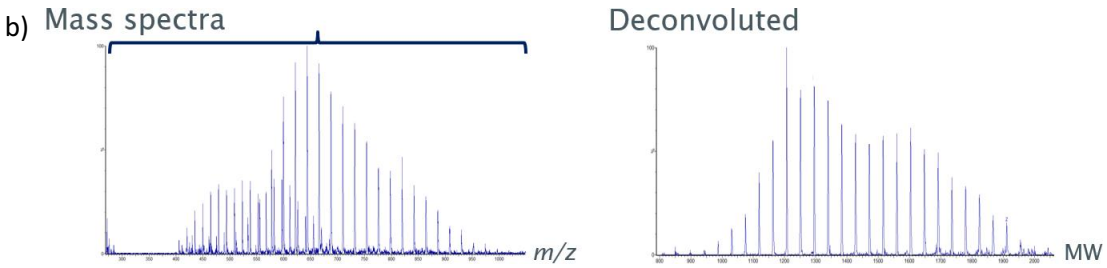

Figure 179. Quantitation approaches of PEGs using the whole distribution: a) sum of the RICCs of all PEG ions in the mass spectra, and b) sum of the oligomer Transform™ deconvoluted response

5.3.3 Comparison of quantitative approaches

The previous approaches based on the surrogate oligomer and the whole distribution were compared using PEG 600, 1000, 1450 and 2000 standards, and the differences were assessed using the linear dynamic range (LDR) and the correlation coefficient (R^2) (see the comparison in Table 53). Examples of the calibration curves for PEG 600 are shown in Figure 180 and Figure 181. The rest of the calibration curves can be found in Appendix B. Overall, similar values of the LDR were obtained independently of the approach used, except when using SIM acquisition of the most intense ion, where the improvement in the S/N resulted in a lower limit of quantitation (LOQ) concentration achieved. Whilst SIM achieved an improved detection limit, the data is targeted and only recorded for one *m/z* value selected. SIM data cannot be revisited to search for other species, a downfall that does not occur with full *m/z* range data acquisitions. When comparing R^2 values, procedures that followed a deconvolution approach showed slightly lower (0.998 compared to 0.999). The outstanding R^2 value shown in Table 53 suggests that these approaches can be used.

	Approach		**PEG 600**	**PEG 1000**	**PEG 1450**	**PEG 2000**
Surrogate oligomer	SIM	LDR (µg/mL)	0.0 1-10	0.5-15	0.5-50	2.5-100
		R^2	0.9999	0.9999	0.9999	0.9999
	RICC	LDR (µg/mL)	1-75	10-200	50-300	100-500
		R^2	0.9984	0.9993	0.9992	0.9984
	Deconvoluted mass spectra	LDR (µg/mL)	1-75	10-200	50-300	100-500
		R^2	0.9958	0.9994	0.9983	0.9957

Whole distribution	Sum peak areas of RICC	LDR (µg/mL)	1-75	10-200	50-300	100-500
		R^2	0.9981	0.9979	0.9977	0.9979
	Mass spectra deconvolution	LDR (µg/mL)	1-75	10-200	50-300	100-500
		R^2	0.9977	0.9981	0.9976	0.9971

Table 53. Comparison of different approaches for external calibration quantitation based on the LDR and R^2

Notably, the presence of ions in the background isobaric to the ions produced by PEG derivatives was negligible in most cases and did not affect the analytical result. However, the presence of multiple isobaric ions in complex PEGs requires careful examination when analysing data (*e.g.*, Tween® 80).

a)

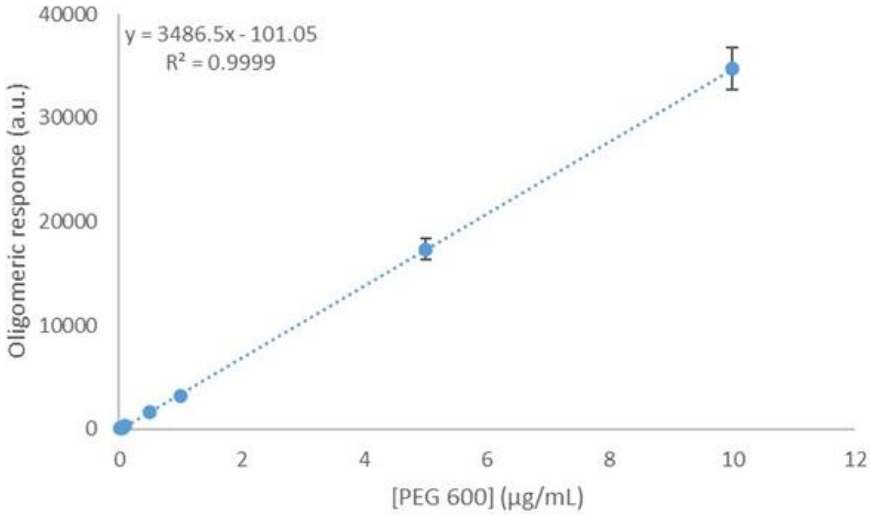

b)

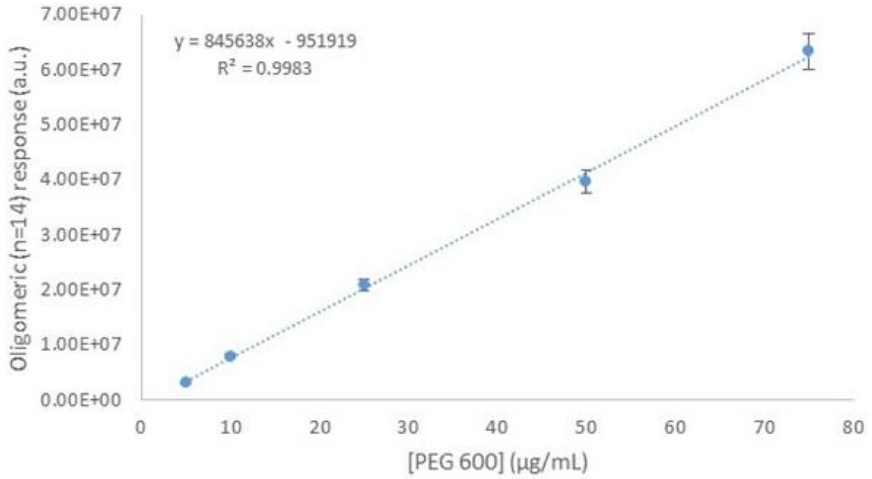

c)

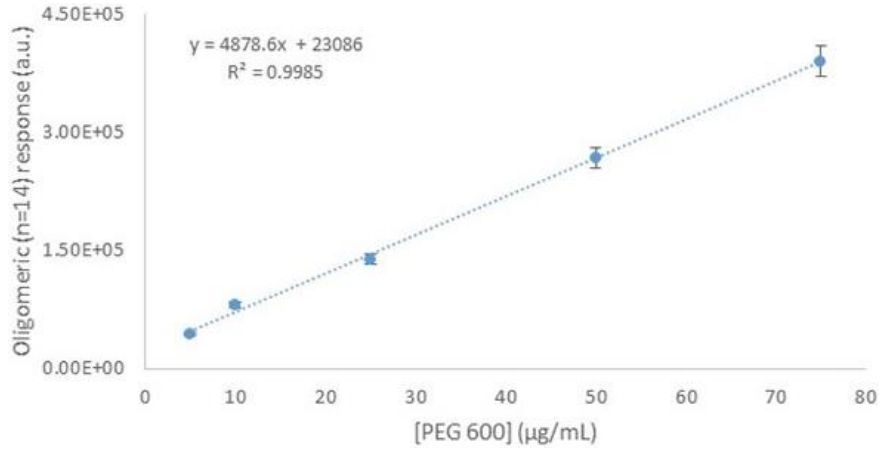

Figure 180. Examples of calibration curves for quantitation using a surrogate oligomer: a) SIM acquisition, b) use of the RICC, and c) deconvolution of the mass spectra (samples analysed in triplicates, the error bars correspond to 1 stdev)

a)

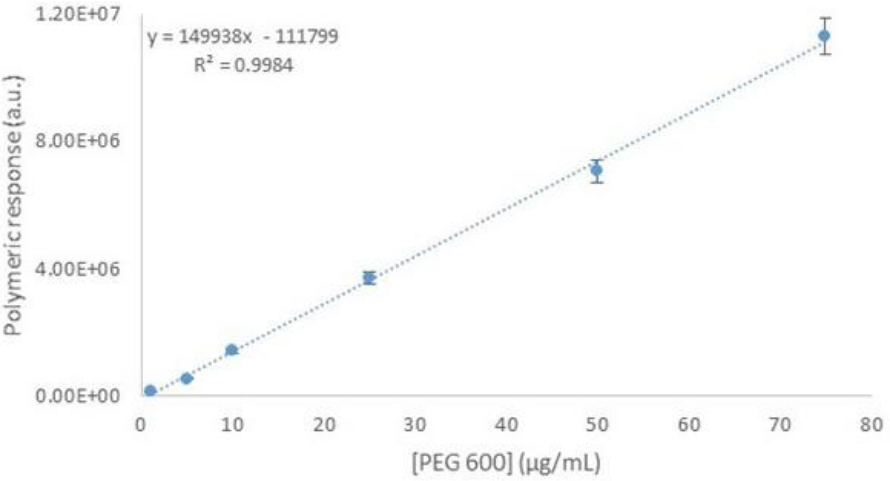

b)

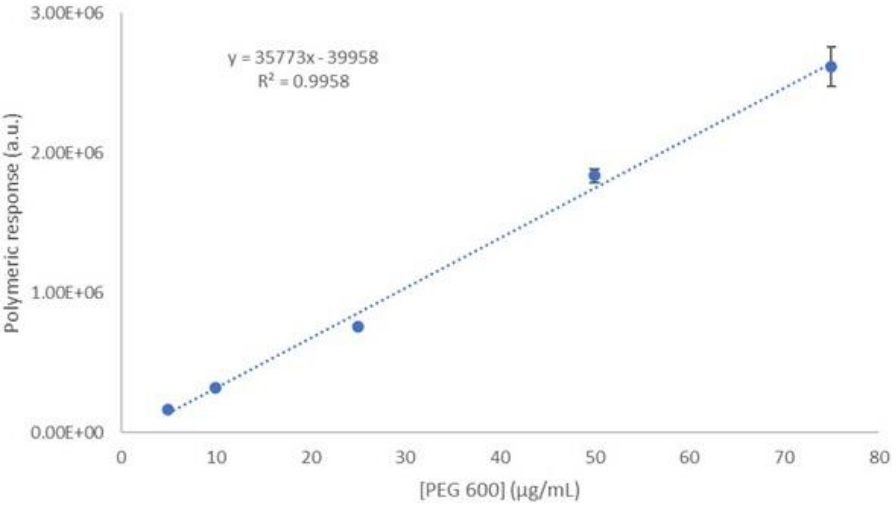

Figure 181. Examples of calibration curves for quantitation using the whole distribution: a) Sum of the peak areas of the RICC of all ions, and b) sum of the oligomer Transform™

deconvoluted response (samples analysed in triplicates, the error bars correspond to 1 stdev)

When comparing data processing of the different approaches (Table 54), approaches that used the whole distribution took significantly longer than approaches that used the surrogate oligomer. However, automating data processing or machine learning can be accelerated and reduce these times even further. The speed of automatisation was shown using TargetLynx™ Application Manager, an add-on within the MassLynx™ software package that automates data acquisition, processing, and reporting. This incorporates a wide range of confirmatory checks that identify samples falling outside the user-specified or regulatory thresholds, providing confidence in quantitative results. Automatisation using TargetLynx™ was applied to surrogate oligomers based on the RICC of the most intense ion with/without SIM acquisition, resulting in data processing that was extremely fast, as the calibration curve was obtained immediately without data processing.

	Approach	**Data processing time per sample (min)**
Surrogate oligomer	RICC with SIM	0.5
	RICC without SIM	0.5
	Deconvoluted mass spectra	1
Whole distribution	Mass spectra deconvolution	20
	Sum peak areas of RICC	35

Table 54. Comparison of different approaches for external calibration quantitation based on the data processing time

5.4 Intercomparison study: effect of the mass analyser

Quantitation of large biomolecules and polymers requires understanding the generation of the mass spectra as many aspects affect the ions produced [159] (refer to section 1.3.9, page 33), resulting in differences in the reported M_n, M_w and PDI values. The effect of the mass analyser was studied using different mass analysers available in the laboratory.

5.4.1 Effect on the mass spectra and deconvoluted mock spectra

The effect of the ion transmission and the collision gas were evaluated by coupling the Waters® UPC^2 instrument to the Waters® Xevo SQD 2 (quadrupole mass analyser (Q)), the Waters® Xevo TQD (triple quadrupole mass analyser (QqQ)) and the Waters® Synapt™ G2-*Si* (quadrupole time-of-flight (QToF) mass analyser) (Figure 182). It is noteworthy that the Q and the QqQ transmit ions using a beam design, whilst the QToF uses a pulse to transmit ion packets. Similarly, the QqQ and the QToF include the use of a collision gas that can induce charge stripping and collision-induced dissociation (CID) of ammoniated molecules (see 5.2.2, page 190 for further information).

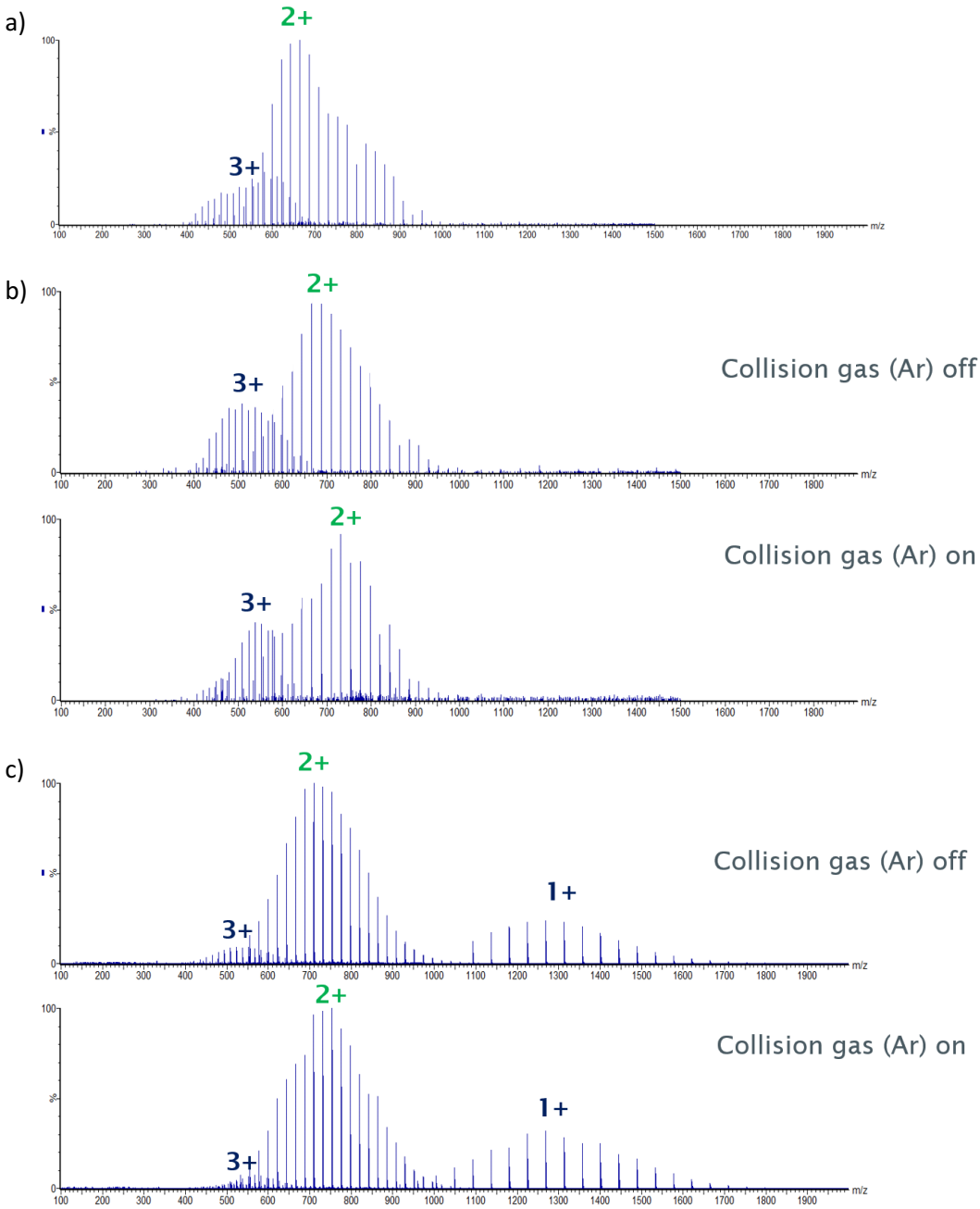

Figure 182. Evaluation of the effect of the mass analyser ion transmission and collision gas in the mass spectra of PEG 1450: a) Q: beam mass analyser without collision gas Q, b) QqQ: beam mass analyser with collision gas QqQ, and c) QToF: pulsed mass analyser with collision gas

When comparing mass analysers, both with a beam design (Figure 182 a Q *vs* Figure 182 b QqQ), the effect of the collision gas was observed. Even with the collision gas set to off in the QqQ, low levels of the remaining gas in the ion path caused charge stripping and a degree of uncontrolled CID of the ammoniated molecules; however, increased ion count was noticed (*ca.* 50%). When comparing mass analysers, one with a beam design (Figure 182 b QqQ) and one with a pulse design (Figure 182 c QToF pulsed), the shifting toward lower charge states in the QToF resulted from the change in the ion path and the longer distance that the ion beam travels.

The Q cannot resolve the $^{12}C/^{13}C$ isotopic distribution for highly charged species of the oligomers (resolving power SQD 2 is a unit *vs* 10,000 for the Synapt™ QToF), involving that the ion count for ions of these oligomers can vary from ions of oligomers with lower MW, where the isotopic distribution is resolved. This phenomenon was associated to the formation of different charged states varies based on the oligomer chain length (Figure 183), as discussed in section 3.5, page 142, and it is affected by the scan line rate of the Q.

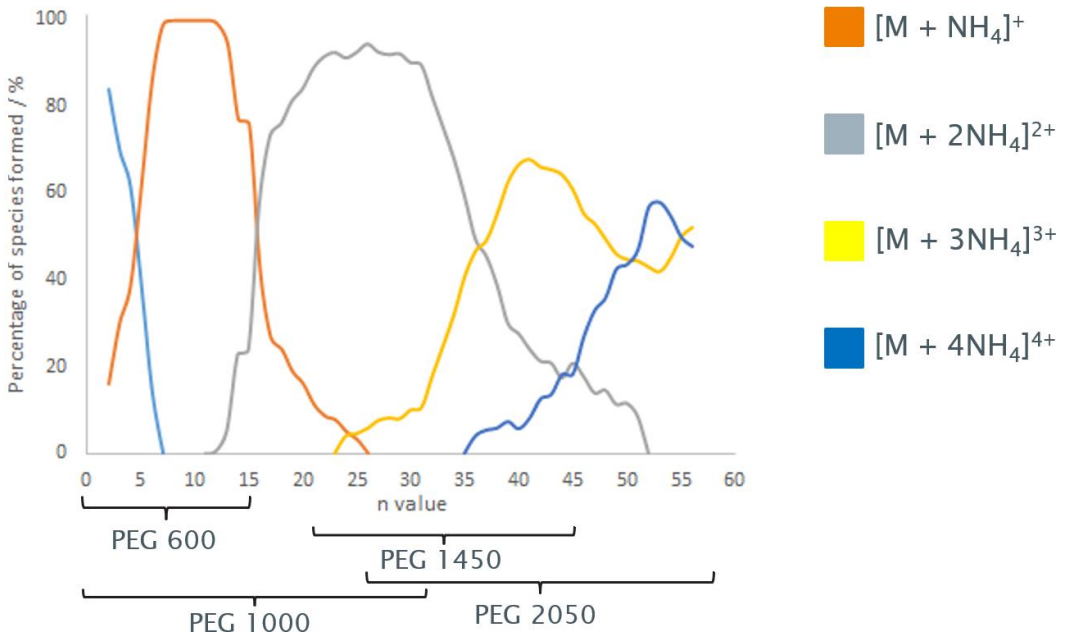

Figure 183. Ionisation current trends of different ionisation events of alcohol PEG oligomers. Data acquired using UHPSFC positive ion ESI Q MS and mixture of 50 µg/mL in CH_3CN (per component) of PEG 600, 1000, 1450 and 2000

It is worth remembering that the difference in the $^{12}C/^{13}C$ isotopic distribution for singly charged species is Δ*m/z* 1.0 *m/z* units, for doubly charged species Δ*m/z* 0.5 *m/z* units, for triply charged species is Δ*m/z* 0.33 *m/z* units, *etc.* When using the Q, singly charged species of the $^{12}C/^{13}C$ isotopic distribution were fully resolved. The resolution of the doubly charged species was differentiated depending on the oligomer *m/z* value (*i.e.*, the scan rate line), whilst higher charges species showed an unresolved isotopic distribution. Conversely, the QToF can resolve up to Δ*m/z* 0.0001 *m/z* units (resolving power 10,000), meaning that the $^{12}C/^{13}C$ isotopic distributions were resolved no matter the observed charged state.

The low-mass resolution (LM) and the high-mass resolution (HM) values of the Q were varied to improve the $^{12}C/^{13}C$ isotopic distribution resolution for the doubly charged species and improve the deconvoluted traces obtained to improve polymer quantitation. LM and HM are Waters® vendor-specific values, and these set the resolving DC on the Qs, involving that at LM=HM=15, the unit resolution is achieved at 20% peak height. These values relate to the slope (HM) and the y-offset (LM) of the scan line rate of the Q; as such, modifying these values moves the scan line away from the stability region of the Matthieu diagram of the Q, changing the ion response (sensitivity) if the scan line leverage down with a compromise in the mass resolution (see section 1.5.3.3.1, page 77). Examples of how these parameters affect the mass spectra are shown in Figure 184. Increasing HM (Figure 184 a) significantly decreased sensitivity and did not improve the mass resolution between ions, while decreasing HM led to a similar mass resolution. Increasing or decreasing LM (Figure 184 b) showed improvements in the sensitivity as a sacrifice in the mass resolution. The modification of HM or LM did not benefit the mass resolution between ions and suggested that the optimal values were LM 14 and HM 16, leading to an ion separation of up to 0.5 *m/z* units apart.

a)

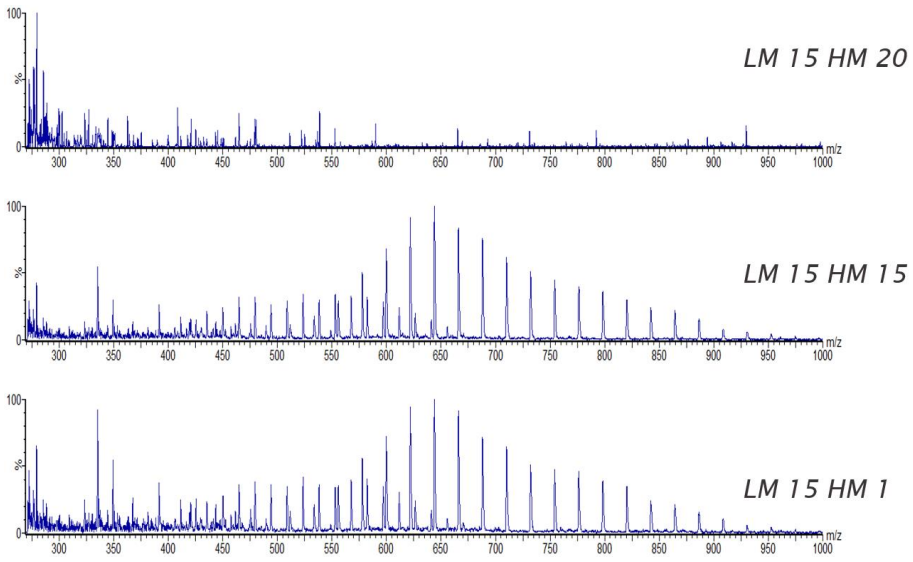

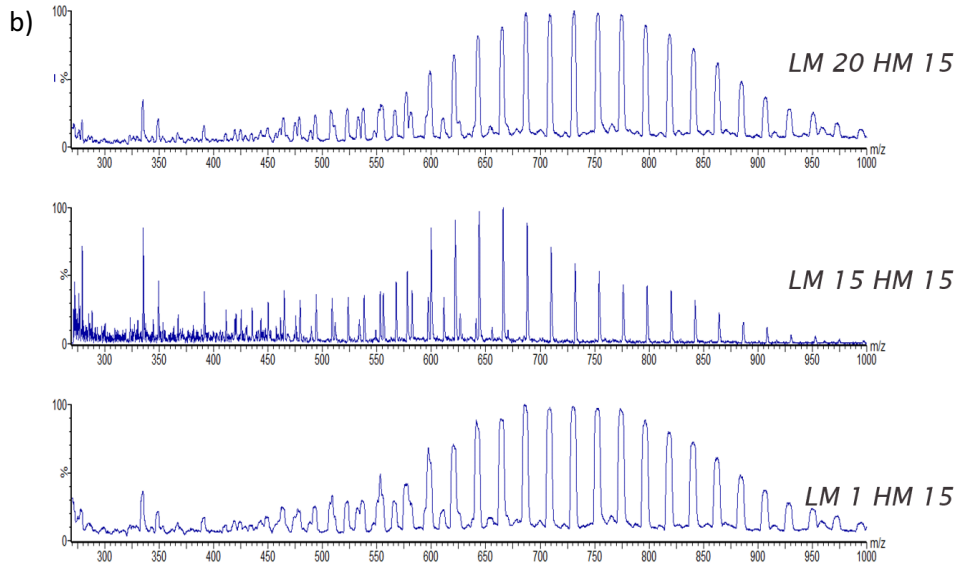

Figure 184. UHPSFC positive ion Q MS. Mass spectra. 100 µg/mL PEG 1450 in CH_3CN. Effect of a) HM, and b) LM in the sensitivity and resolving power of the Q mass analyser

The differences in the resolving power of the $^{12}C/^{13}C$ isotopic distribution of multiply charged species between both mass analysers required conversion of the Transform™ deconvoluted traces to allow comparison. Two data treatment procedures were applied: (i) changing the x-axis from the MW scale to the n value scale and (ii) re-scaling the response of the Transform™ deconvoluted traces. The first data treatment consisted in changing the mass scale of the *x*-axis from the MW scale to the n value scale. The redrawn figure (Figure 185 b) is equivalent to the deconvoluted traces previously shown (Figure 185 a). The second data treatment is related to the differences in the S/N between the designs, with a higher sensitivity observed in the QToF.

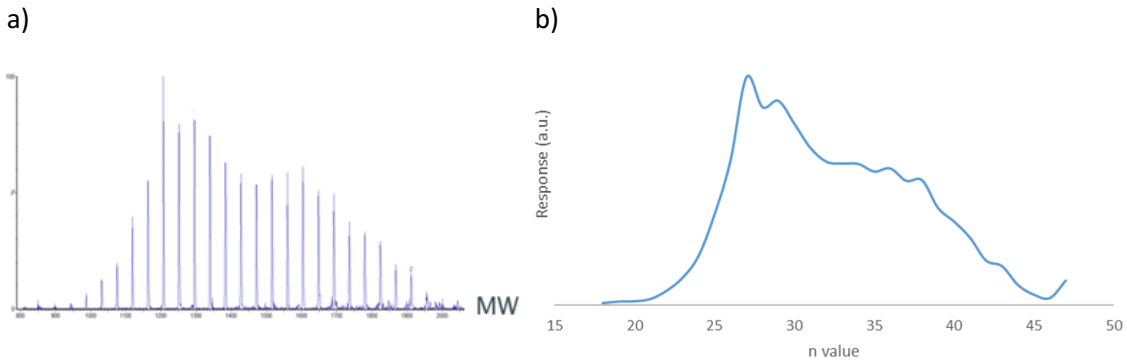

Figure 185. Simplification of the deconvolution trace of PEG 1450 to allow data analysis comparison between mass analysers. The response of the Q was increased by a factor corresponding to the relative differences between the oligomer intensity of the most intense oligomer in each deconvoluted trace

The redrawn deconvoluted traces were superposed (Figure 186), with the curves in blue curve relating to the Q Transform™ response and the orange curve relating to the QToF Transform™ response. The apparent deconvoluted traces between both mass analysers were associated with the resolving power $^{12}C/^{13}C$ isotopic distribution of Q and how the charge state of the ions affects the separation of the $^{12}C/^{13}C$ isotopic distribution.

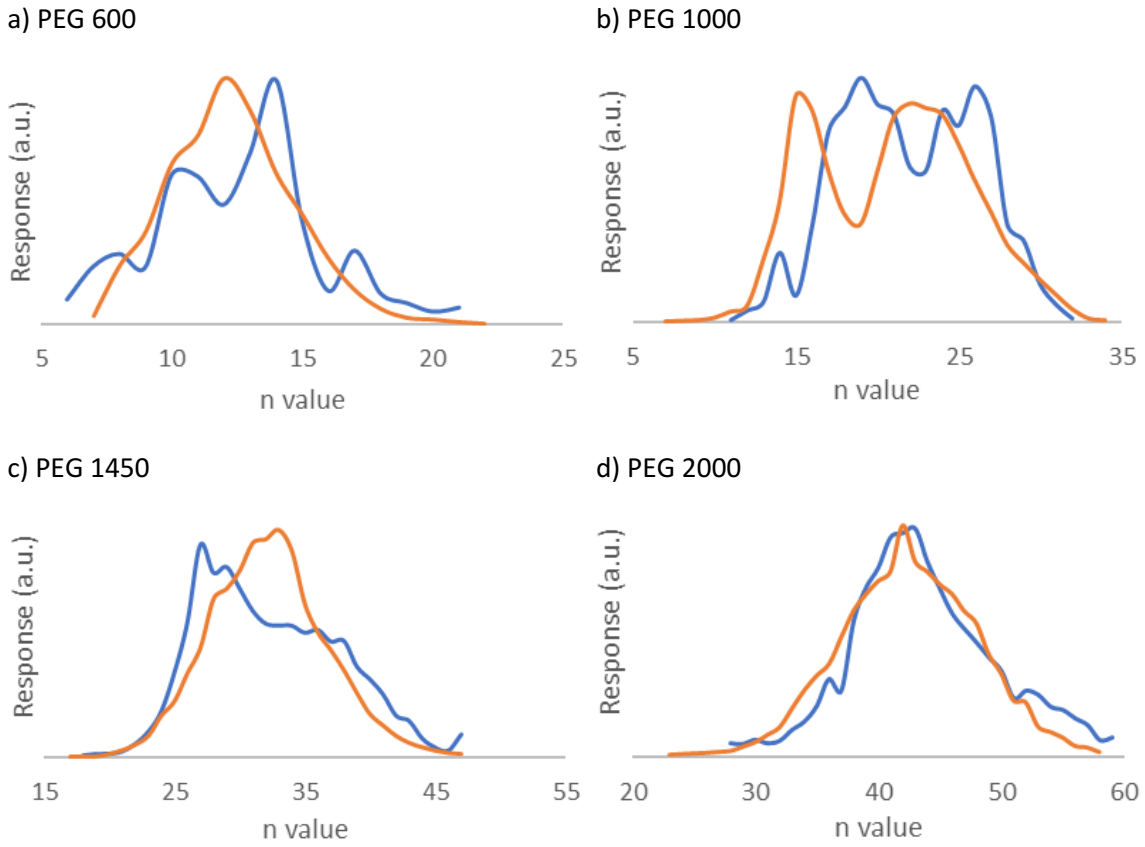

Figure 186. UHPSFC positive ESI MS. PEG 600, 1000, 1450 and 2000. Comparison of the mass spectra deconvolution traces of a) PEG 600, b) PEG 1000, c) PEG 1450, and d) PEG 2000 when using the Q (blue) and QToF (orange) mass analysers. Note that the Q mass analyser response was adjusted to align the graphs based on sensitivity and concentration differences

The deconvoluted traces were compared to the proposed visual representations of the relative contribution of each charged state to the polymer response (Figure 187; discussed in section 3.5, page 142) to allow an understanding of the influence of the resolving power $^{12}C/^{13}C$ isotopic distribution based on the polymer MW.

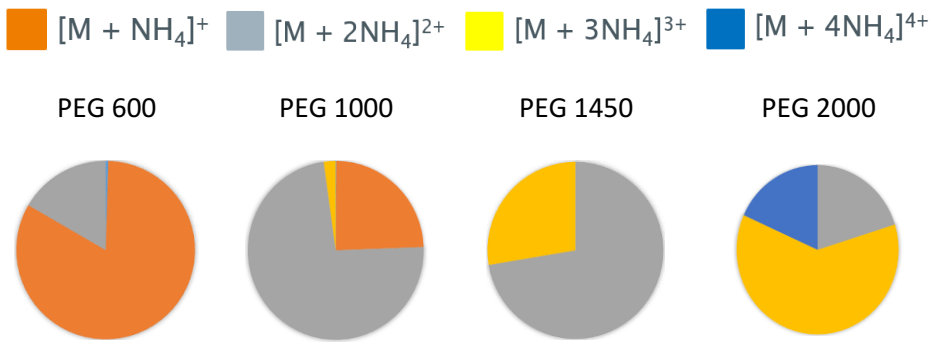

Figure 187. UHPSFC positive ion ESI Q MS. PEG 600, 1000, 1450 and 2000. Ionisation current trends when using the Q mass analyser

As discussed previously, the resolving power of the Q mass analyser mainly affects the $^{12}C/^{13}C$ isotopic distribution of the doubly charged species. When evaluating Figure 186 and Figure 187 and Figure 196, the significant contribution of the doubly charged species (grey area) highlighted the abnormal features observed in the deconvolution traces (Figure 186), affecting oligomers that ionise towards doubly charged species (Figure 183). For PEG 1000 and 1450 (Figure 186 b and c), the presence of doubly charge state species was significant (Figure 187, > 75%), whilst for PEG 600 and 2000 (Figure 186 a and d), their presence is smaller (Figure 187 < 25%); however, the higher amount of background ions in the *m/z* range 100-1000 led to the highest differences in the deconvoluted traces of PEG 600.

The differences in the resolution of the $^{12}C/^{13}C$ isotopic distribution between mass analysers showed the higher similarity of the deconvoluted trace when using the QToF to the typical Gaussian-type distribution of polymers. For beam instrumentation such as Q mass analysers, the scan rate and duty cycle of modern instrumentation are fast (typically 15-20,000 *m/z* units per second) and can deliver the appropriate number of scans across an SFC peak to give a truly representative peak profile; this with the caveat of the scan rate being *m/z* range dependent. Note here that the isotopic information of measured ions may be compromised at very fast scan rates (approaching their theoretical limit). The QToF pulsed ion beam instrumentation provided similar quantitation to the one obtained using the Q with the advantage of the high resolution resulting in the confidence of up to 4 decimal places in the *m/z* value allowing to postulate chemical formulae.

5.4.2 Effect on the quantitation and polydispersity

The quantitation capacity of the QToF was compared to the Q using the LDR and R^2 (Table 55). The QToF led to a significant improvement in sensitivity and a narrower LDR, with an improved

coefficient of variance (CV 9% for Q *vs* 5% for QToF, without ISTD). The improved sensitivity in the QToF was associated with a larger hole in the sampling cone and the step wave located in the Synapt G2-*Si*, resulting in improved LDR values. The dimensions of the sampling cones are 0.50 mm in the Waters® ZSpray® ESI source of the Waters® SQD 2 and 0.80 mm in the Waters® ZSpray® ESI source of the Waters® Synapt G2-*Si*. The sampling cone hole was 2.56-times larger in the QToF, which led to an increased ion transmission entering into the mass analyser.

Deconvolution approach	**Mass analyser**		**PEG 600**	**PEG 1000**	**PEG 1450**	**PEG 2000**
Surrogate oligomer	Q	LDR (µg/mL)	1-75	5-130	5-150	10-300
		R^2	0.9958	0.9994	0.9983	0.9957
	QToF	LDR (µg/mL)	0.5-25	1-50	1-60	5-75
		R^2	0.9997	0.9999	0.9995	0.9995
Whole distribution	Q	LDR (µg/mL)	1-75	10-200	50-300	100-500
		R^2	0.9958	0.9994	0.9983	0.9957
	QToF	LDR (µg/mL)	0.5-25	1-50	1-60	5-75
		R^2	0.9997	0.9998	0.9993	0.9992

Table 55. Effect of the mass analyser (Q and QToF) in the quantitation, compared based on the LDR and R^2

Figure 188 and Figure 189 show examples of these improvements for PEG 600. The reader is referred to Appendix B for the calibration curves of the other PEGs.

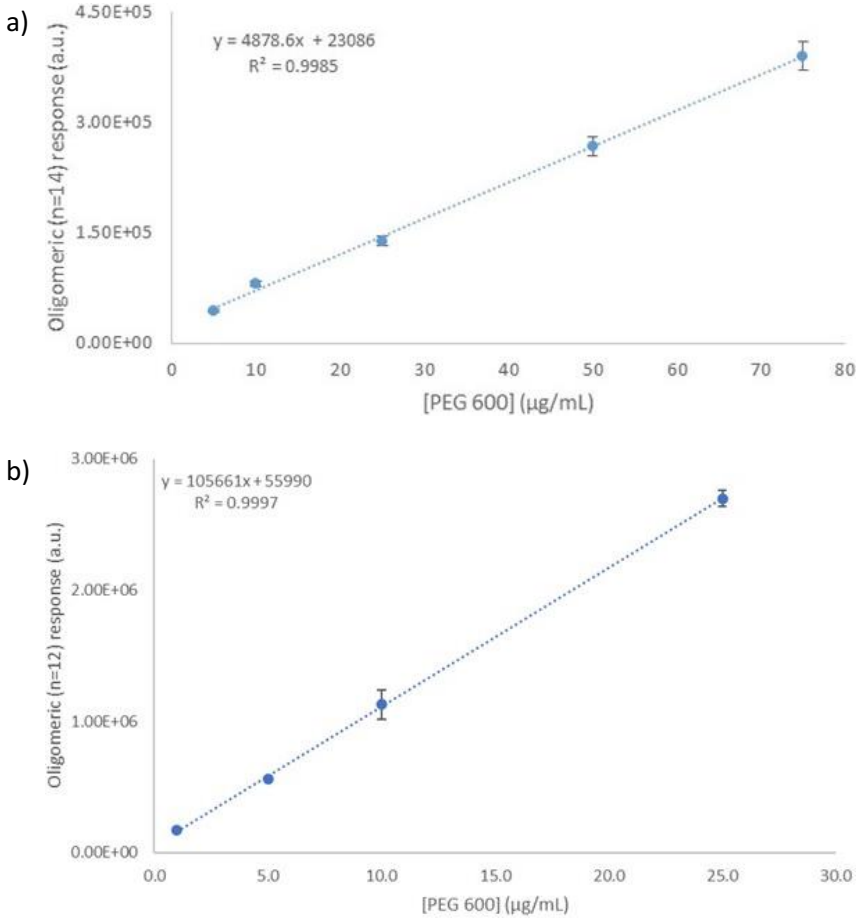

Figure 188. Examples of calibration curves of PEG 600 using deconvolution approaches of a surrogate oligomer. Effect of the mass analyser: a) Q, b) QToF (samples analysed in triplicates, the error bars correspond to 1 stdev)

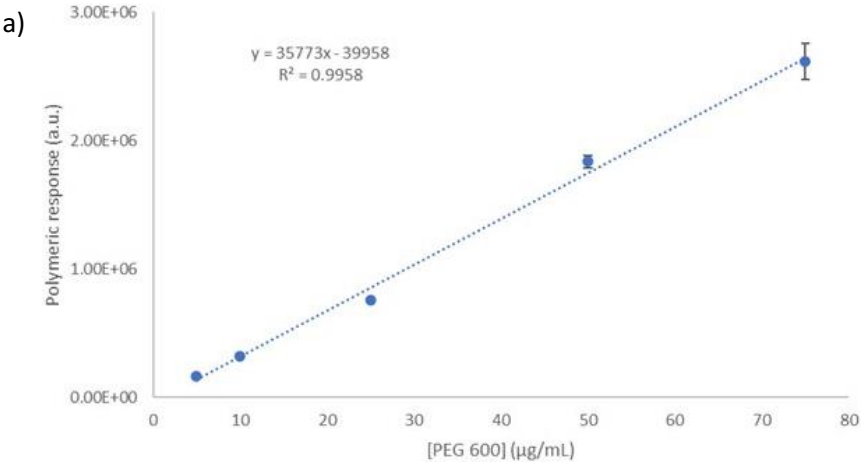

b)

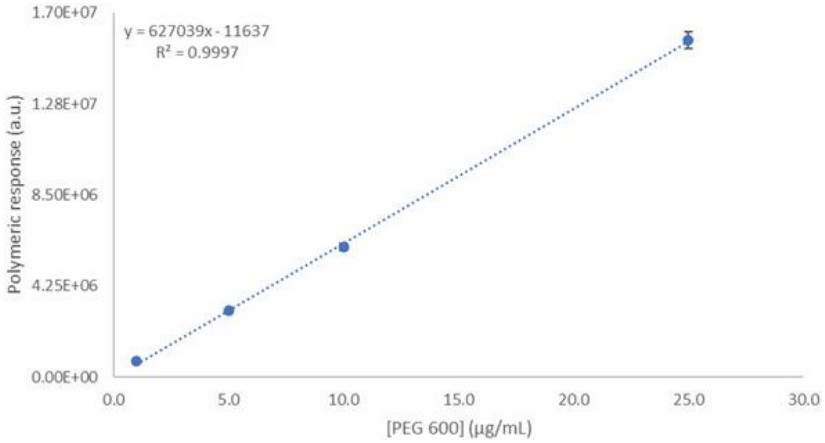

Figure 189. Examples of calibration curves of PEG 600 using deconvolution approaches of the whole distribution. Effect of the mass analyser: a) Q, and b) QToF (samples analysed in triplicates, the error bars correspond to 1 stdev)

When comparing data processing of the different approaches (Table 56), data processing time increased due to the larger size of QToF data files due to the acquisition of high-resolution data.

	Approach	**Data processing time per sample (min)**
Surrogate oligomer	Q	1
	QToF	3
Whole distribution	Q	20
	QToF	60

Table 56. Comparison of the effect of the mass analyser on the data processing time for external calibration quantitation

Similarly, the comparison of the experimental values of M_n, M_w and PDI acquired using the Q and the QToF were highly similar to the values reported by the manufacturer using gel permeation chromatography and highlighted the validity of the method for PEG quantitation (Table 57). Although differences were observed in the deconvoluted traces, both mass analysers resulted in accurate and precise values of M_n, M_w and PDI in the range of those reported by the manufacturer. It is worth reporting that the lack of resolving power in the Q did not significantly impact the obtained values, and still, both approaches showed very high R^2 values, independently of the mass analyser.

PEG 600	Experimental Q	Experimental QToF	Manufacturer
M_n	581 ± 1.5% (-1.5%)	581 ± 0.4% (-1.4%)	590
M_w	600 ± 1.5% (-1.3%)	602 ± 0.4% (-1.0%	609
PDI	1.033 ± 0.002	1.034 ± (0.001)	1.032
PEG 1000	**Experimental Q**	**Experimental QToF**	**Manufacturer**
M_n	991 ± 1.7% (+1.0%)	982 ± 0.2% (-0.5%)	987
M_w	1027 ± 1.6% (+0.7%)	1015 ± 0.2% (-0.5%)	1020
PDI	1.036 ± 0.002	1.034 ± 0.001	1.033
PEG 1450	**Experimental Q**	**Experimental QToF**	**Manufacturer**
M_n	1437 ± 0.2% (-0.9%)	1440 ± 0.4% (-0.8%)	1451
M_w	1477 ± 0.2% (-0.9%)	1485 ± 0.4% (-0.4%	1491
PDI	1.028 ± 0.001	1.031 ± 0.001	1.028
PEG 2000	**Experimental Q**	**Experimental QToF**	**Manufacturer**
M_n	1944 ± 0.9% (-1.1%)	1954 ± 0.4% (-0.5%)	1965
M_w	1979 ± 1.1% (-1.4%)	1995 ± 0.4% (-0.6%)	2007
PDI	1.018 ± 0.001	1.020 ± 0.001	1.021

Table 57. Comparison of the effect of the mass analyser (Q *vs* QToF) in the M_n, M_w and PDI of different PEGs as obtained using UHPSFC positive ESI MS and 0.5 µg/mL (Q) and 0.2 µg/mL (QToF) of 18-crown-6 in acetonitrile. Samples analysed in triplicates. The error corresponds to 1 stdev. Manufacturer values acquired using SEC

5.5 Evaluation of an internal standard for quantitation

In quantitative analysis, internal standards (ISTD) are added at a constant concentration to all standards, blanks, controls, and unknown solutions to account for variations occurring during the sample preparation and compensate for injection irreproducibility or retention time drifts that may occur. The response is represented related to the amount of ISTD added (Equation 42). The ISTD must not be present in the sample and must have a defined purity and give a reliable MS

response without interfering with the analysis (no ionisation enhancement or suppression). Two criteria are used for selecting an ISTD: (i) the ISTD must not be present in the sample, and (ii) the ISTD must have similarities in the molecular structure with the analyte, especially when analysing using MS. Using PEGs or PPGs is impractical due to their presence as excipients or impurities in the formulation. Using other polymers is impractical due to the complexity added to the analysis and the intrinsic differences in PDI, resulting in less robust quantitation methods. Chen and He reported some of these challenges [151].

$$Response\ ratio = \frac{Peak\ area_{Analyte}}{Peak\ area_{ISTD}}$$ Equation 42

The resemblance of crown ethers to cyclic PEGs suggests that these molecules could be used as a monodispersed ISTD. These molecules were designed to capture cations selectively: 12-crown-4 for Li^+, 15-crown-5 for Na^+ and 18-crown-6 for K^+. Studies found that 18-crown-6 can bind to ammonium salts, especially in CH_3OH or CH_3CH_2OH media [386, 387]. Still, size similarities of the Na^+ and NH_4^+ cations suggested that 15-crown-5 should be more appropriate to capture NH_4^+ than 18-crown-6 (see Figure 190). These findings suggested that both 15-crown-5 and 18-crown-6 can be evaluated as possible candidates as ISTD for this quantitation.

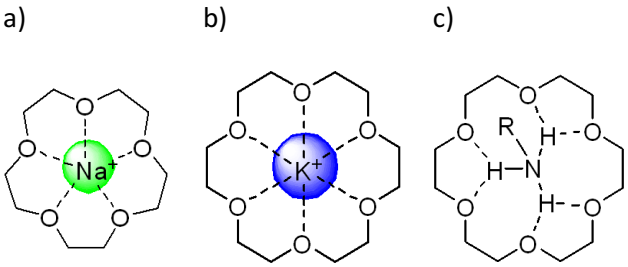

Figure 190. Crown ethers evaluated in this research and their chelation to different cations: a) 15-crown-5 for Na^+, b) 18-crown-6 for K^+, and c) 18-crown-6 for NH_4^+

The chromatographic peak shape was symmetric for both crown ethers (Figure 191 a); however, selective ionisation was only achieved for 18-crown-6 (Figure 191 b), resulting in designating this crown ether as the ISTD for this quantitation.

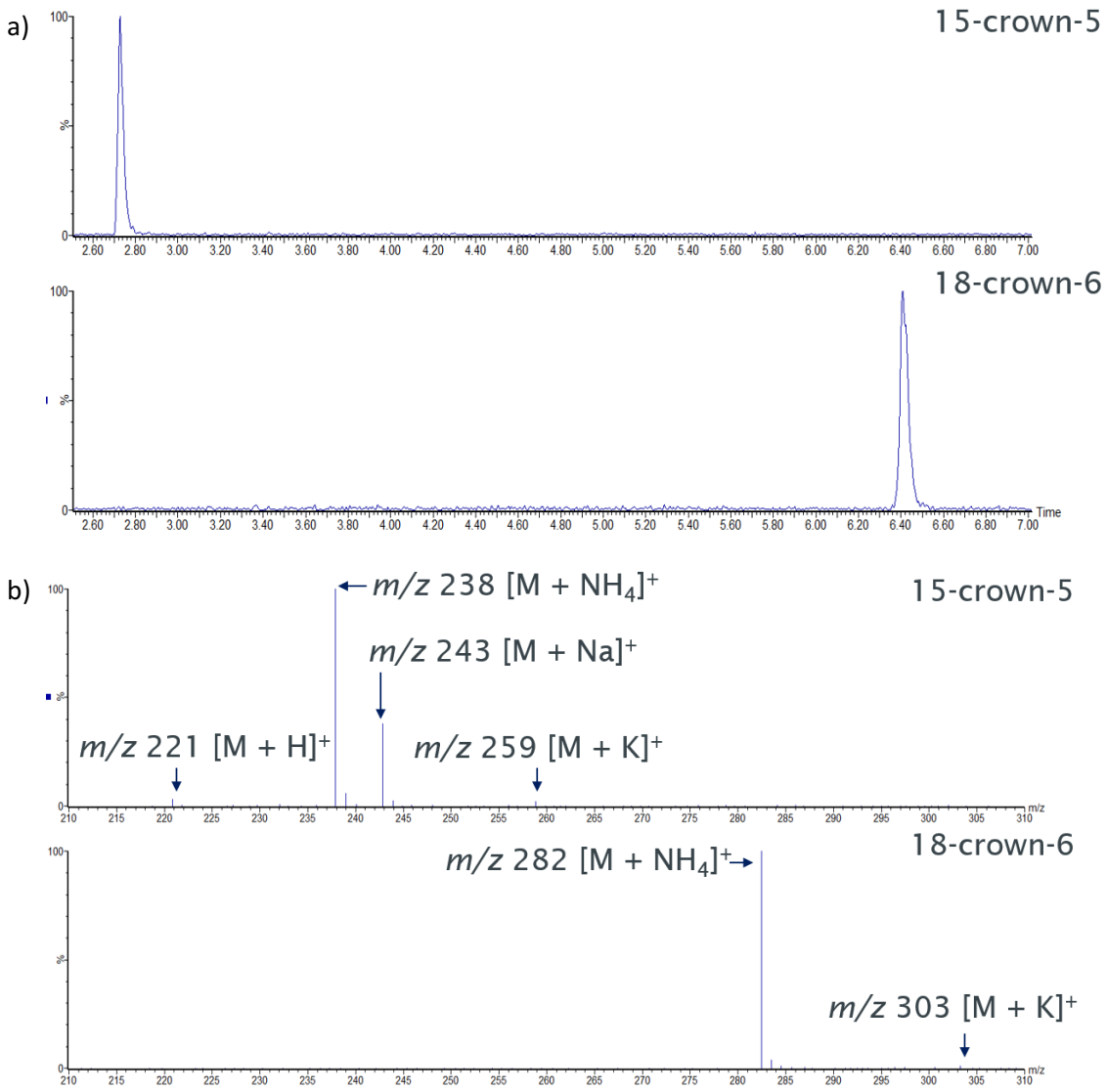

Figure 191. UHPSFC positive ion ESI Q MS. 50 µg/mL 15-crown 5 (*m/z* 238) and 18-crown-6 (*m/z* 282) in CH_3CN: a) BPICC, and b) mass spectra

The calibration curve for 18-crown-6 showed a linear response in a concentration range of *ca.* 0.1-20 µg/mL (Figure 192,. A final ISTD concentration of 0.5 µg/mL (S/N 12) was selected as the peak area response was in the lower 1/3 region of the working standard curve of PEG 1000.

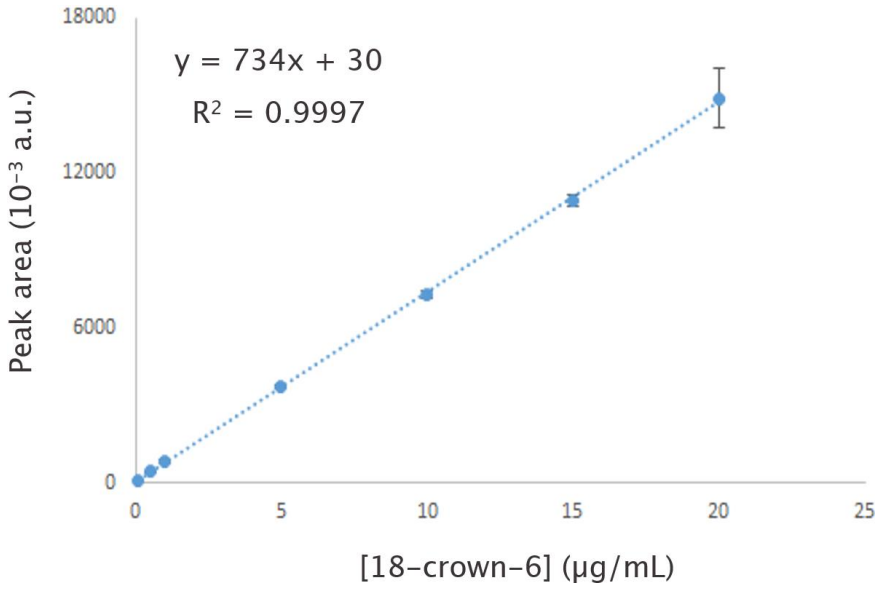

Figure 192. Linear range scoping for 18-crown-6 using UHPSFC positive ion ESI Q MS (samples analysed in triplicates, the error bars correspond to 1 stdev)

PEG 1000 was selected to evaluate the ion suppression produced by the ISTD due to a co-elution observed (Figure 193) between 18-crown-6 and the PEG oligomer with 14 repeating units (P14). The co-elution suggested that 18-crown-6 could affect the oligomer ionisation, or vice versa, resulting in an error in calculating M_n, M_w and PDI.

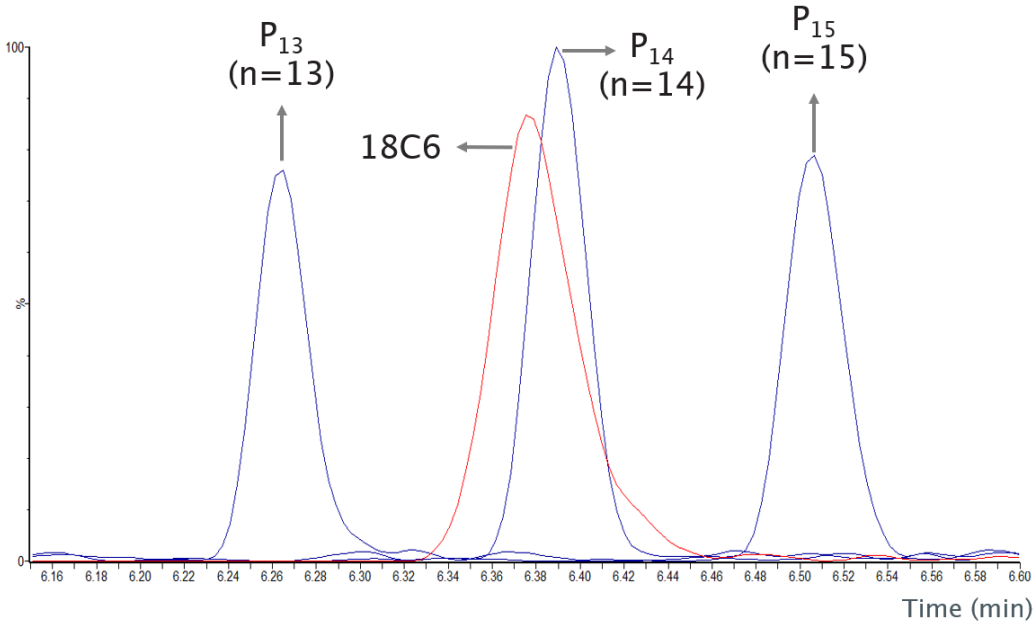

Figure 193. UHPSFC positive ion ESI Q MS. BPICC. 50 µg/mL PEG 1000 + 0.5 µg/mL 18-crown-6 (18C6) in CH_3CN. Co-elution between the ISTD and the oligomer P_{14} of PEG 1000

Different samples in CH_3CN containing 50 µg/mL PEG 1000, 0.5 µg/mL of 18-crown-6, or both were tested to evaluate ion suppression. Analysis of the mixtures (Figure 194) showed ion suppression on the co-eluted oligomer (P_{14}) of *ca.* -13% with an enhanced response of the ISTD of *ca.* +11% (Figure 194 a). The matrix effects induced by the ISTD were insignificant when calculating M_n, M_w, and PDI (Figure 194 b) as only P_{14} partially co-elutes with the ISTD. These minor differences were associated with the baseline separation of the oligomers, as only one oligomer suffers the ion suppression. These low levels of signal suppression of P_{14} and the enhanced response of the ISTD suggest that finding an alternative ISTD that is well resolved from the polymeric distribution is required for the quantitation of more complex PEG mixtures.

a)

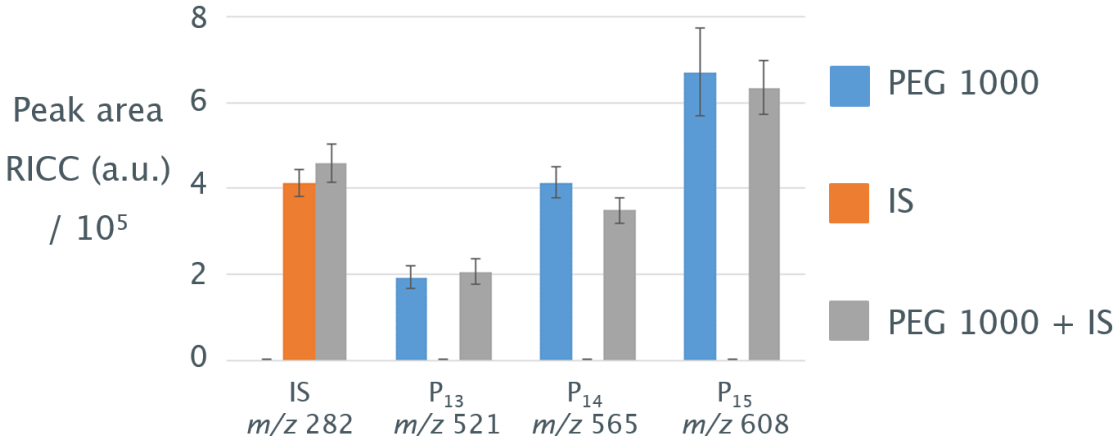

b)

PEG 1000	Experimental without ISTD	Experimental with ISTD	Manufacturer
M_n	991 ± 1.7% (+1.0%)	983 ± 0.2% (-0.4%)	987
M_w	1027 ± 1.6% (+0.7%)	1017 ± 0.2% (-0.3%)	1020
PDI	1.036 ± 0.002	1.034 ± 0.001	1.033

Figure 194. Evaluation of the interference produced by the ISTD in the response of PEG 1000. 50 µg/mL PEG 1000 + 0.5 µg/mL 18-crown-6 in CH_3CN. a) Evaluation of the matrix effect based on the peak area. b) Effect of introducing the ISTD when calculating M_n, M_w and PDI. Samples analysed in triplicates. The error correspond to 1 stdev

The use of the ISTD improved R^2 values from 0.998 to 0.999 and the precision of the analysis (measured as the coefficient of variation (CV)) from 10% to 4%, independently of the approach. Figure 195 shows an example of these improvements for PEG 600. The reader is referred to Appendix B for the calibration curves of the other PEGs.

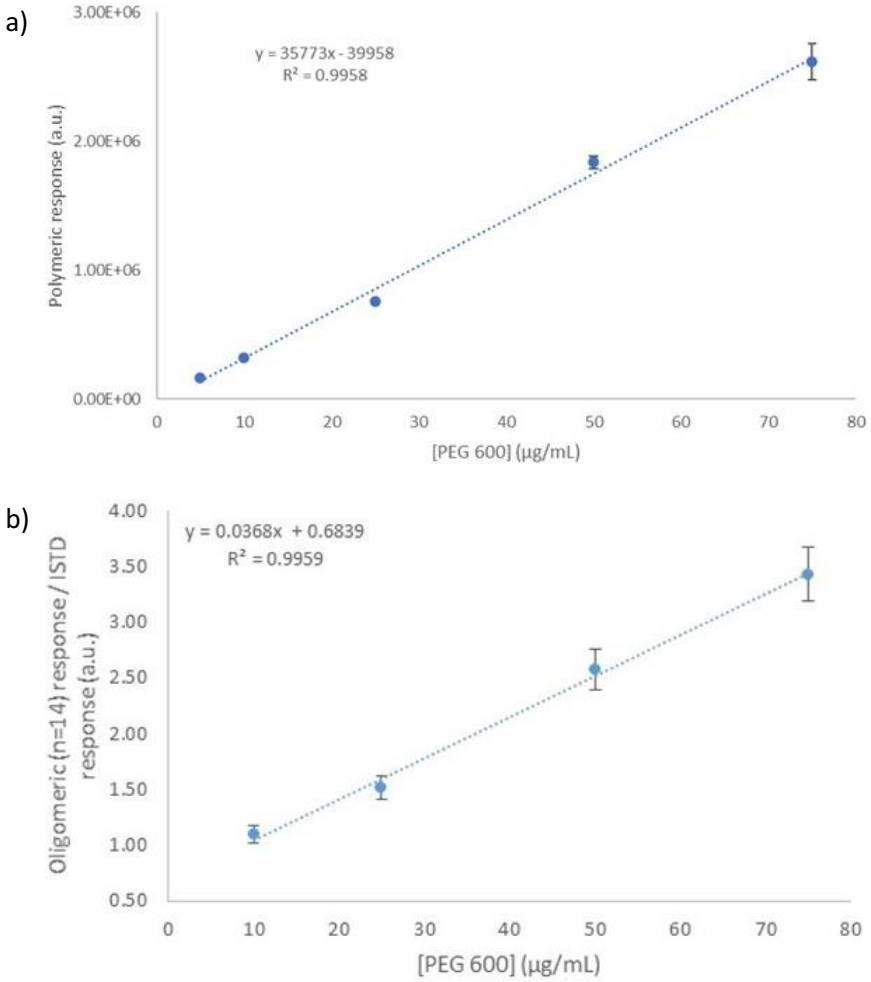

Figure 195. Effect of the ISTD of 18-crown-6 in the calibration curve of PEG 600. a) External calibration, and b) Internal calibration (samples analysed in triplicates, the error bars correspond to 1 stdev)

5.6 Final chapter remarks

This chapter focused on developing a deconvolution approach for polymer analysis and its use to quantify key quality parameters of PEGs: the number average (M_n) and weight average (M_w) MWs and the polydispersity (PDI). The different quantitative approaches resulted in the first work where polymer quantitation can be achieved using deconvolution of the oligomer mass spectra. Using the Waters® Transform™ algorithm resulted in faster data processing than using the standard sum of all RICCs. If this algorithm could be executed using Scripting software, then even a higher data processing speed may be achieved, making it better suited for quality control or high throughput environments. The deconvolution approach was less prone to human errors

since fewer processing steps were used. However, further investigation of the background ions is required to avoid artefacts and quantify more complex PEG polymers (*i.e.*, Tween® 80).

The intercomparison study showed that the mass analyser and data acquisition modes were critical factors for quantitation. For beam instrumentation such as Q mass analysers, the scan rate and duty cycle of modern instrumentation are fast (typically 15-20,000 *m/z* units per second) and can deliver the appropriate number of scans across the SFC peak to give a truly representative peak profile, this with the caveat of the scan rate being *m/z* range dependent. Note that the isotopic information of measured ions may be compromised at very fast scan rates (approaching their theoretical limit). Whilst SIM achieved improved detection limits, the data is targeted and only records data for known species, so revisiting data to search for other species is impossible. QToF instrumentation, a pulsed ion beam, delivers high-resolution mass measurements, and because there is no *m/z* scan, all the ions are recorded simultaneously. The result is that the high-resolution capability allows for nominally isobaric species to be separated. Further, ions can be measured accurately, typically to the 4th place decimal, allowing possible chemical formulae to be postulated for the ion. The ion identification is further enhanced by comparing the measured and theoretical isotope patterns.

Alternative algorithms were recently developed to transform centroid into profile data and vice versa. Their development is crucial when implementing high-resolution mass analysers into routine quality control environments. Even though there are challenges using the Q mass analyser related to the resolution of multiply charged species, the quantitation capabilities of both Q and QToF mass analysers were similar to the manufacturer values of M_n, M_w and PDI. Using a QqQ could be a reasonable intermediate cost-effective alternative between mass analysers for PEG mixtures with low complexity; however, the use of a QToF is highly recommended for complex mixtures such as Tween® 80.

Additionally, the precision of the analysis was improved when using a monodispersed ISTD such as 18-crown-6, which, due to the baseline resolution of the oligomers, did not compromise M_n, M_w or PDI calculations. However, the low level of ion suppression observed suggests the need to find an alternative monodisperse ISTD that elutes at higher percentages of organic solvent (higher than 30%), especially when quantifying complex PEG mixtures.

From these observations, the following quantitation protocol was proposed (Figure 196):

- Prepare calibration solutions of PEG 600, 1000, 1450 and 2000 with the addition of 0.5 µg/mL final concentration of 18-crown-6 (when analysed using a Q)

- Analyse the samples using UHPSFC positive ESI Q MS or QToF MS without collision gas
- Obtain the base peak ion current chromatogram. Obtain the mass spectra of the polymeric distribution, and apply deconvolution using the Transform™ algorithm
- Calculate M_n, M_w and PDI values from the deconvoluted spectra by using the *m/z*, *i.e.*, MW of the oligomers and the deconvoluted oligomer response
- Sum all the deconvoluted oligomer responses from the deconvoluted spectra and use this value as the total polymer response at that specific concentration
- Divide the polymer response by the internal standard ion response, and use it to create the calibration curve

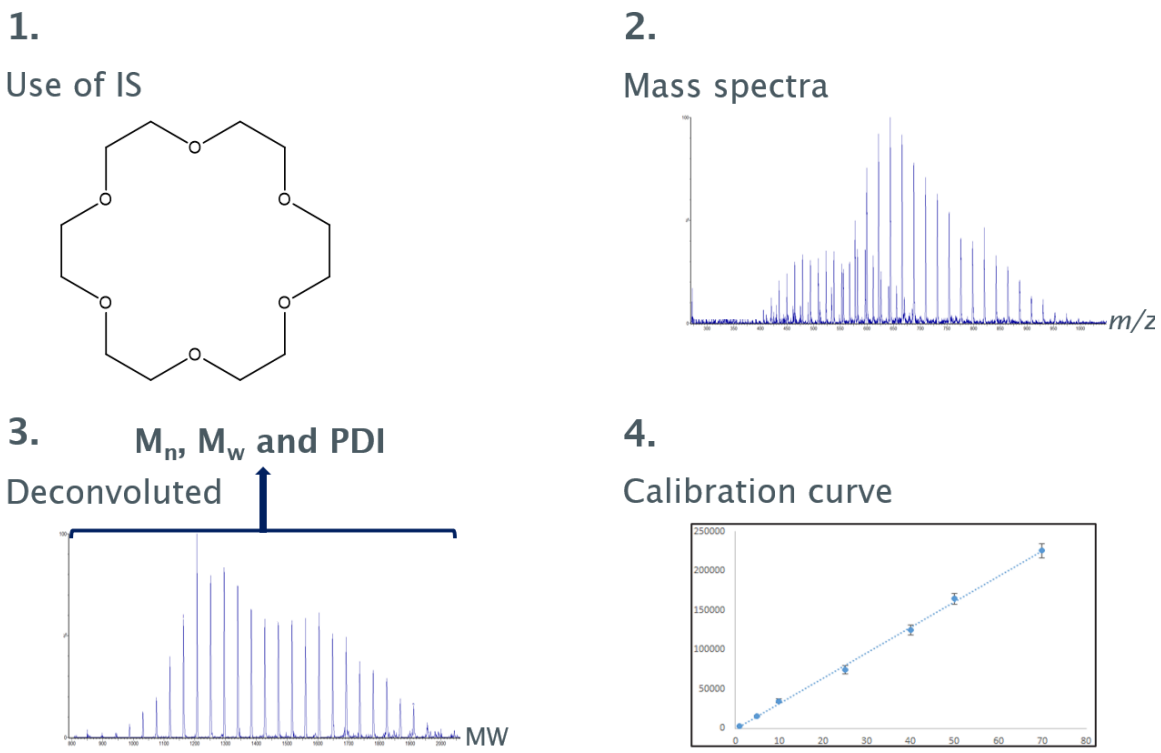

Figure 196. Proposed protocol for PEG quantitation using Transform™ deconvolution

Still, the current work did not explore the applicability of the developed quantitation approach for the complex PEGs used in this research. The presence of isobaric ions in the background was negligible in most cases and can be easily identified; however, analysis of complex PEGs requires careful examination when applying the deconvolution due to the presence of multiple isobaric ions (e.g., Tween® 80). Even though further research is required, the deconvolution approach is likely to be applicable to other areas where polymer quantitation is needed, such as an alternative to the strategy developed by Lingaityte for the quantitation of methylene diphenyl diisocyanate oligomers or the calculation of the degree of substitution of cyclodextrins. Additionally, the current work did not explore the quantitation of low-level impurities, an important area of

research in any pharmaceutical formulation, especially in recent times with the concerns about a rare allergic reaction to PEG in specific individuals that might cause anaphylaxis [388]. The characterisation and quantitation of PEGs have become critical to accelerating the development of vaccines based on lipid nanoparticles (such as the CoViD-19 vaccine Comirnaty) or in oligonucleotide therapeutics that contain PEGs to improve delivery.

Chapter 6 Optimisation of the separation and ionisation of (2-hydroxypropyl)-β-cyclodextrins

6.1 Understanding the mass spectra

6.1.1 Evaluation of the direct infusion mass spectra

A direct infusion (DI) analysis of the 2HPBCD into the QToF MS source was performed to understand the ionisation behaviour of the molecule. The positive ion ESI mass spectrum (Figure 197) obtained showed that the 2HPBCD preferred the formation of sodiated singly, doubly and triply charged species $[M + nNa]^{n+}$. Similarly, the different ions observed with the same charged state alerted about the polymeric character of the molecule.

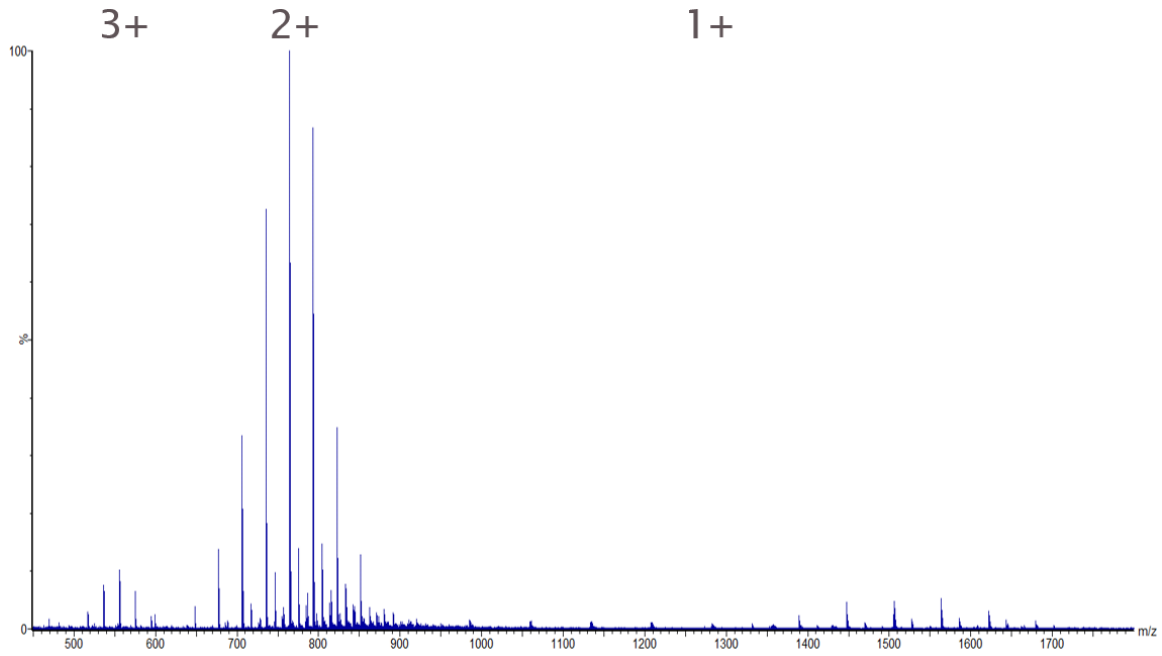

Figure 197. DI positive ion ESI QToF MS. Mass spectra. 10 µg/mL of 2HPBCD in H_2O. The formation of the multiply charged ions in the 2HPBCD are highlighted

A closer look at the singly charged region of the mass spectrum (Figure 198) suggested that the differences between ions corresponded to the molecular weight (MW) of the hydroxypropyl (HP) chain (58 Da) (Equation 43), *i.e.*, the 2HPBCD "oligomers" at specific DS within the central β-CD ring. The 21 positions of the cyclodextrin ring are randomly substituted, resulting in a 2HPBCD with different DS and several positional isomers for the same DS.

$$\Delta m/z = \frac{MW\ hydroxypropyl\ chain}{charge\ state\ (n)} = 58/n \qquad \text{Equation 43}$$

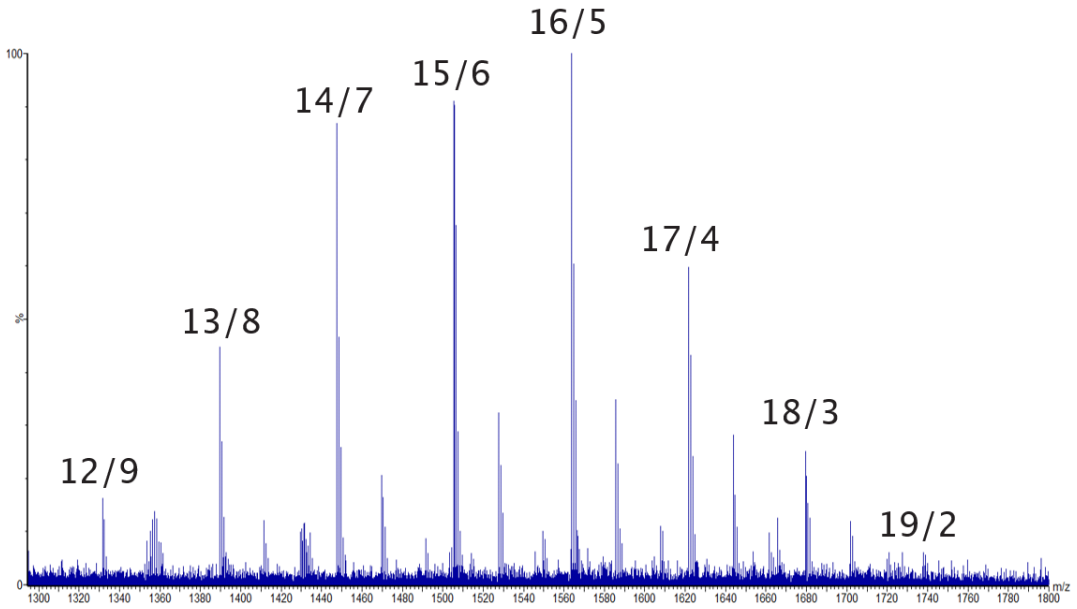

Figure 198. DI positive ion ESI QToF MS. Mass spectra. 10 µg/mL of 2HPBCD in H_2O. The degree of substitution of the singly charged area of the mass spectra showing the polymeric character. Oligomer ions were labelled based on the DS of the central β-CD ring. The first number corresponds to the number of positions substituted by the HP chain, and the second number is the amount of free hydroxy groups

The polymer mass spectra suggested that the ion formation was compromised by an excess presence of Na ions resulting in the formation of salts (Δ*m/z* 22 *m/z)* $[M + (n+x)Na – xH]^{n+}$ ions in the free hydroxy end groups (either in the OH-2, 3 or 6 from the 2HPBCD or the HP chain) (Figure 199). These were indicated in the mass spectra using the symbol $ throughout the chapter.

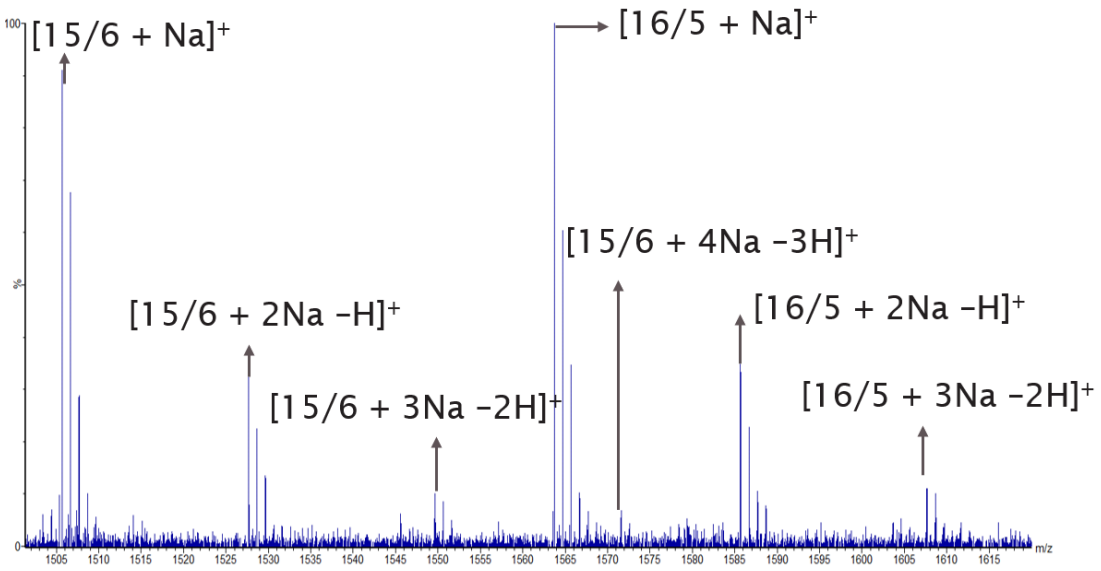

Figure 199. DI positive ion ESI QToF MS. Mass spectra. 10 µg/mL of 2HPBCD in H_2O. The formation of Na salts of 2HPBCD. An example is shown for singly charged species

6.1.2 Initial considerations of the analysis

6.1.2.1 Excessive retention and evaluation of the gradient elution

The analysis of the base peak ion current chromatogram (BPICC) when using a 5-40% gradient of co-solvent (Figure 200) showed a non-observation of the analyte when using different columns and suggested that 2HPBCD was either excessively retained or completely unretained on the stationary phase (SP). The elution of the analyte in bypass (injection in the chromatographic system but avoiding the column) suggested excessive retention. Subsequently, a gradient using 5-50% CH_3OH allowed the elution of the analyte.

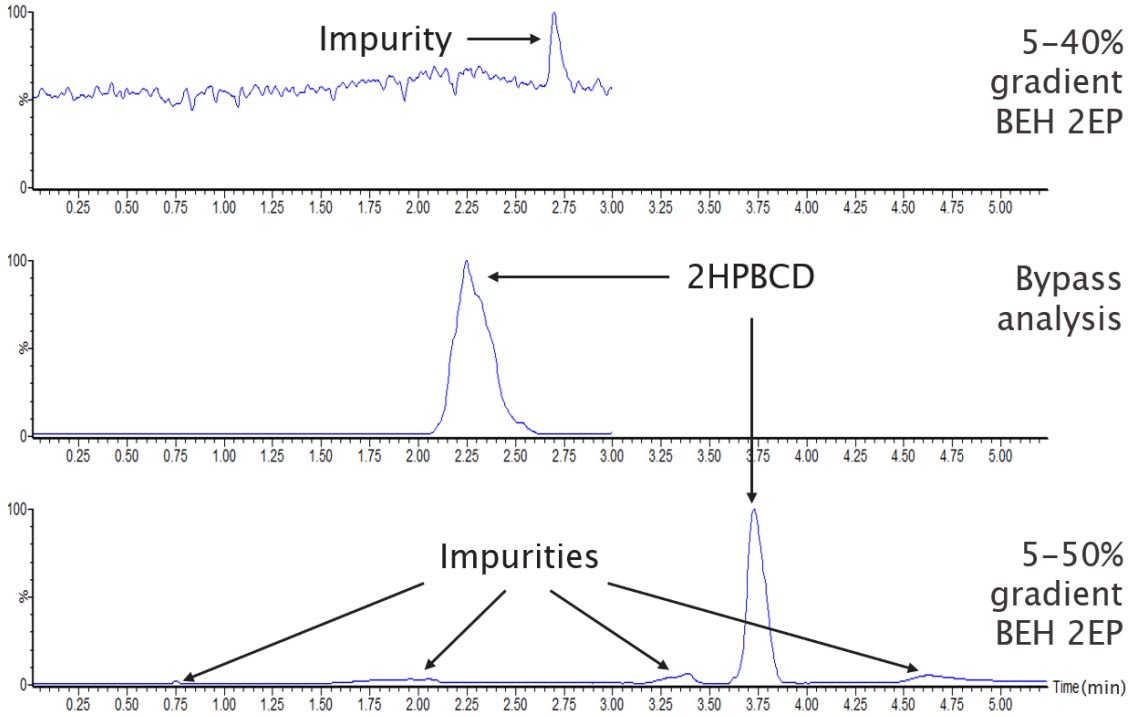

Figure 200. UHPSFC positive ion ESI QToF MS. BPICC. 1000 µg/mL in CH_3OH + 1% HCOOH. The requirement to increase the gradient percentage

6.1.2.2 Benefits of changing the mass analyser

The lower S/N observed when using the quadrupole (Q) or the triple quadrupole (TQD) mass analysers suggested that changing to the QToF mass analyser was beneficial. The data were visualised using ion maps through the MZmine software (described in detail in section 5.4, page 198). The higher background when using the Q (Figure 201 a) barely allowed the observation of the analyte. However, the higher sensitivity and inherent S/N when using the quadrupole time of flight mass analyser (QToF) facilitated the data analysis (Figure 201 b) due to a larger hole in the sampling cone and shifting of the ions formed to produce fewer charge states.

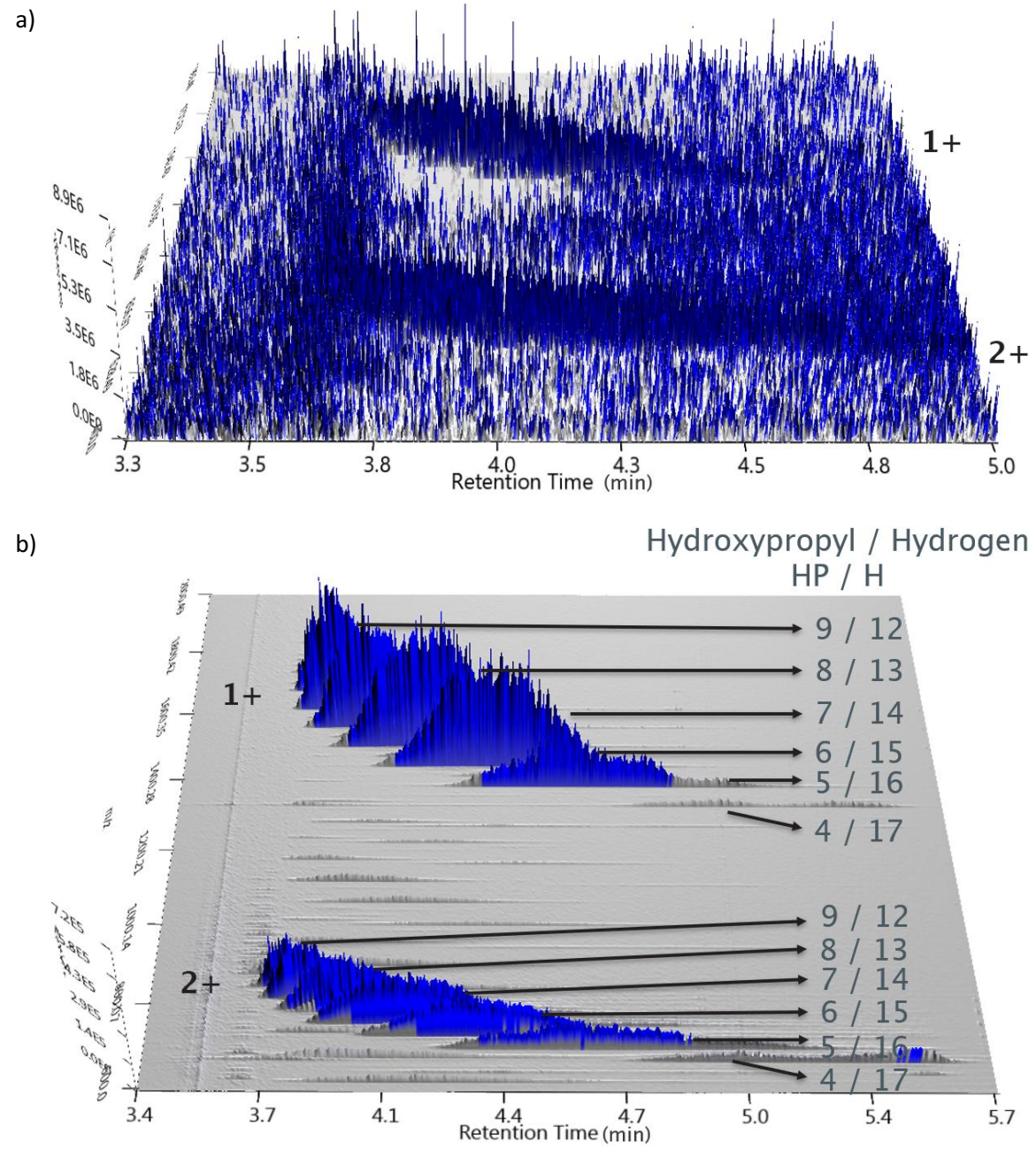

Figure 201. UHPSFC positive ion ESI MS. Ion map. Effect of the mass analyser in the ion map of 2HPBCD. a) Q 1000 µg/mL in CH_3OH + 1% HCOOH, b) QToF 100 µg/mL in CH_3OH + 1% HCOOH

6.2 Evaluation of the injection, mobile phase, and mass spectrometry make-up solvents

The higher tendency of CDs to capture Na^+ requires that the salt formation should be considered during the chromatographic method optimisation, as their formation compromises the S/N and

the calculation of the DS. Selective ionisation was therefore required to improve detection and increase the S/N. Accordingly, the optimisation of the mobile phase was investigated.

6.2.1 Evaluation of the injection and mass spectrometry make-up solvents

The lack of solubility of CDs in many organic solvents limits the selection of the sample diluent and co-solvent. An initial solubility test suggested that β-CD was soluble in H_2O whilst the 2HPBCD derivative was soluble in H_2O and CH_3OH, indicating that both solvents were plausible. Different injection solvents were tested to evaluate their impact on the peak shape. The addition of HCOOH was tested to minimise the formation of Na salts. The analysis of the chromatographic peak shape under the three solvents (Figure 202) showed that CH_3OH + 1% HCOOH provided the best results, and this solvent was selected.

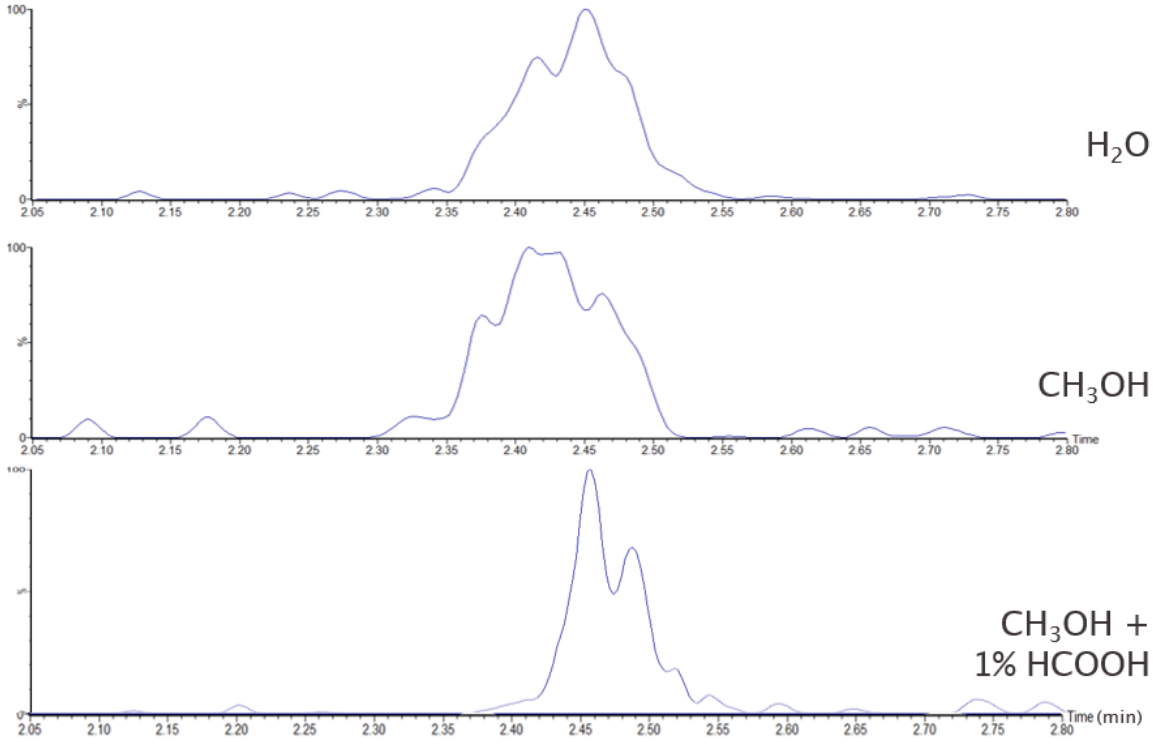

Figure 202. UPSFC positive ion ESI QToF MS. RICC (*m/z* 1448). 10 mg/mL 2HPBCD. Peak shapes when using three different injection solvents

Evaluation of the mass spectra when using make-up solvents (Figure 203) suggested that the salt formation compromised the coupling with UHPSFC due to the higher amount of Na^+ ions present within the system, suggesting the use of acidic make-up solvents. Similarly, the preference in the positive ion ESI MS ionisation of sugar-based molecules for Na^+, such as the β-CDs, involved that using ammonium salts was possible; however, basic mobile phases should promote the formation of Na salts. These valuations involved that acidic mobile phases and make-up solvents were required; however, a basic make-up solvent such as CH_3OH + 50 µM CH_3COONH_4 could be used

when other molecules prefer the ionisation towards ammoniation due to the low impact in the mass spectra of the 2HPBCD (Figure 203). At the same time, make-up solvents based on salts of Na such as HCOONa should be avoided due to a higher formation of Na salts of the 2HPBCD. As a result, the selection of CH_3OH + 1% HCOOH as the injection and the make-up solvents is recommended.

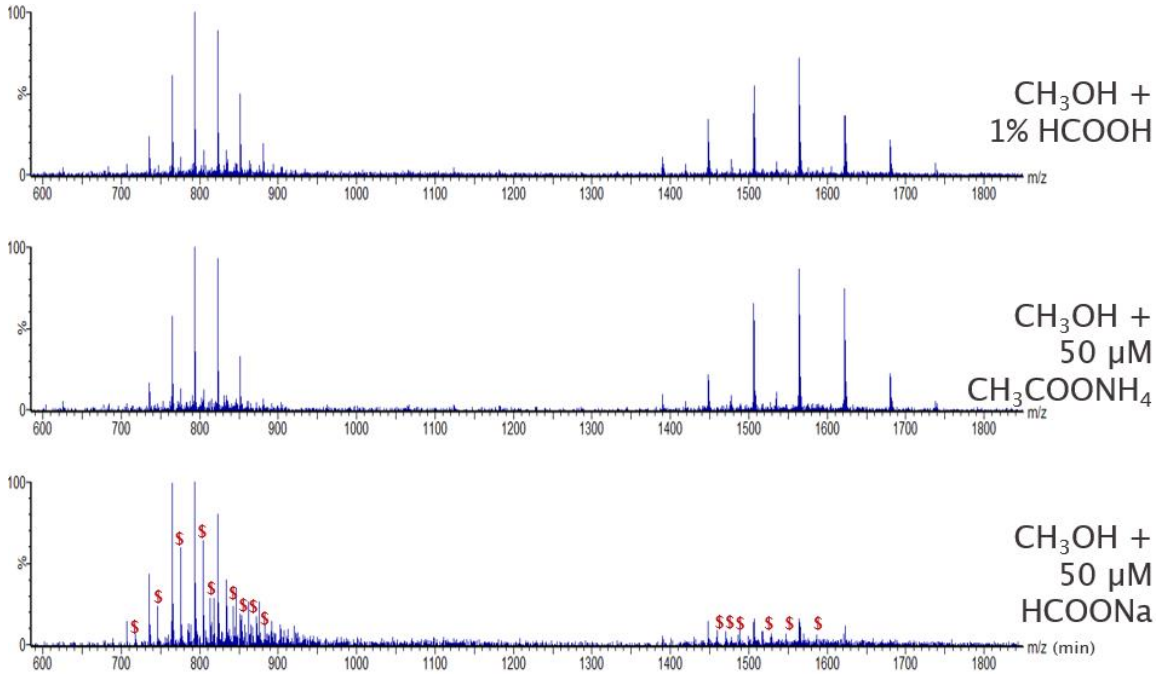

Figure 203. UPSFC positive ion ESI QToF MS. Mass spectra. 10 mg/mL 2HPBCD using of CH_3O+ 1% HCOOH. Mass spectra obtained when using three different make-up solvents. Notice the formation of Na salts when using 50 µM HCOONa showing low levels of Na salt ($)

6.2.2 Optimisation of the mobile phase and achievement of selective ionisation

The Na salt formation suggested the use of an acidic additive in the mobile phase. The addition of HCOOH to the methanolic co-solvent improved the peak shape as the secondary formation of Na salts was minimised (Figure 204). A more symmetrical peak shape was achieved when increasing the amount of HCOOH from 0.1 to 1% due to the higher acidity of the mobile phase.

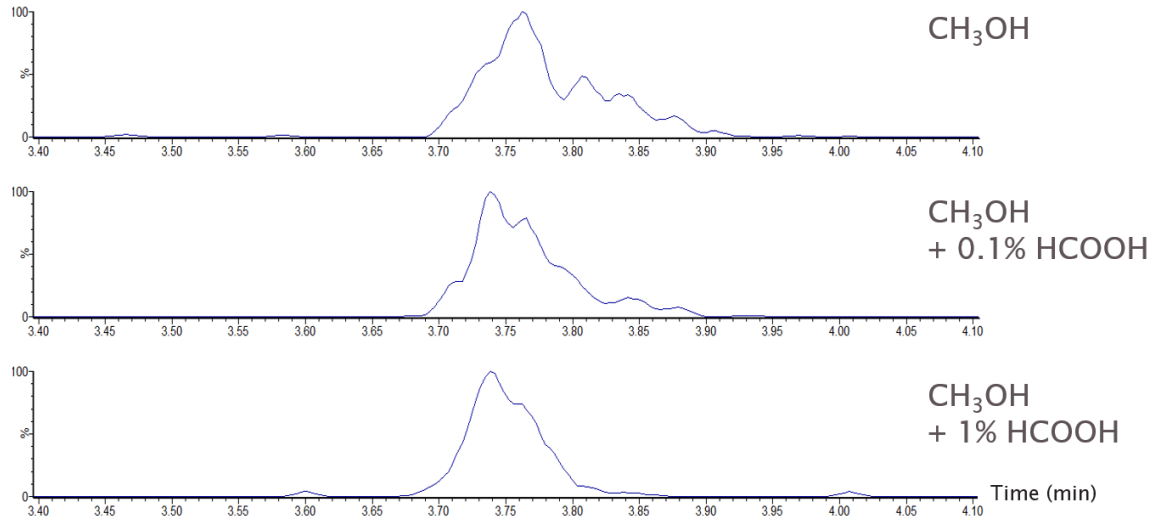

Figure 204. UHPSFC positive ion ESI QToF MS. RICC (*m/z* 1448). 10 mg/mL 2HPBCD in CH_3OH + 1% HCOOH. Optimisation of HCOOH concentration in the mobile phase

The improved S/N when using the acidic conditions described above led to a minimisation of Na salt formation and illustrated that selective ionisation had been mainly achieved (Figure 205).

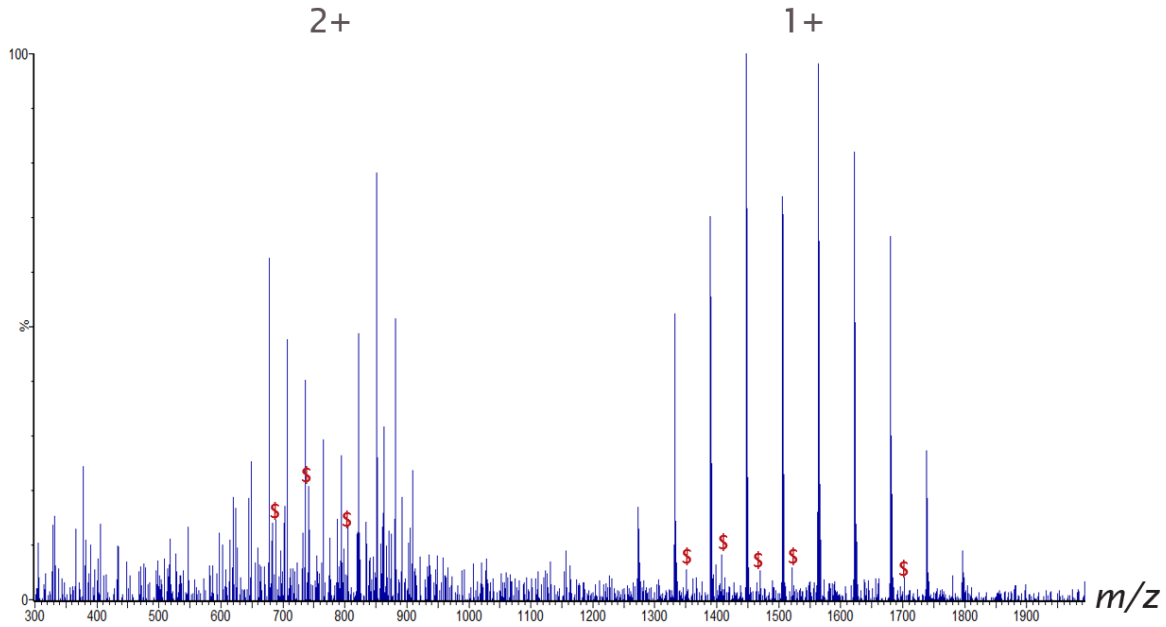

Figure 205. UPSFC positive ion ESI QToF MS. 10 mg/mL 2HPBCD using of CH_3OH + 1% HCOOH. Mass spectra obtained using CH_3OH + 1% HCOOH showing low levels of Na salt ($)

Partial substitution of the methanol-formic acid co-solvent for H_2O improved chromatographic resolution at the cost of deteriorating the peak shape. The use of H_2O increased the basicity of the mobile phase and resulted in the formation of a higher amount of Na salts meaning that this co-solvent was discarded.

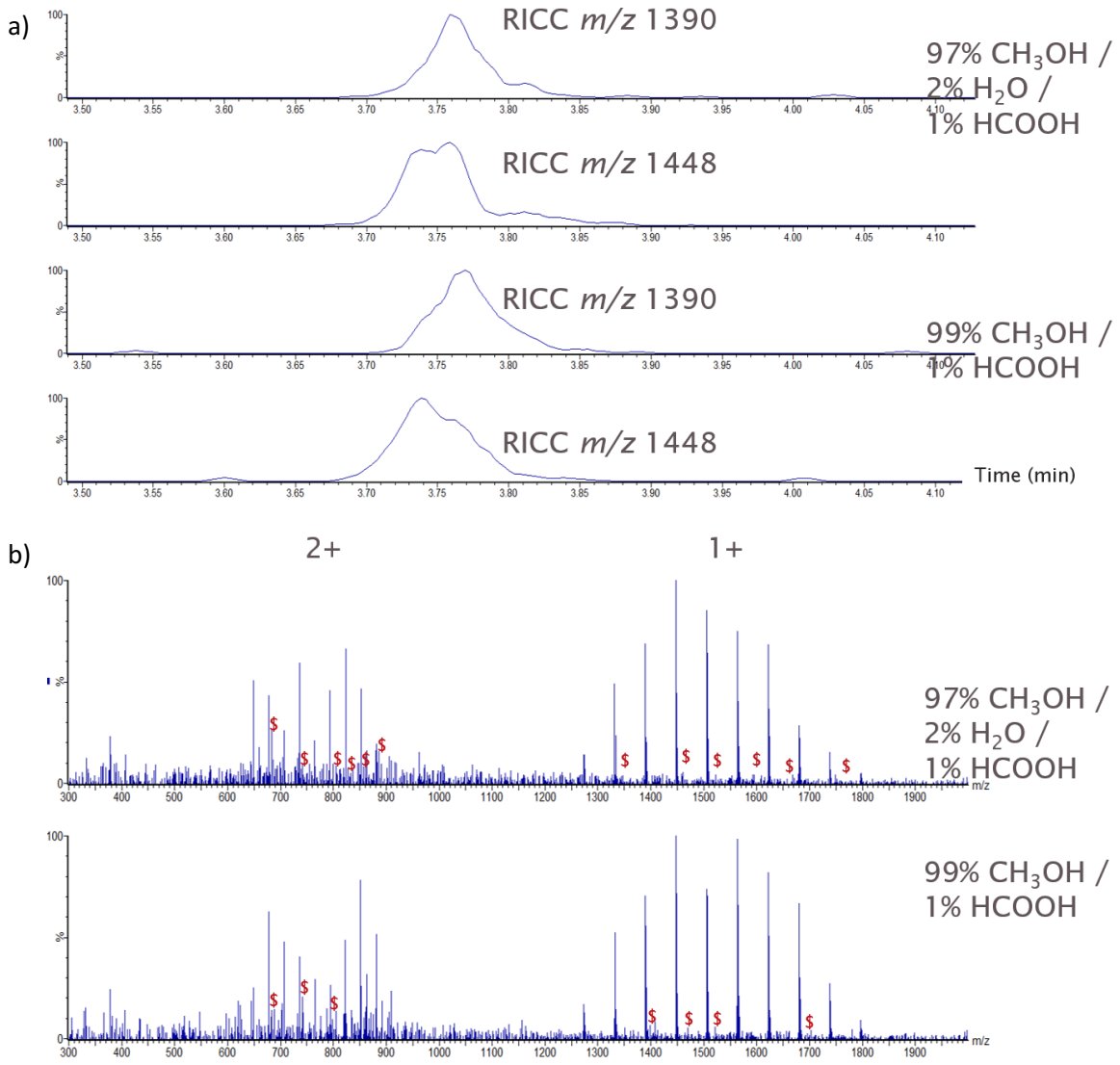

Figure 206. UHPSFC positive ion ESI QToF MS. 10 mg/mL 2HPBCD in CH_3OH + 1% HCOOH. Optimisation of the H_2O concentration in the mobile phase. a) RICC of two consecutive oligomers, and b) mass spectra showing relative levels of Na adducts ($)

6.2.3 Investigation of the effect of the column temperature and ABPR

Varying the column temperature (Figure 207) exhibited little influence on the separation due to a low impact of the mobile phase density on the inclusion-exclusion equilibria. The minor impact of the column temperature in the chromatographic separation was associated with little dependence on the temperature in the inclusion mechanism of the SP ligands inside the 2HPBCD cavity.

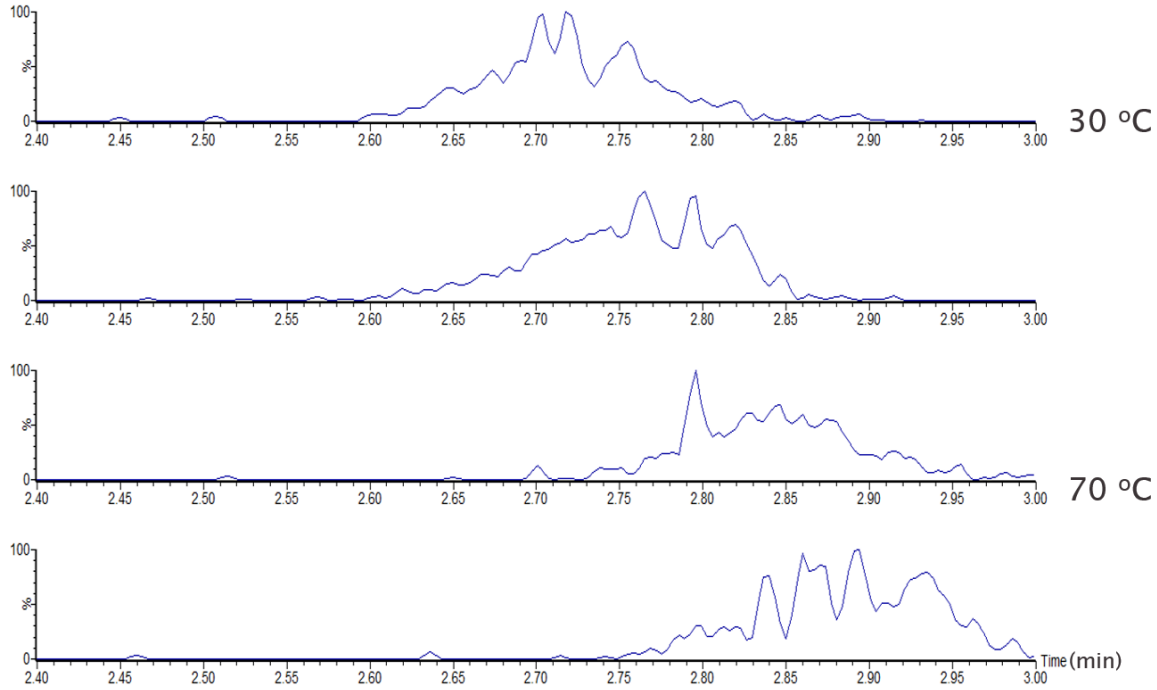

Figure 207. UHPSFC positive ion ESI QToF MS. RICC *m/z* 1622 and *m/z* 1564. 1000 µg/mL 2HPBCD in CH_3OH. Effect of the column temperature in the separation

Similarly, increasing the ABPR value (Figure 208) decreased chromatographic retention. The low impact of the ABPR in the peak shape and the chromatographic retention suggested the material could show low solubility in CO_2. Lower ABPR was considered more appropriate to decrease the mass transfer and increase the chromatographic resolution, and as such, a value of 105 bar was selected.

A lower column temperature and ABPR were proposed to improve chromatographic separation, with a final value of 30 °C and 105 bar chosen. Also, the observations in the column temperature and the ABPR suggested that the chromatographic separation required subcritical conditions and that further investigation of the APBR pressure was not required. Increasing the percentage of the organic co-solvent above 50%] would lead to increased mobile phase viscosity and lower analyte diffusion, resulting in higher backpressure and the risk of mobile phase separation [389]. When percentages higher than 50% are used, the technique is usually called enhanced-fluidity liquid chromatography [389]. An investigation on the use of this technique for the chromatographic separation of this mixture is proposed for their characterisation.

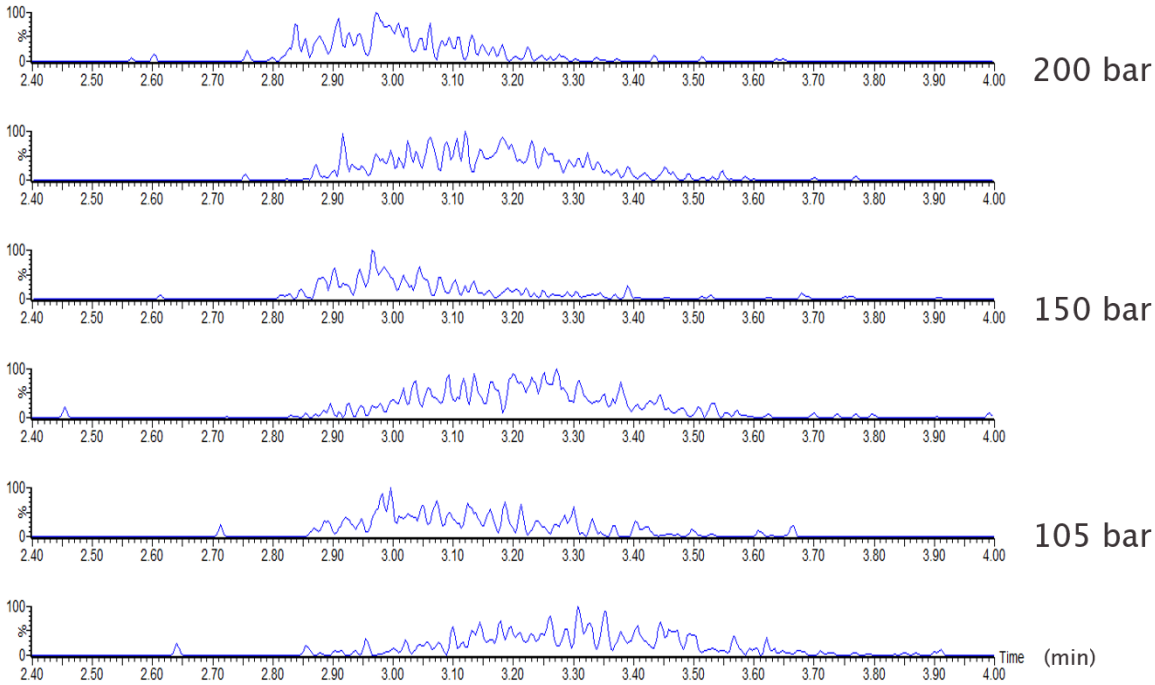

Figure 208 UHPSFC positive ion ESI QToF MS. RICC *m/z* 1622 and *m/z* 1564. 1000 µg/mL 2HPBCD in CH_3OH. Effect of the ABPR in the separation

6.3 Investigation of achiral stationary phase

6.3.1 Elution order of oligomers

When polymers are analysed using SFC, the elution of oligomers typically occurs via a size-exclusion mechanism, with shorter MW oligomers eluting earlier than larger MW ones (see section 4.2 for a typical elution of polymers in SFC).

A counterintuitive inverse elution was observed when evaluating the reconstructed ion current chromatograms (RICC) of the singly charged sodiated ions $[M + Na]^+$ of the 2HPBCD oligomers (Figure 209). CDs that showed a higher degree of hydroxypropylation, *i.e.*, with a greater DS, *i.e.*, oligomers with higher MW eluted earlier than the less substituted lower MW oligomers. The independence of these observations to the column suggested that the ethylpyridine ligands in the SP of the BEH-2EP were included inside the 2HPBCD cavity, *i.e.*, the formation of an inclusion-exclusion complex controlled the separation of oligomers based on their DS.

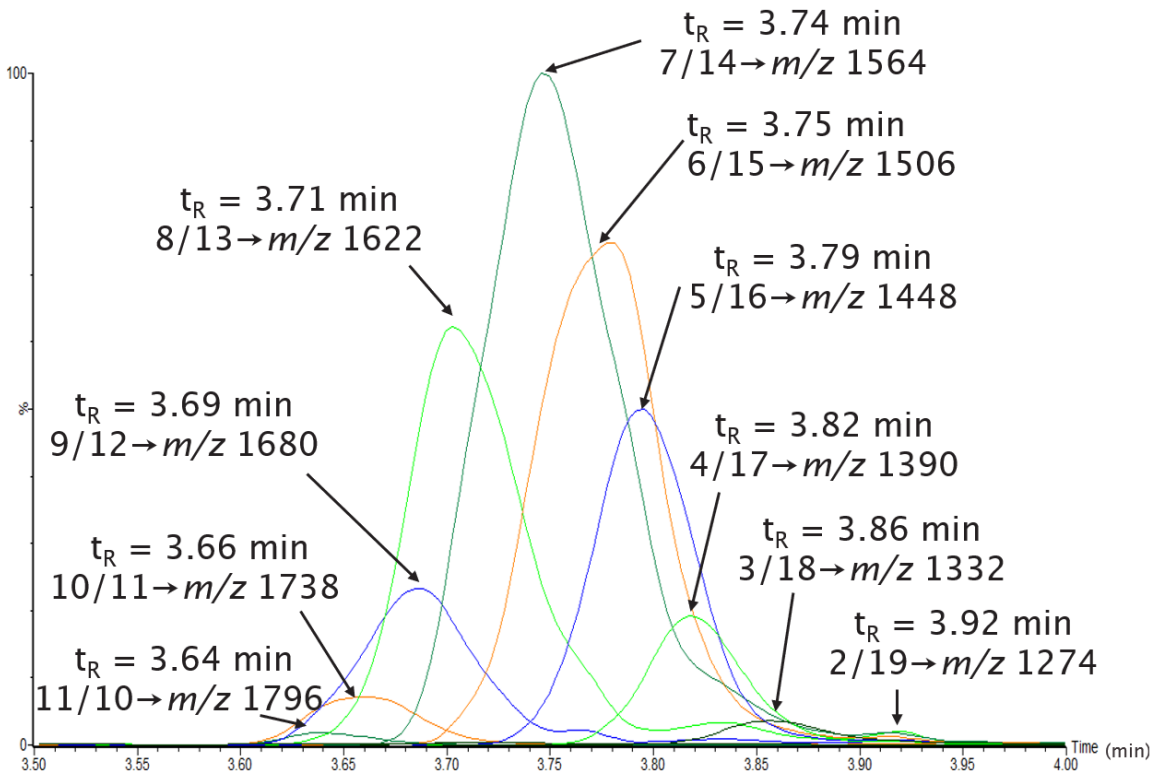

Figure 209. UHPSFC positive ion ESI MS. 1000 µg/mL 2HPBCD in CH_3OH. RICC of the singly charged species showing the oligomer elution. Data acquired using the BEH-2EP SP

6.3.2 Separation using achiral stationary phases

The inclusion-exclusion mechanism separation observed when using the BEH-2EP suggested that a further investigation into the formation of an inclusion complex of the ligands within the SP was required. Even though a range of SPs was tested, the columns presented in Table 58 provided insight into the inclusion mechanism. Fully porous particle (FPP) (1.7 µm, 2.1 mm X 100 mm) and superficially porous particle (SPP) (2.7 µm, 3.0 mm X 100 mm) columns for achiral analyses were tested.

Their selection was based on aiming to understand the possible inclusion of the SP ligand in the 2HPBCD and a further understanding of other possible separation mechanisms that could participate in the separation of the oligomers. BEH-2-EP and T2PIC were selected as they contain ligands that can be included in the 2HPBCD cavity. The TDEA SP was investigated due to its use in sugar analysis. SPP versions of the C18 (C18+) were considered to examine the influence of partitioning mechanisms in the separation of 2HPBCD oligomers.

Particle type and column size	Stationary phase	Particle size (µm)	Abbreviation
FPP for achiral analysis (3.0 mm x 100 mm)	Waters® Acquity™ UPLC™ HSS Perfluorophenyl	1.8	PFP
	Waters® Acquity™ UPC² BEH 2-Ethylpyridine	1.7	BEH 2EP
	Acquity™ UPC² Torus™ 2-Picolamine	1.7	T2Pic
	Acquity™ UPC² Torus™ Diethylamine	1.7	DEA
SPP for achiral analysis (3.0 mm x 100 mm)	Acquity™ Cortecs™ C18+	2.7	C18+

Table 58. Investigated columns with achiral SPs for the evaluation of the oligomer elution and the inclusion-exclusion mechanism for SP selection

The formation of the inclusion complex and the lack of other secondary mechanisms are shown in Figure 210 in the peak shape of the analyte when using the BEH-2EP. Compared to other SPs, the higher symmetry of the peak suggested that isomers with the same DS have the same K_A/K_D constant when forming the inclusion complex, resulting in less complex patterns.

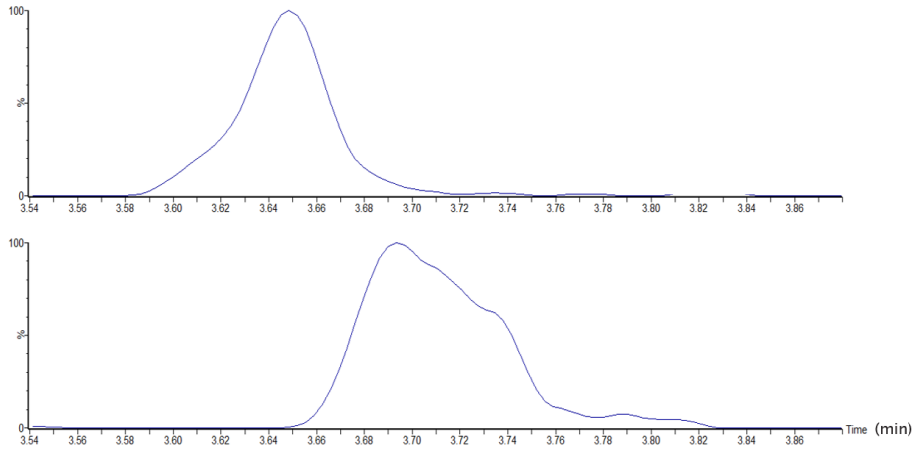

Figure 210. UHPSFC positive ion ESI MS. 1000 µg/mL 2HPBCD in CH_3OH + 1% HCOOH. RICC *m/z* 1448 (top) and *m/z* 1622 (bottom) when using the BEH-2EP SP

A larger resolution in the chromatographic peaks (between the RICCs of *m/z* 1448 and *m/z* 1662) was observed when using the T2Pic SP (Figure 211). The improved separation of the positional

isomers may be due to a secondary interaction of the 2HPBCD with the amino group in the SP ligand that provides the selective formation of an inclusion complex.

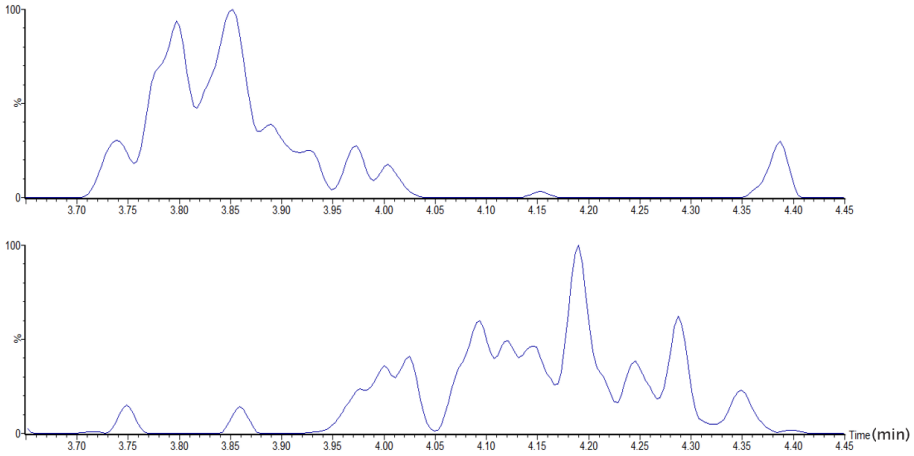

Figure 211. UHPSFC positive ion ESI MS. 1000 µg/mL 2HPBCD in CH_3OH + 1% HCOOH. RICC *m/z* 1448 (top) and *m/z* 1622 (bottom) when using the T2Pic SP

The TDiol showed the poorest separation (Figure 212), as the SP chains did not form inclusion species, and only polarity and partition governed the separation. The description of the SP proposed by Gross *et al.* suggested that the lack of inclusion complex for achiral compounds was associated with the relatively small length of the SP ligands. The shorter length of the SP ligands means their inclusion in the 2HPBCD cavity is insignificant, and the CD might only be "entrapped" within the pores of the SPs (130 Å). Note that the diameter of the cavity of β-CD is 6 Å [390].

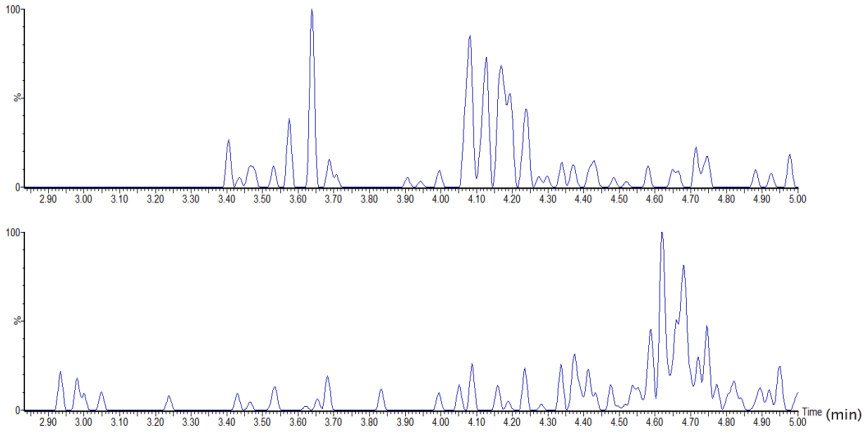

Figure 212. UHPSFC positive ion ESI MS. 1000 µg/mL 2HPBCD in CH_3OH + 1%HCOOH. RICC *m/z* 1448 (top) and *m/z* 1622 (bottom) when using the TDiol SP

Even with a similar chain length between the DEA and the Diol ligands, the DEA SP (Figure 213) showed chromatographic peak shapes comparable to those obtained when using the BEH 2-EP (Figure 210). The similarities between the DEA and the BEH-2EP SPs were associated with

favourable interactions of the amino group located in the DEA or the pyridine in the BEH-2EP ligands of the SP with the 2HPBCD cavity.

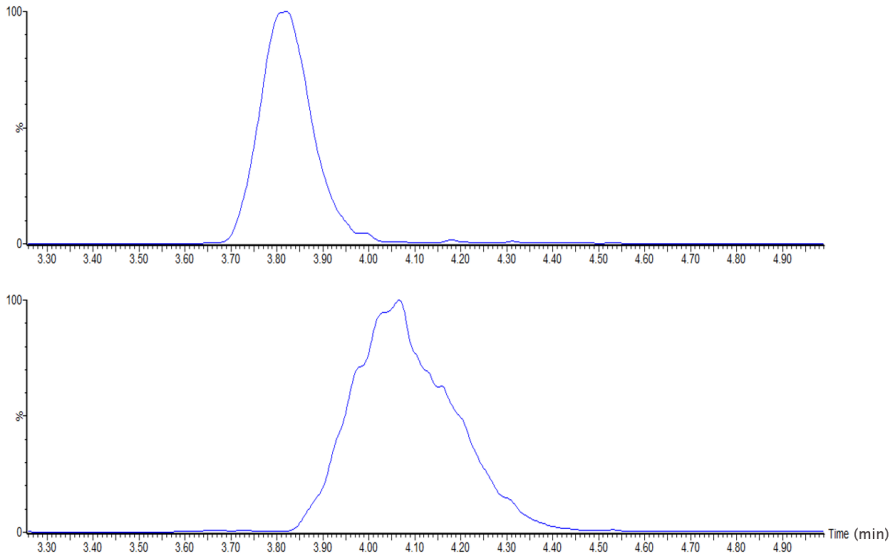

Figure 213. UHPSFC positive ion ESI MS. 1000 µg/mL 2HPBCD in CH_3OH + 1% HCOOH. RICC *m/z* 1448 (top) and *m/z* 1622 (bottom) when using the DEA SP

When using an SP with longer aliphatic chains such as the C18+, the formation of an inclusion complex was possible, as reported by Gros *et al.* [391]. The introduction of secondary interactions (partitioning, induced dipole) between the SP ligands and the 2HPBCD possibly explained the distorted peak shape observed (Figure 214). Still, the distortion of the peak shapes of the RICCs was related to the positive charge in the SP ligands. Their interaction with the hydroxy groups in the 2HPBCD could explain the separation of positional isomers.

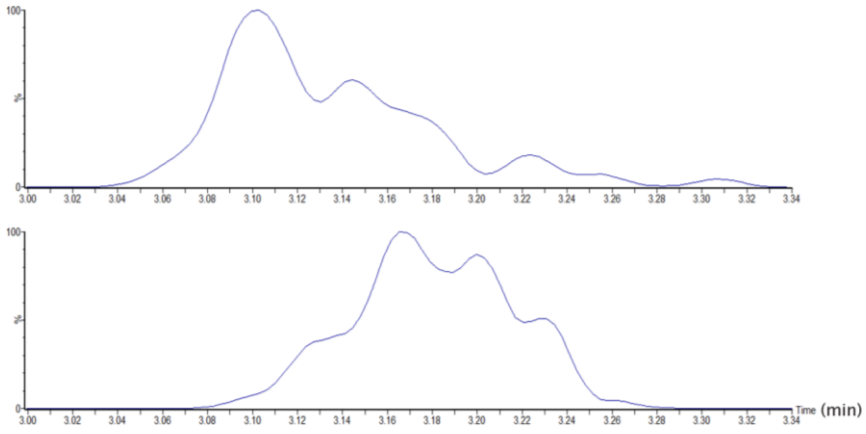

Figure 214. UHPSFC positive ion ESI MS. 1000 µg/mL 2HPBCD in CH_3OH + 1% HCOOH. RICC *m/z* 1448 (top) and *m/z* 1622 (bottom) when using the C18+ SP

As shown in Figure 210, Figure 211, Figure 213 and Figure 214 (but not in Figure 212), the analysis of the SPs suggests that the formation of an inclusion complex between the SP ligands and the 2HPBCD was vital for successful oligomer separation. Even though the chromatographic conditions could be optimised for each specific SP, the improved peak shape achieved when using the BEH 2-EP SP (Figure 210) suggested that unless secondary interactions were present, the current mobile phase is appropriate independently of the selected SP. This conclusion was possible due to the explanation of an inclusion complex between SP ligands and 2HPBCD oligomers, suggesting exploitation of the inclusion complexes to improve the chromatographic separation of the 2HPBCD oligomers. The resemblance of the ligand of chiral polysaccharide SPs resulted in the evaluation of these SP.

6.4 Need for chiral stationary phases

6.4.1 Method translation

The lack of fully porous particle (FPP) chiral columns with similar dimensions to the FPP achiral columns available (1.7 µm, 2.1 mm, 100 mm) in the laboratory required the use of columns with larger dimensions (3 µm, 4.6 mm, 250 mm) for screening due to their availability. Their use presented an instrumental challenge due to the differences in their dimensions compared to the FPP or superficially porous particle SPP columns (Figure 215 a). The longer length of the FPP chiral columns prevented their fitting in the instrument column compartment (Figure 215 b) and required locating an alternative column pre-heater sited outside the oven to be used. Notice that a larger column compartment can be purchased for the instrument but was unavailable in the laboratory when the analyses were performed.

a)

b)

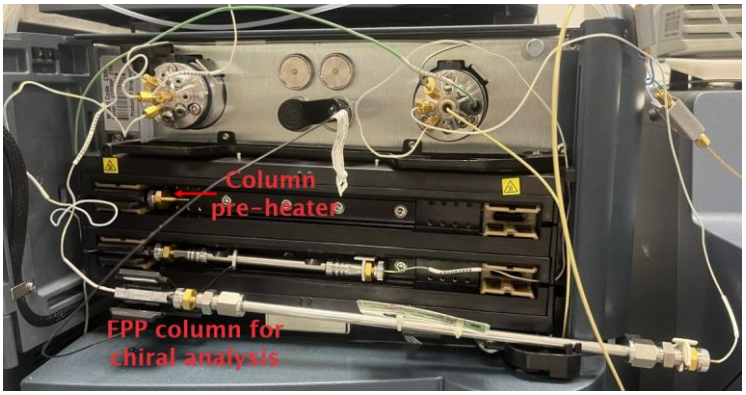

Figure 215. The instrumental challenge of using HPLC columns (250 mm) in a UPC^2 system: a) Differences in column size between FPP for achiral analysis (100 mm), SPP for achiral analysis (100 mm) and FPP for chiral analysis (250 mm) columns, and b) the set-up of the FPP for chiral analysis column in the UPC^2 column compartment

A method translation was needed due to the higher dimensions of the FPP chiral columns and the inability to work with the column temperature control. The method column temperature was translated as follows: (i) the column temperature was assumed to be (and reported as) room temperature, and (ii) the flow rate (F) was scaled from 1.1 to 2.5 mL/min (Equation 44) due to the differences in column length (L) to particle diameter (d_p) ratio (Table 59).

$$F_2 = \frac{F_1 x L_2^2 x d_{p,1}}{L_1^2 x d_{p,2}} \qquad \text{Equation 44}$$

Column type	**Column dimensions**	**L/d_p**	**Column temperature (°C)**	**Flow rate (mL/min)**
FPP for achiral analysis	1.7 µm, 2.1 mm x 100mm	58,824	30	1.1
SPP for achiral analysis	2.7 µm, 3.0 mm x 100mm	40,000	30	2.5
FPP for chiral analysis	3 µm, 4.6 mm x 250mm	50,000	Room temperature	2.5

Table 59. Method translation from sub-2 µm/SPP particles to HPLC columns

The use of modern sub 2 µm chiral columns would not require a method translation as shown, and the proposed conditions could be used. Also, notice that the L/d_p ratio does not consider that similar efficiencies can be achieved between SPP and FPP with sub-2 µm particles.

6.4.2 Separation using chiral stationary phases

Several chiral FPP columns for chiral analyses based on polysaccharides with a wide range of substituents were assessed (Table 60) with dimensions (3 µm x 4.6 mm x 250 mm). The selection of these SPs resulted from the resemblance of their ligand structures to drug molecule; and as such, they allowed the investigation of the theory that inclusion complexes between the SP ligands and the 2HPBCD were being formed.

Column	Ligand	Column	Ligand
Chiralcel OD	Tris(3,5-dimethylphenyl carbamate) 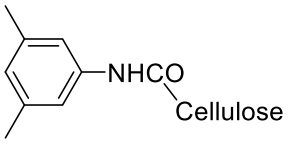	Chiralpack AD	Tris(3,5-dimethylphenyl carbamate) 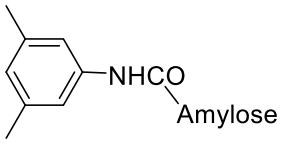
Chiralcel OD-H	Tris(3,5-dimethylphenyl) carbamate 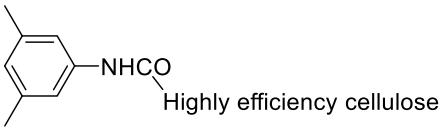	Chiralpack AS	Tris[(S)-1-phenyl ethyl carbamate] 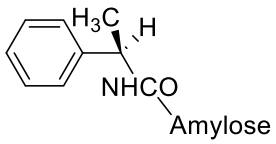
Chiralcel OG	Tris(4-methylphenyl carbamate) 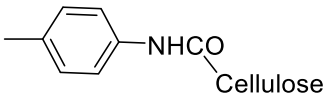		

Table 60. Chiral SPs selected to investigate the possible inclusion-exclusion mechanism

Comparing the Chiralcel OD and the Chiralpack AD allowed the investigation of the differences between cellulose-based and amylose-based SPs (Figure 216). The significant differences in the baseline (0.6 min for the Chiralcel OD and 0.25 min for the Chiralpack OD) were possibly linked to the rigidity of the SP in the stacking of secondary π interactions between the SP ligands. Cellulose-based SPs are more rigid (Chiralcel columns), resulting in stacked π interactions and stronger inclusion-exclusion equilibria, leading to a higher peak width (0.5 to 1.7 min). Conversely, the conformation of amylose-based SP (Chiralpack columns) is less constrained, resulting in a lower degree of stacked π interactions, causing a lower peak width (0.2 to 0.7 min).

When comparing ligands (Figure 216), the size and 3D structure of the ligand were key factors for the formation of the inclusion complex within the CD cavity. Larger ligands such as the tris(3,5-dimethyl phenyl carbamate) provided a shorter peak width (0.6 min for Chiralcel OD, 0.4 min for Chiralcel OD-H and 0.25 min for Chiralpack AD) due to a partial inclusion in the cavity. Besides, those with a more linear structure, such as the tris(4-methyl phenyl carbamate) (Chiralcel OG) or the tris[(S)-1-phenyl ethyl carbamate] (Chiralpak AS), showed a higher peak width (1.7 min). The larger peak width was associated with a stronger inclusion-exclusion mechanism promoted by a preferential formation of dipole and H-bonding interactions of the SP ligands with the cavity.

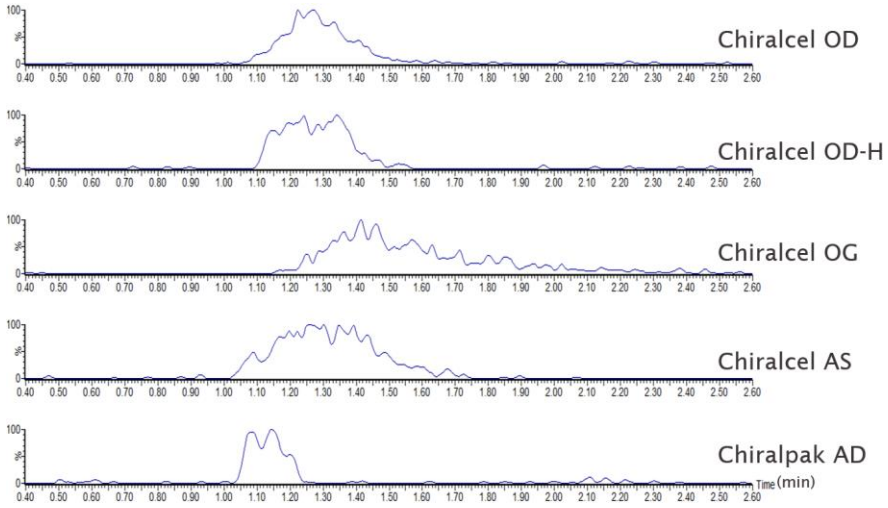

Figure 216. UHPSFC positive ion ESI TQD MS. BPICC. 1000 µg/mL 2HPBCD in CH_3OH + 1% HCOOH. Analysis of 2HPBCD using FPP columns designed for chiral screening

Evaluation of SPs for chiral analyses suggested that using the Chiralcel OD and Chiralpack AD would provide comparable results to SPs designed for achiral analyses with ligands that resemble drug molecules and provide a higher formation of the proposed inclusion-exclusion mechanism.

6.5 Final column evaluation

6.5.1 Stationary phase evaluation using high-resolution mass spectrometry

Previous experiments showed the 2HPBCD oligomer separation related to the inclusion of the SP ligands in the 2HPBCD cavity. This process was similar to the interactions of the CD with the drug molecule. Several SPs with ligands resembling a drug molecule that could be included in the CD cavity were selected (Table 61). The C18+ was evaluated due to a possible partitioning mechanism participating in the separation.

Particle type and column size	**Stationary phase**	**Particle size (µm)**
FPP for achiral analysis (3.0 mm x 100 mm)	Acquity™ UPLC™ HSS PFP	1.8
	Acquity™ UPC² BEH 2-Ethylpyridine	1.7
	Acquity™ UPC² Torus™ 2-Picolamine	1.7
SPP for achiral analysis (3.0 mm x 100 mm)	Acquity™ Cortecs™ C18+	2.7

FPP for chiral analysis (4.6 mm x 250 mm)	Chiralcel OD	3
	Chiralpack AD	3

Table 61. Columns selected for 2HPBCD screening

A more symmetric peak shape was achieved using the Chiralcel OD and the T 2-Pic (Figure 217 a) phases. Their similar degree of selectivity and oligomer separation was associated with the lack of positional isomer separation in these SPs, suggesting that both SPs have a similar degree of occupation of ligands in the SP support and minimal input of secondary interactions in the separation.

When comparing the Chiralcel OD and the Chiralpack AD columns (Figure 217 a and b), the lack of oligomer separation in the Chiralpack AD suggested that the tris(3,5-dimethyl phenyl carbamate) ligand in the polysaccharide was not included in the CD which appears to be critical to providing good oligomer separation. The wider open structure of the amylose-based SPs (Chiralpack AD) suggested a less favourable formation of an inclusion complex that could relate to secondary π stacking interactions between the SP ligands in the Chiralcel OD, explaining the differences in the peak shape and baseline.

The different peak shapes and the observation of "mountains" when using the C18+, the PFP and the BEH 2-EP SPs (Figure 217 b) were related to secondary interactions that altered the peak shape and allowed the differentiation of the positional isomers of the 2HPBCD, as previously discussed in section 6.4.

a)

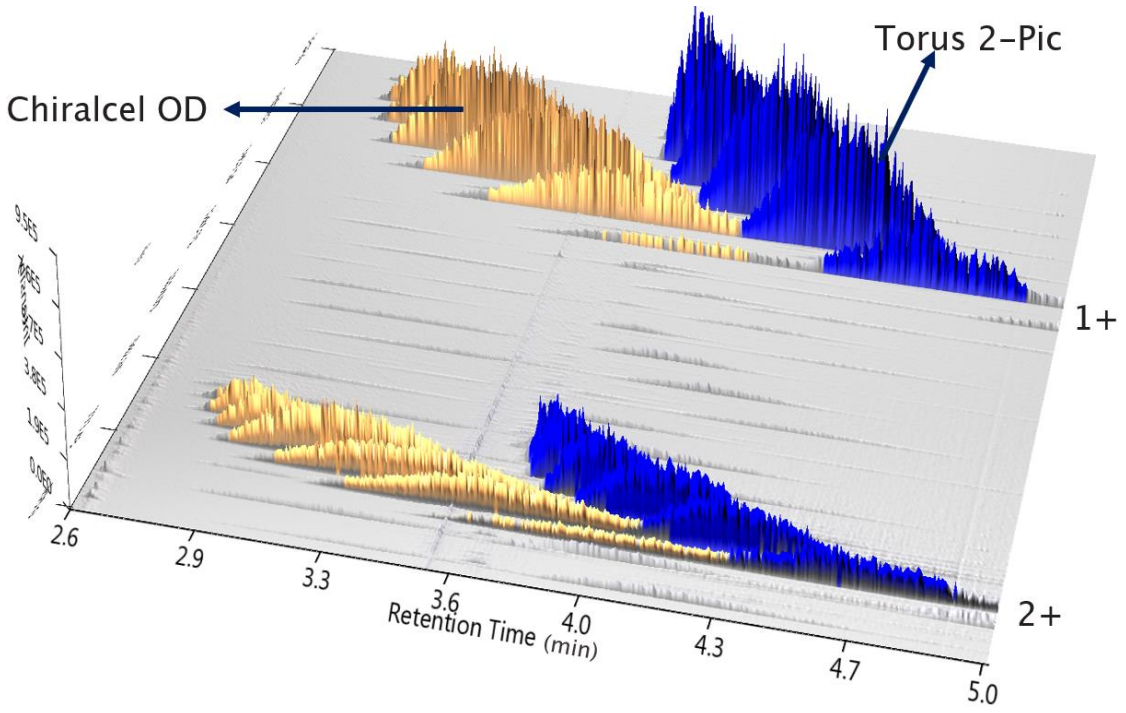

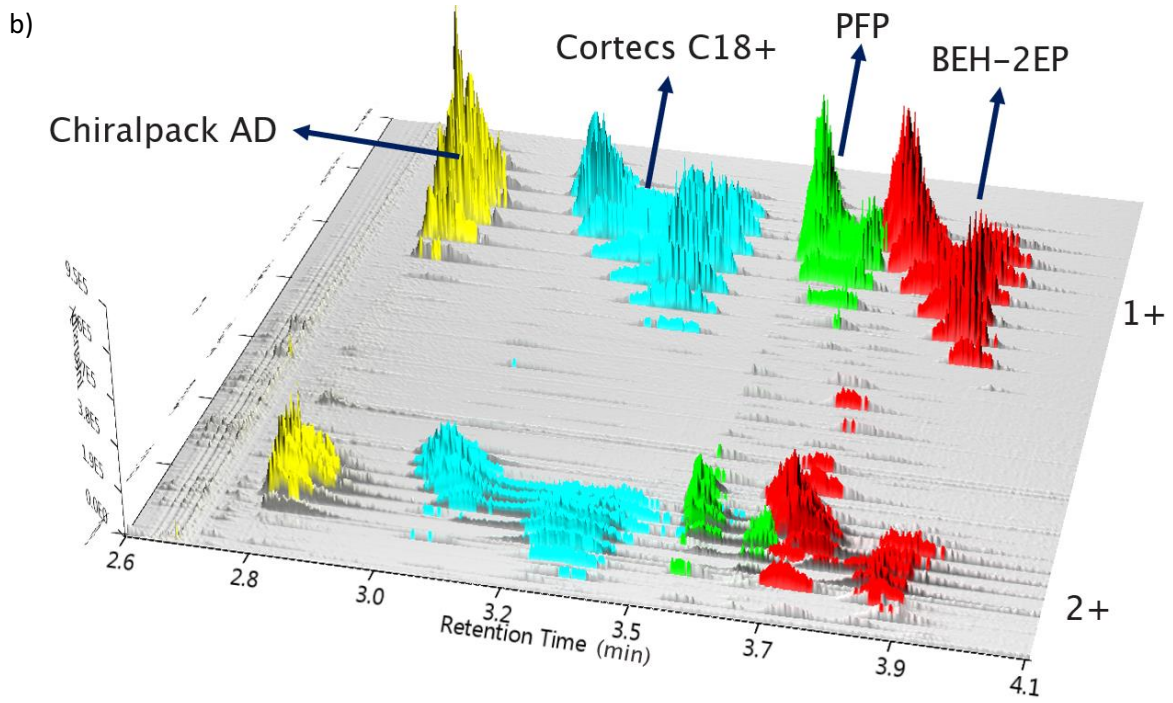

Figure 217. UHPSFC positive ion ESI QToF MS. Ion map. 1000 µg/mL 2HPBCD in CH_3OH + 1% HCOOH. Comparison of the selected columns screened for the 2HPBCD separation

6.5.2 Stationary phase selection using ion mobility mass spectrometry

The unusual chromatographic peak shape observed when using the different SPs was investigated using selective ion monitoring (SIM) acquisition and ion mobility mass spectrometry (IMMS). The experiment selected the ion with *m/z* 1506 $[6HP/15H + Na]^+$ in the Q (Figure 218) shows that the conformers were separated by shape and size using TWIMS, and the masses were accurately represented and measured using ToF MS. The measured drift times of the components were converted to $^{TW}CCS_{N2}$ values following established procedures using a mixture of 0.1 µg/mL acetaminophen and 10 µg/mL poly-DL-alanine in 50%/50% (v/v) CH_3CN/H_2O for calibration [360]. The obtained collisional cross-section (CCS) values are called $^{TW}CCS_{N2}$ as the CCS values of molecules depend on the ion mobility technique (TWIMS = TW) and the gas used for the separation (N_2).

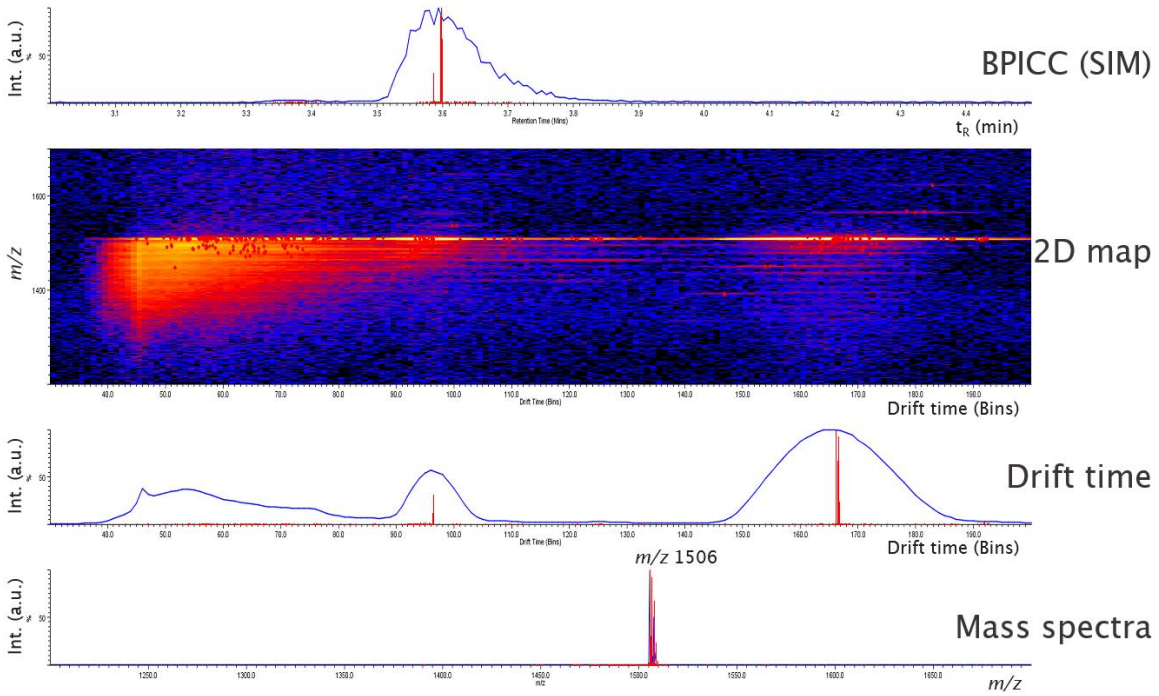

Figure 218. Different representations of UHPSFC positive ion ESI Q IM ToF MS

The data acquired using UHPSFC positive ion ESI Q IM ToF MS can be viewed in different representations. The correlations between the BPICC, the mass spectra and the mobiligram are shown in Figure 219; however, the representation of mobiligrams in 3D provided insight into the different conformers for the established ion. The 3D mobiligrams represented the chromatographic retention (t_R) on the *x*-axis, the drift time (min) on the *y*-axis and the ion current on the *z*-axis.

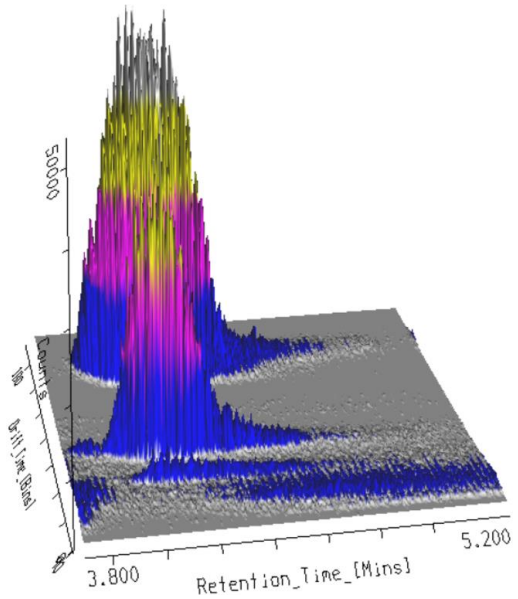

Figure 219. UHPSFC positive ion ESI Q IM ToF MS. 100 µg/mL 2HPBCD in CH_3OH + 1% HCOOH. Mobiligrams (retention time *vs* drift time) were acquired using SIM *m/z* 1506

The analysis of the mobiligrams of the selected ion with *m/z* 1506 $[6HP/15H + Na]^+$ (Figure 220) provided insight into the different chromatographic peak shapes observed in Figure 217. A study of the conformer retention time (t_R) allowed the Chiralpak AD, PFP, and BEH-2EP SPs to be discarded. The Chiralcel OD, the T2Pic and the C18+ SPs provided some conformer separation due to the presence of secondary interactions within the SP ligand that allowed for the higher conformer separation. The data showed the power of the added degree of separation when combining TWIMS with chromatography for characterisation. The co-eluted conformers could be resolved due to the coupling, which allowed for the correct selection of the SP. Further investigation is required that is outside of the scope of this project.

SP	Mobiligram	$^{TW}CCS_{N2}$ (Å^2)	t_R (min)
a) Chiralcel OD	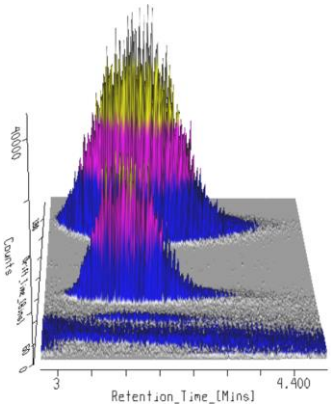	202 ± 2	3.41
		140 ± 1	3.45
b) Torus 2-Pic	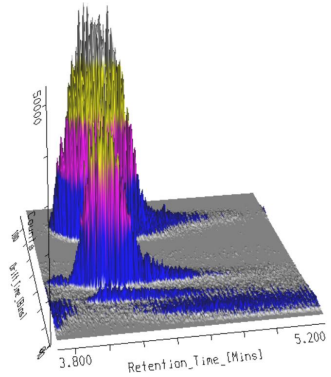	140 ± 1	3.89
		202 ± 2	3.96
c) Chiralpack AD	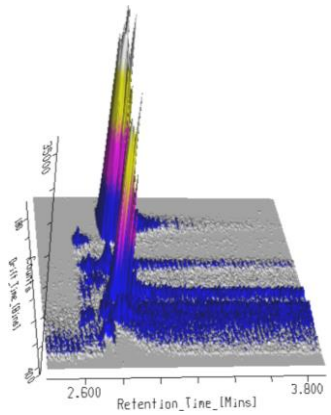	202 ± 2	2.82
		140 ± 1	2.82

d) Cortecs C18+

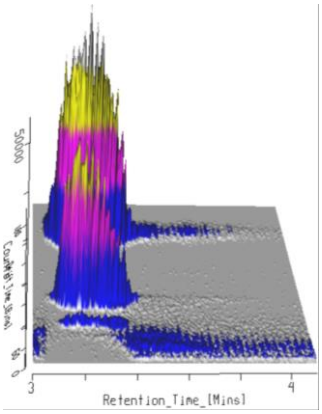

140 ± 1 3.6

202 ± 2 3.68

e) PFP

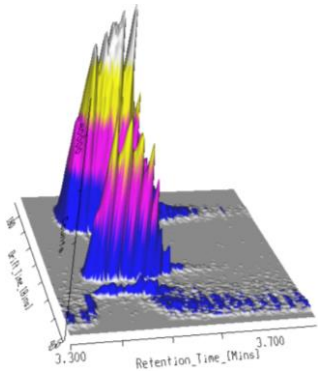

140 ± 1 3.43

202 ± 2 3.44

f) BEH 2-EP

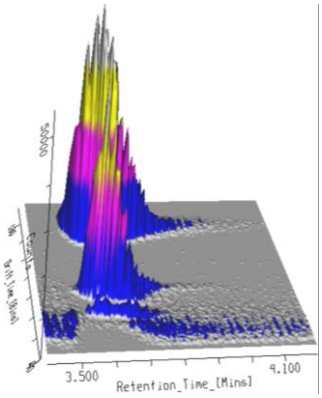

140 ± 1 3.59

202 ± 2 3.59

Figure 220. UHPSFC positive ion ESI Q IM ToF MS. 100 µg/mL 2HPBCD in CH_3OH + 1% HCOOH. Mobiligrams (retention time *vs* drift time) were acquired using SIM *m/z* 1506. Separation of up to 4 conformers of the 2HPBCD oligomer with 6 hydroxypropyl and 15 hydrogens. Comparison between a) Chiralcel OD, b) 2-PIC, c) Chiralpack AD, d) C18+, e) PFP, and f) BEH 2-EP SPs

6.5.3 Peak shape explanation using ion mobility mass spectrometry

An IMMS separation of the ion $[6HP/15H + Na]^+$ with *m/z* 1506 was performed. An evaluation of the $^{TW}CCS_{N2}$ in the mobiligram showed two different types of conformers under the chromatographic peak shape, one with 140 ± 2 $Å^2$ (Table 62) and one with 202 ± 2 $Å^2$ (Table 63).

m/z	t_R (min)	Intensity (counts)	$^{TW}CCS_{N2}$ ($Å^2$)	Assignation
1505.034	3.6	314224	139.9 ± 1.4	Conformer A
1505.357	3.6	82173	140.6 ± 1.4	Conformer A
1505.539	3.6	6116939	140.9 ± 1.4	Conformer A
1505.726	3.6	132005	140.5 ± 1.4	Conformer A

Table 62. Detected peak list for *m/z* 1506 and $^{TW}CCS_{N2}$ 140 ± 2 $Å^2$ using the C18+

m/z	t_R (min)	Intensity (counts)	$^{TW}CCS_{N2}$ ($Å^2$)	Assignation
1505.322	3.68	336737	202.4 ± 2.2	Conformer B
1505.535	3.68	38318036	202.1 ± 2.2	Conformer B
1505.743	3.67	213188	203.4 ± 2.3	Conformer B

Table 63. Detected peak list for *m/z* 1506 and $^{TW}CCS_{N2}$ 202 ± 2 $Å^2$ using the C18+

Additionally, the acquisition of experimental $^{TW}CCS_{N2}$ values of α-CD (149 ± 2 $Å^2$) and β -CD (180 ± 2 $Å^2$) (Table 64) allowed confirmation of the substitution pattern in 2HPBCD.

	Ion detected	Experimental $^{TW}CCS_{N2}$ ($Å^2$)
α-CD	$[M + H]^+$ *m/z* 973.8	149 ± 2
β-CD	$[M + 2Na]^{2+}$ *m/z* 590.2	180 ± 2

Table 64. Experimental $^{TW}CCS_{N2}$ ($Å^2$) of α-CD and β-CD. Data obtained by infusion of 50 µg/mL solution in H_2O + 1% HCOOH

Thompson reported that substitutions in OH-6 narrow the cone rim [392], and as such, these observations could suggest that substitutions that only occur in OH-6 should result in smaller $^{TW}CCS_{N2}$ values. Similarly, as substitutions in the OH-2 and OH-3 groups broaden the rim of the cavity, molecules substituted in these positions should result in higher values. This evidence allowed the association of the conformers with 140 ± 2 $Å^2$ with at least one hydroxypropylation occurring in OH-6, whilst conformers with 202 ± 2 $Å^2$ were linked with hydroxypropylation in OH-2 and OH-3 positions only. The analysis of the reported intensities (Table 62 and Table 63) showed *ca.* 25% of conformers with $^{TW}CCS_{N2}$ equal to 140 ± 2 $Å^2$ and *ca.* 75% of conformers with $^{TW}CCS_{N2}$ values equal to 202 ± 2 $Å^2$ (Table 65). These values suggested that the

hydroxypropylation occurs in the β-CD central ring and not in the HP chains. Also, the hydroxypropylation is not equal, and hydroxypropylation in the OH-6 position was observed, which indicated a non-regioselective formation of the 2-hydroxy derivative.

$^{TW}CCS_{N2}$ (Å^2)	Relative proportion	Assigned conformer
140 ± 2 Å^2	25%	2HPBCD with at least one HP occurring in OH-6
202 ± 2 Å^2	75%	2HPBCD with HP in OH-2 and/or OH-3

Table 65. Experimental $^{TW}CCS_{N2}$ (Å^2) of α-CD and β-CD. Data obtained by infusion of 50 µg/mL solution in H_2O + 1% HCOOH and using polyalanine/acetaminophen as calibrants

6.6 Final chapter remarks

The current chapter showed the challenges in the method development using UHPSFC positive ion ESI MS of 2HPBCD and confirmed the complexity of the mixture. Data showed the challenge in developing a UHPSFC MS for 2HPBCD and the complexities involved in the method development and characterisation. Whilst an acidic mobile phase was required to eliminate the formation of Na salts, an inclusion complex governed the separation and complicated the selection of the SP.

Additionally, the source design of the mass spectrometer is important to allow more ions to be introduced into the mass analyser to improve sensitivity and lower the number of charge states to simplify the mass spectra.

When evaluating the different SPs, the main observation was that the oligomer separation was favoured by ligands in the SP with structures that resembled drug molecules. When selecting these ligands, any possible secondary interaction (H-bonding, partitioning, etc.) of the ligand with the 2HPBCD should be carefully evaluated. Similarly, the L/d_p values of the different SPs suggested that either FPP achiral or chiral columns could be used (achiral = 58,824, chiral = 50,000) and that purchasing the Chiralcel OD with sub 2 µm x 3.0 mm x 100 mm dimensions would be beneficial for further understanding of the proposed inclusion-exclusion mechanism and the differences between SPs.

Also, the addition of IMMS revealed the hidden complexity of the different conformers and positions of substitutions, suggesting that a deeper characterisation is possible. The use of IMMS is a powerful tool for polymer characterisation and adds extra levels of detail to the structure of the polymer.

Finally, the formation of different charged states suggests an approach for quantitation of PEGs and calculation of the degree of substitution of the 2HPBCD can be developed. However, a deeper understanding of the presence of other substitutions on the β-CD ring is required as this investigation showed that hydroxypropylation in the OH-2 position was not complete, resulting in a compromise of the pharmaceutical characteristics of the final drug product.

Chapter 7 Conclusions and future work

7.1 Research summary

The research undertaken focused on developing new analytical methods for understanding the composition of polymeric pharmaceutical additives used in industry, hoping to identify and quantify unknown impurities and investigate how ultra-high-performance supercritical fluid chromatography coupled to mass spectrometry (UHPSFC-MS) can provide answers in their analysis. The focus was on expanding the capabilities of the technique for polymeric excipients used in the pharmaceutical industry. These polymers are added to many drug formulations to improve drug solubility and delivery. The emphasis was on the characterisation and quantitation of poly(ethylene) glycols (PEGs) and the characterisation of (2-hydroxypropyl)-β-cyclodextrin (2HPBCD).

7.2 Summary of contributions in poly(ethylene) glycol analysis

7.2.1 Primary contributions

A generic UHPSFC-MS approach for PEG characterisation was developed that was independent of the end group analysed. The chromatographic method showed the need to use a co-solvent based on CH_3OH, H_2O and CH_3COONH_4. The optimised method showed minor dependence on the end group chemistry; however, the mobile phase composition significantly impacted the chromatographic separation and the peak shape of PEG with acidic end groups. While CH_3COONH_4 and H_2O favoured the chromatographic peak shape, CH_3COONH_4 improved the chromatographic resolution between oligomers. Similarly, the interactions of the ammonium ions with the stationary phase and the PEG chain and the size-related mechanism suggested that the selection of the stationary phase was not critical in the oligomer separation. Also, even though the column temperature minorly affected the chromatographic separation between consecutive oligomers, a large increase in the separation was noticed between the first and the last chromatographic peak that was considered to be required to minimise the ion suppression of possible impurities and facilitate their identification. Contrary, the interactions of the end groups with the stationary phase played an important role when separating PEG distributions and advised that the selection of the stationary phase should be based on the interactions with the end group and not on the chain itself.

In terms of the ionisation by positive ion ESI MS, cationisation is favoured for PEG analysis. The extensive range of molecular weights of PEGs in the industry means that both singly single and multiply charged species could be observed in daily analyses of these molecules, resulting in a complicated mass spectrum. Cationisation of PEGs *via* ammoniation adducts was selected from the added benefits of CH_3COONH_4 during the chromatographic separation and, as such, the preferred formation of ammoniated molecules under the analysis conditions. Even under these circumstances, other ionisation events can occur, with the predominant event being the formation of protonated molecules or sodiated adducts. The lack of selectivity in the ionisation complicated the positive ion ESI data and subsequently benefitted from selectively forming one species over another. Achieving selective ionisation of PEGs to form ammoniated adducts provided a cleaner mass spectrum that facilitated impurity observation and decreased the variance in the measured signal, resulting in improved characterisation and quantitation of the material.

The analysis of the ionisation of PEG oligomers confirmed the conclusions of Gidden *et al.* about the influence of chain length; however, the influence of the end group or the importance of the end group in the ionisation when compared to the chain itself were never shown [364]. This research showed how ionisation occurs at an oligomer level. The ionisation of oligomers was influenced mainly by the chain length of the oligomer (repeating unit) and, to a lesser extent, by the end group. Even though longer PEG chains allow the accommodation of more charges in the structure because Coulombic repulsions are minimised (size-related effect), this research quantified the effect of the cation incorporation by evaluating the average charge state (z_{avg}) and the relative formation of one charge state over another based on the oligomer repeating unit. Similarly, data showed that the end group affected the ionisation due to an inductive effect that disturbs the lone pair of electrons of the neighbouring O atoms and alters the chelation event of the cation. The influence of the electron-donating groups destabilises the closest O of the PEG chain (more electronegative), pushing the electron density towards the PEG chain, resulting in fewer charges being accommodated. The length of the aliphatic chain could explain differences observed between PEGs with different aliphatic end groups, as the longer the aliphatic chain, the stronger this effect. Contrary to this, electron-withdrawing groups deactivate the O of the PEG chain (less electronegative). The more delocalised electron cloud allowed for a larger number of charges.

Even positive ionisation ESI MS was favoured due to the PEG chain; the use of the negative ion polarity or other ionisation sources helped the characterisation. The direct infusion of PEGs with

acidic groups into the negative ion ESI MS provided good results; however, those with only one site for deprotonation resulted in the formation of ions that fell outside the range of the mass analyser (for quadrupole mass analysers). Still, positive ion ESI MS was selected over the negative polarity due to the lack of selectivity in positive ion ESI MS allowed for detecting an impurity of PEG diacid 2000 not observed when the source was used in the negative polarity. While ESI MS is still a common ionisation source choice within the industry, the extension to other sources can simplify characterisation and may aid the identification of components within these complex mixtures due to the selectivity in the ionisation, improving confidence when assigning chemical structures. Atmospheric pressure chemical ionisation (APCI MS) provided similar results to ESI MS with a lower sensitivity, implying that this ionisation source should be avoided. Atmospheric pressure photoionisation (APPI MS) confirmed the characterisation of polymers with unsaturated sites in Tween® 80.

The foremost challenge in the characterisation is related to the presence of isobaric species in many complex polymeric mixtures. The powerful combination of the two techniques improved characterisation. The use of ion maps and base peak ion current chromatogram (BPICC) allowed the characterisation of several PEGs of different levels of complexity in different scenarios for the pharmaceutical industry. Whilst the BPICC worked as a screening tool to differentiate polymers and highlight differences in the material source from several suppliers, using the BPICC on its own is not enough to interpret polymeric mixtures. The data visualisation of ion maps using MZmine resulted in an information-rich visual representation of the distribution of the polymer ionisation charged states. SFC-MS ion maps proved an excellent tool for characterising polymeric chains at different charge states and facilitated the identification of impurities. These tools excel when complemented with other analytical techniques or knowledge of different ionisation approaches, with examples illustrated in this research by the quantitation of free lauric acid using negative ion ESI MS in Tween® 20 for comparison of suppliers and product qualities or the complementary examination of Gelucire® 44/14 degradation with differential scanning calorimetry.

A change in the mass analyser from a low-resolution quadrupole (Q) to a high-resolution quadrupole time-of-flight (QToF) accelerated the characterisation due to shifting the mass spectra to ions with lower charge states that simplified the ion map. The increased sensitivity facilitates observation of the polymeric trends at the different charged states and their impurities. Increased sensitivity was afforded by the design of the Synapt™ G2-*Si,* and, similarly, the addition of a QToF increased the resolution power with regards to the Q mass analyser and provided more insight into the characterisation of the polymers. The high-resolution capability allows for nominally isobaric species to be separated, and ions can be measured accurately (typically to the fourth decimal place), allowing possible chemical formulae to be postulated for the ion. The

confidence in the identity of the ion is further enhanced by comparing the measured and theoretical isotope patterns.

Furthermore, the enhanced oligomer separation provided by UHPSFC-MS allowed the proposal of the first work where polymer quantitation can be achieved using deconvolution of the oligomer mass spectra based on the Waters® Transform™ algorithm, independently of the oligomer molecular weight. The deconvolution approach was also less prone to human errors since fewer processing steps were used. Their use provided confidence in the quantitative results of number average (M_n) and weight average (M_w) molecular weights and polydispersity (PDI) that were compatible with established size exclusion chromatography (SEC) approaches.

Also, the comparative study of the mass analysers showed that the mass analyser and data acquisition modes were critical factors for quantitative analysis. For beam instrumentation such as Q mass analysers, the scan rate and duty cycle of modern instrumentation are fast (typically 15-20,000 *m/z* units per second) and can deliver the appropriate number of scans across the SFC peak to give a truly representative peak profile, with the caveat of the scan rate being *m/z* range dependent. However, data processing is time-consuming and cannot provide accurate mass measurements. Note here that the isotopic information of measured ions may be compromised at very fast scan rates (approaching their theoretical limit) and induce errors in the assignation of polymeric trends. Despite the lack of isotopic resolution, quantitative results were obtained that were compatible with SEC. A benefit of Q or QToF data is that data can be revisited to search for other species (non-targeted analysis). However, while SIM provides improved detection limits, the data is targeted and only recorded for known species; thus, revisiting data and searching for other species is impossible. The precision of the analysis improved when introducing a monodispersed internal standard (ISTD, 18-crown-6) without compromising the calculation of M_n, M_w and PDI due to the baseline resolution of the oligomers. From these observations, a quantitation protocol was proposed (see section 5.6, page 213 for further information).

When comparing the data processing time of the different quantitation methods, for Q data, approaches that used the whole distribution took significantly longer than approaches that used the surrogate oligomer (20 min *vs* 1 min per sample). However, both approaches are recommended as both may be automated. Automated data processing is advised when using QToF data due to the increase in the time required for data processing (35 min per sample for the deconvolution of the whole distribution mass spectra).

Incorporation of the proposed deconvolution approach to the TargetLynx™ Application Manager resulted in data processing becoming a simpler task when using surrogate oligomers. TargetLynx™ is an add-on within the MassLynx™ software package that automates data acquisition, processing, and reporting. This software incorporates a wide range of confirmatory checks that identify samples falling outside the user-specified or regulatory thresholds, providing confidence in quantitative results. Automation using TargetLynx™ was applied to surrogate oligomers based on the RICC of the most intense ion with/without SIM acquisition, resulting in extremely fast data processing, as the calibration curve was obtained immediately without user input.

7.2.2 Limitations of the research and future work

The main limitation of the UHPSFC-MS approach developed in this thesis is that PEGs with amino or basic end groups were not considered as they were out of the scope of this project; however, further investigation is required due to their enhanced use in modern mRNA formulations [393]. As such, the incorporation of the UHPSFC-MS methods developed should be considered to investigate the wide range of other end groups of PEGs used in the industry. Additionally, the current work did not explore the quantitation of low-level impurities, an essential area of research in any pharmaceutical formulation, especially with the recent research showing an allergic reaction to PEG in specific individuals that might cause anaphylaxis [83, 388]. The characterisation and quantitation of polymeric excipients have become critical in recent times to enable faster development of vaccines based on lipid nanoparticles (such as the CoViD-19 vaccine Comirnaty) or the PEG materials used in formulations in oligonucleotide therapeutics.

Even though UHPSFC-MS is appropriate for investigating PEG materials, other techniques are required to provide a complete picture of the polymeric mixture. This limitation is familiar within the polymer analysis field, with constraints in analysing minor components within a mixture. For example, the analysis of small drug molecules and excipients can be affected by the ion suppression produced by the polymeric chain, and their detection or quantitation might be compromised. Using SEC or a temperature-gradient analysis with atmospheric solids analysis probe sources in MS (ASAP MS) could allow the investigation of low levels of suppressed small molecule impurities. SEC is a well-established technique in routine analysis for analysis of small molecules in polymeric samples, and ASAP can be added as a technique for on-process analysis for facile and rapid detection of impurities.

Additionally, the research did not explain the unusual chromatographic peak shapes of poly(oxyethylene) sorbitan-based polymers observed, and further investigation might be required

with proposals including (i) the use of ion mobility mass spectrometry to add an extra dimension in the separation and (ii) use of 2D hyphenated chromatographic techniques or (iii) the coupling of several columns in series to improve peak resolution and peak capacity within the chromatographic separation. The presence of possible initial cyclisation subproducts of sorbitol in polysorbate materials could provide insights into formulation development and suggests that current synthetic routes require improvement. Further investigation is required into the interactions of the different cyclisation subproducts of sorbitol with the drug molecule or the biological entities and how the molecule is delivered when these cyclisation subproducts are present.

An example of the benefit of different ionisation sources was shown when using negative ion ESI MS to quantify free lauric acid in Tween®20, which provided an approach to compare suppliers and product qualities. Even though the proposed approach of quantitation of free lauric acid eliminates most of the sample preparation steps used in the standardised method using a liquid chromatography-charged aerosol detector [377], the drawback is the lack of detection of free ethylene oxide or dioxin from the synthesis or degradation or other volatile molecules present in the mixture, which is possible when using headspace or liquid injection gas chromatography-MS (GC-MS) [378]. These techniques allow the simultaneous identification and quantitation of synthetic (ethylene oxide or dioxin) or oxidative degradation (formic acid) subproducts, saving time during the analysis. It is worth noticing that their control is critical due to their carcinogenic characteristics and the possible interactions of these impurities with the drug molecule.

In terms of the quantitation, changing the mass analyser from the Q to the QToF did not result in significant improvements. Even with the challenges of the Q mass analysers related to the resolution of multiply charged species, the quantitation capabilities of both mass analysers were in a similar range with concordances in the calculated and manufacturer values of M_n, M_w and PDI. The use of a triple quadrupole mass analyser (QqQ) could be a reasonable, cost-effective alternative between mass analysers for PEG mixtures with low complexity, but a QToF mass analyser is highly recommended for complex mixtures. The use of a QToF mass analyser is recommended when quantifying complex PEG polymers (*i.e.*, Tween® 80); however, investigation of background ions is required to avoid artefacts. Moreover, the precision of the analysis was improved when using a monodispersed internal standard (ISTD); however, the low level of ion suppression observed when using 18-crown-6 suggests the need to find an alternative monodispersed ISTD that elutes at higher percentages of organic solvent (higher than 30%), especially when quantifying complex PEG mixtures.

Quantitative data processing can be accelerated by executing the mass spectra deconvolution algorithm using scripting software. Quantitative approaches using a surrogate oligomer can benefit from the incorporation of the proposed deconvolution approach to the TargetLynx™ Application Manager and add-on within the MassLynx™ software. An example of automation using TargetLynx™ was its application to surrogate oligomers based on the RICC of the most intense ion with/without SIM acquisition. This resulted in an extremely fast data processing with the calibration curve immediately obtained without user input. When analysing QToF data, the longer data processing times compared to Q data (60 min *vs* 20 min) suggest that adding a scripting software to accelerate the data processing (such as TargetLynx™) is highly advisable. Using the QToF MS alongside scripting software should increase the suitability of the mass analyser in quality control or high throughput environments. Some of these challenges can be avoided with recent developments in transforming centroid into profile data and *vice versa*. Their development is undoubtedly crucial when implementing high-resolution mass analysers into routine quality control environments by reducing data file size, as demonstrated in this research. Still, the use of a black-box approach of continuous data generation, processing, backup and elimination with minimal user input or expert understanding can be used to mitigate some of these challenges.

The current work did not explore the applicability of the developed quantitation approach for the complex PEGs used in this research. The presence of isobaric ions in the background was negligible in most cases and can be easily identified; however, analysis of complex PEGs requires careful examination when applying data deconvolution due to the presence of multiple isobaric ions (*e.g.*, Tween® 80). Even though further research is required, the deconvolution approach is expected to apply to other areas where polymer quantitation is needed, such as an alternative to the method developed by Lingaityte for the quantitation of methylene diphenyl diisocyanate oligomers [158] or the calculation of the degree of substitution of CDs.

7.2.3 Final remarks

The UHPSFC-MS method developed for PEG analysis herein has been shown to be fit-for-purpose and can be used in the pharmaceutical industry for investigation and quality control purposes. The addition of UHPSFC-MS is recommended to investigate samples that cannot meet specifications due to in-process degradation, suppliers, or batches - *e.g.*, by using the benefit of the selectivity of the ionisation to unravel polymer complexity.

7.3 Summary of contributions in (2-hydroxypropyl)-β-cyclodextrins

7.3.1 Primary contributions

Additionally, the research investigated the challenges in developing a UHPSFC-MS assay for 2HPBCD analysis and the complexities involved in the method development and characterisation. Whilst an acidic mobile phase was required to eliminate the formation of Na salts, an inclusion complex governed the separation and complicated the selection of the stationary phase. The selection of the stationary phase pointed to the formation of an inclusion complex between the stationary phase ligand intruding into the 2HPBCD cavity.

Similar benefits of changing the mass analyser from a Q to the QToF were found to those encountered in the analysis of PEGs, with the higher sensitivity afforded by the design of the Synapt^{TM} G2-*Si* being the most relevant aspect. Also, the addition of ion mobility mass spectrometry (IMMS) revealed the hidden complexity of the different conformers and positions of substitutions and showed how the coupling of SFC becomes a powerful tool for polymer characterisation due to the additional detail achieved in the structure of the polymer and is recommended when characterising these excipients. Finally, the formation of different charged states suggests an approach for the quantitation of PEGs and the calculation of the degree of substitution of 2HPBCD can be developed.

7.3.2 Limitations of the research and future work

One of the main concerns when developing the method was the significant differences of the solubility of the native α-, β- or γ- cyclodextrins (CD) compared to 2HPBCD in solvents commonly used as SFC diluents/mobile phases. The result is that the poor solubility of β-CD in the mobile phase might limit the observation of this component and compromise the applicability of the technique to perform an investigation of the formulation. The extensive differences in the solubility between CDs suggest that the development of a generic method for CD characterisation is doubtful. Further efforts should be made to elucidate the substitution pattern of 2HPBCD - with the formation of an inclusion complex between 2HPBCD and the stationary phase ligands being a possible route for separation. Both achiral and chiral stationary phases with ligands that resemble small drug molecules were proposed; however, a deeper study of secondary interactions that participate in the inclusion is required to develop a method that is fit-for-purpose.

The characterisation of 2HPBCD benefited when adding IMMS, as a deeper understanding of substitution positions on the β-CD ring and conformers of the 2HPBCD was possible. This work showed that hydroxypropylation in the OH-2 position was not regioselective and could compromise the pharmaceutical characteristics of the final drug product. Even with this limitation, the formation of different charged states suggested that an approach for quantitation to calculate the degree of substitution of the 2HPBCD can be developed based on the proposed deconvolution approach of PEG mass spectra to correlate chemical structure and the performance properties of the formulated drug.

7.3.3 Final remarks

Even though UHPSFC-MS provided insights into the characterisation of 2HPBCD, a deeper understanding of the chromatographic method is required to evaluate the capability of including the developed method technique in the routine analysis of these excipients.

7.4 Final thesis remarks

The research presented in this thesis has demonstrated that SFC-MS with various ion sources can provide deep insight into the characterisation of complex polymeric materials used in the pharmaceutical industry. The information provided is complementary and, in some aspect, superior to the current gold standard of SEC. Of particular note is:

- The use of ammonium acetate mobile phases to force the formation of ammoniated adducts over sodiated molecules, which are more straightforward to process
- The improved data visualisation of ion maps, especially when using MZmine, which facilitates the observation of the polymeric chains and the impurities present
- The use of high-resolution mass spectrometry to tackle the higher degree of isobaric masses that are present in most of the polymeric mixtures
- The use of deconvolution algorithms based on the oligomer for improved quantitation, which is recommended in conjunction with automated data processing algorithms
- The benefits of the coupling of ion mobility mass spectrometry with supercritical fluid chromatography, which facilitate the observation of conformers and interpretation of challenging polymeric mixtures

Appendix A Prediction of acidic dissociation constants of acidic PEGs using surrogate molecules

Surrogates of acidic PEGs with two repeating units were selected to account for electrostatic, hydrogen bonding, and other possible interactions to predict their pKa values using ACDLabs 2017.1.

A.1 Acidic dissociation constant prediction for mPEG acid 2000

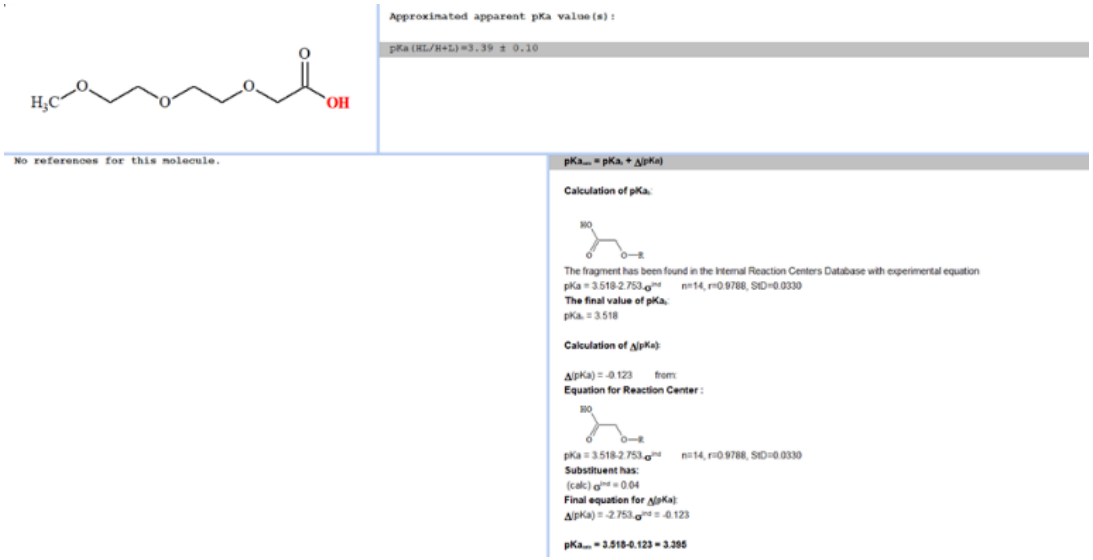

A.2 Acidic dissociation constant prediction for PEG diacid 2000

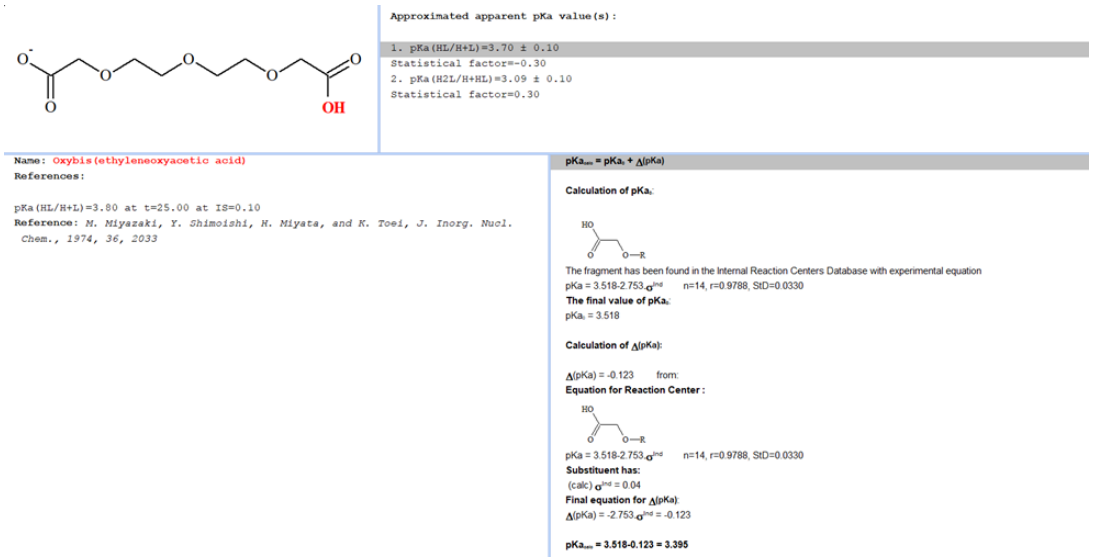

Appendix B Calibration curves used in poly(ethylene) glycol quantitation

In chapter 5, several approaches were proposed to quantify PEG materials. Here, the calibration curves and the residuals of each approach are shown. Samples were analysed in triplicates.

B.1 Approaches for quantitation using a surrogate oligomer and quadrupole mass analyser. External calibration linear fittings

B.1.1 Selective ion monitoring acquisition of the most intense ion in the mass spectra. External calibration linear fittings

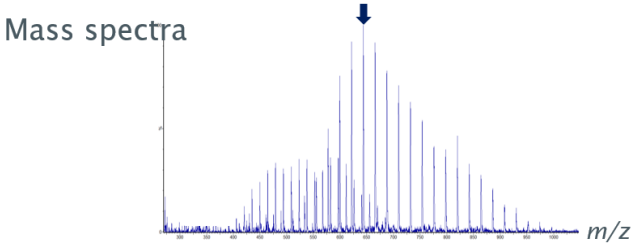

B.1.2 Use of the reconstructive ion current chromatogram of the most intense oligomer. External calibration linear fittings

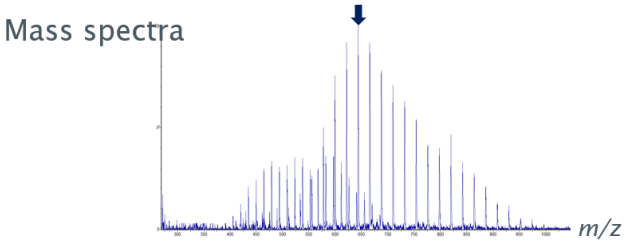

B.1.3 Deconvolution of the mass spectra of a surrogate oligomer. External calibration linear fittings

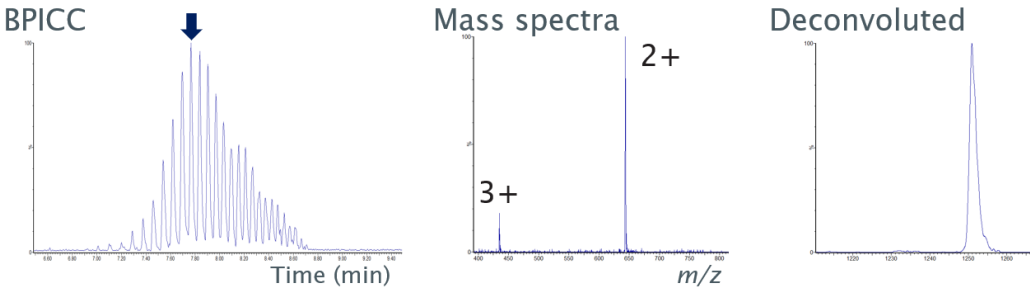

B.1.1 Selective ion monitoring acquisition of the most intense ion in the mass spectra. External calibration linear fittings

PEG 600

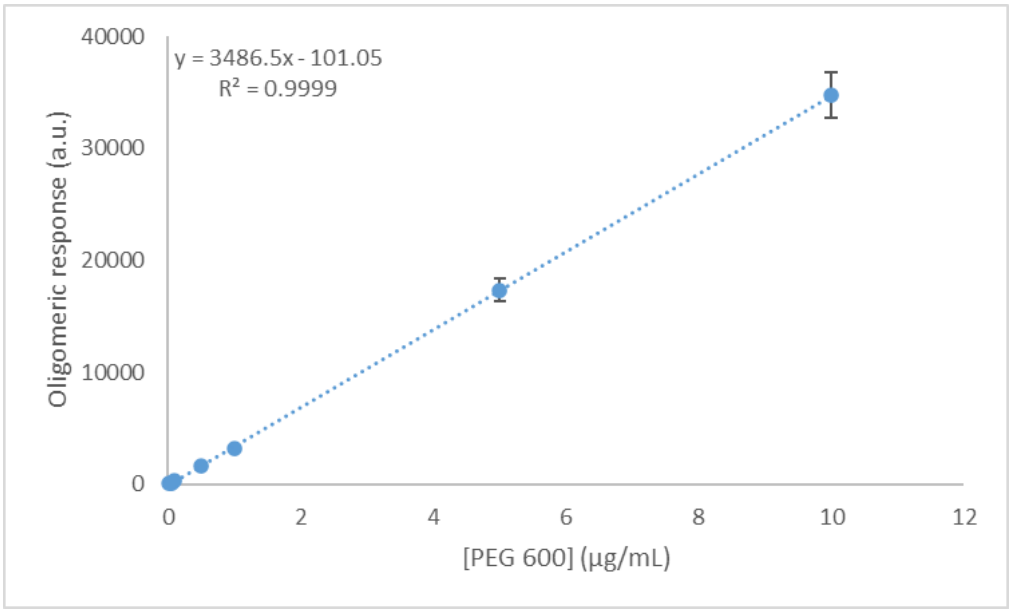

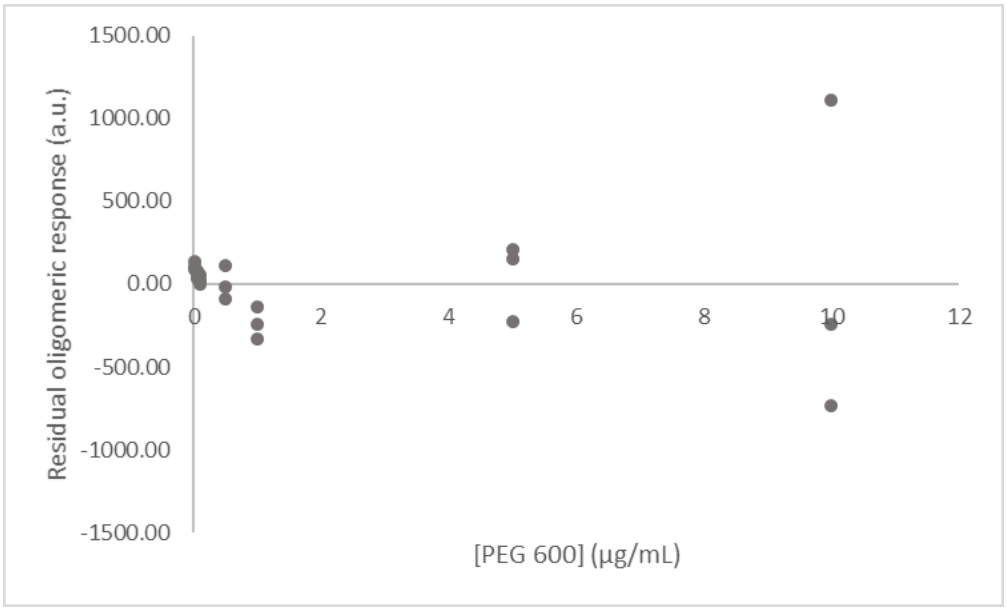

PEG 1000

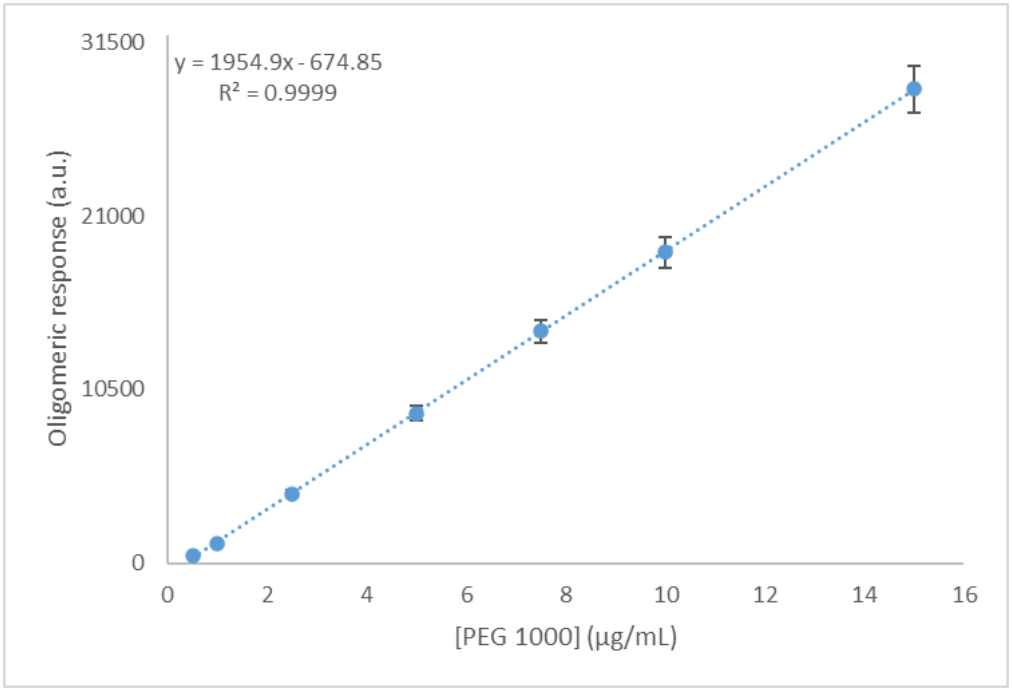
y = 1954.9x - 674.85
R² = 0.9999
Oligomeric response (a.u.)
31500
21000
10500
0
0
2
4
6
8
10
12
14
16
[PEG 1000] (µg/mL)

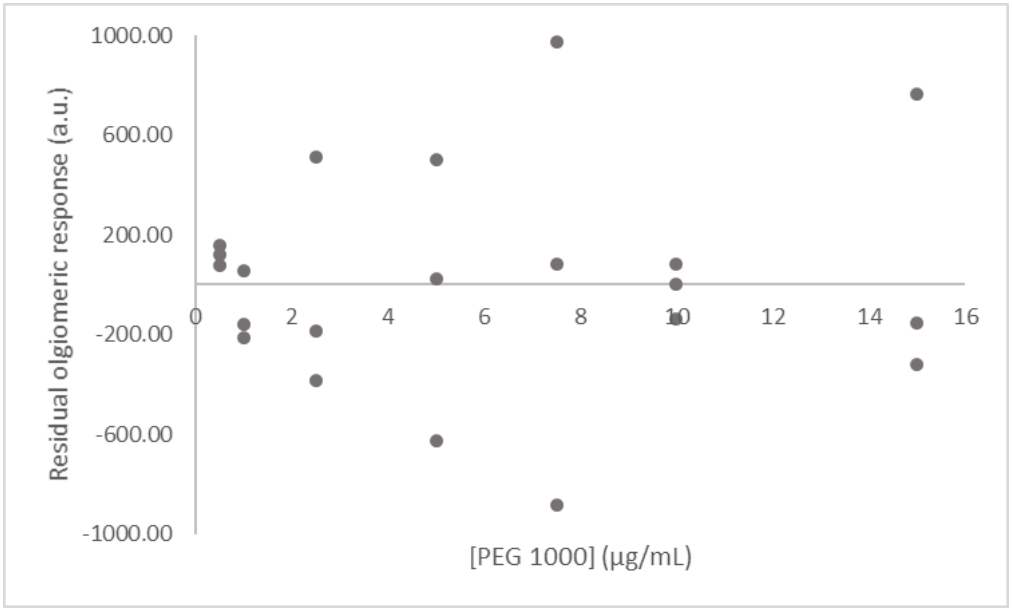
Residual olgiomeric response (a.u.)
1000.00
600.00
200.00
-200.00
-600.00
-1000.00
0
2
4
6
8
10
12
14
16
[PEG 1000] (µg/mL)

PEG 1450

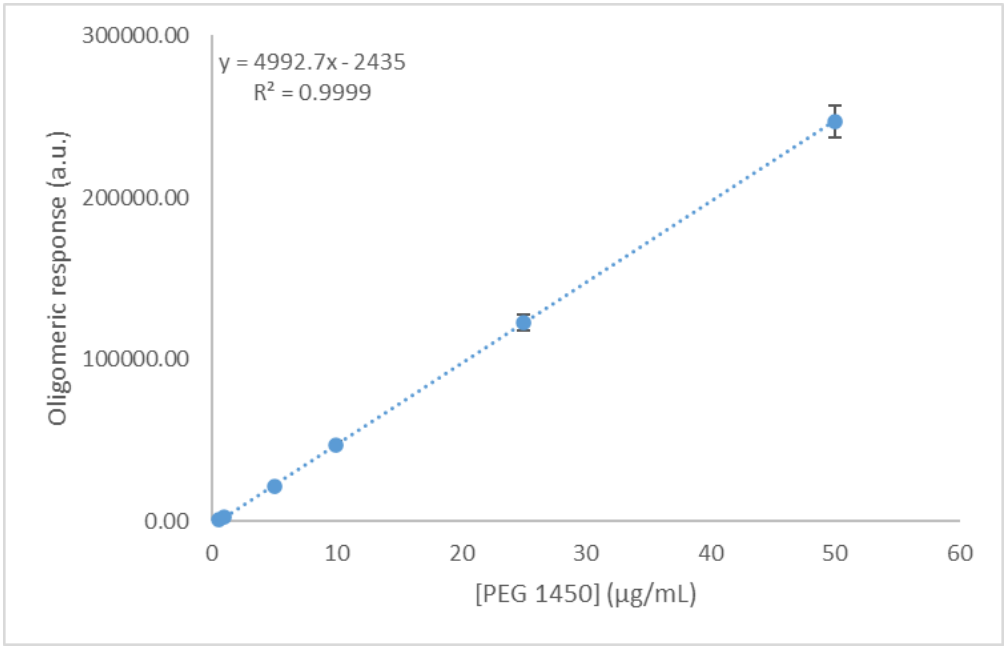
y = 4992.7x - 2435
R² = 0.9999
Oligomeric response (a.u.)
300000.00
200000.00
100000.00
0.00
0
10
20
30
40
50
60
[PEG 1450] (µg/mL)

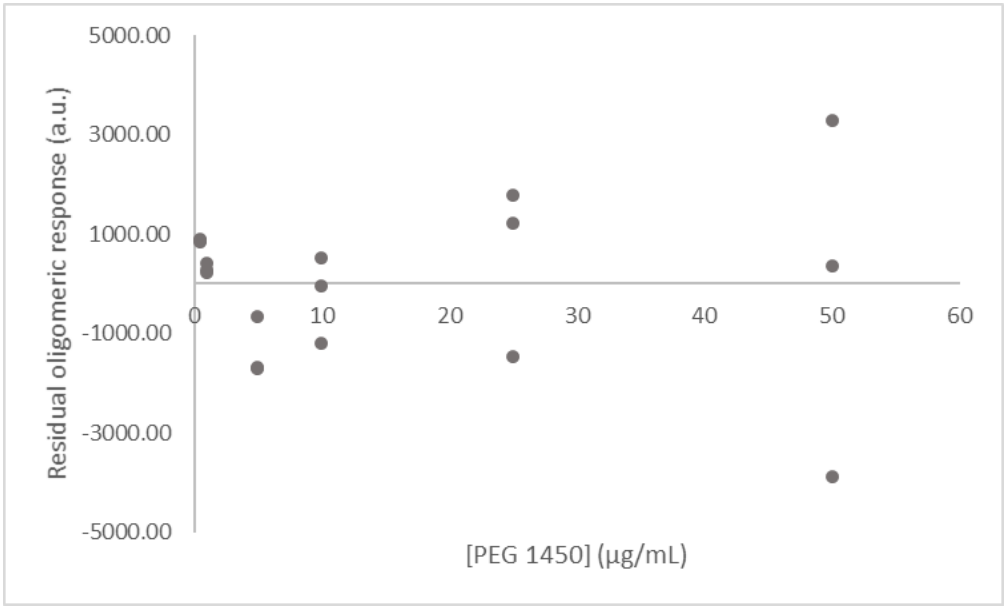
Residual oligomeric response (a.u.)
5000.00
3000.00
1000.00
-1000.00
-3000.00
-5000.00
0
10
20
30
40
50
60
[PEG 1450] (µg/mL)

PEG 2000

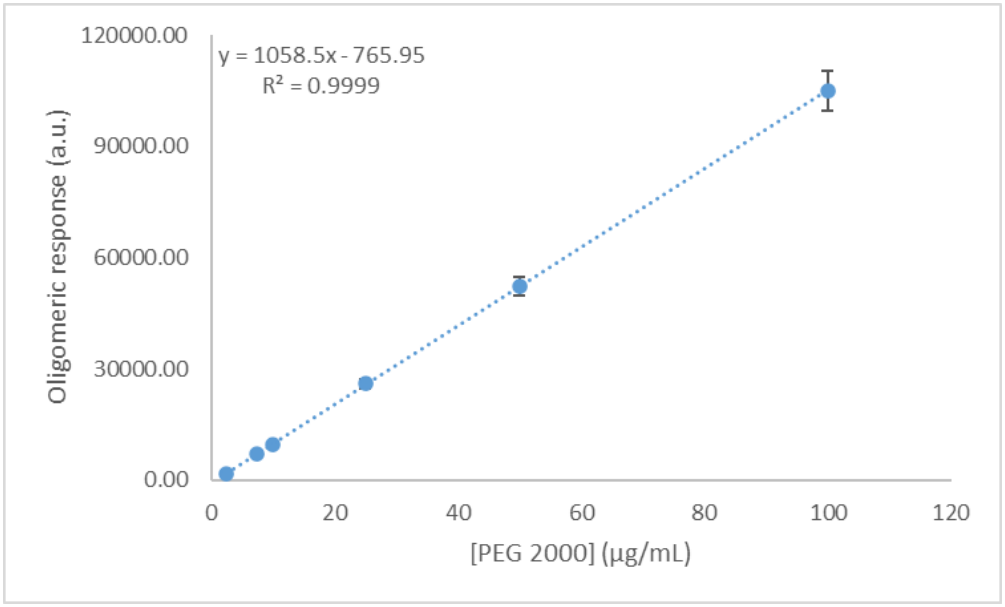
y = 1058.5x - 765.95
R² = 0.9999
Oligomeric response (a.u.)
120000.00
90000.00
60000.00
30000.00
0.00
0
20
40
60
80
100
120
[PEG 2000] (µg/mL)

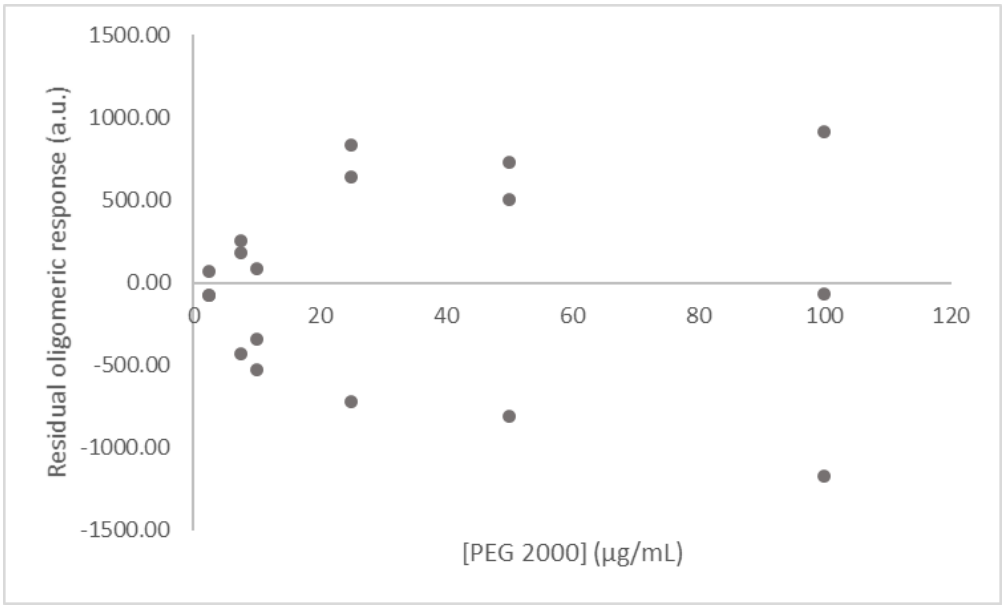
Residual oligomeric response (a.u.)
1500.00
1000.00
500.00
0.00
-500.00
-1000.00
-1500.00
0
20
40
60
80
100
120
[PEG 2000] (µg/mL)

B.1.2 Use of the reconstructive ion current chromatogram of the most intense oligomer. External calibration linear fittings

PEG 600

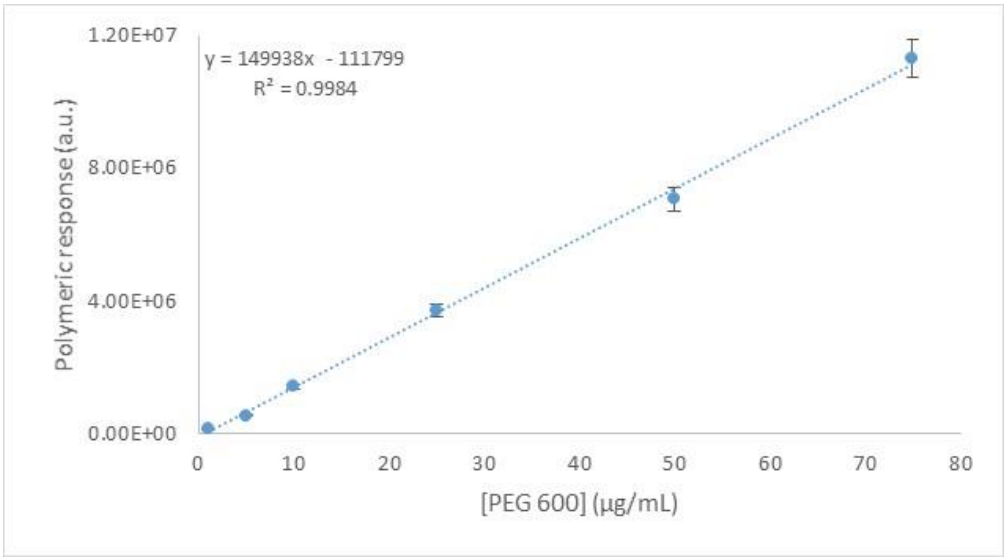

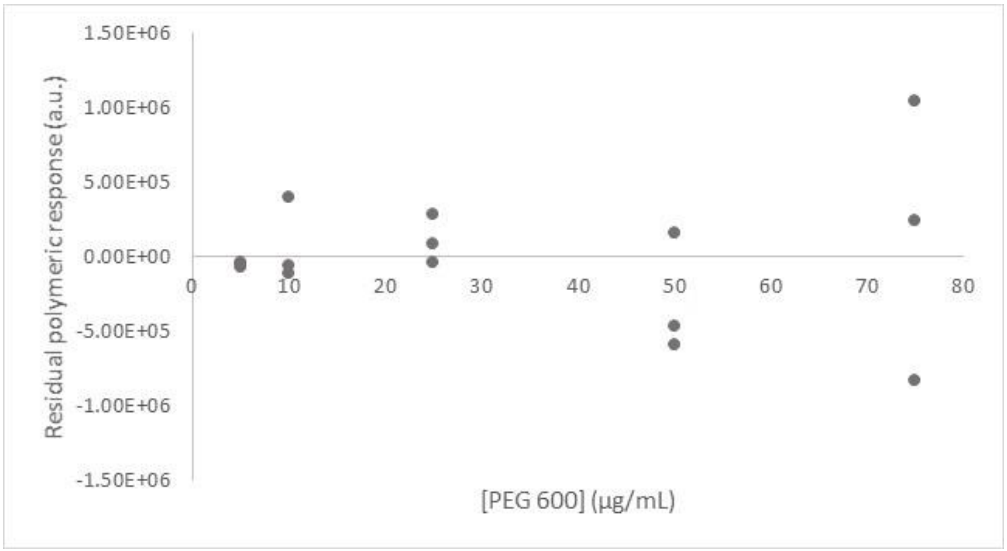

PEG 1000

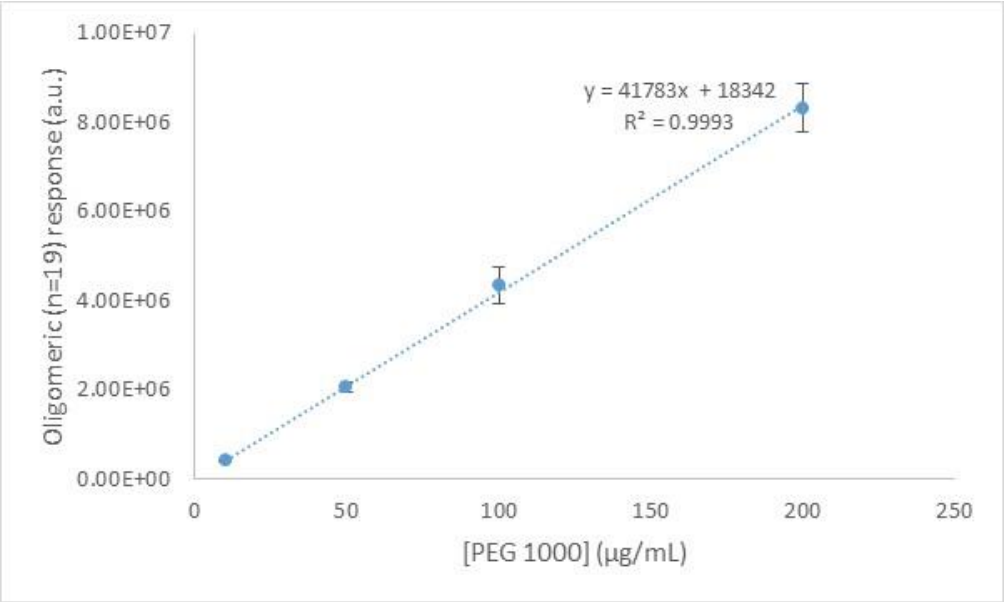
1.00E+07
8.00E+06
6.00E+06
4.00E+06
2.00E+06
0.00E+00
Oligomeric (n=19) response (a.u.)
y = 41783x + 18342
R² = 0.9993
0
50
100
150
200
250
[PEG 1000] (µg/mL)

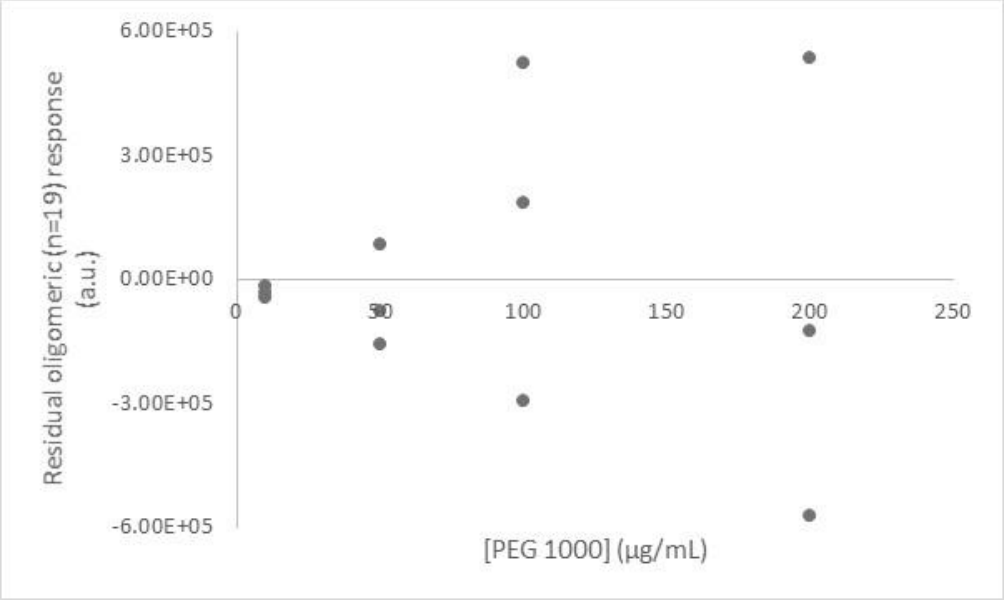
6.00E+05
3.00E+05
0.00E+00
-3.00E+05
-6.00E+05
Residual oligomeric (n=19) response (a.u.)
0
50
100
150
200
250
[PEG 1000] (µg/mL)

PEG 1450

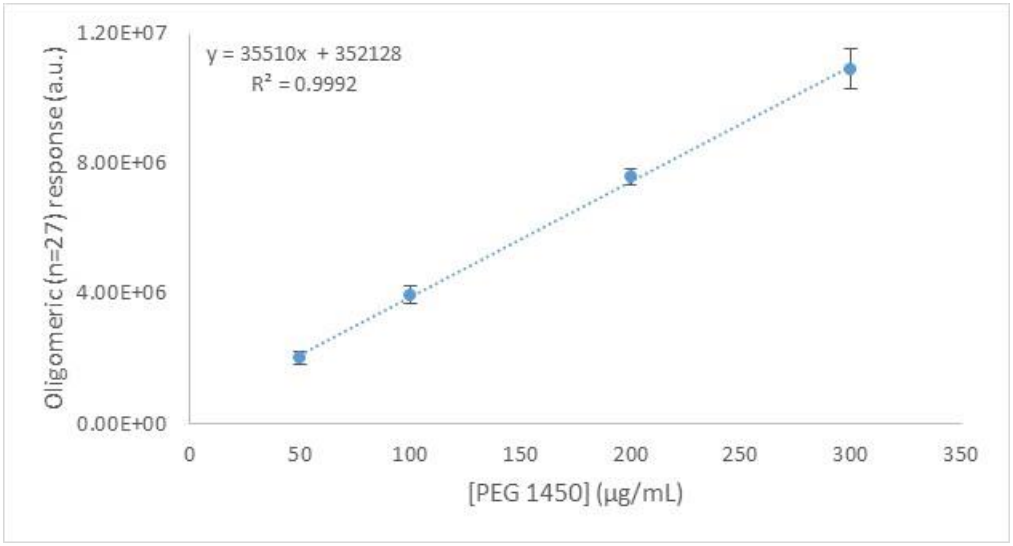
y = 35510x + 352128
R² = 0.9992
Oligomeric (n=27) response (a.u.)
1.20E+07
8.00E+06
4.00E+06
0.00E+00
0
50
100
150
200
250
300
350
[PEG 1450] (µg/mL)

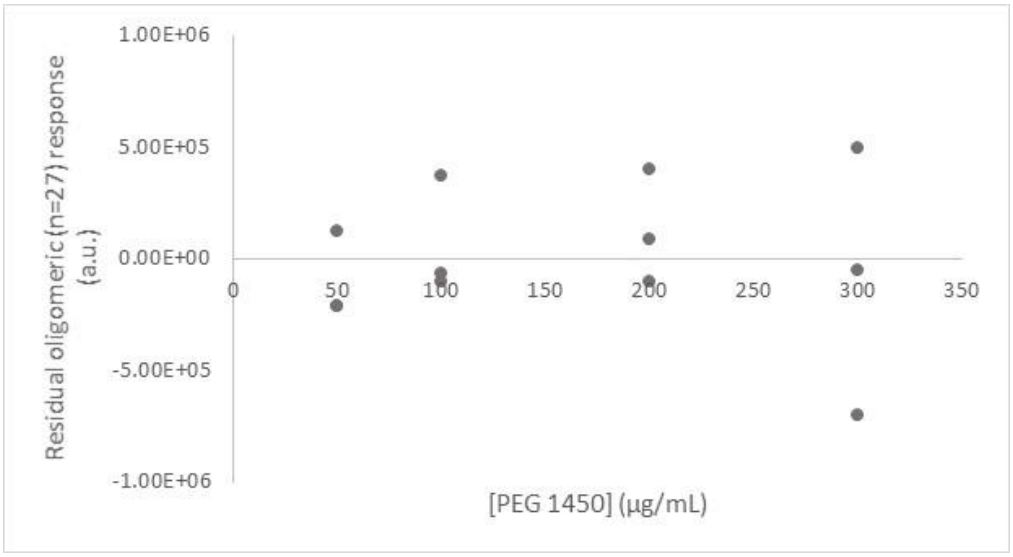
Residual oligomeric (n=27) response (a.u.)
1.00E+06
5.00E+05
0.00E+00
-5.00E+05
-1.00E+06
0
50
100
150
200
250
300
350
[PEG 1450] (µg/mL)

PEG 2000

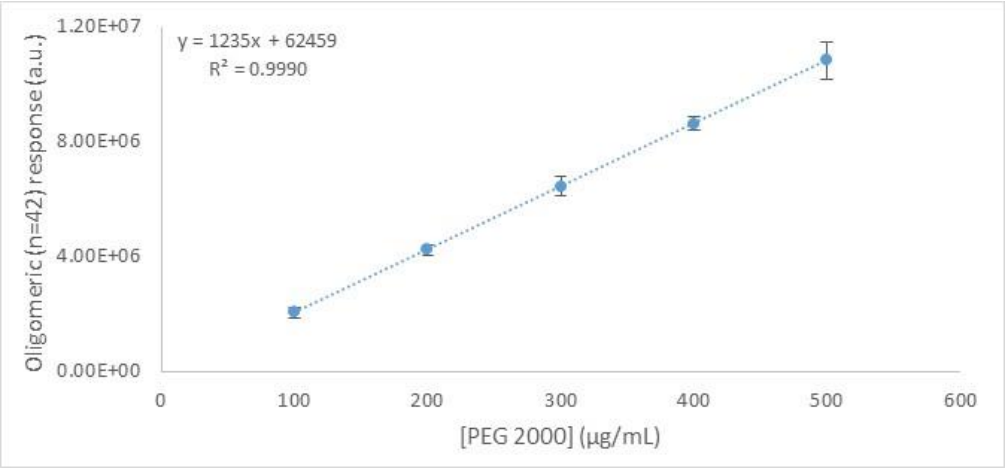
y = 1235x + 62459
R² = 0.9990
Oligomeric (n=42) response (a.u.)
1.20E+07
8.00E+06
4.00E+06
0.00E+00
0
100
200
300
400
500
600
[PEG 2000] (µg/mL)

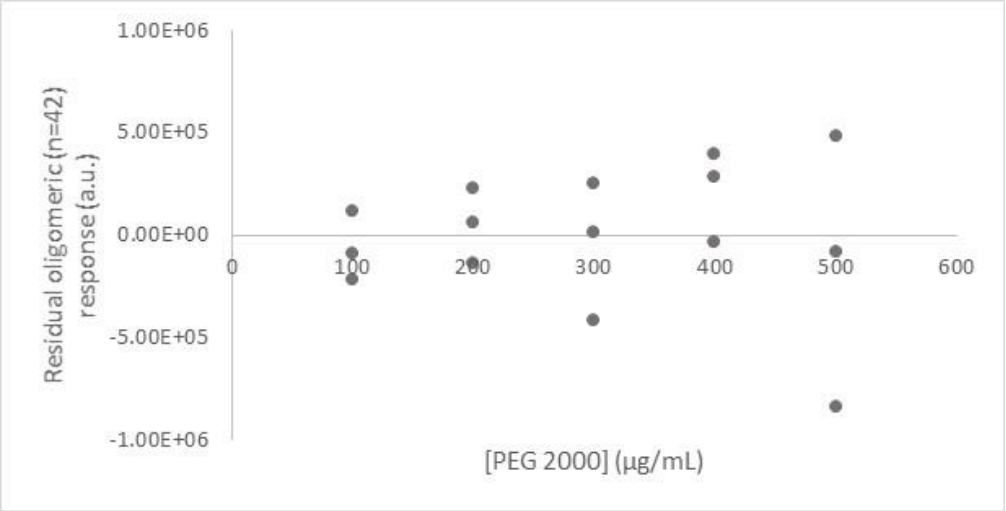
Residual oligomeric (n=42) response (a.u.)
1.00E+06
5.00E+05
0.00E+00
-5.00E+05
-1.00E+06
0
100
200
300
400
500
600
[PEG 2000] (µg/mL)

B.1.3 Deconvolution of the mass spectra of a surrogate oligomer. External calibration linear fittings

PEG 600

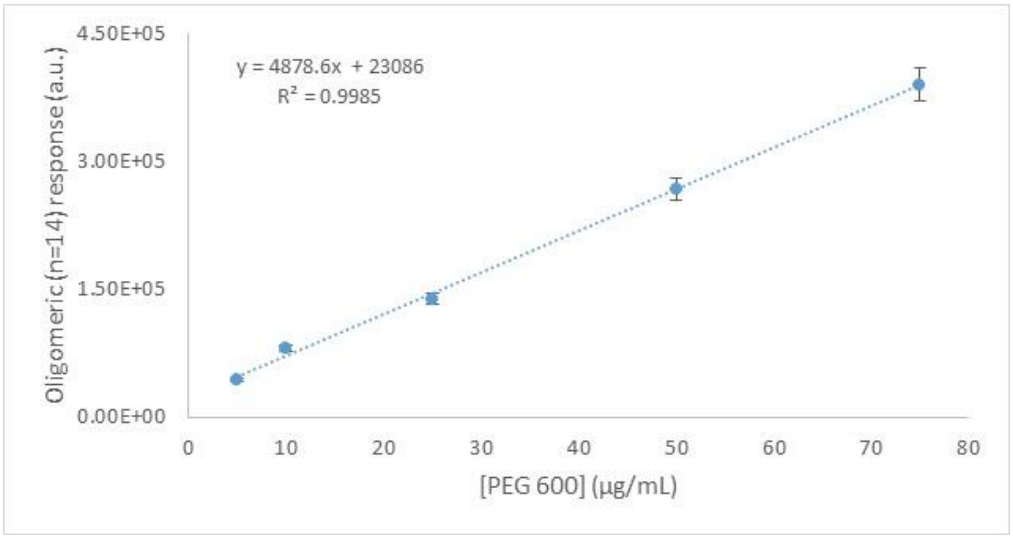

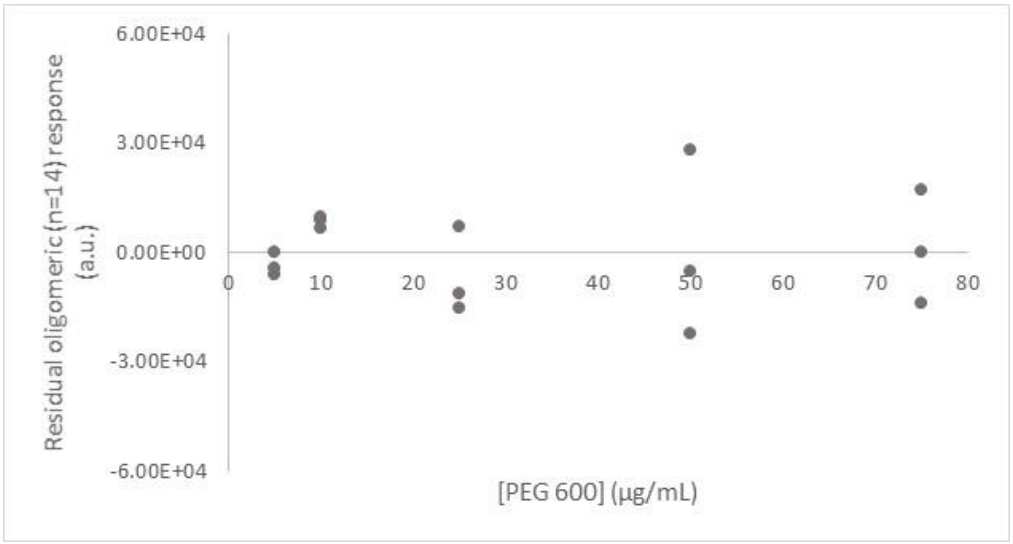

PEG 1000

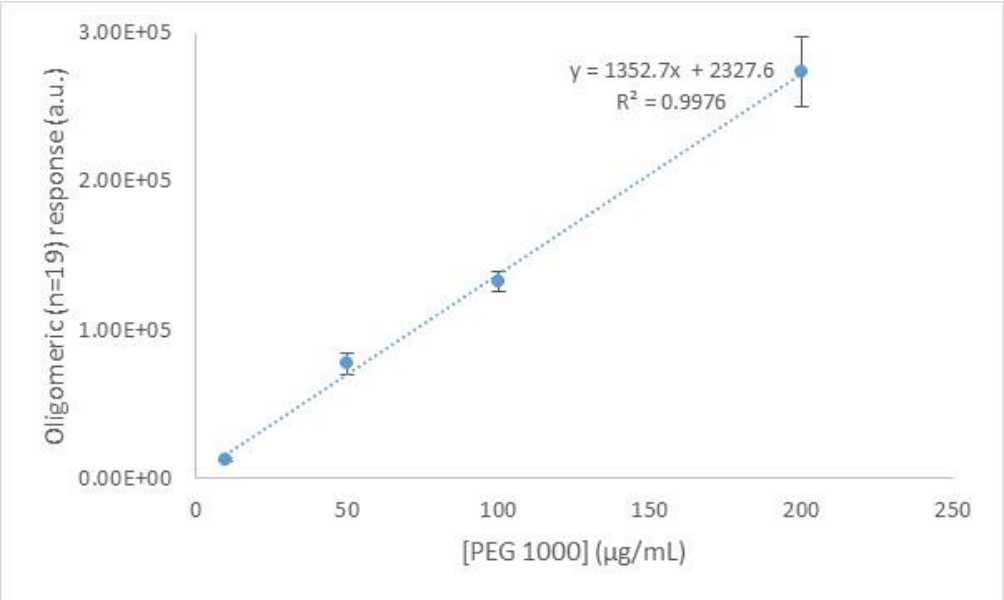
3.00E+05
2.00E+05
1.00E+05
0.00E+00
Oligomeric (n=19) response (a.u.)
y = 1352.7x + 2327.6
R² = 0.9976
0
50
100
150
200
250
[PEG 1000] (µg/mL)

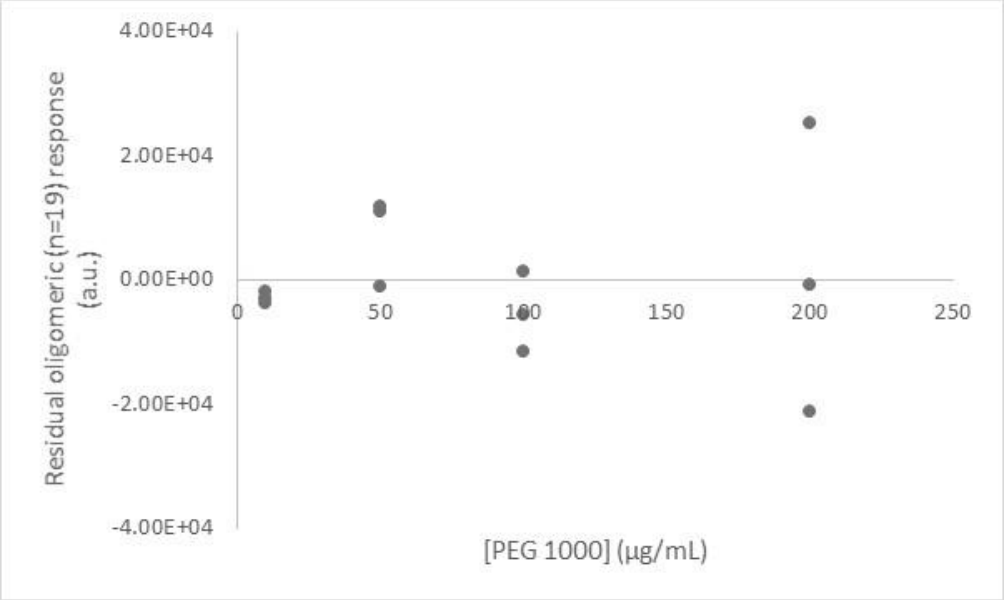
4.00E+04
2.00E+04
0.00E+00
-2.00E+04
-4.00E+04
Residual oligomeric (n=19) response (a.u.)
0
50
100
150
200
250
[PEG 1000] (µg/mL)

PEG 1450

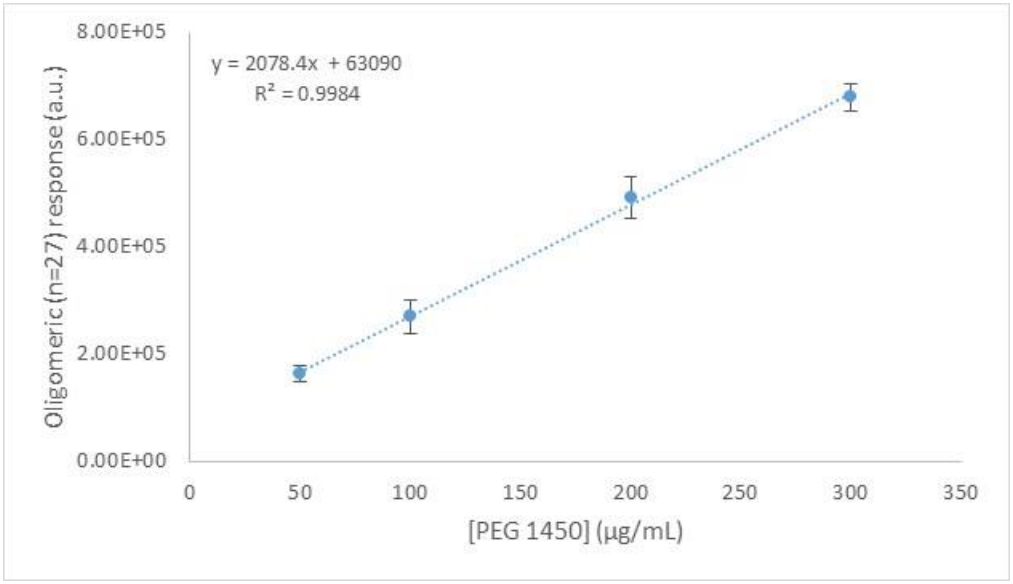
y = 2078.4x + 63090
R² = 0.9984
Oligomeric (n=27) response (a.u.)
8.00E+05
6.00E+05
4.00E+05
2.00E+05
0.00E+00
0
50
100
150
200
250
300
350
[PEG 1450] (µg/mL)

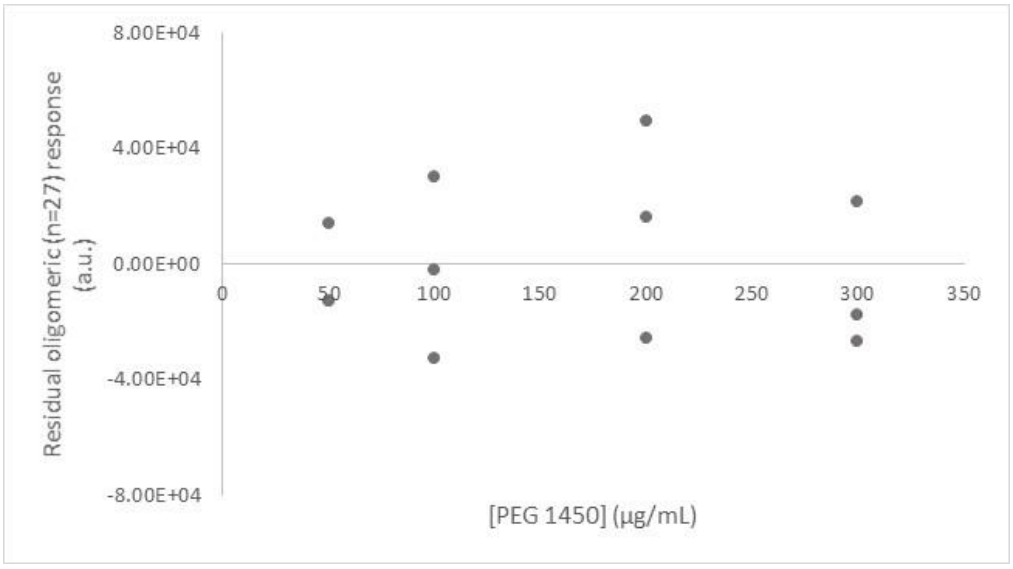
Residual oligomeric (n=27) response (a.u.)
8.00E+04
4.00E+04
0.00E+00
-4.00E+04
-8.00E+04
0
50
100
150
200
250
300
350
[PEG 1450] (µg/mL)

PEG 2000

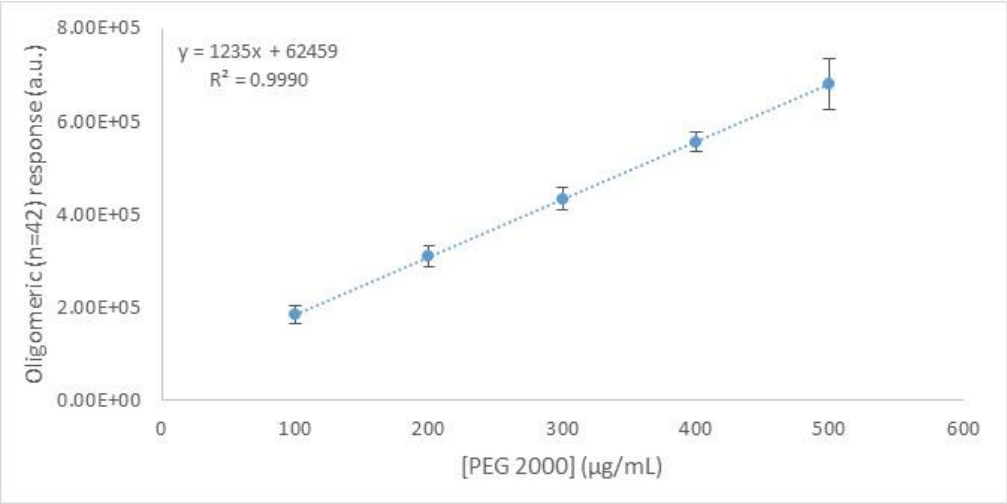
y = 1235x + 62459
R² = 0.9990
Oligomeric (n=42) response (a.u.)
8.00E+05
6.00E+05
4.00E+05
2.00E+05
0.00E+00
0
100
200
300
400
500
600
[PEG 2000] (µg/mL)

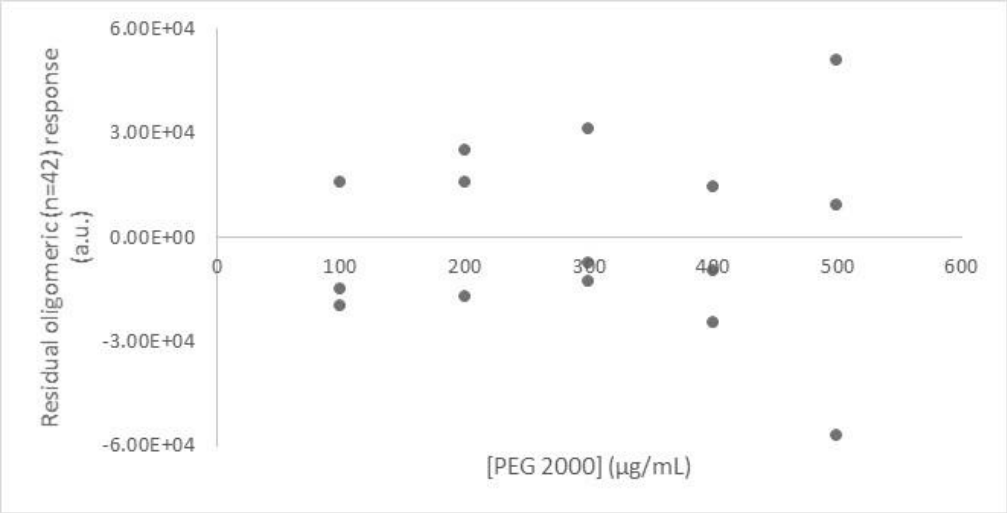
Residual oligomeric (n=42) response (a.u.)
6.00E+04
3.00E+04
0.00E+00
-3.00E+04
-6.00E+04
0
100
200
300
400
500
600
[PEG 2000] (µg/mL)

B.2 Approaches for quantitation using the whole distribution and quadrupole mass analyser. External calibration linear fittings

B.2.1 Sum of the peak areas of the reconstructive ion current chromatograms of all ions in the whole distribution. External calibration linear fittings

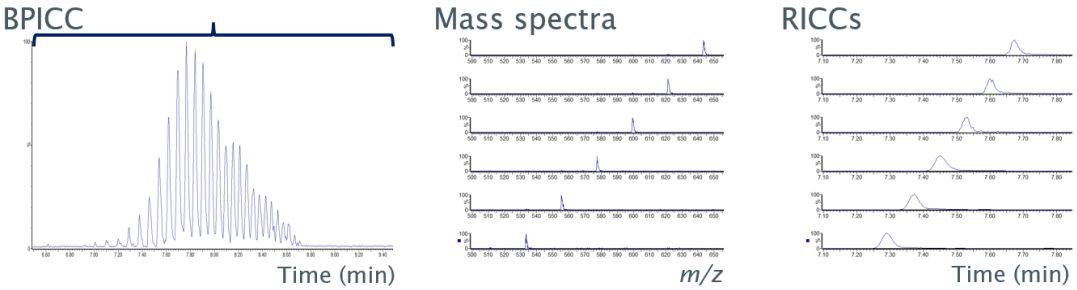

B.2.2 Sum of all the oligomer Transform™ deconvoluted response. External calibration linear fittings

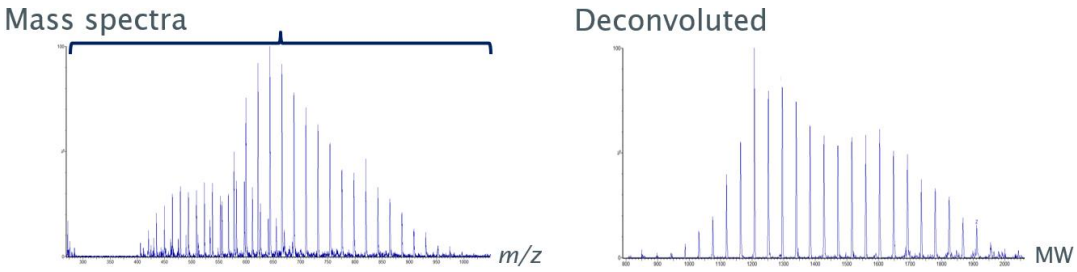

B.2.1 Sum of the peak areas of the reconstructive ion current chromatograms of all ions in the whole distribution. External calibration linear fittings

PEG 600

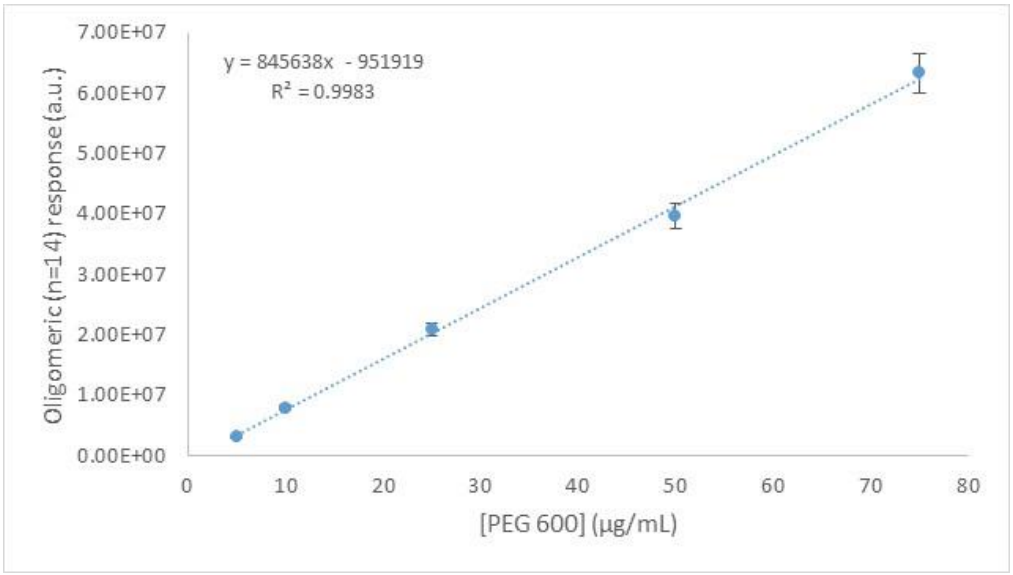

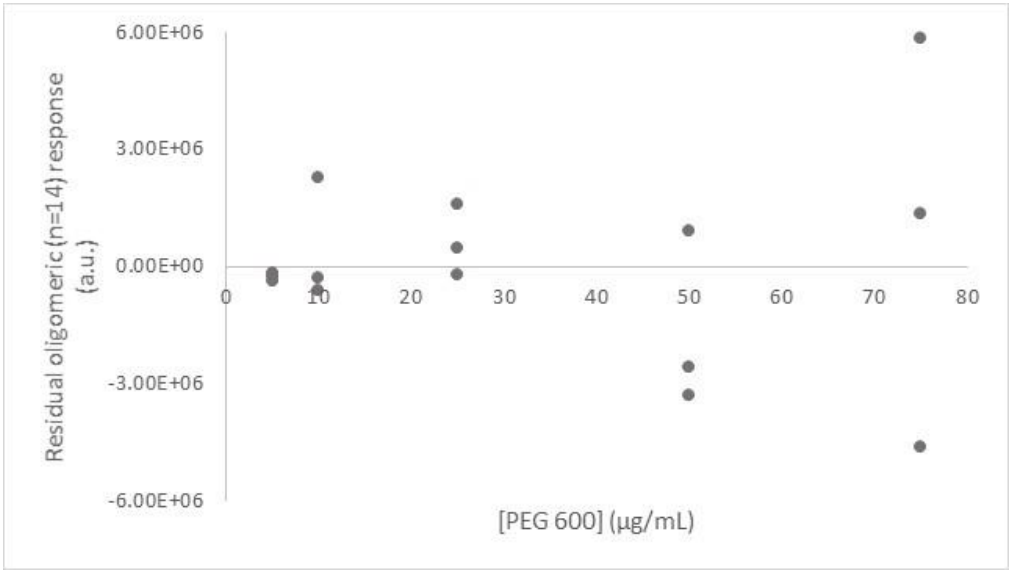

PEG 1000

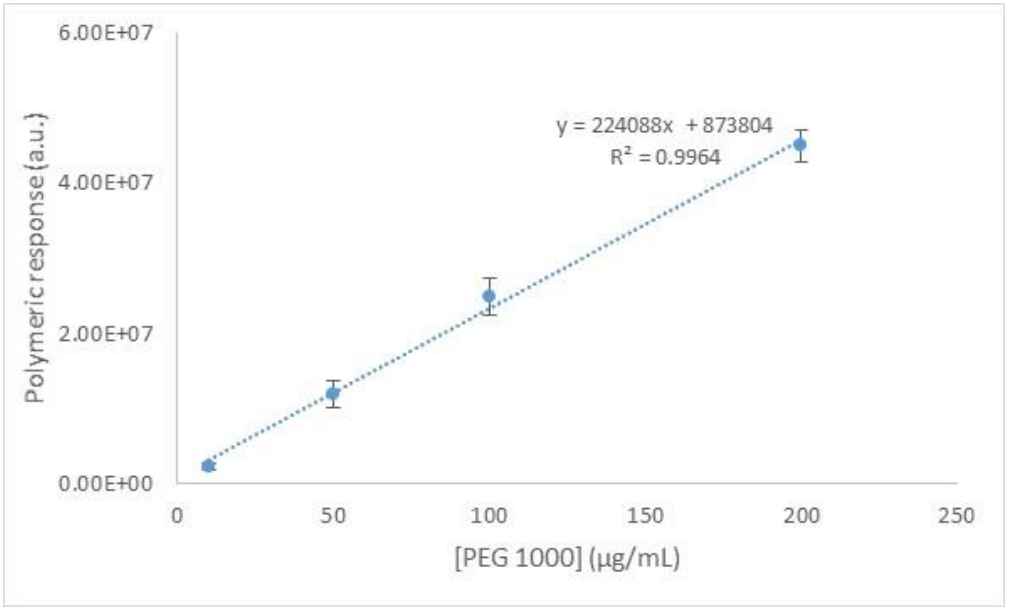
6.00E+07
4.00E+07
2.00E+07
0.00E+00
Polymeric response (a.u.)
y = 224088x + 873804
R² = 0.9964
0
50
100
150
200
250
[PEG 1000] (µg/mL)

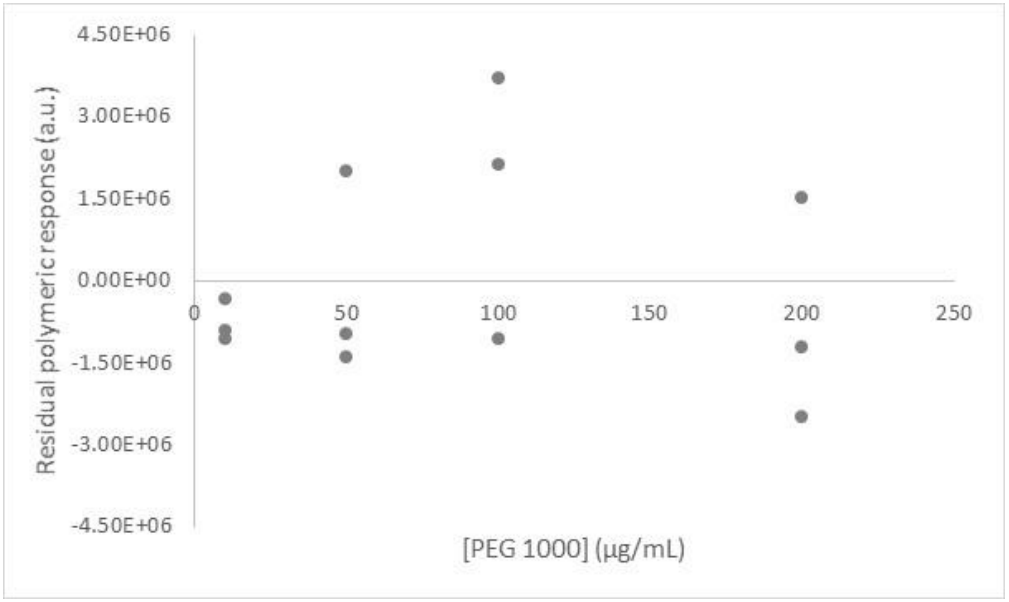
4.50E+06
3.00E+06
1.50E+06
0.00E+00
-1.50E+06
-3.00E+06
-4.50E+06
Residual polymeric response (a.u.)
0
50
100
150
200
250
[PEG 1000] (µg/mL)

PEG 1450

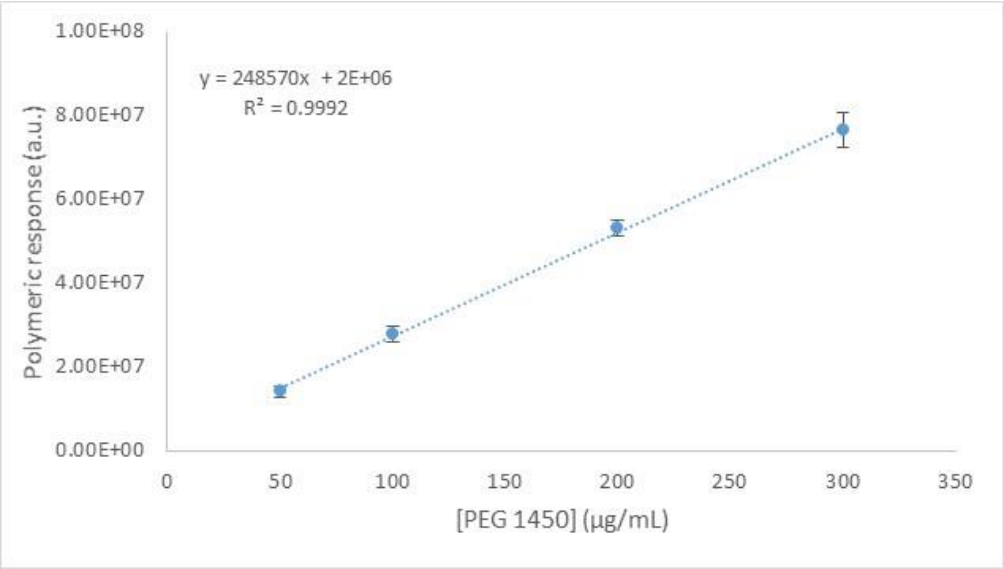
y = 248570x + 2E+06
R² = 0.9992
Polymeric response (a.u.)
1.00E+08
8.00E+07
6.00E+07
4.00E+07
2.00E+07
0.00E+00
0
50
100
150
200
250
300
350
[PEG 1450] (µg/mL)

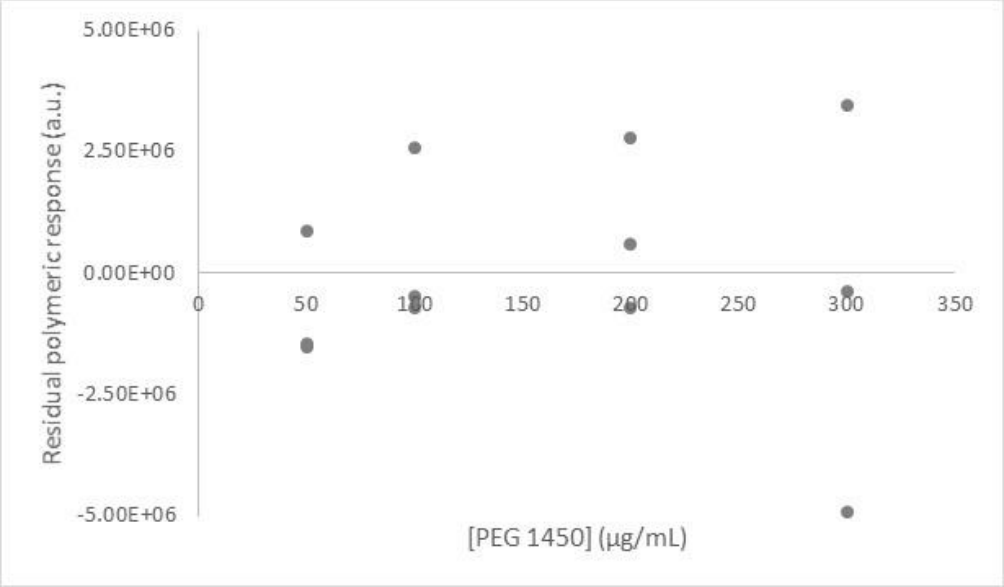
Residual polymeric response (a.u.)
5.00E+06
2.50E+06
0.00E+00
-2.50E+06
-5.00E+06
0
50
150
250
300
350
[PEG 1450] (µg/mL)

PEG 2000

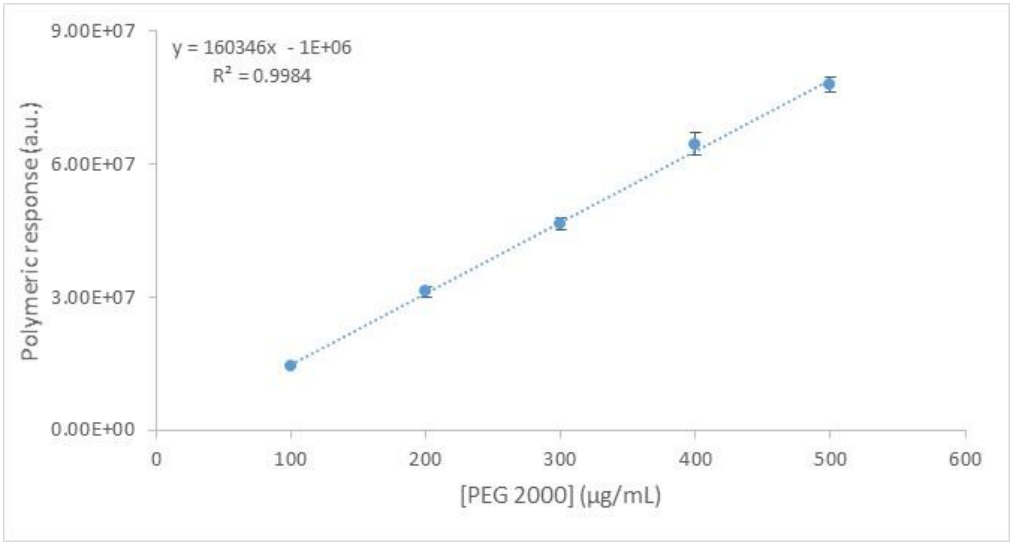
9.00E+07
6.00E+07
3.00E+07
0.00E+00
y = 160346x - 1E+06
R² = 0.9984
Polymeric response (a.u.)
0
100
200
300
400
500
600
[PEG 2000] (µg/mL)

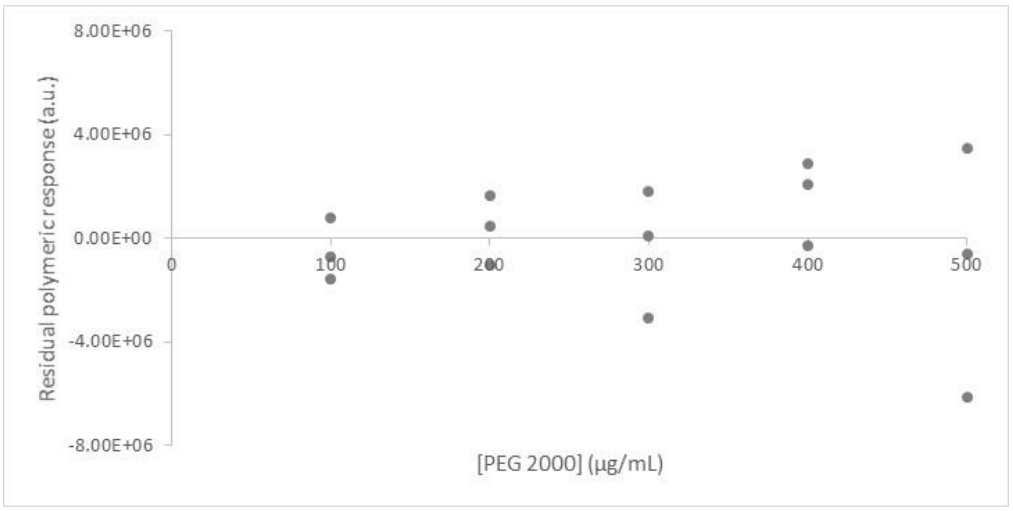
8.00E+06
4.00E+06
0.00E+00
-4.00E+06
-8.00E+06
Residual polymeric response (a.u.)
0
100
200
300
400
500
[PEG 2000] (µg/mL)

B.2.2 Sum of all the oligomer Transform™ deconvoluted response. External calibration linear fittings

PEG 600

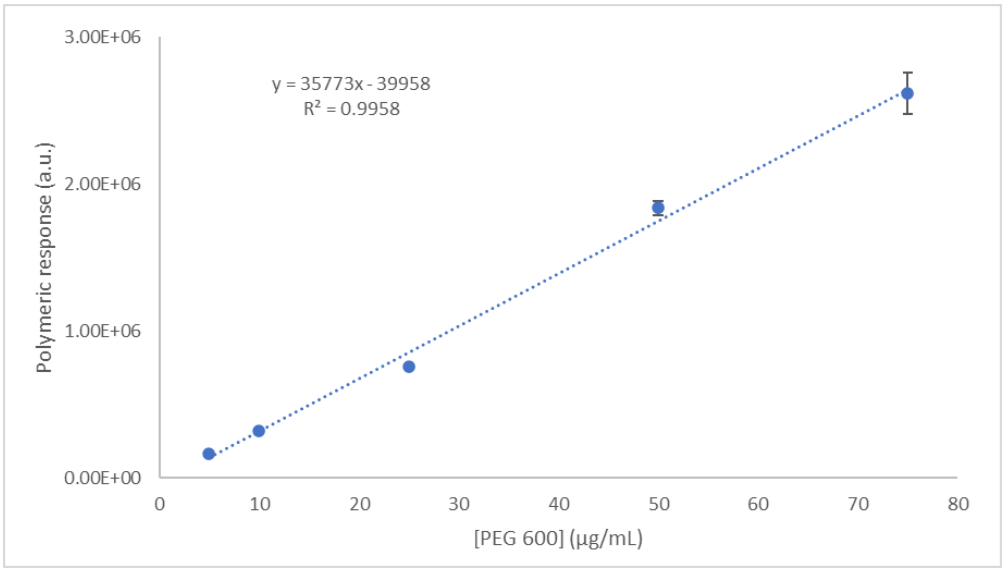

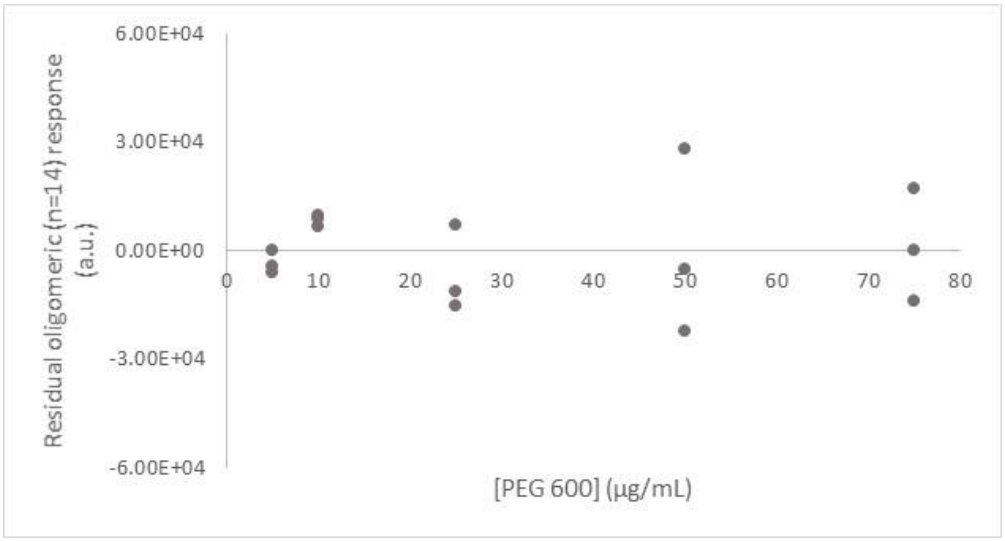

PEG 1000

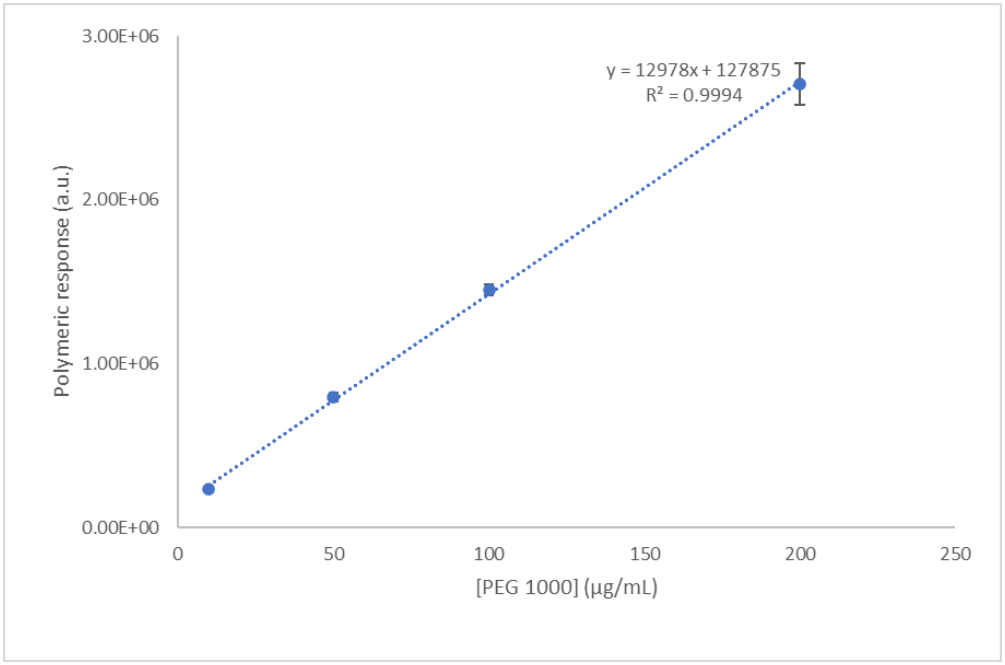
3.00E+06
2.00E+06
1.00E+06
0.00E+00
Polymeric response (a.u.)
y = 12978x + 127875
R² = 0.9994
0
50
100
150
200
250
[PEG 1000] (µg/mL)

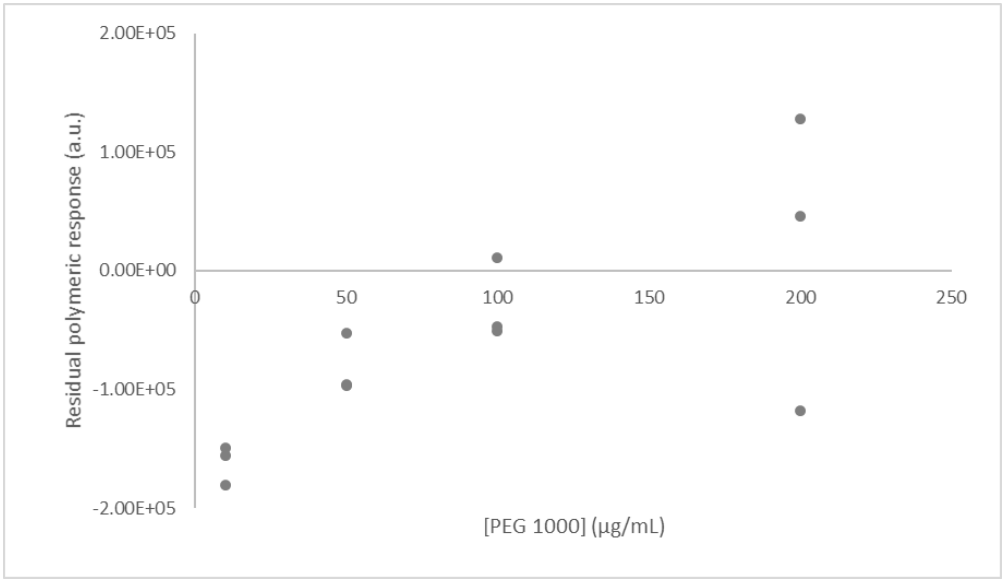
2.00E+05
1.00E+05
0.00E+00
-1.00E+05
-2.00E+05
Residual polymeric response (a.u.)
0
50
100
150
200
250
[PEG 1000] (µg/mL)

PEG 1450

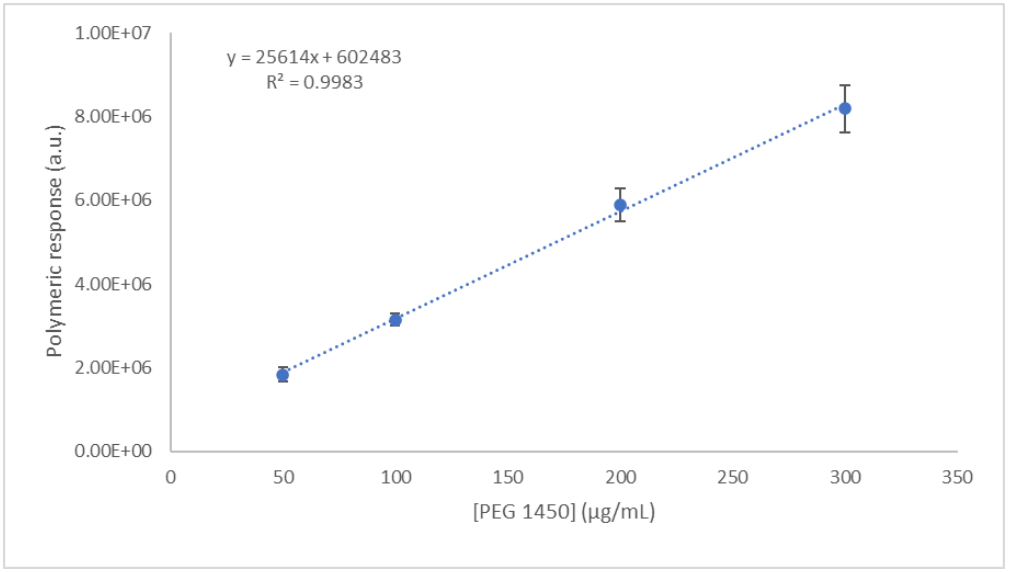
y = 25614x + 602483
R² = 0.9983
Polymeric response (a.u.)
1.00E+07
8.00E+06
6.00E+06
4.00E+06
2.00E+06
0.00E+00
0
50
100
150
200
250
300
350
[PEG 1450] (µg/mL)

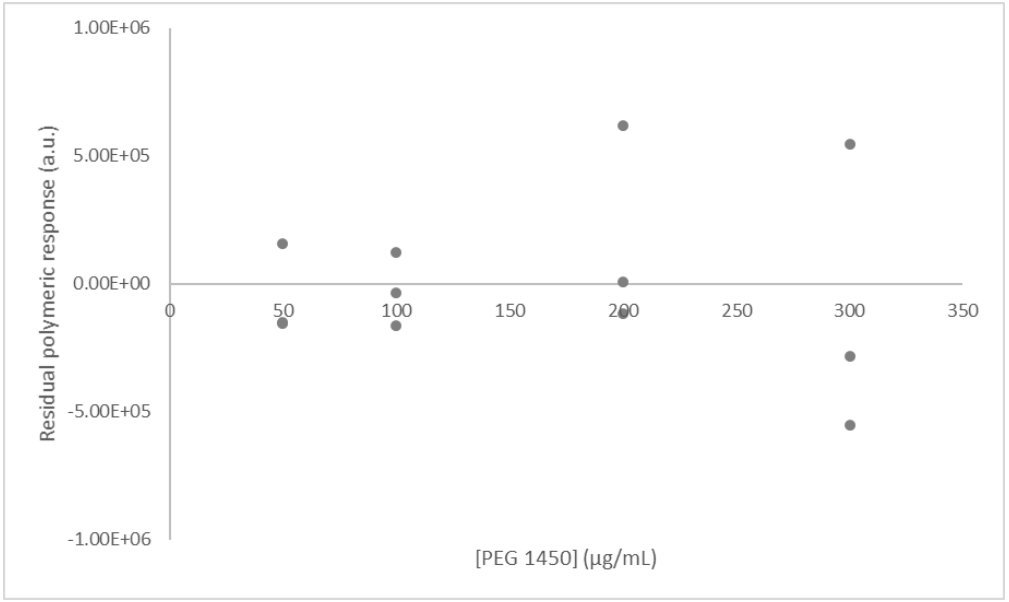
Residual polymeric response (a.u.)
1.00E+06
5.00E+05
0.00E+00
-5.00E+05
-1.00E+06
0
50
100
150
200
250
300
350
[PEG 1450] (µg/mL)

PEG 2000

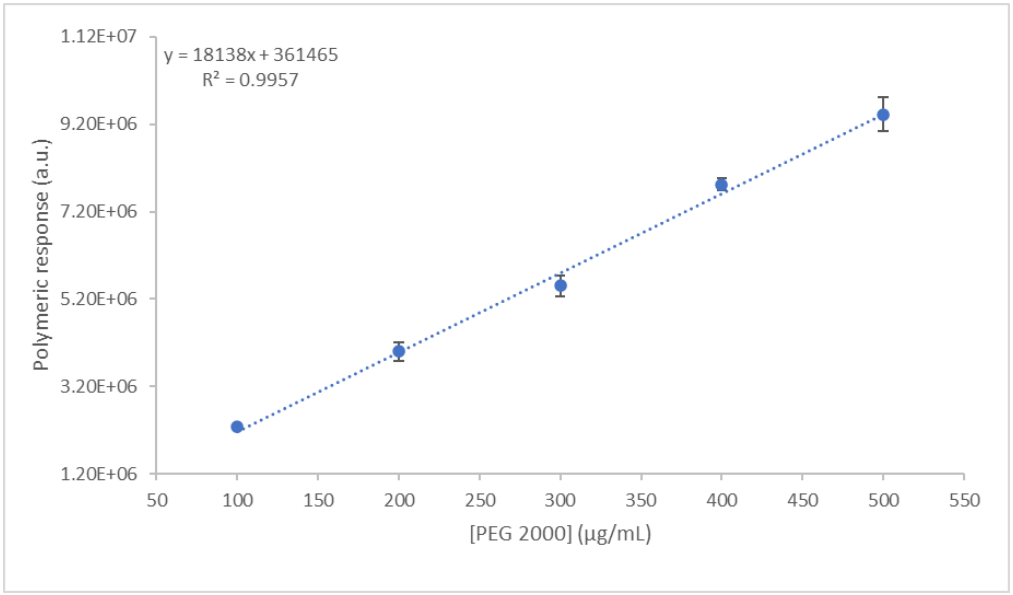
y = 18138x + 361465
R² = 0.9957
Polymeric response (a.u.)
1.12E+07
9.20E+06
7.20E+06
5.20E+06
3.20E+06
1.20E+06
50
100
150
200
250
300
350
400
450
500
550
[PEG 2000] (µg/mL)

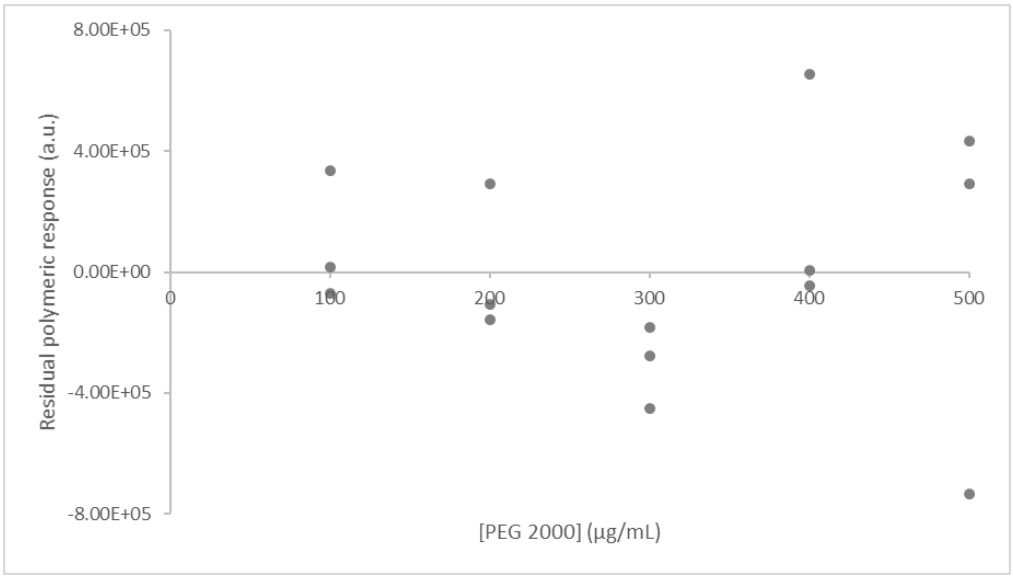
Residual polymeric response (a.u.)
8.00E+05
4.00E+05
0.00E+00
-4.00E+05
-8.00E+05
0
100
200
300
400
500
[PEG 2000] (µg/mL)

B.3 Approaches for quantitation using the quadrupole time-of-flight mass analyser. External calibration linear fittings

B.3.1 Mass spectra deconvolution of a surrogate oligomer. External calibration linear fittings

B.3.2 Mass spectra deconvolution of the whole distribution. External calibration linear fittings

B.3.1 Mass spectra deconvolution of a surrogate oligomer. External calibration linear fittings

PEG 600

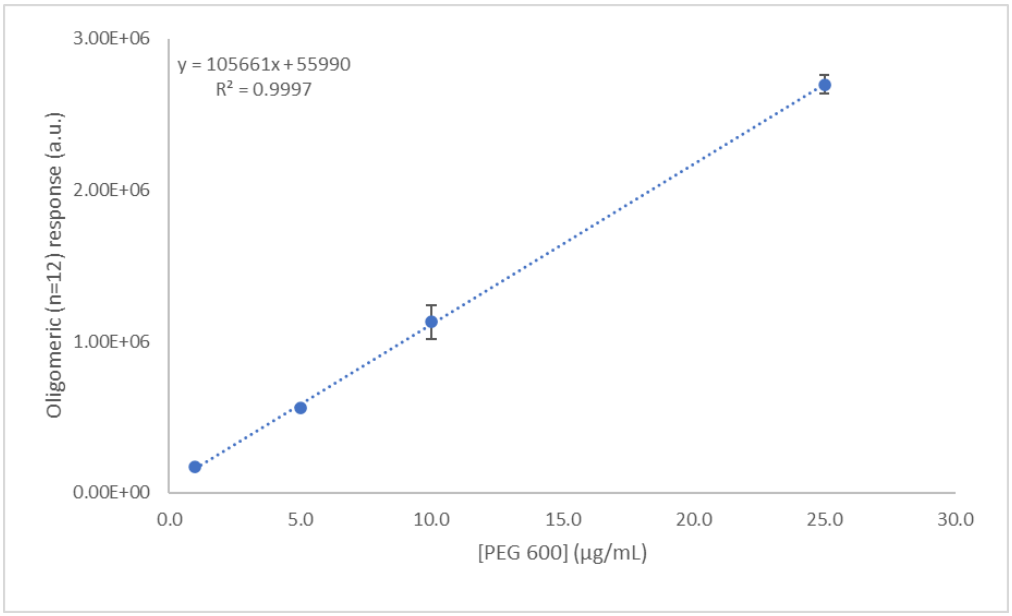

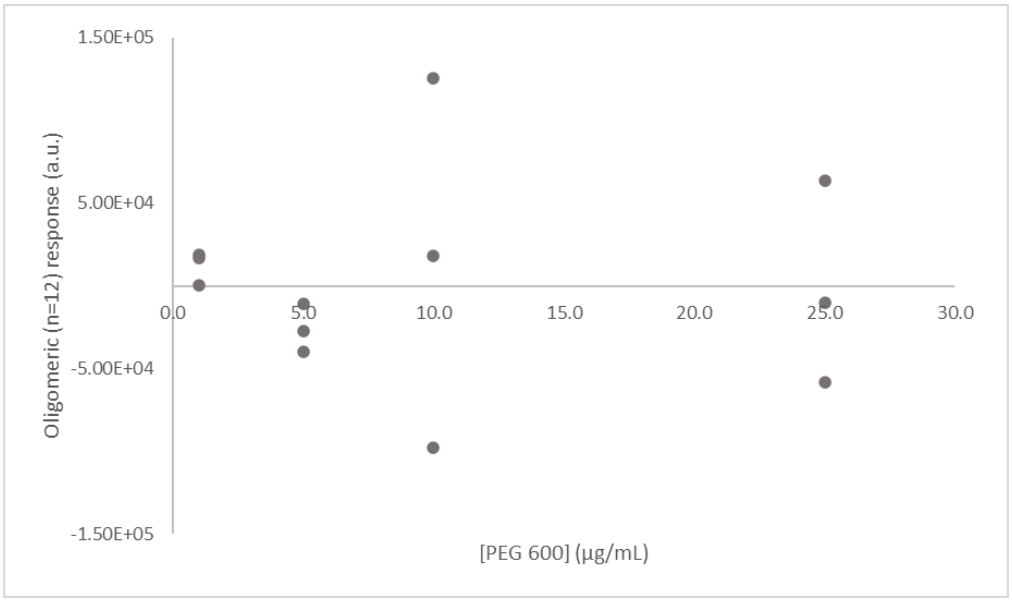

PEG 1000

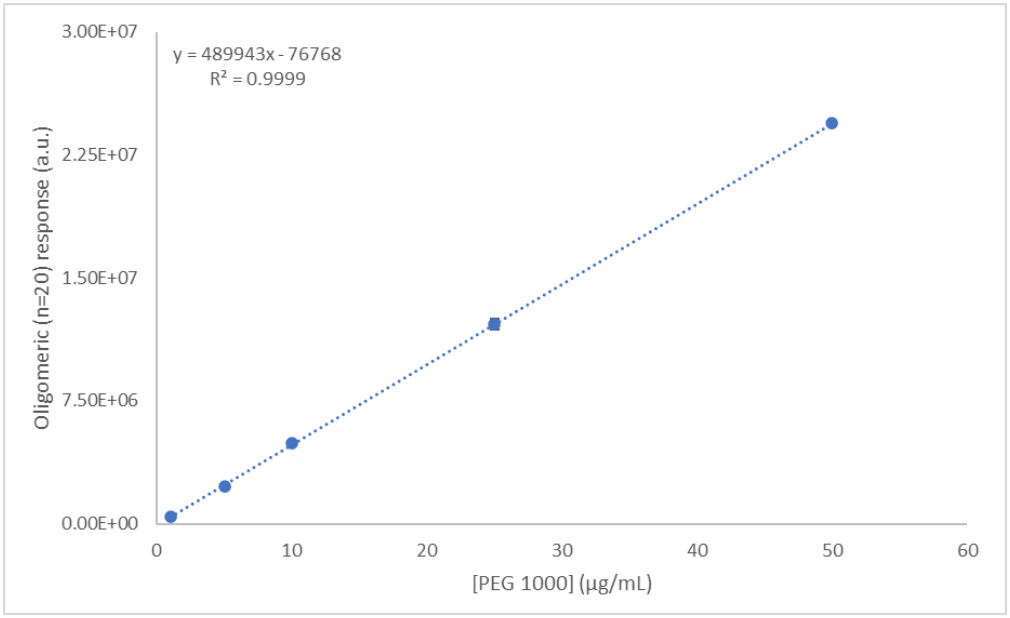
y = 489943x - 76768
R² = 0.9999
Oligomeric (n=20) response (a.u.)
3.00E+07
2.25E+07
1.50E+07
7.50E+06
0.00E+00
0
10
20
30
40
50
60
[PEG 1000] (µg/mL)

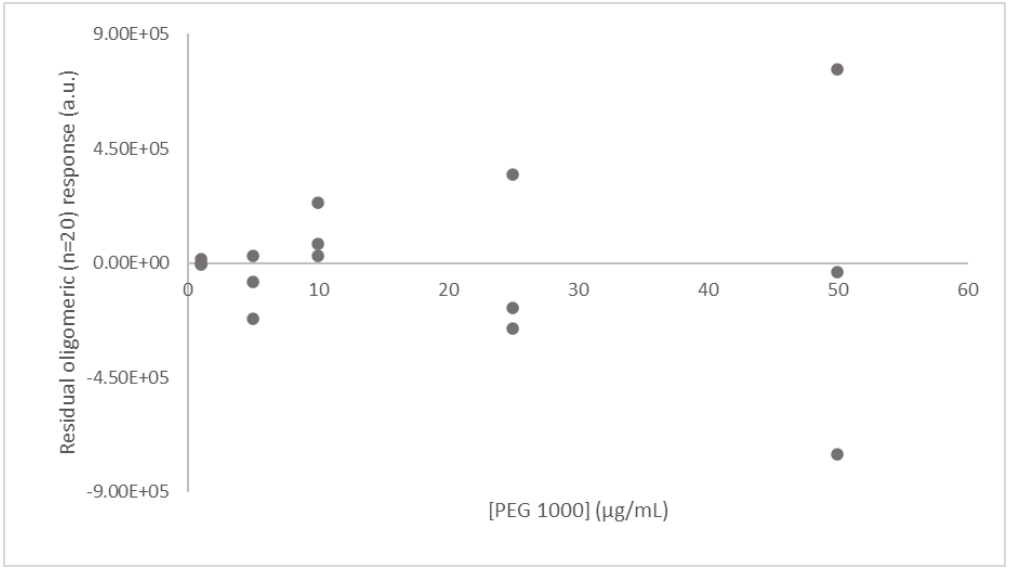
Residual oligomeric (n=20) response (a.u.)
9.00E+05
4.50E+05
0.00E+00
-4.50E+05
-9.00E+05
0
10
20
30
40
50
60
[PEG 1000] (µg/mL)

PEG 1450

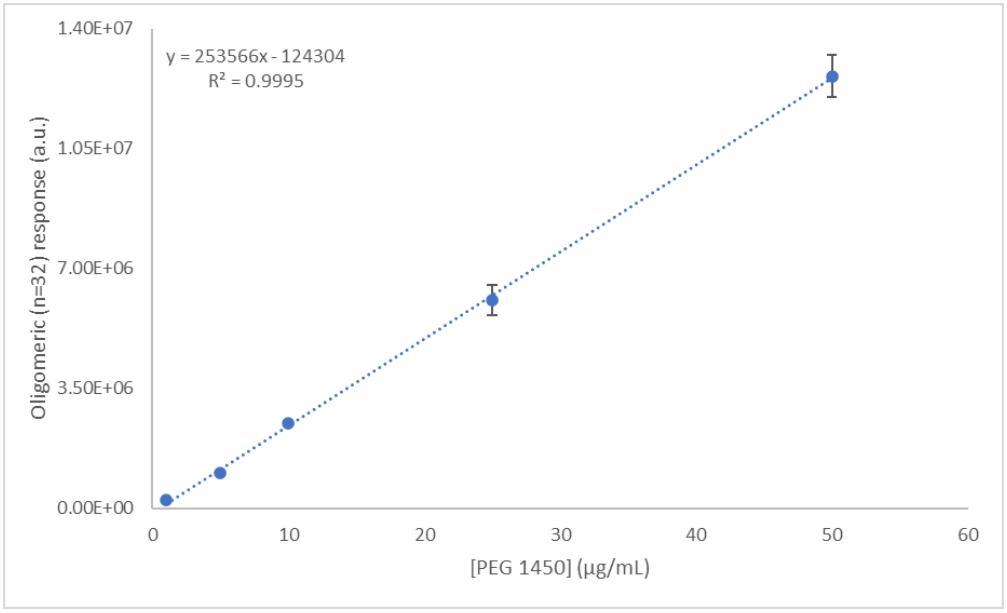
y = 253566x - 124304
R² = 0.9995
Oligomeric (n=32) response (a.u.)
1.40E+07
1.05E+07
7.00E+06
3.50E+06
0.00E+00
0
10
20
30
40
50
60
[PEG 1450] (µg/mL)

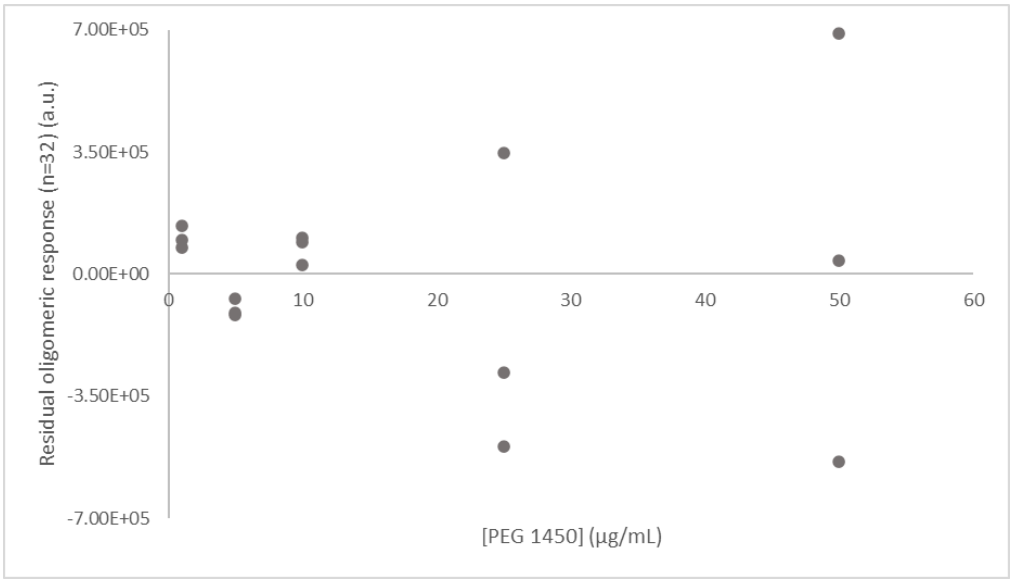
Residual oligomeric response (n=32) (a.u.)
7.00E+05
3.50E+05
0.00E+00
-3.50E+05
-7.00E+05
0
10
20
30
40
50
60
[PEG 1450] (µg/mL)

PEG 2000

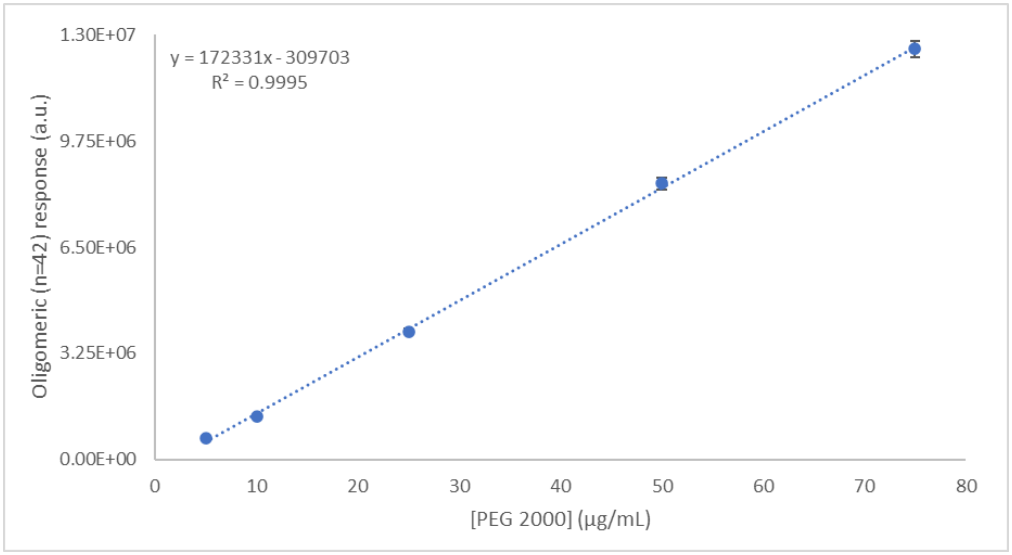
y = 172331x - 309703
R² = 0.9995
Oligomeric (n=42) response (a.u.)
1.30E+07
9.75E+06
6.50E+06
3.25E+06
0.00E+00
0
10
20
30
40
50
60
70
80
[PEG 2000] (µg/mL)

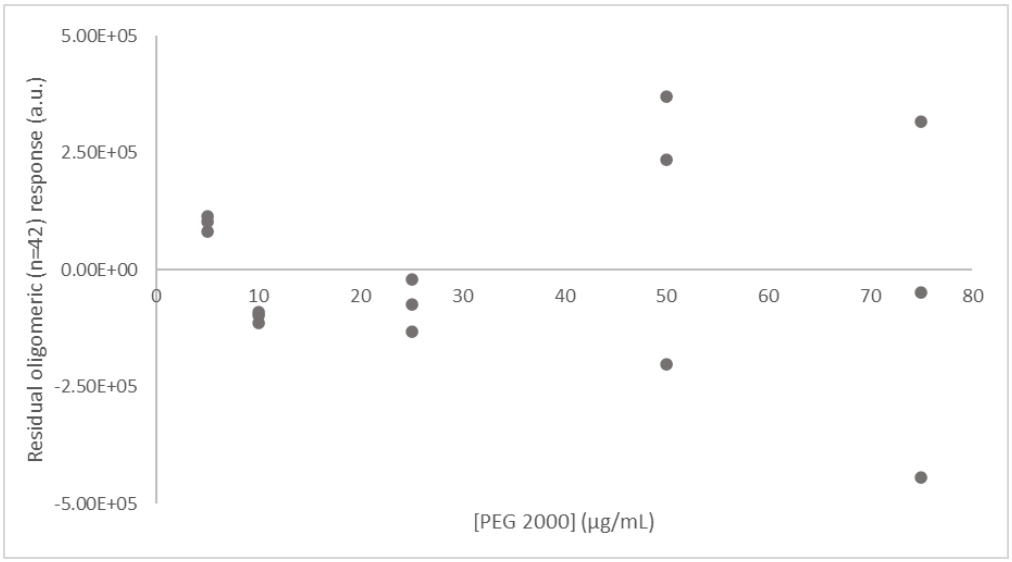
Residual oligomeric (n=42) response (a.u.)
5.00E+05
2.50E+05
0.00E+00
-2.50E+05
-5.00E+05
0
10
20
30
40
50
60
70
80
[PEG 2000] (µg/mL)

B.3.2 Mass spectra deconvolution of the whole distribution. External calibration linear fittings

PEG 600

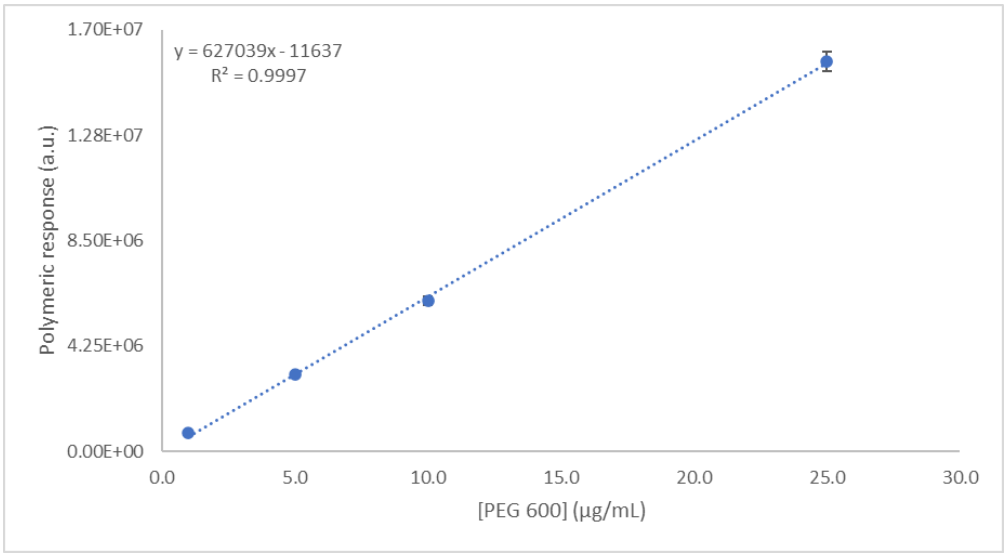

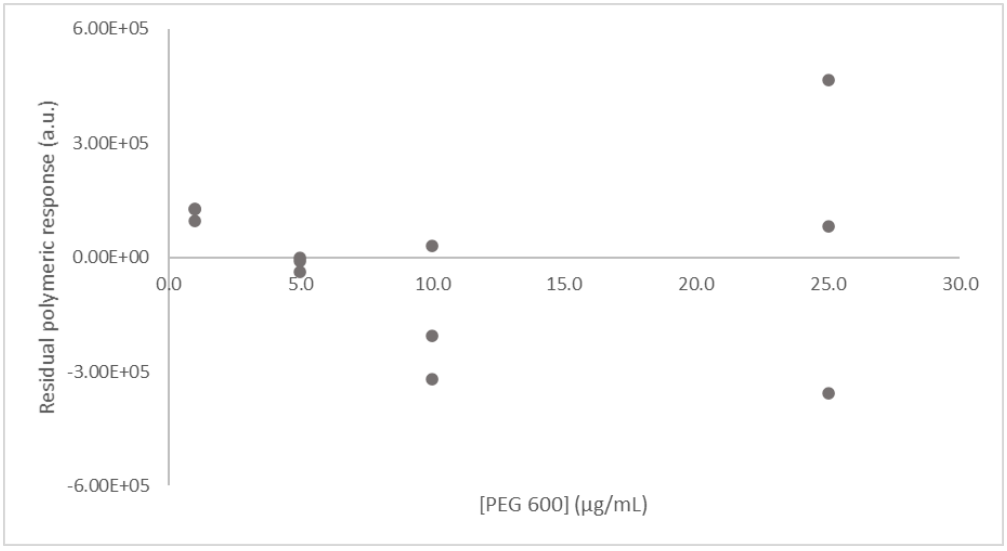

PEG 1000

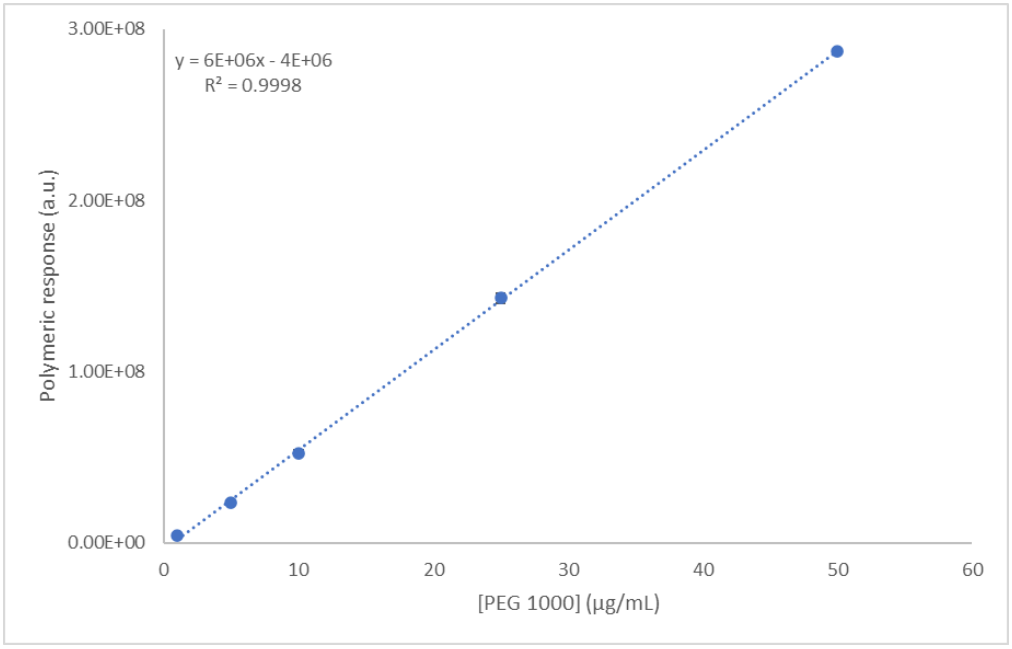
y = 6E+06x - 4E+06
R² = 0.9998
Polymeric response (a.u.)
3.00E+08
2.00E+08
1.00E+08
0.00E+00
0
10
20
30
40
50
60
[PEG 1000] (µg/mL)

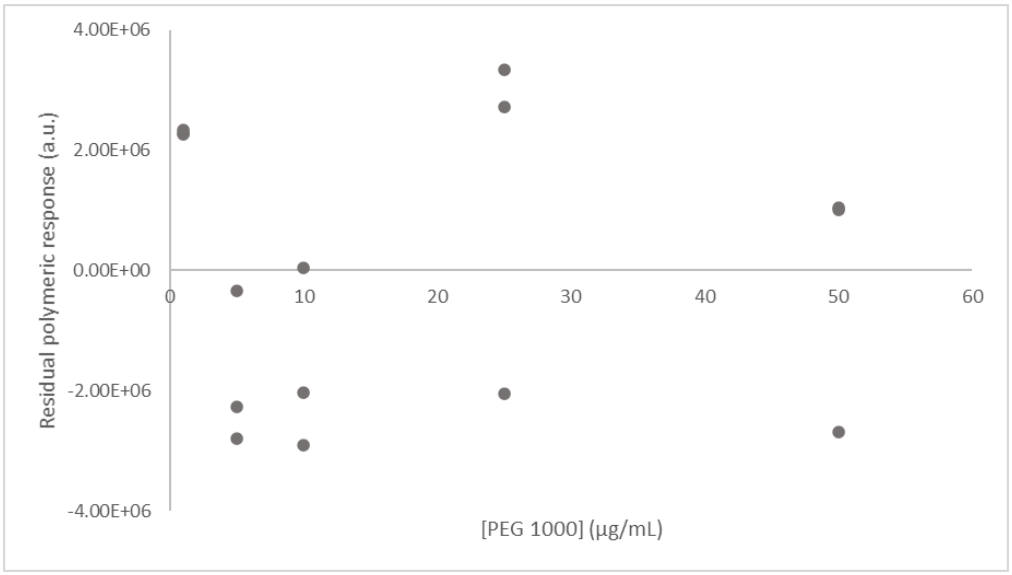
Residual polymeric response (a.u.)
4.00E+06
2.00E+06
0.00E+00
-2.00E+06
-4.00E+06
0
10
20
30
40
50
60
[PEG 1000] (µg/mL)

PEG 1450

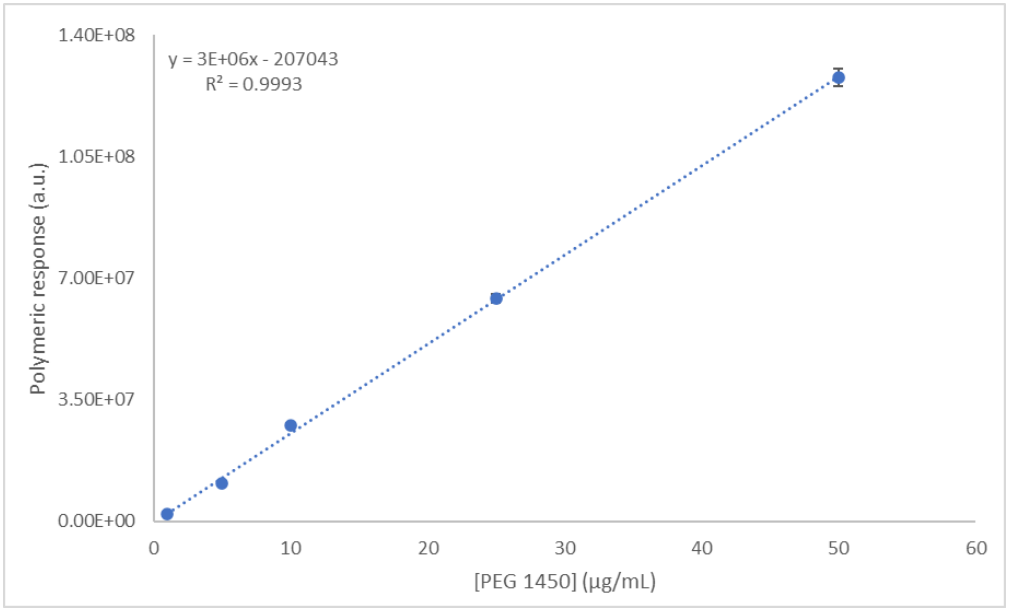
y = 3E+06x - 207043
R² = 0.9993
Polymeric response (a.u.)
1.40E+08
1.05E+08
7.00E+07
3.50E+07
0.00E+00
0
10
20
30
40
50
60
[PEG 1450] (µg/mL)

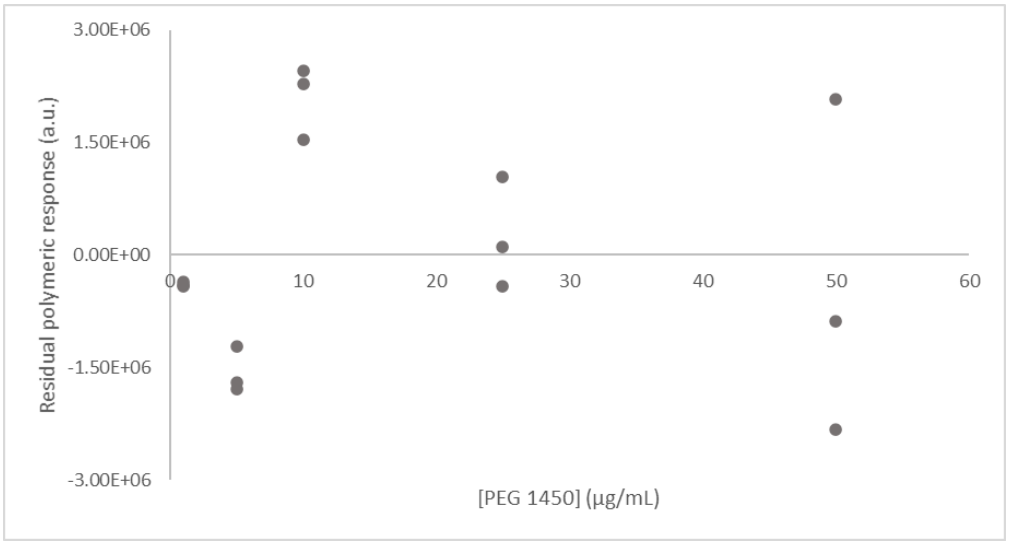
Residual polymeric response (a.u.)
3.00E+06
1.50E+06
0.00E+00
-1.50E+06
-3.00E+06
0
10
20
30
40
50
60
[PEG 1450] (µg/mL)

PEG 2000

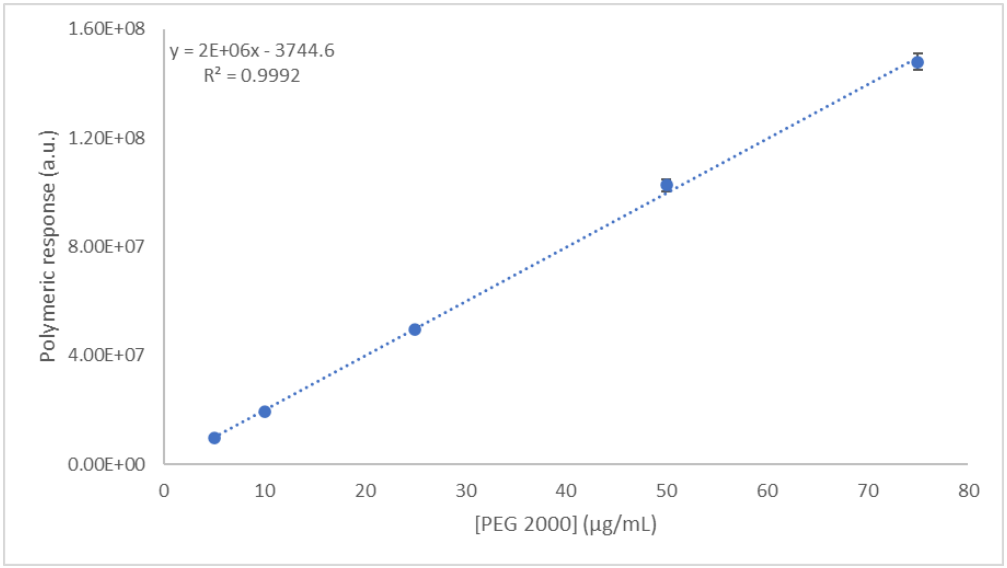
y = 2E+06x - 3744.6
R² = 0.9992
Polymeric response (a.u.)
1.60E+08
1.20E+08
8.00E+07
4.00E+07
0.00E+00
0
10
20
30
40
50
60
70
80
[PEG 2000] (µg/mL)

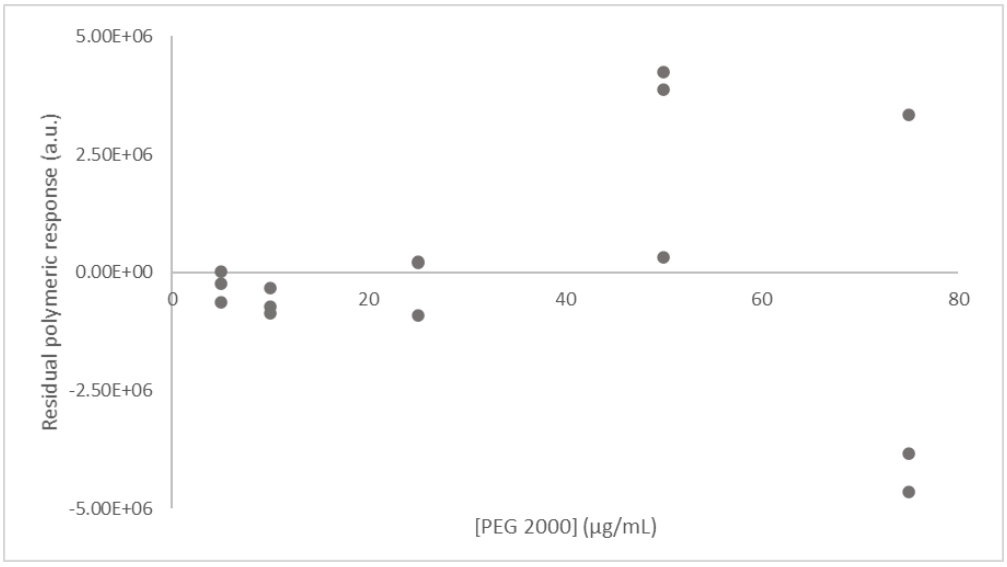
Residual polymeric response (a.u.)
5.00E+06
2.50E+06
0.00E+00
-2.50E+06
-5.00E+06
0
20
40
60
80
[PEG 2000] (µg/mL)

B.4 Approaches for quantitation using the quadrupole mass analyser and internal calibration linear fitting

B.4.1 Mass spectra deconvolution of a surrogate oligomer. Internal standard calibration linear fittings

B.4.2 Mass spectra deconvolution of the whole distribution. Internal calibration linear fittings (0.5 µg/mL 18-crown-6 in CH3CN)

B.4.1 Mass spectra deconvolution of a surrogate oligomer. Internal standard calibration linear fittings

PEG 600

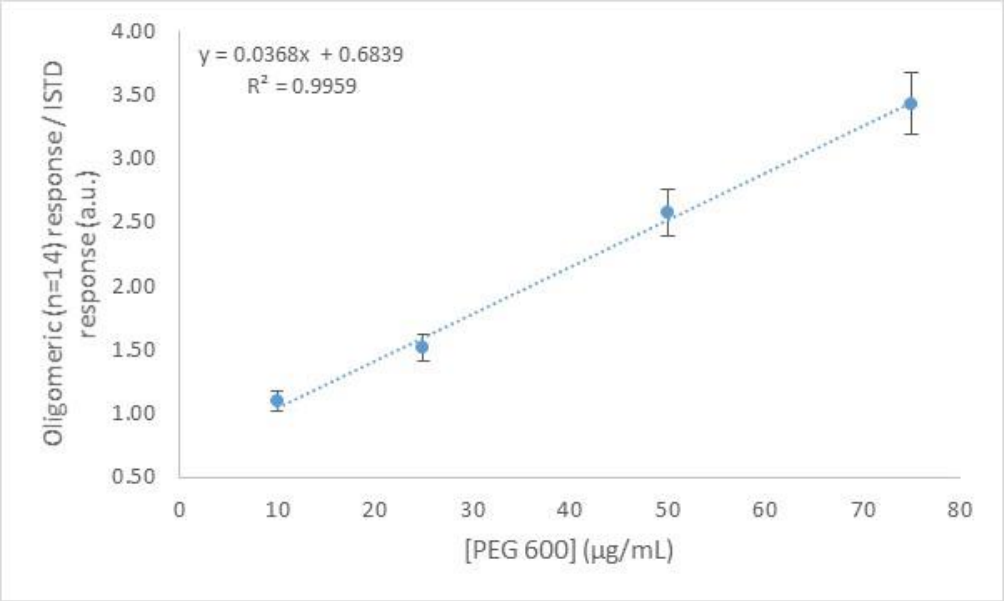

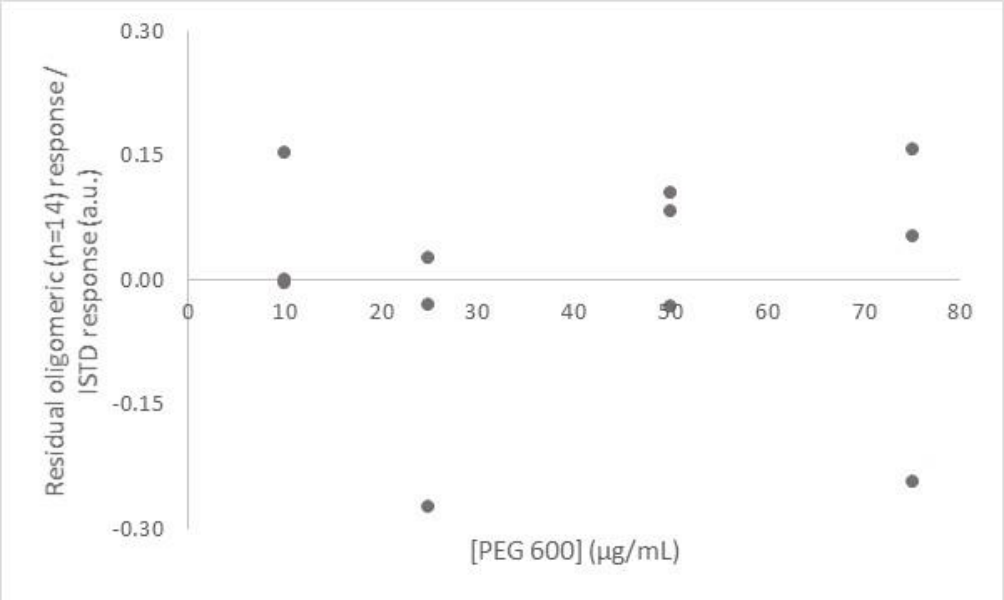

PEG 1000

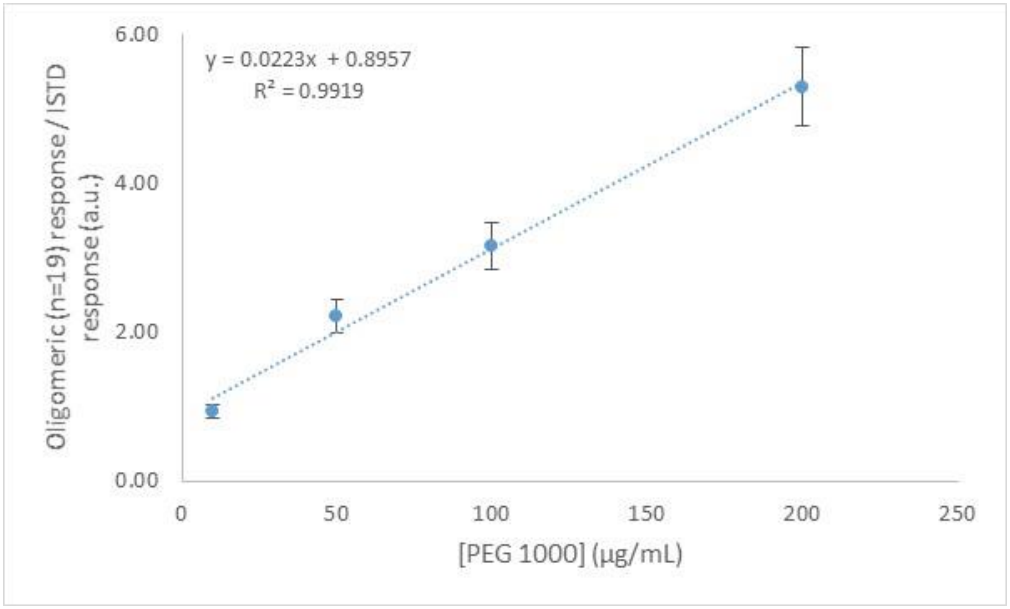
y = 0.0223x + 0.8957
R² = 0.9919
Oligomeric (n=19) response / ISTD response (a.u.)
6.00
4.00
2.00
0.00
0
50
100
150
200
250
[PEG 1000] (µg/mL)

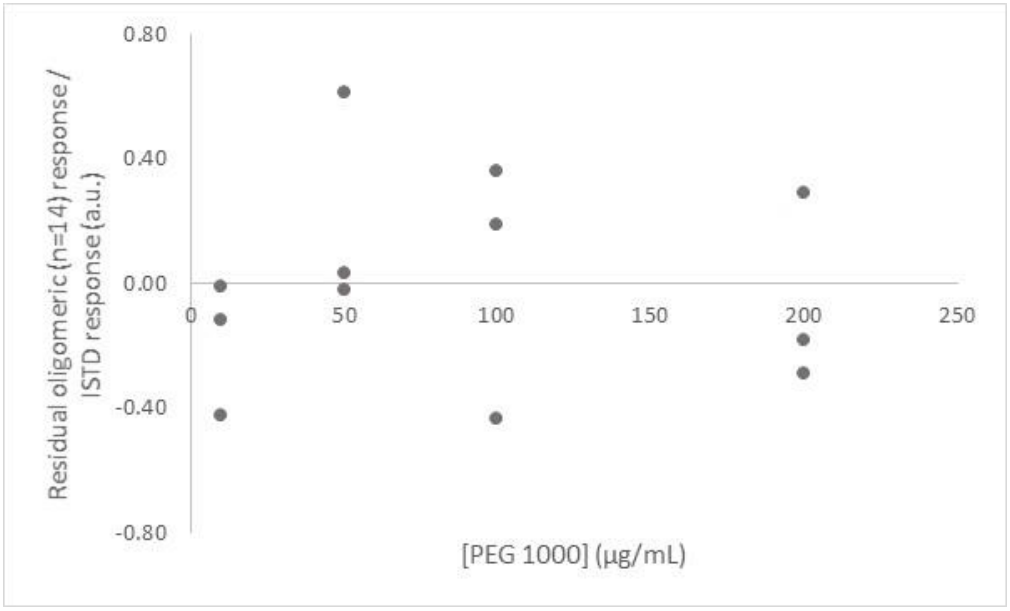
Residual oligomeric (n=14) response / ISTD response (a.u.)
0.80
0.40
0.00
-0.40
-0.80
0
50
100
150
200
250
[PEG 1000] (µg/mL)

PEG 1450

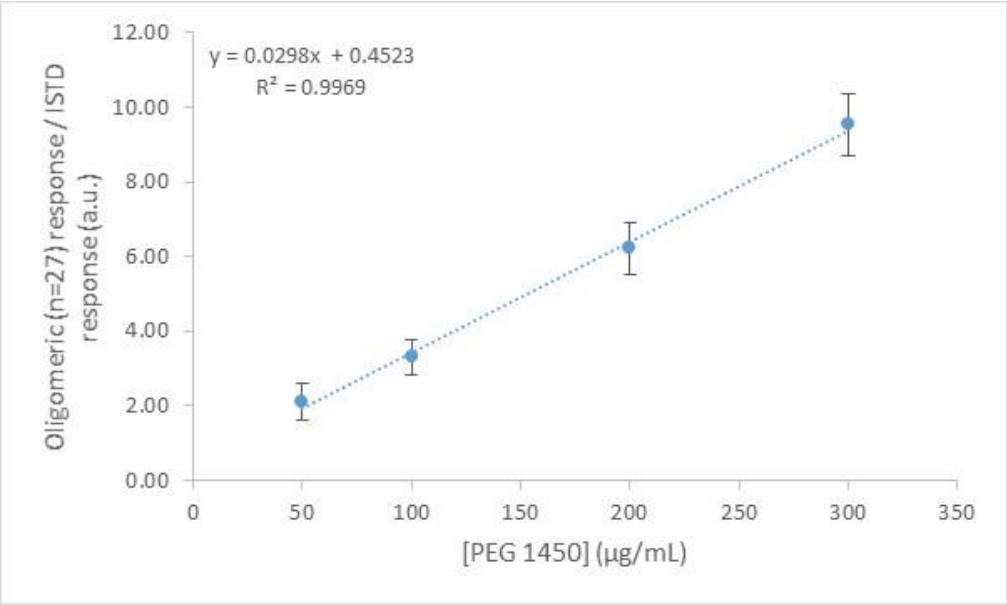
y = 0.0298x + 0.4523
R² = 0.9969
Oligomeric (n=27) response / ISTD response (a.u.)
[PEG 1450] (µg/mL)
12.00
10.00
8.00
6.00
4.00
2.00
0.00
0
50
100
150
200
250
300
350

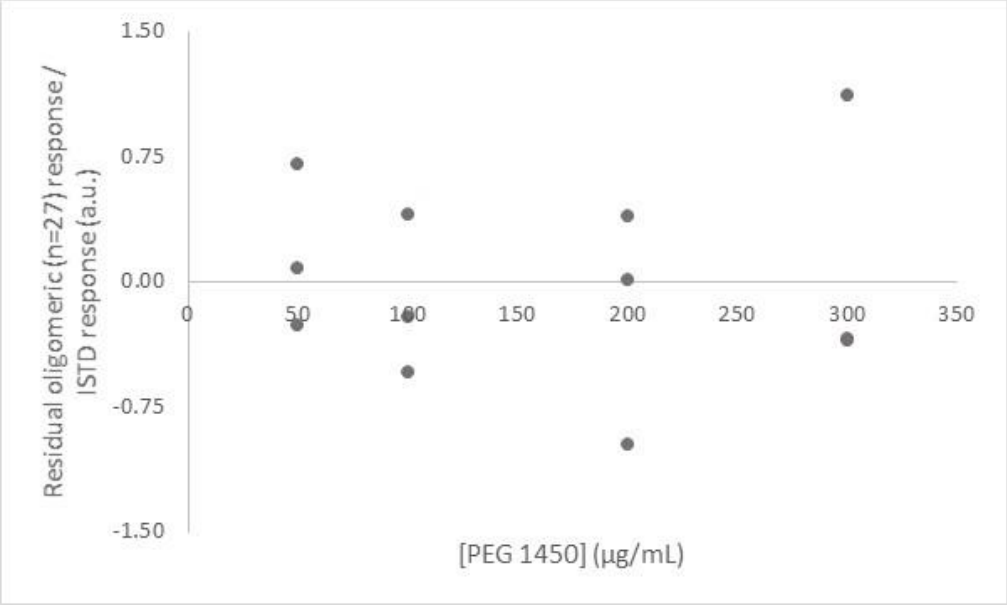
Residual oligomeric (n=27) response / ISTD response (a.u.)
[PEG 1450] (µg/mL)
1.50
0.75
0.00
-0.75
-1.50
0
50
100
150
200
250
300
350

PEG 2000

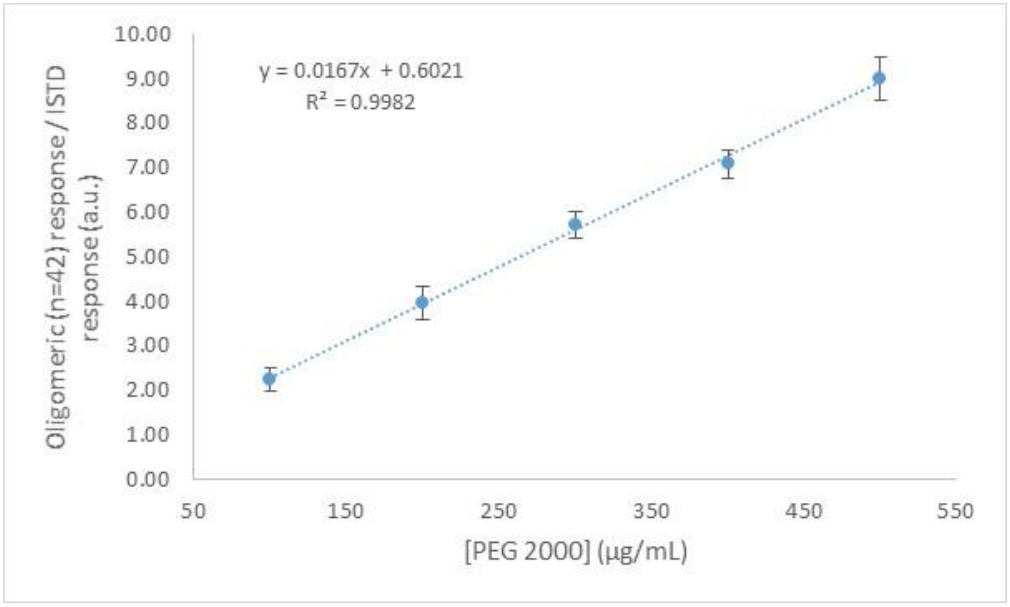
y = 0.0167x + 0.6021
R² = 0.9982
Oligomeric (n=42) response / ISTD response (a.u.)
[PEG 2000] (µg/mL)
10.00
9.00
8.00
7.00
6.00
5.00
4.00
3.00
2.00
1.00
0.00
50
150
250
350
450
550

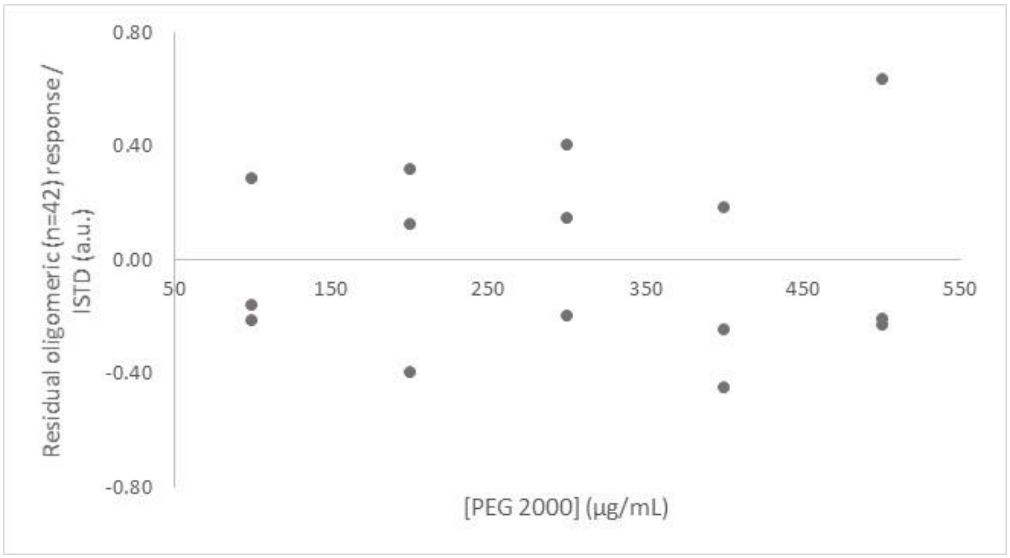
Residual oligomeric (n=42) response / ISTD (a.u.)
[PEG 2000] (µg/mL)
0.80
0.40
0.00
-0.40
-0.80
50
150
250
350
450
550

B.4.2 Mass spectra deconvolution of the whole distribution. Internal calibration linear fittings (0.5 µg/mL 18-crown-6 in CH_3CN)

PEG 600

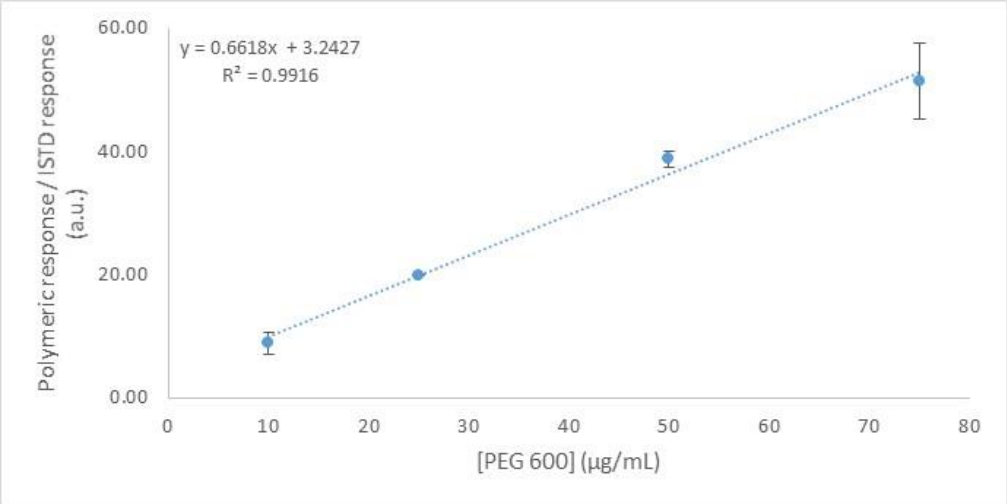

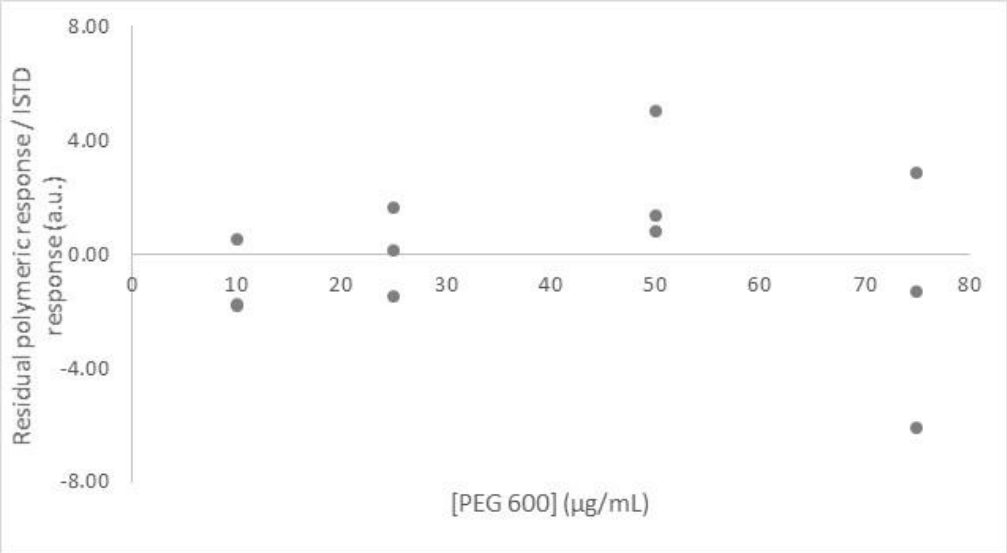

PEG 1000

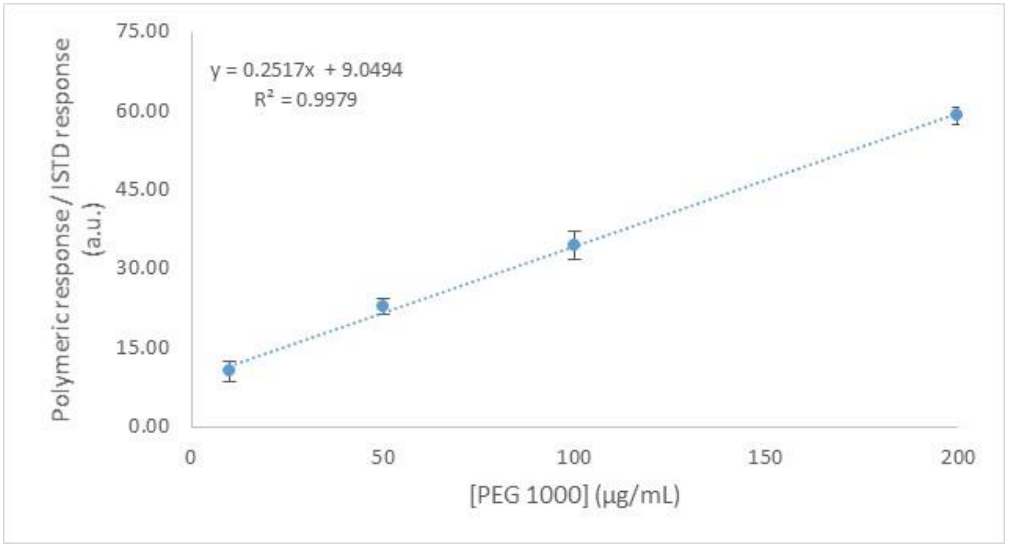
y = 0.2517x + 9.0494
R² = 0.9979
Polymeric response / ISTD response (a.u.)
75.00
60.00
45.00
30.00
15.00
0.00
0
50
100
150
200
[PEG 1000] (µg/mL)

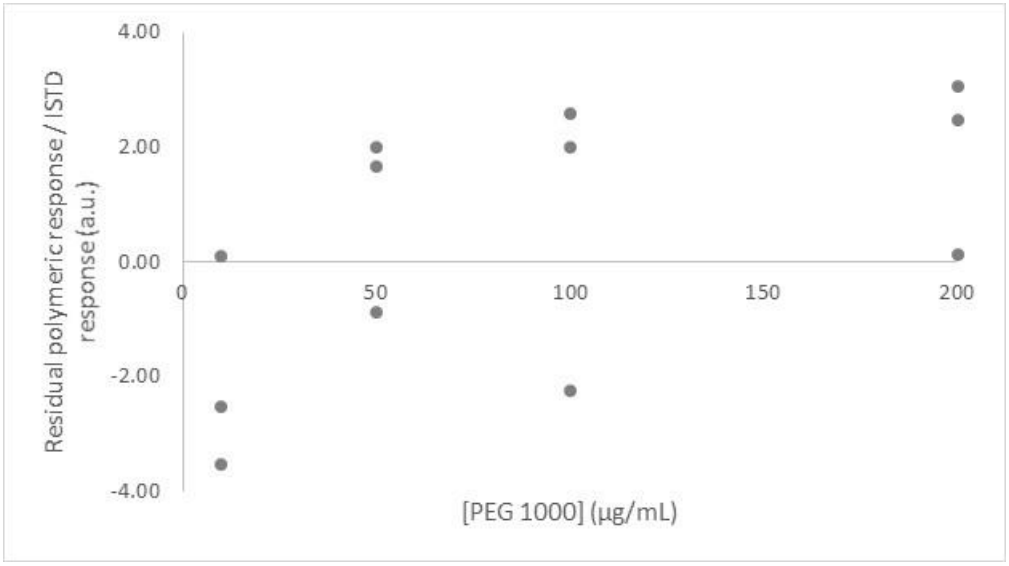
Residual polymeric response / ISTD response (a.u.)
4.00
2.00
0.00
-2.00
-4.00
0
50
100
150
200
[PEG 1000] (µg/mL)

PEG 1450

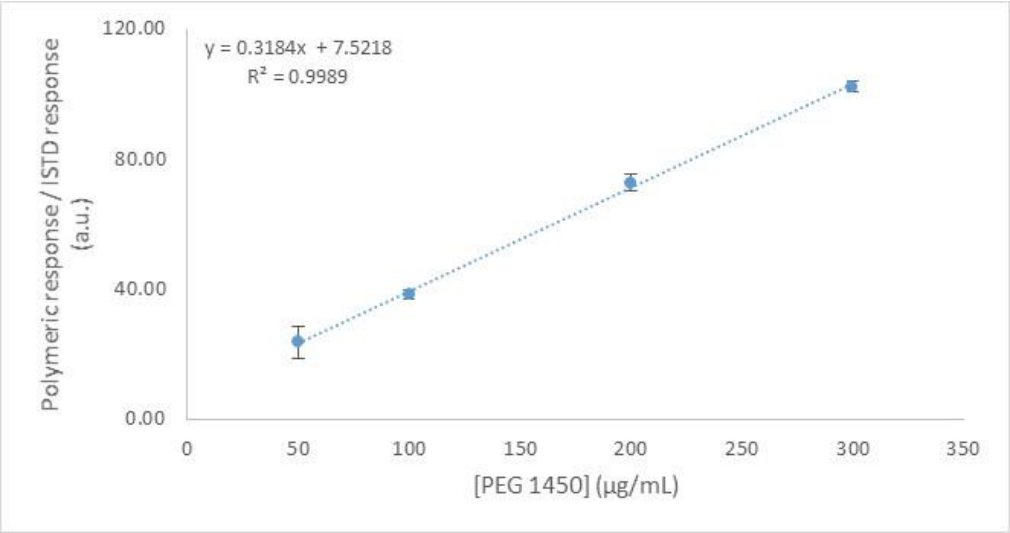
y = 0.3184x + 7.5218
R² = 0.9989
Polymeric response / ISTD response (a.u.)
120.00
80.00
40.00
0.00
0
50
100
150
200
250
300
350
[PEG 1450] (µg/mL)

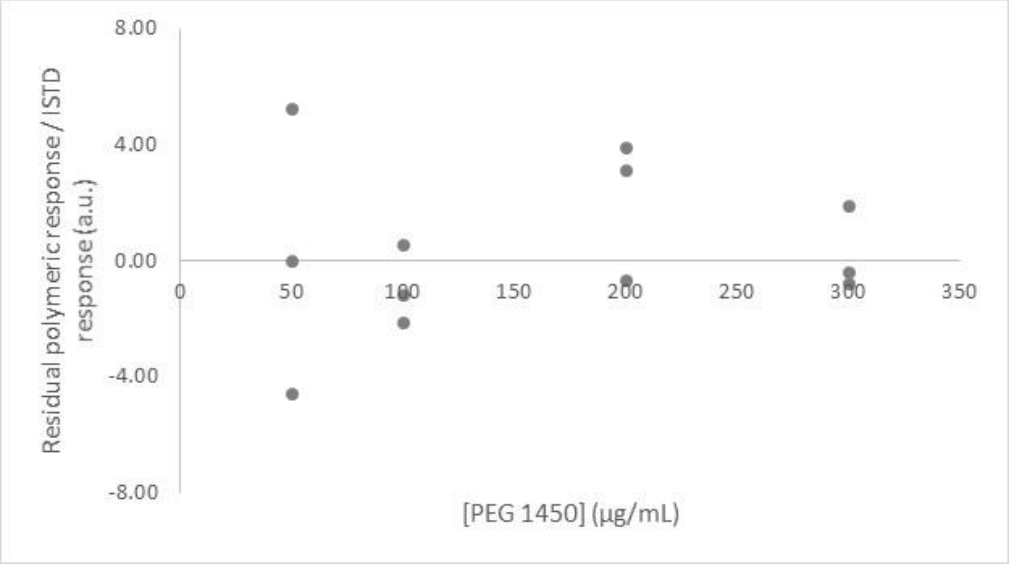
Residual polymeric response / ISTD response (a.u.)
8.00
4.00
0.00
-4.00
-8.00
0
50
100
150
200
250
300
350
[PEG 1450] (µg/mL)

PEG 2000

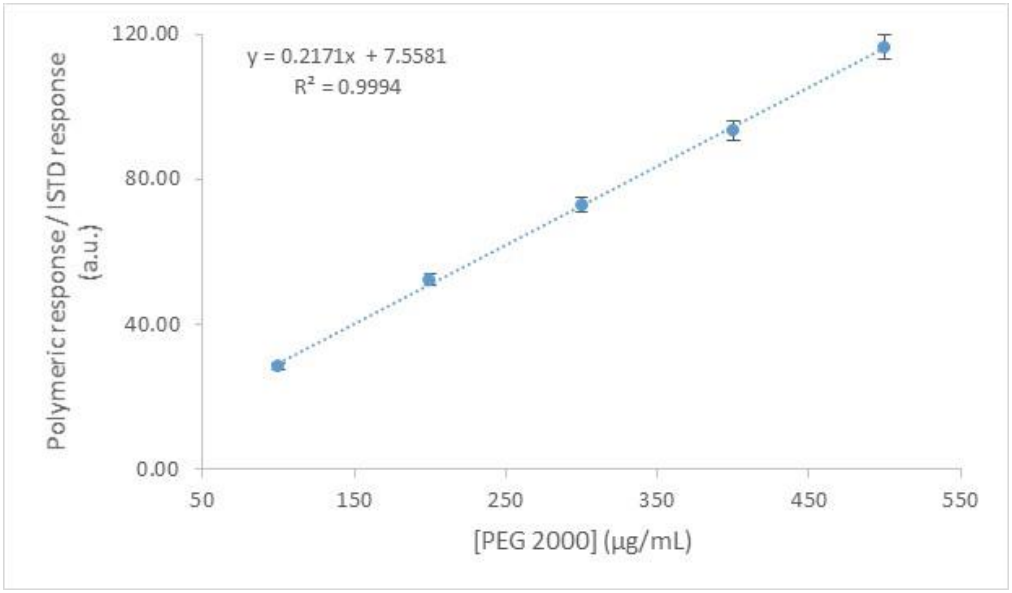
y = 0.2171x + 7.5581
R² = 0.9994
Polymeric response / ISTD response (a.u.)
120.00
80.00
40.00
0.00
50
150
250
350
450
550
[PEG 2000] (µg/mL)

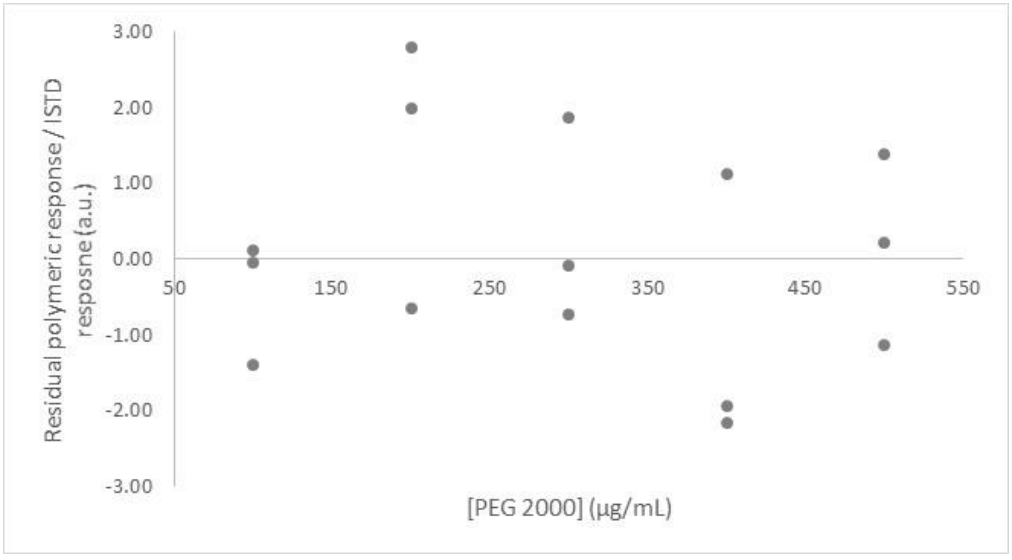
Residual polymeric response / ISTD resposne (a.u.)
3.00
2.00
1.00
0.00
-1.00
-2.00
-3.00
50
150
250
350
450
550
[PEG 2000] (µg/mL)

List of References

1. G. L. Patrick, *An Introduction to Medicinal Chemistry*, Oxford university press, 2013.
2. K. Stromgaard, P. Krogsgaard-Larsen and U. Madsen, *Textbook of Drug Design and Discovery*, CRC press, 2009.
3. S. F. Zhou and W. Z. Zhong, *Mol.*, 2017, **22**, 279.
4. D. P. Elder, M. Kuentz and R. Holm, *Eur. J. Pharm. Sci.*, 2016, **87**, 88-99.
5. C. K. Ozkan, O. Esim, A. Savaser and Y. Ozkan, *Curr. Pharm. Anal.*, 2021, **17**, 360-374.
6. A. S. Narang and S. H. S. Boddu, *Excipient Applications in Formulation Design and Drug Delivery*, Springer International Publishing, 2015.
7. C. A. Lipinski, *Am. Pharm. Rev.*, 2002, **5**, 82-85.
8. G. Pifferi, P. Santoro and M. Pedrani, *Farmaco*, 1999, **54**, 1-14.
9. A. M. Vargason, A. C. Anselmo and S. Mitragotri, *Nat. Biomed. Eng.*, 2021, **5**, 951-967.
10. C. A. Lipinski, F. Lombardo, B. W. Dominy and P. J. Feeney, *Adv. Drug Delivery Rev.*, 1997, **23**, 3-25.
11. C. A. Lipinski, *Drug Discovery Today: Technol.*, 2004, **1**, 337-341.
12. R. P. Ribeiro, J. T. S. Coimbra, M. J. Ramos and P. A. Fernandes, *Theor. Chem. Acc.*, 2017, **136**, 46.
13. B. E. Gidal, J. DeCerce, H. N. Bockbrader, J. Gonzalez, S. Kruger, M. E. Pitterle, P. Rutecki and R. E. Ramsay, *Epilepsy Res.*, 1998, **31**, 91-99.
14. A. T. Serajuddin, *J. Pharm. Sci.*, 1999, **88**, 1058-1066.
15. G. R. Jang, R. Z. Harris and D. T. Lau, *Med. Res. Rev.*, 2001, **21**, 382-396.
16. F. Hannauer, R. Black, A. D. Ray, E. Stulz, G. J. Langley and S. W. Holman, *Anal. Sci. Adv.*, 2022, **3**, 90-102.
17. Novel drug delivery systems, https://www.pharmaguideline.com/2021/06/novel-drug-delivery-system.html?m=1, (accessed June 2022).
18. V. S. V. Priya, H. K. Roy, N. jyothi and N. L. Prasanthi, *Sch. Acad. J. Pharm.*, 2016, **5**, 305-308.
19. H. Priya James, R. John, A. Alex and K. R. Anoop, *Acta Pharm. Sin. B*, 2014, **4**, 120-127.
20. W. B. Liechty, D. R. Kryscio, B. V. Slaughter and N. A. Peppas, *Annu. Rev. Chem. Biomol. Eng.*, 2010, **1**, 149-173.
21. D. Jones, *Pharmaceutical Applications of Polymers for Drug Delivery*, iSmithers Rapra Publishing, 2004.
22. C. Englert, J. C. Brendel, T. C. Majdanski, T. Yildirim, S. Schubert, M. Gottschaldt, N. Windhab and U. S. Schubert, *Prog. Polym. Sci.*, 2018, **87**, 107-164.
23. N. Larson and H. Ghandehari, *Chem. Mater.*, 2012, **24**, 840-853.
24. K. Hoste, K. De Winne and E. Schacht, *Int. J. Pharm.*, 2004, **277**, 119-131.
25. X. Pang, H. L. Du, H. Q. Zhang, Y. J. Zhai and G. X. Zhai, *Drug Discovery Today*, 2013, **18**, 1316-1322.
26. M. E. Brewster and T. Loftsson, *Adv. Drug Delivery Rev.*, 2007, **59**, 645-666.
27. H. Schellekens, W. E. Hennink and V. Brinks, *Pharm. Res.*, 2013, **30**, 1729-1734.
28. A. M. Doweyko and L. M. Doweyko, *Future Med. Chem.*, 2009, **1**, 1029-1036.
29. S. Rizwan, A. Mehmood, I. Khalid, M. S. Khan, Q. Yousafi, S. Kalsoom and H. Rashid, *Curr. Comput.-Aided Drug Des.*, 2018, **14**, 385-390.
30. L. Xu, N. Grandi, C. Del Vecchio, D. Mandas, A. Corona, D. Piano, F. Esposito, C. Parolin and E. Tramontano, *J. Microbiol.*, 2015, **53**, 288-293.
31. I. Ekladious, Y. L. Colson and M. W. Grinstaff, *Nat. Rev. Drug Discovery*, 2018, **18**, 273-294.
32. O. Chambin and V. Jannin, *Drug Dev. Ind. Pharm.*, 2005, **31**, 527-534.
33. S. Fernandez, J. D. Rodier, N. Ritter, B. Mahler, F. Demarne, F. Carriere and V. Jannin, *Biochim. Biophys. Acta*, 2008, **1781**, 367-375.

34. M. G. Sarpietro, G. Pitarresi, S. Ottimo, M. C. Giuffrida, M. C. Ognibene, C. Fiorica, G. Giammona and F. Castelli, *Mol. Pharmaceutics*, 2011, **8**, 642-650.
35. P. Muller, *Pure Appl. Chem.*, 1994, **66**, 1077-1184.
36. I. Ekladious, Y. L. Colson and M. W. Grinstaff, *Nat. Rev. Drug Discovery*, 2019, **18**, 273-294.
37. H. Schott, *J. Pharm. Sci.*, 1995, **84**, 1215-1222.
38. R. C. Pasquali, M. P. Taurozzi and C. Bregni, *Int. J. Pharm.*, 2008, **356**, 44-51.
39. T. Chmiel, A. Mieszkowska, D. Kempińska-Kupczyk, A. Kot-Wasik, J. Namieśnik and Z. Mazerska, *Microchemical Journal*, 2019, **146**, 393-406.
40. M. M. Miller, S. P. Wasik, G. L. Huang, W. Y. Shiu and D. Mackay, *Environ. Sci. Technol.*, 1985, **19**, 522-529.
41. J. D. Hughes, J. Blagg, D. A. Price, S. Bailey, G. A. Decrescenzo, R. V. Devraj, E. Ellsworth, Y. M. Fobian, M. E. Gibbs, R. W. Gilles, N. Greene, E. Huang, T. Krieger-Burke, J. Loesel, T. Wager, L. Whiteley and Y. Zhang, *Bioorg. Med. Chem. Lett.*, 2008, **18**, 4872-4875.
42. J. A. Arnott and S. L. Planey, *Expert Opin. Drug Discovery*, 2012, **7**, 863-875.
43. A. Kolate, D. Baradia, S. Patil, I. Vhora, G. Kore and A. Misra, *J. Controlled Release*, 2014, **192**, 67-81.
44. M. S. Thompson, T. P. Vadala, M. L. Vadala, Y. Lin and J. S. Riffle, *Polymer*, 2008, **49**, 345-373.
45. J. Li and W. J. Kao, *Biomacromolecules*, 2003, **4**, 1055-1067.
46. J. M. Harris, *J. Macromol. Sci., Chem.*, 2007, **25**, 325-373.
47. N. N. Reed and K. D. Janda, *J. Org. Chem.*, 2000, **65**, 5843-5845.
48. A. D'Souza A and R. Shegokar, *Expert Opin. Drug Delivery*, 2016, **13**, 1257-1275.
49. J. Khandare and T. Minko, *Prog. Polym. Sci.*, 2006, **31**, 359-397.
50. F. M. Veronese and M. Morpurgo, *Farmaco*, 1999, **54**, 497-516.
51. Y. H. Choe, C. D. Conover, D. Wu, M. Royzen and R. B. Greenwald, *J. Controlled Release*, 2002, **79**, 41-53.
52. Y. H. Choe, C. D. Conover, D. Wu, M. Royzen, Y. Gervacio, V. Borowski, M. Mehlig and R. B. Greenwald, *J. Controlled Release*, 2002, **79**, 55-70.
53. M. Swierczewska, K. C. Lee and S. Lee, *Expert Opin. Emerging Drugs*, 2015, **20**, 531-536.
54. M. C. Garnett, *Adv. Drug Delivery Rev.*, 2001, **53**, 171-216.
55. P. L. Turecek, M. J. Bossard, F. Schoetens and I. A. Ivens, *J. Pharm. Sci.*, 2016, **105**, 460-475.
56. G. Pasut, A. Guiotto and F. M. Veronese, *Expert Opin. Ther. Patents*, 2005, **14**, 859-894.
57. L. S. Lee, C. Conover, C. Shi, M. Whitlow and D. Filpula, *Bioconjugate Chem.*, 1999, **10**, 973-981.
58. A. Berthod, S. Tomer and J. G. Dorsey, *Talanta*, 2001, **55**, 69-83.
59. D. A. McKenzie, *J. Am. Oil Chem. Soc.*, 1978, **55**, 93-97.
60. N. M. van Os, *Nonionic surfactants: Organic chemistry*, Marcel Dekker, New York, 1998.
61. B. Lindman, B. Medronho and G. Karlstrom, *Curr Opin Colloid In*, 2016, **22**, 23-29.
62. L. Chiappisi, S. Prevost, I. Grillo and M. Gradzielski, *Langmuir*, 2014, **30**, 10608-10616.
63. R. Dong and J. Hao, *Chem. Rev.*, 2010, **110**, 4978-5022.
64. L. Chiappisi, *Adv. Colloid Interface Sci.*, 2017, **250**, 79-94.
65. Gattefosse, https://www.gattefosse.com/, (accessed (accessed June 2022).
66. A. Svensson, C. Neves and B. Cabane, *Int. J. Pharm.*, 2004, **281**, 107-118.
67. R. Zhang, Y. Wang, L. Tan, H. Y. Zhang and M. Yang, *J. Chromatogr. Sci.*, 2012, **50**, 598-607.
68. H. Kato, Y. Nagai, K. Yamamoto and Y. Sakabe, *J. Assoc. Off. Anal. Chem.*, 1989, **72**, 27-29.
69. J. Giacometti, C. Milin, N. Wolf and F. Giacometti, *J. Agric. Food Chem.*, 1996, **44**, 3950-3954.
70. D. Wilkinson, G. Ramjee, M. Tholandi and G. Rutherford, *Cochrane Database Syst. Rev.*, 2002, DOI: 10.1002/14651858.CD003939, CD003939.

71. J. B. Farcet, J. Kindermann, M. Karbiener, R. Scheinecker, O. Kostner and T. R. Kreil, *J. Med. Virol.*, 2021, **93**, 3880-3889.
72. R. White, S. Jobling, S. A. Hoare, J. P. Sumpter and M. G. Parker, *Endocrinol.*, 1994, **135**, 175-182.
73. Candidate list of substances of very high concern for authorisation. European Chemicals Agency. An agency of the European Union., https://echa.europa.eu/candidate-list-table/-/dislist/details/0b0236e1807db570, (accessed (accessed June 2022).
74. REACH Legislation. European Chemicals Agency., https://echa.europa.eu/regulations/reach/legislation, (accessed June 2022).
75. Authorisation List. European Chemicals Agency, https://echa.europa.eu/authorisation-list, (accessed June 2022).
76. R. Schueller and P. Romanowski, *Conditioning Agents for Hair and Skin*, Online, 1998.
77. H. I. Maibach, A. O. Barel and M. Paye, *Handbook of Cosmetic Science and Technology*, CRC Press, 2014.
78. P. Alexandridis and T. A. Hatton, *Colloid Surface A*, 1995, **96**, 1-46.
79. S. Janssens, H. N. de Armas, J. P. Remon and G. Van den Mooter, *Eur. J. Pharm. Sci.*, 2007, **30**, 288-294.
80. R. Ghasemi, M. Abdollahi, E. Emamgholi Zadeh, K. Khodabakhshi, A. Badeli, H. Bagheri and S. Hosseinkhani, *Sci. Rep.*, 2018, **8**, 9854.
81. K. Knop, R. Hoogenboom, D. Fischer and U. S. Schubert, *Angew. Chem., Int. Ed. Engl.*, 2010, **49**, 6288-6308.
82. C. P. Carpenter, M. D. Woodside, E. R. Kinkead, J. M. King and L. J. Sullivan, *Toxicol. Appl. Pharmacol.*, 1971, **18**, 35-40.
83. V. Erdeljic Turk, *Clin. Immunol.*, 2021, **227**, 108748.
84. R. P. Gullapalli and C. L. Mazzitelli, *Int. J. Pharm.*, 2015, **496**, 219-239.
85. M. Ito, D. Watanabe, M. Kobayashi, Y. Tamada and Y. Matsumoto, *Contact Dermatitis*, 2006, **54**, 225.
86. E. T. Dams, P. Laverman, W. J. Oyen, G. Storm, G. L. Scherphof, J. W. van Der Meer, F. H. Corstens and O. C. Boerman, *J. Pharmacol. Exp. Ther.*, 2000, **292**, 1071-1079.
87. T. Ishida, R. Maeda, M. Ichihara, K. Irimura and H. Kiwada, *J. Controlled Release*, 2003, **88**, 35-42.
88. R. I. Mahato, *Biomaterials for Delivery and Targeting of Proteins and Nucleic Acids*, CRC Press, 2004.
89. D. A. Herold, K. Keil and D. E. Bruns, *Biochem. Pharmacol.*, 1989, **38**, 73-76.
90. H. G. Elias, *Pure Appl. Chem.*, 1975, **43**, 115-147.
91. M. Rogošić, H. J. Mencer and Z. Gomzi, *Eur. Polym. J.*, 1996, **32**, 1337-1344.
92. R. G. Jones, J. Kahovec, R. Stepto, E. S. Wilks, M. Hess, T. Kitayama and W. V. Metanomski, *Compendium of Polymer Terminology and Nomenclature*, RSC Publishing, 2008.
93. E. Tokunaga, T. Yamamoto, E. Ito and N. Shibata, *Sci. Rep.*, 2018, **8**, 1-7.
94. *ICH Q3A Impurities in new drug substances*, International conference for harmonisation, 2006.
95. *ICH Q3B Impurities in new drug substances*, International conference for harmonisation, 2006.
96. M. Saraji and N. Shirvani, *Int. J. Cosmet. Sci.*, 2017, **39**, 36-41.
97. J. Glastrup, *Polym. Degrad. Stab.*, 1996, **52**, 217-222.
98. M. N. Nassar, V. N. Nesarikar, R. Lozano, W. L. Parker, Y. Huang, V. Palaniswamy, W. Xu and N. Khaselev, *Pharm Dev Technol*, 2004, **9**, 189-195.
99. The International Agency for Research on Cancer (IARC), https://www.iarc.who.int/, (accessed July 2022).
100. K. C. Waterman, W. B. Arikpo, M. B. Fergione, T. W. Graul, B. A. Johnson, B. C. Macdonald, M. C. Roy and R. J. Timpano, *J. Pharm. Sci.*, 2008, **97**, 1499-1507.

101. J. D. Franolic, G. J. Lehr, T. L. Barry and G. Petzinger, *J. Pharm. Biomed. Anal.*, 2001, **26**, 651-663.
102. X. Fang, R. T. Bibart, S. Mayr, W. Yin, P. A. Harmon, J. F. McCafferty, R. J. Tyrrell and R. A. Reed, *J. Pharm. Sci.*, 2001, **90**, 1800-1809.
103. D. S. Bindra, T. D. Williams and V. J. Stella, *Pharm. Res.*, 1994, **11**, 1060-1064.
104. Y. Sato, D. Breslin, H. Kitada, W. Minagawa, T. Nomoto, X. Z. Qin and S. B. Karki, *Int. J. Pharm.*, 2010, **390**, 128-133.
105. *Lipid Oxidation*, Oily Press Lipid Library Series, 2005.
106. P. K. Working, M. S. Newman, J. Johnson and J. B. Cornacoff, *Safety of poly(ethylene) glycol and poly(ethylene) glycol derivatives*, ACS Symposium Series, 1997.
107. R. Duncan and F. Spreafico, *Clin. Phormocokinet.*, 1994, **27**, 290-306.
108. K. Ulbrich, V. Subr, J. Strohalm, D. Plocova, M. Jelinkova and B. Rihova, *J. Controlled Release*, 2000, **64**, 63-79.
109. B. Rihova, M. Jelinkova, J. Strohalm, V. Subr, D. Plocova, O. Hovorka, M. Novak, D. Plundrova, Y. Germano and K. Ulbrich, *J. Controlled Release*, 2000, **64**, 241-261.
110. C. Theiss and U. Holzgrabe, *J. Pharm. Biomed. Anal.*, 2018, **160**, 212-221.
111. B. N. Barman, D. H. Champion and S. L. Sjoberg, *J. Chromatogr. A*, 2009, **1216**, 6816-6823.
112. Y. H. Lee, E. S. Jeong, H. E. Cho and D. C. Moon, *Talanta*, 2008, **74**, 1615-1620.
113. D. Brinz and U. Holzgrabe, *Electrophoresis*, 2008, **29**, 3605-3611.
114. M. R. Plata, A. M. Contento and A. Rios, *Electrophoresis*, 2010, **31**, 679-687.
115. U. Just, H. R. Holzbauer and M. Resch, *J. Chromatogr. A*, 1994, **667**, 354-360.
116. K. Takahashi, *J. Biosci. Bioeng.*, 2013, **116**, 133-140.
117. A. M. Schou-Pedersen, J. Ostergaard, M. Johansson, S. Dubant, R. B. Frederiksen and S. H. Hansen, *J. Pharm. Biomed. Anal.*, 2014, **88**, 256-261.
118. B. J. Hoffman, L. T. Taylor, S. Rumbelow, L. Goff and J. D. Pinkston, *J. Chrom. A*, 2004, **1034**, 207-212.
119. K. Takahashi, S. Kinugasa, M. Senda, K. Kimizuka, K. Fukushima, T. Matsumoto, Y. Shibata and J. Christensen, *J. Chromatogr. A*, 2008, **1193**, 151-155.
120. K. Takahashi, S. Kinugasa, R. Yoshihara, A. Nakanishi, R. K. Mosing and R. Takahashi, *J. Chromatogr. A*, 2009, **1216**, 9008-9013.
121. K. Takahashi, S. Matsuyama, S. Kinugasa, K. Ehara, H. Sakurai, Y. Horikawa, H. Kitazawa and M. Bounoshita, *Metrologia*, 2015, **52**, 8-16.
122. B. Trathnigg, B. Maier, G. Schulz, R.-P. Krüger and U. Just, *Macromol. Symp.*, 1996, **110**, 231-240.
123. E. Hvattum, W. L. Yip, D. Grace and K. Dyrstad, *J. Pharm. Biomed. Anal.*, 2012, **62**, 7-16.
124. L. Huang, P. C. Gough and M. R. Defelippis, *Anal. Chem.*, 2009, **81**, 567-577.
125. Z. Wang, Y. Wang, C. Tie and J. Zhang, *J. Chromatogr. A*, 2020, **1609**, 460450.
126. A. M. Poulton, R. C. Poulten, A. Baldaccini, A. Gabet, R. Mott, K. E. Treacher, E. Roddy and P. Ferguson, *J. Chromatogr. A*, 2021, **1638**, 461839.
127. Q. Ma, Y. Zhang, J. Zhai, X. Chen, Z. Du, W. Li and H. Bai, *Anal. Bioanal. Chem.*, 2019, **411**, 2759-2765.
128. S. D. Hanton, *Chem. Rev.*, 2001, **101**, 527-569.
129. S. Koster, M. C. Duursma, J. J. Boon and R. M. Heeren, *J. Am. Soc. Mass Spectrom.*, 2000, **11**, 536-543.
130. P. Perez Hurtado, P. Y. Lam, D. Kilgour, A. Bristow, E. McBride and P. B. O'Connor, *Anal. Chem.*, 2012, **84**, 8579-8586.
131. T. N. J. Fouquet, *J. Mass Spectrom.*, 2019, **54**, 933-947.
132. F. G. Hoogland and J. J. Boon, *Int. J. Mass Spectrom.*, 2009, **284**, 66-71.
133. F. O. Ayorinde, S. V. Gelain, J. H. Johnson and L. W. Wan, *Rapid Commun. Mass Spectrom.*, 2000, **14**, 2116-2124.
134. W. Schrader and H. W. Klein, *Anal. Bioanal. Chem.*, 2004, **379**, 1013-1024.

135. L. Charles, C. Chendo and S. Poyer, *Rapid Commun. Mass Spectrom.*, 2020, **34**, 1-23.
136. J. R. Snelling, C. A. Scarff and J. H. Scrivens, *Anal. Chim.*, 2012, **84**, 6521-6529.
137. N. S. Erdem, N. Alawani and C. Wesdemiotis, *Anal. Chim. Acta*, 2014, **808**, 83-93.
138. Q. Zhang, A. Wang, Y. Meng, T. Ning, H. Yang, L. Ding, X. Xiao and X. Li, *Anal. Chim.*, 2015, **87**, 9810-9816.
139. G. K. Webster and M. A. Gragg, *Anal Methods-Uk*, 2019, **11**, 3314-3323.
140. B. Trathnigg, S. Feichtenhofer and M. Kollroser, *J. Chromatogr. A*, 1997, **786**, 75-84.
141. L. Prokai and W. J. Simonsick, *Rapid Commun. Mass Spectrom.*, 1993, **7**, 853-856.
142. K. K. Lee, Y. Z. Sahin, R. Neeleman, B. L. Trout and V. Kayser, *Hum. Vaccines Immunother.*, 2016, **12**, 1757-1765.
143. T. Gruendling, M. Guilhaus and C. Barner-Kowollik, *Anal. Chem.*, 2008, **80**, 6915-6927.
144. S. F. Wong, C. K. Meng and J. B. Fenn, *J. Phys. Chem.*, 2002, **92**, 546-550.
145. B. B. Reinhold and V. N. Reinhold, *J. Am. Soc. Mass Spectrom.*, 1992, **3**, 207-215.
146. S. M. Kay and S. L. Marple, *Proceedings of the IEEE*, 1981, **69**, 1380-1419.
147. *Maximum Entropy and Bayesian Methods*, Kluwer Academics, Santa Fe, New Mexico, U.S.A., Proceedings of the Fifteenth International Workshop on Maximum Entropy and Bayesian Methods, 1995.
148. P. C. Kooijman, S. Kok and M. Honing, *Rapid Commun. Mass Spectrom.*, 2017, **31**, 362-370.
149. J. Axelsson, E. Scrivener, D. M. Haddleton and P. J. Derrick, *Macromolecules*, 1996, **29**, 8875-8882.
150. M. Lichtenegger and M. Rychlik, *J. Chromatogr. B*, 2015, **1001**, 182-190.
151. H. Chen and M. He, *J. Am. Soc. Mass Spectrom.*, 2005, **16**, 100-106.
152. R. Szyszka, S. D. Hanton, D. Henning and K. G. Owens, *J. Am. Soc. Mass Spectrom.*, 2011, **22**, 633-640.
153. Z. Walterova and J. Horsky, *Anal. Chim. Acta*, 2011, **693**, 82-88.
154. C. M. Guttman, K. M. Flynn, W. E. Wallace and A. J. Kearsley, *Macromol.*, 2009, **42**, 1695-1702.
155. K. Takahashi, S. Matsuyama, T. Saito, H. Kato, S. Kinugasa, T. Yarita, T. Maeda, H. Kitazawa and M. Bounoshita, *J. Chromatogr. A*, 2008, **1193**, 146-150.
156. J. Gong, X. Gu, W. E. Achanzar, K. D. Chadwick, J. Gan, B. J. Brock, N. S. Kishnani, W. G. Humphreys and R. A. Iyer, *Anal. Chem.*, 2014, **86**, 7642-7649.
157. H. Sun, Q. Zhang, Z. Zhang, J. Tong, D. Chu and J. Gu, *J. Pharm. Biomed. Anal.*, 2017, **145**, 255-261.
158. D. Lingaityte, PhD thesis, University of Southampton, 2020.
159. R. Cole, *Electrospray ionization mass spectrometry: fundamentals, instrumentation, and applications*, Wiley-Blackwell, 1997.
160. R. Erb and H. Oberacher, *Electrophoresis*, 2014, **35**, 1226-1235.
161. D. C. Muddiman, X. Cheng, H. R. Udseth and R. D. Smith, *J. Am. Soc. Mass Spectrom.*, 1996, **7**, 697-706.
162. X. Cheng, D. C. Gale, H. R. Udseth and R. D. Smith, *Anal. Chem.*, 1995, **67**, 586-593.
163. E. S. Park, W. E. Wallace, C. M. Guttman, K. M. Flynn, M. C. Richardson and G. A. Holmes, *J. Am. Soc. Mass Spectrom.*, 2009, **20**, 1638-1644.
164. H. Zhu, T. Yalcin and L. Li, *J. Am. Soc. Mass Spectrom.*, 1998, **9**, 275-281.
165. A. Premstaller, K. H. Ongania and C. G. Huber, *Rapid Commun. Mass Spectrom.*, 2001, **15**, 1045-1052.
166. A. Premstaller and C. G. Huber, *Rapid Commun. Mass Spectrom.*, 2001, **15**, 1053-1060.
167. A. Biwer, G. Antranikian and E. Heinzle, *Appl. Microbiol. Biotechnol.*, 2002, **59**, 609-617.
168. S. Kobayashi, *Cyclodextrin producing enzyme (CGTase)*, Elsevier, 1996.
169. J. Szejtli, *Chem. Rev.*, 1998, **98**, 1743-1754.
170. A. Garcia, J. Priotti, A. V. Codina, M. D. Vasconi, A. D. Quiroga, L. I. Hinrichsen, D. Leonardi and M. C. Lamas, *Drug Delivery Transl. Res.*, 2019, **9**, 273-283.

171. P. Jansook, N. Ogawa and T. Loftsson, *Int. J. Pharm.*, 2018, **535**, 272-284.
172. A. Garcia, D. Leonardi, M. O. Salazar and M. C. Lamas, *PLoS One*, 2014, **9**, 1-8.
173. H. J. Schneider, F. Hacket, V. Rudiger and H. Ikeda, *Chem. Rev.*, 1998, **98**, 1755-1786.
174. D. O. Thompson, *Crit. Rev. Ther. Drug Carrier Syst.*, 1997, **14**, 1-104.
175. S. H. Khalid, M. Bashir, S. Asghar, T. H. Mallhi and I. U. Khan, *Colloid Sci. Pharm. Nanotechnol.*, 2019, DOI: 10.5772/intechopen.90364.
176. A. Garcia, D. Leonardi and M. C. Lamas, *Bioorg. Med. Chem. Lett.*, 2016, **26**, 602-608.
177. *Europe Pat.,* 0149197, 1983.
178. *US Pat.,* 4,727,064, 1984.
179. Cyclodextrin News Database, www.cyclodextrin.net, (accessed July 2022).
180. E. M. Agency, Background Review for Cyclodextrins Used as Excipients, http://www.ema.europa.eu/docs/en_GB/document_library/Report/2014/12/WC500177936.pdf, July 2022).
181. L. Kritharides, M. Kus, A. J. Brown, W. Jessup and R. T. Dean, *J. Biol. Chem.*, 1996, **271**, 27450-27455.
182. T. Irie, K. Fukunaga, M. K. Garwood, T. O. Carpenter, J. Pitha and J. Pitha, *J. Pharm. Sci.*, 1992, **81**, 524-528.
183. D. R. Graham, E. Chertova, J. M. Hilburn, L. O. Arthur and J. E. Hildreth, *J. Virol.*, 2003, **77**, 8237-8248.
184. S. Barman and D. P. Nayak, *J. Virol.*, 2007, **81**, 12169-12178.
185. G. Senti, R. Iannaccone, N. Graf, M. Felder, F. Tay and T. Kundig, *Dermatology*, 2013, **226**, 247-252.
186. A. A. Wolf, Y. Fujinaga and W. I. Lencer, *J. Biol. Chem.*, 2002, **277**, 16249-16256.
187. M. Yokoo, Y. Kubota, K. Motoyama, T. Higashi, M. Taniyoshi, H. Tokumaru, R. Nishiyama, Y. Tabe, S. Mochinaga, A. Sato, N. Sueoka-Aragane, E. Sueoka, H. Arima, T. Irie and S. Kimura, *PLoS One*, 2015, **10**, 1-20.
188. J. Pitha, J. Milecki, H. Fales, L. Pannell and K. Uekama, *Int. J. Pharm.*, 1986, **29**, 73-82.
189. M. Malanga, J. Szeman, E. Fenyvesi, I. Puskas, K. Csabai, G. Gyemant, F. Fenyvesi and L. Szente, *J. Pharm. Sci.*, 2016, **105**, 2921-2931.
190. C. Trinadha Rao, J. Pitha, B. Lindberg and J. Lindberg, *Carbohydr. Res.*, 1992, **223**, 99-107.
191. C. Novák, G. Pokol, J. Sztatisz, L. Szente and J. Szejtli, *Anal. Chim. Acta*, 1993, **282**, 313-316.
192. O. Reer and B. W. Muller, *Int. J. Pharm.*, 1994, **104**, 239-246.
193. C. Yuan, B. Liu and H. Liu, *Carbohydr. Polym.*, 2015, **118**, 36-40.
194. J. Szemán, R. Kedei, S. Gergely, I. Kolbe, L. Szente and A. Salgó, Torino, 2006.
195. Y. M. Zhang, F. Bao, Z. F. Zhang and Q. Zhou, *Fenxi Huaxue*, 2007, **35**, 1055-1058.
196. M. Agueros, M. A. Campanero and J. M. Irache, *J. Pharm. Biomed. Anal.*, 2005, **39**, 495-502.
197. N. Rabearimonjy, S. Ounnar, M. Righezza and M. Dreux, Dordrecht, 1998.
198. H. Jiang, R. Sidhu, H. Fujiwara, M. De Meulder, R. de Vries, Y. Gong, M. Kao, F. D. Porter, N. M. Yanjanin, N. Carillo-Carasco, X. Xu, E. Ottinger, M. Woolery, D. S. Ory and X. Jiang, *J. Lipid Res.*, 2014, **55**, 1537-1548.
199. T. A. Maryutina, E. Y. Savonina, P. S. Fedotov, R. M. Smith, H. Siren and D. B. Hibbert, *Pure Appl. Chem.*, 2018, **90**, 181-231.
200. L. M. Polo-Diez, *Fundamentos de cromatografia*, Dextra, 2015.
201. M. W. Dong, *HPLC and UHPLC for Practicing Scientists*, John Willey & Sons, 2019.
202. J. J. van Deemter, F. J. Zuiderweg and A. Klinkenberg, *Chem. Eng. Sci.*, 1956, **5**, 271-289.
203. A. T. James and A. J. Martin, *Biochem. J.*, 1952, **52**, 238-242.
204. K. Klesper, *J. Org. Chem.*, 1962, **27**, 700-701.
205. R. L. Synge, *Biochem. J.*, 1950, **2**, 41-42.
206. R. M. Wheaton and W. C. Bauman, *Ann. N. Y. Acad. Sci.*, 1953, **57**, 159-176.

207. L. S. Ettre, M.S. Tswett and the invention of chromatography, http://www.chromatographyonline.com/centenary-chromatography?id=&pageID=1&sk=&date=, (accessed May 2020).
208. H. H. Strain and J. Sherma, *J. Chem. Educ.*, 1967, **44**, 238.
209. A. T. James and A. J. Martin, *Br. Med. Bull.*, 1954, **10**, 170-176.
210. G. A. Howard and A. J. Martin, *Biochem. J.*, 1950, **46**, 532-538.
211. A. J. Alpert, *J. Chromatogr. A*, 1990, **499**, 177-196.
212. H. P. Jennissen and L. M. Heilmeyer, Jr., *Biochemistry*, 1975, **14**, 754-760.
213. C. A. Lucy, *J. Chrom. A*, 2003, **1000**, 711-724.
214. J. C. Whitehorn, *J. Biol. Chem.*, 1923, **56**, 751-764.
215. A. J. Martin and R. L. Synge, *Biochem. J.*, 1941, **35**, 1358-1368.
216. A. P. McKeown, A Simple, Generally Applicable HILIC Method Development Platform Based Upon Selectivity, https://www.chromatographytoday.com/article/hplc-uhplc/31/advanced-chromatography-technologies/a-simple-generally-applicable-hilic-method-development-platform-based-upon-selectivity/1958, (accessed (accessed June 2022).
217. R. D. Mountain, *J. Phys. Chem. B*, 2010, **114**, 16460-16464.
218. Z. L. Nikolov and P. J. Reilly, *J. Chromatogr.*, 1985, **325**, 287-293.
219. P. Hemström and K. Irgum, *J. Sep. Sci.*, 2006, **29**, 1784-1821.
220. Z. Hao, B. Xiao and N. Weng, *J. Sep. Sci.*, 2008, **31**, 1449-1464.
221. C. West, *Anal. Bioanal. Chem.*, 2018, **410**, 6441-6457.
222. M. Saito, *J. Biosci. Bioeng.*, 2013, **115**, 590-599.
223. S. Sie, W. Van Beersum and G. Rijnders, *Sep. Sci.*, 1966, **1**, 459-490.
224. J. C. Giddings, M. N. Myers and J. W. King, *J. Chromatogr. Sci.*, 1969, **7**, 276-283.
225. R. Jentoft and T. Gouw, *J. Chromatogr. Sci.*, 1970, **8**, 138-142.
226. H. B. Patel and T. M. Jefferies, *J. Chromatogr.*, 1987, **389**, 21-32.
227. S. R. Springston and M. Novotny, *Chromatographia*, 1981, **14**, 679-684.
228. D. R. Gere, R. Board and D. McManigill, *Anal. Chem.*, 1982, **54**, 736-740.
229. L. T. Taylor, *J. Supercrit. Fluids*, 2009, **47**, 566-573.
230. L. Novakova, A. G. Perrenoud, I. Francois, C. West, E. Lesellier and D. Guillarme, *Anal. Chim. Acta*, 2014, **824**, 18-35.
231. M. Saito, Y. Yamauchi, H. Kashiwazaki and M. Sugawara, *Chromatographia*, 1988, **25**, 801-805.
232. E. Ibanez and F. J. Senorans, *J. Biochem. Biophys. Methods*, 2000, **43**, 25-43.
233. T. A. Berger, Supercritical Fluid Chromatography Primer, Agilent Technologies, https://www.agilent.com/cs/library/primers/public/5991-5509EN.pdf, (accessed (accessed June 2022).
234. C. F. Poole, *J. Biochem. Biophys. Methods*, 2000, **43**, 3-23.
235. J. M. Levy and W. M. Ritchey, *J. Chromatogr. Sci.*, 1986, **24**, 242-248.
236. T. A. Berger, *J. Chromatogr. A*, 1997, **785**, 3-33.
237. M. Ashraf-Khorassani, M. G. Fessahaie, L. T. Taylor, T. A. Berger and J. F. Deye, *J. High Resolut. Chromatogr. Chromatogr. Commun.*, 1988, **11**, 352-353.
238. T. A. Berger and J. F. Deye, *J. Chromatogr.*, 1991, **547**, 377-392.
239. A. Giorgetti, N. Pericles, H. M. Widmer, K. Anton and P. Datwyler, *J. Chromatogr. Sci.*, 1989, **27**, 318-324.
240. K. N. West, C. Wheeler, J. P. McCarney, K. N. Griffith, D. Bush, C. L. Liotta and C. A. Eckert, *J. Phys. Chem. A*, 2001, **105**, 3947-3948.
241. C. West and E. Lemasson, *J. Chromatogr. A*, 2019, **1593**, 135-146.
242. J. Liu, E. L. Regalado, I. Mergelsberg and C. J. Welch, *Org. Biomol. Chem.*, 2013, **11**, 4925-4929.
243. L. T. Taylor, *J. Chromatogr. A*, 2012, **1250**, 196-204.

244. M. O. Kostenko and O. I. Pokrovskiy, *J. Chromatogr. A*, 2019, **1586**, 154-158.
245. A. Grand-Guillaume Perrenoud, J. Boccard, J. L. Veuthey and D. Guillarme, *J. Chromatogr. A*, 2012, **1262**, 205-213.
246. J. Zheng, L. T. Taylor, J. D. Pinkston and M. L. Mangels, *J. Chromatogr. A*, 2005, **1082**, 220-229.
247. J. Zheng, T. Glass, L. T. Taylor and J. D. Pinkston, *J. Chromatogr. A*, 2005, **1090**, 155-164.
248. J. Zheng, L. T. Taylor and J. D. Pinkston, *Chromatographia*, 2006, **63**, 267-276.
249. A. Cazenave-Gassiot, R. Boughtflower, J. Caldwell, L. Hitzel, C. Holyoak, S. Lane, P. Oakley, F. Pullen, S. Richardson and G. J. Langley, *J. Chromatogr. A*, 2009, **1216**, 6441-6450.
250. B. Kucerova, L. Krcmova, D. Solichova, J. Plisek and P. Solich, *J. Sep. Sci.*, 2013, **36**, 2223-2230.
251. M. Díaz-Bao, R. Barreiro, J. Miranda, A. Cepeda and P. Regal, *Chromatography*, 2015, **2**, 79-95.
252. *US Pat.,* 6,686,035, 2001.
253. P. C. Iraneta, K. D. Wyndham, D. R. McCabe and T. H. Walter, A review of Waters Hybrid Particle Technology. Part 3. Charged Surface Hybrid (CSH) Technology and Its Use in Liquid Chromatography, https://www.waters.com/webassets/cms/library/docs/720003929en.pdf, (accessed July 2022).
254. W. Stöber, A. Fink and E. Bohn, *J. Colloid Interface Sci.*, 1968, **26**, 62-69.
255. R. Hayes, A. Ahmed, T. Edge and H. Zhang, *J. Chromatogr. A*, 2014, **1357**, 36-52.
256. G. Guiochon and F. Gritti, *J. Chromatogr. A*, 2011, **1218**, 1915-1938.
257. V. R. J. Acquaro, F. M. Lancas and M. E. Queiroz, *J. Chromatogr. B*, 2017, **1048**, 1-9.
258. K. Nagai, T. Shibata, S. Shinkura and A. Ohnishi, *J. Chromatogr. A*, 2018, **1572**, 119-127.
259. E. Lesellier and C. West, *J. Chromatogr. A*, 2015, **1382**, 2-46.
260. C. West and E. Lesellier, *J. Chromatogr. A*, 2006, **1110**, 200-213.
261. C. West, L. Fougere and E. Lesellier, *J. Chromatogr. A*, 2008, **1189**, 227-244.
262. C. West, E. Lemasson, K. Nagai, T. Shibata, P. Franco, S. Bertin, P. Hennig and E. Lesellier, *Chromatographia*, 2018, **82**, 143-152.
263. Y. Okamoto, M. Kawashima, K. Yamamoto and K. Hatada, *Chem Lett*, 1984, **13**, 739-742.
264. Y. Okamoto, M. Kawashima and K. Hatada, *J. Am. Chem. Soc.*, 2002, **106**, 5357-5359.
265. Y. Okamoto and T. Ikai, *Chem. Soc. Rev.*, 2008, **37**, 2593-2608.
266. T. Ikai, C. Yamamoto, M. Kamigaito and Y. Okamoto, *J. Chromatogr. B*, 2008, **875**, 2-11.
267. G. Felix, *J. Chromatogr. A*, 2001, **906**, 171-184.
268. W. A. Etzel, W. Gau, W. Kramer, U. Stelzer and J. Weissmuller, *Magn Reson Chem*, 1998, **36**, 64-68.
269. G. K. E. Scriba, *Trends Anal. Chem.*, 2019, **120**, 115639.
270. P. Franco, A. Senso, L. Oliveros and C. Minguillon, *J. Chromatogr. A*, 2001, **906**, 155-170.
271. G. Subramanian, *Chiral Separation Techniques: A Practical Approach*, Wiley, 2006.
272. G. Gübitz and M. G. Schmid, *Chiral Separations: Methods and Protocols*, Humana Press, 2004.
273. V. Desfontaine, A. Tarafder, J. Hill, J. Fairchild, A. G.-G. Perrenoud, J. L. Veuthey and D. Guillarme, *J. Chromatogr. A*, 2017, **1511**, 122-131.
274. V. Abrahamsson and M. Sandahl, *J. Chromatogr. A*, 2013, **1306**, 80-88.
275. P. Vajda and G. Guiochon, *J. Chromatogr. A*, 2014, **1333**, 116-123.
276. A. Tarafder, K. Kaczmarski, M. Ranger, D. P. Poe and G. Guiochon, *J. Chromatogr. A*, 2012, **1238**, 132-145.
277. B. E. Richter, D. J. Bornhop, J. T. Swanson, J. G. Wangsgaard and M. R. Andersen, *J. Chromatogr. Sci.*, 1989, **27**, 303-308.
278. H. Liu, G. Raffin, G. Trutt and J. Randon, *J. Chromatogr. A*, 2017, **1530**, 171-175.

279. M. Noll-Borchers, T. Hölscher, E. Naegele and M. Becker, Determination of Aromatic Content in Diesel Fuel According to ASTM D5186, 5991-5682EN https://sim-gmbh.de/images/PDF_Dokumente_neu/ASTM_D5186_App_Note_Aromatics.pdf, July 2022).
280. M. Noll-Borchers, T. Hölscher, E. Naegele and M. Becker, Determination of Olefin Content in Denatured Ethanol According to ASTM D7347, 5991-7271EN, https://www.agilent.com/cs/library/applications/5991-7271EN.pdf, (accessed July 2022).
281. M. Noll-Borchers, T. Hölscher, E. Naegele and M. Becker, Determination of Olefin Content in Gasoline According to ASTM D6550, 5991-6434EN, https://sim-gmbh.de/images/PDF_Dokumente_neu/ASTM_D6550__App_Note_Olefins.pdf, (accessed July 2022).
282. M. Swartz, *J. Liq. Chromatogr. Relat. Technol.*, 2010, **33**, 1130-1150.
283. K. G. Kraiczek, R. Bonjour, Y. Salvade and R. Zengerle, *Anal. Chem.*, 2014, **86**, 1146-1152.
284. L. M. Miller, J. D. Pinkston and L. T. Taylor, *Modern Supercritical Fluid Chromatography: Carbon Dioxide Containing Mobile Phases*, Wiley, 2019.
285. T. A. Berger and B. K. Berger, *J. Chromatogr. A*, 2011, **1218**, 2320-2326.
286. M. Dreux and M. Lafosse, *LC GC International*, 1997, **10**, 382–390.
287. E. Lesellier, A. Valarche, C. West and M. Dreux, *J. Chromatogr. A*, 2012, **1250**, 220-226.
288. N. C. Megoulas and M. A. Koupparis, *Crit. Rev. Anal. Chem.*, 2005, **35**, 301-316.
289. M. Laffose, in *Practical supercritical fluid chromatography and extractions*, ed. T. Caudell, Harwood academic publishers, 1999.
290. V. Camel, D. Thiebaut, M. Caude and M. Dreux, *J. Chromatogr. A.*, 1992, **605**, 95-101.
291. X. D. Bu, E. L. Regalado, J. Cuff, W. Schafer and X. Y. Gong, *J. Supercrit. Fluids*, 2016, **116**, 20-25.
292. T. Gorecki, F. Lynen, R. Szucs and P. Sandra, *Anal. Chem.*, 2006, **78**, 3186-3192.
293. J. Prothmann, M. Sun, P. Spegel, M. Sandahl and C. Turner, *Anal. Bioanal. Chem.*, 2017, **409**, 7049-7061.
294. B. Bolaños, M. Greig, M. Ventura, W. Farrell, C. M. Aurigemma, H. Li, T. L. Quenzer, K. Tivel, J. M. R. Bylund, P. Tran, C. Pham and D. Phillipson, *Int. J. Mass Spectrom.*, 2004, **238**, 85-97.
295. J. D. Pinkston, *Eur. J. Mass. Spectrom.*, 2005, **11**, 189-197.
296. R. W. Dixon and D. S. Peterson, *Anal. Chem.*, 2002, **74**, 2930-2937.
297. R. D. Cohen and Y. Liu, in *Advances in chromatography*, eds. E. Grushka and N. Grinberg, CRC Press, 2014, vol. 52.
298. T. H. Mourey and L. E. Oppenheimer, *Anal. Chem.*, 1984, **56**, 2427-2434.
299. J. M. Charlesworth, *Anal. Chem.*, 1978, **50**, 1414-1420.
300. A. Kuch and R. Saari-Nordhaus, *Am. Lab.*, 2001, **33**, 61.
301. C. R. Mitchell, Y. Bao, N. J. Benz and S. Zhang, *J. Chromatogr. B*, 2009, **877**, 4133-4139.
302. M. Lafosse, C. Elfakir, L. Morinallory and M. Dreux, *J. High Resolut. Chromatogr.*, 1992, **15**, 312-318.
303. J. T. B. Strode and L. T. Taylor, *J. Chromatogr. Sci.*, 1996, **34**, 261-271.
304. J. H. Arndt, T. Macko and R. Brull, *J. Chromatogr. A*, 2013, **1310**, 1-14.
305. T. Vehovec and A. Obreza, *J. Chromatogr. A*, 2010, **1217**, 1549-1556.
306. J. P. Hutchinson, G. W. Dicinoski and P. R. Haddad, in *Charged Aerosol Detection for Liquid Chromatography and Related Separation Techniques*, ed. P. H. Gamache, John Wiley & Sons, 2017, ch. 4.
307. P. H. Gamache, R. S. Mccarthy, S. M. Freeto, D. J. Asa, M. J. Woodcock, K. Laws and R. O. Cole, *LC GC North America*, 2005, **23**, 150-161.
308. S. Almeling, D. Ilko and U. Holzgrabe, *J. Pharm. Biomed. Anal.*, 2012, **69**, 50-63.
309. K. K. Murray, R. K. Boyd, M. N. Eberlin, G. J. Langley, L. Li and Y. Naito, *Pure Appl. Chem.*, 2013, **85**, 1515-1609.

310. J. B. Fenn, M. Mann, C. K. Meng, S. F. Wong and C. M. Whitehouse, *Science*, 1989, **246**, 64-71.
311. M. Yamashita and J. B. Fenn, *J. Phys. Chem.*, 2002, **88**, 4451-4459.
312. J. B. Fenn, M. Mann, C. K. Meng, S. F. Wong and C. M. Whitehouse, *Mass Spectrom. Rev.*, 1990, **9**, 37-70.
313. J. F. De la Mora and I. G. Loscertales, *J. Fluid Mech.*, 1994, **260**, 155-184.
314. M. S. Wilm and M. Mann, *Int. J. Mass Spectrom. Ion Processes*, 1994, **136**, 167-180.
315. J. F. Mora, G. J. Van Berkel, C. G. Enke, R. B. Cole, M. Martinez-Sanchez and J. B. Fenn, *J. Mass Spectrom.*, 2000, **35**, 939-952.
316. E. Janusson, A. V. Hesketh, K. L. Bamford, K. Hatlelid, R. Higgins and J. S. McIndoe, *Int. J. Mass Spectrom.*, 2015, **388**, 1-8.
317. J. V. Iribarne and B. A. Thomson, *J. Chem. Phys.*, 1976, **64**, 2287-2294.
318. M. Dole, L. L. Mack, R. L. Hines, R. C. Mobley, L. D. Ferguson and M. B. Alice, *J. Chem. Phys.*, 1968, **49**, 2240-2249.
319. L. Konermann, E. Ahadi, A. D. Rodriguez and S. Vahidi, *Anal. Chem.*, 2013, **85**, 2-9.
320. E. Ahadi and L. Konermann, *J. Am. Chem. Soc.*, 2011, **133**, 9354-9363.
321. N. B. Cech and C. G. Enke, *Mass Spectrom. Rev.*, 2001, **20**, 362-387.
322. M. Mann, C. K. Meng and J. B. Fenn, *Anal. Chem.*, 1989, **61**, 1702-1708.
323. T. M. Annesley, *Clin. Chem.*, 2003, **49**, 1041-1044.
324. H. Awad, M. M. Khamis and A. El-Aneed, *Appl. Spectrosc. Rev.*, 2014, **50**, 158-175.
325. S. Bajic, Waters UniSpray Ionization Source, https://www.waters.com/waters/library.htm?cid=134891755&lid=134939768&locale=en_US, (accessed April 2020).
326. O. Ciclet, D. Barron, S. Bajic, J. L. Veuthey, D. Guillarme and A. G.-G. Perrenoud, *J. Chromatogr. B*, 2018, **1083**, 1-11.
327. A. Raffaelli and A. Saba, *Mass Spectrom. Rev.*, 2003, **22**, 318-331.
328. P. Terrier, B. Desmazieres, J. Tortajada and W. Buchmann, *Mass Spectrom. Rev.*, 2011, **30**, 854-874.
329. E. Horning, D. Carroll, I. Dzidic, K. Haegele, M. Horning and R. Stillwell, *J. Chromatogr. A*, 1974, **99**, 13-21.
330. D. B. Robb, T. R. Covey and A. P. Bruins, *Anal. Chem.*, 2000, **72**, 3653-3659.
331. D. B. Robb and M. W. Blades, *J. Am. Soc. Mass Spectrom.*, 2005, **16**, 1275-1290.
332. D. B. Robb and M. W. Blades, *J. Am. Soc. Mass Spectrom.*, 2006, **17**, 130-138.
333. J. Drzeżdżon, D. Jacewicz, A. Sielicka and L. Chmurzyński, *Trends Anal. Chem.*, 2019, **115**, 121-128.
334. P. B. O'Connor and F. Hillenkamp, in *MALDI MS: A Practical Guide to Instrumentation, Methods and Applications*, eds. F. Hillenkamp and J. Peter-Katalinić, 2007, ch. 2.
335. C. Menzel, K. Dreisewerd, S. Berkenkamp and F. Hillenkamp, *J. Am. Soc. Mass Spectrom.*, 2002, **13**, 975-984.
336. J. Soltwisch and K. Dreisewerd, *Rapid Commun. Mass Spectrom.*, 2011, **25**, 1266-1270.
337. E. de Hoffmann, *J. Mass Spectrom.*, 1996, **31**, 129-137.
338. W. Paul and H. Steinwedel, *Zeitschrift fuer Naturforschung divided into Inorg. Chem., Org. Chem., Biochem., Biophys.*, 1953, **8**.
339. P. E. Miller and M. B. Denton, *J. Chem. Educ.*, 1986, **63**, 617-622.
340. J. H. Batey, *Vacuum*, 2014, **101**, 410-415.
341. B. A. Thomson, D. J. Douglas, J. J. Corr, J. W. Hager and C. L. Jolliffe, *Anal. Chem.*, 1995, **67**, 1696-1704.
342. A. C. C. Voo, R. Ng, J. J. Tunstall and S. Taylor, *J Vac Sci Technol A*, 1997, **15**, 2276-2281.
343. M. Zeller and S. Konig, *Anal. Bioanal. Chem.*, 2004, **378**, 898-909.
344. B. A. Mamyrin, V. I. Karataev, D. V. Shmikk and V. A. Zagulin, *Zhurnal Ehksperimental'noj i Teoreticheskoj Fiziki*, 1973, **64**, 82-89.

345. S. G. Alikhanov, *Sov. Phys. JETP-USSR*, 1957, **4**, 452-453.
346. W. C. Wiley and I. H. McLaren, *Rev. Sci. Instrum.*, 1955, **26**, 1150-1157.
347. B. A. Mamyrin, V. I. Karataev, D. V. Shmikk and V. A. Zagulin, *Sov. J. Exp. Theor. Phys.*, 1973, **64**, 82–89.
348. J. A. Rodrigues, A. M. Taylor, D. P. Sumpton, J. C. Reynolds, R. Pickford and J. Thomas-Oates, *Adv Carbohydr Chem Biochem*, 2007, **61**, 59-141.
349. N. Mirsaleh-Kohan, W. D. Robertson and R. N. Compton, *Mass Spectrom Rev*, 2008, **27**, 237-285.
350. C. J. Brais, J. O. Ibanez, A. J. Schwartz and S. J. Ray, *Mass Spectrom Rev*, 2021, **40**, 647-669.
351. J. T. Watson and O. D. Sparkman, *Introduction to Mass Spectrometry: Instrumentation, Applications and Strategies for Data Interpretation*, John Wiley & Sons, 2007.
352. J. Franzen, *Int. J. Mass Spectrom. Ion Processes*, 1997, **164**, 19-34.
353. E. W. McDaniel, D. W. Martin and W. S. Barnes, *Rev. Sci. Instrum.*, 1962, **33**, 2-7.
354. J. C. May, C. B. Morris and J. A. McLean, *Anal. Chem.*, 2017, **89**, 1032-1044.
355. A. B. Kanu, P. Dwivedi, M. Tam, L. Matz and H. H. Hill, Jr., *J. Mass Spectrom.*, 2008, **43**, 1-22.
356. C. J. Gray, B. Thomas, R. Upton, L. G. Migas, C. E. Eyers, P. E. Barran and S. L. Flitsch, *Biochim. Biophys. Acta*, 2016, **1860**, 1688-1709.
357. C. Bleiholder, N. R. Johnson, S. Contreras, T. Wyttenbach and M. T. Bowers, *Anal. Chem.*, 2015, **87**, 7196-7203.
358. T. M. Allison, M. Landreh, J. L. P. Benesch and C. V. Robinson, *Anal. Chem.*, 2016, **88**, 5879-5884.
359. K. Giles, J. P. Williams and I. Campuzano, *Rapid Commun. Mass Spectrom.*, 2011, **25**, 1559-1566.
360. B. T. Ruotolo, J. L. Benesch, A. M. Sandercock, S. J. Hyung and C. V. Robinson, *Nat. Protoc.*, 2008, **3**, 1139-1152.
361. C. A. Scarff, K. Thalassinos, G. R. Hilton and J. H. Scrivens, *Rapid Commun. Mass Spectrom.*, 2008, **22**, 3297-3304.
362. D. P. Smith, T. W. Knapman, I. Campuzano, R. W. Malham, J. T. Berryman, S. E. Radford and A. E. Ashcroft, *Eur. J. Mass Spectrom.*, 2009, **15**, 113-130.
363. K. Thalassinos, M. Grabenauer, S. E. Slade, G. R. Hilton, M. T. Bowers and J. H. Scrivens, *Anal. Chem.*, 2009, **81**, 248-254.
364. J. Gidden, T. Wyttenbach, A. T. Jackson, J. H. Scrivens and M. T. Bowers, *J. Am. Chem. Soc.*, 2000, **122**, 4692-4699.
365. A. N. Swinburne and J. W. Steed, *Supramol. Chem.: Mol. Nanomater.*, 2012.
366. M. J. Bogan and G. R. Agnes, *J. Am. Soc. Mass Spectrom.*, 2002, **13**, 177-186.
367. T. Pluskal, S. Castillo, A. Villar-Briones and M. Oresic, *BMC Bioinf.*, 2010, **11**, 395.
368. E. M. J. Wilmot, PhD thesis, University of Southampton, 2017.
369. T. R. Covey, B. A. Thomson and B. B. Schneider, *Mass Spectrom. Rev.*, 2009, **28**, 870-897.
370. C. West, E. Lemasson, S. Bertin, P. Hennig and E. Lesellier, *J. Chromatogr. A*, 2016, **1440**, 212-228.
371. C. West and E. Lesellier, *J. Chromatogr. A*, 2008, **1203**, 105-113.
372. C. West and E. Lesellier, *J. Chromatogr. A*, 2008, **1191**, 21-39.
373. P. Liigand, K. Kaupmees, K. Haav, J. Liigand, I. Leito, M. Girod, R. Antoine and A. Kruve, *Anal. Chem.*, 2017, **89**, 5665-5668.
374. C. West, J. Melin, H. Ansouri and M. Mengue Metogo, *J. Chromatogr. A*, 2017, **1492**, 136-143.
375. A. T. Iavarone and E. R. Williams, *J. Am. Chem. Soc.*, 2003, **125**, 2319-2327.
376. V. Jannin, *OCL: Oilseeds Fats, Crops Lipids*, 2009, **16**, 267-272.
377. D. Ilko, A. Braun, O. Germershaus, L. Meinel and U. Holzgrabe, *Eur. J. Pharm. Biopharm.*, 2015, **94**, 569-574.

378. J. Hoisington and J. S. Herrington, *Separations*, 2021, **8**, 35.
379. A. Seidel, *Characterization and Analysis of Polymers*, 2008.
380. D. Jenke, *J. Liq. Chromatogr. Relat. Technol.*, 2003, **26**, 2417-2447.
381. K. Yamamoto, K. Machida, A. Kotani and H. Hakamata, *Chem. Pharm. Bull (Tokyo)*, 2021, **69**, 970-975.
382. R. K. Boyd, *Trace Quantitative Analysis by Mass Spectrometry*, 2008.
383. J. C. Cottrell, B. N. Green and S. A. Jarvis, Transform, Proceedings of the 39th Conference on Mass Spectrometry and Allied Topics, American Society for Mass Spectrometry, Nashville, TN, 1991.
384. S. Powley, PhD thesis Doctoral, University of Southampton, 2018.
385. M. T. Marty, A. J. Baldwin, E. G. Marklund, G. K. Hochberg, J. L. Benesch and C. V. Robinson, *Anal. Chem.*, 2015, **87**, 4370-4376.
386. J. S. Bradshaw and R. M. Izatt, *Acc. Chem. Res.*, 1997, **30**, 338-345.
387. V. Rüdiger, H.-J. Schneider, V. P. Solov'ev, V. P. Kazachenko and O. A. Raevsky, *Eur. J. Org. Chem.*, 1999, 1847-1856.
388. K. Wylon, S. Dolle and M. Worm, *Allergy, Asthma, Clin. Immunol.*, 2016, **12**, 67.
389. S. V. Olesik, *J. Chromatogr. A*, 2004, **1037**, 405-410.
390. L. Szente, A. Singhal, A. Domokos and B. Song, *Molecules*, 2018, **23**, 1228.
391. Q. Gros, J. Molineau, A. Noireau, J. Duval, T. Bamba, E. Lesellier and C. West, *J. Chromatogr. A*, 2021, **1639**, 461923.
392. D. O. Thompson, *Crit. Rev. Ther. Drug Carrier Syst.*, 1997, **14**, 1-104.
393. A. J. Barbier, A. Y. Jiang, P. Zhang, R. Wooster and D. G. Anderson, *Nat. Biotechnol.*, 2022, **40**, 840-854.